ЖУРНАЛ ФИЗИЧЕСКОЙ ХИМИИ

СОДЕРЖАНИЕ

Том 81, номер 9, 2007

METHODS AND TECHNIQUES
OF PHYSICOCHEMICAL INVESTIGATIONS

ХИМИЧЕСКАЯ КИНЕТИКА И КАТАЛИЗ

ФИЗИЧЕСКАЯ ХИМИЯ ПОВЕРХНОСТНЫХ ЯВЛЕНИЙ

Contents

METHODS AND TECHNIQUES
OF PHYSICOCHEMICAL INVESTIGATIONS

CHEMICAL KINETICS AND CATALYSIS

PHYSICAL CHEMISTRY OF SURFACE PHENOMENA

8ᵗʰ International Conference on Fundamental and Applied
══ Aspects of Physical Chemistry: PHYSICAL CHEMISTRY 2006 ══
(Belgrade, September. 26–29. 2006)

ПРЕДИСЛОВИЕ

Данный номер "Журнала физической химии" включает Материалы 8-й Международной конференции по фундаментальным и прикладным аспектам физической химии, которая проходила в Белграде с 26 по 29 сентября 2006 г. Такое представление материалов конференции – результат сотрудничества Общества физикохимиков Сербии и "Журнала физической химии". Идея сотрудничества возникла в ходе 7-й Международной конференции (сентябрь 2004 г.), была активно поддержана академиком РАН, директором Института катализа им. Борескова, членом редколлегии Журнала В.Н. Пармоном и академиком РАН, главным редактором Журнала В.В. Луниным. Материалы собраны и представлены к публикации группой сотрудников Белградского университета под руководством проф. Слободана Анича – основных организаторов данной конференции.

Конференции по фундаментальным и прикладным аспектам физической химии Общество физикохимиков Сербии организует раз в два года, начиная с 1992 г., в последние годы совместно с Институтом катализа СО РАН и Институтом катализа Болгарской академии наук. Проблематика конференций охватывает широкий спектр направлений современной физической химии, в их работе участвует большое число физикохимиков из различных стран мира (Япония, Китай, США, Франция, Бельгия и многие другие страны). Об уровне Конференций свидетельствует и то, что рефераты всех статей, опубликованных в Proceedings 4-й – 7-й Конференций, в полном объеме приведены в Chemical Abstracts.

На 8-й Конференции представлен широкий спектр работ по различным направлениям физической химии, в частности, по химической термодинамике, кинетике и катализу, спектроскопии и проблемам структуры молекул, биофизической и радиационной химии, физической химии конденсированных фаз и поверхности и т.д. Устные доклады были, в основном, посвящены проблемам кинетики и катализа, электрохимии, биофизической химии, радиационной химии и физико-химическим аспектам материаловедения. Работы секции кинетики и катализа включали проблемы определения и моделирования поверхностно-активных центров катализаторов, поиска новых катализаторов, динамики каталитических реакций в твердых телах.

Особо следует отметить большое число докладов, посвященных исследованиям нелинейной динамики конкретных химических реакций, колеба-

тельных процессов и хаоса в многомерных пространствах, осцилляторного переноса веществ через мембраны, влияния внешних условий на осуществление таких реакций, а также работ по анализу возможных практических приложений колебательных реакций. Работы в этом направлении активно развиваются в Белградском университете совместно с коллегами из Бельгии (Свободный университет Брюсселя). Сообщения по электрохимии носили в заметной степени прикладной характер, связанный, например, с созданием новых электродных материалов, материалов для батарей и топливных элементов, а также с электрохимическими методами определения различных веществ. Прикладная направленность характеризовала и большое число работ, представленных на секции материаловедения. Тем не менее, такая направленность проявлялась на фоне физико-химических аспектов исследования соответствующих веществ и материалов.

Работы по спектроскопии и структуре молекул в основной своей массе были связаны с изучением сравнительно больших органических и элементоорганических молекул. На конференции были представлены работы и по защите окружающей среды, точнее, по анализу поллютантов различными физико-химическими методами. К сожалению, секция физико-химического образования включала всего один стендовый доклад.

Следует отметить, что полный перечень материалов 8-й Конференции представлен в "Proceedings of the 8th International Conference on Fundamental and Applied Aspects of Physical Chemistry", volumes 1 and 2.

Организаторы конференций пользуются случаем сообщить всем работающим в области физической химии, что они могут представить свои результаты на следующей конференции, которая состоится в сентябре 2008 г., и надеются, что наиболее существенные из этих результатов могут быть в качестве оригинальных научных статей представлены в соответствующем номере "Журнала физической химии".

Председатель международного оргкомитета Конференции Слободан Анич

Председатель программного комитета Анкица Антич-Йованович

Вице-председатель локального оргкомитета Желько Чупич

Заместитель главного редактора "Журнала физической химии" Н.Ф. Степанов

CHEMICAL THERMODYNAMICS
AND THERMOCHEMISTRY

HIGH PRESSURE BEHAVIOUR OF CARBON BY LASER-GENERATED SHOCKS

© 2007   D. Batani*, H. Stabile*, F. Canova*, M. Koenig**, A. Benuzzi**,
H. Nishimura***, Y. Ochi***, J. Ullschmied****, J. Skala****,
B. Kralikova****, M. Pfeifer****, T. Mocek****, A. Präg****

*Dipartimento di Fisica "G. Occhialini", Universita degli Studi di Milano Bicocca and INFM, Piazza della Scienza 3,
20126 Milano, Italy
**Laboratoire pour l' Utilisation des Lasers Intenses, UMR 7605 CNRS-CEA-Ecole Polytechnique-Paris VI,
Palaiseau, France
***ILE, Osaka University, 2–6 Yamadaoka, Suita City, Osaka 565-0871, Japan
****PALS Research Centre, Za Slovankou 3, 18221 Prague 8, Czech Republic
E-mail: batani@mib.infn.it

Abstract – We present experimental data for carbon equation of state (EOS) at Megabar pressures, obtained by laser-driven shock waves. Experiments were performed at the PALS and LULI laboratories using carbon samples with two different values of initial density, in order to explore a wider region of the phase diagram. Previously unreached pressures were obtained. Results are compared with previous experiments and with available theoretical models and seem to show high compressibility of carbon at Megabar pressures.

INTRODUCTION

The equation of state (EOS) of carbon at high pressures (Megabar or Multimegabar regime) is of interest for several branches of physics, namely:

Material Science: carbon is a unique element due to its polymorphism and the complexity and variety of its state phases. The EOS of carbon has been the subject of several recent important experimental and theoretical scientific works [1–15]. The important phenomenon of carbon metallization at high pressure has long been predicted theoretically but until now never experimentally proved. At very high pressures the regime of non-ideal strongly-correlated and partially-degenerate plasmas is approached which is characterized by an almost complete absence of experimental data [15–18].

Astrophysics: description of high pressures phases is essential for developing realistic models of planets and stars [19, 20]. Carbon is a major constituent (through methane and carbon dioxide) of giant planets like Uranus and Neptune. High pressures are thought to produce methane pyrolysis with a separation of the carbon phase and possible formation of a diamond or metallic layer [21–23]. Metallization of the carbon layer in the mantle of these planets (the "ice" layers") could give high electrical conductivity and, by dynamo effect, be the source of the observed large magnetic fields [24, 25].

Concerning carbon metallization, the first theoretical estimates (Van Vechten [1]) set the triple point for the transition among diamond (α), liquid metal (βl), and solid metal (βs) at 1.7 Mbar and 3100 K, a prediction not in agreement with experimental results by Shaner and Brown [2] and Grover [3]. More recent

works set the metallic transition at much larger pressures: Yin and Cohen [4] predict a transition from diamond to a BC-8 semi-metallic phase $at \approx 11$ Mbar (and a second transition to a SC-4 metallic phase $at \approx 27$ Mbar). in fair agreement with the calculations by Biswas et al. [5] who put the upper limit of diamond stability $at \approx 12$ Mbar, and with the calculations by Fahy and Louie [6] (11.1 Mbar). Ruoff and Luo [7], working on experimental data on gap closure by Mao et al. [8], put the metallic transition $at \approx 8.4$ Mbar. Such pressures can be easily generated in the laboratory by using laser-driven shocks.

At higher temperatures, liquid phases are predicted, going from non-metallic at low pressures to semi-metallic and metallic as the pressure is increased. The first experimental evidence of a liquid metallic phase was given by Bundy [9]. Nowadays, the probably most accepted phase diagram of carbon by Grumbach and Martin [10] sets the structural changes in liquid carbon at pressures of 4 and 10 Mbar and suggests that laser driven shocks ($P = 2$–6 Mbar, $T > 20000$ K) should reach a liquid metallic phase. In Fig. 1 we have reported a simplified version of Grumbach and Martin's phase diagram to which we added the Hugoniot curves corresponding to the initial densities $\rho_0 = 1.6$ g/cm^3 and $\rho_0 = 1.45$ g/cm^3 (the two values used in our experiment). Again, the liquid metallic phases can be easily reached with laser shocks. These are indeed nowadays the only laboratory tool which can achieve pressures of a few tens Mbars [18].

In this paper, we present the first Hugoniot data for carbon obtained with laser-driven shocks. In recent years, it has been well established that laser-shocks are

a useful tool for high-pressure physics, to compress materials at Megabar pressures and measure their EOS [26, 27]. The goal of our experiment was to begin the exploration of carbon EOS in the pressure range 1–15 Mbar. We got the first experimental points at pressures higher than 8 Mbar. Moreover, we substantially increased the number of EOS data for carbon at pressures >1 Mbar (here we present 9 new EOS points against a total, of about 20 points which, to our knowledge, were available in literature [28–32]).

One general limitation of shock-wave EOS experiments is that only data on the Hugoniot curve of the material are obtained. This is due to the fact that shocks compress and heat the material at the same time, so pressure and temperature are no longer two independent variables. One way to overcome such limitation is to use a sample with reduced density ρ_0 (porous or foam target). This changes the initial conditions in the material so that data along *different* Hugoniot curves are obtained. Hence by changing ρ_0 the whole EOS plane can be explored. In particular, by reducing the initial density ρ_0 of the sample, the same shock pressure P will correspond to a higher temperature T (internal energy E) and a reduced final density ρ.

The experiment is based on generating high quality shocks and using "two steps–two materials" targets (Fig. 2). Relative EOS data of "unknown" materials (here C) are obtained by using a "well-known" reference (here Al). Al behavior at high pressure is well known, making it a typical reference material for shock experiments. The method is described in detail in [27].

Some laser shots were done at LULI where three laser beams at $\lambda = 0.53$ μm were focused at intensities of $\approx 5 \times 10^{13}$ W/cm². The pulse was Gaussian in time with a full width at half maximum (FWHM) of 600 ps. In order to increase laser energy (and shock pressure), other shots were done with the PALS iodine laser [33], with typical energy of 250 J per pulse at a wavelength of 0.44 μm, focused up to 2×10^{14} W/cm². The pulse was Gaussian with a FWHM of 450 ps. In both cases, large focal spots and Phase Zone Plates (PZP) [26] were used to get uniform laser illumination and avoid 2D effects in the propagation of the shock.

Two diagnostics systems (Fig. 2), based on streak cameras coupled to a photographic objectives and 12 bit CCD cameras, were used: a) rear-side time-resolved imaging (to record target self-emissivity), and, b) time resolved visible reflectometry (at LULI only). Both diagnostics allow the measurements of the shock breakout times from the base and steps of the "two steps – two materials" target (see Fig. 2). Hence we measured the shock velocity in Al and C simultaneously on the same laser shot. Details on the experimental set-up are reported in [34] for PALS, and in [26] for LULI (and for the reflectivity diagnostics in [35]). Time and spatial resolution of both diagnostics, in both laboratories, were typically of the order of 10 ps and 10 μm.
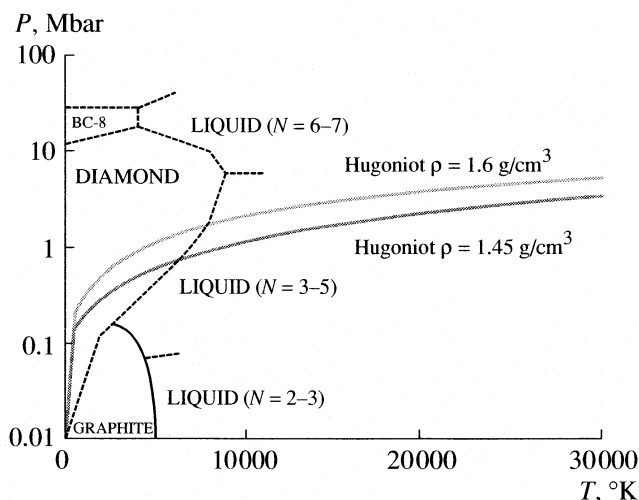
Fig. 1. Grumbach and Martin's phase diagram (after [12]) and the two Hugoniot curves corresponding to the initial densities $\rho_0 = 1.6$ g/cm³ and $\rho_0 = 1.45$ g/cm³.
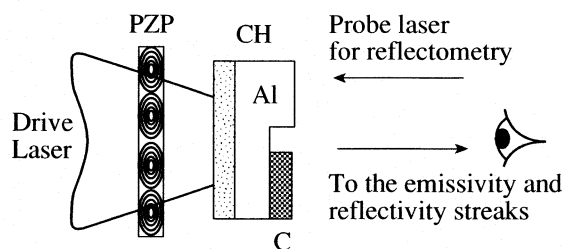
Fig. 2. Scheme of the experimental set-up. The CH layer may be (or may be not) present in order to reduce X-ray emission from laser irradiated side. The probe laser, used at LULI only, was a Nd:YAG converted to 2ω with pulse duration of 8 ns.

The reflectivity temporal behavior is important since it can provide evidence of insulator to metal transitions (optical reflectivity is directly related to the density of free charge carriers in the material [35]). However this requires a different target configuration, and no attempt was done in this direction in this first experiment.

Targets, and in particular the carbon layers, are an important part of the experiment. Some carbon depositions were done at the University of Milan using the Supersonic Cluster Beam Deposition (SCBD) technique with appropriate masks [36] which allows quite uniform layers and steep steps to be deposited. The particular deposition system allows carbon to stick on Al avoiding usual de-lamination problems. More important, it is possible to deposit carbon layers with densities variable between 1 and 2 g/cm³. In our experiment, carbon layers with initial density $\rho_0 = 1.45 \pm 0.10$ g/cm³ were used. The deposition technique allowed the realization of targets with an acceptable surface roughness (less than 0.5 micron, i.e. $\approx 3\%$ of step thickness which
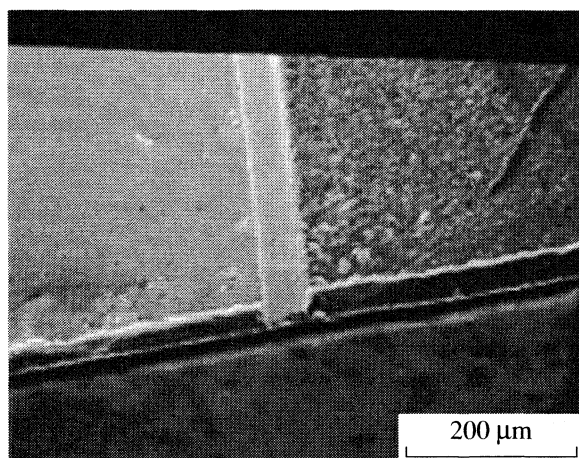
Fig. 3. SEM image of double step target produced at General Atomics, with density $\rho_0 = 1.6$ g/cm^3.
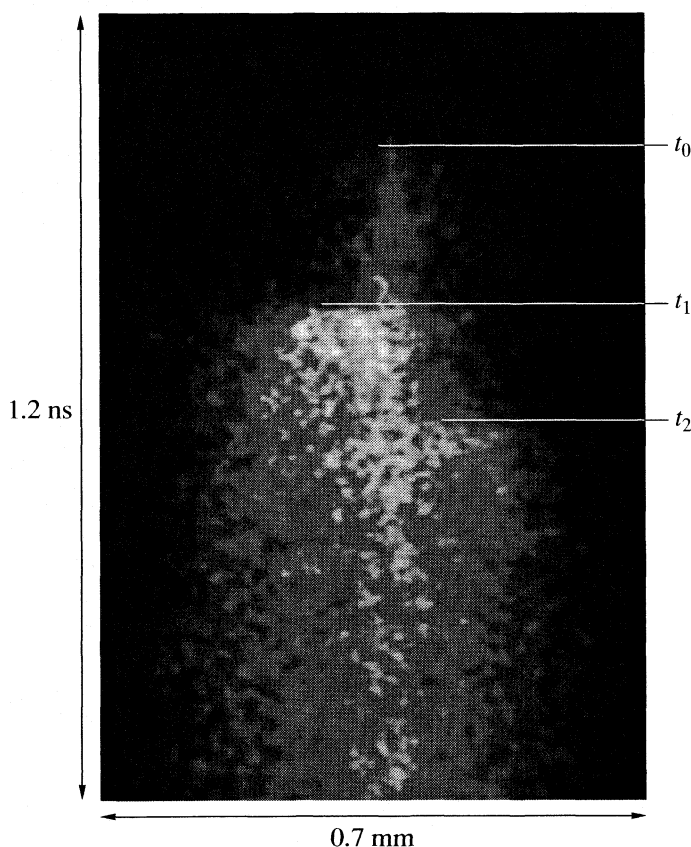
Fig. 4. Shock breakout streak image of the target rear side in emission, target produced at General Atomics. Shot made at PALS with energy $E = 108$ J. Lines indicate the shock break-out from the Al step (left) and from the C step (right). Al step gave $t_1 - t_0 = 205$ ps, $D_{Al} = 38.8$ km/s, $P_{Al} = 33$ Mbar. C step gave: $t_2 - t_0 = 295$ ps, $D_c = 32.2$ km/s, $P_c = 18$ Mbar.

was of the order of 15 μm). These give an error comparable to the typical ≤5% due to streak camera resolution. The Al step thickness was 5 μm.

Other carbon targets were fabricated at General Atomics [37] (see Fig. 3) using a completely different technique based on the use of colloidal carbon. In this case, carbon with initial density $\rho_0 = 1.6 \pm 0.10$ g/cm^3 was produced. Stepped targets were made of lathe machining of bulk aluminum. The Al base was ≈8 μm, and the step thickness was ≈8.5 μm. The carbon layer was then produced and the target was machined again to produce the C step (with thickness ≈10 μm). The use of two different type of targets allow a comparison of measurements and a better confidence in our results. Fig. 4 shows a typical results obtained from the emissivity diagnostics. In total we obtained 5 good experimental points at LULI (2 for $\rho_0 = 1.45$ g/cm^3 and 3 for $\rho_0 = 1.6$ g/cm^3) and 4 good points at PALS (all for $\rho_0 = 1.6$ g/cm^3). These are shown in Fig. 5 with all the other experimental results already available in the literature in the pressure range $P \geq 1.5$ Mbar. Data, grouped according to their initial density ρ_0, are compared to the shock polar curve derived from the Sesame tables (the model QEOS [38] yields practically identical results for carbon, even if usually it does not describe the Hugoniot with the same accuracy like the SESAME EOS does).

The errors on pressure and fluid velocity are ≈15% and ≈20% respectively; these error bars have been estimated by calculating the propagation of experimental errors on shock velocity (5%) on the quantities determined by the mismatch method. The error on shock velocity is instead determined from the experimentally measured uncertainties in step thickness and by streak-camera temporal resolution.

All our data, for both initial densities, are below the shock polar curve derived from the Sesame tables. Despite our quite large error bars (which make most points compatible with the theoretical curve), such results show a systematic deviation, and indicate a compressibility of carbon, at these pressures, much higher than what predicted by most models (the density ρ of the compressed sample is obtained from the Hugoniot Rankine relations for shocks, namely from $\rho(D-U) = \rho_0 D$). However such behavior could be also due to the presence of systematic errors in our experiment. One possible cause often cited for explaining errors in laser-shock EOS experiments is preheating induced by X-rays. In our case, preheating was surely small for the points at LULI due to the rather low laser intensity and the presence of a CH layer on laser irradiated side, which reduces X-ray generation (as shown experimentally in [35]). On the contrary, for the shots at PALS preheating was measured by calibrating the emissivity diagnostics and, for the two shots at higher energy (pressure), it was as high as a couple of eV [34]. Despite this, the LULI points are as far from Sesame as the PALS points. Therefore preheating is probably not the cause of deviation from theoretical curves (or at least not of the whole deviation). Another possible systematic effect could be due to the high porosity of the targets, even if porous and foam targets are routinely used in

Pressure, Mbar
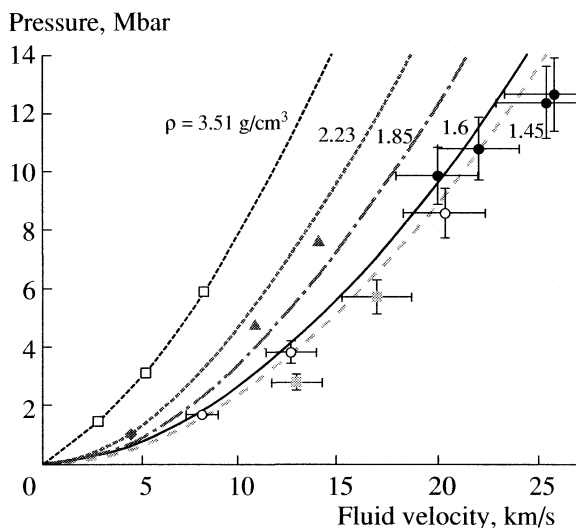
Fig. 5. Experimental EOS results from shock experiments. Only data with $P \geq 1.5$ Mbar and corresponding Hugoniot are shown. Our points: full squares, 1.45 g/cm^3 LULI; empty circles, 1.6 g/cm^3 LULI; full circles, 1.6 g/cm^3 PALS. Previous points: empty diamond, 1.85 g/cm^3 Pavlovskii et al. [28]; triangles, 2.2 g/cm^3 Nellis [29]; full diamond, 2.23 g/cm^3 Pavlovskii et al. [28]; empty squares, 3.51 g/cm^3 (diamond) Pavlovskii [30].

EOS experiments. Hence, even if this point requires further future work and analysis, for the moment we can conclude that at very high pressures carbon is likely to be more compressible than predicted by Sesame or QEOS. Let's notice that a deviation from Sesame is also observed for other points obtained at high shock pressure (for instance the point at ≈ 3 Mbar for carbon with $\rho_0 = 1.85$ g/cm^3 reported by Pavlovskii and Drakin [28]). Even more interestingly, the same behavior was observed by Nellis et al. [29] who, using underground nuclear explosions as a compression tool, report two EOS points for graphite ($\rho_0 = 2.2$ g/cm^3) at 4.76 and 7.61 Mbar.

The relation between shock velocity D and fluid velocity U for carbon in the Megabar range is linear ($D = C + SU$, where C is the sound velocity in the material in that pressure range). For carbon with $\rho_0 = 1.6$ g/cm^3, from Sesame (or QEOS), we get $C \approx 5$ km/s and $S \approx 1.27$ [39]. A linear interpolation of our points instead yields $S \approx 1.08$–1.14 (depending on whether we consider or not the two "preheated" points). From this we get an "experimental" shock polar $P = \rho_0 DU = \rho_0 U(C + SU)$ which of course nicely interpolates our results in the (P, U) plane. This curve is above the thermodynamic limit $P = \rho_0 U^2$ corresponding to infinite compressibility (all our experimental points are above such limit). However, it seems too close to the shock polar for a perfect gas, which again could indicate an influence from systematic effects. For the case $\rho_0 = 1.45$ g/cm^3 we didn't make any attempt to determine S since we had two points only.

CONCLUSIONS

The observed increased compressibility of carbon, suggests that at a given pressure along the Hugoniot, the density in the final state (liquid) is smaller than that for solid. Transitions to less dense phases also enhance thermal contributions, explaining the observed pressure discrepancy. This agrees with conclusions by Nellis et al. [4] and reinforces their observations.

ACKNOWLEDGMENTS

REFERENCES

1. J. A. Van Vechten, Phys. Rev. B, **7**, 1479, (1973).
2. J. W. Shaner and J. M. Brown, **45**, 235, (1984).
3. R. Grover, J. Chem. Phys. **71**, 3284 (1979).
4. M. T. Yin. M. L. Cohen, Phys. Rev. Lett., **50**, 2006. (1983); M. T. Yin, Phys. Rev. B. **30**. 1773 (1984).
5. R. Biswas, R. M. Martin, et al., Phys. Rev. B, **30**, 3210 (1984).
6. S. Fahy, S. G. Louie. Phys. Rev. B, **36**, 3373 (1987).
7. A.L. Ruoff, H. Luo, J. Appl. Phys. **70**, 2066 (1991).
8. H. K. Mao, P. M. Bell, Science, **200**, 1145, (1978); H. K. Mao, R. J. Hemley, Nature, **351**, 721 (1991).
9. F. P. Bundy, Physica A, **156**, 169 (1989); F. P. Bundy, J. Chem. Phys., **38**, 631 (1963); F. P. Bundy, H. M. Strong, R. H. Wentorf, J. Chem. Phys., 10, 213, (1973).
10. M. Grumbach, R. Martin, Phys. Rev. B, **54**, 15730 (1996).
11. T. Sekine, Appl. Phys. Lett., **74**, 350 (1999).
12. L. Benedetti, et al., Science, **286**, 100 (1999).
13. S. Scandolo, et al., Phys. Rev. B, **53**, 5051 (1996).
14. A. Cavalleri, et al., Europhys. Lett., **57**, 281 (2002).
15. In this regime, the most complete EOS are the SESAME tables developed at the Los Alamos Laboratory (SESAME Report on the Los Alamos Equation-of-State library. Report No. LALP-83-4, T4 Group LANL, Los Alamos, 1983).
16. M. Ross, Rep. Prog. Phys. **48**, 1 (1985).
17. S. Eliezer, A. Ghatak, H. Hora "Equation of state: theory and applications" Cambridge Univ. Press. Cambridge (1986).
18. Y. Gupta, S. Sharma. Science, **277**, 909 (1997).
19. S. Saumon, G. Chabrier, et al., Ap. J. Suppl., **99**, 713 (1995).
20. T. Guillot, Science, **286**, 72 (1999).
21. M. Ross, Nature, **292**, 435 (1981).

22. F. Ancillotto, G. Chiarotti et al., Science, **275**, 1288 (1997).

23. W. J. Nellis, N. C. Holmes, et al., J. Chem. Phys. **107**, 9096 (1997); W. J. Nellis, et al., Science, **240**, 779 (1988).

24. N. F. Ness, et al., Science, **240**, 1473 (1989); N. F. Ness, et al., Science, **233**, 85 (1986).

25. J. E. Connerney, et al., J. Geophys. Rev., **92**, 15329 (1987).

26. M. Koenig, et al., Phys. Rev. E, **50**, R3314 (1994).

27. M. Koenig, et al., Phys. Rev. Lett., **74**, 2260 (1995); D. Batani, et al., Phys. Rev. B, **61**. 9287 (2000); D. Batani, A. Morelli, et al., Phys. Rev. Lett., **88**, 235502 (2002).

28. M. N. Pavlovskii, V. P. Drakin, JETP Lett., **4**, 116 (1966).

29. W. J. Nellis, et al., J. Appl. Phys., **90**, 696 (2001).

30. M. N. Pavlovskii, Sov. Phys. Solid State, **13**, 741 (1971).

31. W. H. Gust, Phys. Rev. B, **22**, 4744 (1980).

32. *LASL Shock Hugoniot Data*, edited by S. P. Marsch (University of California, Berkeley. 1980). pp. 28–51.

33. K. Jungwirth, et al., Phys. Plasmas, **8**, 2495 (2001).

34. D. Batani, H. Stabile, et al., Phys. Rev. E (2003).

35. A. Benuzzi. et al., Phys. Plasmas, **5**, 2410 (1998).

36. E. Barborini. et al., J. Phys. D: Appl. Phys. 32, LI05 (1999); E. Barborini, et al., Appl. Phys. Lett. 77, 1059 (2000); P. Piseri, et al., Rev. Sci. Instrum. 72, 2261 (2001).

37. special thanks to J. Kaae, General Atomics, S. Diego, USA, for target fabrication.

38. R. M. More et al., Phys. Fluids, **31**, 3059 (1988).

39. This is true for QEOS and the Sesame table 7830. Other carbon tables give different, but close, values.

УДК 541.183

ПРОСТЫЕ МОЛЕКУЛЫ НА АКЦЕПТОРНОМ ЦЕНТРЕ ЦЕОЛИТА: КВАНТОВО-ХИМИЧЕСКИЙ ПОДХОД

© 2007 г.   Н. Ф. Степанов, А. А. Кубасов, Я. В. Тихий

Московский государственный университет им. М.В. Ломоносова, Химический факультет
E-mail: kubasov@comp.chem.msu.su

На основе различных квантово-химических методов и сопоставления с данными непосредственных измерений показана эффективность и достоверность кластерного подхода к моделированию взаимодействия ряда простых молекул (CO, вода, аммиак, этилен, метанол) с акцепторными центрами цеолитов. Установлено, что в комплексе молекул CO с трехкоординированным атомом алюминия образуются связи Al···CO, что позволяет использовать эту молекулу как тест на акцепторные свойства цеолитов. Сопоставление опытных и расчетных данных для взаимодействия от одной до трех молекул типа RH с фрагментом цеолита позволяет утверждать, что вода, аммиак, этилен и метанол в поле акцепторного центра цеолита приобретают протонодонорные свойства, аналогичные свойствам мостиковых групп OH в водородных формах цеолитов. Отмечено, что при построении вероятных схем катализа цеолитами необходимо учитывать возможное участие акцепторных центров в превращении молекул указанного типа.

В последние годы развитие теории и практики сделало квантово-химические расчеты одним из основных методов непосредственного изучения свойств различных молекулярных систем. При этом перешли от исследования взаимодействия двух или трех молекул между собой к взаимодействию кластеров (ассоциатов) с одной или несколькими другими молекулами. Такой переход явился качественным скачком, поскольку при этом изучают наноструктуры, отличающиеся по свойствам как от индивидуальных молекул, так и от объемных фаз. Становится возможным моделирование свойств олигомеров и объектов супрамолекулярной химии.

Расчетные исследования, проводимые в сочетании с непосредственным экспериментом, позволяют более глубоко и достоверно устанавливать закономерности формирования структур, содержащих сравнительно небольшое число индивидуальных молекул, и оценивать вероятность их устойчивого состояния. Особенно полезен такой комплексный подход, когда энергетические различия между гипотетическими структурами не позволяют делать надежные выводы. Другим немаловажным обстоятельством является и то, что проведение теоретических расчетов позволяет повысить достоверность интерпретации результатов различных физических методов исследования. Эти новые, современные подходы используют при изучении самых разнообразных систем, но наибольшее распространение получили они в изучении биологических систем, в частности при выяснении механизма действия ферментов, и в катализе комплексами переходных металлов, кластерами и твердыми телами (цеолитами).

При изучении модельных структур гетерогенного катализатора и их взаимодействий с адсорбирующимися и превращающимися молекулами очевидно необходимым этапом является построение сравнительно небольших кластеров твердого тела. В связи с жесткостью неорганических систем, являющихся основой большинства гетерогенных катализаторов, для моделирования свойств активного центра представляется вполне достаточным учитывать только ближайшее его окружение. Такие представления дают возможность, используя рентгеноструктурные данные, выбирать сравнительно небольшой и жесткий кластер, передающий свойства твердого тела. При этом возникают две серьезные проблемы. Во-первых, выбор фрагмента катализатора, имитирующего активный центр, а во-вторых, выбор числа и вида достаточно простых молекул, взаимодействие которых с модельным активным центром (кластером) позволит сделать обоснованные заключения о механизмах адсорбции и катализа.

В последние годы в нашей группе были разработаны соответствующие подходы и проведено неэмпирическое моделирование различных кластеров. Так, с целью более глубокого понимания атмосферных процессов исследованы свойства кластеров, включающих до 100 молекул воды и взаимодействующих с озоном или диоксидом азота [1]. Другим направлением работ было изучение свойств промышленно важных цеолитных катализаторов, для чего использовались циклические фрагменты структуры, содержащие три, четыре, шесть, восемь тетраэдрических атомов алюминия и кремния, взаимодействующих с од-

ной–тремя молекулами воды, аммиака, этилена, метанола в составе кластера.

Структура и свойства цеолитных катализаторов весьма разнообразны, но общим для всех является высокая степень упорядоченности расположения составляющих их атомов. Поэтому изучение активных центров цеолитов возможно при моделировании свойств сравнительно малых структур, состоящих из цеолитного фрагмента и нескольких сравнительно небольших молекул, используемых при изучении адсорбционных и каталитических свойств катализаторов. Именно этому разделу наших работ посвящена данная публикация.

В работах по моделированию цеолитных катализаторов наибольшее внимание различные исследовательские группы уделяют изучению свойств протонодонорных центров. Однако в непосредственных опытах показано, что во многих случаях активность цеолитов связана качественно и количественно с акцепторными центрами. Такие центры возникают за счет того, что дегидроксилирование кристаллического алюмосиликата при повышенной температуре приводит к уменьшению координации тетраэдрического атома алюминия и, тем самым, к образованию структурного дефекта. Свойства акцепторных центров и взаимодействие с ними разных молекул изучены в значительно меньшей степени. Ряд исследователей, кроме того, полагает, что они не являются активными центрами кислотного катализа.

Нами ранее изучались каталитические свойства цеолитов, обладающих центрами такого типа. На основании корреляции экспериментальных результатов и ИК-спектрального изучения адсорбции различных оснований показано, что акцепторные центры могут быть активными в кислотном катализе. Кроме того, предположено, что взаимодействие с ними молекул типа RH может приводить к образованию новых протонодонорных центров [2]. Именно это вызвало постановку систематического квантово-химического изучения свойств акцепторных центров и моделирования взаимодействия с ними различных молекул.

Результаты неэмпирических квантово-химических расчетов дают основу для глубокого понимания природы и свойств адсорбционных комплексов (CO, вода, аммиак, этилен, метанол), образующихся при взаимодействии с модельными фрагментами структуры цеолита, содержащими координационно ненасыщенный тетраэдрический атом алюминия. Показано, что в поле акцепторного центра молекулы типа RH способны проявлять свойства донора протона.

КВАНТОВО-ХИМИЧЕСКИЕ РАСЧЕТЫ И ВЫБОР МОДЕЛЬНОГО ФРАГМЕНТА

Для проведения расчетов в качестве первого приближения использовали полуэмпирический метод PM3 (MOPAC 93), а затем проводили расчеты ограниченным методом Хартри–Фока, по теории возмущений Меллера–Плессе второго порядка (MP2 и LMP2, PC GAMESS) и методом функционала плотности с нелокальным функционалом BLYP и гибридным функционалом B3LYP (программный пакет JAGUAR). Поскольку разные неэмпирические подходы приводили к качественно и количественно совпадающим результатам, основная информация была получена с использованием функционала BLYP (базисы 6-31G** и 6-31++G** для оценки энергии отрыва протона). Выбор сделан на основе предварительных расчетов с использованием различных базисов и сопоставления полученных результатов. Во всех случаях (кроме оценки энергии отрыва протона) проводили полную оптимизацию геометрии анализируемых молекулярных систем [3]. Оценку величины заряда на атоме проводили по Малликену.

Для моделирования акцепторного центра использовали замкнутые циклические фрагменты, содержащие два–семь атомов кремния и один атом алюминия. Небольшое число тетраэдрических атомов облегчало проведение вычислений, но обеспечивало структурную жесткость, свойственную цеолитным структурам. Предварительно было показано, что структуры с тремя тетраэдрическими (обозначение 3Z) атомами достаточны для моделирования взаимодействия с малыми молекулами (вода, аммиак), так как расширение фрагмента не приводило к заметным различиям. Структуры типа 8Z необходимы для анализа систем, содержащих молекулы спирта. Обе выбранные модели структуры являются фрагментами реальных цеолитов: 3Z содержится в ZSM-18, а 8Z в структуре фожазита, рис. 1.

Некоторые из полученных результатов можно сопоставить с литературными данными, что позволило подтвердить достоверность нашего подхода.

ОБСУЖДЕНИЕ РЕЗУЛЬТАТОВ

Взаимодействие с одной молекулой

Изучение адсорбции молекулы CO показало, что энергия диссоциации 3Z–CO на 35 кДж/моль выше, чем энергия диссоциации 3Z–OC, а расстояние C···Al в 3Z–CO на 27 пм меньше, чем расстояние O···Al в 3Z–OC, так что предпочтительным оказывается образование комплексов Al···CO, а не Al···OC. При этом значение теплоты адсорбции (50–60 кДж/моль) и синий сдвиг (54–62 см$^{-1}$) полос ИК-спектра были воспроизведены с хорошей точностью. Отмечен существенный перенос
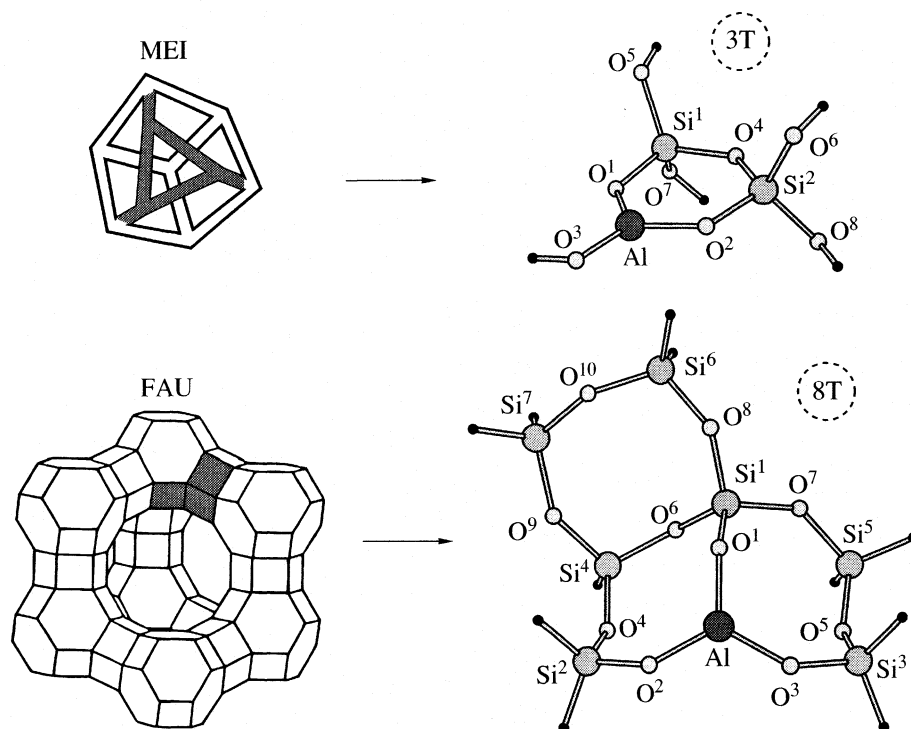
Рис. 1. Фрагменты 3Z и 8Z в цеолитах.

электронной плотности от CO на трехкоординированный атом алюминия (0.347 а.е. по сравнению с 0.151 а.е. в свободной молекуле CO), что соответствует литературным данным [4].

Координационное взаимодействие молекулы воды с акцепторным центром приводит к изменению ее свойств, указывающему на облегчение отрыва протона от связанной молекулы воды по сравнению со свободной. Главный вклад в такое изменение вносит сам акцепторный центр, а влияние его окружения носит вторичный характер. Диссоциация воды в поле кластера 8T приводит к образованию протонного центра той же силы, что и координация. Получены практически совпадающие значения энергии отрыва протона (1354 ± 0.5 кДж/моль), длины связей OH (98.2 ± ± 0.05 пм) и зарядов на атомах H (0.370 ± 0.002 а.е.) соответствующих комплексов. В то же время, характеристики диссоциативного комплекса ($\nu_{OH} =$ = 3635 см$^{-1}$, R_{HAl} = 240 пм) оказываются близки к экспериментальным данным, относящимся к мостиковой группе OH фожазита, фрагментом которого является кластер 8T. Следовательно, можно предположить, что координация воды на акцепторном центре также приводит к образованию протонного центра, который близок по силе к мостиковой группе OH.

Координация молекулы аммиака на акцепторном центре [5] приводит к такому возмущению молекулы, что на одном из атомов водорода положительный заряд возрастает на 0.07–0.10 а.е. и

этот атом становится потенциальным центром протонодонорной кислотности. Молекула аммиака образует координационную связь N$\cdots$Al длиной 203.3 пм, а также водородную связь H$\cdots$O с атомом кислорода в составе кластера 3T. Длина этой водородной связи составляет 208 пм, а соответствующий угол NHO равен 147 град. Диссоциация в составе ионной пары образует более сильный центр бренстедовской кислотности, но энергетически менее (130 кДж/моль) выгодна, чем координационное связывание молекулы. Рассчитанные величины энергии координации (адсорбции) и синий сдвиг (δ_s колебания на 140–160 см$^{-1}$) адсорбированной молекулы хорошо согласуются с литературными данными. Связывание аммиака уменьшает энергию его депротонизации на 203–257 кДж/моль в комплексах 3Z и 8Z соответственно. Полученные результаты аналогичны полученным ранее как в наших исследованиях, так и в работах других авторов по изучению адсорбции воды на акцепторных центрах. Однако в комплексах с водой энергия депротонизации ниже, т.е. молекула аммиака, возмущенная акцепторным центом, будет более слабым, чем адсорбированная вода, протонным центром.

При адсорбции этилена преимущественным является образование плоского и стабильного π-комплекса, в котором связь атома водорода становится слабее: по сравнению со свободной молекулой энергия депротонизации уменьшается на 110 и 150 кДж/моль на комплексах 3Z и 8Z соот-

ветственно. Заряды на атомах водорода возрастают в среднем на 0.07 а.е. Ориентация этих атомов относительно атома алюминия незначительно влияет на приобретаемый избыточный заряд. Сама молекула приобретает частичный положительный заряд на концевых атомах водорода: 0.255 а.е. Это приводит к ослаблению связи С=С, что находит отражение в ее удлинении на 1.5 пм и красном сдвиге частоты ее валентного колебания[1] на 38–41 см$^{-1}$, т.е. адсорбированная молекула может обладать свойствами протонной кислоты. Из этого следует, что протонодонорные свойства молекул RH в поле акцепторного (трехкоординированного атома Al) заметно возрастают.

Для молекул метанола [6] при связывании на 3Z- и 8Z-фрагментах координация также энергетически (на ~40 кДж/моль) более выгодна, чем диссоциация. Влияние акцепторного центра выражается в облегчении отрыва протона от OH-группы. Вследствие этого она приобретает свойства протонной кислоты и по силе донорной способности приближается к мостиковой OH-группе в водородных формах цеолитов. Образующаяся в результате такого взаимодействия метоксигруппа CH$_3$O по длине связей, значениям валентных углов и частотам колебаний практически не отличается от мостиковой метоксигруппы в H-формах цеолитов: длины связей С–Н отличаются на 0.1–0.3 пм, длины связей С–О на 1.3–1.5 пм, углы НСН на 0.2–0.5 град., заряды CH$_3$-группы на 0.017–0.019 а.е., а частоты гармонических колебаний на 0–15 см$^{-1}$. Можно полагать, что и реакционная способность их будет весьма близкой.

Изменения структуры цеолитного фрагмента в результате взаимодействия с адсорбируемыми молекулами отмечены во фрагменте AlO$_3$. Изменения зарядов на атомах и межатомных расстояний связей, прилегающих к этому фрагменту или минимальны (вторая сфера), или не регистрируемы. Так, изменение длин связей Si–О в Z3 составляет лишь 0–3 пм, тогда как основная часть связей Si–О кластера 8Z в его бинарных комплексах вообще остается невозмущенной в пределах ±0.5 пм. В кластере 3Z возмущение зарядов на удаленных атомах не превышает 0.02 а.е., а в кластере 8Z заряды на большинстве атомов изменяются не более чем на 0.01 а.е. Тем самым подтверждается принятая нами идея, что малые фрагменты и образуемые ими кластеры могут быть надежной моделью взаимодействий в системе цеолит–индивидуальная молекула.

Адсорбция молекул типа RH приводит к образованию новых протонодонорных центров, что объясняет полученные нами ранее данные об увеличении активности цеолитов при адсорбции малых количеств воды, аммиака и сероводорода.

Общий вывод данной части исследований состоит в том, что взаимодействие молекул типа RH с акцептором может привести к такому возмущению адсорбированных молекул, которое позволяет рассматривать их как потенциальные доноры протона.

Взаимодействие с цеолитным фрагментом двух или трех молекул

Присутствие нескольких молекул вблизи акцепторного центра приводит к образованию организованных структур, как правило циклических, а нарастание числа адсорбированных молекул приводит к образованию цепочек адсорбата. При адсорбции нескольких молекул воды происходит существенное изменение их электронной плотности. Так, на протоне молекулы, непосредственно связанной с атомом алюминия, заряд возрастает на 0.11–0.12 а.е., а суммарный заряд молекулы достигает 0.13–0.15 а.е. Из этого следует, что молекула воды в поле цеолита проявляет свойства, аналогичные гидратированному протону. Во второй молекуле заряды на атомах водорода возрастают на 0.03–0.04 а.е. Третья молекула воды связывается наименее прочно. Энергия отрыва составляет всего 66 кДж/моль, в то время как отрыв второй молекулы в адсорбированном димере требует 106 кДж/моль (32 кДж/моль в свободном димере). Этот результат обосновывает представление о последовательном сдвиге протона в цепочке нескольких молекул воды. Такой эффект аналогичен происходящему в цепочках нескольких аминокислот и некоторых других соединений.

Высказанное предположение о том, что в поле акцептора молекула воды может стать донором протона, подтверждается расчетом кластера цеолит–вода–аммиак. Показано, что связанная в комплекс молекула аммиака аналогична связанному иону аммония (рис. 2). Частоты гармонических колебаний структуры 3Z–OH–NH$_4$ (перенос протона воды) воспроизводят основные особенности ИК-спектра аммиака, адсорбированного на протонном кислотном центре: присутствует полоса 1467 см$^{-1}$ в области деформационных колебаний 1450–1500 см$^{-1}$. Это позволяет утверждать, что адсорбция с образованием достаточно сложного и упорядоченного комплекса нескольких молекул воды или аммиака должна быть свойственна цеолитам.

Нами проведены также расчеты комплексов СО или C$_2$H$_4$ и молекул воды, координированных на акцепторном центре. Сравнение со свойствами комплексов этих же молекул со структурными OH-группами H-форм цеолитов показало практически полное совпадение рассчитанных характеристик. Это позволяет заключить, что молекула воды, координированная на акцепторном центре,

---

[1] Колебание, участие в котором связи С=С максимально.
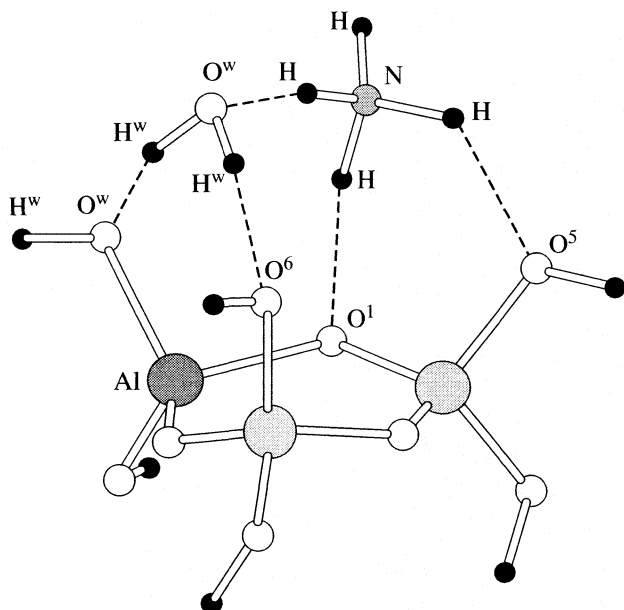
Рис. 2. Комплекс $3Z-2H_2O-NH_3$.
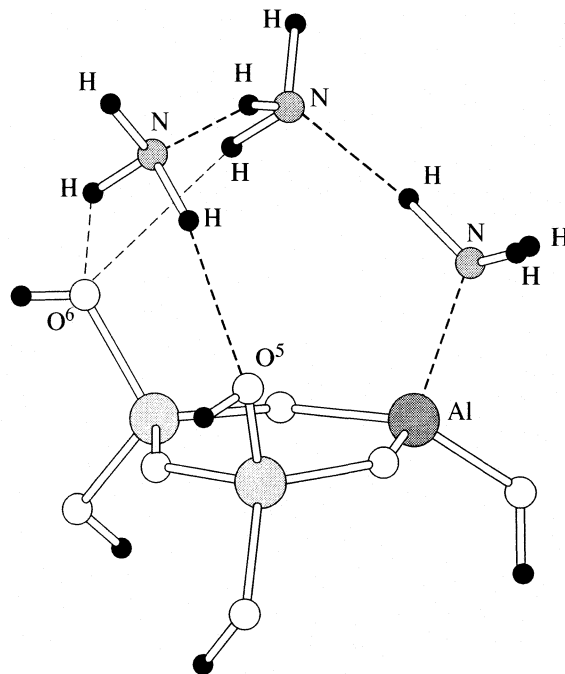
Рис. 3. Комплекс фрагмента $3Z$ и 3 молекул аммиака.

по своей протонодонорной способности весьма близка к хорошо изученным центрам бренстедовской кислотности.

Протонодонорная активность возрастает также и в молекулах аммиака, непосредственно связанных с акцепторным центром, что отражается в относительно высокой энергетической стабильности ассоциатов $(NH_3)_n$, где $n = 2$ или 3. Ступенчатый отрыв сначала одной адсорбированной молекулы, а затем второй от комплекса $3Z-(NH_3)_3$ (рис. 3) требует энергии 36 и 71 кДж/моль, в то время как энергия диссоциации свободного димера аммиака составляет 17 кДж/моль. Координированные молекулы аммиака приобретают способность образовывать Н-связи с адсорбированными на них одной или несколькими молекулами воды, что не наблюдается при их взаимодействии в газовой фазе. Возмущенные в поле акцепторного центра молекулы аммиака способны связывать СО или C_2H_4. Но при этом прочность образующейся между ними связи (~29 и 25 кДж/моль соответственно) меньше, чем в аналогичных комплексах СО или C_2H_4 с водой. Тем самым подтверждается, что протонная кислотность, обусловленная молекулами аммиака, будет слабее, чем образующаяся при адсорбции воды на акцепторном центре. Отметим, что влияние акцепторного центра передается по цепочке адсорбированных молекул, и это еще раз подтверждает предлагаемые в литературе аналогии цеолитного и ферментативного катализа.

При взаимодействии двух молекул метанола с фрагментом Z8 ступенчатая координация также является предпочтительной. Хотя вторая молеку-

ла непосредственно не связана с цеолитом, ее геометрия и распределение электронной плотности существенно меняются. Так, заряд на атоме водорода гидроксильной группы по сравнению с индивидуальной молекулой возрастает на 0.08 а.е., а частота колебаний ОН примерно на 300 см$^{-1}$ ниже, чем в свободном димере метанола. При этом энергетически взаимодействие не очень сильное. Однако и в этом случае акцепторный центр играет решающую роль в упорядочении и характере взаимодействия двух молекул спирта. По сравнению со свободным димером, поле цеолитного фрагмента увеличивает энергию взаимодействия между двумя молекулами метанола на ~60 кДж/моль. Если в свободном димере метанола заряд на атомах Н составляет 0.307 а.е., то в адсорбированном димере в зависимости от расположения молекулы спирта он колеблется в пределах от 0.366 до 0.443 а.е.

Если же к комплексу цеолит–метанол присоединить молекулу аммиака (общепринятый способ оценки протонодонорной способности поверхностных центров), то в отличие от комплекса цеолит–вода–аммиак перенос протона на молекулу аммиака не происходит. Тем не менее, взаимодействие метанол–аммиак достаточно сильное (~100 кДж/моль), что отражает возмущающее действие цеолита.

Остановимся теперь на указанной выше важности таких теоретических работ для интерпретации результатов непосредственных опытов. Так, в спектрах термопрограммированной де-

сорбции (ТПД) аммиака наблюдают низкотемпературные пики (энергии активации десорбции ~80 кДж/моль), обычно интерпретируемые как десорбция аммиака со слабых кислотных центров цеолитов. Нами были рассчитаны значения энергии разложения бимолекулярных ассоциатов на обоих типах кислотных центров (71 и 59 кДж/моль соответственно). Причем ассоциаты на акцепторном центре более устойчивы. Это позволяет предложить отличную от общепринятой интерпретацию: низкотемпературный пик в спектрах может быть обусловлен разрушением ассоциатов аммиака на цеолитных ЛКЦ и БКЦ, в которых непосредственно связанная с кислотным центром молекула обладает свойствами протонной кислоты.

При регистрации спектров ТПД после предварительной обработки образца цеолита парами воды наблюдали только один пик, что обычно объясняли удерживанием аммиака на сильных протонных центрах. Нами показано, что ассоциаты, внешнюю сферу в которых занимает молекула воды, оказываются устойчивее их аналогов с молекулой аммиака в той же позиции. Энергия диссоциации кластера равна 298 и 268 кДж/моль соответственно. Следовательно, вода может вытеснять аммиак из внешней сферы ассоциатов, что и приводит к удалению низкотемпературного пика на кривых ТПД аммиака. Однако анализ наших результатов позволяет утверждать, что имеет место и образование гидрата, связанного на акцепторном центре иона аммония. Образование полимолекулярных ассоциатов, обнаруженных нами, несколько меняет и интерпретацию ИК-спектров аммиака и метанола, адсорбированных на цеолитах.

В области 3300–2400 см$^{-1}$ наблюдается сложный спектр, который относят к валентным колебаниям связей N–H ионов аммония, участвующих в образовании водородных связей с атомами цеолитного каркаса. Нами показано, что образование ассоциатов приводит к поглощению в области 2500–1900 см$^{-1}$, отвечающей колебаниям внутренних мостиковых связей N–H(···N). Следовательно, полосы в ИК-спектре аммиака, адсорбированного Н-формой цеолита, могут быть отнесены не только к связанному иону аммония, но также к комплексам и ассоциатам аммиака на акцепторных центрах.

Расчеты показали, что при недиссоциативной адсорбции метанола происходит существенный красный сдвиг полосы ν ОН; появление в спектре комплекса CH$_3$–8Z–ОН полосы 3700–3800 см$^{-1}$, характерной для групп ОН алюмосиликатов, обусловлено формированием группы AlOH; в спектрах комплексов Н–8Z–ОCH$_3$ и CH$_3$–8Z–ОН полоса δ ОН метанола исчезает; для мостикового комплекса CH$_3$–8Z–ОН и координированной молекулы метанола характерен сдвиг полосы ν СО в красную область спектра; образование метоксигруппы в комплексе Н–8Z–ОCH$_3$ вызывает сдвиг полосы ν СО в синюю область спектра, но не сопровождается заметным (~100–150 см$^{-1}$) сдвигом валентных колебаний CH$_3$ в синюю область. Эти соображения могут существенно влиять на интерпретацию ИК-спектров адсорбированного метанола.

Одним из важных результатов проведенных расчетов, позволяющим более обоснованно представлять механизмы превращений на цеолитах является анализ спектров адсорбированного этилена. В комплексе с акцептором удлиняется связь С=С (1.5 пм), а красный сдвиг колебания ν$_{CC}$ (на ~40 см$^{-1}$) относительно свободной молекулы оказывается вдвое больше, чем у комплексов, в которых молекула этилена связана с группой ОН цеолита. Следовательно, акцепторный центр ослабляет связь С=С более существенно. Очевидно, что одним из вероятных активных центров превращения по кислотному механизму может быть акцепторный центр, возникающий при предкаталитическом прокаливании катализатора.

Таким образом, проведенное систематическое квантово-химическое исследование свойств комплексов фрагмента цеолита, имитирующего акцепторный центр (трехкоординированный атом алюминия), с некоторыми простыми молекулами показало, что в поле этого центра возможно такое возмущение адсорбированной молекулы, содержащей атом водорода, при котором она приобретает свойства донора протона. Это предположение, выдвинутое ранее на основе изучения явлений кислотного катализа и ИК-спектров, получило подтверждение при анализе свойств комплексов цеолит-цепочка из двух-трех изучаемых молекул. Сам по себе такой эффект достаточно хорошо изучен при адсорбции малых количеств воды на дегидроксилованных формах цеолитов. Нами ранее отмечалось промотирующее действие аммиака, проведенные расчеты же позволяют утверждать, что такое влияние возможно и при адсорбции этилена и метанола. Эффект такого воздействия будет зависеть от природы адсорбируемой молекулы.

При этом акцептор взаимодействует не только с непосредственно связанной с ним простой молекулой, но и с молекулами второй и третьей координационной сферы, образующими достаточно гибкую, но упорядоченную цепочку, что позволяет проводить аналогию между действием цеолитного и ферментативного катализатора.

В цеолитном катализаторе изменение свойств потенциального каталитического центра практически не сказывается на свойствах его ближайшего окружения в твердом теле. Этот важный результат служит обоснованием использования кластерного подхода и модели локальных взаи-

модействий при квантово-химическом изучении адсорбционных и каталитических свойств цеолитов.

Исследование свойств комплексов с акцепторным центром этилена или метанола, т.е. молекул, превращение которых протекает на цеолитах по кислотному механизму, показало, что кислотные центры, структуру которых обычно представляют как группы OH водородных форм цеолитов, могут быть не единственными каталитически активными центрами. Сила воздействия акцепторного центра на изученные молекулы и свойства образующихся комплексов сопоставимы с наблюдаемой при взаимодействии с кислотными группами OH структуры водородных форм цеолитов.

СПИСОК ЛИТЕРАТУРЫ

1. *Домрачева Т.М., Новаковская Ю.В., Кубасов А.А., Степанов Н.Ф.* // Журн. физ. химии. 1999. Т. 73. № 7. С. 1249.

2. *Кубасов А.А., Топчиева К.В.* // Тез. докл. II Всесоюз. конф. "Применение цеолитов в катализе". М., 1981. С. 254.

3. *Тихий Я.В., Кубасов А.А., Степанов Н.Ф.* // Журн. физ. химии. 2003. Т. 77. № 8. С. 1496.

4. *Солтанов Р.И.* // Кинетика и катализ. 1990. Т. 31. № 2. С. 438.

5. *Тихий Я.В., Кубасов А.А., Степанов Н.Ф.* // Журн. физ. химии. 2005. Т. 79. № 9. С. 1684.

6. *Stepanov N.F., Kubasov A.A., Tikhii Ya.V.* // Int. J. Quantum Chem. 2005. V. 104. № 2. P. 214.

CHEMICAL KINETICS
AND CATALYSIS

TEMPERATURE DEPENDENCE OF OXYGEN EVOLUTION THROUGH CATALASE-LIKE ACTIVITY OF HORSERADISH PEROXIDASE

© 2007   A. Popović-Bijelić*, G. Bijelić**, L. Kolar-Anić*, V. Vukojević***

*Faculty of Physical Chemistry, University of Belgrade
Studentski trg 12–16, 11000 Belgrade, Serbia
**Center for Multidisciplinary Studies, University of Belgrade
Kneza Višeslava 1, 11000 Belgrade, Serbia
***Department of Clinical Neuroscience, Karolinska Institute CMM L8:01, 17176 Stockholm, Sweden
E-mail: ana@ffh.bg.ac.yu

Abstract – By experimental investigations of the temperature dependence of catalase-like activity of horseradish peroxidase in the temperature range 278–328 K, different kinetic profiles for oxygen evolution were found below and above 298 K. Extension of the model is proposed to account for these observations. By numeric simulations of the reaction kinetics at different temperatures it was found that enhanced evaporation of molecular oxygen from the reaction solution is the main root through which oxygen is lost at elevated temperatures in laboratory conditions.

INTRODUCTION

Horseradish peroxidase (HRP) is an extracellular plant enzyme known to oxidize a variety of substrates at the expense of hydrogen peroxide thus generating free radical intermediates necessary for polymerization and cross-linking of cell wall components, oxidation of secondary metabolites, regulation of cell wall components and regulation of cell growth and differentiation [1].

The general mechanism of HRP catalyzed oxidation of substrates by H_2O_2 proceeds in three distinct steps [2]. First, the native ferric enzyme reacts with the oxidizing substrate to yield compound I, an oxyferryl iron porphyrin π radical. In the presence of an aromatic compound, which is a two-electron reductant, compound II is formed. Compound II oxidizes the second substrate molecule and is converted back into the native ferric enzyme.

In the absence of the usual reducing substrates, H_2O_2 performs a dual role – as an oxidant in the formation of compound I, and as a typical one-electron donor (reducing) substrate for peroxidase [3]. In these conditions a progressive loss of enzymatic activity takes place due to the formation of verdohemoprotein (P-670) that is devoid of catalytic activity. Also, a catalase-like activity of HRP is observed: HRP catalyzes hydrogen peroxide heterolysis into molecular oxygen and water. Catalase-like activity of HRP is weak compared to true catalases but it is a principal protective mechanism against oxidative inactivation.

The catalase-like activity of horseradish peroxidase is protective in plants and is typically being activated in response to environmental stress (pH, temperature, drought) or pathogen attack [1, 3]. In addition, this reactive pathway is attracting considerable attention in food processing because of its impact on food quality [4] and in advanced technology for the building of biosensors [5]. Therefore, a renewed interest in studying and modeling [3–6] the reaction mechanism of this pathway has arisen.

EXPERIMENTAL

Purified horseradish peroxidase was obtained from Sigma, type II, R_Z (A_{403}/A_{275}) = 1.8. Hydrogen peroxide (30%, v/v) and buffer substances (analytical reagent grade) were obtained from Merck.

The reaction was initiated by adding 1.0 × $\times 10^{-6}$ mol dm^{-3} HRP to the reaction medium containing 5.0×10^{-3} mol dm^{-3} H_2O_2 in 5.0×10^{-2} mol dm^{-3} sodium phosphate buffer, pH 6.0. The ratio of initial concentrations of hydrogen peroxide and HRP, $[H_2O_2]_0/[HRP]_0$, was set to 1000. The temperature was controlled within ±0.01°C. The course of the reaction was monitored spectrophotometrically and potentiometrically. The concentration of H_2O_2 was determined by measuring the absorbance at 240 nm, taking $\varepsilon_{240\,nm}$ = = 41.25 × 10^3 mol^{-1} dm^3 cm^{-1} [6], the enzyme concentration was estimated using the Soret extinction coefficient, $\varepsilon_{403\,nm}$ = 102 × 10^3 mol^{-1} dm^3 cm^{-1} [2] and oxygen production was measured using an oxygen electrode.

RESULTS AND DISCUSSION

Oxygen production curves (Fig. 1) show distinct kinetic profiles, suggesting a change in the reaction mechanism due to the increase in temperature.

Initial rates of oxygen formation (v_0) were determined from oxygen production measurements during the initial 25 s. They exhibit linear dependence on the initial concentration of the enzyme in the concentration

$[O_2] \times 10^4$, mol dm^{-3}
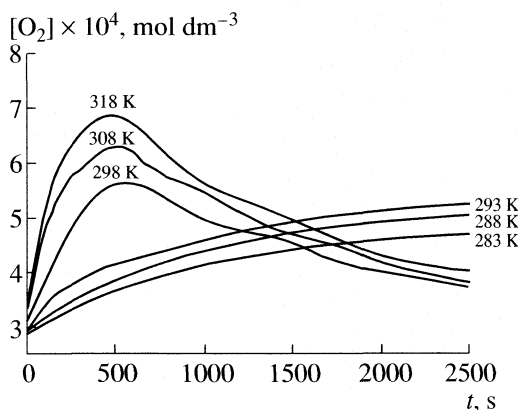
Fig. 1. Oxygen production at different temperatures. At temperatures lower then 298 K, a hyperbolic production profile typical for a product can be observed, whereas at higher temperatures the kinetic profile of oxygen production changes and resembles a profile of an intermediate.

$v_0(O_2) \times 10^6$, mol dm^{-3} s^{-1}
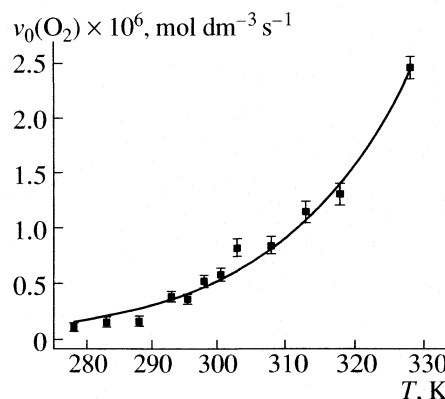
Fig. 2. Exponential increase of the initial rates of oxygen production at elevated temperatures.

range $7 \times 10^{-7} \le [\mathrm{HRP}]_0 \le 5 \times 10^{-6}$ mol dm^{-3} [6] and exponential dependence on temperature (Fig. 2).

To account for the consumption of oxygen (parabolic kinetic profile) in the range 298–328 K we assumed that when the concentration of dissolved oxygen in the reaction mixture becomes very high it is either consumed by a reactant or it simply evaporates from the reaction mixture. To test if oxygen is being consumed, an elementary step describing interaction between oxygen and the protonated form of the enzyme (EH$^+$) that was proposed in [3] and [7] was added to a previously proposed model [6]:

$$\mathrm{EH}^+ + \mathrm{O}_{2(1)} \underset{k_{-1}}{\overset{k_1}{\rightleftarrows}} \mathrm{Co(III)}. \qquad (1)$$
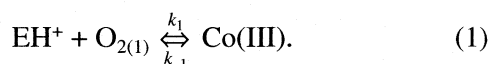
To simulate the kinetics of the temperature dependence of the catalase-like activity of HRP, we integrated numerically the set of ordinary differential equations

derived from the chemical equations given in Table (Steps R1–R10) through the mass-action law. Values of the rate constants are given in Table.

These simulations agreed well with the experimental results obtained for temperatures below 298 K, but did not agree with those above 298 K.

To test if the parabolic shape is due to oxygen evaporation, we assumed that when the reaction is conducted in a solution, evaporation of oxygen from the reaction solution might become significant at higher temperatures. Therefore, evaporation of dissolved oxygen from the reaction mixture is introduced [8]:

$$\mathrm{O}_{2(1)} \underset{k_{-11}}{\overset{k_{11}}{\rightleftarrows}} \mathrm{O}_{2(g)}. \qquad (2)$$

Results of numerical simulations by the extended reaction scheme (Steps R1–R11) are given in Fig. 3; they correspond to experimental conditions given in Fig. 1.

Enlarged reaction scheme describing the pH and temperature dependence of the catalase-like activity of horseradish peroxidase

(R1)	$\mathrm{E} + \mathrm{H}^+ \longleftrightarrow \mathrm{EH}^+$	$k_1 = 1.0 \times 10^8$ M^{-1} s^{-1}; $k_{-1} = 1.0 \times 10^{-3}$ M^{-1} s^{-1};
(R2)	$\mathrm{E} + \mathrm{H}_2\mathrm{O}_2 \longrightarrow \mathrm{coI} + \mathrm{H}_2\mathrm{O}$	$k_2 = 1.0 \times 10^7$ M^{-1} s^{-1};
(R3)	$\mathrm{coI} + \mathrm{H}_2\mathrm{O}_2 \longleftrightarrow \mathrm{coI} \cdot \mathrm{H}_2\mathrm{O}_2$	$k_3 = 4.0 \times 10^3$ M^{-1} s^{-1}; $k_{-3} = 1.0 \times 10^{-1}$ s^{-1};
(R4)	$\mathrm{coI} \cdot \mathrm{H}_2\mathrm{O}_2 \longrightarrow \mathrm{E} + \mathrm{O}_{2(1)} + \mathrm{H}_2\mathrm{O}$	$k_4 = 1.62$ s^{-1};
(R5)	$\mathrm{EH}^+ + \mathrm{O}_{2(1)} \longleftrightarrow \mathrm{coIII}$	$k_5 = 5.3 \times 10^4$ M^{-1} s^{-1}; $k_{-5} = 1.0 \times 10^{-1}$ s^{-1};
(R6)	$\mathrm{coI} \cdot \mathrm{H}_2\mathrm{O}_2 \longrightarrow \mathrm{coII} + \mathrm{H}^+ + \mathrm{HO}_2^{\bullet}$	$k_6 = 5.0 \times 10^{-3}$ s^{-1};
(R7)	$\mathrm{coII} + \mathrm{H}_2\mathrm{O}_2 \longleftrightarrow \mathrm{coII} \cdot \mathrm{H}_2\mathrm{O}_2$	$k_7 = 1.0 \times 10^7$ M^{-1} s^{-1}; $k_{-7} = 1.0 \times 10^{-7}$ s^{-1};
(R8)	$\mathrm{coII} \cdot \mathrm{H}_2\mathrm{O}_2 \longrightarrow \mathrm{coIII} + \mathrm{H}_2\mathrm{O}$	$k_8 = 2.0$ s^{-1};
(R9)	$\mathrm{coIII} \longrightarrow \mathrm{O}_2^{-\bullet} + \mathrm{E}$	$k_9 = 8.2 \times 10^{-3}$ s^{-1};
(R10)	$\mathrm{coI} \cdot \mathrm{H}_2\mathrm{O}_2 \longrightarrow \mathrm{Ei}$	$k_{10} = 2.9 \times 10^{-3}$ s^{-1};
(R11)	$\mathrm{O}_{2(1)} \longleftrightarrow \mathrm{O}_{2(g)}$	$k_{11} = 6.0 \times 10^{-3}$ s^{-1}; $k_{-11} = 6.0 \times 10^{-3}$ s^{-1}

Note: E and Ei are the native and inactive enzyme, respectively. EH$^+$ is the protonated form of enzyme, coI, coII, and coIII are enzyme intermediates, compounds I, II, and III, respectively. coI $\cdot$ H$_2$O$_2$ and coII $\cdot$ H$_2$O$_2$ are complexes between the respective enzyme intermediate and H$_2$O$_2$.
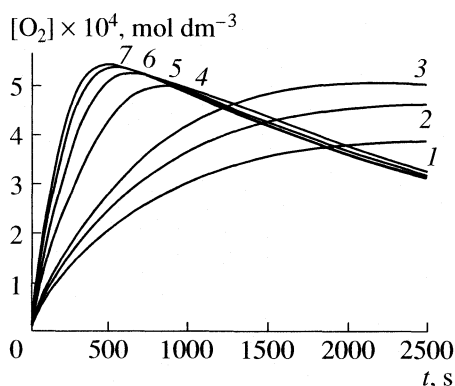
Fig. 3. Numeric simulations of the temperature dependence of oxygen production. Curve *3* is a simulation of actual oxygen production at 293 K. Curves *1*, *2* and *4–7* were obtained by multiplying the relevant kinetic constants (k_4, k_5 and k_{-5} from Table) by factors 0.7, 0.85, 2, 4, 8 and 15 respectively.

CONCLUSION

Experimental investigations of temperature dependence of the catalase-like activity of horseradish peroxidase in the temperature range 278–328 K revealed different kinetic profiles for oxygen evolution below and above 298. To account for these observations, an extended model is proposed that successfully emulates the pH and temperature dependence of the catalase-like activity of horseradish peroxidase in a wide range of conditions.

In the numerical simulations, we first optimized the set of rate constants to account for oxygen evolution at 298 K. To model the temperature dependence the rate constants k_4, k_5 and k_{-5} were scaled with the same proportionality factor, as discussed above. Values of other rate constant were not modified. This approach was applied because values of activation energies (E_a) for reaction steps 4 and 5 are not known.

Model simulations indicate that in conventional laboratory experiments enhanced evaporation of molecular oxygen from the reaction solution is the main root through which oxygen is lost at elevated temperatures. However, in living plants or in technological processing, where the partial pressure of oxygen can be much higher, its catalytic degradation by HRP can become prominent. In plants this may be a secondary defense mechanism against oxidative stress.

ACKNOWLEDGMENTS

REFERENCES

1. *Plant Peroxidases*; 1980–1990, Ed. by C. Penel, T. H. Gaspar, and H. Greppin (University of Geneva, Geneva, 1992).
2. H. B. Dunford, *Heme Peroxidases,* (J. Wiley and Sons Inc., New York, 1999).
3. J. Hernandez-Ruiz, M. B. Arnao, A. N. P. Hiner, F. Garcia-Canovas and M. Acosta, Biochem. J., **354**, 107 (2001).
4. M. H. Dicko, H. Gruppen, A. S. Traoré, A. G. J. Voragan and W. J. H. van Berkel, Biotechnol. Mol. Biol. Rev., **1**, 21 (2006).
5. N. Dimcheva and E. Horozova, Anal. Bioanal. Chem. **382**, 1374 (2005).
6. A. Popović-Bijelić, G. Bijelić, Lj. Kolar-Anić and V. Vukojević, Ann. N.Y. Acad. Sci., **1048**, 457 (2005).
7. J. N. Rodriguez-Lopez, A. T. Smith and R. N. F. Thorneley, J. Biol. Chem., **272**, 389 (1997).
8. L. F. Olsen, M. J. B. Hauser and U. Kummer, Eur. J. Biochem., **270**, 2796 (2003).

CHEMICAL KINETICS
AND CATALYSIS

KINETICS OF Cu²⁺ BINDING TO THE POLY(ACRYLIC ACID) HYDROGEL

© 2007   A. Kostić*, J. Jovanović**, B. Adnadjević**, A. Popović***

Faculty of Agriculture, Nemanjina 6, Zemun, Belgrade, Serbia
**Faculty of Physical Chemistry, Studentski Trg 12–16, Belgrade, Serbia*
***Faculty of Chemistry, Studentski Trg 12–16, Belgrade, Serbia*
E-mail: bora@ffh.bg.ac.yu

Abstract – Isothermal kinetics of copper (ion) binding to the poly(acrylic acid) (PAA) hydrogel at 20°, 25°, 35° and 45°C was investigated. Isothermal conversions and kinetics curves of Cu²⁺ binding to the PAA hydrogel were determined. It was found that the well known kinetics models of Peppas can not be applied for describing the entire process of Cu²⁺ binding. The new method for determination the kinetics model of Cu²⁺ binding process, as well as the activation energy density distribution functions of PAA hydrogel interaction with Cu²⁺, were established. It was found that dominant influence on the kinetics of the process, at temperatures $T \geq 30°C$ has Cu²⁺ diffusion to the active centers (with $E_a = 9$ kJ/mol), but at $T \geq 30°C$ and for the degree of bound Cu²⁺ $\alpha = \geq 0.2$, the interaction of Cu²⁺ from the adsorption center with $E_a = 26$ kJ/mol is dominant.

INTRODUCTION

Polymer materials are widely used type of materials and very popular in present time are hydrogels. Polyelectrolytes hydrogels have been attracted much attention as functional polymers that possess properties of water absorption. In recent time environmental protection has been confronted with increased contamination of waste water by heavy metals ions. They are metabolic poisons and enzyme inhibitors. The polyelectrolyte hydrogels can be applied to the problems of the recovery of precious metal, removal of toxic or radioactive elements from various effluents, and metal preconcentration for environmental sample analysis [1]. It has been shown that metal absorption is generally limited by metal diffusion inside the hydrogel and the hydrogel-water interfacial area [2]. Coordination resins have been used in metal extractions [3] but they demonstrate poor swelling in water, limiting the mobility of ligands. If we considered this fact, hydrophilic polymeric networks (polyacrylamide, polymethacrylic and poly-acrylic acid) will be very advantageous, as they can absorb an amount of water that can be thousand times larger than the mass of the original dry polymer. Fundamental studies on the complexation of metal cations with polyelectrolyte hydrogels have been carried out and used successfully in the recovery of metal ions [4]. Thus, the swelling of a polyelectrolyte network in metal aqueous solution can be applied to the treatment of diluted aqueous effluents in environmental studies [5]. The below cited papers illustrated this application and dealt with the absorption of copper ions with different types of hydrogels.

Recently, H. Kaşgöz and co-workers dealt with development and investigation of the sorbents for removal Cu(II) and other metal ions [6–8]. They prepared and used modified polyacrylamide (PAAm) hydrogels for removal of Cu(II) ion at pH 5.5 (which was considered to be optimal) by the batch equilibrium technique [6, 7]. They found that unmodified PAAm was not effective in removal of Cu(II) ions since amide groups alone cannot form complexes with copper ions. They found that the hydrogels of the modified polymers obtained by transa-midation of PAAm exhibited promising properties as complexing agents for Cu(II) ion removal [6, 7]. The maximum Cu(II) ion removal capacity of 4.07 mmol/g has been obtained with hydrogel based on sulfomethylation reaction products of PAAm [7]. The reported results were based solely on the determined Cu(II) ion removal capacity and there was not any information about the kinetics of the investigated process. Also, the new sorbent hydrogels based on poly(N-hydroxymethylacryla-mide)modified with introduced amine groups, were developed and used as sorbent for removal of Cu(II) ion (as a model metal ion) from aqueous solutions. The adsorption properties of the hydrogels were investigated at 25°C depending on pH, time and Cu(II) ion concentration. The results obtained from adsorption isotherm were evaluated by using Langmuir and Freundlich adsorption models. It was found that Langmuir isotherm model provided the best fit for the adsorption of Cu(II)ion as well as indigo carmine [8].

The work of I. Katime and E. Rodriguez [5] dealt with the absorption of copper and zinc with poly(acrylic acid–co–itaconic acid) hydrogel. The swelling process of xerogels of different compositions in water and salt solutions has been studied at 25°C and influence of pH on the adsorption process was examined. The swelling kinetics, kinetics order and rate constant of the investigated hydrogels have been determined. The swelling processes satisfied to a second–order kinetics. They found that metal absorption increased when pH, salt concentration in external solution and itaconic acid

content were levelled. They suggested that a complexation of –COO⁻ groups with Cu^{2+} happened forming neutral –COOCuOOC-group.

Some authors suggested that copolymer of a polyacrylamide and polyacrylic acid should be of use for the recovery of copper from environment [9]. Hydrogels based on acrylic acid are known as specific materials because of their biocompatibility, nontoxicity, hydrophilicity, etc. Due to this properties they have been used in medicine and pharmacy [10, 11], environmental protection, and agriculture. The aim of this paper was to investigate the kinetics of Cu^{2+} ion binding to the poly(acrylic acid) hydrogel.

EXPERIMENTAL

Materials. Acrylic acid (99.5%) (AA) in glacial form was supplied by Merck A.G., Germany. N,N-methylene bisacrylamide (p.a) (MBA) was purchased from Aldrich Chemical Co., Milwaukee, USA. The initiator, 2,2-Azobis-[2-(2-imidazolin–2-il)-propan dihydrochlorid (VA044), (99.8%) was supplied by Wako Pure Chemicals Industries, Ltd, USA. Copper-sulfate pentahydrate, $CuSO_4 \cdot 5H_2O$ (99.8%) was purchased from Zorka Pharma, Sabac, SCG. All substances were used as received without further purification.

Synthesis. *Poly(acrylic acid) hydrogels (PAA)* were synthesized by simultaneous radical polymerization and crosslinking using AIPD as an initiator and MBA as a cross-linking agent, in general using experimental procedure previously described [12, 13]. This procedure consists in follows: solution of acrylic acid in the form of 20% (wt) solution was prepared and mixed with solution of MBA ($0.1\%_w$). After good stirring of these mixtures to assue the homogenity of reaction mixture and nitrogen bubbling through the mixture for half an hour, initiator solution (0.06 mol % of the monomer) was added and reaction mixture was once again rapidly homogenized with stirring. The prepared solution was placed in Petri dish and stored in a dry oven for 5 hours at 80°C. After the polymerization was finished, the obtained gel-type product was transformed into the Na⁺ form (60%) by neutralization with a 3% solution of Na_2CO_3. The resulting hydrogel was cut to approximately equal discs and placed in excess of distilled water. The water was changed 7-times every 5 hours (or 12 hours during the night), in order to remove the unreacted monomers and the sol fraction of polymer. Then the obtained hydrogel was dried in an air oven in temperature regime 80° C for 2 hours, 90°C for 3 hours and 105°C to constant mass. The obtained product was stored in a vacuum exicator before use.

Binding of copper to the PAA hydrogel. Preweighed dry hydrogel (xerogel) samples, with average weight of 0.1 g, were immersed in solution of 0.01 M $CuSO_4$ at different temperatures. Aliquots of solution were taken at predetermined time intervals. The amount of copper was determined by atomic absorption spec-

trometry using Varian Spectra AA55 atomic absorption spectrometer. Specific quantity of binded Cu^{2+} (X) was determined according to (1):

$$X = \frac{C_0 - C_i}{m} V \qquad (1)$$

where C_0 is the Cu^{2+}-concentration of the starting copper solution and C_i is the Cu^{2+} concentration at time t, V is the volume of the Cu^{2+} solution, and m is the hydrogel sample mass.

Determination of the degree of bound Cu²⁺ (α): degree of bound Cu^{2+} (α) was determined according to eq. (2):

$$\alpha = X/X_{max}, \qquad (2)$$

where X_{max} is the maximal quantity of bound Cu^{2+}.

Methods used to evaluate kinetics parameters of Cu²⁺ ion binding to PAA hydrogel

Peppas' method [14]: To determine the kinetics parameters of Cu^{2+} ion binding to PAA hydrogel, the results were analyzed applying the linearized form of well-known equation (3):

$$\alpha = kt^n, \qquad (3)$$

where n is an exponent indicative for the mechanism of the process, coefficient k is the apparent release rate and t is the interaction time.

Friedman's differential iso-conversional method [15]: the kinetic analysis of experimental data is based on the rate equation:

$$\frac{d\alpha}{dt} = Af(\alpha)\exp\left(-\frac{E}{RT}\right), \qquad (4)$$

where T is the temperature, A is the pre-exponential factor, E is the apparent activation energy, $f(\alpha)$ is the kinetics model function of the degree of Cu^{2+} ion binding and R is the gas constant. The logarithm form of equation (4) leads to:

$$\ln\frac{d\alpha}{dt} = \ln A + \ln f(\alpha) - \frac{E}{RT}. \qquad (5)$$

For $f(\alpha)$ = const, the plot $\ln(d\alpha/dt)$ vs. $1/T$, obtained from conversional curve should be a straight line whose slope allowed to evaluate the apparent activation energy.

RESULTS AND DISCUSSION

Figure 1 presents kinetic curves of isothermal binding of Cu^{2+} to the PAA hydrogel at different temperatures.

At the kinetic curves of isothermal binding of Cu^{2+} to the PAA hydrogel, two characteristic shapes of the changes of the specific quantity of the bound Cu^{2+} with interaction time, i.e. a linear and non-linear ones can be easily observed at all investigated temperatures. The interaction temperature increase, especially for $T \geq 30°C$, leads to an abrupt increase of Cu^{2+} bound to PAA hy-

drogel and the duration of the linear changes of the bound Cu^{2+} also increase.

Figure 2 presents the isothermal dependence of $\ln\alpha$ vs. $\ln t$.

As can be seen from the Fig. 2, the plot of $\ln\alpha$ vs. $\ln t$ for all the temperatures gave straight lines in the limited ranges of the investigated release process, which is called the range of applicability (α_{ap}). From the plot of $\ln\alpha$ vs. $\ln(t)$ (Fig. 3) the kinetic parameters, n and k, were calculated for corresponding range of applicability (α_{ap}).

Table 1 presents the results of the temperature influence on the results obtained for the parameters (n and k) determined applying the so called "Peppas" eq. (3), the ranges of applicability for the determined parameters, as well as the values of E_a and $\ln A$ which were calculated based on them.

As can be seen from the results presented in Table 1, the temperature increase has no important influence on the range of applicability of Peppas' equation applied to Cu^{2+} binding to the PAA hydrogel, while constant k increase. The exponential constant n, which is indicative for the mechanism of the Cu^{2+} binding to the PAA hydrogel, is for $T \leq 30°C$ equal to 0.5, but for $T \geq 30°C$ increase as the temperature increase.

Bearing in mind that the Peppas' equation can be applied in limited stages of the investigated process of the Cu^{2+} binding to the PAA hydrogel, a new method that is so called "method of the reduced time" [16] was applied to determine the kinetic model of the Cu^{2+} binding to the PAA hydrogel. According to that method, the kinetic model Cu^{2+} binding to the PAA was determined by comparison (graphical and analytical) of the experimentally obtained function for investigated Cu^{2+} binding to the PAA hydrogel $\alpha_e = f(t_N)$, with the curves of the theoretical functions $\alpha = f(t_N)$, for different solid state reaction models [16]. There t_N is the so-called reduced time:

$$t_N = t/t_{0.9}, \qquad (6)$$

where $t_{0.9}$ is the interaction time at $\alpha = 0.9$.

The kinetics models used for the determination of the model best describing the kinetics of the MEPBA release process from PAA–co–MA hydrogel is shown in Table 2.

Based on the obtained results, it was found that the investigated process of Cu^{2+} binding to PAA at temperatures below $30°C$ might be well-described with the model of one dimensional diffusion (D1) and with the model of second order (F2) for temperatures above $30°C$. Figures 3 and 4 present dependences of α^2 on interacting time (for temperatures below $30°C$) and $1/(1 - \alpha)$ on interacting time (for temperatures above $35°C$), respectively.

As usually, the rate constant for the presented process of Cu^{2+} binding were determined and their changes with temperature are presented in Table 3.
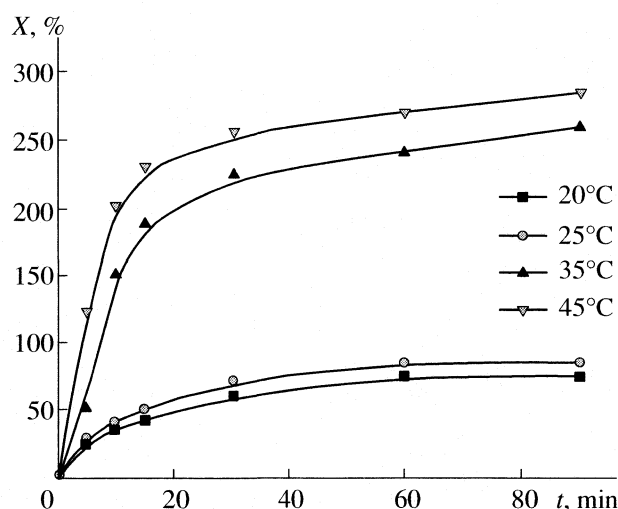
Fig. 1. Isothermal kinetics curves of Cu^{2+} binding to the PAA hydrogel.
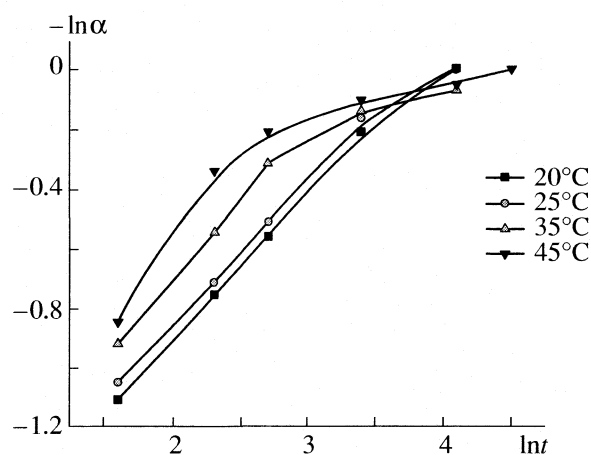
Fig. 2. A plot of $\ln\alpha$ versus $\ln t$ for Cu^{2+} binding to the PAA hydrogel.
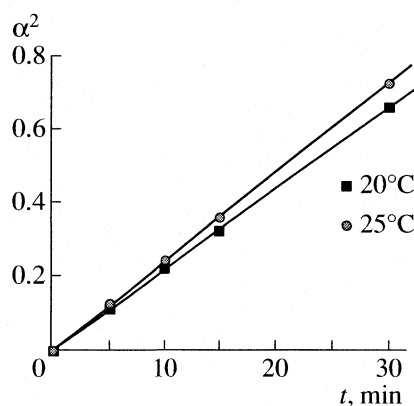
Fig. 3. A plot of α^2 from time.

Table 1. The temperature influence on the kinetics parameters (n and k), corresponding α_{ap} and calculated E_a and $\ln A$ for Cu^{2+} binding to the PAA hydrogel

T, °C	α_{ap}	$-k$, min^{-1}	n	E_a, kJ/mol	$\ln A$
20	0.3–0.81	1.91	0.5	4.14	4.96
25	0.3–0.85	1.85	0.5		
35	0.4–0.81	1.80	0.55		
45	0.4–0.81	1.77	0.59		

Kinetics parameters (E_a and $\ln A$) of the process of isothermal binding of Cu^{2+} to the PAA are determined by applying Arrhenius equation and the calculated values are presented in column 3 and 4. According to the obtained results for the kinetics of process of isothermal binding of Cu^{2+} to the PAA, different kinetics models appear to have a limited range of applicability and give different values for the kinetics parameters. The Friedman's isoconversion methods was applied to determine dependence of E_a and $\ln A$ on the degree of bound Cu^{2+} (α). Because the changes of E_a with the changes of α follow the functional dependence of $\ln A$ with α according to the eq. (7) (compensation effect):

$$\ln A_\alpha = -2.32 + 0.364 E_{a,\,\alpha}, \qquad (7)$$

we can state in agreement with Vyzovkin et al. [17, 18] that process of isothermal Cu^{2+} binding to the PAA hydrogel may be described with the model of two independent first-order reactions at two well defined adsorptions centers whose ratio in the kinetics of the process changes with the changes of the degree of bound Cu^{2+} at PAA hydrogel.

To determine activation energy of the activation centers we use the following theoretical model.

Let us assume that due to the different energies of the adsorption centers there exists the distribution of the active centers, than function of the distribution of the probability values of activation energies ($f(E)$) could be defined. Because the kinetics of Cu^{2+} bonding could be described with the model of first order reaction, than we can propose that the following is valid:

$$\alpha = 1 - \int_0^\infty \Phi\,(E,\,T)f(E)dE, \qquad (8)$$

where $\Phi(E, T)$ is equat to

Table 2. The set of the kinetics models used for determination the kinetics model of MEPBA release process from PAA-co-MA hydrogel

Model	Kinetics mechanism	General.expression of kinetics model, $f(\alpha)$	Integral form of kinetics model, $g(\alpha)$
P1	Power law	$4\alpha^{3/4}$	$\alpha^{1/4}$
P2	Power law	1	$\alpha^{1/3}$
P3	Power law	$2\alpha^{1/2}$	$\alpha^{1/2}$
P4	Power law	$2/3\alpha^{-1/2}$	$\alpha^{3/2}$
R1	Zero-order (Polany-Winger equation)	1	α
R2	Phase-boundary controlled reaction (contracting area, i.e., bidimensional shape)	$2(1-\alpha)^{1/2}$	$[1-(1-\alpha)^{1/2}]$
R3	Phase-boundary controlled reaction (contracting volume, i.e., tridimensional shape)	$3(1-\alpha)^{2/3}$	$[1-(1-\alpha)^{1/3}]$
F1	First-order (Mampel)	$(1-\alpha)$	$-\ln(1-\alpha)$
F2	Second-order	$(1-\alpha)^2$	$(1-\alpha)^{-1}$
F3	Third-order	$(1-\alpha)^3$	$0.5[(1-\alpha)^{-2}-1]$
A2	Avrami-Erofe'ev	$2(1-\alpha)[-\ln(1-\alpha)]^{1/2}$	$[-\ln(1-\alpha)]^{1/2}$
A3	Avrami-Erofe'ev	$3(1-\alpha)[-\ln(1-\alpha)]^{2/3}$	$[-\ln(1-\alpha)]^{1/3}$
A4	Avrami-Erofe'ev	$4(1-\alpha)[-\ln(1-\alpha)]^{3/4}$	$[-\ln(1-\alpha)]^{1/4}$
D1	One-dimensional diffusion	$1/2\alpha$	α^2
D2	Two-dimensional diffusion (bidimensional particle shape)	$1/[-\ln(1-\alpha)]$	$(1-\alpha)\ln(1-\alpha)+\alpha$
D3	Three-dimensional diffusion (tridimensional particle shape) Jander equation	$3(1-\alpha)^{2/3}/2[1-(1-\alpha)^{1/3}]$	$[1-(1-\alpha)^{1/3}]^2$
D4	Three-dimensional diffusion (tridimensional particle shape) Ginstling-Brounshtein equation	$3/2[(1-\alpha)^{-1/3}-1]$	$(1-2\alpha/3)-(1-\alpha)^{2/3}$
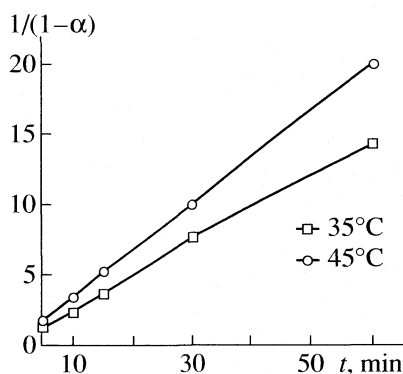
Fig. 4. A plot of $1/(1 - \alpha)$ from time.

$$\Phi(E, T) = \exp\left(-A_0 \int_0^T \exp\left(-\frac{E}{RT}\right) dT\right). \qquad (9)$$

By using a variable $x = E/RT$, eq. (9) is rewritten as follows:

$$\Phi(E, T) =$$

$$= \exp\left\{-\frac{A_0 E}{R}\left(\frac{e^{-x}}{x} - \int_x^\infty \frac{e^{-x}}{x} dx\right)\right\} = \exp\left\{-\frac{A_0 E}{R} p(x)\right\}, \qquad (10)$$

where $p(x)$ is the so called "p-function" that is well known in the field of thermal analysis. By employing an approximation $p(x) = e^{-x}/x^2$, we can write that

$$\Phi(E, T) = \exp\left[-\frac{A_0 RT^2}{E} \exp\left(-\frac{E}{RT}\right)\right]. \qquad (11)$$

To estimate the $f(E)$ curve from the experimental data of α vs. time the possibility of approximate representation for eq. (8) was examined. Since the $\Phi(E, T)$ function changes rather steeply with E at a given temperature, it seems to be allowable to assume $\Phi(E, T)$ by step function U at an activation energy $E = E_s$ as:

$$\Phi(E, T) = U(E - E_s). \qquad (12)$$

This approximation corresponds to assumption only single reaction whose activation energy is E_s at a given temperature T. Then eq. (8) is simplified to:

$$\alpha = 1 - \int_{E_s}^\infty f(E) dt. \qquad (13)$$

According to eq. (13) we can write that:

$$\alpha = 1 - \int_0^{E_s} f dE. \qquad (14)$$
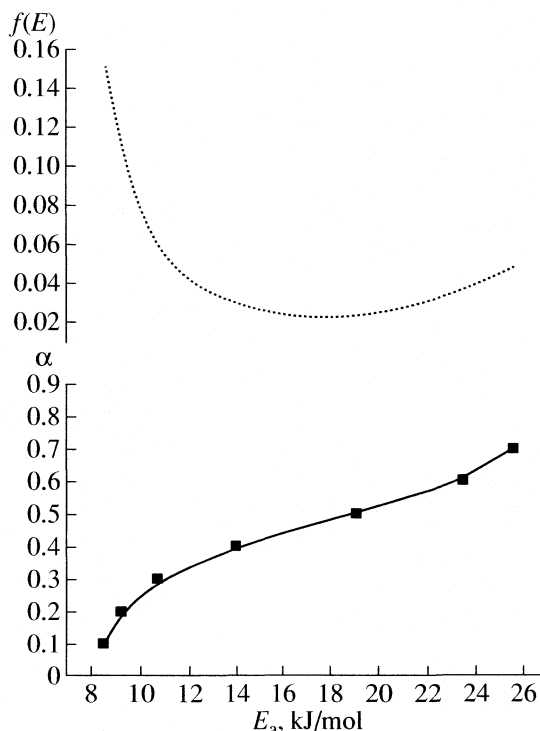
Fig. 5. A plot of degree of Cu^{2+} binding to PAA hydrogel (α) vs. single reaction activation energy (E) and its density distribution function $f(E)$.

Therefore, $f(E_s)$ is given by differentiating eq. (13) by E_s as:

$$f(E_s) = d\alpha/dE_s. \qquad (15)$$

Therefore, the density function of the distribution of the probability of activation energies could be directly obtained from the experimentally determined relationship: α vs. E, by its differentiating, i.e. $f(E) = d\alpha/dE$. Figure 5 presents dependences of isothermal binding of Cu^{2+} to PAA hydrogel (α) vs. single reaction activation energy (E) and corresponding function of the density distribution $f(E)$.

The function of the density distribution of the probability of activation energy shows two well-signed maxima for values of E_a at 9 kJ/mol and 26 kJ/mol. The last E_a value is in good correspondence with E_a value for saturation rate of the Cu^{2+} binding to the PAA hydrogel.

Table 3. Model constants of the Cu^{2+} binding rate

T, °C	k, min^{-1}	E_a, kJ/mol	ln$A$
20	0.022	10.45	0.48
25	0.024		
35	0.250	25.67	8.65
45	0.350		

CONCLUSIONS

The investigated process of isothermal binding of Cu^{2+} to PAA hydrogel at temperatures below 30°C is a complex kinetic process that can be described with two independent reactions which occurred at two well-defined adsorption centers at PAA hydrogel.

It was found that at temperatures $T \leq 30°C$ the dominant influence on the kinetics of the process has Cu^{2+} diffusion to the active centers (with $E_a = 9$ kJ/mol) and at $T \geq 30°C$ and the degree of bound Cu^{2+}, $\alpha \geq 0.2$ the dominant influence has the kinetics of the interaction of Cu^{2+} from the adsorption center with $E_a = 26$ kJ/mol.

The function of the density distribution of the probability of activation energy shows two well signed maxima for values of E_a at 9 kJ/mol and 26 kJ/mol. The last E_a value is in good correspondence with E_a value for saturation rate of the Cu^{2+} binding to the PAA hydrogel.

ACKNOWLEDGEMENTS

REFERENCES

1. D. K. Hale, *Methods or Processing of Extracting a Solute from a Solution*, British Patent 738.500, 1955.
2. A. G. Andreopulus, Eur. Polym. J. **25(9)**, 977 (1989).
3. M. J. F. Zirnhelt, J. P. Leory, Y. Brunette. Sci & Technolgy, **28**, 2419 (1993).
4. E. H. Rifi, F. Rastegar, J. P. Brunette, Talanta, **42(6)**, 811 (1995).
5. I. Katime, E. Rodriguez, J. Macromol. Sci.-Pure. Appl. Chem., **A38(5 & 6)**, 543 (2001).
6. H. Kaşgöz; S. Özgümüş; M. Orbay, Polymer, **42**, 7497 (2001).
7. H. Kaşgöz; S. Özgümüş; M. Orbay, Polymer, **44**, 1785 (2003).
8. H. Kaşgöz, Polymer Bulletin **56**, 517 (2006).
9. W. Li; H. Zhao; P. R. Teasdole; R. John; S. Zhang, Reactive & Functional Polymer, **52**, 31 (2002).
10. N. A. Peppas; A. G. Mikos, *"Hydrogels in Medicine and Pharmacy"*, Vol. **I**: *Fundamentals*, CRC Press, Boca Raton, Florida, p. 2–23, 1986.
11. B. D. Ratner; A. S. Hoffman, in *"Hydrogels for Medical and Related Applications"*, Andrade and Andrade, eds., American Chemical Society, Washington DC, p. 1–36, 1976.
12. J. Jovanović, B. Adnadjević, S. Ostojić, M. Kicanović, Mater. Sci. Forum, **453–454**, 543 (2004).
13. J. Jovanović, B. Adnadjević, Poll. Bull. **58**, 243 (2007).
14. N. Peppas. Pharm. Acta. Helv **60(4)**, 110 (1985).
15. H. L. Friedman, J. Polym. Sci., Part **C6**, 183 (1963).
16. M. E. Brown, D. E. Dollimore, A. K. Galwey, *Reactions in the solid state, Comprehensive chemical kinetics*, Vol. **22**, Elsevier pp. 87–91, 1980.
17. S. Vyzovkin; C. A. Wight. Thermochimica Acta, **53**, 340 (1999).
18. S. Vyazovkin, W. Linert, Int. Rev. Phys. Chem. **14**, 355 (1995).

THE STATE SPACE OF A MODEL FOR THE OSCILLATING BRAY-LIEBHAFSKY REACTION

© 2007   G. Schmitz*, Lj. Kolar-Anić**

*Université Libre de Bruxelles, Faculté des Sciences Appliqués, CP165/63, Av. F. Roosevelt 50, 1050 Bruxelles, Belgium
**University of Belgrade, Faculty of Physical Chemistry, P.O. Box 137, Studensky trg 12–16, YU-11001 Belgrade, Serbia
E-mail: <gschmitz@ulb.ac.be>

Abstract – It is known from a long time that the decomposition of hydrogen peroxide catalyzed by hydrogen and iodate ions, the Bray-Liebhafsky reaction, can give oscillations in a batch reactor. Recently, mixed-mode oscillations and chaos were also observed in a CSTR. The model we had proposed to explain the kinetics in a batch reactor can as well simulate these new complex behaviours. Time series give only a limited view of the features of the calculated behaviours and more information is obtained studying the properties of the state space. We use projections of the trajectories, calculation of the correlation dimension of the attractor, Poincaré sections, and return maps. As the state space of the model is six-dimensional, we try to answer two questions: Do the projections into a $3D$ subspace give correct pictures of the real trajectories? Have we reasons to prefer a special subspace?

INTRODUCTION

The decomposition of hydrogen peroxide in the presence of hydrogen and iodate ions, known as the Bray-Liebhafsky oscillatory reaction [1, 2], is the result of two complex pathways in which hydrogen peroxide acts either as Reducing (R) or Oxidizing (O) agent.

$$2IO_3^- + 2H^+ + 5H_2O_2 \longrightarrow I_2 + 5O_2 + 6H_2O \quad \text{(R)}$$

$$I_2 + 5H_2O_2 \longrightarrow 2IO_3^- + 2H^+ + 4H_2O. \quad \text{(O)}$$
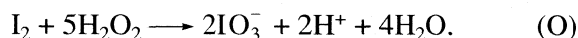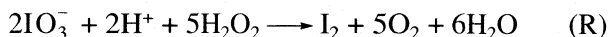
The dynamics of this reaction has been studied extensively in batch reactors [3–9] and its main features can be simulated by the model we have proposed [10–13]. Recently, complex oscillations and chaos were also observed experimentally in a continuous well-stirred tank reactor (CSTR) [14–16] and simulated numerically using the same model [17, 18]. Fig. 1 gives examples of calculated behaviours at different specific flow rates j_0 (total volume flow divided by the reactor volume). However, such time series give only a limited view of the features of the calculated behaviours, simple oscillations, mixed-mode oscillations or chaos. In order to obtain more information, identify fundamental properties and compare them with other known systems, we have to use other representations and different tools. This work discusses $3D$ views, calculations of the correlation dimension, Poincaré maps and relation between phenomena in three and more than three dimensions.

The composition of a system can be represented as a point in the space of the concentrations, called the state space, and its evolution with time as the trajectories of this point. The number of dimensions of this space is the number of concentrations. Periodic oscillations give closed curves and aperiodic oscillations give unclosed curves known as chaotic attractors. Such representations help in analyzing the structure of the state space, identifying attracting and repelling regions in transient regime, revealing common properties of sets of trajectories, and visualizing the shape of attractors. Fig. 2 shows trajectories corresponding to the time series in Fig. 1. For $j_0 = 4.825 \times 10^{-3}$ min^{-1}, Fig. 1a suggests that we have simple oscillations but Fig. 2a reveals that, instead of a limit cycle, we have a chaotic attractor discussed in details later. Fig. 2b and 2d show two examples of mixed-mode oscillations, several large amplitude oscillations separated by one small amplitude oscillation or several small ones separated by a large one. Fig. 2c illustrates a chaotic window in the region of mixed-mode oscillations. These $3D$ views are more informative than the time series but still insufficient to understand the dynamics of the system. A problem comes from the dimension of the state space. The mechanism of reactions (R) and (O) is not simple and beside the chemical species IO_3^-, H^+, H_2O_2 and I_2 we have, at least, four intermediate species, I^-, IOH, IO_2H and I_2O. Thus, the state space has more than three dimensions and Fig. 2 shows only projections of the trajectories into a $3D$ subspace. We shall try to answer two questions: Do these projections give correct pictures of the real trajectories? Do we have reasons to prefer a special subspace?

MODEL

Our model is given in Table and its dynamics is described by the six differential equations hereafter. Iodate and acid are in large excess and their concentrations were maintained constant, $[IO_3^-] = 0.0474$ and

$[I_2] \times 10^4$
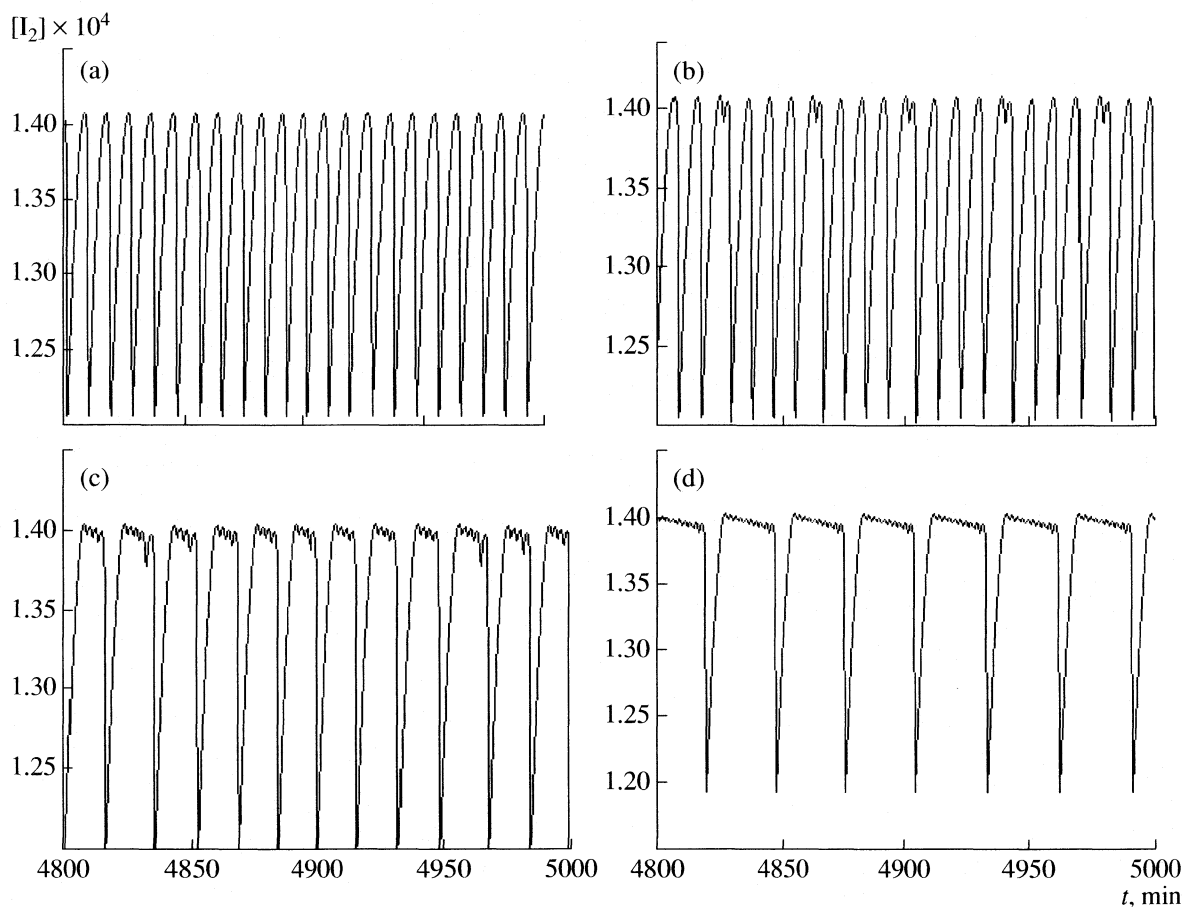
Fig. 1. Time series for $j_0 = 4.825 \times 10^{-3}$ (a), 4.828×10^{-3} (b), 4.9466×10^{-3} (c) and 5.02×10^{-3} min^{-1} (d).

$[H^+] = 0.0958$ mol/dm^3. Adding two differential equations to account for their temporal evolution does not alter the dynamics of the system, but only slightly shifts the position of the bifurcation points [17]. The hydrogen peroxide in the input flow was $[H_2O_2]_{in} = 0.155$ mol/dm^3. Calculations were performed using the MATLAB program package as explained previously [18]:

$$d[H_2O_2]/dt = -r_5 - r_6 - r_7 - r_8 + j_0([H_2O_2]_{in} - [H_2O_2]),$$

$$d[I_2]/dt = r_4 - j_0[I_2],$$

$$d[I^-]/dt = -r_1 - r_2 - r_4 + r_5 - j_0[I^-],$$

$$d[HIO]/dt = r_1 + 2r_3 - r_4 - r_5 + r_6 - j_0[HIO], \tag{1}$$

$$d[HIO_2]/dt = r_1 - r_2 + r_6 - r_7 + r_8 - j_0[HIO_2],$$

$$d[I_2O]/dt = r_2 - r_3 - r_6 - j_0[I_2O],$$

Model of the Bray-Liebhafsky reaction

Reactions	Rate constants*	no.
$IO_3^- + I^- + 2H^+ \rightleftharpoons HIO + HIO_2$	$k_1 = 3.18 \times 10^5$; $k_{-1} = 7.91 \times 10^7$	(R1, R-1)
$HIO_2 + I^- + H^+ \longrightarrow I_2O + H_2O$	$k_2 = 5.0 \times 10^{11}$	(R2)
$I_2O + H_2O \rightleftharpoons 2HIO$	$k_3 = 5.0 \times 10^3$; $k_{-3} = 3.15 \times 10^8$	(R3, R-3)
$HIO + I^- + H^+ \rightleftharpoons I_2 + H_2O$	$k_4 = 3.0 \times 10^{11}$; $k_{-4} = 4.5$	(R4, R-4)
$HIO + H_2O_2 \longrightarrow I^- + H^+ + O_2 + H_2O$	$k_5 = 1.20 \times 10^4 + 3.0 \times 10^{4*}$ [H$^+$]	(R5)
$I_2O + H_2O_2 \longrightarrow HIO + HIO_2$	$k_6 = 5.0 \times 10^5$	(R6)
$HIO_2 + H_2O_2 \longrightarrow IO_3^- + H^+ + H_2O$	$k_7 = 2.0 \times 10^3$	(R7)
$IO_3^- + H^+ + H_2O_2 \longrightarrow HIO_2 + O_2 + H_2O$	$k_8 = 9.5 \times 10^{-4} + 3.92 \times 10^{-2*}$ [H$^+$]	(R8)

* We keep the units mol · dm^{-3} and min used in the previous papers [11–13].
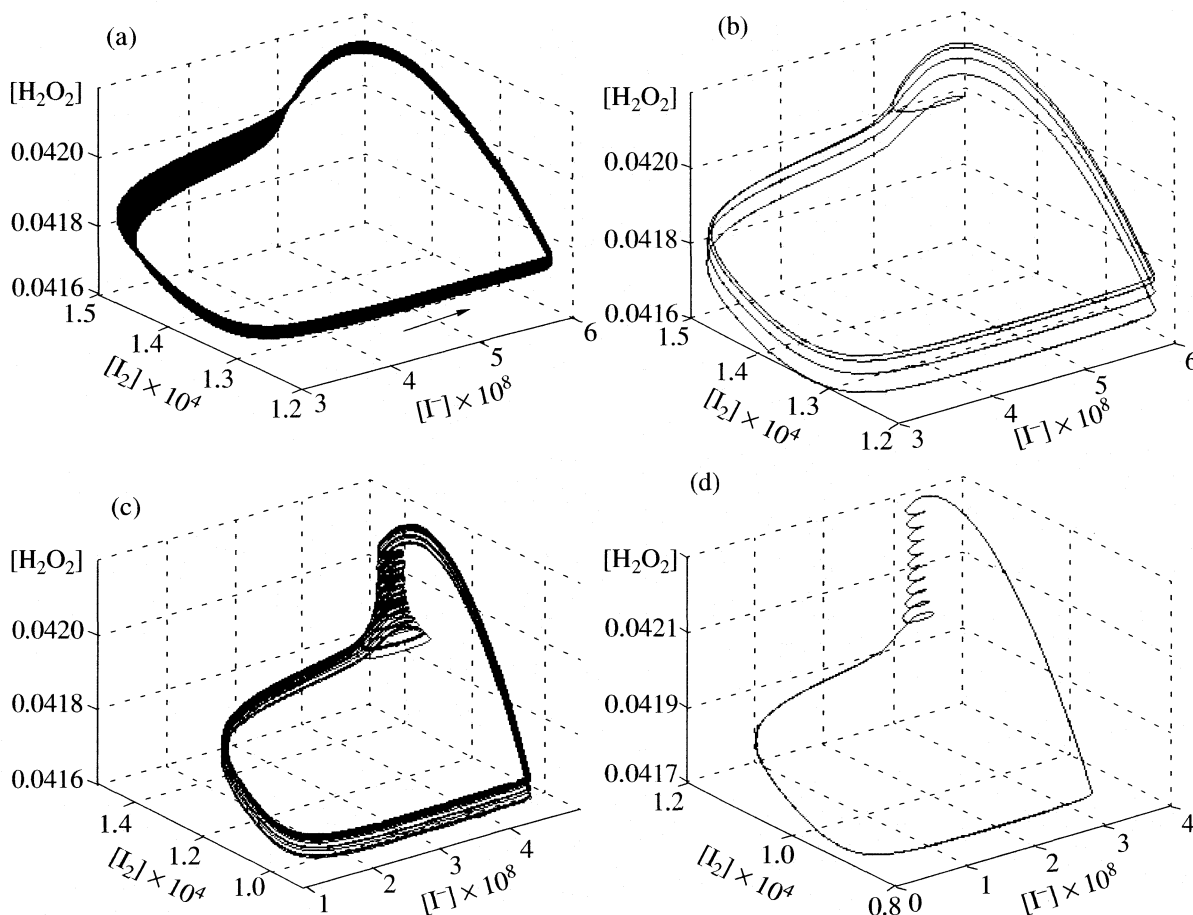
Fig. 2. $3D$ projections of the trajectories in the $6D$ state space for the same j_0 values as in Fig. 1.

where $[H_2O_2]_{in}$ is the hydrogen peroxide concentration in the input flow and

$$r_1 = k_1[IO_3^-][I^-][H^+]^2 - k_{-1}[HIO][HIO_2],$$

$$r_2 = k_2[HIO_2][I^-][H^+],$$

$$r_3 = k_3[I_2O] - k_{-3}[HIO]^2,$$

$$r_4 = k_4[HIO][I^-] - k_{-4}[I_2]/[H^+],$$

$$r_5 = k_5[HIO][H_2O_2],$$

$$r_6 = k_6[I_2O][H_2O_2],$$

$$r_7 = k_7[HIO_2][H_2O_2],$$

$$r_8 = k_8[IO_3^-][H_2O_2].$$

This model simulates a number of periodic and aperiodic dynamic states under CSTR conditions discussed in our previous publication [18]. Some other examples are shown in Figs. 1 and 2. With increasing the flow rate, a Hopf bifurcation point, simple large oscillations, mixed mode oscillations with an increasing ratio between the numbers of small and large amplitude oscillations, simple small oscillations and a reverse Hopf bifurcation are observed. In the region of mixed-mode

oscillations, period-doubling sequences lead to chaotic windows. Chaotic mixtures of mixed-mode patterns were also found.

RESULTS AND DISCUSSION

Correlation dimension

Periodic trajectories are $1D$ objects and their projections from a $6D$ state space into a $3D$ subspace don't raise special problems. This is not so for chaotic attractors like those in Figs. 2a and 2c. To characterize them we have calculated their fractal dimension, or more precisely one of their fractal dimensions [19], the correlation dimension introduced by Grassberger and Procaccia [20]. They take N trajectory points and count the fraction $p_i(R) = N_i/(N - 1)$ of these points within a distance R of a given point i. (The expression is divided by $N - 1$ since there are at most $N - 1$ other points in the neighbourhood of the point i.) Then, they calculate the correlation sum defined as

$$C(R) = \frac{1}{N}\sum_{i=1}^{N} p_i(R),$$
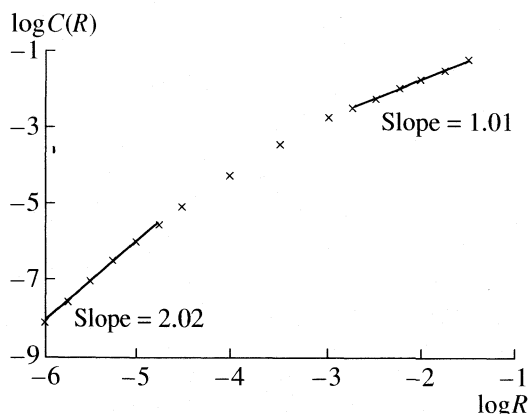
Fig. 3. Correlation sum and correlation dimension for the chaotic attractor of Fig. 2a.

$C(R)$ would be proportional to R if the trajectory points were located on a line and proportional to R^2 if they were located on a surface. This suggest the definition of the correlation dimension as the number D_c that satisfies

$$C(R) = \lim_{R \to 0} kR^{D_c}.$$

In practice, it is impossible to calculate the limit for $R \longrightarrow 0$ because the number of points used to calculate $C(R)$ is finite and there is some minimum distance between them. When R is less than this minimum $C(R)$ is equal to zero. The best that can be done is to plot $\log(C(R))$ as a function of $\log(R)$, look for a linear relation at small R values and take the slope as D_c. Figure 3 shows a typical example of the correlation sums calculated for chaotic attractors obtained with our model. To avoid scaling problems, these calculations use the dimensionless form of the kinetic equations discussed below. When R is not much smaller than the size of the attractor, the slope of the plot is just a little larger than one. When R decreases, it increases and tends to about two. These results, obtained in the $6D$ state space, support the geometrical picture given by the $3D$ projections. The trajectory remains close to the periodic orbits obtained at slightly different j_0 values, which is one-dimensional, and the correlation sums at the higher R values are not very different from the correlation sums for these periodic orbits. The fractal dimension can only be obtained when R is much smaller than the thickness of the attractor. Then, the number of pairs of points in the calculation of D_c is significant only if N is very large and the precision becomes limited by the calculation times. The obtained information is nevertheless very enlightening: the dimension of the chaotic attractor is close to two. It is a thin band in the $6D$ state space and its projection in $3D$ subspaces could distort it but preserves this fundamental property.

Poincaré sections

To characterize trajectories in $3D$ state spaces it is useful to make Poincaré sections, i.e. to study their intersections with a half plane. If the Poincaré plane is correctly selected, a simple limit cycle gives just an intersection point, complex oscillations give a finite number of points, quasi-periodic oscillations on a torus give a closed curve and a chaotic attractor gives more or less complicated structures of points in the plane. However, in our $6D$ state space, the Poincaré "plane" has five dimensions and we can only see projections of the Poincaré sections. They are nevertheless useful. Figure 4a shows sections of the attractor in Fig. 2a projected in the subspace $[H_2O_2]$–$[I_2]$. They reveal a feature of the attractor not observable in this figure, the attractor has the shape of a folded strip and its Poincaré sections are nearly lines. As the intersection of an attractor of dimension D_a with a Poincaré plane has $D_a - 1$ dimensions, the Poincaré sections in Fig. 4a indicate that D_a is close to two, in accordance with the correlation dimension calculations. Actually, for any chaotic attractor D_a must be larger than two and zooms on other projections of the Poincaré section reveal that it is a "thick" line.

Poincaré sections don't only help to build geometrical representations of attractors; they also give information about the motion on it through return maps. The values of $[H_2O_2]$ at the intersections points in Fig. 4a are plotted in Fig. 4b as a function of the preceding values giving the first return map $[H_2O_2]_{n+1} = F_{H_2O_2}([H_2O_2]_n)$. In the general case of j concentrations, they are j functions represented in vectorial form by $\mathbf{X}_{n+1} = \mathbf{F}(\mathbf{X}_n)$ where $\mathbf{X} = \{X_1...X_j\}$. The theorem of existence and uniqueness of the trajectories imply the existence of these functions. They simplify greatly the description of the system's dynamics and still contain important information about it [19]. The example in Fig. 4b shows a surprising simplification: $[H_2O_2]_{n+1}$ depends only on $[H_2O_2]_n$ and not on the other concentrations allowing comparisons of the behaviour of this complicated system with well known one-dimensional maps. At the crossing point between the return map and the diagonal line $[H_2O_2]_{n+1}$ is equal to $[H_2O_2]_n$. This point is the intersection with the Poincaré plane of a period-one closed orbit, which must be unstable. Actually, a chaotic attractor is associated with an infinite number of closed orbits of any order. Important properties of the attractor can be extracted from these orbits [21–24]. The return map for $[I_2]$ in Fig. 4c seems also one-dimensional but with two branches giving two $[I_2]_{n+1}$ values for one $[I_2]_n$ value, which seems to be in contradiction with the uniqueness of the solutions of the differential equations. A closer look at the results shows that there is no contradiction because the $[H_2O_2]$ values are different on the two branches. The period-one unstable orbit crosses the Poincaré plane at point O near $[I_2]_{n+1} = [I_2]_n = 1.20644 \times 10^{-4}$ and $[H_2O_2]_{n+1} = [H_2O_2]_n = 0.041778$. At the other crossing point with

Fig. 5. Mixed-mode oscillations on a folded slow manifold.

the diagonal line $[H_2O_2]_{n+1}$ and $[H_2O_2]_n$ have different values and we have no periodic orbit. In conclusion, Poincaré sections and return maps reduce the study of the main features of our $6D$ system to the study of $2D$ maps for $[H_2O_2]$ and $[I_2]$. We now show why and when this reduction is possible.

Dimensionless kinetic equations

The kinetic equations (1) describing the dynamics of our model can be transformed into the useful dimensionless form (2) as explained in the annex

$$c_1 dy_1/d\tau = -\rho_5 - \rho_6 - \rho_7 - \rho_8 + c_1(1 - y_1) + c_2,$$

$$dy_2/d\tau = \rho_4 - y_2,$$

$$c_3 dy_3/d\tau = -\rho_1 - \rho_2 - \rho_4 + \rho_5 - c_3 y_3,$$

$$c_4 dy_4/d\tau = \rho_1 + 2\rho_3 - \rho_4 - \rho_5 + \rho_6 - c_4 y_4,$$

$$c_5 dy_5/d\tau = \rho_1 - \rho_2 + \rho_6 - \rho_7 + \rho_8 - c_5 y_5,$$

$$c_6 dy_6/d\tau = \rho_2 - \rho_3 - \rho_6 - c_6 y_6. \tag{2}$$

The y_i are the ratios between the actual concentrations $[H_2O_2]$, $[I_2]$, $[I^-]$, $[IOH]$, $[IO_2H]$ and $[I_2O]$ and their values at the steady state, the ρ_i are dimensionless forms of the rates r_i and the c_i are dimensionless parameters. Beside the benefit of these dimensionless equations pointed out in the annex, we show here that they throw light on the behaviour of the trajectories. The values of the parameters c_3, c_4, c_5 and c_6 calculated with the rate constants in Table are smaller than 10^{-2}. One consequence of this smallness can be understood considering the simpler system (3) where ε is a small parameter. We suppose that the surface $F_3 = 0$, called the slow manifold, has the folded shape represented in Fig. 5. Its upper and lower part are stable, its middle part is unstable

$$dx_1/dt = F_1(x_1, x_2, x_3),$$

$$dx_2/dt = F_2(x_1, x_2, x_3),$$

$$\varepsilon dx_3/dt = F_3(x_1, x_2, x_3). \tag{3}$$

As ε is small, dx_3/dt remains large until x_3 takes a value such that $F_3(x_1, x_2, x_3)$ is also small. The trajectories ap-

Fig. 4. Poincaré sections in the chaotic attractor of Fig. 2(a) for $[I^-] = 4.5 \times 10^{-8}$ and $d[I^-]/dt < 0$ (upper part) or $d[I^-]/dt > 0$ (lower part) (a) and first return maps for $d[I^-]/dt > 0$ (b and c).

proach quickly the slow manifold and then move slowly on it. When they eventually reach a point at the borderline between its stable and unstable folds, as points A and C in Fig. 5, they jump onto the other stable fold at points B and D. This motion gives normally simple or mixed-mode oscillations. It is also possible that the successive transition points are all different, which gives a chaotic attractor. The no-intersection theorem [19, p. 77] is not violated because the trajectories do not follow exactly the $2D$ slow manifold. However, a consequence of the smallness of ε is that they remain very close to it and the dimension of the chaotic attractor is close to two. The solution of the system (3) is nearly always close to the solution of the simpler system $dx_1/dt = F_1(x_1, x_2, x_3)$, $dx_2/dt = F_2(x_1, x_2, x_3)$ and $F_3(x_1, x_2, x_3) = 0$. The last equation gives the so-called "fast" variable x_3 in function of to the "slow" variables x_1 and x_2. If it is written $x_3 = G(x_1, x_2)$, the approximate equations take the form $dx_1/dt = F_1(x_1, x_2, G(x_1, x_2))$, $dx_2/dt = F_2(x_1, x_2, G(x_1, x_2))$, showing that the main features of the motion are given by the behaviour of x_1 and x_2.

Our system is more complicated but the simplification is similar. There are six variables but only two of them are slow, $[H_2O_2]$ and $[I_2]$. The slow manifold is two-dimensional and the correlation dimension of the chaotic attractor is close to two because c_3, c_4, c_5 and c_6 are small. This reduces the effective dimension of the motion in the $6D$ state space. Let us underline that the slow variables are the concentrations of species appearing in the stoichiometric equations (R) and (O). Looking at the definitions of the small parameters, we see that this is not fortuitous. The return maps for $[H_2O_2]$ and $[I_2]$ are two-dimensional because the motion remains close to the two-dimensional slow manifold. This could help to identify specific properties of our chaotic attractors. However, if many theoretical results have been obtained for one-dimensional maps, bi-dimensional maps are less known, with the noticeable exception of the Hénon map [19]. Further theoretical works would be useful.

As a final comment, we mention that if we use the values of the parameters giving chaos but replace the first equation of our differential system with the "pool approximation" $[H_2O_2]$ = constant, the solutions are simply stable steady states or limit cycles, depending on $[H_2O_2]$. This suggests that at least two slow variables are needed to get chaos and shows the danger of the pool approximation.

CONCLUSION

Our previous work [18] showed that our model for the Bray-Liebhafsky reaction can simulate mixed-mode oscillations and chaos in a CSTR. In this work, we analyze the characteristics of the trajectories. The model involves six concentrations, $[H_2O_2]$, $[I_2]$, $[I^-]$, $[IOH]$, $[IO_2H]$ and $[I_2O]$, and the trajectories are located in a $6D$ state space. However, correlation dimensions calcu-

lations and Poincaré sections reveal that the chaotic attractors remain close to $2D$ surfaces. The return maps for $[H_2O_2]$ and $[I_2]$ are bi-dimensional. The dimensionless form of the kinetic equations explains this reduction of the number of effective dimensions. The four variables $[I^-]$, $[IOH]$, $[IO_2H]$ and $[I_2O]$ are "fast" variables and the trajectories are strongly attracted by a $2D$ slow manifold. The main features of the dynamics are found out in the behaviour of the "slow" variables, $[H_2O_2]$ and $[I_2]$, and we do have reasons to prefer subspaces including these variables. Models in chemical kinetics often lead to this particular kind of autonomous equations with several "fast" variables and only a few "slow" variables. Writing them in a dimensionless form should reveal the distinction between these two kinds of variables and the associated simplifications. We suggest a link with the chemical intuition: the slow variables are those appearing in the stoichiometric equations.

ANNEX: KINETIC EQUATIONS IN DIMENSIONLESS FORM

A convenient form of the kinetic equations (1) is obtained replacing the concentrations with the ratios between their actual values and their values at the steady state:

$$y_1 = [H_2O_2]/[H_2O_2]_{ss}; \quad y_2 = [I_2]/[I_2]_{ss}; \quad y_3 = [I^-]/[I^-]_{ss};$$

$$y_4 = [HIO]/[HIO]_{ss}; \quad y_5 = [HIO_2]/[HIO_2]_{ss};$$

$$y_6 = [I_2O]/[I_2O]_{ss}.$$

The concentrations $[\ldots]_{ss}$ at the steady state are solutions of the following equations derived from the six equations $d[\ldots]_{ss}/dt = 0$:

$$j_0([H_2O_2]_{in} - [H_2O_2]_{ss}) = (k_5[HIO]_{ss} + k_6[I_2O]_{ss} +$$

$$+ k_7[HIO_2]_{ss} + k_8[IO_3^-][H^+])[H_2O_2]_{ss},$$

$$j_0[I_2]_{ss} = k_4[HIO]_{ss}[I^-]_{ss}[H^+] - k_{-4}[I_2]_{ss},$$

$$j_0(2[I_2]_{ss} + [I^-]_{ss} + [HIO]_{ss} + [I_2O]_{ss}) =$$

$$= k_3[I_2O]_{ss} - k_{-3}[HIO]_{ss}^2,$$

$$j_0(2[I_2]_{ss} + [I^-]_{ss} + [HIO]_{ss} + 2[I_2O]_{ss}) =$$

$$= k_2[HIO_2]_{ss}[I^-]_{ss}[H^+] - k_6[I_2O]_{ss}[H_2O_2]_{ss},$$

$$j_0(2[I_2]_{ss} + [I^-]_{ss} + [HIO]_{ss} + [HIO_2]_{ss} + 2[I_2O]_{ss}) =$$

$$= k_1[IO_3^-][I^-]_{ss}[H^+]^2 - k_{-1}[HIO]_{ss}[HIO_2]_{ss} -$$

$$- k_7[HIO_2]_{ss}[H_2O_2]_{ss} + k_8[IO_3^-][H^+][H_2O_2]_{ss},$$

$$j_0(5[I_2]_{ss} + 3[I^-]_{ss} + 2[HIO]_{ss} +$$

$$+ [HIO_2]_{ss} + 4[I_2O]_{ss}) =$$

$$= (k_5[HIO]_{ss} - k_6[I_2O]_{ss} - k_7[HIO_2]_{ss} +$$

$$+ k_8[IO_3^-][H^+][H_2O_2]_{ss}.$$

These equations have no explicit solution but can be solved by an iterative method. Beside the used solution in the region of the state space were we get the oscillations, there is another solution, always unstable, given by

$$[I_2]'_{ss} = [I^-]'_{ss} = [HIO]'_{ss} = [I_2O]'_{ss} = 0,$$

$$j_0([H_2O_2]_{in} - [H_2O_2]'_{ss}) =$$

$$= (k_7[HIO_2]'_{ss} + k_8[IO_3^-][H^+])[H_2O_2]'_{ss},$$

$$j_0[HIO_2]'_{ss} = (-k_7[HIO_2]'_{ss} + k_8[IO_3^-][H^+])[H_2O_2]'_{ss}.$$

This steady state is not directly related to the oscillations but could be important for the analysis of the structure of the state space. To put the kinetic equations in a dimensionless form, the eleven kinetic constants are replaced with eleven dimensionless parameters. Taking j_0 as the unit of time and $[I_2]_{ss}$ as the unit of concentrations, they are

$$c_1 = [H_2O_2]_{ss}/[I_2]_{ss};$$

$$c_2 = ([H_2O_2]_{in} - [H_2O_2]_{ss})/[I_2]_{ss};$$

$$c_3 = [I^-]_{ss}/[I_2]_{ss};$$

$$c_4 = [HIO]_{ss}/[I_2]_{ss}; \quad c_5 = [HIO_2]_{ss}/[I_2]_{ss};$$

$$c_6 = [I_2O]_{ss}/[I_2]_{ss};$$

$$a_1 = k_{-1}[HIO]_{ss}[HIO_2]_{ss}/(j_0 \times [I_2]_{ss});$$

$$a_2 = k_{-3}[HIO]_{ss}^2/(j_0 \times [I_2]_{ss});$$

$$a_3 = k_{-4}/j_0;$$

$$a_4 = k_7[HIO_2]_{ss}/(j_0 \times [I_2]_{ss});$$

$$a_5 = k_8[IO_3^-][H^+][H_2O_2]_{ss}/(j_0 \times [I_2]_{ss}).$$

Introducing the dimensionless time $\tau = j_0 \times t$ and dimensionless rates of reactions $\rho_i = r_i/(j_0 \times [I_2]_{ss})$, the kinetic equations become

$$c_1 dy_1/d\tau = -\rho_5 - \rho_6 - \rho_7 - \rho_8 + c_1(1 - y_1) + c_2,$$

$$dy_2/d\tau = \rho_4 - y_2,$$

$$c_3 dy_3/d\tau = -\rho_1 - \rho_2 - \rho_4 + \rho_5 - c_3 y_3,$$

$$c_4 dy_4/d\tau = \rho_1 + 2\rho_3 - \rho_4 - \rho_5 + \rho_6 - c_4 y_4,$$

$$c_5 dy_5/d\tau = \rho_1 - \rho_2 + \rho_6 - \rho_7 + \rho_8 - c_5 y_5,$$

$$c_6 dy_6/d\tau = \rho_2 - \rho_3 - \rho_6 - c_6 y_6,$$

where

$$\rho_1 = (2 + c_3 + c_4 + c_5 + 2c_6 + a_1 + a_4 - a_5)y_3 - a_1 y_4 y_5,$$

$$\rho_2 = 0.5(c_2 - 1 - c_3 - c_5 - 2a_4)y_3 y_5,$$

$$\rho_3 = (2 + c_3 + c_4 + c_6 + a_2)y_6 - a_2 y_4^2,$$

$$\rho_4 = (1 + a_3)y_3 y_4 - a_3 y_2,$$

$$\rho_5 = 0.5(5 + c_2 + 3c_3 + 2c_4 + c_5 + 4c_6 - 2a_5)y_1 y_4,$$

$$\rho_6 = 0.5(c_2 - 5 - 3c_3 - 2c_4 - c_5 - 4c_6 - 2a_4)y_1 y_6,$$

$$\rho_7 = a_4 y_1 y_5,$$

$$\rho_8 = a_5 y_1.$$

This form of the kinetic equations gives convenient representations of the state space with unit concentrations at the steady state and uses parameters with a direct chemical meaning: the c_i are ratios of concentrations and a_1 to a_3 are characteristics of the reversibility of reactions (1), (3) and (4). The superiority of these equations is also a result of the smallness of the parameters c_3, c_4, c_5 and c_6 calculated with the rate constants in Table. As long as they remain small, the permanent trajectories are nearly independent on their values. The original system depends on 13 parameters, j_0, $[H_2O_2]_{in}$ and eleven kinetic constants but we don't need to know exactly all these constants. The dynamics of the system depends only on c_1, c_2 and five a_i. The dimensionless equations show which values, or ratios of values, are important and which are not. Moreover, they reduce some numerical problems associated with the stiffness of the classical equations.

REFERENCES

1. W. C. Bray, *J. Am. Chem.* Soc. **43**, 1262 (1921).

2. W. C. Bray and H. A. Liebhafsky, J. Am. Chem. Soc. **53**, 38 (1931).

3. S. D. Furrow, in *Oscillations and Traveling Waves in Chemical Systems*, Ed. by R. J. Field, M. Burger, (J. Wiley, New York, 1985), p. 171.

4. S. Anić, D. Mitić, and Lj. Kolar-Anić, J. Serb. Chem. Soc. **50**, 53 (1985).

5. S. Anić and Lj. Kolar-Anić, Bunsenges Ber., Phys. Chem. **90**, 1084 (1986).

6. S. Anić and Lj. Kolar-Anić, J. Chem. Soc. Faraday Trans. 1 **84**, 3413 (1988).

7. F. G. Buchholtz and S. Broecker, J. Phys. Chem. A **102**, 1556 (1988).

8. S. Anić, D. Stanisavljev, G. Kr. Belovljev, and Lj. Kolar-Anić, Bunsenges Ber., Phys. Chem. **93**, 488 (1989).

9. S. Anić, D. Stanisavljev, Ž. Čupić, M. Radenković, V. Vukojević and Lj. Kolar-Anić, Science of Sintering, **30**, 49 (1998).

10. G. Schmitz, J. Chim. Phys. Chim. Biol. **84**, 957 (1987).

11. Lj. Kolar-Anić and G. Schmitz, J. Chem. Soc. Faraday Trans. **88**, 2343 (1992).

12. Lj. Kolar-Anić, D. Mišljenović, S. Anić and G. Nicolis, React. Kinet. Catal. Lett. **54**, 35 (1995).

13. Lj. Kolar-Anić, Ž. Čupić, S. Anić and G. Schmitz, J. Chem. Soc. Faraday Trans. **93**, 2147 (1997).

14. V. Vukojević, S. Anić and Lj. Kolar-Anić, J. Phys. Chem. A **104**, 10731 (2000).

15. V. Vukojević, S. Anić and Lj. Kolar-Anić, Phys. Chem. Chem. Phys. **4**, 1276 (2002).

16. Lj. Kolar-Anić, V. Vukojević, N. Pejić, T. Grozdić and S. Anić, in *Experimental Chaos*, Ed. by S. Boccaletti, B. J. Gluckman, J. Kurths, L. Pecora, R. Meucci, O. Yordanov, (Melville, New York, American Institute of Physics, AIP Conference Proceedings, Volume 742, 2004), p. 3–8.

17. Lj. Kolar-Anić, T. Grozdić, V. Vukojević, G. Schmitz and S. Anić, in *Selforganization in nonequilibrium sys-*

tems, Ed. by S. Anić, Ž. Čupić and Lj. Kolar-Anić, (Society of Physical Chemists of Serbia, Belgrade, 2004), pp. 115–118.

18. G. Schmitz, Lj. Kolar-Anić, S. Anić, T. Grozdić and V. Vukojević, J. Phys. Chem. A **110**, 10361 (2006).

19. R. C. Hilborn, *Chaos and Nonlinear Dynamics*, Second edition, (Oxford University Press, Oxford, 2000).

20. P. Grassberger and I. Procaccia, Phys. Rev. Lett., **50**, 346 (1983).

21. D. Auerbach, P. Cvitanović, J. P. Eckmann, G. Gunarante and I. Procaccia, Phys. Rev. Lett. **58**, 2387 (1987).

22. P. Cvitanović, Phys. Rev. Lett. **61**, 2729 (1988).

23. Y. C. Lai, Y. Nagai and C. Grebogi, Phys. Rev. Lett. **79**, 649 (1997).

24. R. Gilmore, M. Lefranc, *The Topology of Chaos*, (Wiley, New York, 2002).

CHEMICAL KINETICS
AND CATALYSIS

REMOVAL OF VOLATILE ORGANIC COMPOUNDS FROM ACTIVATED CARBON BY THERMAL DESORPTION AND CATALYTIC COMBUSTION

© 2007   D. Ranković*, Z. Arsenijević**, N. Radić**, B. Grbić**, Ž. Grbavčić***

*Faculty of Physical Chemistry, University of Belgrade, Studentski trg 12–16, 11000 Belgrade, Serbia
**IChTM-Center for Catalysis and Chemical Engineering, Njegoševa 12, 11000 Belgrade, Serbia
***Faculty of Technology and Metallurgy, University of Belgrade, Karnegijeva 4, 11000 Belgrade, Serbia
E-mail: ranko@ffh.bg.ac.yu

Abstract – Thermal desorption of saturated activated carbon, discharged from industrial adsorber, and catalytic oxidation of desorbed products over Pt/Al_2O_3 catalyst have been investigated. The activated carbon are almost completely regenerated by flushing with air at 200°C during 30 min. Desorbed products are fully oxidized over Pt/Al_2O_3 catalyst above the temperature of 275°C.

INTRODUCTION

Volatile organic compounds (VOCs) can be considered as a major source of air pollution, and in many cases, legislation has already been introduced to reduce their emissions. VOCs can be produced from a variety of industrial and commercial processes, including printing, metal decorating, paint drying, metal degreasing, manufacturing of organic compounds and polymers, food processing, etc. [1]. These VOCs have been generally implicated in the formation of photochemical smog and destruction of ozone layer. Incineration, condensation, scrubbing, adsorption or catalytic oxidation can remove VOCs from exhaust gases. Thermal incineration, the most often used method, destroys these compounds by burning them at temperatures higher than 1000°C. These high temperatures generate the formation of undesirable by-products such as nitrogen oxides, dibenzofurans and dioxins. Catalytic oxidation offers high destructive efficiency, lower operating temperature than thermal combustion systems, lower capital costs, and smaller units [1]. This process can be considered as an effective way for reducing VOCs emissions from stationary sources [2–4]. One of the widespread technologies for the removal of low concentrations of VOCs from the air is based on VOCs adsorption on activated carbon (AC), either in the powdered or in granular form [5–7]. The surface characteristics of AC are crucial for adsorption process. The AC microstructure comprises of a cross-linked aromatic sheets with graphite or structured carbons scattered on surfaces randomly [8]. The saturated AC, however, must be regenerated before reuse. The regeneration methods are based either on desorption, induced by increasing temperature or by displacement with a suitable solvent. Desorbed products must be further removed by thermal or catalytic oxidation or by appropriate chemical, electrochemical or microbial processes. Both noble metals and mixed metal oxides can be used as catalysts

for VOCs combustion [9–15]. Noble metals are generally supported on alumina; however, other supports and particularly zeolites can be also used.

Our previous work have been directed to development of combined adsorber – desorber – catalytic reactor system, nominal capacity 3.5 m³/h, using modified spouted bed (i.e. spouted bed with axially inserted draft tube) loaded with activated carbon for xylene removal [16]. Combustion of desorbed organics was conducted in separate catalytic reactor loaded with platinum catalyst.

Within this work investigation of thermal desorption of spent activated carbon, discharged from industrial adsorber, and catalytic oxidation of desorbed products over Pt/Al_2O_3 catalyst, are presented.

EXPERIMENTAL

Activated carbon, type K81/B (Trayal Corporation, Kruševac), in the form of granulate, with mean granule size of 1 mm, was used as a sorbent for the removal of pollutants from industrial waste gasses. Characteristics of AC K81/B are presented in Table 1. Samples used in laboratory investigations were discharged from commercial adsorption unit. Adsorption unit was placed within pesticide production plant and served as control device for VOCs emission.

Catalyst. Characteristics of Pt/Al_2O_3 catalyst are presented in Table 2 [17]. For laboratory investigation, catalyst was ground and grain size of 0.1 to 0.2 mm was used for catalytic combustion of desorbed products from AC.

Apparatus is made of two independently heated reactors, connected in series, presented on Fig. 1. Both reactors are situated within Gas Chromatograph Shimadzu 14-A. The first, desorption reactor, consisted of stainless steel tube, OD 6 mm, ID 4 mm and 115 mm in length. Desorption reactor (3) was placed in the oven

Table 1. Activated carbon (AC K81/B) characteristics

Index in benzene	40–45%	
Specific capacity	$0.3 \, kg_{VOC}/kg_{AC}$	
BET surface area	$1200 \, m^2/g$	
Volume micro pore	$0.45–0.50 \, cm^3/g$	
Cumulative production volume pore	$0.8–1.0 \, cm^3/g$	
Mean size particle	0.9–1.1 mm	
Bulk density	$564.4 \, kg/m^3$	
Hardness	74–76%	
Size particle (DIN 4188)	>1.6 mm	1.5–2%
	(0.425–1.6) mm	97–98%
	<0.425 mm	0.5–1%
	<0.355 mm	0.1–0.2%

Table 2. Catalyst characteristics

Mean diameter (mm)	3.3	Porosity (%)	66
Surface area (m^2/g)	96	Pt loading (wt %)	0.12
Density (kg/m^3)	3329	Pt dispersion (%)	86
Apparent density (kg/m^3)	1300	Pt distribution	Egg shell
Pore volume (m^3/kg)	0.58	Width of Pt band (μm)	~100

that was originally designed for commercial on-column injector OCI–14. Desorption reactor oven (4) is capable of being temperature programmed from other heated sections of gas chromatograph. Samples of AC (0.12 g–0.23 cm^3) were placed in the middle of desorber (3), housed on quartz wool holder, with thermocouple on the top of the bed. Air and nitrogen were used as desorption fluids. The air flow corresponded to the space velocity of 12000 h^{-1}. The second, catalytic reactor (6) was also made of stainless steel tube, with the same dimensions as desorption reactor. Catalytic reactor was situated in the column oven of the gas chromatograph (Shimadzu 14-A). Reactor was loaded with 0.15 g of crushed commercial Pt/Al_2O_3 catalyst. Applied flow rates through the catalyst bed corresponded to the space velocity of 13500 h^{-1}. Temperature of the reactor was maintained by column oven temperature controller, while the temperature of the catalyst bed was recorded by thermocouple situated at the outlet of the catalyst layer.

Temperature programmed desorption of organics from AC was investigated in the temperature range from 50 to 300°C with programmed temperature rise of 5, 10, 20 and 50 K/min.

Taking into account that the catalytic reactor was placed in the column oven, analysis of unreacted organic products was restricted only to the total organic content, using empty column and FID detector. Therefore,

in order to determine catalytic activity, desorption products (at the inlet of catalytic reactor) were analyzed using the same method. Also, quantitative and qualitative analysis of desorption products, without catalytic reactor, were performed by means of stainless steel column, 6.5 ft. long and 1/8 in. in diameter, containing 23% SP 1700 on chromosorb PAW.

RESULTS AND DISCUSSION

Desorption of organics from activated carbon conducted in the air stream caused burning of AC. The AC light off started at temperatures above 280°C. Therefore, further desorption experiments have been done with nitrogen as effluent fluid. Fig. 2 presents mass loss of AC in the temperature range from 120 to 300°C with heating rate of 10 K/min.

The AC mass loss gradually increases from 5 to 19% up to the temperature of 260°C. Further temperature rise does not affect the AC mass loss. Also, mass loss of 19% was obtained at lower temperatures (200°C) with the same rate of heating, but with prolonged temperature hold time of desorber reactor for 30 min.

Overall analysis of desorption products from AC in the temperature range from 120 to 300°C with programmed temperature rise of 10 K/min revealed that major constituent of adsorbed organics is xylene (about 90%). The rest of desorbed organics belong mainly to SOLVESSO 100 that is commercial name for industrial solvent containing C9-C10 dialkyl and trialkyl-benzenes. Up to the temperature of 160°C xylene is the only organics that appeared in the effluent gas, while the SOLVESSO 100 constituents appear at higher temperatures and their amount gradually increase with temperature and prolonged desorption time.

The adequate adoption of gas flow rate and temperature regime in desorption unit can provide targeted dynamics and composition of desorbed organics. Therefore, heating rate of 10 K/min from 70 to 200°C with hold time of 30 min at 200°C was chosen for catalytic activity tests.

Catalytic activity test expressed as function of time on stream are presented on Fig. 3, along with temperature regime in the desorption unit. Although real gas compositions are the mixture of xylene and ingredients of commercial solvent SOLVASSOL 100, all concentrations of organics, including the inlet concentration, are expressed as total organics calibrated with respect to the xylene. Therefore, portions of these constituents varied with time on stream. At lower temperatures xylene is dominant within total organics concentration, but above 200°C concentration of SOLVASSOL 100 compounds are increasing and participate in total organics up to 15 vol %. Consequently, time on stream activity tests should be analyzed from this point of view.

Catalytic activity tests can be considered for two different concentration regions, upward and downward curves. Obviously, activity of the catalyst is higher in
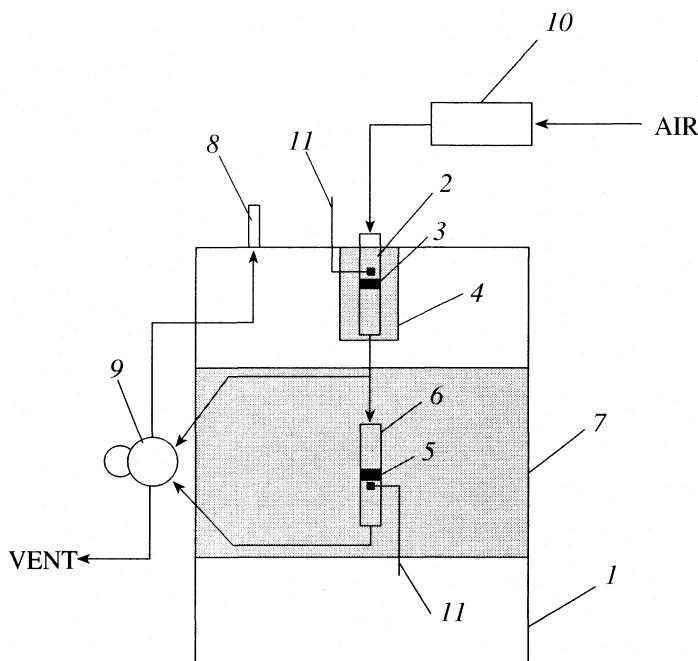
Fig. 1. Schematic diagram of apparatus: *1* – gas chromatograph, *2* – AC, *3* – desorption reactor, *4* – desorption reactor oven, *5* – catalyst, *6* – catalytic reactor, *7* – catalytic reactor – column oven, *8* – FID detector, *9* – 6-port valve, *10* – flow controller and *11* – thermocouples.
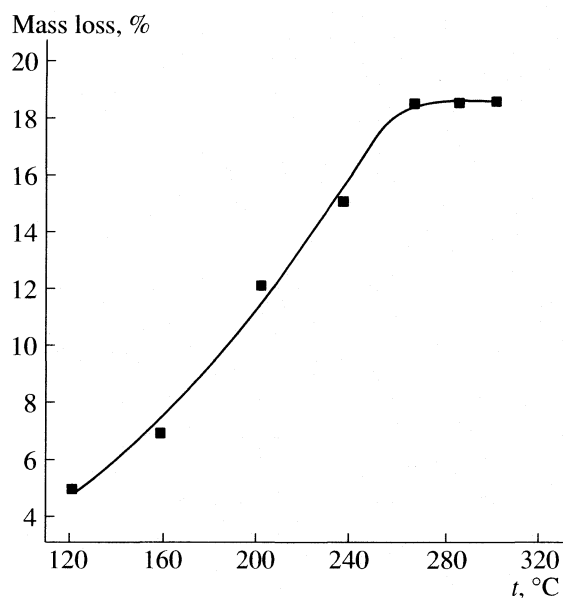
Fig. 2. Mass loss of AC as a function of desorption temperature.
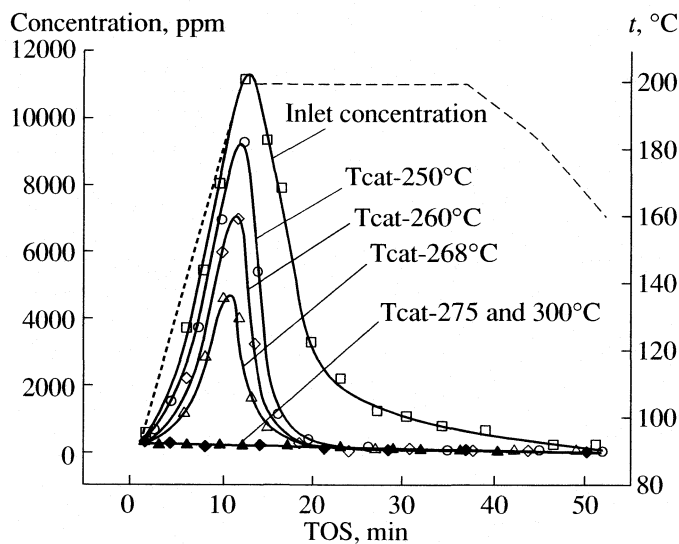
Fig. 3. Conversion of VOCs and desorption regime vs. time on stream; filled lines – VOCs concentration, dashed line – temperature of desorber.

downward region with respect to upward part. It may be concluded that the presence of C9–C10 dialkyl and trialkyl-benzenes increase conversion of xylene, this suggests that products of reactions are somehow speeding up the rate. Systems in which this occurs are often referred as autocatalytic [18], but it is only the speculation. Further experiments are necessary for confirma-

tion of this assumption. Also, such behavior can be explained by heat effect in catalytic bed due to released heat of combustion. There is possibility that the temperatures in catalyst bed are higher than recorded by thermocouple, placed just at the outlet of catalytic bed. It should be mentioned that catalytic reactor is situated in relatively high volume column oven of gas chro-
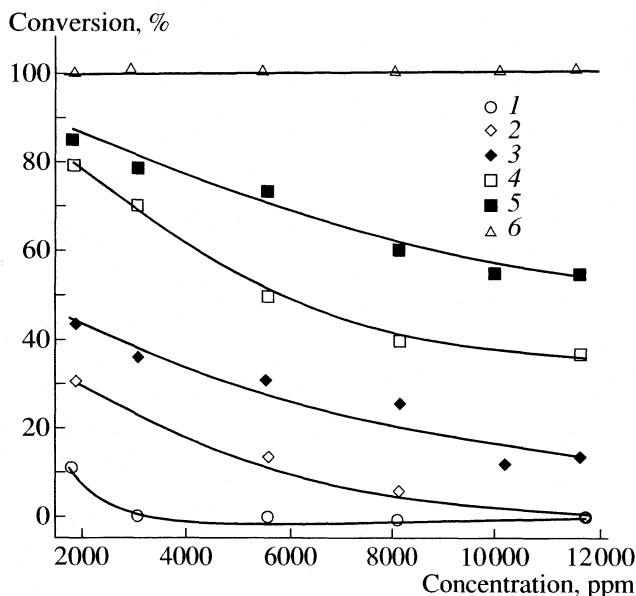
Conversion, %

Fig. 4. Conversion of VOCs as a function of concentration in upward concentration regime at differ temperatures: 230 (*1*), 240 (*2*), 250 (*3*), 260 (*4*), 268 (*5*), 275 and 300°C (*6*).

matograph that provide suitable heat transfer conditions. However, activity tests show that catalysts temperatures of 275°C is sufficient to burn up all desorbed organics.

For this reasons, effects of concentrations on catalytic activity have been envisaged only in upward concentration regime that is presented on Fig. 4.

Increase of concentration of organics decreases catalyst efficiency. These results could indicate possible mechanism of catalytic reaction. Probably, surface concentrations of organics remain constant regardless the organics concentrations in the gas phase. This should be the basis for further research about kinetics of xylene oxidation over Pt/Al_2O_3 catalysts employing a gradientless reactor.

CONCLUSION

Thermal desorption of organics by the air from saturated AC, discharged from commercial adsorber, enables satisfactory regeneration of AC. The AC saturated mainly by xylene and partly by SOLVESSO 100 is almost completely regenerated by flushing with air at 200°C during 30 min.

Desorbed products are fully oxidized over Pt/Al_2O_3 catalyst above the temperature of 275°C.

These results show that removal of low concentrations of organic compounds by adsorption on AC, thermal regeneration of AC and post-treatment of desorbed products from AC over Pt/Al_2O_3 catalyst can be successfully applied for removal of organic pollutants from waste gases.

REFERENCES

1. E. Noordally, J. R. Richmond, and S. F. Tahir, Catal. Today **17**, 359 (1993).
2. J. J. Spivey, Ind. Eng. Chem. Res. **26**, 2165 (1987).
3. J. N. Armor, Appl. Catal. B: Env. **1**, 221 (1992).
4. J. Hermia and S. Vigneron, Catal. Today **17**, 349 (1993).
5. J. Tsou, L. Pinard, P. Magnoux, J. L. Figueiredo, and M. Guisnet, Appl. Catal. B: Env. **46**, 371 (2003).
6. J. C. S. Wu, Z. A. Lin, F. M. Tsai, and J. W. Pan, Catal. Today 63, 419 (2000).
7. N. Kawasaki, H. Kinoshita, T. Oue, T. Nakamura, and S. Tanada, J. Coll. Inter. Sci. **275**, 40 (2004).
8. R. C. Bansal, J. B. Donnet, and F. S. Stoeckli, *Active Carbon* (Marcel Dekker, New York, 1988, Chapters 1–3).
9. H. Sinjoh, H. Muraki, and Y. Fujitani, Appl. Catal. **49**, 195 (1989).
10. A. Schwartz, L. L. Holbrook, and H. Wise, J. Catal. **21**, 199 (1971).
11. M. Skoglundh, L. O. Löwendhal, and J. E. Ottersted, Appl. Catal. **77**, 9 (1991).
12. Y. Moro-oka, Y. Morikawa, and A. Ozaki, J. Catal. **7**, 23 (1967).
13. Y. F. Yu Yao, Ind. Eng. Chem. Process Des. Dev. **23**, 60 (1984).
14. Ph. Dégé, L. Pinard, P. Magnoux, and M. Guisnet, C. R. Acad. Sci., Ser. IIc: Chim. **4**, 41 (2001).
15. P. Marecot, A. Fatche, B. Kellali, G. Mabillon, M. Prigent, and J. Barbier, Appl. Catal. B: Env. **3**, 282 (1994).
16. Ž. Grbavčić, D. Ranković, Z. Arsenijević, in "*Proceedings of the 7th International Conference on Fundamental and Applied Aspects of Physical Chemistry 2004 "Physical Chemistry 2004"*, Vol. II, 709 (Society of Physical Chemists of Serbia, Belgrade, 2004).
17. N. Radic, B. Grbic, and A. Terlecki-Baricevic, Appl. Catal. B: Env. **50**, 153 (2004).
18. S. Gangwal, K. Ramanathan, P. Caffrey, M. Mullins, and J. Spivey, in "*Mixture Effects in the Catalytic Oxidation of VOCs in Air, Report No. EPA 600/7-88-017*" (US Environmental Protection Agency, Research Triangle Park, NC, 1988).

CHEMICAL KINETICS
AND CATALYSIS

MECHANISM OF THE KOLBE–SCHMITT REACTION WITH LITHIUM AND SODIUM PHENOXIDES

© 2007   S. Marković*, Z. Marković**, Ne. Begović***, Ne. Manojlović****

*Faculty of Science, University of Kragujevac, 12 Radoja Domanovića, 34000 Kragujevac, Serbia
**Faculty of Agronomy, University of Kragujevac, 34 Cara Dušana, 32000 Čačak, Serbia
***Institute of General and Physical Chemistry, 12/V Studentski trg, 11000 Belgrade, Serbia
****Faculty of Medicine, University of Kragujevac, 69 Svetozara Markovića, 34000 Kragujevac, Serbia
E-mail: mark@kg.ac.yu; mark@tcf.kg.ac.yu

Abstract – The mechanisms of the carboxylation reactions of lithium and sodium phenoxides are investigated by means of DFT method with CEP-31 + G(d) basis set. The introduction of diffusion functions does not affect the outcome of the calculations. As a consequence, the results of this investigation are in good agreement with the findings obtained by means of LANL2DZ basis set. Lithium phenoxide yields only salicylic acid in the Kolbe–Schmitt reaction. The reaction of sodium phenoxide can proceed in the *ortho* and *para* positions, but the para substituted product can be expected at a very low concentration in the reaction mixture. The deviation of lithium and sodium phenoxides from the mechanisms of carboxylations of other alkali metals is a consequence of small ionic radii of lithium and sodium.

INTRODUCTION

The Kolbe–Schmitt reaction is a carboxilation reaction of alkali metal phenoxides with carbon dioxide where hydroxybenzoic acids are formed [1–3]. This reaction has been used for more than a century for industrial production of aromatic hydroxy acids, such as salicylic acid, p-hydroxybenzoic acid, 3-hydroxy-2-naphtoic acid, 6-hydroxy-2-naphtoic acid, etc. These acids play a significant role in the synthesis of numerous products, such as pharmaceuticals, antiseptic, fungicidal, and color-developing agents, textile assistants, polyesters, high-polymeric liquid crystals and dyes [4, 5]. The reaction scheme is presented in Fig. 1.

The mechanism of the Kolbe–Schmitt reaction has been the subject of investigations of many experimental and theoretical studies. The early results on the Kolbe–Schmitt reaction mechanism can be found in the review [6], and references cited there. In this work we refer to the later results concerning the Kolbe–Schmitt reaction mechanism. The work of Kunert et al. [7] provided valuable information on the mechanism of the Kolbe–Schmitt reaction. On the basis of FT-IR spectra and DTA analysis the presence of the intermediate NaOPh-CO$_2$ complex was confirmed. It was also found that the complex changed to a further intermediate at increased temperature (75–80°C). It was concluded that a direct carboxylation could be excluded from the Kolbe–Schmitt reaction mechanism.

Kosugi [8] investigated the Kolbe–Schmitt reaction mechanism of phenol and 2-naphthol. It was concluded, on the basis of C-13 NMR and MOPAC/PM3 calculations, that a direct carboxylation of phenoxide with carbon dioxide took place, and KOPh–CO$_2$ (or NaOPh–CO$_2$) was not an intermediate in the reaction.

This study was focused on the carbonation of potassium phenoxide, and an exact mechanism of the reaction was not put forward.

A DFT study on the mechanism of the carboxylation reaction of sodium phenoxide was performed by means of Gaussian 98 software package at B3LYP level of theory with LANL2DZ basis set [9]. A mechanism including three transition states and three intermediates was proposed. A quantitative explanation for the low yield of p-hydroxybenzoic acid and the equilibrium behavior of the Kolbe–Schmitt reaction was provided. In order to investigate solvent effects on the Kolbe–Schmitt reaction kinetics Stanescu et al. [10, 11] performed theoretical DFT studies, where Jaguar 4.2 program package at the B3LYP level of theory was used. The investigations of Achenie and Stanescu confirmed the mechanism proposed in [9].

In a recent research [12, 13] the mechanisms of the carboxylation reactions of lithium, potassium, rubidium and cesium phenoxides were investigated at the DFT/LANL2DZ level of theory. It was observed that the mechanism of the carboxylation reaction of lithium phenoxide was significantly different from those of other alkali metal phenoxides, but it was not studied in details. It was also observed that there was a significant resemblance between the mechanisms of the carboxylation reactions of lithium and sodium phenoxides. This provoked us to reinvestigate the mechanism of the Kolbe–Schmitt reaction of lithium and sodium phenoxides using different basis set.

alkali metall phenoxide

+

intermediate complex

ortho route

para route
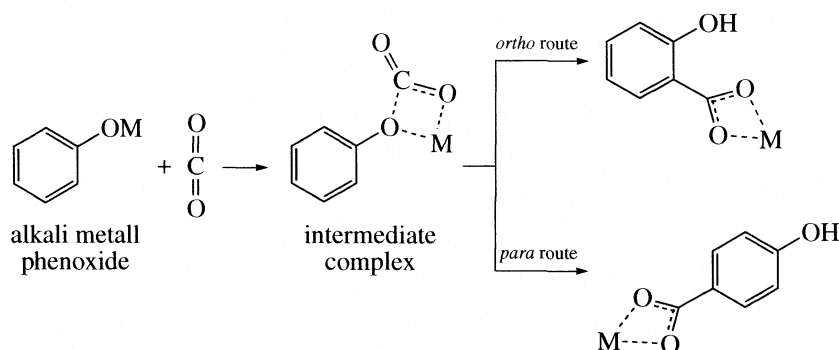
Fig. 1. Reaction scheme for the Kolbe–Schmitt reaction. M represents alkali metals.

COMPUTATIONAL METHODS

Geometrical parameters of all stationary points and transition states for the reactions of lithium and sodium phenoxides with carbon dioxide are optimized in vacuum, employing analytic energy gradients by means of the Becke-type three-parameter hybrid combined with the gradient-corrected correlation functional of Lee, Yang, and Parr [14, 15]. This functional, commonly known as B3LYP [15, 16], implemented in GAUSSIAN98 program package [17], turned out to be quite reliable for geometrical optimizations [18]. All theoretical calculations are carried out by employing the CEP-31 + G(d) basis set. CEP-31 + G(d) uses Stevens/Basch/Krauss ECP split-valence basis set and includes a set of polarization functions [19]. It also includes corrections for relativistic effects. The vibrational analysis and the natural bond orbital (NBO) analysis [20, 21] are performed for all structures at the all B3LYP/CEP-31 + G(d) level. All the fully optimized transition state structures are confirmed by the existence of a sole imaginary frequency, whereas the optimized intermediate structures possess only real frequencies. From the transition state structures, the intrinsic reaction coordinates (IRCs) are obtained, and

the free energies are maximized along these paths. These paths and free energies maxima are obtained using the IRC routine in GAUSSIAN98. The analysis of the vibrational frequencies is performed by means of the Molden program, version 3.7 [22].

RESULTS AND DISCUSSION

The mechanism of the reaction of carbon dioxide with PhO-M (M stands for Li and Na) is examined. It is found out that the Kolbe–Schmitt reaction of lithium phenoxide and sodium phenoxide proceeds via three transition states and three intermediates. The three transition states are verified by the intrinsic reaction coordinate (IRC) calculations. A general outline of the mechanism is presented in Fig. 2.

Direct carboxylation of benzene ring is investigated by performing a forced attack of carbon dioxide to the *ortho*, *meta* and *para* positions of PhO-M. This attack does not reveal any possible reaction path. On the other hand, a stable intermediate complex B-M is formed by approaching the reactants to each other. This step of the reaction proceeds smoothly, with the stabilization of the system, and without any activation barrier. This is in agreement with the finding that not all chemical reactions proceed via transition states, particularly in the gas phase [23]. The existence of the intermediate B-M in the Kolbe–Schmitt reaction has been confirmed experimentally [7, 8]. This reaction path is supported by theoretical results, as follows.

The APT (atomic polar tensors) charge distribution [24] of the reactants (Table 1) shows that in PhO-M the positive charge is located on the metal, whereas the negative charge is distributed among the oxygen and *ortho* and *para* carbons of the benzene ring. The charge distribution analysis undoubtedly indicates that the oxygen of carbon dioxide will bond to the alkali metal, and the carbon of carbon dioxide will bond to the adjacent oxygen of PhO-M, thus forming the intermediate B-M. The optimized geometry of B-M is presented in Fig. 2, whereas the bond lengths in B-Li and B-Na are given in Tables 2 and 3, respectively. It is worth men-

Table 1. APT (atomic polar tensors) charge distribution in reactants and first intermediate

	PhO–M		B–M	
	Li	Na	Li	Na
M	0.91	0.92	0.83	0.88
O	−1.29	−1.23	−1.21	−1.20
o-C	−0.19	−0.20	−0.10/−0.12	−0.10/−0.13
m-C	0.11	0.13	0.04/0.02	0.05/0.03
p-C	−0.20	−0.24	−0.07	−0.09
Carbon dioxide				
C	1.15		1.80	1.82
O	−0.57		−1.07	−1.09
O	−0.57		−0.80	−0.83

PhO-M + CO₂ B-M

C-M TS2-M D-M

TS3-M E-M
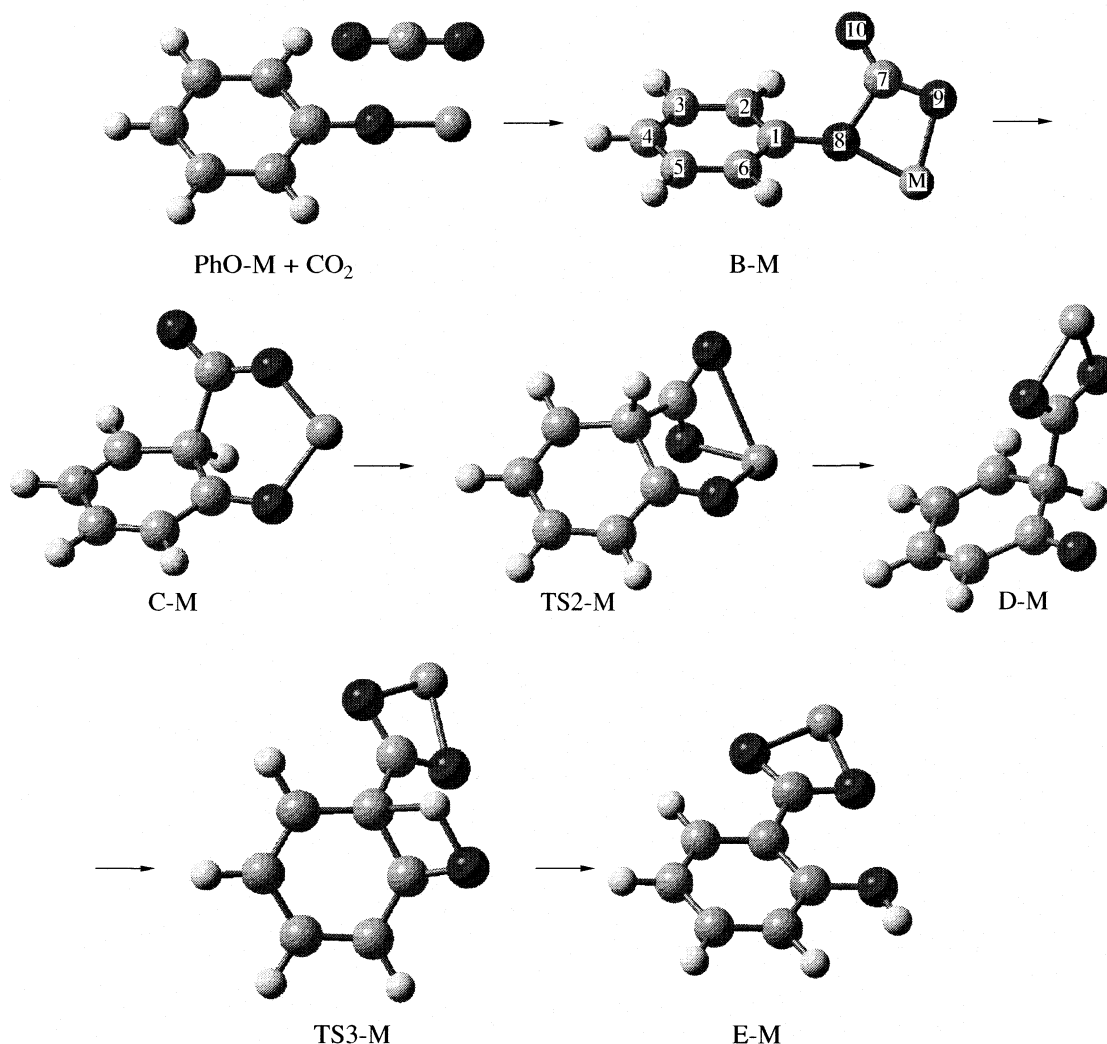
Fig. 2. Mechanism of the Kolbe–Schmitt reaction of lithium and sodium phenoxides. M stands for Li and Na. B–M, C–M and D–M represent the first, second and third intermediates, whereas TS2-M and TS3-M represent the second and third transition states, respectively. The geometry of oTS1-M is not presented because it is very similar to that of C–M. E–M represents alkali metal salt of hydroxybenzoic acid.

tioning that the distances of 1.602 Å in B–Li and 1.586 Å in B–Na reveal the formation of weak C7–O8 bonds.

Now, the intermediate complex undergoes further conversion. A direct carboxylation with another molecule of carbon dioxide is examined, but this attack does not reveal any possible reaction path. On the other hand, Table 1 clearly reveals that the carbon of the CO_2 moiety in B–M is strongly electrophilic, indicating that an electrophilic attack of the CO_2 moiety to the benzene ring can be expected as a plausible step of the reaction. For this reason the reaction paths for electrophilic attacks of this carbon to the *ortho*, *meta* and *para* positions of B–M are examined. The meta route is not revealed. This finding is in agreement with Table 1 which shows that the *ortho* and *para* carbons in the benzene ring are nucleophilic.
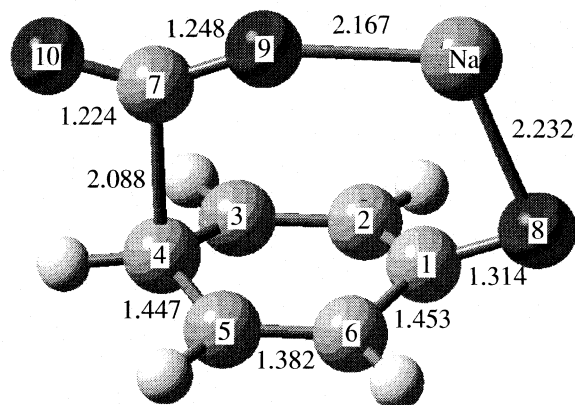
Fig. 3. Optimized geometry of the first transition state in the carboxylation reaction of sodium phenoxide in the *para*-position.

Table 2. Bond lengths and free energies (G^{298}) of the intermediates, transition states and product in the carboxilation reaction of lithium phenoxide. The atoms are labeled in accordance with Fig. 2

Bond length (Å)	B–Li	TS1–Li	C–Li	TS2–Li	D–Li	TS3–Li	E–Li
C1–C2	1.414	1.469	1.513	1.540	1.547	1.478	1.429
C2–C3	1.413	1.448	1.493	1.506	1.518	1.459	1.420
C3–C4	1.416	1.388	1.373	1.369	1.364	1.391	1.408
C4–C5	1.415	1.441	1.457	1.465	1.473	1.450	1.415
C5–C6	1.414	1.394	1.385	1.382	1.373	1.399	1.410
C1–C6	1.414	1.452	1.458	1.463	1.484	1.436	1.421
C1–O8	1.389	1.294	1.273	1.260	1.236	1.296	1.374
O8–M	1.796	1.764	1.807	1.948			
O9–M	1.831	1.828	1.763	1.888	1.878	1.871	1.859
O10–M				2.471	1.885	1.874	1.860
C2–C7		2.086	1.705	1.580	1.561	1.535	1.514
C7–O9	1.263	1.240	1.274	1.284	1.278	1.281	1.283
C7–O10	1.207	1.198	1.227	1.254	1.282	1.286	1.293
G^{298} (kcal/mol)	0.40	8.46	7.55	18.97	16.18	63.87	2.26

Table 3. Bond lengths and free energies (G^{298}) of the intermediates, transition states and product in the carboxilation reaction of sodium phenoxide. The atoms are labeled in accordance with Fig. 2

Bond length (Å)	B–Na	TS1–Na	C–Na	TS2–Na	D–Na	TS3–Na	E–Na
C1–C2	1.417	1.478	1.509	1.523	1.544	1.475	1.429
C2–C3	1.413	1.453	1.488	1.500	1.515	1.456	1.420
C3–C4	1.416	1.386	1.373	1.370	1.365	1.394	1.409
C4–C5	1.415	1.444	1.457	1.462	1.472	1.448	1.415
C5–C6	1.414	1.391	1.384	1.383	1.374	1.400	1.410
C1–C6	1.416	1.458	1.465	1.464	1.484	1.435	1.422
C1–O8	1.385	1.284	1.269	1.261	1.237	1.299	1.376
O8–M	2.215	2.148	2.183	2.300			
O9–M	2.180	2.201	2.137	2.227	2.227	2.221	2.212
O10–M				2.972	2.240	2.232	2.214
C2–C7		2.026	1.739	1.621	1.577	1.555	1.526
C7–O9	1.263	1.241	1.264	1.275	1.273	1.275	1.278
C7–O10	1.258	1.205	1.228	1.251	1.277	1.280	1.288
G^{298} (kcal/mol)	−1.35	9.87	9.05	14.91	13.26	61.52	1.22

For conversion of B–Li a reaction path for an attack in the *para* position is not revealed. Conversion of B–Na proceeds in both *ortho* and *para* positions, via the transition states oTS1–Na and pTS1–Na. The optimized geometry of pTS1–Na is presented in Fig. 3.

By inspecting Tables 2 and 3 one can conclude that all corresponding bond lengths in the species containing lithium and sodium are mutually very similar, with the exception of O8–M and O9–M. These bonds are significantly longer in the species containing sodium, which is a consequence of the larger ionic radius of sodium. In pTS1–Na the O8–Na and O9–Na bonds form

a bridge that enables the bonding of C7 to the *para* carbon. For this reason the lengths of bonds O8–M and O9–M are of crucial significance for the pTS1–Na geometry. In pTS1–Na these bonds are even longer than they are in oTS1–Na. Still, in pTS1–Na C1, C4 and O8 deviate from the plane of the benzene ring by 8.6°, 9.7° and 26°, respectively. The ionic radius of lithium is only 0.60 Å. This implies that a possible geometry of pTS1–Li would require significant deformations of benzene ring. For this reason pTS1–Li does not form, thus explaining the experimental finding that *o*-hydroxy-

benzoic acid is the only product of the reaction of lithium phenoxide with carbon dioxide [6].

The activation barriers for the conversions of B–Na in the ortho and para positions amount 11.22 and 14.01 kcal/mol, respectively. According to the Curtin–Hammond principle, the distribution of products is determined by the difference of free energies of the *ortho* and *para* transition states. It is clear that the intramolecular conversion of the B–Na complex is the most responsible for the products distribution in the Kolbe–Schmitt reaction. The free energy difference of 2.8 kcal/mol between the two transition states for the conversion of B–Na results in a 1 : 0.009 ratio of the product concentrations. On the basis of this, one should expect the *para* substituted product (sodium 4-hydroxybenzoate) at a very low yield in the reaction mixture, which agrees well with the experimental results [25]. For this reason the *para* route of the carboxylation reaction of sodium phenoxide is excluded from this investigation.

The reactions in the *ortho* positions proceed via the transition states oTS1–Li and oTS1–Na, with the formation of the intermediates C–Li and C–Na (Fig. 2). Since oTS1–M is a late transition state, the structure and energy of the intermediate C–M is similar to that of oTS1–M. Tables 2 and 3 show that a new C2–C7 bond in C–M is partially formed. On the basis of the natural bond order (NBO) analysis [20, 21], there is $\sigma(C2–C7) = 0.761C2(sp^{4.33}) + 0.648C7(sp^{2.61})$ in C–Li and $\sigma(C2–C7) = 0.764C2(sp^{4.82}) + 0.645C7(sp^{2.79})$ in C–Na. The predominant p character of these C atoms with little s mixing indicates that the C2–C7 bond is weak. The length of C2–C7 bond (about 1.7 Å) is in agreement with the NBO analysis. A consequence of the formation of this weak bond is that in C–M the geometry of the benzene ring is slightly deformed in the ortho position.

The next step of the reaction is a conversion of the intermediate C–M into D–M via TS2-M transition state (Fig. 2, Tables 2 and 3). The results obtained from the IRC calculations for the formation of TS2-Li are presented in Fig. 4. In TS2-M a new O10-M bond is being formed. In D–M the bond C2–C7 is almost completely formed, though it is still longer than ordinary single bonds. The NBO analysis of D–M reveals an increase of the contribution of s orbital in sp hybridization on C2 and C7: $\sigma(C2–C7) = 0.728C2(sp^{3.27}) + 0.686C7(sp^{1.66})$ for D–Li and $\sigma(C2–C7) = 0.735C2(sp^{3.46}) + 0.678C7(sp^{1.91})$ for D–Na. The geometries of D–Li and D–Na are significantly different from that of the third intermediate in the carboxylation reaction of other alkali metals (i.e. potassium, cesium and rubidium) [12]. This can be explained by the short ionic radii of lithium and sodium which do not enable the formation of structures where the metal is chelated with three oxygens.

As for the last step of the Kolbe–Schmitt reaction a 1,3 hydrogen shift from C2 to O8 is considered as a plausible reaction step. This step of the reaction proceeds via TS3 transition state (Fig. 2), and requires the
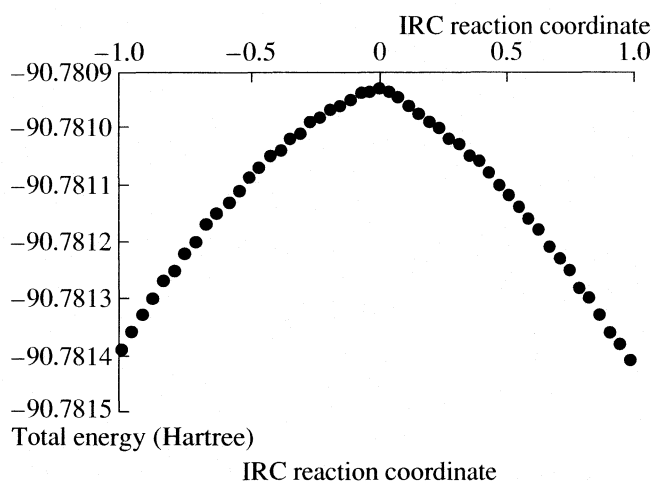
Fig. 4. Plot of total energy versus IRC reaction coordinate for the formation of TS2-Li.

highest energy barrier (Tables 2 and 3), implying that it is the rate limiting step of the Kolbe–Schmitt reaction. This relatively high activation energy is supported by the experimental fact that the reaction mixture has to be heated for 1 hour at 150–250°C under high pressure [6] in order to form corresponding salt of hydroxy benzoic acids. Similarly, 1,3-shift of hydrogen atom in the conversion process for vinyl-acetaldehyde tautomerization requires activation energy of 56.4 kcal/mol [26].

The results of this investigation confirm the mechanisms of the carboxylation reactions of lithium and sodium phenoxides obtained by means of the LANL2DZ basis set [9–12]. The introduction of diffusion functions does not affect the outcome of the calculations. Lithium phenoxide yields only salicylic acid in the Kolbe–Schmitt reaction. This is a consequence of very short ionic radius of lithium, so that possible geometries of the intermediates and transition states that would appear in the Kolbe–Schmitt reaction of lithium phenoxide in the *para* position would require significant deformations of the benzene ring. The reaction of sodium phenoxide can proceed in both *ortho* and *para* positions, with pronounced deformations of the benzene ring in the *para* route of the reaction. For this reason the *para* substituted product can be expected at a very low concentration in the reaction mixture. The deviation of lithium and sodium phenoxides from the mechanisms of carboxylations of other alkali metals is a consequence of small ionic radii of lithium and sodium.

ACKNOWLEDGEMENT

REFERENCES

1. H. Kolbe, Liebigs Ann. **113**, 125 (1860).

2. H. Kolbe, and E. Lautemann, Liebigs Ann. **115**, 157 (1860).

3. R. Schmitt, J. Prakt. Chem. **31**, 397 (1985).

4. M. Windholz, The Merck Index; Merck & Co Inc.: Rahway, 1983; 10th edition, p. 8190.

5. J.E.F. Reynolds, Salicylic acid in: Martindale The Extra Pharmacopoeia; The Royal Pharmaceutical Society, London, 1996; 31st Edition, pp. 1093–1105.

6. A. S. Lindsey and H. Jeskey, Chem. Rev. 583 (1957).

7. M. Kunert, E. Dinjus, M. Nauck and J. Sieler, Chem. Ber./Recueil **130**, 1461 (1997).

8. Y. Kosugi, Y. Imaoka, F. Gotoh, M. A. Rahim, Y. Matsui, and K. Sakanishi, Org. Biomol. Chem. **1**, 817 (2003).

9. Z. Marković, J.P. Engelbrecht, and S. Marković, Z. Naturforsch. **57a**, 812 (2002).

10. I. Stanescu, and L. E. K. A. Achenie, Chem. Eng. Sci. **61**, 6199 (2006).

11. I. Stanescu, R. R. Gupta, and L. E. K. Achenie, Mol. Sim. **32**, 279 (2006).

12. Z. Marković, S. Marković, and N. Begović, J. Chem. Inf. Model. **46(5)**, 1957 (2006).

13. Z. Marković, S. Marković, and N. Begović, 8th International Conference on Fundamental and Applied Aspects of Physical Chemistry Belgrade (2006) **C**-6-P.

14. A. D. Becke, Phys. Rev. A. 2098 (1988).

15. C. Lee, W. Yang, and R.G. Parr, Phys. Rev. B. 785 (1988).

16. A.D. Becke, J. Chem. Phys. **98**, 5648 (1993).

17. Frisch, M. J., Trucks, G. W., Schlegel, H. B., Scuseria, G. E., Robb, M. A., Cheeseman, J. R., Zakrzewski, V. G., Montgomery, J. A. Jr., Stratmann, R. E., Burant, J. C., Dapprich, S., Millam, J. M., Daniels, A. D., Kudin, K. N., Strain, M. C., Farkas, O., Tomasi, J., Barone, V., Cossi, M., Cammi, R., Mennucci, B., Pomelli, C., Adamo, C., Clifford, S., Ochterski, J., Petersson, G. A., Ayala, P. Y., Cui, Q., Morokuma, K., Malick, A. D., Rabuck, K. D., Raghavachari, K., Foresman, J. B.; Cioslowski, J., Ortiz, J. V., Baboul, A. G., Stefanov, B. B., Liu, G., Liashenko, A., Piskorz, P., Komaromi, I., Gomperts, R., Martin, R. L., Fox, D. J., Keith, T., Al-Laham, M. A., Peng, C. Y., Nanayakkara, A., Challacombe, M., Gill, P. M. W., Johnson, B., Chen, W., Wong, M. W., Andres, J. L., Gonzalez, C., Head-Gordon, M., Replogle, E. S., Pople. J. A. *Gaussian 98, Revision A.9*, Gaussian, Inc.: Pittsburgh, PA, 1998.

18. *Chemical Applications of Density Functional Chemistry*, Laird, A., Ross, R. B., Zeigler, T., Eds., American Chemical Society: Washington, 1996.

19. W. J. Stivens, H. Bach, and J. Krauss, J. Chem. Phys. **81**, 6026 (1984).

20. J. P. Foster, and F. Weinhold, J. Am. Chem. Soc. **102**, 7211 (1980).

21. A. E. Reed, R. B. Weinstock, and F Weinhold, J. Chem. Phys. **83**, 735 (1985).

22. G. Schaftenaar, *MOLDEN 3.7*; CAOS/CAMM Center: The Netherlands, 1998.

23. W. J. Hehre, A. J. Shusterman, and W. W. Huang, *A Laboratory Book of Computational Organic Chemistry*, Wavefunction Inc. Irvine, California, 1996.

24. J.A. Marti, Chem. Phys. **265**, 263 (2001).

25. O. Baine, G. F. Adamson, J. W. Barton, J. L. Fitch, D. R. Swayampati, and H.A.J. Jeskey, J. Org. Chem. **19**, 510 (1954).

26. K. Suenobu, M. Nagaoka, and T. Yamabe, J. Mol. Struc. (Theochem) **461–462**, 581 (1999).

CHEMICAL KINETICS
AND CATALYSIS

TEMPERATURE DEPENDENCE OF CATALYTIC CYCLOHEXANE PARTIAL OXIDATION IN POLYTETRAFLUOROETHYLENE REACTOR

© 2007   D. Lončarević*, J. Krstić*, P. Banković*, S. Anić**, Ž. Čupić*

*Institute of Chemistry, Technology and Metallurgy, Department of Catalysis, Njegoševa 12, 11000 Belgrade, Serbia
E-mail: davorl@verat.net
**Faculty for Physical Chemistry, University of Belgrade, P.O. Box 137, Studentski trg 16, 11001 Belgrade, Serbia*

Abstract – Polymer-supported Co(II) catalyst was prepared and its activity and selectivity in the partial oxidation of cyclohexane was determined at several temperatures, in a polytetrafluoroethylene reactor (PTFE). The catalyst was characterized by means of SEM-EDX, FTIR, diffuse reflectance UV-Vis, N_2 sorption and mercury porosimetry. Activation energies were determined at steady state conditions for the net production of cyclohexanone and cyclohexanol and for cyclohexane and oxygen net consumption. Some activation energies were lower than the ones reported for uncatalysed process, indicating that the catalyst exhibit important role in the initiation of the free radical reaction.

INTRODUCTION

Selective oxidation of cyclohexane to a mixture of cyclohexanone and cyclohexanol under mild conditions is an industrial process important for the manufacture of nylon-6 and nylon-66. The system, currently in use for partial oxidation of cyclohexane (Ch) to the mixture of cyclohexyl hydroperoxide (Chhp), cyclohexanol (Chl) and cyclohexanone (Chn), employs 0.3–3.0 ppm of a soluble cobalt catalyst, at temperature and pressure value range of 150–175°C and 0.8–1.0 MPa respectively [1].

The mechanism of non-catalytic cyclohexane oxidation is important since it significantly contributes to the catalytic process as well. The reaction scheme of Khar'kova [2] was reported to give a good correlation with experiments. The application of this model is limited to conversion levels lower than 8%.

In general, the temperature dependence of the oxidation of alkanes is determined by their high stability, and they do not react below approximately 400 K. Above 400 K, the parent alkane molecule (RH) decomposition is initiated by the removal of an atom of hydrogen by molecular oxygen. This step, called abstraction reaction, is highly endothermic, with enthalpy value in the range of roughly 180–230 kJ/mol, depending on the bond energy of the abstracted H atom in the parent alkane, and requires activation energy proportional to the endothermicity. This energy may be provided by collision with a third species, which can be any component of the mixture, either a radical or a stable molecule. Therefore, it is very common in this system that even walls of the reaction vessel influence propagation of the chain [3]. Hence, an investigation in a high pressure reactor with chemically inert walls is necessary for the catalyst effect study.

Investigations have extensively been performed in the heterogenization of batch reactions, on various solid supports (inorganic oxides, zeolites etc.) [4, 5]. Metal ions act as the initiators of free radical auto-oxidation which proceeds further via radical chain reaction [5]. Our previous results, obtained using stainless steel reactor, show that polymer-supported Co(II) catalyzes cyclohexane partial oxidation at 170°C and 2.8 MPa, with high conversion and good selectivity towards desired products [6, 7].

The goal of present work was to examine the temperature influence on the cyclohexane oxidation in a polytetrafluoroethylene (PTFE) reactor. Activation energies were calculated at isothermal regimes for several temperatures and a hypothesis of the catalyst role in the reaction mechanism was derived.

EXPERIMENTAL

Macroreticular copolymer of poly-4-vinylpyridine and divinylbenzene (REILLEX–425), produced by Reilly Tarr & Chemical Corporation, was used as a support. Catalyst was prepared from ethanol solutions of cobalt(II)-nitrate, $Co(NO_3)_2 \cdot 6H_2O$ and the solid polymer. The Co^{2+} content of the catalyst was 5.72 wt. % (cobalt was quantitatively bound to the polymer).

The catalyst was characterized by means of SEM-EDX (automated system JSM–6460LV JOEL with EDX), FTIR Nicolet Avatar 320 and diffuse reflectance UV-Vis (Nicolet Evolution 500 spectrometer). Reflectance (R) data were converted to pseudo-absorbance f(R) using the Kubelka–Munk equation.

The specific surface area was estimated by the BET method from N_2 sorption measured on Sorptomatic 1990 Thermo Finnigan automatic system. Pore size and pore volume distribution were determined by mercury porosimetry (Carlo Erba 2000 porosimeter with Macropores unit 120).
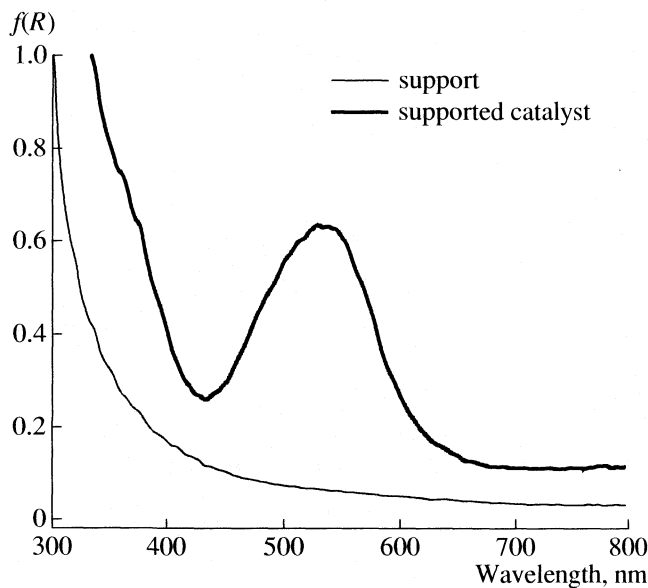
Fig. 1. Diffuse reflectance spectra of the polymer support and polymer supported cobalt catalyst, $f(R)$ is the Kubelka–Munk pseudo-absorbance.
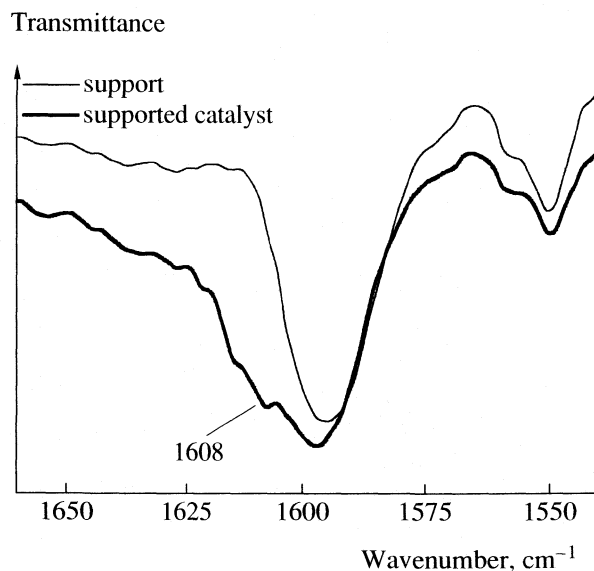
Fig. 2. The IR spectra of the polymer support and polymer supported cobalt catalyst.

Activity tests were performed in a stainless steel, laboratory scale (100 cm³), stirred autoclave with PTFE liner. In all catalytic runs, the following conditions were used: the reaction mixture contained 35 g Ch and 0.5 g of the catalyst (1.43 wt. % of the catalyst with respect to cyclohexane), air pressure was 2.8 MPa, and stirrer speed was 350 rpm. Air-flow rate was maintained at about 100 cm³ min⁻¹. Gas and liquid samples were periodically taken at predetermined periods of time.

The activity tests were performed under isothermal conditions: after an initial fast heating up to the working temperature, the system was maintained at this temperature for 120 min before the reaction was stopped. In each experiment, a fresh charge of the catalyst was used. Tests were performed at 130, 140, 150, 160 and 170°C.

The composition of the liquid samples was analyzed by gas chromatography using stainless steel column packed with 10% Carbowax 20M on Chromosorb WAW, coupled to a flame ionization detector, isothermally at 150°C. The Chhp concentration was determined by iodometric titration and indirectly by reduction with triphenylphosphine [8].

RESULTS AND DISCUSSION

The specific surface area of catalyst samples (S_{BET}) was calculated according to Brunauer–Emmett–Teller method [9] from the nitrogen adsorption isotherms to be S_{BET} = 52 m²/g. This value is only slightly lower then the one obtained for the polymer support (S_{BET} = 59 m²/g), and it is not dependent on the Co content [7]. This catalytic material exhibits a broad pore size distribution

with the pore diameter ranging from 60–110 nm and its mean value about 90 nm.

SEM-EDX analysis of Co^{2+} ions fraction over the catalyst bead revealed non-uniform distribution of the egg-shell type.

At the molecular level, diffuse reflectance UV-Vis spectra with broad band at 535 nm indicated octahedral Co^{2+} coordination (Fig. 1). Moreover, FTIR spectra of the catalyst (Fig. 2) revealed that the pyridine nitrogen lone pair coordinates to the cobalt. When Co^{2+} ions are introduced into the polymer support [10] a new shoulder appears at 1609 cm⁻¹.

Preliminary tests were performed in order to estimate the influence of the oxygen concentration and mixing on the distribution of the products. There were no significant changes in the reaction rate and the product distribution in wide range of the mixing rate and the oxygen feed values. These tests confirmed that the reaction proceeds in kinetic regime and with no kinetic changes with different oxygen feed.

With increasing reaction temperature in the catalytic tests a higher consumption was observed for both Ch and oxygen. Reaction at 130°C wasn't used for the further calculation because this temperature seems to be too low for the initiation of the process.

After an initial period, the oxygen consumption determined from the experimental data at different temperatures evolves to a constant reaction rate, which decreases with the increase of temperature (Fig. 3). Hence, zero order reaction rate was used, with respect to oxygen (equation (1)), according to [11] and our preliminary tests. All Arrhenius plots from evaluated rate constants (in mol dm⁻³ s⁻¹) are shown in Fig. 4. Activation energy calculated from the oxygen consumption
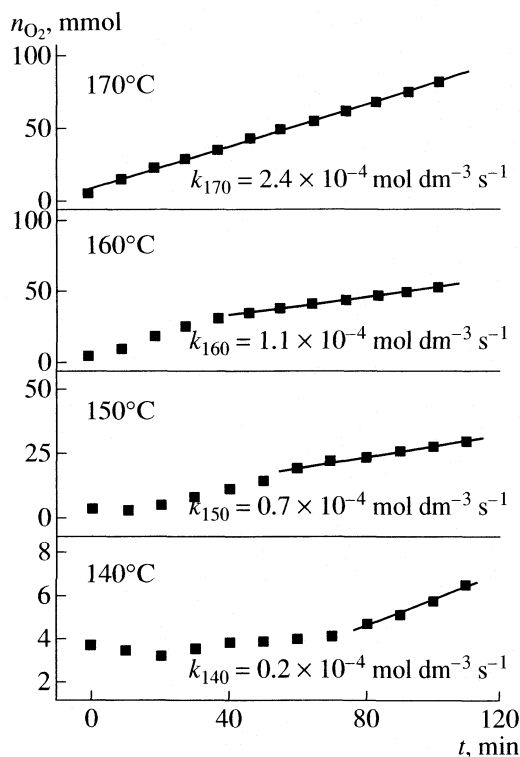
Fig. 3. Quantity of the spent oxygen at different temperatures.
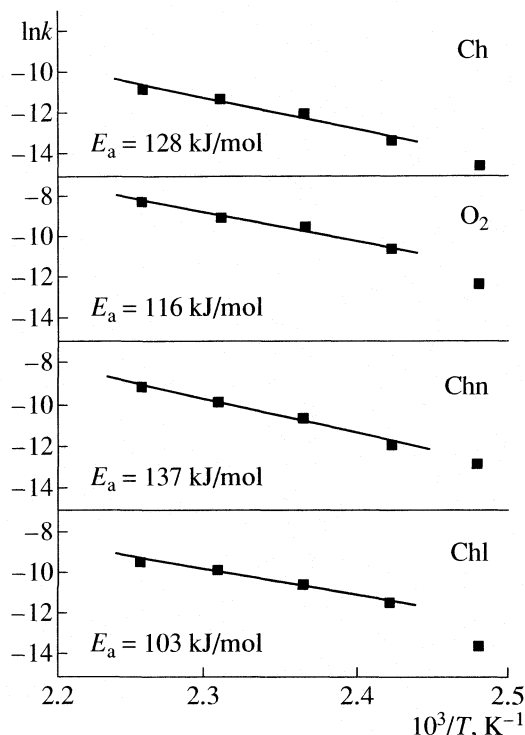
Fig. 4. Arrhenius plots for cyclohexane and oxygen consumption and cyclohexanol and cyclohexanone production.

was $E_a = 116$ kJ/mol which is nearly the same as the one ($E_a = 113$ kJ/mol) reported by Berezin [11] for metal reactor.

$$-d[O_2]/dt = k_2. \tag{1}$$

Decomposition of the cyclohexane molecule is initiated by the removal of hydrogen by molecular oxygen. This step is highly endothermic and requires activation energy of 176 kJ/mol, as reported by (Khar'kova) for cyclohexane in a metal reactor with no catalyst. The hydrogen abstraction is a rate limiting step as the slowest reaction in the mechanism. It was calculated from the Ch consumption according to the equation for the first order reaction Eq. (2) that our catalytic system requires activation energy as low as 128 kJ/mol. The Arrhenius plot from these rate constants in s^{-1} is shown in (Fig. 4) as well. The obtained activation energy value indicates that the catalyst improves the initiation of the radical reaction through the alkyl radicals production reaction.

$$-d[Ch]/dt = k_1[Ch]. \tag{2}$$

Furthermore, higher yields were obtained for both Chn and Chl, at higher reaction temperatures. Activation energies for the Chn and Chl production were evaluated from Eq. (3), for steady state conditions. The production rate of both products is proportional to the concentration of cyclohexylperoxy radical [ChOO$^\bullet$] and Ch [11]:

$$d[P]/dt = k_i'[Ch][ChOO^\bullet] = k_i, \quad k_i = k_3 \text{ or } k_4, \tag{3}$$

where P is any of the products (Chn or Chl), and the rate constants k_3 and k_4 correspond to each product, respectively. The same rate law for the two products is a consequence of the parallel reactions mechanism, since both Chn and Chl are produced from ChOOH as a common precursor. After some initial time, the concentrations of both products increased with approximately constant rate in the used temperature interval and reaction time interval. The constant rate is here a consequence of constant free radical intermediary concentrations in steady state and rather small changes of the [Ch] value due to low conversion levels. Therefore, it was possible to evaluate activation energies of the steady state overall production for both Chl and Chn. The Arrhenius plots calculated from rate constants in mol dm^{-3} s^{-1} are shown in Fig. 4 for both products. The obtained activation energy value for the Chl production process (103 kJ/mol) is lower then for the Chn production process (137 kJ/mol).

Moreover, we can compare the obtained values of the activation energies for both products with the values published by Khar'kova for the uncatalyzed process. Most free radical processes from this model have too low activation energies to be kinetically important for the examined catalytic pathways.

The published activation energies of the reactions:

$$ChOOH \longrightarrow ChO^{\bullet} + OH^{\bullet}, \quad E_a = 135.8 \text{ kJ/mol},$$

$$ChOOH + Ch \longrightarrow ChO^{\bullet} + Ch^{\bullet} + H_2O,$$
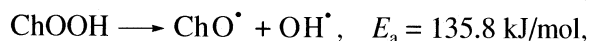
$$E_a = 134.0 \text{ kJ/mol},$$

observed in uncatalyzed system, are both very close to the value obtained for the Chn production in our catalytic system. Chn can be obtained directly by simple recombination-dehydrogenation reaction between the products of these two reactions. It is therefore reasonable to assume that in both catalyzed and uncatalyzed systems, Chn is produced mostly by the same reaction mechanism.

On the other side, the activation energy value accepted for the uncatalyzed reaction:

$$2ChOO^{\bullet} \longrightarrow Ch=O + ChOH + O_2,$$
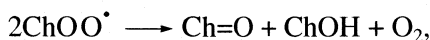
$$E_a = 117.1 \text{ kJ/mol},$$

(in which both Chl and Chn are produced in equal amounts) is significantly higher than our value for the activation energy of Chl production (103 kJ/mol). It can be deduced that catalyst generates new catalytic pathway, favoring the Chl production at lower temperatures. However, activation energies alone are not sufficient to reason on the product distribution, which also depends on time. Therefore, it is still not possible to propose a catalytic mechanism for the Chl and Chn production.

The most significant effect of the catalyst seems to be the lowering of the activation energy for the initiation reaction (hydrogen abstraction) and an appropriate reaction mechanism can be derived to explain the observed catalytic effects. In accordance with our UV-Vis and FTIR spectra, cobalt ions are in octahedral coordination with pyridine rings of the polymer support. The activation of oxygen in the reaction with the central Co ion of the coordination sphere is the most probable path. Activated oxygen in the ligand position is probably more active in the hydrogen abstraction than free dissolved oxygen indicating the formation of cobalt superoxo species on the catalyst surface. Hence, the initiation of the free radical mechanism probably depends on the following reaction:

$$[(P)-Py-Co-O-O^{\bullet}] + Ch \longrightarrow$$

$$\longrightarrow [(P)-Py-Co-O-OH] + Ch^{\bullet},$$
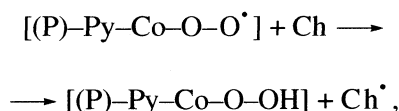
where $Ch^{\bullet}$ represents cyclohexyl radical and [(P)–Py–Co–O–O$^{\bullet}$] is a polymer supported cobalt complex with one axial pyridine ligand and activated dioxygen at the opposite side [12].

CONCLUSION

Results obtained in cyclohexane partial oxidation over the macroporous polymer supported cobalt catalysts confirmed that the reaction proceeds selectively to cyclohexanone and cyclohexanol, with a very low extent of deep oxidation.

The influence of the temperature was characterized through the Arrhenius type behavior and the activation energies were evaluated for both cyclohexane and oxygen consumption and for cyclohexanone and cyclohexanol overall production processes. The catalyst exhibits important role in the initiation of the free radical reaction by lowering the activation energy for the production of alkyl radicals.

ACKNOWLEDGEMENT

REFERENCES

1. D. E. Danley, C. R. Campbell, *Kirk Othmer Encyclopedia of Chemical Technology* (3rd Ed.) (John Willey & Sons; New York, **1**, 514 (1978)).

2. T. V. Khar'kova, I. L. Arest-Yakubovich, V. V. Lipes, Kinetika i Kataliz **30**, 954 (1989).

3. N. N. Semenov, *Some problems relating to chain reactions and to the theory of combustion* (Nobel Lecture, December 11, 1956).

4. G. L. Goe, C. R. Marston, E. F. V. Scriven, E. E. Sowers, *Catalysis of Organic Reactions* (Ed. D. W. Blackburn, Marcel Dekker, Inc., New York, p. 275 (1989)).

5. I. W. C. E. Arends, R. A. Sheldon, Appl. Catal. A **212**, 175 (2001).

6. D. Lončarević, Ž. Čupić, M. Odović, J. Serb. Chem. Soc. **70**, 209 (2005).

7. D. Lončarević, Ž. Čupić, Material Sciences Forum, **494**, 363 (2005).

8. G. B. Shul'pin, J. Mol. Cat. A: Chemical **189**, 36 (2002).

9. F. Rouquerol, J. Rouquerol, K. Sing, *Adsorption by Powders and Porous Solids* (Academic Press, London, 1999).

10. L. A. Belfiore, M. P. McCurdie, E. Ueda, Macromolecules, **26**, 6908 (1993).

11. I. V. Berezin, E. T. Denisov, N. M. Emanuel, *The oxidation of cyclohexane* (Moscow University Publishing, Moscow, pp. 89, 13, 103 (1962)) [in Russian].

12. B. S. Tovrog, D. J. Kitko and R. S. Drago, J. Am. Chem. Soc. **98**, 5144 (1976).

CHEMICAL KINETICS
AND CATALYSIS

TIME DEPENDENT INHIBITION OF Na+/K+-ATPase INDUCED BY SINGLE AND SIMULTANEOUS EXPOSURE TO LEAD AND CADMIUM IONS

© 2007   V. Vasić, D. Kojić, K. Krinulović, M. Čolović, A. Vujačić, D. Stojić

Department of Physical Chemistry, Institute of Nuclear Sciences Vinča, P.O. Box 522, 11001 Belgrade, Serbia
E-mail: evasic@vin.bg.ac.yu

Abstract – Time dependent interactions of Na+/K+-ATPase, isolated from the rat brain synaptic plasma membranes (SPMs), with Cd^{2+}- and Pb^{2+}-ions by single exposure and in the mixture, were investigated *in vitro*. The interference of the enzyme with these metal ions was studied as a function of different protein concentrations and the exposure time. The aim of the work was to investigate the possibility for selective recognition of Cd^{2+}- and Pb^{2+}-ions in the mixture, on the basis of the various rate of their protein – ligand interactions. The decreasing protein concentration increased the sensitivity of Na+/K+-ATPase towards both metals. The selectivity in the protein – ligand interactions was obtained by variation of preincubation time (incubation before starting enzymatic reaction).

INTRODUCTION

The membrane enzyme Na+/K+-ATPase is expressed in synaptic plasma membranes (SPM) of almost all animal cells, as functions to maintain sodium and potassium gradients across the membrane that subserve cellular activities, such as volume regulation, action potential and secondary active transport [1, 2].

It is well known that some heavy metals (Pb^{2+}, Hg^{2+}, Cd^{2+} etc.), as well as many organic compounds (pesticides, drugs), are potent inhibitors of Na+/K+-ATPase in concentration dependent manner [3–10].

The investigation of corresponding biosensing system, using this enzyme, for selective recognition of toxic agents in water solutions is of interest. The measure of ATPase activity is temporal change of the concentration of inorganic orthophosphate (P_i) liberated by enzymatic catalyzed hydrolysis of ATP. It is usually determined by spectrophotometric methods [11]. Development of test method, for detection Na+/K+-ATPase inhibitors based on the color reaction for orthophosphate determination, seems reasonable.

Several enzyme-based sensors for determination of the total heavy metals have been reported, but heavy metals show, in general, non-selective effects on the enzymatic activity [12–14]. The earlier investigations of metal ion effects and organic compounds on synaptic plasma membrane Na+/K+-ATPase pointed out that the percent of the inhibited activity depended of many factors, such as the presence of chelators, protein concentration and the duration of the enzyme-ligand interaction [15, 16].

The aim of this work was to investigate the possibility for selective recognition low concentration of Cd^{2+} and Pb^{2+} as the inhibitors of Na+/K+-ATPase activity

based on the difference in their interactions with the protein.

EXPERIMENTAL

Chemicals and material

All chemicals for medium assay were commercially available from Sigma (St. Louis, MO, USA) and of reagent grade. The metal ion salts: lead (II) nitrate, cadmium (II) nitrate, NaCl, KCl, stannous chloride, ammonium molybdate, were from Merck (Darmstadt, Germany). All solutions were prepared using de-ionized water.

Synaptic plasma membranes (SPM) were isolated from the whole rat brain of 3-month-old male Wistar albino rats from the local colony. Animals were kept under controlled illumination (lights on: 5:00 a.m.–5:00 p.m.) and temperature ($23 \pm 2°C$), and had free access to food and water. After decapitation, brains were rapidly excised and pooled (6/pool) for immediate preparation of SPM. The SPM were isolated according to the method of Cohen et al. [17], as modified by Towle and Sze [18]. The preparation procedure and the purity of SPM preparations were described previously [19]. The mitochondrial contamination, based on both morphological and biochemical markers, was less than 7%. Protein content was determined by the method of Lowry et al., as modified by Markwell et al. [20].

ATPase assay

Total ATPase activity was determined in 0.2 ml standard incubation medium containing 0.05 M Tris-HCl (pH 7.4), 0.1 M NaCl, 0.02 M KCl, 5×10^{-3} M $MgCl_2$, 2×10^{-3} M ATP and 25 μg protein, and final volume of 2 ml contains 0.05 M Tris-HCl (pH 7.4),

Table 1. Spectrophotometric response of the colorimetric assay as the function of the reaction mixture volume and incubation time τ (containing 25 µg protein)

Volume, ml	A_{690} (control*)		
	τ = 10 min	τ = 20 min	τ = 40 min
0.2	0.445 ± 0.005	0.675 ± 0.006	0.750 ± 0.007
1	0.250 ± 0.003	0.465 ± 0.002	0.545 ± 0.005
2	0.220 ± 0.002	0.310 ± 0.003	0.330 ± 0.002
4	0.150 ± 0.001	0.255 ± 0.002	0.310 ± 0.003

Notes. The standard concentrations of constituents and buffer as described in Experimental.

0.1 M NaCl, 0.02 M KCl, 5×10^{-4} M MgCl$_2$, 4×10^{-4} M ATP and 25 µg protein in the presence or absence (control) of the desired concentration of inhibitors or their mixtures. The activity obtained without NaCl and KCl in the medium assay was attributed to Mg^{2+}-ATPase. Na$^+$/K$^+$-ATPase activity was calculated as a difference between the total ATPase and Mg^{2+}-ATPase activity.

Incubation mixtures were incubated before enzymatic reaction for different preincubation time, keeping the reaction time constant and vice versa, at 37°C. All experiments were carried out by starting the reaction with ATP, to minimize the possibility that the inhibitory effect may be reduced through the time-dependent formation of an inactive metal-ATP complex. After the required incubation period, the reaction was stopped by addition of 22 µl ice-cold 3M HClO$_4$, and cooled by ice water for 15 min. The results were expressed as the relative activity, i.e., the specific activity of enzyme at a particular concentration of metal ion divided by the specific activity of the control specimen (in the absence of metal) and represent the mean values of at least three independent experiments made in duplicate. The specific activity was expressed in µmol P$_i$/mg protein/g.

Monitoring enzyme activity

After the enzymatic reaction was stopped, the reagents for color development using the modified spectrophotometric procedure [7] based on the modified stannous chloride method were added. The solution was developed to 5 ml. P$_i$ liberated from the hydrolysis of ATP during the course of the reaction was measured by reading the absorbance at 690 nm after 20 min.

Apparatus

The spectrophotometric measurements were performed on Beckman 5260 UV VIS spectrophotometer.

RESULTS AND DISCUSSION

The effect of reaction mixture volume and reaction time on the absorbance of the colorimetric assay for Na,K-ATPase activity determination

Three series of experiments were performed in order to investigate the optimal conditions for measuring the enzyme activity. The aim was to find out the conditions for decreasing the detection limit of Na,K-ATPase activity in the presence of inhibitors due to the decreasing of protein concentration.

In the first series of experiments the response of colorimetric assay for Na$^+$,K$^+$-ATPase activity was measured varying the volume of the reaction mixture from 0.2 to 4 ml. The amount of protein (25 µg), ATP, and Mg^{2+}-ions was kept constant (as in standard incubation mixture 0.2 ml), and the varying of reaction mixture volume led to the lowering of the concentration of these reaction mixture components. Besides, the concentration of Na$^+$- and K$^+$-ions in various reaction mixture volumes was kept constant. The concentration of P$_i$ as a measure of Na$^+$,K$^+$-ATPase activity was determined using the modified spectrophotometric procedure [11]. The values of the absorbance of the colorimetric assay for standard (10 min) incubation time as the function of the reaction mixture volume are presented in Table 1. The results showed that the absorbance of the colorimetric assay decreased by increasing the reaction mixture volume from 0.2 ml to 4.0 ml. Consequently, it was concluded that the measurable signal (absorbance above 0.1) was obtained by increasing the reaction volume from 0.2 to 4.0 ml.

In the second series of experiments the activity of the enzyme in various reaction volumes was measured as the function of incubation time. The values of the absorbance of the colorimetric assay are also presented in Table 1. As can be seen, the prolongation of the reaction time from 10 to 40 minutes also induced the increasing of absorbance of the colorimetric assay. It was worthy to notice that this effect was lowered by reaction medium volume above 2.0 ml. As conclusion, the enzymatic reaction in reaction mixture volume 2.0 ml after 10 min incubation gave the measurable and convenient spectrophotometric response concerning the enzymatic activity, and these parameters were used in further experiments.

In the third series of experiments the activity of Na$^+$/K$^+$-ATPase was followed by varying the concentration of ATP from 0.1 mM to 1 mM in the above mentioned conditions. The aim was to find out the range of ATP concentration for constant specific activity of the enzyme. The change of the specific activity of Na$^+$/K$^+$-ATPase vs. ATP concentration is presented in Fig. 1. It can be seen from the results that the reaction rate reached its plateau at ATP concentration above 0.4 mM. In further experiments ATPase activity was investigated in medium assay of 2 ml in the presence of 0.4 mM ATP.

Na$^+$/K$^+$-ATPase activity, μmol P$_1$/min per mg protein
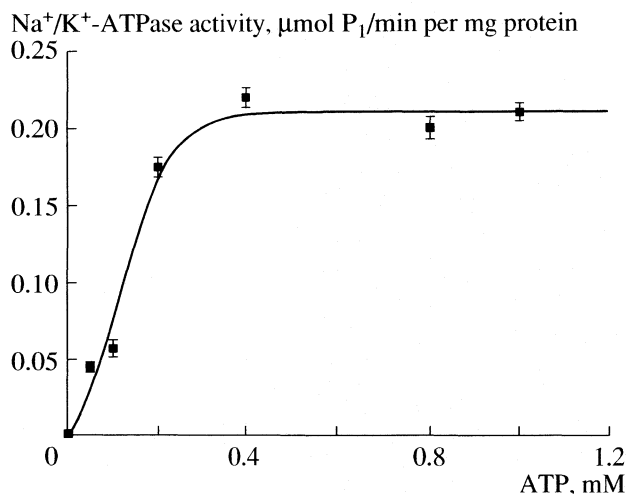
Fig. 1. Activity of SPMs Na$^+$/K$^+$-ATPase as a function of ATP concentration. Final reaction volume was 2ml and composition of medium assay as described in *Experimental*.

In all cases concentration dependent sigmoid inhibition curves were obtained. The IC$_{50}$ values (metal ion concentration which produced 50% inhibition of the enzymatic activity) were calculated from experimental results. The obtained values are presented in Table 2. As the results indicated, decreasing the protein concentration induced the lower IC$_{50}$ values in both cases. The results presented in Table 2 show, that in the presence of 12.5 μg/ml protein the metal concentration which produced 50% of enzyme activity inhibition was lower than the maximal allowed concentration of this metal in water [21]. It is worthy to notice, that IC$_{50}$ values for Pb^{2+} and Cd^{2+} induced inhibition, under these experimental conditions are about 10 fold lower compared to the other studies [3, 4]. These differences may be resulted from different membrane systems (SPMs in this work), but the protein concentration and composition of medium assay are the most important for these observations.

Effect of protein concentration on the IC$_{50}$ values of Pb^{2+} and Cd^{2+} induced inhibition of Na$^+$/K$^+$-ATPase

The influence of protein concentration on the IC$_{50}$ values for the measurement of Na$^+$,K$^+$-ATPase activity were investigated in the presence of Cd^{2+} and Pb^{2+} ions. Na$^+$/K$^+$-ATPase activity was investigated by varying the concentrations of Pb(NO$_3$)$_2$ and Cd(NO$_3$)$_2$ from 1×10^{-9} to 1×10^{-3} M in reaction mixture containing 125 μg/ml or 12.5 μg/ml protein. The tubes were incubated for 10 minutes at 37°C before starting enzymatic reaction, and after addition of ATP the tubes were incubated for a future 10 minutes. The results are presented in Fig. 2.

Effects of metal-enzyme contact time on inhibition of Na$^+$/K$^+$-ATPase activity by single and simultaneous exposure to Pb^{2+} and Cd^{2+} ions

Inhibition of Na$^+$/K$^+$-ATPase activity in the presence of 12.5 μg/ml protein in 2.0 ml reaction medium by 1×10^{-4} M Pb^{2+} and 2×10^{-6} M Cd^{2+} by single and simultaneous exposure (in the mixture) was investigated as a function of the preincubation time.

The results presented in Fig. 3 showed that the variation of the preincubation time, produced the various effects on the enzyme activity. As it could be seen from Fig. 3 (curve *1*), Cd^{2+} induced about 35% inhibition during the first 5 minutes, by single exposure. The pro-
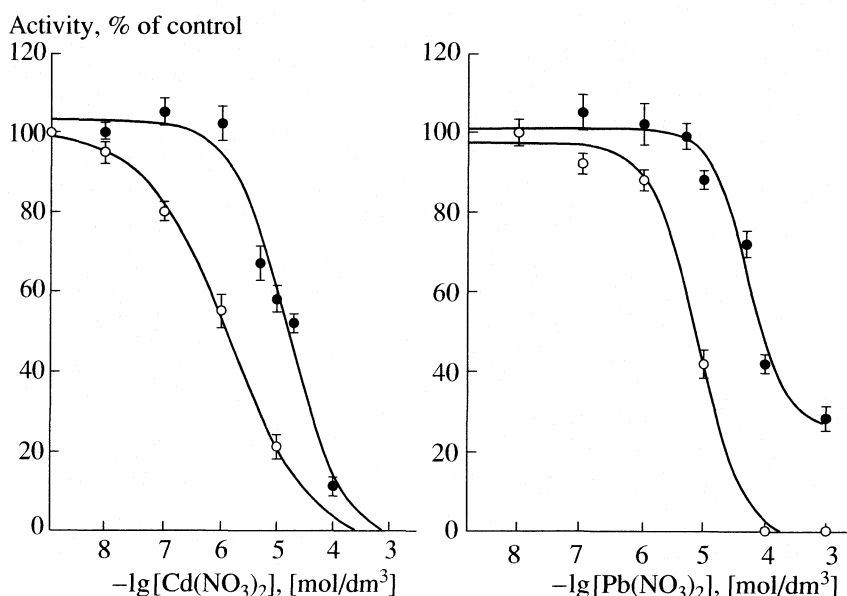
Fig. 2. Effects of Pb^{2+} and Cd^{2+} on the activity of Na$^+$/K$^+$-ATPase in the presence of different protein concentration (125.0 μg/ml protein - solid symbols; 12.5 μg/ml protein – open symbols).

Table 2. The inhibitory efficiency (IC_{50} values, M) of Cd^{2+} and Pb^{2+} for Na^+/K^+-ATPase as a function of protein concentration

Protein concentration, µg/ml	Cd^{2+}	Pb^{2+}
125.0	$(2.0 \pm 0.1) \times 10^{-5}$	$(1.0 \pm 0.1) \times 10^{-4}$
12.5	$(2.0 \pm 0.2) \times 10^{-6}$	$(7.0 \pm 0.3) \times 10^{-6}$

longed contact time did not influence the change of the enzyme inhibition. On the contrary, the effect of Pb^{2+} (Fig. 3, curve 2) on the enzyme activity was dependent on exposure time in the interval from 1 to 40 minutes. It is significant, that in the first five minutes the change of the activity by single exposure on Pb^{2+}, remained in the range of the experimental error. However, the inhibition continually increased, being near 100% after 40 min.

Various effects of preincubation time on the inhibition of Na^+/K^+-ATPase activity by Cd^{2+} and Pb^{2+} could be explained by the difference in the reaction rate of solvent exchange (water) in coordination sphere of the metal ion [22] during the ligand-protein interactions. Namely, the rate of Cd^{2+} ions bonding to the inhibitory sites of enzyme was faster compared to this rate for Pb^{2+} ions, and the results show that the equilibrium was achieved in the first five minutes. On the contrary, the reaction of Pb^{2+} ions with enzyme inhibitory sites was much slower, but this metal exerted more toxic effect, since it inhibited the enzyme activity completely after 40 min exposure.

Our investigations also showed that the reaction time, after the start of the enzymatic reaction by adding

ATP, did not influence the degree of the inhibition (data not shown) by single exposure to the both metal ions. The high concentration of substrate molecules in the reaction medium during the enzymatic reaction and their competition with metal ions for same bonding sites are probably the reason for insignificant effect of the reaction time, since it was reported that Cd^{2+} and Pb^{2+} are competitive inhibitors of Na^+/K^+-ATPase [3, 10].

The experimental data in Fig. 3 (curve 3, points) present the enzyme inhibition after the exposure to the mixture containing 1×10^{-6} M Pb^{2+} and 2×10^{-6} Cd^{2+}, under the same experimental conditions as above. The results obtained for the mixture of inhibitors fit very well with the calculated values (curve 3, dash line) for the single exposure (Fig. 3, curves 1 and 2). The simultaneous exposure to the mixture of metal ions induced an additive effect on the enzyme activity in all cases. Moreover, the inhibition was complete after 25 min. The additive inhibition of SPM Na^+/K^+-ATPase activity with Pb^{2+} and Cd^{2+} suggests that both metals are competing for the same set of inhibitory binding sites. This competition is in agreement with the high, similar affinities that Pb^{2+} and Cd^{2+} have for binding to sulfhydril groups [22, 23].

The variation of preincubation time by simultaneous exposure can enable the selective recognition of inhibition induced by these ions. Keeping the short preincubation time between the mixture of these ions and protein, the inhibition is mainly due to Cd^{2+} ions. If the enzyme activity insignificantly decreased after 5 minutes of contact time, but continually increased by prolonged contact time under the same experimental conditions, the inhibition can probably be induced by the presence of Pb^{2+} ions. If activity of enzyme decreased significantly in the first 5 min and continually to 25 min, both metal ions are present in the reaction mixture.

This difference in time dependent protein – ligand interactions may enable possible application of this enzyme system (SPM) for selective recognition of these ions. As reported in previous study [24], immobilization increased the stability of this enzyme system, and preserved the sensitivity to divalent heavy metals, such as Cd^{2+} and Hg^{2+}. Investigation of the time effects on the inhibition of these metals on immobilized SPM for their selective detection is the subject of further investigations.

Fig. 3. Effect of preincubation time on Na^+/K^+-ATPase activity in presence of 2×10^{-6} M Cd^{2+} (curve 1), 1×10^{-6} M Pb^{2+} (curve 2) and the mixture of 2×10^{-6} M Cd^{2+} and 1×10^{-6} M Pb^{2+} (curve 3 – experimental data open triangle; calculated data dash line).

REFERENCES

1. Rodrigez de Lores Arnaiz, G.; Pena, C. *Neurochem. Int.* **27**, 319 (1995).

2. Vasilets, L. A., Schwarz, W., *Biochem. Biophys. Acta* **1154**, 201 (1993).

3. Rajanna, B., Hobson, M., Bansal, S.K., Desaiah, D., *Toxicol. Lett.* **18**, 331 (1983).

4. Carfagna, M. A., Ponsler, G. D., Muhoberac, B. B., *Chem. Biol. Interact.* **100**, 53 (1996).

5. Vasić, V., Jovanović, D., Krstić, D., Vučković, D., Nikezić, G., Horvat, A., Vujisić, Lj., Radak, B., *Arch. Toxicol. Kinet. Xenobiot. Metab.* **5**, 279 (1997).

6. Jovanović, D., Vasić, V., Nikolić, V., Ćetković, S., Nikezić, G., *Arch. Toxicol. Kinet. Xenobiot. Metab.* 8 (3), 152 (2000).

7. Nikezić, G., Horvat, A., Nedeljković, N., Todorović, S., Nikolić, V., Kanazir, D., Vujisić, Lj., Kopečni, M. *Gen. Phisiol. Biophis.* **17**, 15 (1998).

8. Horvat, A., Vujisić, Lj., Nedeljković, N., Todorović, S., Vasić, V., Nikolić, V., Nikezić, G., *Arch. Toxicol. Kinet. Xenobiot. Metab.* **5**, 267 (1997).

9. Vasić, V., Krinulović, K., Krstić, D., Momić, T., Horvat, A., *Monats. Chem.* **135**, 605 (2004).

10. Hexum, T. D., *Biochem. Pharmacol.* **23**, 3441 (1974).

11. Taras, M. J., Greenberg, A. E., Hoak, R. D., Rand, M. C., In *Standard Methods for the Examination of Water and Wastwater* (13thedition), American Public Health Association, Washington, p. 530 (1971).

12. Toren, E. C., Burger, F. J., *Microchim. Acta*, 1049 (1968).

13. Preininger, C., Wolfbeis, O., *Biosens. Bioelectron.* **11**, 981 (1996).

14. Gayet, J. C., Haouz, A., Geloso-Meyer, A., Burstein, C., *Biosens. Bioelectron.* **8**, 177 (1993).

15. Vasić, V., Jovanović, D., Krstić, D., Nikezić, G., Horvat, A., Vujisić, Lj., Nedeljković, N., *Toxicol. Lett.*, **110**, 95 (1999).

16. Peyser, Y. M., Ben-Hur, M., Weher, M. M., Muhlrad, A., *Biochemisry* **35**, 4409 (1996).

17. Cohen, R. S., Blomberg, F., Berzins, K., Siekevits, P., *J. Cell. Biol.* **74**, 181 (1977).

18. Towle, A. C., Sze, P. Y., *J. Steroid. Biochem.* **18**, 135 (1983).

19. Horvat, A., Nikezić, G., Martinović, *J. Experientia* **51**, 11 (1995).

20. Markweel, A. K., Hass, S. M., Bieber, L. L., Tolbert, N. E.; *Anal. Biochem.* **87**, 206 (1978).

21. EPA. *Safe Drinking Water Act*, 1974.

22. Sillen, L. G., Martell, A. E., In *Stability Constants of Metal-Ion Complex*, Special Publication No. 1, Chem Soc, London, 1971.

23. Martin, B. R., *Bioorganic chemisty of toxicity*. In Handbook on Toxicity of Inorganic Compounds (Seiler H.G., Sigel H., Siegel A., Eds.), Dekker, New York, 1988.

24. Vasić, V., Jovanović, D., Horvat, A., Momić, T., Nikezić, G., *Anal. Biochem.* 300, 113 (2002).

CHEMICAL KINETICS
AND CATALYSIS

ANALYSIS OF COMPLEX OSCILLATORY DYNAMICS
OF A pH OSCILLATOR

© 2007   D. Bakeš*, L. Schreiberová*, I. Schreiber*, M. J. B. Hauser**

*Department of Chemical Engineering and Center for Nonlinear Dynamics of Chemical and Biological Systems,
Prague Institute of Chemical Technology, Technická 5, 166 28 Prague 6, Czech Republic
**Institut für Experimentelle Physik, Abteilung Biophysik, Otto-von-Guericke-Universität Magdeburg, Universitätsplatz 2,
39106 Magdeburg, Germany
E-mail: Igor.Schreiber@vscht.cz

Abstract – Reaction systems that display pronounced periodic and aperiodic variations in the pH value of the reaction medium are known as pH oscillators. A member of this family of reactions studied here, the Cu(II)-catalyzed oxidation of thiosulfate by hydrogen peroxide in acidic solution, is known to display rich variety of oscillatory dynamics. We focus on experimental time series showing complex aperiodic dynamics that simultaneously possess the characteristics of period-doubled large-amplitude oscillations and irregular small-amplitude oscillations, reminiscent of mixed-mode dynamics. An analysis based on the reconstruction of the attractor from the measured time series by two different methods and a subsequent calculation of the maximal Lyapunov exponent reveals that this interesting dynamical regime is a manifestation of deterministic chaos.

Oscillatory dynamics is of great importance in biological and physiological reaction systems [1, 2]. Most of them are characterized by a multitude of highly regulated biochemical components. Chemical reaction systems are often much simpler, hence providing more systematic insights into the fundamental mechanisms leading to such complex dynamics. So far, a big variety of chemical oscillators has been designed and studied. Among them, the family of so-called pH oscillators has recently attracted considerable scientific interest, since these reactions lead to substantial oscillations in the pH value of the reaction medium, making the pH value a suitable parameter for inducing changes in key physiological and technical parameters in the environment of the oscillator. Thus, combinations of pH oscillators and pH-responsive gels and membranes [3–5], or of pH oscillators and pH-activated enzymes [6, 7] are studied and discussed.

Although glycolysis [8] and the Bray-Libhafsky reaction [9] have been shown to support pH oscillations, a systematic design of a family of pH oscillators based on a common sulfur chemistry has been started some two decades ago [10, 11]. This family is based on the autocatalytic pH dependent oxidation of sulfite by H_2O_2 [11–15] and reactions which consume H^+ thus providing for negative feedback. The latter include reactions with hexacyanoferrate [11, 16], carbonate [12, 13, 15], the enzyme model compound hemin [17, 18], thiosulfate [10, 19], and a series of sulfur-containing compounds [20]. These systems were reported to display rich dynamics when investigated in a continuous-flow stirred tank reactor (CSTR). The behaviour of pH oscillators ranges from stationary dynamics, coexisting stationary states [14], to simple periodic oscillations [13, 15], and to a more complex behaviour, such

as complex mixed-mode oscillations [17, 18], or even chaotic dynamics [12, 21]. It should be noted, however, that the degree of dynamical complexity varies from one pH oscillator to another.

In the present letter, we investigate the complex dynamics occurring in the oxidation of thiosulfate catalyzed by cupric ions, the so-called HPTCu system. This pH-oscillatory reaction system has been shown experimentally to display periodic oscillations as well as compound mixed-mode oscillations [10]. In addition, parameter regions where multistability occurs have been reported [10] and all these dynamics were also obtained by simulation [22]. When studying the complex dynamics of the HPTCu system, we monitored complex aperiodic time series that simultaneously show the characteristics of period-doubled large-amplitude oscillations and a series of irregular small amplitude oscillations, reminiscent of mixed-mode states. In the following, we wish to characterize the nature of this type of dynamics.

MATERIALS AND METHODS

Experimental

Experiments were carried out in a CSTR of 12.5 ml volume equipped with a thermostating jacket. Reaction solutions were delivered to the reactor by a stepping motor-driven syringe pump holding three syringes with stock solutions, while superfluous reaction medium was removed from the reactor at the same flow rate. The flow rate k_0 corresponds to the inverse mean residence time of the reactants in the reactor and this parameter was varied in our experimental studies. All experiments were performed at $25.0 \pm 0.1°C$.

Reactant solutions were prepared daily from reagent grade chemicals and water produced by an ion-exchanger membrane filtration purifying system. Three solutions with inlet concentrations of $[H_2O_2]_0 = 0.1$ mol/l, $[Na_2S_2O_3 \cdot 5H_2O]_0 = 0.008$ mol/l, and $[CuSO_4]_0 = 5.0 \times \times 10^{-5}$ mol/l in 0.001 mol/l H_2SO_4 were delivered from either 50 or 100 ml syringes by a syringe pump.

The dynamics in the reactor was monitored by a pH glass microelectrode (Mettler-Toledo). These data were sampled at a frequency of 3 Hz and stored in a computer for later analysis.

Methods of time series analysis

To characterize the type of dynamics presented by the HPTCu reaction, the experimentally measured time series were subjected to different methods of time series analysis.

In a preliminary effort, the periodicities encoded in a time series were investigated by Fourier transformation. However, while the Fourier spectra are useful in characterizing periodic and quasiperiodic data, their interpretation becomes difficult when it comes to noisy and chaotic time series. In fact, the distinction of noisy and chaotic dynamics is hardly feasible from the Fourier spectra.

The analysis of complex time series relies on attractors that are reconstructed from experimental time series. Since further evaluation and characterization of the data depends on these attractors and their "quality", we reconstructed the attractors by two independent methods and analyzed the differences in attractor characteristics implied by the reconstruction methods. The attractors were obtained either by the method of time delays according to Takens [23], or by subjecting the time series to singular value decomposition (SVD) and reconstructing the attractor from the obtained modes.

The reconstruction of attractors by time-delays was carried out using the program package TISEAN [24]. A discrete time series $y_i = (x_1, x_2, ..., x_n)$ was plotted against time-delayed versions of itself, i.e. $y_j = (x_{1 + j\tau_d}, x_{2 + j\tau_d}, ..., x_{n + j\tau_d})$, where τ_d is a chosen discrete time delay, $j = 1, ..., m$, and m is the dimension of the reconstructed phase space. The crucial point for this reconstruction method consists in defining the optimal delay time τ_d such that the time series and its time-delayed counterpart are as independent of each other as possible. To find the optimal time delay τ_d we calculated the minima of the mutual information $I(\tau_d)$ [25]

$$I(\tau_d) = \sum_i \sum_j p_{ij}(\tau_d) \ln \frac{p_{ij}(\tau_d)}{p_i p_j},$$

where p_i and p_j are the probabilities to find the time series in the a i-th and j-th intervals, respectively, while $p_{ij}(\tau_d)$ is the joint probability that the time series value

is in the i-th interval and after time τ_d, the value is in the j-th interval.

The second method used is the reconstruction by singular value decomposition (SVD) [26]. Here, the trajectory matrix X having as columns the time-delayed series, is obtained by applying a series of minimal time-delays (i.e. $\tau_d = 1$, corresponding to 0.333 s) to the original data. According to SVD, the matrix X is decomposed into three matrices

$$X = USV^T$$

where U and V are orthogonal matrices. The matrix V serves as the new orthonormal basis onto which the original time series is projected to yield the new attractor matrix U. S is a diagonal matrix containing the singular values which are usually sorted by decreasing values of s_{ii}. The attractor can be reconstructed by using a few leading modes, while modes associated with very low singular values may be neglected, since they usually reflect experimental noise. In fact, criteria for cutting off insignificantly low singular values have been developed in order to provide for reliable noise filters, which suppress noise while still retaining a maximum of useful information [26].

RESULTS AND DISCUSSION

Measured time series

After sufficiently long time (a couple of hours) it is assumed that the system reaches a sustained asymptotic regime. This regime can be a steady state, periodic or aperiodic oscillations. The aperiodic regime seems to arise via a period-doubling bifurcation from simple periodic oscillations. For $k_0 < 0.0075$ s^{-1} simple large-amplitude oscillations with period of ~500 s are observed. Upon a slight increase in the flow rate the system undergoes a period-doubling bifurcation leading to larger and smaller peaks and, almost simultaneously, low-amplitude, high-frequency oscillations emerge on the descending shoulder of the larger peak having the duration of about 200 s. This feature reveals the complex nature of the reaction dynamics, and for $k_0 > 0.01$ s^{-1}, highly complex mixed-mode aperiodic oscillations are well developed. A typical example of such dynamics is shown in Fig. 1.

In the present letter we focus on these aperiodic dynamics and examine whether they are a manifestation of deterministic chaos. The time series in Fig. 1 is characterized by large-amplitude peaks with widely varying amplitudes on the order of a pH unit, within which shorter episodes of rapid, small-amplitude irregular oscillations (some being just ramps) are interspersed, both on the descending and ascending shoulders of the larger peaks. The overall length of the measured data is a maximum allowed by the syringe pumps used. While this length may be generally considered as somewhat restricted for the time series analysis, it does show suffi-
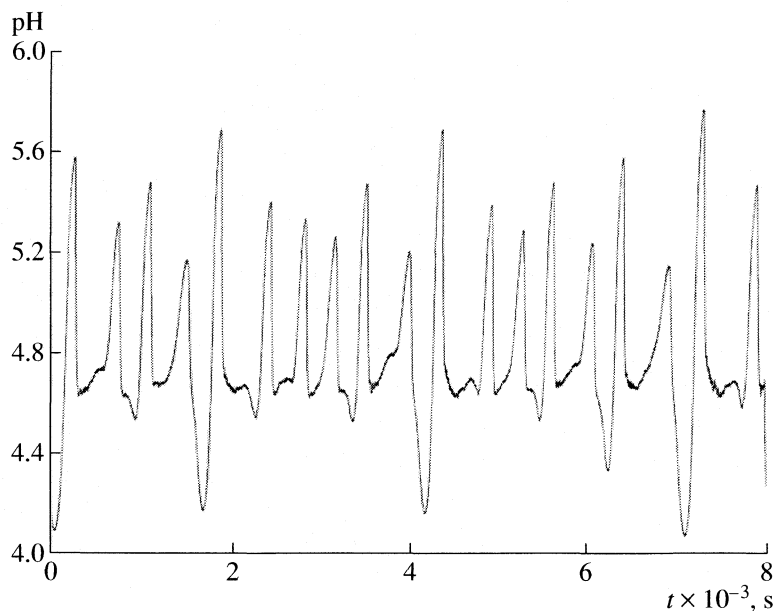
Fig. 1. Complex time series at a flow rate $k_0 = 0.0109$ s^{-1}. It simultaneously shows characteristics of period-doubled large-amplitude oscillations and that of a series of irregular small amplitude oscillations, reminiscent of mixed-mode states.
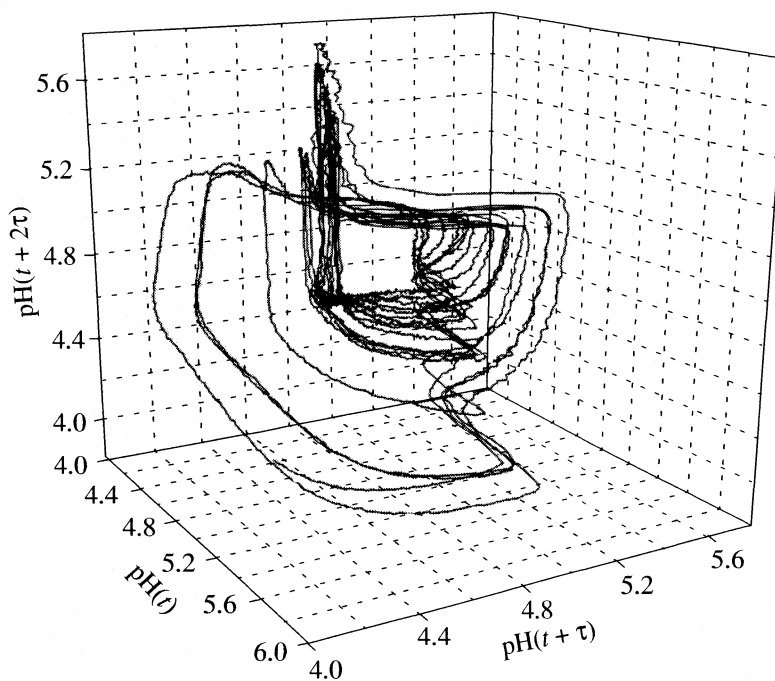
Fig. 2. Attractor reconstructed from the time series (Fig. 1) by the method of time delay, using $\tau_d = 300$ (corresponding to a delay time of 100 s).

cient repetition of features to be well reflected in the re-constructed attractor as shown below.

Phase space reconstruction

First, the experimental data are analyzed by the method of delay. A three dimensional plot of the recon-structed attractor with a time delay $\tau_d = 300$ (corresponding to a delay time of 100 s) obtained from the minimum of mutual information is shown in Fig. 2. The Figure suggests a sheet-like arrangement with the internal part of the attractor having a complex multi-layered structure characteristic of low-dimensional chaotic dynamics.
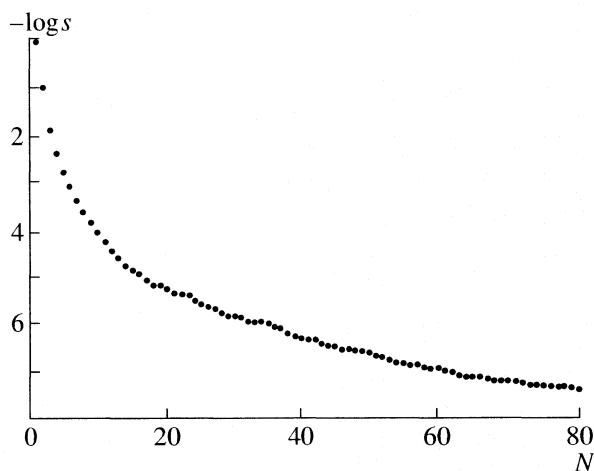
Fig. 3. Spectrum of the normalized singular values (s); N – ordinal number.

Next, the singular value decomposition method was employed. The decomposition provides the spectrum of the normalized singular values s which are arranged according to their magnitude in decreasing order and plotted in logarithmic scale, see Fig. 3. The singular value of a given mode represents the "quantity of information" contained in this mode. In general, it is expected that there exists a constrained number N_e of modes carrying all essential information about the decomposed signal; N_e corresponds to the embedding dimension of the attractor. The modes with greater ordinal number than N_e carry predominantly the information about noise. This is normally indicated by a sudden change in the slope of the graph of singular values. But it is also possible that the embedding dimension is high, therefore the breakpoint is not well discernable. In Fig. 3 the dependence of the singular values on ordinal number is quite smooth, which seems to suggest that the embedding dimension is high.

Two different applications of the SVD method are used after decomposition into the modes: (i) the data are filtered by removing modes associated with small singular values and then the method of delay is applied to the reconstructed time series, and (ii) selected modes are used for the visualization of the trajectory in the phase space.

Following the first approach with the same time delay τ_d as in the case of the reconstruction from the prime data and with the use of about ten first modes, the attractor is smoother than that in Fig. 2, making thus the structure of the attractor more easy to discern. In this regard, the SVD method provides a good tool for smoothing out the prime data, but one has to be careful with the number of modes used for the reconstruction, particularly because we do not have a clear indication in Fig. 3, where to cut off the modes.

Using the second approach, the first three modes are plotted, see Fig. 4. In general, the first few dominant modes are expected to represent the large- and medium-scale dynamics of the system. Higher modes involve mainly the small-amplitude oscillations and even higher modes become dominated by noise. Thus the
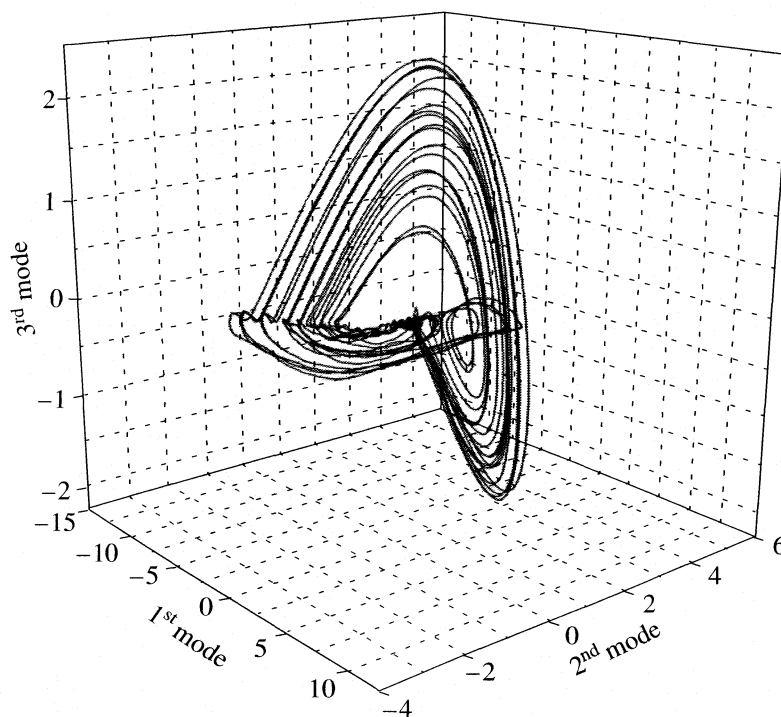
Fig. 4. Attractor reconstructed from the leading three modes obtained by SVD the time series of Fig. 1.
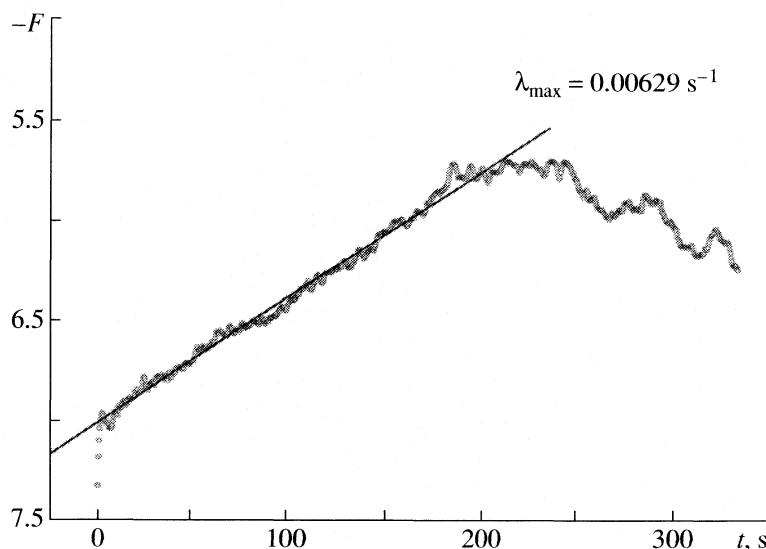
Fig. 5. Plot of the stretching factor (F) against time. The slope corresponds to the maximal Lyapunov exponent λ_{max}.

use of different combinations of modes in the phase space plot represents the "local" dynamics of the system on different scales. Unlike deterministic dynamics, noise fills the space uniformly providing no visible structure. By inspecting Fig. 4, the trajectory clearly extends along a large-scale folded two-dimensional sheet and, in addition, makes small-scale loops within a subsheet embedded in the middle part of the reconstructed attractor. This corresponds well to large- and small-amplitude oscillations in the prime time series while omitting higher SVD modes mostly removes fuzziness of the smallest scales, thus supporting the presence of deterministic chaotic dynamics.

Lyapunov exponents

As it was shown above, the visualization is a convenient method to study the geometric complexity of the attractor reconstructed from the data. However, it is also desirable to characterize the assumed deterministic chaos by examining temporal dynamics on the attractor. Chaotic dynamics should exhibit local exponential divergence of nearby trajectories in at least one direction within the attractor. This sensitivity is expressed in terms of positive Lyapunov exponents associated with expanding directions. To this purpose, we use the method of calculating the maximal Lyapunov exponent provided by the TISEAN package [24]. For a chosen embedding dimension and a radius of a sphere surrounding any particular point on the attractor, a stretching factor F providing a measure of exponential expansion averaged over different points on the attractor is calculated in dependence on time. The choice of the embedding dimension, radius and other parameters may strongly influence results, therefore the interpretation of calculations must be done very carefully.

The stretching factor F for the examined time series was calculated as shown in Fig. 5. There is a distinct linear part with positive slope in this plot spanning approximately 200 s, which indicates an average exponential expansion along an unstable direction within the attractor. The slope of the relevant linear part yields the maximal Lyapunov exponent $\lambda_{max} = 0.00629$ s^{-1}. Hence, we can conclude that the trajectory is generated by deterministic chaos. A characteristic time $1/\lambda_{max} = 160$ s within which the chaotic dynamics amplifies any fluctuation and makes prediction ineffective is in fact shorter than the average interval of ~500 s between large-amplitude spikes.

CONCLUSIONS

We have examined geometric and temporal characteristics of the dynamics observed experimentally in the HPTCu reaction run in a CSTR. A close inspection of the geometric features of the attractor reconstructed from the measured time series as well as the calculation of the maximal Lyapunov exponent leads to the conclusion that the dynamics is indeed deterministically chaotic. The particular feature of interest is that the observed oscillations are of a mixed-mode type with large irregular spikes intermingled with equally irregular episodes of small and fast oscillations. The theoretical background for explanation of such dynamics may involve a Shil'nikov type of chaos or different, competing oscillatory sources in the complex reaction network of the HPTCu system. These questions will be addressed in future studies.

REFERENCES

1. A. Goldbeter, "Biochemical oscillations and cellular rhythms. The molecular bases of periodic and chaotic behaviour", Cambridge University Press, Cambridge, 1996.

2. L. Glass and M. C. Mackey, "From clocks to chaos. The rhythms of life", Princeton University Press, Princeton, N.J., 1988.

3. C. J. Crook, A. Smith, R. A. L. Jones, and A. J. Ryan, Phys. Chem. Chem. Phys. **4**, 1367 (2002).

4. I. Varga, I. Szalai, R. Meszaros, and T. Gilanyi, J. Phys. Chem. B **110**, 20297 (2006).

5. S. A. Giannos, S. M. Dinh, and B. Berner, J. Pharm. Sci. **84**, 539 (1995).

6. T. Ohmori, W. Yu., T. Yamamoto, A. Endo, M. Nakaiwa, T. Amemiya, T. Yamaguchi, Chem. Phys. Lett. **407**, 48 (2005).

7. V. K. Vanag, D. G. Miguez, and I. R. Epstein, J. Chem. Phys, **125**, 194515 (2006).

8. B. Hess, A. Boiteux, and J. Krüger, Adv. Enzym Regul., **7**, 149 (1969).

9. I. Matsuzaki, J. H. Woodson, and H. A. Liebhafsky, Bull. Chem. Soc. Japan, **43**, 3317 (1970).

10. M. Orbán and I. R. Epstein, J. Am. Chem. Soc. **109**, 101 (1987).

11. G. Rábai, K. Kustin, and I. R. Epstein, J. Am. Chem. Soc. **111**, 3870 (1989).

12. G. Rábai, J. Phys. Chem. A **101**, 7085 (1997).

13. G. A. Frerichs and R. C. Thompson, J. Phys. Chem. A, **102**, 8142 (1998).

14. I. Hanazaki, N. Ishibashi, H. Mori, and Y. Tanimoto, J. Phys. Chem. A **104**, 7695 (2000).

15. G. Rábai, N. Okazaki, and I. Hanazaki, J. Phys. Chem. A, **103**, 7224 (1999).

16. G. Rábai, A. Kaminaga, and I. Hanazaki, Chem. Commun. **1996**, 2181.

17. M. J. B. Hauser, A. Strich, R. Bakos, Zs. Nagy-Ungvárai, S. C. Müller, Faraday Discuss. **120**, 229 (2001).

18. M. J. B. Hauser, N. Fricke, U. Storb, S. C. Müller, Z. Phys. Chem. **216**, 375 (2002).

19. G. Rábai and I. Hanazaki, J. Phys. Chem. A, **103**, 7268 (1999).

20. G. Rábai, M. Orbán, and I. R. Epstein, J. Phys. Chem. **96**, 3870 (1992).

21. G. Rábai and I. Hanazaki, J. Am. Chem. Soc. **119**, 1458 (1997).

22. K. Kurin-Csörgei, M. Orbán, G. Rábai, and I. R. Epstein, J. Chem. Soc. Faraday Trans. **92**, 2851 (1996).

23. F. Takens, "Detecting strange attractors in turbulence", in "Dynamical systems and turbulence", Lecture Notes in Mathematics **898**, Springer, Berlin, 1981, p. 366.

24. R. Hegger, H. Kantz, and T. Schreiber, Chaos, **9**, 413 (1999).

25. A. M. Fraser and H. L. Swinney, Phys. Rev. A **33**, 1134 (1986).

26. D. S. Broomhead and G. P. King, Physica D **20**, 217 (1986).

STRUCTURE OF MATTER
AND QUANTUM CHEMISTRY

УДК 541.65

Yb³⁺ DOPED DYPHILLOSILICATES PREPARED BY THERMALLY INDUCED PHASE TRANSFORMATION OF ZEOLITES

© 2007   B. Nedić*, V. Dondur*, A. Kremenović**, ***, R. Dimitrijević**, B. Antić***,
J. Blanuša***, D. Vasiljević-Radović****, M. Stojiljković*****

*Faculty of Physical Chemistry, University of Belgrade, Studentski trg 12–16, Belgrade, Serbia

**Faculty of Mining and Geology, University of Belgrade, Djusina 7, Belgrade, Serbia

***Institute of Nuclear Sciences "Vinca", Condensed Matter Physics Laboratory, PO Box 522, 11001 Belgrade, Serbia

****Institute of Chemistry, Technology and Metallurgy – Center of Microelectronic Technologies
and Single Crystals, 11000 Belgrade, Serbia

*****Institute of Nuclear Sciences "Vinca", Laboratory of Physical Chemistry, P.O. Box 522, 11001 Belgrade, Serbia

E-mail: bojana@ffh.bg.ac.yu

Abstract – Yb³⁺ doped Ba and Sr diphyllosilicates (hexacelsians) have been synthesized using Na form of LTA zeolite by ion exchange procedure and thermal treatment. Crystal structures of both doped samples have been refined and described in this article. Results of Rietveld refinements clearly indicate that Yb³⁺ ions are incorporated into hexacelsians` structure. AFM microphotographs were shown round shape of particles with size of few microns. The magnetization measurements were done within 2–300 K temperature range, revealing the enhancement of magnetization with temperature that is not in accordance with simple paramagnetic behaviour.

INTRODUCTION

Alkaline earth aluminates, silicates and aluminosilicates [1–6] are used as matrix materials for doping with transition and, especially, rare earth ions. These doped materials have wide applications, such as phosphors for plasma display panels (PDP), field emission displays and fluorescence lamps [7–9]. For PDP applications, phosphors should efficiently absorb vacuum ultraviolet light. Also, phosphors with a spherical shape and size less than 1 μm are required because the process for making a uniform phosphor layer depends on these physical properties [10]. $BaMgAl_{10}O_{17}$ (BAM) doped with Eu^{2+} ions is used as blue phosphor for PDP because it has deep blue color, a short decay time and high vacuum ultraviolet (VUV) efficiency [11]. However, it has been found that this blue phosphor is less stable than its red and green counterparts. The causes for this degradation process are thermal treatment during PDP manufacturing as well as irradiation by VUV photons [12]. The thermal degradation process is particularly serious because it is probably related with change in valence of Eu^{2+} to Eu^{3+} or in crystal structure of BAM [13].

It has recently been found that celsian could be adequate substitute for BAM [14]. It is well known that celsian is thermally very stable material. Kim et al. [14] have been found that celsian, doped with Eu^{2+} ions, preserved Eu^{2+} ions from oxidation. Doped celsian was synthesized using mixture of oxides as initial materials. Also, recent study describes structural and spectroscopic properties of Eu^{3+} doped hexacelsian [15].

In this work, Ba and Sr hexacelsians doped with Yb³⁺ ions were synthesized using zeolite as starting material and ion-exchange procedure for doping. Crystal structures and microstructures were described as well as magnetic properties of these doped samples.

EXPERIMENTAL PART

Sodium form of LTA (Si/Al = 1.00) zeolite was used as initial material. Barium and strontium exchanged zeolites (Ba–LTA and Sr–LTA, respectively) were obtained by aqueous ion-exchange procedure, which was repeated several times and was performed in diluted solutions [16]. The presence of Na⁺ in Ba–LTA and Sr–LTA was checked by Atomic Absorption Spectrophotometry (AAS), using Varian Spectra AA55 Spectrometer. Ba–LTA and Sr–LTA were than doped with Yb³⁺ (Ba–LTA:Yb³⁺ and Sr–LTA:Yb³⁺, respectively) also using ion-exchange procedure. Samples were thermally treated at 1000°C for 4 hours, and were spontaneously cooled to the room temperature.

The elemental analysis on the barium, strontium and ytterbium content were performed by inductively coupled plasma – atomic emission spectroscopy (ICP–OES), using Spectroflame ICP, operating at 2.5 kW and

Table 1. Comparison of unit cell parameters for doped and non-doped samples [18]

	BAS [19]	BAS : Yb³⁺	SAS [20]	SAS : Yb³⁺
a, Å	5.29645(2)	5.29776(8)	5.1974(5)	5.1967(2)
c, Å	7.78874(4)	7.7854(2)	15.1984(2)	15.1795(4)
V, Å³	189.22	189.226(6)	355.561(7)	355.01(2)

Table 2. Fractional coordinates, site occupation factors and isotropic vibrational parameters for both doped samples

Atom	SAS : Yb^{3+}					BAS : Yb^{3+}				
	x	y	z	S.O.F.	B_{iso}	x	y	z	S.O.F.	B_{iso}
M*	0	0	0	0.159(6)	0.87(2)	0	0	0	0.140(2)	0.86(4)
Yb	0	0	0	0.00443	0.87(2)	0	0	0	0.00067	0.86(4)
Al	1/3	2/3	0.3593(4)	1/3	1.02(4)	1/3	2/3	0.2865(8)	1/3	1.27(8)
Si	1/3	2/3	0.1423(4)	1/3	1.02(4)	1/3	2/3	0.7105(8)	1/3	1.27(8)
O1	1/3	2/3	0.2467(4)	1/3	1.4(5)	1/3	2/3	0.5074(8)	1/3	1.6(2)
O2	0.406(1)	−0.015(2)	0.1039(2)	1	1.4(5)	0.984(2)	0.437(2)	0.2071(6)	1	1.6(2)

* M represents Sr for SAS : Yb^{3+}, and Ba for BAS : Yb^{3+} sample.

27 MHz. Two sets of standard solutions ranging from 1 ppm to 10 ppm of barium, strontium and ytterbium were prepared and used for calibration. Spectral lines 407.771 nm for Sr, 455.403 nm for Ba and 369.419 nm for Yb were used.

X-Ray Powder Diffraction (XRPD) patterns of doped and non-doped thermally treated samples (BAS:Yb^{3+}, SAS:Yb^{3+}, BAS and SAS) were collected on a Philips PW-1710 automated powder diffractometer, using a Cu tube operating at 40 kV and 35 mA. Rietveld refinements were performed with the aid of Full-Prof software package [17]. Magnetic susceptibility measurements were done with Quantum design MPMS squid magnetometer in a temperature range 2 K < T < 300 K and DC magnetic field of 500 Oe.

For the AFM measurements, Ba–LTA and Sr–LTA, as well as doped counterparts were pressed into pellets, and then thermally treated at 1000°C for 4 hours. AFM measurements were performed using AutoProbe CP Research manufactured by TM Microscopes.

RESULTS AND DISCUSSION

Atomic absorption spectroscopy indicates that Na$^+$ ions are completely substituted with Ba^{2+} ions, as well as with Sr^{2+} ions. After doping with Yb^{3+} ions and thermal treatment, it is confirmed by XRPD [18] that both samples contain hexacelsian phase. SAS:Yb^{3+} has a small amount of Sr-feldspar phase, too. The structure of BAS:Yb^{3+} is refined into the space group $P\bar{3}$, while the structure of SAS:Yb^{3+} is refined into the space group $P\bar{3}c1$. The initial model of Ba–hexacelsian structure is adopted from Kremenovic et al. [19], while the initial model for Sr–hexacelsian structure is adopted from Nedić et al. [20]. The values for unit cell parameters, fractional coordinates, isotropic vibrational parameters and site occupation factors for both samples are listed in Tables 1 and 2. Isotropic vibrational parameters for Si and Al are restrained by the same value and the site occupation factors are constrained, due to similar number of electrons. Also due to very low amount of Yb ions in the samples, isotropic vibrational parameters for

Ba and Yb, as well as for Sr and Yb, are restrained to the same value. From the values of unit cell parameters and site occupation factors for Yb^{3+} ions, it can be concluded that, for both samples, Yb^{3+} ions are successfully incorporated into the structure. The interatomic distances and angles (Table 3) are in agreement with previously published works [19, 20].

Figure 1 represents the crystal structure of BAS:Yb^{3+} projected in bc plane. Due to great similarity, structure of SAS:Yb^{3+} is not shown. The ion-exchange procedure, comparing with usual synthetic methods, has one advantage – certainty that doped ions could only occupy extra-framework positions. In this case, the extra framework cations are Ba and Sr.

The chemical formulas calculated on the basis of the results of ICP-OES analysis are given in Table 4. SAS:Yb^{3+} sample contains more Yb^{3+} ions than BAS:Yb^{3+} sample. This is expected, because Yb^{3+} has ionic radius which is closer to ionic radius of Sr^{2+}, than to ionic radius of Ba^{2+}. Comparing these results with chemical formulas calculated from values of site occupation factors [18], a slight disagreement is observed. There is a possibility that doping caused slight symmetry lowering, which will be the subject of future investigations.

As mentioned above, particle size is very important for application of these materials, because the morphol-
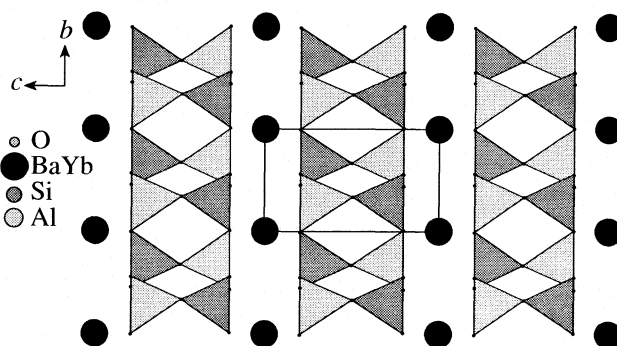
Fig. 1. Crystal structure of BAS:Yb^{3+} (projected in bc plane).

Table 3. Chemical formulas calculated from ICP–OES

	Chemical formula
BAS : Yb^{3+}	$Ba_{5.97}Yb_{0.03}Al_{12}Si_{12}O_{48}$
SAS : Yb^{3+}	$Sr_{5.82}Yb_{0.11}Al_{12}Si_{12}O_{48}$

Table 4. Interatomic distances and angles for both doped samples

Distance [Å]/Angle [°]	SAS : Yb^{3+}	BAS : Yb^{3+}	Multiplicity
M–O2	2.669(6)	2.857(7)	6
Si–O1	1.585(9)	1.581(9)	1
Si–O2	1.609(7)	1.616(8)	3
⟨Si–O⟩	1.603(9)	1.607(9)	–
Al–O1	1.709(9)	1.720(9)	1
Al–O2	1.724(4)	1.744(8)	3
⟨Al–O⟩	1.720(9)	1.738(9)	–
O1–O2	2.636(7)	2.672(8)	3
O1–O2	2.793(8)	2.850(8)	3
⟨O1–O2⟩	2.714(9)	2.761(8)	–
O2–Al–O1	108.9(5)	108.1(5)	3
O2–Al–O2	110.0(5)	110.8(5)	3
O2–Si–O1	111.2(6)	113.4(8)	3
O2–Si–O2	107.6(5)	105.3(8)	3

Table 5. The values of effective magnetic numbers and energy levels obtained from the fit of equations (1)

Parameter	SAS : Yb^{3+}	BAS : Yb^{3+}
E_1 [K]	0	0
E_2 [K]	31(1)	9(1)
M^2_{1eff}	2.41(3)	0.56(1)
M^2_{2eff}	4.2(1)	1.79(6)

ogy of phosphor particles plays an important role in improving the brightness of PDPs [21]. In order to describe morphology of samples, AFM microphotographs for doped and non-doped samples are obtained and shown in Fig. 2. It is visible that samples have, more or less, round shape and their size is approximately few microns. It has to be noticed that these samples are prepared (grinded) for XRPD analysis, and that with further grinding the size and shape of grains will be more suitable for applications.

The results of magnetization measurements $M(T)$ for both samples show the behavior that is not inherent to an isolated Yb^{3+} in dielectric crystal environment. For comparison, Fig. 3 represents the inverse susceptibility curves of SAS:Yb^{3+}, BAS:Yb^{3+} and diluted

$(Yb,Y)_2O_3$. There is a relative agreement at low temperatures, but approximately above 40 K the susceptibility of both SAS:Yb^{3+} and BAS:Yb^{3+} becomes significantly larger, and in the case of BAS:Yb^{3+} it even increases with temperature (note that Fig. 3 shows the inverse susceptibility). The susceptibilities are calculated per one mole of Yb in all samples, which illustrate the differences between states of Yb ion in different crystal matrices. These are mostly due to crystal field influence or the presence of collective phenomena (exchange interactions). Considering the very low Yb concentration in the samples, the direct exchange or superexchange is negligible.

The inverse molar susceptibilities of SAS:Yb^{3+} and BAS:Yb^{3+} could suggest the contribution of Van Fleck temperature independent paramagnetism. However, due to the odd number of 4f electrons, Yb^{3+} has no singlet levels in a crystal field of whatever low symmetry, and since the first excited manifold level of Yb^{3+} is over 13000 cm^{-1} above the ground level, the Van Fleck contribution has to be neglected in this case. Moreover, the magnetization (per Yb ion) in SAS:Yb^{3+} and BAS:Yb^{3+} at room temperature is over three (SAS:Yb^{3+}) or four (BAS:Yb^{3+}) times larger then in typically paramagnetic $(Yb,Y)_2O_3$, which eliminates the crystal field also as a dominant interaction within the whole temperature range. This fact points to the presence of correlation between localized magnetic moments at elevated temperatures, the nature of which will be subject of our future investigations.

The similarity of SAS:Yb^{3+} and Yb_2O_3 susceptibilities below 40 K led us to assumption that the crystal field influence may still be dominant in this temperature range, though this seems to be less true for BAS:Yb^{3+} sample. Through this approach, within the 2–40 K we can express the susceptibility of the samples as [22]:

$$\chi_M = \frac{N g_J^2 \mu_B^2}{kT}\left(\sum_i M_{ieff}^2 e^{-\frac{E_i}{kT}} \Big/ \sum_i e^{-\frac{E_i}{kT}}\right), \qquad (1)$$

where N, g_J, k and μ_B have their usual meaning, E_i is the energy gap between the ground and the i-th excited Kramer's doublet, and M_{ieff} denotes linear combinations of the free ion magnetic quantum numbers M_J:

$$M_{ieff} = \sum_{M_J}\left|\alpha_{M_J}^i\right|^2 M_J. \qquad (2)$$

In (2), $\alpha_{M_J}^i$ are coefficients from the linear expansion of the i-th level wave function over the free ion states:

$$|i\rangle = \sum_{M_J}\alpha_{M_J}^i|LSJM_J\rangle. \qquad (3)$$

By fitting the experimental data between 2 K and 40 K (Fig. 4), we can deduce the approximate values of energy and magnetic numbers M_{ieff} of the ground and first
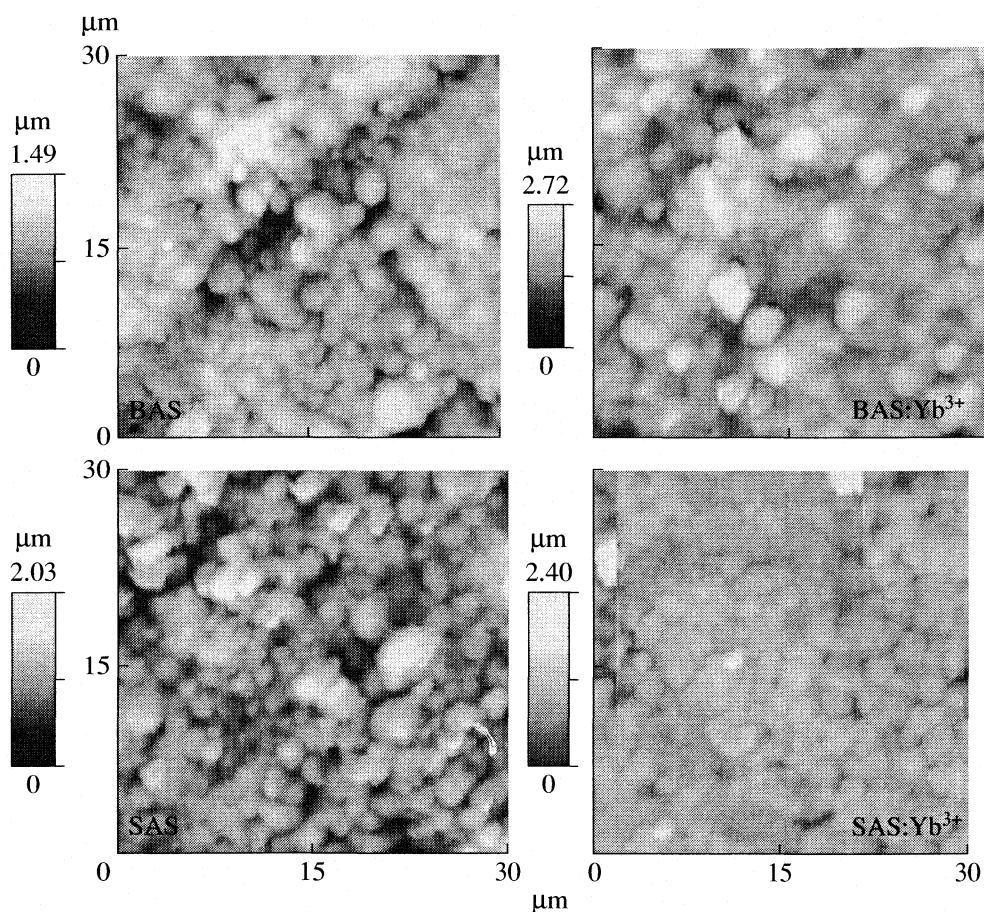
Fig. 2. AFM microphotographs of doped and non-doped samples.
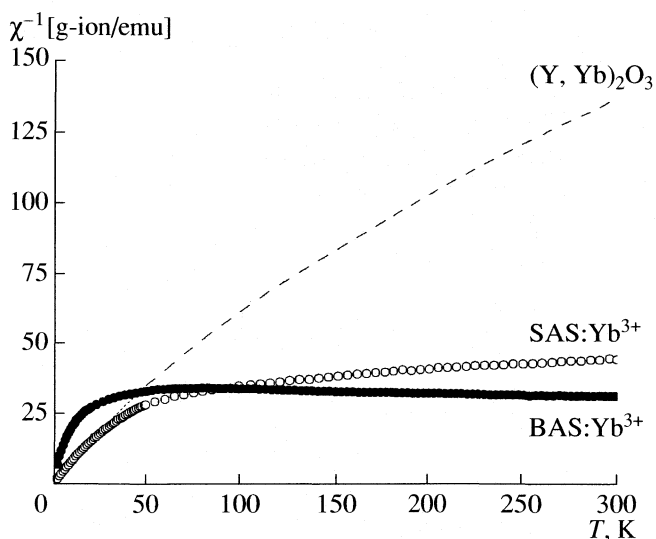
Fig. 3. The inverse gram ion susceptibility of SAS:Yb^{3+}, BAS:Yb^{3+} and diluted (Yb,Y)$_2$O$_3$ versus temperature.
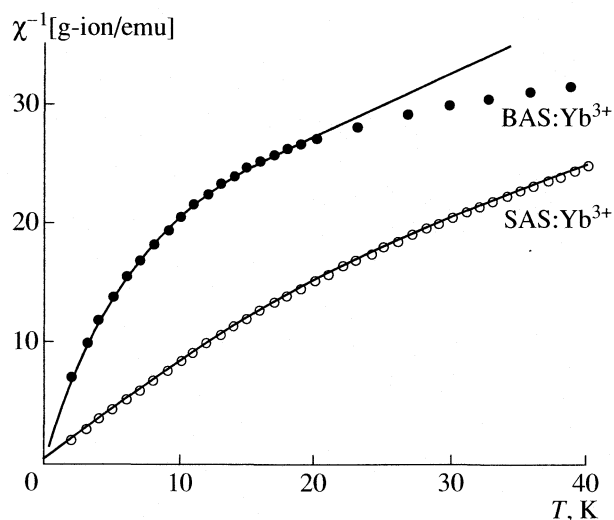
Fig. 4. Low temperature susceptibilities of SAS:Yb^{3+} and BAS:Yb^{3+} fitted to Eq. (1).

excited doublets, which are listed in Table 5. There is a pronounced difference between the parameters of two samples, with unusually low values in the case of BAS:Yb^{3+} sample for which the model (1) appeared to be actually not applicable above 20 K (Fig. 4).

CONCLUSION

In this work, Yb^{3+} doped Ba- and Sr-diphyllosilicates are synthesized using LTA zeolite as initial material by ion-exchange procedure and thermal treatment

at 1000°C for 4 hours. Chemical analysis show that the amount of Yb^{3+} ions is greater in SAS:Yb^{3+} sample than in BAS:Yb^{3+} sample. Results of Rietveld refinements clearly indicate that Yb^{3+} ions are incorporated into hexacelsians structure. AFM microphotographs show approximately round particles. The magnetic measurements clearly illustrate the existence of some kind of correlation between magnetic moments at room temperature, by giving the values of moment larger then the free ion value (4 μ_B). This implies the long range indirect interactions (due to the low Yb concentration). It is interesting that the effect is enhanced with raise of the temperature, which points to the probable coupling role of delocalized carriers. Another point of interest is that this long range coupling is of ferromagnetic character (increased magnetization compared to paramagnetic or free ion ensemble). However, magnetization measurements alone can not provide us the origin of observed interactions; other experimental techniques sensitive to the carrier concentration are suggested for further investigations.

ACKNOWLEDGEMENTS

REFERENCES

1. F. Lahoz, I. R. Martin, U. R. Rodriguez-Mendoza, I. Iparraguirre, J. Azkargorta, A. Mendioroz, R. Balda, J. Fernandez, V. Lavin, Optical Materials, **27**, 1762 (2005).

2. G. Wang, O. Marty, C. Garapon, A. Pillonnet, W. Zhang, Appl. Phys. A, **79**, 1599 (2004).

3. T. Aitasalo, J. Holsa, H. Jungner, J. Krupa, M. Lahtinen, M. Lastusaari, J. Legendziewicz, J. Niittykoski and J. Valkonen, Radiat Eff. Defects Solids **158**, 209 (2003).

4. T. Aitasalo, P. Deren, J. Holsa, H. Jungner, M. Lastusaari, J. Niittykoski and W. Strek, Radiat. Meas. **38**, 515 (2004).

5. H. Kang, S. Hong, Y, Kang, K. Jung, Y. Shul, S. Park, J. Alloys Compd., **402**, 246 (2005).

6. L. Jiang, C. Chang, D. Mao and C. Feng, J. Alloys Compd. **377**, 211 (2004).

7. C. Kim, I. Kwon, C. Park, Y. Hwang, H. Bae, B. Yu, C. Pyun and G. Hong, J. Alloys Compd. **311**, 33 (2000).

8. C. Ronda, J. Alloys Compd. 225, 534 (1995).

9. A. Talin, K. Dean and J. Jaskie, Solid State Electron. **45**, 963 (2001).

10. K. Jung, H. Lee, Y. Kang, S. Park and Y. Yang, Chem. Mater. **17**, 2729 (2005).

11. K. Kim, Y. Kim, H. Chun, T. Cho, J. Jung, J. Kang, Chem. Mater. **14**, 5045 (2002).

12. B. Dawson, M. Ferguson, G. Marking and A. Diaz, Chem. Mater. **16**, 5311 (2004).

13. K. Kim, K. Koo, T. Cho and H. Chun, Mater. Chem. Phys. 80 (3), 5311 (2003).

14. W. Im, Y. Kim and D. Jeon, Chem. Mater. **18**, 1190 (2006).

15. A. Kremenović, Ph. Colomban, B. Piriou, D. Massiot and P. Florian, J. Phys. Chem. Solids, **64**, 2253 (2003).

16. V. Dondur, R. Dimitrijević, A. Kremenović, Lj. Damjanović, M. Kicanović, H. M. Cheong, S. Macura, Mater. Sci. Forum, **494**, 107 (2005).

17. J. Rodriguez-Carvajal, FullProf.2k (June 2005-LLB JRC) Computer program; www.llb.cea.fr / fullweb/fp2k/fp2k.htm

18. B. Nedić, A. Kremenović, V. Dondur, R. Dimitrijević, Mater. Sci. Forum 219–224, 555 (2007).

19. A. Kremenović, P. Norby, R. Dimitrijević, V. Dondur, Solid State Ionics, 101–103, 611 (1997).

20. B. Nedić, A. Kremenović, V. Dondur, R. Dimitrijević, (submitted).

21. K. Jung and Y. Kang, Mater. Lett. 58 (16), 2161 (2004).

22. M. Mitrić, B. Antić, M. Balanda, D. Rodić and M. Napijalo, J. Phys.: Condens. Matter 9, 4103 (1997).

CHEMICAL OXIDATIVE POLYMERIZATION
OF DIANILINIUM 5-SULFOSALICYLATE

© 2007   G. Ćirić-Marjanović*, A. Janošević*, B. Marjanović**, M. Trchová***,
J. Stejskal***, P. Holler***

*Faculty of Physical Chemistry, University of Belgrade, Studentski Trg 12-16, POB 137, 11001, Belgrade, Serbia

**Centrohem, Karađorđeva 129, 22300 Stara Pazova, Serbia

****Institute of Macromolecular Chemistry, Academy of Sciences of the Czech Republic, Heyrovsky Sq. 2, 162 06 Prague 6,
Czech Republic*

E-mail: gordana@ffh.bg.ac.yu

Abstract – Dianilinium 5-sulfosalicylate was prepared *in situ* and then oxidized in aqueous solution with ammonium peroxydisulfate. The precipitated polyaniline 5-sulfosalicylate was soluble in polar aprotic solvents and showed conductivity of ~0.1 S cm^{-1}. Scanning electron microscopy revealed coexistence of nanorods and granular morphology of the polyaniline 5-sulfosalicylate. The weight-average molecular weight and polydispersity index were determined by gel-permeation chromatography as 53000 and 9.0, respectively. FTIR spectroscopic analysis combined with AM1 and MNDO-PM3 semi-empirical quantum chemical studies of the polymerization mechanism indicate both covalent and ionic bonding of sulfosalicylate to polyaniline chains. Raman spectroscopy proved the presence of substituted phenazine structural units besides ordinary emeraldine segments.

INTRODUCTION

Polyaniline (PANI) is the most important conducting polymer, which has been extensively studied due to its simple preparation, good thermal and environmental stability, structure versatility, and wide applicability. Chemical oxidative polymerizations of commercially available aniline salts, such as hydrochloride and sulfate, lead to the precipitation of polyaniline salts with poor solubility in common solvents. These unacceptable PANI salts must be transformed by dedoping-redoping procedure to more acceptable PANI doped with functionalized acids. Many attempts to synthesize processible PANI salts *via* direct oxidation of various aniline salts with ammonium peroxydisulfate (APS), most often used oxidant in production of PANI, have failed because hydrogen sulfate, formed as a by-product during polymerization, was incorporated into the PANI structure instead of functionalized dopant anion [1]. It was shown that the solubility, crystallinity, thermal stability, electrochemical stability at higher potentials, and anticorrosive properties of PANI have been improved using 5-sulfosalicylic acid (SSA) as a dopant [2–4]. In these reports, PANI 5-sulfosalicylate (PANI.SSA) has been prepared *via* direct oxidation of *in situ* prepared anilinium 5-sulfosalicylate in large excess of SSA, or by doping of PANI base with SSA. As a continuation of our recent work on efficient aniline salt precursor for direct synthesis of processible, soluble conducting PANI salt [5], in the present paper we prepared *in situ* dianilinium 5-sulfosalicylate (DASSA), and performed its polymerization with APS in aqueous solution. The novel polymeric material was character-

ized by the conductivity measurements, scanning electron microscopy (SEM), gel-permeation chromatography (GPC), FTIR, and Raman spectroscopies. The early stages of the polymerization mechanism were theoretically studied by the AM1 and MNDO-PM3 semi-empirical quantum chemical methods combined with conductor-like screening model of solvation.

EXPERIMENTAL

Sample Preparation. The DASSA was prepared *in situ* by the addition of aniline (40 mmol) to the continuously stirred solution of SSA (20 mmol) in distilled water (100 ml), followed by heating of this reaction solution to boiling point, and then by cooling to room temperature. The aqueous solution of APS (50 mmol in 100 ml of water) was added to the solution of DASSA at room temperature, under stirring and the reaction mixture was left for 24 h. The PANI.SSA precipitate was separated by filtration, washed with water (6 × 50 ml) and acetone (4 × 25 ml) (the sample PANI.SSA–H$_2$O), or with 1 M SSA (4 × 25 ml) and acetone (4 × 25 ml) (the sample PANI.SSA-doped), and then dried in vacuum at 70°C. Base form of the polymer (the sample PANI.SSA-deprotonated) was prepared by the addition of large excess 0.5 M NaOH to the reaction mixture after polymerization. The precipitate was collected on filter, washed with water and dried in vacuum at 70°C.

Conductivity. Powdered polymer samples were pressed into pellets, 10 mm in diameter and 1 mm thick, under a pressure of 124 MPa using a hydraulic pellet press. The conductivity was measured between stain-
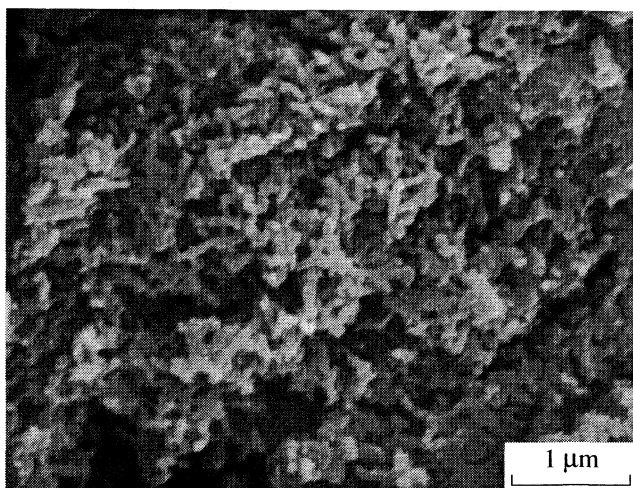
Fig. 1. SEM microphotograph of PANI.SSA–H$_2$O.

Fig. 2. Molecular weight distribution as obtained by GPC of PANI.SSA-deprotonated.

less pistons, at room temperature, by means of an a.c. bridge (Waynne Kerr Universal Bridge B 224), at fixed frequency of 1.0 kHz. During the measurement, pressure was maintained at the mentioned value.

Scanning Electron Microscopy. Scanning electron microphotographs have been taken with a JEOL 6400 microscope.

Gel-Permeation Chromatography. Molecular weights were assessed by a GPC/SEC method using 8 × 500 mm Labio GM 1000 column operating with N-methylpyrrolidone and calibrated by polystyrene standards with a spectrophotometric detection at the wavelength of 650 nm. The samples were dissolved in N-methylpyrrolidone containing 0.025 g cm^{-3} triethanolamine for deprotonation, and 0.005 g cm^{-3} lithium bromide to prevent aggregation.

FTIR Spectroscopy. Infrared spectra in the range of 400–4000 cm^{-1} were recorded at 64 scans per spectrum at 2 cm^{-1} resolution using a fully computerized Thermo Nicolet NEXUS 870 FTIR Spectrometer with a DTGS TEC detector. Measurements were performed after dispersing the powdered samples in potassium bromide pellets. The spectra were corrected for the presence of carbon dioxide and humidity in the optical path.

Raman Spectroscopy. Raman spectra excited in the visible range with a HeNe 633 nm laser were collected on a Renishaw inVia Reflex Raman microscope. Research grade Leica DM LM microscope with objective magnification ×50 was used to focus the laser beam on the sample placed on a X–Y motorized sample stage. The scattered light was analyzed by the spectrograph with a holographic grating 1800 lines mm^{-1}. A Peltier-cooled CCD detector (578 × 385 pixels) registered the dispersed light. The positioning of a sample was controlled, and the data were processed with a Wire 2.2 software.
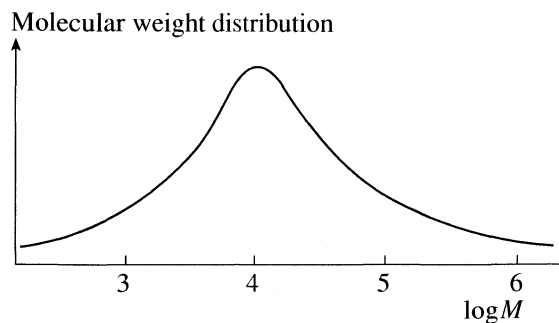
COMPUTATIONAL METHODS

The computational methods used here to obtain the molecular orbitals, the ionization energy, charge distribution (Mulliken charges), and the spin density of individual species are semi-empirical AM1 and MNDO-PM3 models [6, 7] (included in the molecular orbital package MOPAC 97, part of the Chem3D Pro 5.0 package, CambridgeSoft Corporation). The solvation effects in water were taken into account using the conductor-like screening model (COSMO) [8]. The geometry optimization was performed by the EigenFollowing procedure [9, 10]. Input files for the semi-empirical quantum chemical computations were the most stable conformers of investigated molecular structures. The restricted Hartree-Fock method has been used for the molecular structures and the unrestricted Hartree-Fock method for radical species.

RESULTS AND DISCUSSION

Conductivity and Solubility. Obtained green PANI.SSA-doped and PANI.SSA-H$_2$O samples exhibited conductivities ~0.1 S cm^{-1} and ~0.01 S cm^{-1}, respectively. The conductivity of the PANI.SSA-doped is similar to that of the PANI.SSA prepared by Trivedi et al. by using large molar excess of the SSA [2]. The blue coloured sample PANI.SSA-deprotonated has a conductivity of ~4 × 10^{-8} S cm^{-1}.

The synthesized polymer, PANI.SSA-doped, shows good solubility in N-methylpyrrolidone, dimethylsulfoxide and N,N-dimethylformamide.

Morphology. SEM investigations (Fig. 1) revealed that all studied PANI.SSA samples contain nanorods, granular part, and the precipitate of undefined morphology. The nanorods have an average diameter of ~55–70 nm and length of ~200–400 nm.

Molecular Weights. Single large peak appeared in the gel permeation chromatogram of the PANI.SSA-deprotonated (Fig. 2). The weight-average molecular weight, M_w, and the number-average molecular weight M_n, are 53 000 and 5900, respectively, and polydispersity index, M_w/M_n, is 9.0. In comparison with
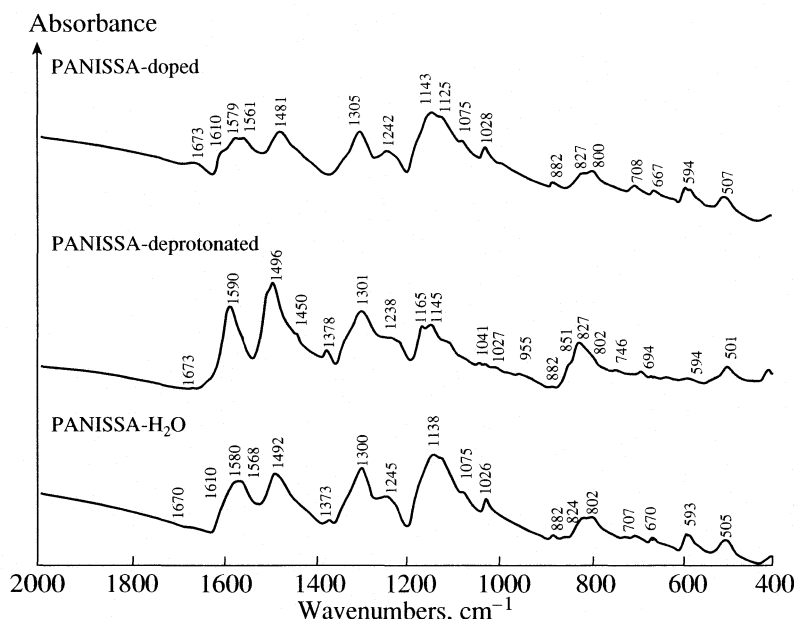
Fig. 3. FTIR spectra of PANI.SSA samples obtained by the oxidative polymerization of DASSA with APS, and treated with 1 M SSA (PANI.SSA-doped), water (PANI.SSA-H$_2$O), or 0.5 M NaOH (PANI.SSA-deprotonated) after polymerization.

PANI.SSA obtained by the chemical oxidative polymerization of the anilinium 5-sulfosalicylate [5], the PANI.SSA obtained by oxidation of DASSA exhibits considerably higher values of M_w.

FTIR Spectra. The FTIR spectra of PANI.SSA samples in the frequency range 2000–400 cm^{-1} are presented at Fig. 3. Main absorption bands in the frequency range 4000–400 cm^{-1} and their assignment are given in Table 1. The bands at 1579 and 1481 cm^{-1}, due to quinonoid (Q) ring and benzenoid (B) ring-stretching vibrations [11–13], respectively, observed in the spectrum of PANI.SSA-doped, show blue-shifting to 1580, 1492 cm^{-1} and 1590, 1496 cm^{-1} in the spectra of PANI.SSA–H$_2$O and PANI.SSA-deprotonated, respectively. Intensity ratio of "benzenoid" (~1500 cm^{-1}) to "quinonoid" (~1600 cm^{-1}) band indicates that the final polymer is in the emeraldine form [12].

The band which has been reported as typical for PANI emeraldine base [12, 14], due to the C–N stretching vibration in QBQ units, is observed at 1373 and 1378 cm^{-1} in the spectra of PANI.SSA-H$_2$O and PANI.SSA-deprotonated, respectively. The secondary amine C–N stretching vibration [4, 14, 15] corresponds to the strong band observed at 1300–1305 cm^{-1} in all spectra. The *para*-coupling between constitutional aniline units is confirmed by the band positioned at 824–827 cm^{-1} for all studied samples [15]. The 1,2,4-trisubstituted benzene rings of the SSA dopant anions are evidenced by the weak band at 882 cm^{-1} [15].

The presence of sulfosalicylate anions as the dopants in the PANI.SSA-doped sample is revealed by the bands at 1673, 1610 (sh), 1561, 1143, 1125 (sh), 1028, 882, 800, 708, 667, and 594 cm^{-1} (Table 1) [4, 15, 16].

The spectrum of PANI.SSA-H$_2$O sample contains the bands of SSA dopant too, at similar positions: 1670, 1610 (sh), 1138, 1026, 882, 802, 707, 670 and 593 cm^{-1}. The spectrum of SSA (dihydrate) itself contains the bands at 1677, 1578, 1149, 1123, 1041, 887, 804, 717, 667 and 586 cm^{-1} [16].

It is interesting to note that we observed very weak bands at 1673 and 882, weak bands at 1027, 694 and 594, and medium one at 1145 cm^{-1} even in the spectrum of the PANI.SSA-deprotonated. This feature could be explained by the covalent bonding between sulfosalicylate and PANI backbone. The shoulder observed at 1075 cm^{-1} in the spectra of PANI.SSA-doped and PANI.SSA–H$_2$O can be attributed to the HSO$_4^-$ ions formed by the reduction of the oxidant during the polymerization [15] or to C–COOH stretching [16].

Raman Spectra. The Raman spectra of the PANI.SSA samples, in the frequency range 2000–300 cm^{-1}, are shown on Fig. 4. The characteristic PANI bands are observed in the Raman spectra of PANI.SSA at wavenumbers 1622–1633 and ~1592 cm^{-1}. The first is assigned to the C~C stretching vibration of the B ring (where ~ denotes the bond intermediate between the single and double bond), and the latter corresponds to C=C and C~C stretching vibrations in the Q and semi-quinonoid (SQ) rings, respectively [17–20]. The most prominent band in the Raman spectrum of PANI.SSA-deprotonated is observed at 1472 cm^{-1}, assigned to the C=N stretching in Q units [19]. This band is also very strong in the spectrum of PANI.SSA–H$_2$O, but it disap-

Table 1. Main FTIR bands of PANI.SSA samples and their assignment

Wavenumber, cm⁻¹			Assignment[a]
PANI.SSA-doped	PANI.SSA–H₂O	PANI.SSA-deprotonated	
3464 vs, br	3459 vs, br	3460 sh, br	ν(N–H)/ν(O–H)
		3380 m, br	ν(O–H)
3244 m–s	3236 m–s	3280 m, br	ν(O–H)
3057 w	3057 w	3057/3028 m	ν(O–H)/ν(C–H)
2965 m	2965 m	2965 w	ν(O–H)/ν(C–H)
2925 m	2925 m	2925 w	ν(O–H)/ν(C–H)
1673 w–m	1670 w	1673 vw	ν(C=O) in COOH or COO⁻
1610 sh	1610 sh		Phenyl ring stretching of SSA
1579 s	1580 s	1590 vs	Q ring-stretching (N=Q=N)/
1561 s	1568 s		Phenyl ring stretching of SSA/asym. ν(COO⁻)
1481 s	1492 s	1496 vs	B ring-stretching (N–B–N)
1450–1400 br	1450–1400 br	1450 sh	ring ν(C~C)/sym. ν(COO⁻)
	1373 w	1378 m	ν(C–N) in QBQ unit
1305 s	1300 s	1301 s	ν(C–N) second. arom. amine
1242 m–s	1245 m–s	1237 m	ν(C–N) in BBB unit/ν(C–O)
		1165 s	N=Q=N
1143 vs	1138 vs	1145 s	asym. ν(SO₃) in SSA/δ(C–H)
1125 sh			Q=N⁺H–B/B–NH–B
1075 sh		1075 sh	sym. ν(SO₃) in HSO₄⁻, ν(C–COOH)
1028 m–s	1026 m–s	1027 w	sym. ν(SO₃) in SSA, ν(S–OH)
882 w	882 w	882 vw	γ(C–H) (1,2,4-trisubstit. ring)
		851 sh	γ(C–H) (1,2,4-trisubstit. ring)
827 m	824 m	827 s	γ(C–H) (1,4-disubstit. ring)
800 m	802 m	802 sh	γ(C–H) (1,2,4-trisubstit. ring) SSA/ν(C–SO₃H)
708 w	707 w	694 w	δ(Phenyl ring) SSA
667 w	670 w	670 vw	γ(Phenyl ring)/δ(Phenyl ring) SSA
594 m	593 m	594 w	γ(Phenyl ring SSA)/γ(OH)/δ(SO₂)

Abbreviations: B – benzenoid ring; Q – quinonoid ring; ν – stretching; δ – in-plane bending; γ – out-of-plane bending; vs – very strong; s – strong; m – medium; w – weak; vw – very weak; sh – shoulder; sym – symmetric; asym – asymmetric.
[a] Assignments based on references [4, 11–16].

pears in the spectrum of PANI.SSA-doped because Q rings are transformed to SQ rings.

The frequency range 1400–1300 cm⁻¹ corresponds to the C~N⁺ stretching vibrations of charged nitrogen segments. In this region the very strong band at ~1338 cm⁻¹ is observed in the spectrum of PANI.SSA-doped, which is assigned to the ν(C~N⁺·) vibration in delocalized polaronic structure, and it is associated with high electron conductivity and the existence of the polaronic lattice [21]. This band is preserved as the strong one at 1337 cm⁻¹ after repeated washing of the polymer with water, and, surprisingly, it is still present but weak, in
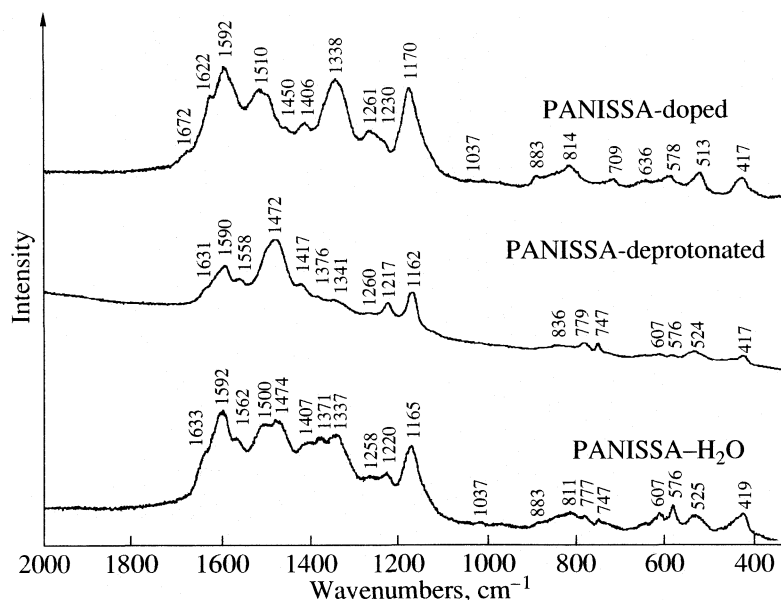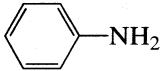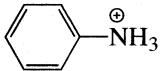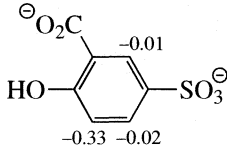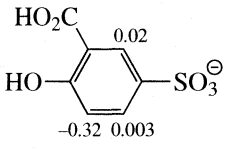
Fig. 4. Raman spectra (λ_{exc} 633 nm) of PANI.SSA samples obtained by the oxidative polymerization of DASSA with APS, and treated with 1 M SSA (PANI.SSA-doped), water (PANI.SSA–H$_2$O), or 0.5 M NaOH (PANI.SSA-deprotonated) after polymerization.

the spectrum of deprotonated sample, at 1341 cm^{-1}. This feature is in accordance with the observed relatively high conductivity of PANI.SSA–H$_2$O sample, and indicates the certain resistance of the polymer toward deprotonation. Mažeikiené et al. reported similar phenomenon for the copolymer of aniline and *m*-aminobenzenesulfonic acid [22]. The strong intra- and intermolecular hydrogen bonding O···H–N between H atom from the NH^{*+} group of PANI.SSA backbone and O atom from SO$_3^-$ group of covalently bonded sulfosalicylate could be proposed as possible explanation. The band at 1341 cm^{-1} in the spectrum of PANI.SSA-deprotonated could be also explained by the presence of phenazine-like structural segments in polymer chains, because the Raman spectrum of phenazine itself shows a band at 1348 cm^{-1}, and such segments are also indicated by the bands observed at 1406 (1417), ~576 and

~417 cm^{-1} in the spectra of all studied PANI.SSA samples [23, 24]. The substituted phenazine segments has been recently connected with the formation of nanostructured PANI, prepared in water without added acid, and in the slightly acidic aqueous medium [11, 25, 26]. The second band in the region 1400–1300 cm^{-1} appears in the spectra of PANI.SSA–H$_2$O and PANI.SSA-deprotonated at 1371 (strong) and 1376 cm^{-1} (weak), respectively, and can be associated with the C~N$^+$ stretching vibrations in more localized polaronic sites [22]. It is correlated with an intermediate level of doping in PANI.SSA–H$_2$O and it is not clearly seen in the spectrum of PANI.SSA-doped.

The very strong band due to C–H bending in-plane vibrations of SQ rings [17] is observed at 1170 and 1165 cm^{-1} in the spectra of PANI.SSA-doped and PANI.SSA–H$_2$O, respectively. This band is weakened

Table 2. Ionization energy (E_i) of hydrated aniline, anilinium cation and 5-sulfosalicylate anions, calculated by AM1 and MNDO-PM3 methods. Mulliken charges, calculated by MNDO-PM3, of the reactive centers of hydrated 5-sulfosalicylate anions, susceptible to electrophilic attack of aniline and oligoaniline cation radicals or nitrenium cations, are also shown

Species	$\langle\!\rangle$—NH$_2$	$\langle\!\rangle$—$\overset{\oplus}{NH_3}$	$^{\ominus}$O$_2$C $\langle\!\rangle$ HO— —SO$_3^\ominus$ −0.01 −0.33 −0.02	HO$_2$C $\langle\!\rangle$ HO— —SO$_3^\ominus$ 0.02 −0.32 0.003
E_i (AM1), eV	8.98	10.18	9.84	10.03
E_i (PM3), eV	9.03	10.25	9.77	9.95
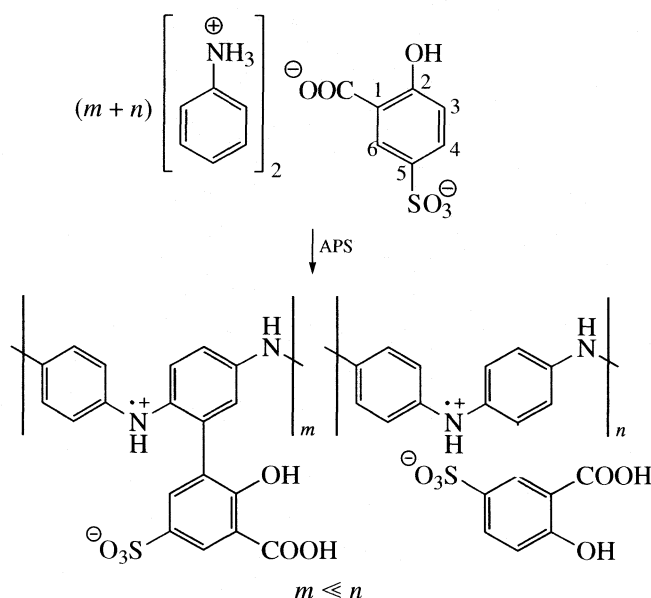
Fig. 5. The formation of functionalized emeraldine salt of PANI.SSA by the oxidation of DASSA with APS.

and shifted to 1162 cm^{-1} after deprotonation, due to transformation of SQ rings in emeraldine salt to Q rings in emeraldine base form.

Theoretical Study. AM1 and MNDO-PM3 semi-empirical quantum chemical calculations show that hydrated 5-sulfosalicylate dianion and monoanion, formed at lower pH during the polymerization, are more oxidizable than anilinium cation and less oxidizable than aniline (Table 2), indicating that polymerization proceeds *via* the generation of both aniline cation radicals and 5-sulfosalicylate radicals, which can be covalently incorporated into the PANI macromolecular structure (Fig. 5). This result is in accordance with the indications from FTIR study that the bands due to SSA vibrations are still present in the deprotonated (dedoped) sample. Based on the charge distribution of SSA anions (Table 2) and the spin density of SSA radicals (Table 3), it was concluded that couplings between growing PANI chain and the 5-sulfosalicylate

reactive species comprise mainly reactions of C3$_{SSA}$ position.

CONCLUSION

The oxidation of the dianilinium 5-sulfosalicylate with ammonium peroxydisulfate, in aqueous solution, leads to the formation of the conducting, processible polyaniline 5-sulfosalicylate, soluble in aprotic polar solvents. 5-Sulfosalicylate anions serve as dopants, as it was revealed by the FTIR spectroscopy. Both AM1 and MNDO-PM3 semi-empirical quantum chemical methods, combined with the conductor-like screening model of solvation, as well as FTIR spectroscopic analysis of deprotonated polyaniline 5-sulfosalicylate indicate some extent of covalent bonding of 5-sulfosalicylate anions to polyaniline chain. The presence of substituted phenazine units, besides benzenoid, quinonoid and semi-quinonoid units, is proved by Raman spectroscopy. Synthesized polymer has a mixed nanostructured and granular morphology.

Table 3. Spin density of the hydrated 5-sulfosalicylate radicals, calculated by MNDO-PM3

Species	5-sulfosalicylate anion radical	5-sulfosalicylate radical
Spin density distribution		

REFERENCES

1. J. Stejskal, D. Hlavatá, P. Holler, M. Trchová, J. Prokeš, I. Sapurina, Polym. Int. **53**, 294 (2004).
2. D. C. Trivedi, S. K. Dhawan, Synth. Met. **58**, 309 (1993).

3. A. Raghunathan, G. Rangarajan, D. C. Trivedi, Synth. Met. **81**, 39 (1996).

4. G. Ćirić-Marjanović, B. Marjanović, M. Popović, V. Panić, V. Mišković-Stanković, Elektrokhimiya **42**, 1497 (2006) [Russ. J. Electrochem. **42**, 1358 (2006)].

5. B. Marjanović, G. Ćirić-Marjanović, I. Juranić, P. Holler, The 7th YUMRS Conference YUCOMAT 2005, Herceg Novi, SCG, Book of Abstracts, p. 75.

6. M. J. S. Dewar, E. G. Zoebisch, E. F. Healy, J. J. P. Stewart, J. Am. Chem. Soc. **107**, 3902 (1985).

7. J. J. P. Stewart, J. Comp. Chem. **10**, 209 (1989).

8. A. Klamt, G. Schüürmann, J. Chem. Soc. Perkin Trans. **2**, 799 (1993).

9. A. Banerjee, N. Adams, J. Simons, R. Shepard, J. Phys. Chem. **89**, 52 (1985).

10. J. Baker. J. Comp. Chem. **7**, 385 (1986).

11. M. Trchová, E. N. Konyushenko, J. Stejskal, I. Šeděnková, P. Holler, G. Ćirić-Marjanović, J. Phys. Chem. B. **110**, 9461 (2006).

12. E. T. Kang, K. G. Neoh, K. L. Tan, Prog. Polym. Sci. **23**, 277 (1998).

13. I. Šeděnková, M. Trchová, N. V. Blinova, J. Stejskal, Thin Solid Films **515**, 1640 (2006).

14. J. Stejskal, I. Sapurina, M. Trchová, J. Prokeš, Chem. Mater. **14**, 3602 (2002).

15. Socrates, G. *Infrared and Raman Characteristic Group Frequencies* (John Wiley & Sons, New York, 2001, pp. 220–222, 272).

16. H. T. Varghese, C. Y. Panicker, D. Philip, J. Raman Spectrosc. 2006, **38**, 309 (2007).

17. M. I. Boyer, S. Quillard, G. Louarn, G. Froyer, S. Lefrant, J. Phys. Chem. B **104**, 8952 (2000).

18. M. Cochet, G. Louarn, S. Quillard, J. P. Buisson, S. Lefrant, J. Raman Spectrosc. **31**, 1041 (2000).

19. G. Louarn, M. Lapkowski, S. Quillard, A. Pron, J. P. Buisson, S. Lefrant, J. Phys. Chem. **100**, 6998 (1996).

20. R. Mažeikiené, G. Niaura, A. Malinauskas. J. Electroanal. Chem. **580**, 87 (2005).

21. M. Bartonek, N. S. Sariciftci, H. Kuzmany, Synth. Met. **36**, 83 (1990).

22. R. Mažeikiené, A. Statino, Z. Kuodis, G. Niaura, A. Malinauskas, Electrochem. Commun. **8**, 1082 (2006).

23. T. J. Durnick, S. C. Wait, J. Mol. Spectrosc. **42**, 211 (1972).

24. G. M. do Nascimento, V. R. L. Constantino, R. Landers, M. L. A. Temperini, Macromolecules **37**, 9373 (2004).

25. G. Ćirić-Marjanović. M. Trchová, J. Stejskal, Collect. Czech. Chem. Commun. **71**, 1407 (2006).

26. J. Stejskal, I. Sapurina, M. Trchová, E. N. Konyushenko, P. Holler, Polymer **47**, 8253 (2006).

УДК 539.192

DECONVOLUTION OF LIGNIN FLUORESCENCE SPECTRA: A CONTRIBUTION TO THE COMPARATIVE STRUCTURAL STUDIES OF LIGNINS

© 2007   D. Djikanović*, A. Kalauzi*, K. Radotić*, C. Lapierre**, M. Jeremić***

*Centre for Multidisciplinary Studies, Laboratory of biophysics, University of Belgrade, 29
Novembra 142, 11000 Belgrade, Serbia
**Institut National Agronomique, 78850 Thiverval-Grignon, France
***Faculty of Physical Chemistry, University of Belgrade, Studentski trg 16, 11000 Belgrade, Serbia
E-mail: xenia@ibiss.bg.ac.yu

Abstract – In this work we deconvoluted fluorescence spectra of lignin and lignin model compound using a combination of one symmetric (Gaussian) and most appropriate number of asymmetric (Log-normal) models. We aimed to obtain the new data on the structural characteristics of lignin as a complex molecule, using fluorescence spectroscopy in combination with FTIR spectra. We analysed emission spectra of lignin model compound, DHP, and isolated lignins from a deciduous tree, poplar, and a conifer tree, spruce. The number of applied asymmetric components is varied for each sample, until component positions obtained from deconvolution of a series of spectra becomes constant. Lignin model compound contains fewer components in the emission spectrum. The same components in the spectra of all three samples show that they contain the same fluorophores. Small shift of peak position can be attributed to the influence of different environments. FTIR spectra of the three polymers show a small difference between their structures. The main difference among the IR spectra of the three samples is in the intensity of some peaks.

INTRODUCTION

Fluorescence spectroscopy is a sensitive tool for structural and kinetic studies of macromolecules. The analysis of fluorescent spectra of polymeric molecules is especially complex, since they may contain different fluorophores or a fluorophore in various microenvironments. Therefore, it is necessary to use computer methods for numerical deconvolution of complex emission spectra into individual components. Lignin, as a major structural polymer in the plant cell walls, is the second most abundant polymer on Earth [1, 2]. Fluorescence is an intrinsic property of lignin. The structural complexity of lignin makes its fluorescence spectra difficult to interpret. In this work we deconvoluted fluorescence spectra of lignin and lignin model compound using a combination of one symmetric (Gaussian) and the most appropriate number of asymmetric (Log-normal) models. We aimed to obtain the new data on the structural characteristics of lignin as a complex molecule, using fluorescence spectroscopy. This approach, combined with analysis of FTIR spectra of lignin, enables comparison of structural characteristics of different lignin samples.

MATERIALS AND METHODS

Lignin model dehydrogenative polymer (DHP) was synthesized according to the procedure of Radotić et al. [3]. DHP was synthesized from coniferyl alcohol, using horseradish peroxidase as an enzymatic catalyst.

Lignins from poplar (*Populus tremuloides*, clone 1214) and spruce (*Picea abies* (L.)) were obtained from wood mill using method of thioacidolysis [4].

Fluorescence spectra were collected using a Fluorolog-3 spectrofluorimeter (Jobin Yvon Horiba, Paris, France) equipped with a 450 W xenon lamp and a photomultiplier tube. The spectra were corrected for the dark counts. In each measurement seven scans were averaged. The emission spectrum of the solvent (dioxane/water, 9/1 v/v) was subtracted. All measurements were performed at controlled temperature of 25°C by means of a Peltier element.

A total of $N_{DHP} = N_{poplar} = N_{spruce} = 22$ emission spectra were collected for each sample (DHP, lignin from poplar and spruce) by excitation at different wavelengths, starting from excitation maximum at 360 up to 465 nm, with a 5 nm-step. Nonlinear fitting of the first 12 spectra was performed using the Nelder-Mead algorithm implemented in Matlab, version 6. There was a significant decrease in intensity of spectra excited by wavelengths higher than 420 nm (13th–22nd spectra). All spectra were deconvoluted by Gaussian and Lognormal models into four components:

$$I(\lambda) = \sum_{i=1}^{n} A_i \frac{1}{\sqrt{2\pi}\sigma_i} \exp\frac{-(\lambda - \lambda_{0i})^2}{2\sigma_i^2}$$

Gaussian model,

where $I(\lambda)$ is the relative fluorescence intensity at wavelength λ, A_i, i-th component area, σ_i, i-th compo-

nent standard deviation (width), λ_{0i}, wavelength of i-th component maximum (position) and n, number of com-

ponents. For each component, all three parameters A_i, σ_i and λ_{0i} were fitted

$$\begin{cases} F_\lambda = F_m \exp\{-(\ln 2/\ln^2\rho)\ln^2[(1/a' - 1/\lambda)/(1/a' - 1/\lambda_m)]\}, & \text{for } \lambda > a', \\ F_\lambda = 0, & \text{for } \lambda \le a' \end{cases}$$

Log-normal model

where F_m is the maximal intensity, ρ the spectral shape asymmetry parameter, a' – function limiting point and λ_m – wavelength at which a maximal fluorescence occurs.

FTIR spectra were collected using a Perkin-Elmer 9836 infrared spectrometer. The dried samples were embedded in KBr pellets in the concentration of 1 mg/60 mg KBr. The spectra were recorded in the transmission band mode in the range 400–4000 cm^{-1}.

RESULTS AND DISCUSSION

Fig. 1 shows emission spectra of lignin model compound, DHP, and isolated lignins from a deciduous tree, poplar, and a conifer tree, spruce. The monomeric building blocks do not vary considerably among the three polymers, all of them containing guaiacyl and/or syringyl unit. However, their ratio vary in the polymers. In deciduous trees (poplar) there are more syringyl than guaiacyl units in lignin structure, while in conifers (spruce) about 95% of monomers are guaiacyl units [5]. In DHP all monomers are guaiacyl ones.

The same maxima positions in the emission spectra of the three samples show similarity of their fluorophores. This is related to the fact that all building monomers in lignins contain substituted benzene rings, which are the main source of their fluorescence. Presence of different side chains on the ring, as well as substitutions at various positions in the ring or side chain, produce variations in the fluorophore emission. There is a high similarity between emission spectra of poplar lignin and DHP. Different ratio of the two emission maxima between spruce, on one side, and poplar and DHP, on the other, shows different structural arrangement of the fluorophores within these polymers. On the other hand, FTIR spectra of the three polymers (Fig. 2) show a small difference between their structures. The main difference among the IR spectra of the three samples is in the intensity of some peaks. The main lignin spectral bands are 1505–1515 cm^{-1} (aromatic skeletal vibrations), 1600 cm^{-1} (aromatic skeletal vibration and C=O stretch), 1660 cm^{-1} (C=C band in the side chain). In the study of FTIR spectra of lignins of different origin, Faix (1991, [6]) found a correlation between syringil to guaiacil (S/G) ratio and intensity of particular IR peaks in a lignin sample. The intensities of the peaks in FTIR spectra of the lignin samples herein presented

(Fig. 2) are in accordance with these S/G ratios. Peak at 966–990 cm^{-1} (–HC=CH– out-of-plane deformation) is present only in DHP. The peak at 1380 cm^{-1} (aliphatic C–H stretch in CH$_3$) is insignificant in the case of spruce sample. Peak at 1740 cm^{-1} (C=O stretch in unconjugated ketone, carbonyl and in ester groups; conjugated aldehydes and carboxylic acids) is absent in the DHP sample and insignificant in poplar lignin. This may be a consequence of oxidative formation of such type of structures during isolation procedure, while in DHP such structures are not formed because harmful processes are avoided and polymerization proceeds in a controlled manner.

In the previous paper [7] we combined a method of continous excitation with a series of wavelengths having a constant difference, and a method of time resolved fluorescence to show that DHP fluorescence originates from discrete fluorophore centers, contrary to the other opinion that charge transfer mechanism operates in lignin emission [8]. Here we applied the same experimental approach to perform a comparative analysis of the emission spectra of lignins shown in Fig. 1. Series of 22 spectra for each sample are excited by wavelenghts differing in 5 nm step. In this way, each fluorophore is excited differently in each step enabling us to check validity of deconvolution procedure.

We analysed first 12 spectra since deconvolution of further spectra did not provide additional data. We used a combination of one symmetric (Gaussian) and various number of asymmetric (Log-normal) models. One Gaussian component in all model combinations was used to compensate for the Raman band, originating from the sample, which appeared in all integral spectra, and arising, as calculated, from OH stretch. The number of applied asymmetric components is varied for each sample, until component positions obtained from deconvolution of a series of spectra becomes constant. For DHP, poplar and spruce, optimal number of asymmetric components in the model is found to be four, five and six, respectively, indicating an increase of complexity of the structure. As an example, results of deconvolution of spruce lignin spectra are given in Fig. 3: deconvolution of one band contour from the series of emission spectra is given in Fig. 3a, as well as fitted component positions as a function of wavelength, for 5 + 1 and 6 + 1 (asymmetric + symmetric) combinations of components (Figs. 3b,c). A comparison of Fig. 3b and
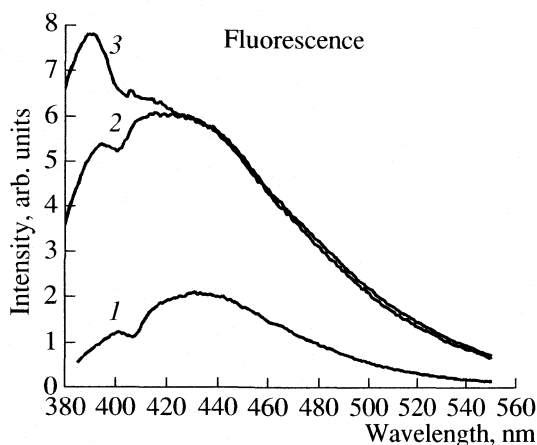
Fig. 1. Emission spectra of DHP (*1*), poplar (*2*) and spruce (*3*) dissolved in dioxane/water mixture (9 : 1, v/v) measured after excitation at 365 nm.

Fig. 3c shows that combination of 6 + 1 component gives better fit. Stepwise increase of wavelength excitation brings one by one fluophores in excited state leaving consequently unexcited those that do not absorb exitation light. Component maxima for the three lignin samples, obtained on the basis of the performed analysis, are given in the Table.

Lignin model compound has simpler structure in comparison with the two isolated lignins, and consequently contains fewer components in the emission spectrum. It is obvious that most components are present in emission spectra of all samples. The same components in the spectra of all three samples show that they contain the same fluorophores, which means that the structure of DHP is very similar to the structure of the two isolated lignins. This fact confirms that DHP is acceptable substitute as model compound for studying the genuine lignin structure and properties. On the other side, difference in positions of some of the components among the three polymers shows that some of the fluorophores that they contain are different, which

Component position (nm) in the emission spectra of lignin model compound and lignins isolated from poplar (*Populus tremuloides*, clone 1214) and spruce (*Picea abies* L.), obtained by spectral deconvolution

DHP	Spruce	Poplar
395	397	397
425	420	420
445	445	442
460	465	460
480	485	480
–	505	505
520	550	530
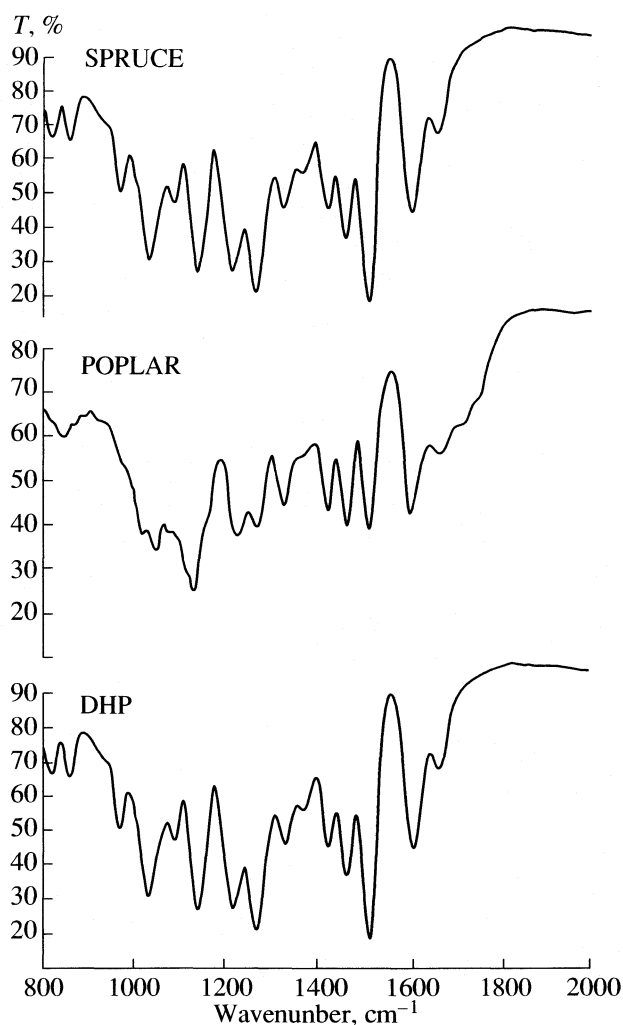
Fig. 2. FTIR spectra of DHP, poplar and spruce.

may be different molecular species or the same species in different environment. Small shift of peak position can be attributed to the influence of different environments. Influence of the environment in the matrix can be multiple, from copigmentation, hydrogen bonding, and dipole induction to steric hindrance [9]. Comparing emission spectra of lignins from a deciduous and conifer trees (Fig. 1), after deconvolution one can see that there are also some similarities and differences (in the region over 500 nm) in spectral component positions (Table). These differences may reflect differences in monomer building blocks in lignin from these two kinds of trees. Machado et al. [10] used life-time quenching of long-lived fluorescent probes to map the energy distribution of the structural units present in lignin fragments from *E. grandis* wood. Their results indicated that the emission spectra of this lignin might be regarded as a superposition of at least four broad spectral envelopes with slightly different emission maxima and widths. They concluded that the majority of the fluorescence complexity of this lignin seems to be associ-

ated with ground state heterogeneity, due to the complex mixture of the different fluorophores, on which different flurophore environments are superimposed [11].
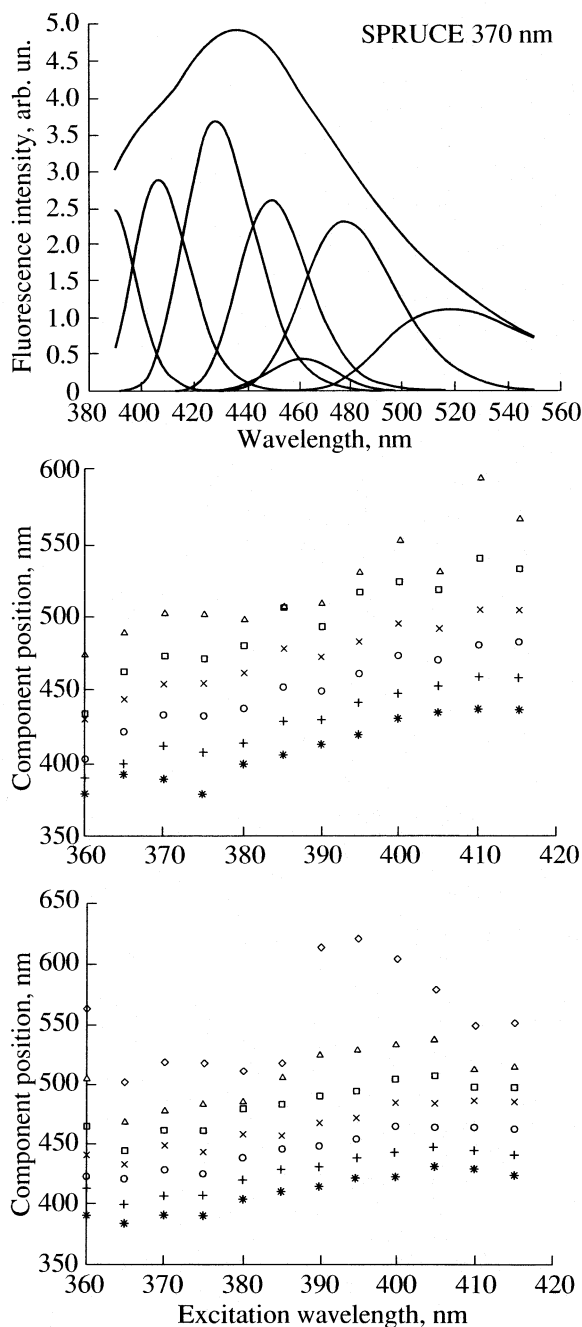
The obtained results show that there are fine structural variations between the three lignin polymers: between DHP as a model compound on one side and natural lignins on the other, or between the two lignins originated from deciduous and conifer trees. This is confirmed by the fine differences in their FTIR spectra (Fig. 2). These data provide an evidence that analysis of fluorescence spectra of complex molecules may give a contribution to the understanding of their structural features. The differences among presented emission spectra (Fig. 1) and their component positions (Table) may be related to the fine differences observed in the FTIR spectra of the three lignins.

ACKNOWLEDGEMENTS

REFERENCES

1. K. Freudenberg, Angew. Chem. **68**, 84 (1956).

2. H. Erdtman, Ind. Eng. Chem. **49**, 1385 (1957).

3. K. Radotić, J. Simić-Krstić, M. Jeremić, M. Trifunović, Biophys. J. **66**, 1763 (1994).

4. C. Lapierre, B. Monties and C. Rolando, Holzforschung **40**, 113 (1986).

5. C. Lapierre, in: Forage cell wall structure and digestibility, Chapter 6, ASA-CSSA-SSSA, 677S.Segoe Rd., Madisson, 133 (1993).

6. O. Faix, Holzforschung **45**, 21 (1991).

7. K. Radotić, A. Kalauzi, D. Djikanović, M. Jeremić, R. M. Leblanc, Z. G. Cerović, J. Photochem. Photobiol. B: Biology **83**, 1 (2006).

8. S. Barsberg, T. Elder, C. Felby, Chem. Mater. **15**, 649 (2003).

9. B. Valeur, Fluorescent probes for evaluation of local physical and structural parameters, in: S.G. Schulman (Ed.), Molecular luminescence spectroscopy methods and applications: Part 3., John Wiley&Sons, New York, 25 (1993).

10. A. E. Machado, D. E. Nicodem, R. Ruggiero, D. S. Perez, A. Castellan, J. Photochem. Photobiol. A: Chem. **138**, 253 (2001).

11. B. Albinsson, S. Li, K. Lundquist, R. Stomberg, J. Mol. Struc. **508**, 19 (1999).

Fig. 3. Uper panel: Example of spruce emission spectrum deconvoluted into one Gaussian and six Log-normal components; excitation wavelength was 370 nm; middle and lower panels: Fitted component positions as a function of the excitation wavelength, after deconvolution into one Gaussian and five Log-normal components, or one Gaussian and six Log-normal components, respectively.

STRUCTURE OF MATTER
AND QUANTUM CHEMISTRY

SURFACE MODIFICATIONS OF TiN COATINGS
BY A PULSED TEA CO_2 LASER: COATING THICKNESS EFFECTS

© 2007   M. S. Trtica*, B. M. Gaković**, B. B. Radak*

Vinča Institute of Nuclear Sciences, P.O. BOX 522, 11001 Belgrade, Serbia
Department of Physical Chemistry
**Atomic Physics Department*
E-mail: bradak@vin.bg.ac.yu

Abstract – Interactions of a Transversely Excited Atmospheric (TEA) CO_2 laser, pulse duration ~2 microseconds (initial spike FWHM ~120 ns), with polycrystalline titanium nitride (TiN) coatings deposited on high quality steel (AISI 316 or M2) were studied. The experiments were carried out in a regime of high laser energy densities: 25, 48, and 50 J/cm^2. The energy absorbed from the laser beam was partially converted to thermal energy, and the effects of the TiN coating thickness on the morphological changes were considered. The morphological features and processes that accompany the interaction can be summarized as follows: (i) exfoliation of the TiN coating in the central zone of the irradiated area (for coating thickness of 1 μm) or appearance of grainy structure (for coating thicknesses 3 μm and 10 μm), (ii) appearance of hydrodynamic changes in the surrounding peripheral zone, and (iii) appearance of plasma in front of the target during sample irradiation.

1. INTRODUCTION

Surface modification studies of titanium-based ceramic coatings, especially titanium nitride deposited on steel substrates, by various types of energetic beams, including laser beams, are of great fundamental and technological interest. The last decade saw some efforts of the studying of laser beam interactions with titanium nitride. Beams of the ruby – [1], Nd:YAG – [2], Ti:Sapphire [3], excimer – KrCl, XeCl [4, 5], and CO_2 [4–6] lasers have so far been employed. Generally, the interaction of pulsed Transversely Excited Atmospheric (TEA) CO_2 laser beams with titanium nitride has not yet been sufficiently explored. Titanium nitride possesses extraordinary physico-chemical properties such as a thermodynamic stability, high hardness, admirable corrosion and erosion resistance, etc. It is therefore attractive for various areas of application, from sensor technologies, industry in general, to applications in biomedicine. In bio-medical applications titanium nitride demonstrates unique properties. It is biocompatible, without toxic effects. It has recently been shown that TiN can be successfully applied as a film coating for blood-contacting implants when deposited on silicon or steel substrates [7, 8].

The present paper deals with effects of a pulsed, energetic, infrared laser emitting at ~10 μm (TEA CO_2 laser) on polycrystalline titanium nitride coatings deposited on high quality steel (AISI 316 or M2). Special attention was paid to morphological surface modifications of the target with respect to the coating thickness. The studies were carried out in the regime of high laser radiation energy densities.

2. EXPERIMENTAL

The TiN coatings (of 1, 3, or 10 μm thickness) used in the experiment were deposited on a steel substrate (AISI 316 or M2) by two methods: (i) reactive d.c. magnetron sputtering [9] or (ii) chemical vapor deposition [10]. Both deposition methods provided good quality coatings. The steel substrate was prepared by the standard metallographic procedure including polishing, rinsing, and drying. Bulk dimensions of rectangularly shaped substrates were typically 20 mm × 12 mm × 2 mm whereas the substrate roughness of AISI 316 or M2 was evaluated to less than 0.1 and 0.4 μm, respectively.

Irradiations were performed with the laser beam focused by a KBr lens of 6.0 cm focal length. The angle of incidence of the laser beam with respect to the surface plane was 90°. The irradiations were carried out in air, at a pressure of 1013 mbar. The TEA CO_2 laser was operated in a multi-mode regime. Nonconventional $CO_2/N_2/H_2$ gas mixtures were used for the TEA CO_2 laser [6], yielding pulses with a gain switched peak followed by a slowly decaying tail.

Various analytical techniques were used for characterization of the samples. X-ray diffraction (XRD) was employed for identifying crystal phases, etc. Surface morphology was monitored by optical microscopy (OM), scanning electron microscopy (SEM), and atomic force microscopy (AFM).

3. RESULTS AND DISCUSSION

The X-ray analysis of the intact titanium nitride coating, prior to laser irradiation, indicated that its polycrystalline structure was similar to published before [6]. The coating showed a cubic B1 structure of the
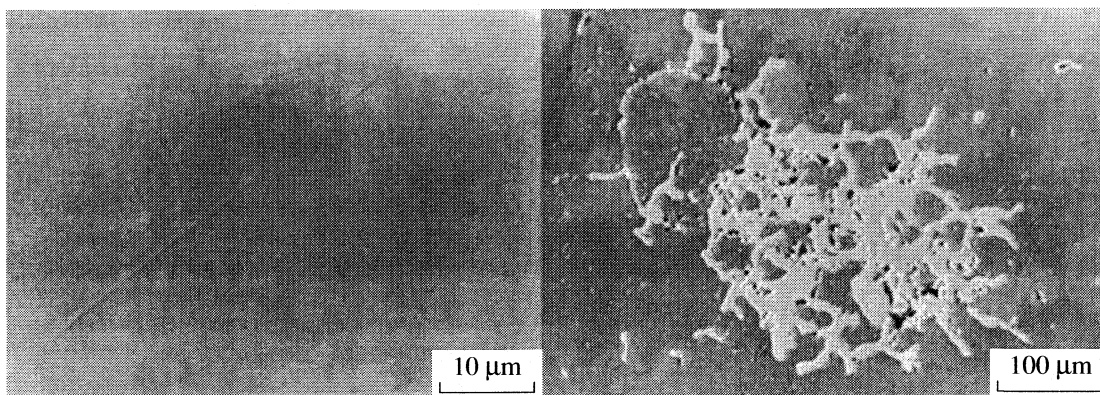
Fig. 1. SEM images of a TiN/steel sample before (*left*) and after (*right*) TEA CO$_2$ laser irradiation by 20 pulses (multi-mode regime; pulse with tail; $\Phi_1 \sim 50$ J/cm^2). TiN coating 1 μm; steel substrate AISI 316.
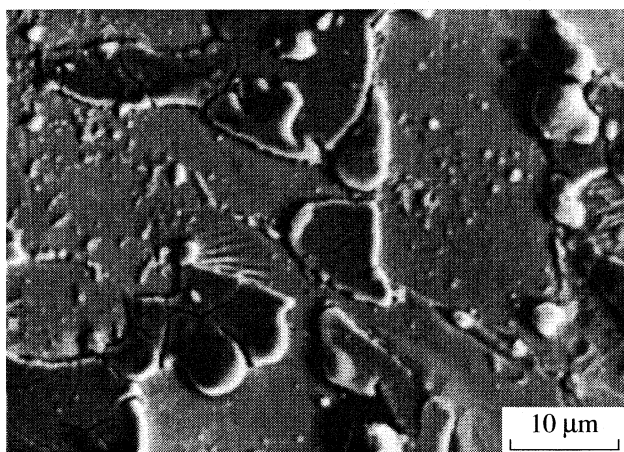
Fig. 2. Morphological changes of a TiN/steel sample after 20 laser pulses (center of the irradiated area). Experimental conditions are the same as in Fig. 1.
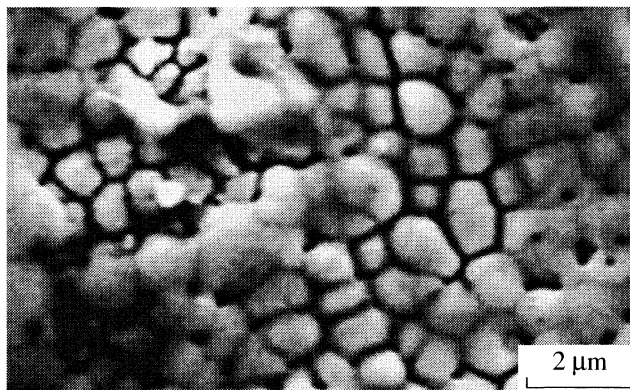
Fig. 3. Topographic features of a TiN/steel sample after 120 pulses (periphery of the irradiated area). Experimental conditions are the same as in Fig. 1.

NaCl-type with a preferred (111) orientation. The TiN coating had a golden-yellow color, typical for stoichiometric composition of [Ti]/[N] = 1. Morphological changes showed dependence on beam characteristics: laser pulse energy density, peak power density, pulse duration, number of accumulated pulses, etc. as well as target characteristics.

The TiN/steel behavior was monitored in the regime of high fluences (Φ, laser radiation energy densities): 25, 48, and 50 J/cm^2. The modifications can be presented as follows:

(*A*) Topographical changes of the sample with the thinnest TiN coating of 1 μm on steel, resulting after 20, 120, and 500 accumulated TEA CO$_2$ laser pulses are presented in Figs. 1–4.

After 20 pulses at 50 J/cm^2 (Figs. 1 on the right, and 2) the damage of the TiN/steel sample can be clearly recognized. Almost complete exfoliation of the TiN coating is observable in the central part of the damage area. The same effect was observed even after just one laser pulse in [4], as well. Cumulative laser pulses (at con-

stant fluence) resulted in the extension of the damaged area, as well as in the modification of the steel substrate. Structures in the form of needle-like and lens-like shapes were observed in the central part at a high number of accumulated pulses. At the periphery of the damaged zone cracking and hydrodynamic effects like resolidified droplets become especially observable after 120 and 500 accumulated pulses, Figs. 3 and 4, respectively.

The evaluation of the TiN/steel surface temperature within each pulse as a function of time was carried out by Equation (1) of our [4], i.e. Eq. (2) [11]:

$$\Delta T(t) = \frac{A}{c\rho(\pi\kappa)^{1/2}} \int_0^t \frac{(\xi)d\xi}{(t-\xi)^{1/2}}, \qquad (1)$$

where absorptivity is denoted as A, specific heat as c, thermal diffusivity as κ, target density as ρ, and the laser beam intensity as I. For the laser pulse shape (with tail) used here, $I_{max} = 115$ MW/cm^2, and an target absorptivity as in [5], the calculation showed that a max-
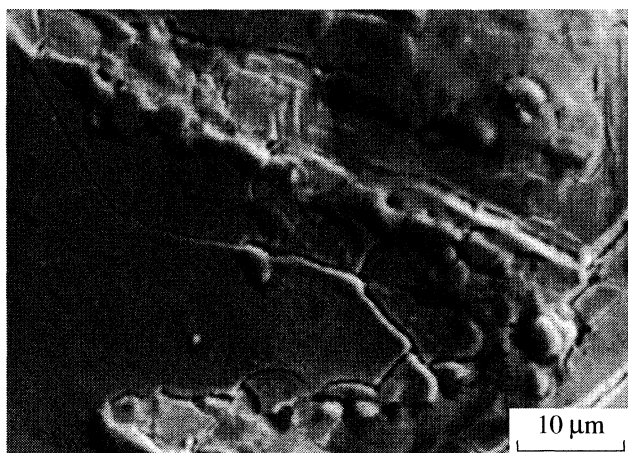
Fig. 4. Topographic features of a TiN/steel sample after 500 pulses (periphery of the irradiated area). Experimental conditions are the same as in Fig. 1.

imum surface temperature of about 3400 K was reached approximately after 1.1 μs. This is approximately the time corresponding to about 2/3 of the tail duration. The high surface temperature led to decomposition/exfoliation of the TiN coating (TiN decomposition temperature is 3252 K [12]) with the first laser pulse, so that each subsequent pulse practically interacted with the steel substrate. The development of the high temperature, as well as the rapid cooling at the steel interface, are drastic events that contribute to the appearance of needle- and lens-like shapes, and hydrodynamic structures. Under these conditions a phase transition within the steel substrate is quite possible. The changes in the central zone can probably be associated with the appearance of the martensite form. It is well known that a phase transition will occur in the

course of steel thermal treatment at higher temperatures, depending on the chemical composition, especially the carbon content [13]. A steel with a low carbon content, like this substrate (AISI 316), will be phase transformed in the temperature interval from 930 to 960 K [13, 14]. A TEA CO_2 laser pulse causes a rapid temperature change on the steel surface, followed by extremely fast cooling, so that the carbon in the steel does not have sufficient time to get completely separated from α-ferrite. The newly created phase becomes oversaturated with carbon, and this structure is known as martensite, characterized by needle- and lens-shaped forms on the surface.

(**B**) Morphological features obtained on the samples with 3 μm and 10 μm TiN coatings after 340 and 500 accumulated TEA CO_2 laser pulses are presented in Figs. 5 and 6, respectively. Morphologically, the central region appears quite different than that obtained after one laser pulse. This region has a predominantly grainy structure. Its distribution is more homogenous with the 3 μm coating than the 10 μm one. The average grain diameter in both cases is about 1 μm. Grain boundary cracking was observed in the central zone, and hydrodynamic effects in the form of resolidified droplets in the outer zones.

The first pulses were not accompanied by any appearance of plasma. Plasma appeared in front of the target only after multiple pulses.

During the TEA CO_2 laser irradiation of a TiN/steel target, the laser source can approximately be considered as a superficial thermal source. In this way, the laser-beam/target interaction can be satisfactorily described by the linear heat conduction theory [15]. After the first high fluence laser pulse the absorptivity of the target changes. As a rule, it increases. The main part of the absorbed laser energy is transformed into heat.
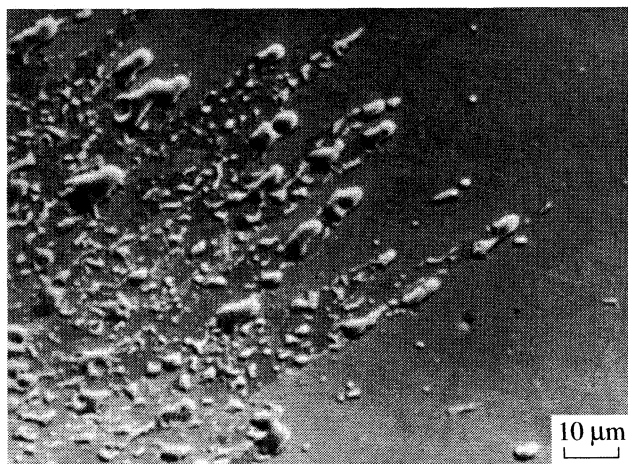
Fig. 5. Topographic features of a TiN/steel sample after 340 pulses (center of the irradiated area). Experimental conditions are the same as in Fig. 1, except for: TiN coating 3 μm; steel substrate AISI M2, Φ ~ 48 J/cm².
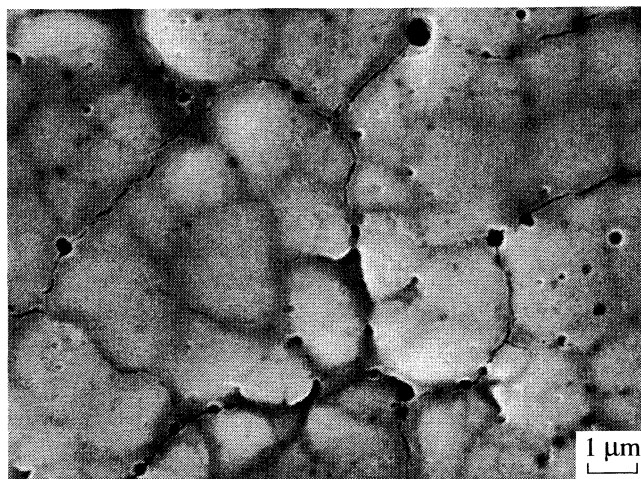
Fig. 6. Topographic features of a TiN/steel sample after 500 pulses (center of the irradiated area). Experimental conditions are the same as in Fig. 1, except for: TiN coating 10 μm; steel substrate AISI 316, Φ ~ 25 J/cm².

Generally, a series of effects such as melting, vaporization, dissociation and ionization of the vaporized material, shock waves in the vapor and the solid, etc. can be generated at the target. The morphological features obtained on the surface are apparently dependent on the thickness of the TiN coating, which controls the presence of interface effects. It can be assessed that the effective laser heat penetration into the sample, for the laser pulse durations used here, does not extend further than the coating thickness. The effective penetration depth can be estimated [2] at about 1 μm, the thickness of the thinnest coating used here. A recent theoretical consideration of in-depth temperature evolution in a titanium sample [15] irradiated by a TEA CO_2 laser of similar intensity as in our case showed that a target temperature of about 3300 K was achieved at a depth of 0.25 μm, and 2000 K at about 1.25 μm, all within one laser pulse. We can safely assume that similar temperatures were reached in our TiN coatings, since Ti and TiN have similar thermal conductivities.

It follows that the TEA CO_2 laser pulses used here interact only superficially with the TiN/steel target. However, in the case of the 1 μm TiN coating the heat effectively reaches the steel interface and the whole surface area sustains the most drastic changes. In this case Figs. 1 and 2 show that the TiN coating is practically removed after the first several laser pulses. In the cases of 3 μm and 10 μm TiN coatings (Figs. 5 and 6, respectively) the effective heat penetration does not reach the interface and the integrity of the TiN coating is maintained. The only direct consequence is the modification of the TiN coating itself.

CONCLUSION

A study of morphological changes of titanium nitride coatings deposited on high quality steel (AISI 316 or M2) induced by a pulsed TEA CO_2 laser is presented. It is shown that this laser induces morphological/structural changes on the target when energy densities are 25, 48, and 50 J/cm^2.

The energy absorbed from the laser beam is mainly converted into thermal energy, causing surface modifications. The level of the modification apparently depends on the coating thickness. Under high fluence the 1 μm TiN coating is removed practically after the first several pulses, whereas the coatings of 3 μm and 10 μm keep their integrity.

The morphological features and processes induced by the CO_2 laser radiation on TiN/steel targets can be summarized as follows: (i) exfoliation of the TiN coating in the central zone of the irradiated area (for the 1 μm coating) or appearance of grainy structure (for 3 μm and 10 μm coatings), (ii) appearance of hydrodynamic changes, like resolidified droplets of the material, in the surrounding peripheral zone, and (iii) appearance of plasma in front of the target during sample irradiation.

REFERENCES

1. M. Zlatanovic, B. Gakovic, A. Radivojevic, P. Drljaca, D. Dukic, S. Ristic, 18th Summer School and International Symposium on the Physics of Ionized Gases, Kotor, Yugoslavia, September 2–6 1996, Contributed Papers, p. 229 (1996).

2. T. V. Kononenko, S. V. Garnov, S. M. Pimenov, V. I. Konov, V. Romano, B. Borsos, H. P. Weber, Appl. Phys. A **71**, 627 (2000).

3. J. Bonse, H. Sturm, D. Schmidt, W. Kautek, Appl. Phys. A **71**, 657 (2000).

4. M. S. Trtica, B. M. Gakovic, Lj. T. Petkovska, V. F. Tarasenko, A. V. Fedenev, E. I. Lipatov, M. A. Shulepov, Appl. Surf. Science **225**, 362(2004).

5. M. S. Trtica, V. F. Tarasenko, B. M. Gakovic, A. V. Fedenev, Lj. T. Petkovska, B. B. Radak, E. I. Lipatov, M. A. Shulepov, Appl. Surf. Science **252**, 474 (2005).

6. B. M. Gakovic, M. S. Trtica, T. M. Nenadovic, B. J. Obradovic, Proceedings of the International Vacuum Congress No14, 31 Aug. 1998, Birmingham, UK, **343-4**, p. 269 (1999).

7. I. Tsyganov, M. F. Maitz, E. Wieser, Appl. Surf. Science **235**, 156 (2004).

8. Ju-Young Yun, Jin-Woo Bae, Ki-Dong Park, Kwang-Wha Chung, 210th Meeting of The Electrochemical Society, Oct. 29–Nov. 3, 2006, Cancun, Mexico, http://ecsmeet2.peerx-press.org/ms-files/ecsmeet2/2005/05/03/00003160/00/3160-0-art-file-0-1115105855.pdf

9. B. M. Gakovic, Z. Rakocevic, T. M. Nenadovic, D. Perusko, M. S. Trtica, S. Zec, Solid State Phenomena **61**, 357 (1998).

10. M. S. Trtica and B. M. Gakovic, 6th International Conference on Fundamental and Applied Aspects of Physical Chemistry, Physical Chemistry 2006, Belgrade, September 26–29, 2006, Proceedings p. 537.

11. J. Hermann, C. Boulmer-Leborgne, I. N. Mihailescu, B. Dubreuil, J. Appl. Phys. **73**, 1091 (1993).

12. L. E. Toth, in "Transition Metal Carbides and Nitrides", Academic Press, New York (1971).

13. Hermann Schuman, "Metallographie", VEB Leipzig (1975).

14. M. S. Trtica, B. M. Gakovic, T. M. Nenadovic, M. M. Mitrovic, Appl. Surf. Science, **177**, 48 (2001).

15. A. L. Thomann, C. Boulmer-Leborgne, C. Andreazza-Vignolle, P. Andreazza, J. Hermann, G. Blondiaux, J. Appl. Phys. **80**, 4673 (1996).

SYNTHESIS AND SPECTROSCOPIC CHARACTERIZATION OF COPPER(II) DEXTRAN COMPLEXES

© 2007   Ž. Mitić*, G. Nikolić**, M. Cakić**, R. Nikolić***, L. Ilić****

*Faculty of Medicine, Department of Pharmacy, 18000 Niš, Serbia
**Faculty of Technology, 16000 Leskovac, Serbia
***Faculty of Sciences and Mathematics, 18000 Niš, Serbia
****Pharmaceutical and Chemical Industry "Zdravlje", Leskovac, Serbia
E-mail: zak_chem2001@yahoo.com

Abstract – Synthesis of the stable copper(II) complexes with reduced dextran derivatives can be realized with low molar polysaccharides at an average molar mass 5000 g mol^{-1}. Copper(II) content of 4–20% is effected at pH 7–8 and at boiling point. Copper(II) complex formation with dextran were analyzed by spectrophotometric VIS methods. IR spectra of copper(II) complexes with dextran were analyzed to find the most stable conformation of glucopyranose unit. ESR parameters of spectrum indicates the square-planar coordination of Cu(II) ion with four oxygen ligand atoms in the same plane.

The copper deficiency causes a number of pathological states [1]. In both human and veterinary medicine commercial copper preparations based on dextran and its derivatives are used for such purpose [2]. According to the literature data dextran has ability of complex formation with various biometals (Zn, Fe, Co, Ca, and Mg) [3–6]. Iron complexes with different polysaccharides have special importance and they have been described in detail [7]. Synthesis procedures for the complex formation of Cu(II) with polysaccharides, including dextran, are described in scientific and patent literature [8]. However, the literature data about the complex formation possibility of Cu(II) ion with dextran derivatives are scarce.

EXPERIMENTAL

Low molar dextran (LMD; M_w = 5000 g mol^{-1}) with reducing groups content (RG) of 12.5% were obtained from pharmaceutical and chemical industry "Zdravlje Actavis Co." (Leskovac, Serbia). The reduction of LMD was performed with NaBH$_4$ (p.a., Merck). The quantity (Q) of NaBH$_4$ necessary for the reduction of LMD depends of (RG, %) and the total polysaccharide mass (m). It was calculated by using the following empirical equitation (1):

$$Q = 3.35 \times 10^{-3} RGm. \qquad (1)$$

The RG values were obtained by using Somogyi method [9]. The reducing group content in the final product was determined by the Somogyi method and found to be below 0.05%. To the solution containing 100 g of ligand (RLMD) in 700 cm^3 H$_2$O the 250 cm^3 of 1.2 mol dm^{-3} NaOH solutions was added. After that drop wise addition of the solution containing 170 mmol of CuCl$_2 \cdot$ 2H$_2$O was performed with continuous stirring until the pH value of about 7 was reached. The synthesis of the complexes was performed at pH values ranging from 7–12 (adjusted by the addition of 10% NaOH solution) by boiling the solution. The change of solution color from blue to green indicated that the synthesis of the complexes was completed. Reaction mixture was than cooled to room temperature and neutralized with 1 mol dm^{-3} HCl. Green solution of the complexes was filtrated and complex precipitated by the addition of the 2.5 dm^3 of 95% ethanol. After overnight standing the ethanol was decanted and precipitate redissolved in 700 cm^3 of redistilled water. The dialysis of the solution was used to remove unbounded ions. Finally, the complex was precipitated from dialyzed solution by the 96% ethanol and after decantation dried for 3 h at 105°C in vacuum oven.

Copper content of the complexes was measured by Atomic Absorption Spectrometry (AAS) on the Philips Pye Unicam SP-9 spectrometer (Cu-lamp λ = 324.8 nm; the breadth of slot 0.5 nm; the flame: acetylene/air), according to the standardized procedure [10]. VIS spectra of the complexes water solutions were recorded on VARIAN Cary-100 Conc. spectrophotometer in quartz cuvettes (1 × 1 cm), with redistilled water as a reference. The IR spectra as average of 10 scans were recorded on IR spectrometer BOMEM MB-100 equipped with standard DTGS/KBr detector, in the range 4000–400 cm^{-1} with resolution of 2 cm^{-1}, by KBr pastille method. ESR spectra of Cu(II) complexes with RLMD were recorded on BRUKER ESR-300 spectrometer at X-band and at room temperature. Measurements were performed on powdered samples in vacuum sealed quartz tubes (3 mm i.d.). g-Values were determined by comparison with potassium nitrozo-disulphonate solution.

RESULTS AND DISCUSSION

The analysis of the synthesis of similar complexes has points to the necessity of defining the physico-chemical properties of the commercial preparations.

Reaction conditions and characteristic physicochemical properties of synthesized Cu(II) complexes with RLMD ligand M_w 5000

Procedure	pH_{synth}	T_{synth}	t_{synth}, min	Color	Cu, %	Water solubility	Stability (Ageing, 6 months)
1	7.5	room	60	light green	7.23	soluble	stable, clear solution
2	7.5	boiling	7	green	19.85	very soluble	stable, clear solution
3	8.0	boiling	7	green-blue	8.12	soluble	stable, clear solution
4	10.0	boiling	7	blue-green	8.20	sparingly soluble	precipitate
5	12.0	boiling	7	dark blue	6.97	slightly soluble	solution layering

By their correlation, the undesired effects can be eliminated and thus considerably improved the pharmacological effect of the complex. For this reason, the choice and optimization of the low molar dextran in the capacity of the ligand have been made.

The reactivity of the dextran primarily depends on the reactivity of the secondary, equatorially oriented hydroxyl-groups (OH-2, OH-3 and OH-4). The contents of the primary OH groups in dextran are slightly increased at lower molar masses (about 2%). As it is the case with the other glucans, the reactivity of the OH-2 group to the alkalizing reagents is higher than of the OH-3 and OH-4 groups. This is rationalized in the context of higher acidity of the OH-2 because of the proximity of anomeric centre [6]. When the OH-2 and OH-4 ionize, reactivity to OH-3 is reduced; however, the substitution on the OH-2 and OH-4 abolish this action and induce the successive increase in the reactivity of OH-3. On applying these generalizations, it is necessary to exercise some precaution, since the potency of the base may affect the relative and absolute reactivities of the hydroxyl.

Through derivatization of the dextran to the reduced form the large number of activation centers with will be at the disposal to the copper ions for the purpose of binding the complex is expected. This creates the possibility of achieving the considerably larger stability of the synthesized complex as well as of its pharmacological effect.

Considering the importance of physicochemical parameters of process and synthesis results, the examination and optimization of ligands in relation to molar mass (M_w) as well as reaction conditions of synthesis (pH, T and t) were investigated in this work. The results of testing are shown in Table.

On the basis of obtained experimental results (Table), a favorable result of Cu(II)-RLMD complexes synthesis is obtained with dextran oligomers M_w 5000, at boiling temperature and pH 7.5–8.0, within 7 min. Synthesis of complexes with the same pH value (7.5) at room temperature or in extreme conditions (autoclave, 130°C) is not performed completely, not even within longer period of time of reaction of 60 min. Complexes obtained under the procedures 4 and 5 (Table), at pH > 8 present unfavorable effects of synthesis. The basic characteristics of synthesized complexes of Cu(II) with

RLMD are given in Table. Comparing the obtained complexes of Cu(II) with RLMD, either in solid state or in solution, it is apparent that depending on pH values various complexes colors are obtained (Table). The change of solutions color during the synthesis may be an indicator whether the syntheses of complexes were successful.

The obtained results shown that the color can vary from light green to dark blue in the range of pH 7.5–12. That is confirmed by the green solution color of the most stable complex of Cu(II) with RLMD (procedure 2, Table), in comparison with indigo-blue alkali solution of decomposed Cu(II) at pH 13, where $[Cu(OH)_4]^{2-}$ ions dominates. Water solubility of synthesized complexes of Cu(II) with RLMD is different. The most water soluble complex is obtained at pH 7.5 (Table). The solution is permanent and stable after a longer period of time (6 months). Complexes that are synthesized at higher pH are less soluble. The solution of complexes (obtained according to the procedure 5, Table), after resting a longer period start layering, releasing precipitate, and become opalescent. Investigation of the applied reaction parameters to the Cu(II) content in complexes have shown that synthesis temperature has s significant influence. When the solution is warmed up to
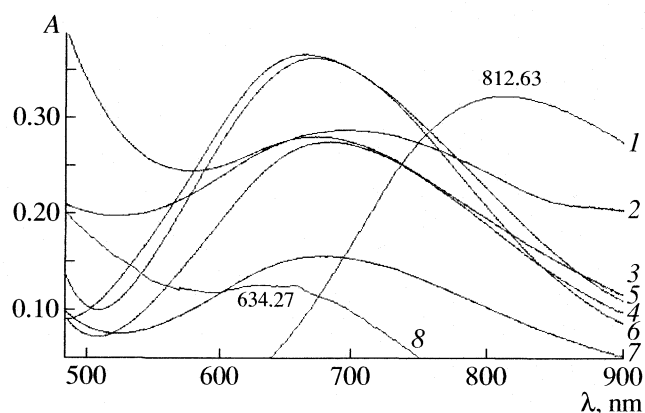
Fig. 1. Absorption light spectra of Cu(II) water solution (1) and complexes Cu(II) with RLMD synthesized: at pH 7.5 and room T (2), at pH 7.5 and temperature of boiling (3), at pH 7.5 in autoclave (4), at pH 8 and temperature of boiling (5), at pH 10 and temperature of boiling (6), at pH 12 and temperature of boiling (7); and complex $[Cu(OH)_4]^{2-}$ at pH 13 (8).

conditions are more extreme (autoclave, 130°C, 1 h), the content of bounded Cu(II) is decreased (4.08%).

Solution pH probably has the influence on the way of binding of Cu(II) into a complex, i.e. on type of bound, because due to the change of pH value the stability, color and solubility of the obtained complex are also changed (Table). Thus, by the increase of solution pH values from 7.5 to 12, the percentage of the bounded Cu(II) with RLMD in complex decreases. Tolmachev et al. [11], in their paper of influence of medium pH on binding Cu(II) with dextran, point out the possibility of gradual complexing, i.e. gradual forming of coordination bonds, where their reforming starts at pH 8. Thus, Cu(II) ions form of three different types of complexes [12] with dextran. Decomposition of Cu(II)-dextran complex begins at pH values higher than 12.

In addition, depending on pH values, complexes of Cu(II) with RLMD also behave differently considering wavelength at which they show absorption maximum.

Fig. 2. ESR spectrum of copper(II) complex with RLMD at pH = 10.

the boiling temperature, the content of bounded Cu(II) in a complex is increased almost three times (19.85%) in comparison to the procedure of synthesis at room temperature (7.23%, Table). However, if the synthesis
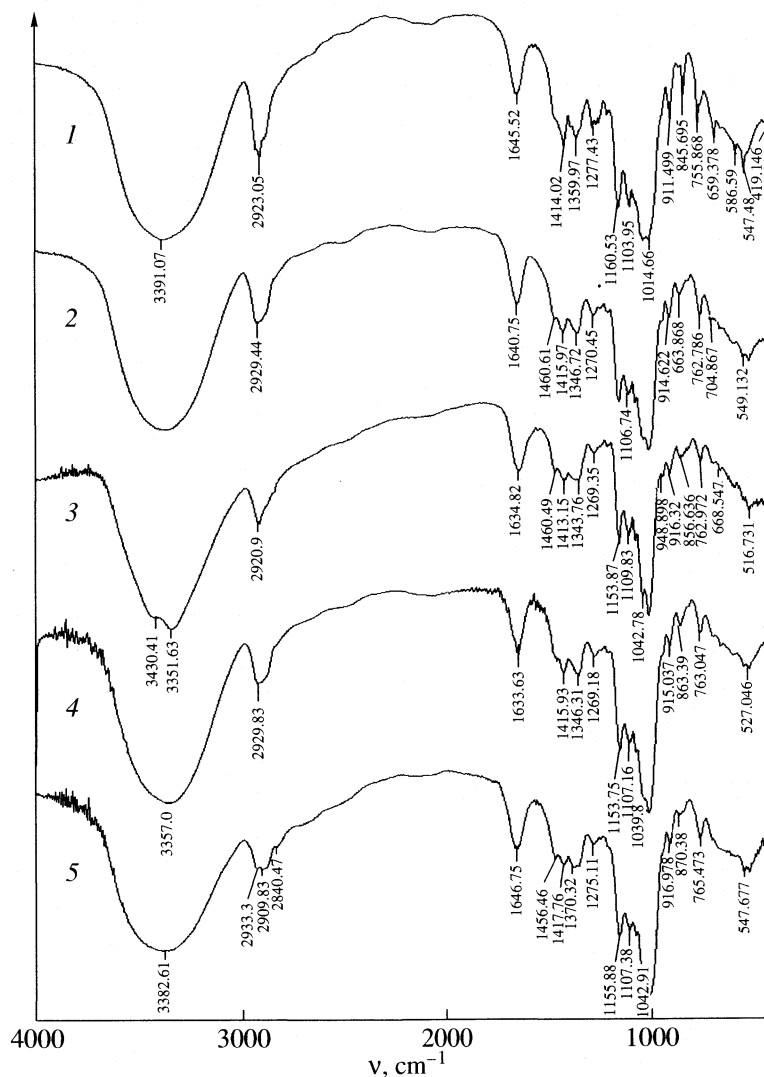
Fig. 3. FTIR spectra of RLMD, $M_w = 5000$ g mol^{-1} (*1*) and Cu(II) complexes with RLMD synthesized at boiling point and pH 8.0 (2), 7.5 (3), 10.0 (4), 12.0 (5).

This range of wavelengths in the VIS spectra is 650–700 nm (Fig. 1).

Hypsochromic effect of complexes absorption maximums with increase of pH solutions (Fig. 1) confirms the presence of different types of complexes. Hexaqua copper(II) ion $[Cu(H_2O)_6]^{2+}$ absorbs at wavelength 812.7 nm, while synthesized complexes absorb within the ranges of 650–700 nm (Fig. 1). With increase in solution pH the absorption maximums change to shorter wavelengths compared with $[Cu(H_2O)_6]^{2+}$ ion. Complex, which has been decomposed at pH values over 12, shows absorption maximum at 634 nm. Thereby, these spectrophotometric criteria can be applied for the confirmation of the success of complex synthesis.

ESR spectrum of complex containing 6.97% of copper synthesized at pH 10 is shown in Fig. 2. The ESR spectra indicate the axial symmetry of synthesized complexes and were typical for the Cu(II) ion with one unpaired electron in $3d$ subshell. Asymmetric appearance of the hyperfine spectral lines originates from the unresolved spectral contributions of two natural isotopes, ^{63}Cu and ^{65}Cu. ESR spectral parameters on Fig. 2 ($A_\parallel = 187 \times 10^{-2}$ cm^{-1}, $g_\parallel = 2.23$ and $g_\perp = 2.03$) point to the tetragonal coordination of Cu(II) with four oxygen atoms from ligands in the same plane [15].

Results of IR spectroscopic investigations show that spectra of Cu(II) ion complexes with polysaccharide and the ligand basically similar (Fig. 3). Dextran and complexes with Cu(II) ion have one crystallographic type of water molecule (1640 cm^{-1}) [13]. Water protons take part in the formation of relatively weak hydrogen bonds. Spectroscopic IR study in particular region of OH (3400, 1420 cm^{-1}) and C–H (2900, 1460, 1350 cm^{-1}) vibrations indicates different binding between central metal ion and ligand, depending on pH and metal contents (Fig. 3). The similarities of the $\gamma(C–H)$ range indicate that there is no difference in the conformation of the glucopyranose unit in the dextran and complex molecule and they probably exhibit C1-chair conformation (916 and 850 cm^{-1}) [14].

On the basis of the obtained results by spectroscopic investigations (UV-VIS, ESR, FTIR) of this complexes, three different types of Cu(II) complexes structure with deprotonized dextran monomer unit (Glc$^-$) are suggested depending on pH synthesis [16]. At pH 7 to 8 $[Cu(Glc)_2(H_2O)_2]$ is formed; at pH 8 to 10 $[Cu(Glc)_2(OH)(H_2O)]^-$ is formed and at pH values over 10 $[Cu(Glc)_2(OH)_2]^{2-}$ is formed.

CONCLUSIONS

Stable Cu(II) complexes with RLMD as a ligand, with the content of Cu(II) from 4–20% are synthesized. The content of copper, which is bound in a complex, is adjusted by variation of pH (7.5–12.0) and temperature (20–130°C) of reaction system.

$[Cu(H_2O)_6]^{2+}$ absorbs at wavelength 812.7 nm, while synthesized complexes absorb within the ranges of 650–700 nm (Fig. 1). With increase in solution pH the absorption maximums change to shorter wavelengths comparing with $[Cu(H_2O)_6]^{2+}$ ion. Complex, which has been decomposed at pH values over 12, shows absorption maximum at 634 nm. These spectrophotometric criteria can be applied for the confirmation of the success of complex synthesis.

The similarities of the $\gamma(C–H)$ range indicate that there is no difference in the conformation of the glucopyranose unit in the polysaccharide dextran and Cu(II) complex molecule and they probably exhibit C1-chair conformation (916 and 850 cm^{-1}).

ESR spectral parameters point to the tetragonal coordination of Cu(II) ion with four oxygen atoms from ligands in the same plane.

REFERENCES

1. EVM/99/19 Draft Review of Copper. Secretariat, UK Government, L., 2002.
2. PCT-WO 02/087598 A1. International Publishing Date, 07.11.2002.
3. Tolmachev, V. N., Lugovaya, Z. A., *Vysokomol. Soedin., Ser.* B, 1976, vol. 18, p. 548.
4. Tolmachev, V. N., Lugovaya, Z. A., *Vysokomol. Soedin, Ser.* B, 1975, vol. 17, p. 756.
5. Lugovaya, Z. A., Tolmachev, V. N., *Vysokomol. Soedin., Ser.* A, 1981, vol. 23, p. 434.
6. Gyurcsik, B., Nagy, L., *Coord. Chem. Rev.,* 2000, vol. 203, p. 81.
7. Nikolić, G., Cakić, M., Ilić, Lj., Ristić, S., Cakić, Ž., *Die Pharmazie,* vol. 57, no. 3, 155.
8. http://www.patents.ibm.com
9. Somogyi, M., *Biol. Chem.,* 1945, vol. 160, p. 61.
10. Djordjević, D., Ilić, Lj., Methods, ev.br. 3766-MO-753/4 CIR "Zdravlje", Leskovac, Serbia, 2003.
11. Tolmachev, V. N., Lugovaya, A. Z., Ischenko, I. K., Valikhanovich, A. I., Zaboronok, V. U., *Vysokomol. Soedin., Ser.* A, 1975, vol. 17, p. 419.
12. Norkus, E., Vaičiuniene, J., Vuorinen, T., Heikkilä, M., *Carbohydr. Polym.,* 2002, vol. 50, p. 159.
13. Cakić, M., Nikolić, G., Ilić, Lj., *Bull. Chem. Technol. Macedonia,* 2002, vol. 12. p. 135.
14. Nikolić, G., Cakić, M., Mitić, Ž., Ilić, Lj. // *Proceeding of the 8th International Conference on Fundamental and Applied Aspects of Physical Chemistry,* Belgrade, 2006, pp. 722–724.
15. Nikolić, G. M., Ilić, Lj., Cakić, M., Nikolić, G. S., Nikolić, R., Mitić, Ž. // *Proceeding of the 7th International Conference of Fundamental and Applied Aspects of Physical Chemistry* (Belgrade, 2004), p. 775.
16. Nikolić G., Mitić Ž., Cakić M., Ilić Lj. // *Proceeding of the 8th International Conference of Fundamental and Applied Aspects of Physical Chemistry* (Belgrade, 2006), p. 719.

STRUCTURE OF MATTER
AND QUANTUM CHEMISTRY

FRANCK–CONDON FACTORS AND r-CENTROIDS
FOR THE $E^1\Pi_u$–$X^1\Sigma_g^+$ SYSTEM OF Ag$_2$

© 2007   M. Kuzmanović*, M. A.Khakoo**, V. Bojović*, A. Antić-Jovanović*

*Faculty of Physical Chemistry, University of Belgrade, P.O. Box 137, 1001 Belgrade, Serbia
**Physical Department, California State University Fullerton, Fullerton, CA 92834, USA
E-mail: ankica@ffh.bg.ac.yu

Abstract – An array of Franck–Condon factors and r-centroids is reported for the bands of $E^1\Pi_u$–$X^1\Sigma_g^+$ system of Ag$_2$ molecule. Both parameters were calculated using the Morse and Rydberg–Klein–Rees potentials. Results showed a reasonable agreement between two sets of data for transitions including lower vibrational levels ($v \le 6$). Differences appear with increasing v, but two sets of calculated Franck–Condon factors follow the same pattern. Predicted intensity distribution was compared with estimated band intensity in experimental spectrum.

INTRODUCTION

For a proper understanding of the intensity distribution in the band systems of the molecules, it is necessary to know accurate values of transition probabilities, $p_{v'v''}$, for individual vibration bands of the corresponding system. They are defined as:

$$p_{v'v''} \equiv \left| \int \psi_{v'} R_e(r) \psi_{v''} dr \right|^2, \quad (1)$$

where $\psi_{v'}$ and $\psi_{v''}$ are the wave functions for the upper and lower vibrational levels, respectively, between which the transition takes place, and $R_e(r)$ is the electronic transition moment.

On the assumption that variation of $R_e(\mathrm{r})$ with internuclear distance r is slow and that $R_e(r)$ may be replaced by an average value of R_e, the relative vibrational transition probabilities are governed mainly by Franck–Condon (FC) factors (square of overlap integrals):

$$p_{v'v''} \cong R_e^2 \left| \int \psi_{v'} \psi_{v''} dr \right|^2. \quad (2)$$

However, if $R_e(r)$ is not independent on internuclear separation in the range of r encountered in the transition, the variations of $R_e(r)$ with r must be taken into account. In such cases, the knowledge of the r-centroids, $r_{v'v''}$, of the bands can be very useful.

Both transition parameters are also essential for a calculation of many important data for molecules, such as a vibrational temperature of the source, populations of upper vibrational levels and radiative lifetimes, among other properties, interesting from different aspects.

In this paper we report the array of FC factors and r-centroids for the $E^1\Pi_u$–$X^1\Sigma_g^+$ band system of ^{107}Ag^{109}Ag molecule (247–262 nm), which, to our best knowledge, are not available in the literature, although the bands are known since 1959 [1]. It is not surprising because the calculation of FC factors and r-centroids requires the knowledge of accurate values of vibrational and rotational constants of the molecule in both states involved in the given transition. The limited resolution in the conventional absorption techniques, used up to 1990, allowed only determination of ω_e and $\omega_e x_e$ in a vibrational analysis of the bands. The rotational constant B_e of the ground X state could only be estimated from the Morse–Clark relation, which states that the product $\omega_e r_e^3$ should be constant for all ground states of similar molecules [2]. Comparing Ag$_2$ with Au$_2$ and Cu$_2$, the ground-state constant $B_e = 0.05122$ cm^{-1} and equilibrium distance $r_e = 0.2496$ nm have been estimated by several authors [3, 4]. Based on these values, the authors could also determine the rotational constant B_e for some other electronic states of Ag$_2$, using the energy separation between band heads and band origins.

Modern laser spectroscopic techniques applied to Ag$_2$ molecule allowed resolution of the rotational structure of the bands and thus direct determination of the rotational constants B_e [5–8]. Results showed that the Morse–Clark rule for Ag$_2$ represents only a crude estimation.

Calculation of FC factors and r-centroids in the present work was performed using very accurate B_e constants for the $X^1\Sigma_u^+$ and $E^{11}\Pi_u$ states [8], derived from high resolution spectra, from which also the vibrational constants ω_e and $\omega_e x_e$ for the $E^{11}\Pi_u$ state have been recalculated and included in calculation.

METHOD OF CALCULATION

The FC factor, $q_{v'v''}$, associated with the v'–v'' band in diatomic band system is defined by the square of overlap integral:

$$q_{v'v''} = \left| \int \psi_{v'} \psi_{v''} dr \right|^2, \qquad (3)$$

while the r-centroid of the band, representing a weighted value of internuclear distance encountered in the v'–v'' transition, is given by the equation:

$$r_{v'v''} = \int \psi_{v'} r \psi_{v''} dr / \int \psi_{v'} \psi_{v''} dr. \qquad (4)$$

The quality of calculation of $q_{v'v''}$ and $r_{v'v''}$, and thus the values of $p_{v'v''}$, relies on the values of $\psi_{v'}$ and $\psi_{v''}$, which depend mainly on the accuracy of the potential curves used to solve Schrödinger vibrational equation. The best results one obtains using Rydberg-Klein-Rees (RKR) potential, but in many cases a Morse approach, particularly for lower part of potential curve, provides a good approximation.

Good agreement between experimental values of the second rotational constants D_e (1.27 × 10⁻⁸ and 1.97 × × 10⁻⁸ cm⁻¹ for the X and E states respectively) and those calculated using Kratzer relation,

$$D_e = 4B_e^3 / \omega_e^2 \qquad (5)$$

(1.26 × 10⁻⁸ and 1.96 × 10⁻⁸ cm⁻¹) suggested that lower part of both states involved in transition X and E, can be well described by a Morse potential.

Since only E–X bands with relatively low v' and v'' have been observed in absorption spectrum ($v' \leq 7$, $v'' \leq 11$), we have calculated 10 × 10 array of $q_{v'v''}$ and $r_{v'v''}$ using a Morse approximation for potential function within the formalism developed by Freser and Jerman [9]. Computation was performed using a modified computer program developed by Felenbok [10] and molecular constants ω_e, $\omega_e x_e$, r_e and μ, listed in Table 1, as input data. μ is reduced mass of the $^{107}Ag^{109}Ag$ isotopomer for which these constants are given. The lower limit, upper limit and interval integration were 2.2, 3.00 and 0.003 Å, respectively.

Since $q_{v'v''}$ and $r_{v'v''}$ are very sensitive to the shape of potential energy curves, we have applied also the RKR approach and calculated large set of both parameters ($v' \leq 30$, $v'' \leq 30$) using RKR program developed by Espy [11] and the constants T_e, D_e, B_e, ω_e, $\omega_e x_e$ and μ from Table 1.

RESULTS AND DISCUSSION

The 10 × 10 array of RKR and Morse FC factors and RKR r-centroids are given in Table 2 together with wavelengths of the corresponding bands [3, 4]. The full set of data is too large to be including here, but it may be obtained from the authors on request. The factors smaller then 10⁻³ are refrained from the presentation in Table 2.

Table 1. Spectroscopic constants (cm⁻¹) for the X and E states of Ag_2 used as input of the Morse and RKR calculations

Constant	$X^1\Sigma_g^+$	$E^1\Pi_u$
T_e	0	40158.6
D_e	15000	3360
B_e	0.048807	0.047171
α_e	0.000208	0.000416
ω_e	192.0 [3]	146.41
$\omega_e x_e$	0.58 [3]	1.595
r_e, Å	2.5303	2.5738
μ, amu	53.94783	

Notes: all constants are used from Table IV in [8]. Values of D_e (dissociation energy) are based on relation $D_e = \omega_e^2 / 4\omega_e x_e$.

FC factors. Differences between RKR and Morse FC factors, are typically in the third decimal place for transitions including lower levels (v' and $v'' < 6$); hence we reported them to that precision. Discrepancies between two set of data slightly increase with v, but the calculated values follow the same pattern: the prominent FC factors form a broader Franck Condon envelope, as a consequence of different equilibrium geometries of the X and E states for which Δr_e is 0.0435 A and $\Delta \omega_e = 45.59$ cm⁻¹. Figure 1 shows the Morse and RKR
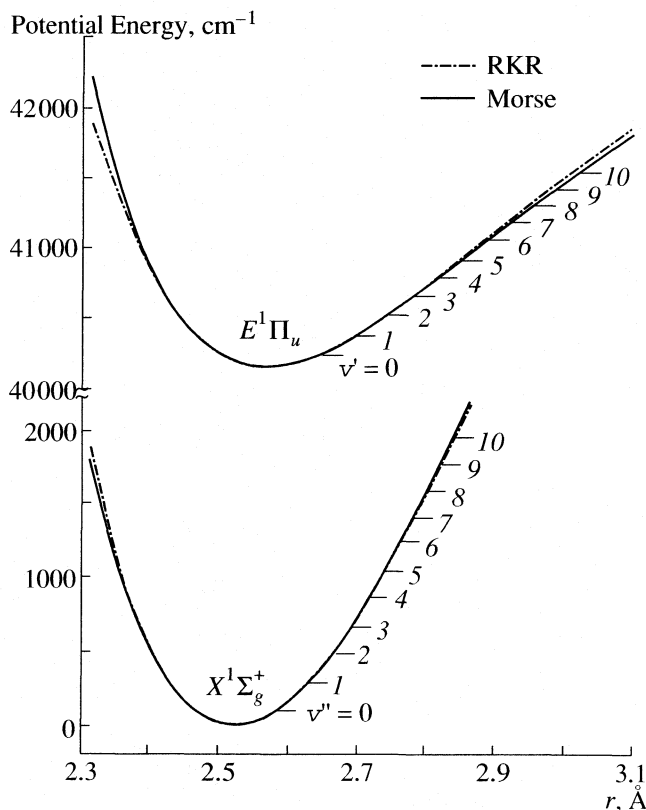
Fig. 1. Potential curves for the X and E states.

Table 2. Franck–Condon factors and r-centroids for the E–X bands of $^{107}Ag^{109}Ag$

v'/v''	0	1	2	3	4	5	6	7	8	9	10	$\Sigma_{q',q''}$
0	0.745	0.201	0.044	0.008	0.001							0.998
	0.740	0.204	0.046	0.009	0.001							1.000
	2.549	2.640	2.686	2.734	2.770							
	2491	2503	2515	–	–							
1	0.225	0.336	0.282	0.116	0.032	0.007	0.001					0.999
	0.228	0.317	0.286	0.120	0.036	0.009	0.002					0.998
	2.481	2.553	2.650	2.696	2.742	2.777	2.816					
	2482	2494	2506	2517	–	–	–					
2	0.028	0.361	0.083	0.245	0.180	0.073	0.023	0.006	0.001			1.000
	0.030	0.363	0.069	0.240	0.183	0.079	0.027	0.007	0.001			0.999
	2.381	2.499	2.537	2.661	2.705	2.751	2.785	2.823	2.851			
	2473	2485	2497	2509	2520	2532	–	–	–			
3	0.001	0.093	0.372	0.000	0.139	0.199	0.121	0.051	0.016	0.004	0.001	0.997
	0.002	0.102	0.364	0.001	0.131	0.192	0.124	0.062	0.020	0.002	0.002	1.000
	2.167	2.417	2.514	1.787	2.672	2.714	2.760	2.794	2.831	2.859	2.892	
	–	2477	2488	–	2512	2524	2536	2548	–	–	–	
4		0.009	0.184	0.274	0.036	0.038	0.162	0.154	0.089	0.037	0.013	0.996
		0.013	0.150	0.257	0.064	0.028	0.145	0.159	0.104	0.049	0.019	0.988
		2.266	2.447	2.524	2.710	2.683	2.722	2.770	2.802	2.838	2.866	
		–	2480	–	–	–	2527	2539	–	–	–	
5			0.033	0.265	0.133	0.099	0.000	0.087	0.150	0.124	0.068	0.959
			0.045	0.271	0.096	0.130	0.000	0.055	0.135	0.134	0.086	0.950
			2.333	2.472	2.519	2.686	2.681	2.727	2.779	2.810	2.847	
			–	2484	2495	2507	–	–	2542	2554	–	
6			0.002	0.082	0.295	0.027	0.117	0.030	0.020	0.105	0.137	0.815
			0.005	0.088	0.262	0.014	0.119	0.055	0.002	0.071	0.127	0.743
			2.020	2.384	2.492	2.454	2.690	2.704	2.720	2.790	2.819	
			–	2476	2487	2499	2510	–	–	2546	2558	
7				0.009	0.152	0.249	0.001	0.074	0.083	0.000	0.043	0.611
				0.022	0.174	0.167	0.030	0.048	0.096	0.000	0.012	0.549
				2.197	2.423	2.504	0.336	2.703	2.714	2.940	2.801	
				2480	–	–	–	–	–	–	–	
8					0.030	0.222	0.147	0.036	0.018	0.101	0.030	0.584
					0.050	0.228	0.051	0.089	0.000	0.074	0.067	0.559
					2.297	2.454	2.503	2.757	2.735	2.722	2.802	
					–	–	–	–	–	–	–	
9					0.001	0.074	0.255	0.047	0.070	0.002	0.067	0.516
					0.003	0.123	0.198	0.000	0.092	0.024	0.018	0.466
						2.363	2.478	2.458	2.730	2.578	2.724	
						–						
10						0.008	0.137	0.225	0.001	0.061	0.037	0.469
						0.027	0.182	0.102	0.034	0.036	0.066	0.447
						2.138	2.411	2.493	1.725	2.741	2.689	
						–	–	–	–	–	–	
$\Sigma_{q'-q''}$	0.999	1.000	1.000	0.999	0.999	0.996	0.964	0.710	0.448	0.434	0.396	
	1.000	0.999	0.965	1.000	0.979	0.997	0.873	0.575	0.471	0.390	0.396	

Notes: first row – RKR FC factors; second row – Morse FC factors; third row – r-centroids (Å); fourth row – wavelengths (Å).

potential energy curves for both states calculated from experimental constants given in Table 1.

It is evident that Morse and RKR curves for the X state match closely in the region of interest while those of E state slightly diverge above $v \geq 6$. This is probably a main reason for larger differences between Morse and RKR FC factors. However, since both sets of calculated FC factors follow the same intensity pattern, they both predict the same intensity fluctuation in the system.

Distribution of the values of FC factors in $v'v''$ scheme covers fairly well the absorption and emission spectra. It indicates the 0–0 band as the strongest one in the system followed by the $\Delta v = \pm 1$, and $\Delta v = \pm 2$ sequence bands, which are much weaker. Also, FC factors predict very small intensity of the following bands: 3–1; 3–3; 4–4; 4–5; 5–6; 5–7; 6–7; and 6–8 and thus their absence in spectrum.

The vibrational sum rule is satisfied for first six v' and v'' progressions indicating that further experimental work will not be helpful to observe more bands in this progressions.

In order to compare predicted and observed intensity distribution in $E–X$ system, we have used the absorption spectrum of Ag_2 obtained by Srdanov and Pesic [4] in a King furnace at temperature of 2100 K. In recorded spectrum, the $E–X$ system contained over 30 bands belonging to $\Delta v = 0$, ± 1, ± 2, -3 and -4 sequences with about five members in each. Since natural silver has two isotopes, ^{107}Ag and ^{109}Ag, in the spectrum appeared bands of three isotopomers: $^{107}Ag_2$, $^{109}Ag_2$ and $^{107}Ag^{109}Ag$. The last is the most abundant (about 50%), so that the bands of this isotopomers are most intense. Visually estimated intensity is generally consistent with that predicted by FC factor: the bands, for which FC factors have negligible value, were not recorded in the spectrum. Figure 2 compares the predicted relative intensities (values FC factors) and measured absorbances of the most prominent heads (belonging to $^{107}Ag^{109}Ag$ isotopomer) of the $\Delta v = -1$, and $\Delta v = -2$ sequence bands. Values of absorbances and FC factors were normalized to 1 for band 1, 2.

Despite the considerable uncertainty in experimentally estimated relative intensity, it is evident that it fairly well follows intensity fluctuation of the FC factors in the scheme 2, and thus offers a good test for reliability of the calculated values.

r-Centroids. The r-centroid values for observed bands vary systematically from band to band of a system following the expectation of in r averiged with $\psi_{v'}\psi_{v''}$. In the case of very small overlap integrals, r-centroids have irregular behaviour and such values are not used in consideration.

Since in the case of $E–X$ transition, $r_{eX} < r_{eE}$, computed r-centroid values increase smoothly with increase of wavelengths of the corresponding $v'v''$ bands in agreement with observation by Nicholls and Jermain [12] for red-degraded band system. Any small scatter about a smooth curve, which is noted, may possibly be
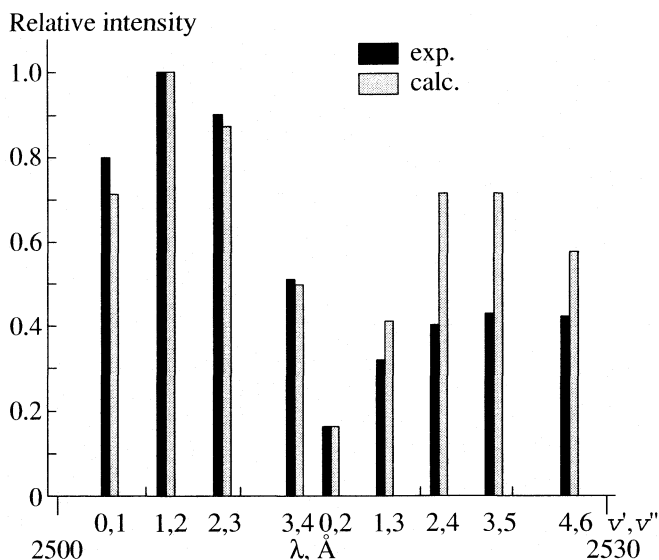
Fig. 2. Comparison of predicted and experimentally estimated intensities for the bands of $\Delta v = -1$, and $\Delta v = -2$ sequences.

attributed to the band-head wavelengths instead of wavelengths of band origins. The smooth relationship between r-centroid and wavelength of observed bands provides a check on the accuracy of calculated FC factors.

The r-centroid value for 0–0 band is approximately equal to $(r'_e + r''_e)/2$ that proves that the potentials are not very anharmonic in the lower part. Further, the sequence differences $\Delta r = (r_{v'+1,\ v''+1} - r_{v',\ v''})$ are found to be constant for a given sequence and varying from about 0.008 to 0.03 Å, suggesting that the potentials of the system are not so broad.

CONCEUSION

The FC factors and r-centroids for the $E^1\Pi_u – X^1\Sigma_g^+$ system of $^{107}Ag^{109}Ag$ isotopomer have been derived for the first time using the Morse and RKR potentials for both electronic states.

It was found a reasonable agreement between two sets of data for transitions including low v-levels, but at higher v (≥ 6) a small deviations appear which, however, do not change the intensity pattern, at least up to $v \approx 10$, as evident from Table 2.

Comparision of predicted and estimated relative band intensity distribution for observed bands supported accuracy of computed FC factors.

Calculated r-centroids will be undoubtedly helpful in the study of variation of electronic transition moment with internuclear separation as in the search of other molecular properties as a function of r.

REFERENCES

1. J. Ruamps, Ann. Phys. **4**, 1111 (1959).
2. G. Herzberg, "*Spectra of Diatomic Molecules*", 2nd ed., Van Nostrand Comp., Princeton (1951).
3. C. M. Brown and M. L. Ginter, J. Mol. Spectrosc., **69**, 25 (1978).
4. V. I. Srdanov and D. S. Pesić, J. Mol. Spectrosc., **90**, 27 (1981).
5. B. Simmard, A. Hackett and A. James, Chem. Phys Letters, **186**, 415 (1991).
6. B. H. G. Kramer, V. Beutel, K. Weyers and W. Demtroder, Chem. Phys. Lett. **193**, 331 (1992).
7. V. Beutel, M. Kuhn and W. Demtroder, J. Mol. Spectrosc., **155**, 343 (1992).
8. V. Beutel, H. G. Kramer, G. L. Bhale, M. Kuhn, K. Weyers and W. Demtroder, J. Chem. Phys., **98**, 2699 (1993).
9. P. A. Fraser and W. R. Jerman, *Proc. Phys. Soc.*, **A66**, 1145 and 1153 (1953).
10. P. Felenbok, Proc. Phys. Soc. **86**, 676 (1965).
11. F. R. Gilmore, R. R. Laher, and P. J. Espy, J. Phys. Chem. Ref. Data, **21**, 1005 (1992).
12. R. W. Nicholls and W. R. Jermain, Proc. Phys. Soc., **69**, 3-A, 253 (1956).

УДК 541.13

ELECTROCHEMICAL DETECTION OF ARSENIC AT A GOLD NANOPARTICLE ARRAY

© 2007 R. Baron*, B. Šljukić*, C. Salter**, A. Crossley**, R. G. Compton*

*Physical and Theoretical Chemistry Laboratory, University of Oxford, South Parks Road, Oxford, OX1 3QZ, UK
E-mail: richard.compton@chem.ox.ac.uk
**Materials Department, University of Oxford, Parks Road, Oxford, OX1 3PH, UK*

Abstract – The detection of As(III) was investigated at a gold nanoparticle array. In the first step, gold nanoparticles were synthesized on glassy carbon microspheres. The resulting hybrid material was characterized by SEM and the sizes of the nanoparticles were found to be in the 20–200 nm range. In the second step, the glassy carbon microspheres decorated with Au nanoparticles were abrasively attached on the surface of a basal plane pyrolytic electrode. The resulting gold nanoarray was characterized by the reduction of surface gold oxides. Furthermore, it was found to have good characteristics for the sensing of arsenic, via anodic stripping voltammetry, with a limit of detection of 0.8 μM and a sensitivity of 0.91 C M^{-1}.

INTRODUCTION

In recent years metal and semiconductor nanoparticles have attracted great interest due to their superior characteristics and possible application in numerous technological areas such as catalysis, optics, microelectronics, and chemical/biological sensors. Therefore, much research has been done into their synthesis and characterization.

Metal nanoparticles have been widely used in the electrochemistry, both in electrocatalysis [1, 2] and electroanalysis and bioelectroanalysis [3–5] for the detection of different electroactive analytes. Nanoparticles exhibit unique advantages over macroelectrodes when used for electroanalysis: enhancement of mass transport, catalysis, high effective surface area and control over electrode microenvironment.

Metallic gold is characterized by chemical inertness, good thermal and electrical conductivity. Bulk gold electrodes have been employed for electrochemical detection of metal ions such as chromium [6, 7] and arsenic [8], as well as amino acids [9] and other organic compounds [10]. Gold has also been used in the detection of hydrogen peroxide [11]. Although gold in its bulk form has shown poor electrocatalytic activity for the reduction and oxidation of hydrogen peroxide, gold nanoparticles have exhibited good catalytic activity due to their high surface area-to-volume ratio and their interface-dominated properties [12]. Gold nanoparticles have also shown an excellent catalytic activity for the oxidation of carbon monoxide [13].

Arsenic is a naturally occurring element widely distributed in the earth's crust. However, exposure to arsenic can cause a variety of serious health problems, such as dermal changes, respiratory, cardiovascular, gastrointestinal, genotoxic, mutagenic and carcinogenic maladies. The arsenic contamination of groundwater and soil in various parts of the world has been widely reported [14–18]. Only in Bangladesh, an estimated 50 million people are at risk that WHO recognizes as the world's worst mass human poisoning disaster [19–21].

In this paper we first present a synthesis of gold nanoparticles on glassy carbon microspheres by electroless deposition and characterization of the resulting material via microscopic and electrochemical techniques. Next, the detection of arsenic was explored on gold nanoparticle-glassy carbon powder decorated basal plane pyrolytic electrode. The modified electrode was found to provide good determination of arsenic.

EXPERIMENTAL

Reagents and materials. Sodium(meta)arsenite (NaAsO$_2$, 99%) was supplied by Fluka and used without further purification. A stock solution of As(III) (4 mM) was prepared from NaAsO$_2$ by dissolving 5.19 mg of NaAsO$_2$ in 10 cm^3 of deionized water. Gold (I) sodium thiosulfate (AuNa(S$_2$O$_3$)$_2$ · H$_2$O, 99.9%) and glassy carbon spherical powder (10–20 microns, type 1) were purchased from Alfa Aesar (Heysham, UK). L-ascorbic acid (C$_6$H$_8$O$_6$, 99.7%) and sulphuric acid (H$_2$SO$_4$) were purchased from BDH and used as received.

All solutions were prepared using deionized water with a resistivity not less than 18.2 MΩ cm at 25°C (Vivendi Water Systems, UK).

Electrochemical measurements. The electrochemical cell was a standard three electrode cell. The reference electrode was an aqueous saturated calomel electrode (SCE, Radiometer Analytical) and the auxiliary electrode was a carbon graphite rod. The working macrodisc electrode was a 5 mm diameter basal plane pyrolytic graphite electrode (BPPG, Le Carbone Ltd, Sussex, UK). The working electrode was used immediately after carrying out a voltammetric scan in the back-
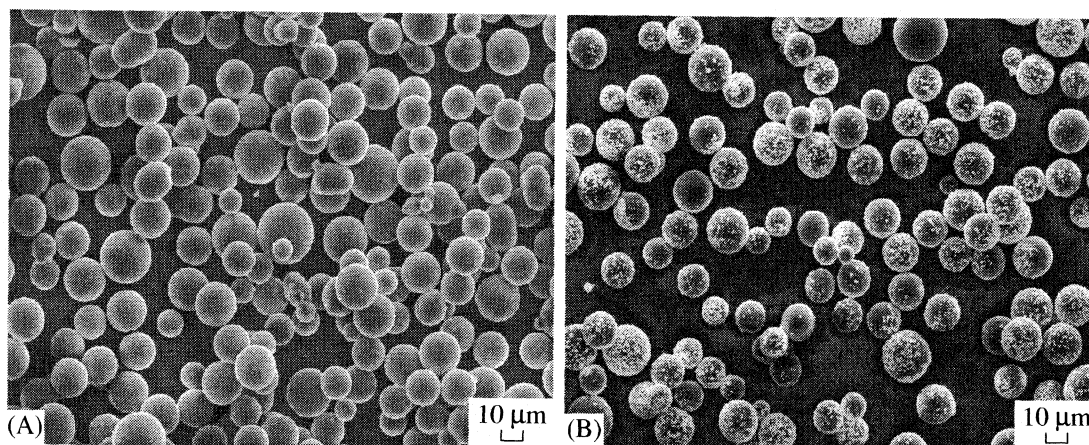
Fig. 1. SEM image of glassy carbon microspheres (A) and Au nanoparticles supported on glassy carbon microspheres (B).
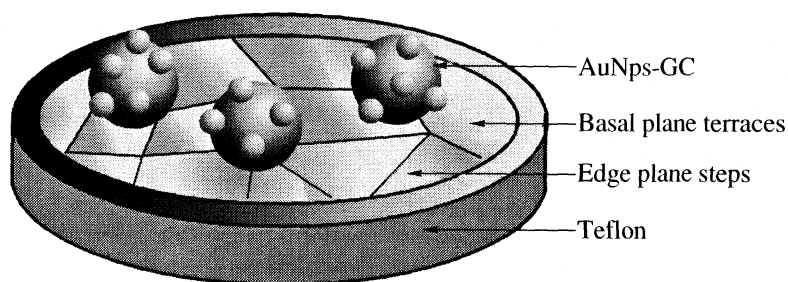
Scheme. Schematic representation of the surface of a BBPG electrode with abrasively attached glassy carbon microspheres decorated with gold nanoparticles (AuNPs-GC).

ground solution (1 M H_2SO_4) at 0.1 Vs^{-1} between 0 and +1.5 V vs. SCE. All experiments were performed at 20°C under a nitrogen atmosphere. The electrochemical investigations were performed using an Eco Chemie μAutolab potentiostat monitored by a PC.

Electroless deposition of metal nanoparticles onto glassy carbon microspheres. Gold nanoparticles were synthesized on glassy carbon spherical powder by an electroless deposition technique. The procedure involved stirring 0.2 g of GC spherical powder into 100 cm^3 of $AuNa(S_2O_3)_2$ solution (0.150 g) with 0.090 g of L-ascorbic acid being added as a reducing agent slowly at the beginning of the reaction. The pH of the reaction mixture was adjusted to 5.2 by adding sodium hydroxide. The reaction mixture was then mixed for 24 h at the room temperature. After reaction was finished, the reaction mixture was filtered and rinsed with water to remove any unreacted species. The resulting powder was left to dry in the air.

Abrasive attachment of carbon microspheres on a basal plane pyrolytic graphite electrode. The abrasive attachment of glassy carbon microspheres decorated by Au nanoparticles (AuNPs-GC) on a basal plane pyrolytic graphite electrode was performed by gently rubbing the electrode surface onto a thin layer of microspheres powder laying on a filter paper (Scheme). The excess of

non attached microspheres on the electrode surface is then removed by the rubbing the electrode surface on a wet cotton cloth. Moreover, after modification of the electrode, its surface was immersed in the solution for 15 minutes before starting the measurements in order to minimize any AuNPs-GC loss during the measurements. The electrode surface can be renewed by pressing cellotape on the electrode surface and removing it along with several surface layers of graphite.

Electron microscopy and elemental analysis. Scanning electron microscopy (SEM) imaging of the electrode surfaces was carried out using a JEOL JMS model 6500F scanning electron microscope.

Calculation limits of detection. The given value corresponds to limit of detection obtained with a standard addition method consisting in 6 additions of 2 μM of arsenic to the sample. The limit of detection was evaluated from the data using 3 sigma method.

RESULTS AND DISCUSSION

Characterisation of the Metal Nanoparticle Modified Glassy Carbon Spheres. Glassy carbon powder modified with gold nanoparticles *via* the electroless deposition technique reported above was characterized
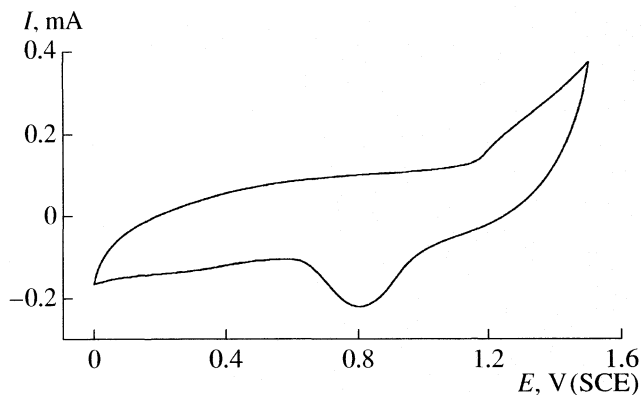
Fig. 2. Cyclic voltammetry at a 5 mm diameter BBPG electrode modified by the abrasive attachment of AuNPs-GC in 1 M H_2SO_4 at scan rate of 0.1 V s^{-1}.

using both spectroscopic and electrochemical techniques.

First, the unmodified GC powder was examined using scanning electron microscopy. The SEM image of the unmodified GC powder verified that it consists of spheres of 10–20 μm diameter according to supplier's specification (Fig. 1A). In addition, some particles of smaller diameter arising from the manufacturing process were observed. Next, GC powder modified with

gold has been examined by SEM. The obtained SEM images of the modified GC spheres (Fig. 1B) showed that randomly distributed metal nanoparticles have been formed on GC spheres. It was found that gold nanoparticle were of 20–200 nm size.

Glassy carbon powder modified via electroless deposition procedure was next characterised using cyclic voltammetry. The modified glassy carbon powder was abrasively attached to basal plane pyrolytic graphite electrode as described in section 2.4 and subsequently qualitatively and quantitatively characterised.

Cyclic voltammograms of AuNPS-GC modified BPPG electrode were run in 0.5 M H_2SO_4 solution from 0 to +1.5 V vs. SCE at scan rate of 0.2 Vs^{-1}. A broad peak could be observed on the cathodic scan at ca. +0.8 V vs. SCE (Fig. 2). This peak potential has been reported as a value characteristic for the reduction of surface oxides of gold [22, 23] confirming that metal gold was synthesized on GC spheres by the electroless deposition method reported above.

The electroactive surface area of the metal formed of GC powder and abrasively attached on BPPG electrode could be evaluated from the area under surface metal reduction peak using literature values for charge passed per unit area on the surface of metal [23].

As(III) detection on a gold nanoparticles – modified electrode. Next we examined the detection of As(III)
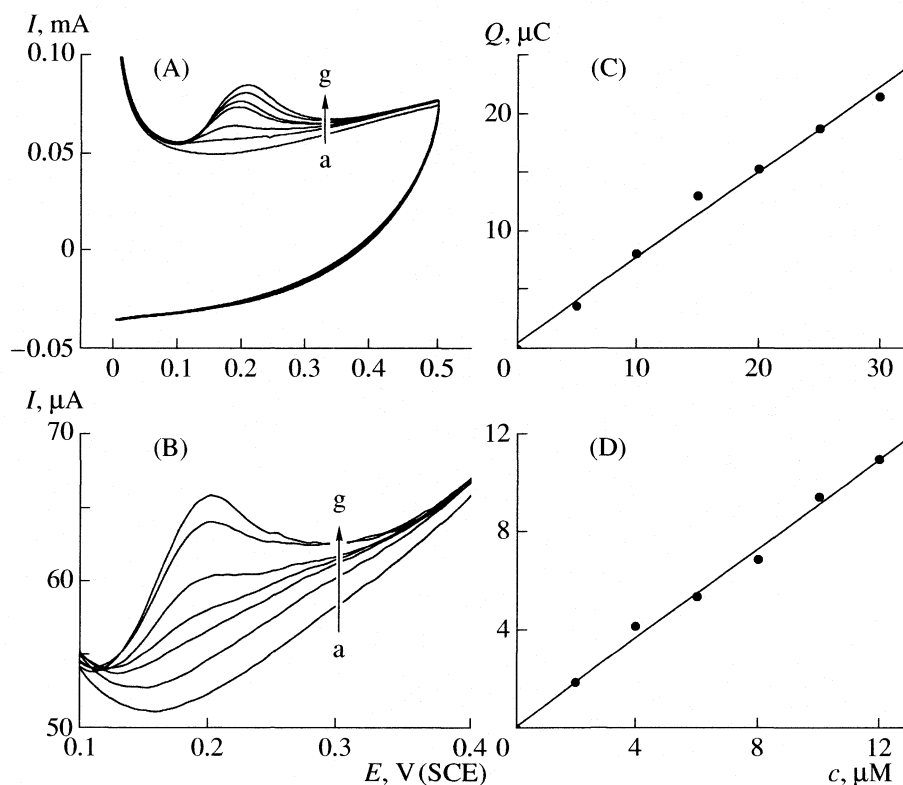
Fig. 3. Cyclic voltammetry at a 5 mm diameter BPPG electrode modified by abrasive attachment of AuNPs-GC at 0.1 V s^{-1}, after holding the potential at – 0.4 V for 40 s in 1 M H_2SO_4 and upon additions of As (III); A: a – 0, b – 5, c – 10, d – 15, e – 20, f – 25, g – 30 μM; B: a – 0, b – 2, c – 4, d – 6, e – 8, f – 10, g – 12 μM; C and D are the corresponding calibration curves.

on BPPG electrode with abrasively attached gold nano-particles – modified GC powder. Note that the abrasive attachment of the metal nanoparticles – modified microspheres is a very quick and efficient way to create a metal array. In addition, it is believed that this procedure reduces formation of nanoparticle agglomerations. AuNPs-GC-BPPG electrode was electrochemically characterised prior to investigation of As(III) detection. Total surface area of gold of the electrode was evaluated from the metal oxide reduction peak area using literature value of 390 μC cm^{-2} [23] for charge passed per unit area on the surface of metal and it was found to be 0.40 cm^2.

Detection of As(III) at AuNPs-GC modified BPPG electrode was investigated in 1 M H$_2$SO$_4$ solution scanning at 0.1 Vs^{-1}, between 0 and 0.5 V versus SCE after holding the potential at ~0.4 V for 40 s. No peak could be observed in the examined potential range in a blank solution without any As(III) added. However, cyclic voltammogram run after adding 0.1 mM As(III) was characterized with a clear peak at ca. +0.2 V vs. SCE. The peak current was found to increase with 5 μM As(III) additions.

The limit of detection of As(III) at AuNPs-GC-BPPG electrode was determined using standard addition method. Figure 3 shows voltammetric response of AuNPs-GC-BPPG electrode obtained for successive 2 μM As(III) additions. Again, a clear peak corresponding to the oxidation of As(III) could be seen, increasing with increased As(III) concentration. The correlation of the peak area for six successive additions was found to be linear with As(III) concentration; limit of detection for As(III) equal μM was calculated based on the peak area vs. As(III) concentration plot data using 3 sigma method. Sensitivity was evaluated from the same set of data and found to be 0.90875 C M^{-1}. With optimization further improvement is likely possible – the limit of detection can be lowered by applying longer deposition time and using more sensitive electrochemical techniques. This is the first time that metal nanoparticles were abrasively attached to the electrode surface without using any binding substances such as nafion. This simple and quick method of modifying electrode surface with metal nanoparticles also provides good contact between electrode and metal nanoparticles as is evidenced by obtained oxidation peak.

CONCLUSIONS

The synthesis of gold nanoparticles on glassy carbon microspheres via electroless deposition has been presented and the formed hybrid material characterised using both spectroscopic and electrochemical techniques evidencing that gold nanoparticles of 20 to 200 nm diameter were prepared. The glassy carbon microspheres decorated with Au nanoparticles synthesized were abrasively attached on the surface of a basal plane py-

rolytic electrode and detection of As(III) was investigated at a gold nanoparticle array. The resulting gold nanoarray showed good characteristics for the sensing of arsenic with a limit of detection of 0.8 μM that can be further optimized.

ACKNOWLEDGEMENTS

REFERENCES

1. A. J. Arvia, R. C. Salvarezza, W. E. Triaca, J. New Mater. Electrochem. Syst. 7, 133 (2004).

2. G. G. Wildgoose, C. E. Banks, R. G. Compton, Small 2, 182 (2006).

3. D. Hernaandez-Santos, M. B. Gonzalez-Garcýa, A. Costa Garcýa, Electroanalysis 14, 1225 (2002).

4. E. Katz, I. Willner, J. Wang, Electroanalysis 16, 19 (2004).

5. Y. Fang, Y. Xu, P. He, J. Biomed. Nanotechnol. 1, 276 (2005).

6. C. M. Welch, M. E. Hyde, O. Nekrassova, R. G. Compton, Phys. Chem. Chem. Phys. 6, 3153 (2004).

7. C. M. Welch, O. Nekrassova, R. G. Compton, Talanta 65, 74 (2005).

8. A. O. Simm, C. E. Banks, R. G. Compton, Electroanalysis 17, 335 (2005).

9. P. J. Vandeberg, D. C. Johnson, Anal. Chem. 65, 2713 (1993).

10. D. C. Johnson, W. R. LaCourse, Anal. Chem. 62, 589A (1990).

11. S. G. Burton, Catal. Today 22, 459 (1994).

12. A. Yu, Z. Liang, J. Cho, F. Caruso, Nano Lett. 3, 1203 (2003).

13. M. Valden, X. Lai, D. W. Goodman, Science 281, 1647 (1998).

14. D. Chakraborti, M. M. Rahman, K. Paul, U. K. Chowdhury, M. K. Sengupta, D. Lodh, C. R. Chanda, K. C. Saha, S. C. Mukherjee, Talanta 58, 3 (2002).

15. B. K. Mandal, K. T. Suzuki, Talanta 58, 201 (2002).

16. D. G. Kinniburgh, W. Kosmus, Talanta 58, 165 (2002).

17. M. Bissen, F. H. Frimmel, A. G. Christ, S. Aesch, Acta Hydrochim. Hydrobiol. 31, 9 (2003).

18. M. Bissen, F. H. Frimmel, A. G. Christ, S. Aesch, Acta Hydrochim. Hydrobiol. 31, 97 (2003).

19. A. H. Smith, E. O. Lingas, M. Rahman, Bull. World Health Org. 78, 1093 (2000).

20. R. Feeney, S. P. Kounaves, Talanta 58, 23 (2002).

21. M. G. M. Alam, G. Allinson, F. Stagnitti, A. Tanaka, M. Westbrooke, Int. J. Environ. Health Res. 12, 236 (2002).

22. H. A. Kozlowska, B. E. Conway, A. Hamelin, L. J. Stoicoviciu, J. Electroanal. Chem. 228, 429 (1987).

23. S. Trasatti, O. A. Petrii, Pure Appl. Chem. 63, 711 (1991).

УДК 543.544

CHEMICAL AND RADIOCHEMICAL CHARACTERIZATION
OF DEPLETED URANIUM IN CONTAMINATED SOILS

© 2007   M. B. Radenković*, A. B. Kandić*, I. S. Vukanać*, J. D. Joksić*, D. S. Djordjević**

*Institute of Nuclear Sciences "Vinča", P.O. Box 522, 11001 Belgrade, Serbia
**ICTM-Centre for Chemistry, Njegoševa 12, 11001 Belgrade, Serbia
E-mail: mirar@vin.bg.ac.yu; jasnaj@vin.bg.ac.yu

Abstract – The main results of chemical and radiochemical characterization and fractionation of depleted uranium in soils contaminated during the Balkan conflict in 1999 are presented in the paper. Alpha-spectrometric analysis of used depleted uranium material has shown the presence of man-made radioisotopes ^{236}U, ^{237}Np and $^{239, 240}Pu$ traces. The fractionation in different soil types was examined by the application of modified Tessier's five-step sequential chemical extraction procedure, specifically selective to certain physical/chemical associations. After ion-exchanged based radiochemical separation of uranium depleted uranium is distinguished from naturally occurring uranium in extracts on the basis of isotopic activities ratios $^{234}U/^{238}U$ and $^{235}U/^{238}U$ and particular substrates for recently present uranium material in soils are indicated.

INTRODUCTION

Depleted uranium (DU) differs from naturally occurring uranium by virtue of having most of its ^{235}U and ^{234}U isotopes removed in the enrichment or fuel reprocessing for the nuclear energy industry. Referred as a low radioactive material, it typically contains 99.7990% of ^{238}U, 0.0010% ^{234}U and 0.2000% ^{235}U by mass, but also may contain traces of transuranic elements indicating irradiated fuel origin [1–3]. Depleted uranium used in Balkans will be characterized in this study by the radiochemical separations of uranium, plutonium and neptunium fractions from DU projectile material and alpha-spectrometric measurements of electrodeposited alpha-sources.

To assess the environmental impact of depleted uranium ammunition used during 1999 in Balkans, a study was done on depleted uranium physical/chemical behavior and its status in some types of contaminated soils some years after the appearance in the environment. For that purpose, the contamination levels are determined and selected soil samples are subjected to a series of successive solid/liquid chemical extractions in a modified Tessier's sequential extraction procedure [4, 5]. Various sequential extractions procedures are developed for metal specification in different soil types but if reliable radiometric measurements are available, the method may be useful for analysis of radionuclides fractionation in soil as well [6, 7]. In this work, the extractive reagents, targeted to a specific physical/chemical association such as ion-exchange, carbonate, iron/manganese oxide, organic and acid soluble methods are applied in five phases to the soil samples contaminated with depleted uranium. The distribution of depleted and naturally occurring uranium in obtained extracts should outline their geochemical fractionation and indicate the mobility and bioavailability of depleted uranium in the soil of investigated environment in local meteorological conditions. Determination of uranium specific activities and isotopic activity ratios $^{234}U/^{238}U$ and $^{235}U/^{238}U$ will be done by high resolution alpha-spectrometry with relatively high sensitivity.

Applied combined physical/chemical procedures and analysis should enable insight into the specific characteristics of depleted uranium behavior in soil and from practical aspect it may help in decision making on the clean-up and remediation strategy for sites contaminated in military actions.

MATERIALS AND METHODS

Depleted uranium of the projectile collected at contaminated area in Southern Serbia, was characterized by the alpha spectrometric analysis. After dissolution of material, relevant standard radiochemical procedures were used to separate uranium fraction as well as a small quantities of plutonium and neptunium isotopes in excess of uranium [8, 9]. The radiochemical procedures involved micro-coprecipitation of actinides on the Fe(III)hydroxide and ion-exchange based acidic extraction using DOWEX 1 × 8 (100–200 mesh) anion resin and di-isopropyl ether liquid/liquid extractions for iron removal. For radiochemical yield recoveries, the aliquots of basic solution were spiked with 0.1 Bq ^{232}U and 0.05 Bq ^{236}Pu diluted tracer solutions, standardized previously by absolute activity measurements in 2π counting geometry. Neptunium fraction was additionally washed and separated by the acetate-based procedure [10] and without tracer added. A thin-layer alpha-sources were prepared for each actinide element by the Talvitie's electrodeposition procedure [11]. Measurements were performed using Canberra 2004 vacuum
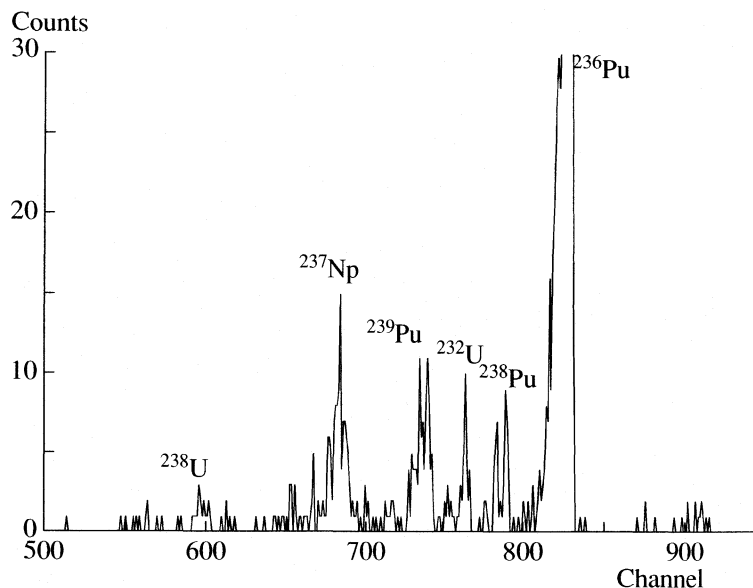
Fig. 1. The spectrum of the alpha-source with ^{237}Np, $^{239,\,240}$Pu, ^{238}Pu from projectile sample, spiked with ^{236}Pu and ^{232}U, and with ^{238}U traces.

chamber (20 mbar) with PIPS detector with 15.3% efficiency. The background was 1.3×10^{-4} imp s^{-1} in the energy range 3.5–9.5 MeV, energy calibration 9.2 keV/channel was done with the thin-layer source of ^{229}Th in equilibrium, with resolution 24 keV for ^{241}Am line. The counting time was $(3–6) \times 10^5$ s.

The soil samples contaminated with depleted uranium were collected in Serbia and Montenegro. Gamma-spectrometric determination of uranium concentrations in soil samples was done using HP Ge detector with 23% efficiency, in 100 ml cylinder geometry, without radioactive equilibrium reached due to the interruption after a fourth ^{238}U-series member at the moment of DU material production.

Selected soil samples (10 g of each) were subjected to a set of five successive solid/liquid extractions, with highly selective extractive reagents simulating mild to seviere environmental conditions. The reagent used in the first phase was 1 M CH$_3$COONH$_4$ (pH 7); the residue was treated with 0.6 M HCl and 0.1 M NH$_2$OH in 0.01 M HCl (pH 4). In the third phase the extractant was 0.2 M (COOH)$_2$/0.2 M NH$_4$H(COO)$_2$ mixture (pH 3); in the forth: 30% H$_2$O$_2$ in 0.01 M HNO$_3$ at 85°C (pH 2), and 6 M HCl at 85°C in the fifth phase. Extractions were performed in mechanical rotational shaker at 20°C and the unusually high solid/liquid ratio 1 : 45 to provide efficient rescue of metals from solid matrix. Replicate measurements were not done.

RESULTS AND DISCUSSION

The specific activities of ^{238}U in top-soil samples taken at the projectile entrance spot and path through the soil were of 10^4 Bq/kg order of magnitude, and in

the nearest soil layer it was 10^5 Bq/kg. The contamination decreases with the distance to 1% of initial value at 120–160 mm to the source (DU kinetic penetrator). The naturally occurring uranium concentration determined by gamma spectrometry was within 20–60 Bq/kg in the soils of investigated areas.

Radiochemical characterization of the projectile has shown specific activity 76 Bq/kg $^{239,\,240}$Pu, 7.70×10^4 Bq/kg ^{236}U and ^{237}Np traces, indicating irradiated fuel origin of depleted uranium material that is in accordance with other reported results [12, 13]. Their relations are shown in the Fig. 1.

All three elements (U, Np and Pu) have a very similar chemical behavior, and separation of neptunium and plutonium traces in the medium with uranium in excess was done by the application of a number of repeated radiochemical treatments. Besides, the alpha-energy line $E = 4.787$ MeV (42%) of ^{237}Np interfere with the ^{234}U line, meaning that almost no uranium should be present to claim that this line (665 channel) belongs to ^{237}Np. As it can be seen in the Fig. 1, this is achieved, since only the ^{238}U traces are visible in spectrum and very low ^{234}U/^{238}U ratio in elemental uranium.

Radionuclides ^{237}Np, $^{239,\,240}$Pu and ^{236}U were not detectable in contaminated soil samples taken in the nearest vicinity of the investigated projectile, using the same methodology. Determined ^{234}U/^{238}U, ^{235}U/^{238}U and ^{236}U/^{238}U ratios are given in the Table 1.

The ^{238}U distribution in five extracted phases obtained for selected soil samples taken at different contaminated areas are presented in the Table 2. The share of uranium quantity of each of five extraction phases in

Table 1. The activity and mass ratios of uranium isotopes determined in the uranium fraction of projectile sample

	Activity ratios	Mass ratios
$^{234}U/^{238}U$	0.125	6.25×10^{-7}
$^{235}U/^{238}U$	0.10	1.54×10^{-3}
$^{236}U/^{238}U$	0.053	3.33×10^{-5}

the total uranium extracted within whole sequential procedure is given in percentiles.

In the first "exchangable" phase of the five-step Tessier's procedure, a non-selectively bonded uranium with both poorly soluble U(IV) and soluble U(VI) forms, is extracted within various substrates in soil samples. In the second step, dissolution of carbonates and manganese hydroxides is provoked where the uranyl-ion (VI) may be expected. The presence of uranium in a high excess in these two phases of extraction is a result of anthropogenic influence and related to contamination. Low clay and humus content in the most of the samples indicated hydrous (crystalline) oxides of the iron and manganese as prevailing substrates for uranium extracted in the third phase [14]. In the forth step of treatment the oxidative degradation of the organic matter and therefore mobilization of organic bonded (humic and fulvic acids) uranium is done [15, 16]. Consequently, only in the surface soil samples, uranium shares are significant in the forth phase extracts. The crystalline iron oxides and partly the silicate matrix are attacked in the fifth phase where acid soluble uranium associations are extracted.

The first group of results concerns samples taken at Cape Arza in Montenegrean coast. The A1, A2 and A3 samples belong to a sandy loam texture class, with 69% sand (2–0.02 mm), 15.8% silt, and 14.9% clay. The B sample is a 99.1% sand, mostly 2–0.2 mm, with negligible percentage of silt and clay. The difference between these two soil types from the same region is obvious. The most of uranium in A samples is extracted in the third and fifth phase and for B sample in the second and forth phases. Therefore, uranium is not very attendant in the first phase, mainly, because the contamination levels are low, and due to a very aggressive environmental conditions.

Uranium distribution is very different for the C-group of soil samples, taken in the continental environment in southern Serbia. There is a strong dependence of the fractionation on the contamination levels as shown in Fig. 2, resulting with weakly bonded exchangeable uranium in highly contaminated soils, regardless of the soil geochemical structure. Assuming the reduction of ^{235}U content to 0.2% in depleted uranium, and prior ^{234}U isotope leaching, the ratios $^{235}U/^{238}U$ and $^{234}U/^{238}U$ determined in the extracts obtained by alpha spectrometric analysis, between 0.1–0.5 and 0.5–1, respectively, may be attributed to the mixture of depleted and naturally occurring uranium in varying proportions.

It appear that depleted uranium "covered" the naturally occurring uranium in highly contaminated samples and naturally ratios were found as dominant in deep-layer soils and uncontaminated samples. Assuming sequential extraction procedure selective enough, these proportions are the result of depleted uranium capability to be incorporated into exchangeable or structural physical/chemical associations and forms in soil in the time of exposition in certain meteorological conditions and geochemical environment. In general, obtained distribution in the sequential extraction phases indicated carbonates and the iron and manganese oxides in soil as the most probable substrates for depleted uranium originated from the weapons. We can conclude that specific chemical forms and types of physi-

Table 2. The ^{238}U distribution in five extracted phases obtained for investigated soil samples

Sample	Phase I	Phase II	Phase III	Phase IV	Phase V
	^{238}U, Bq/kg (%)	^{238}U, Bq/kg (%)	^{238}U, Bq/kg (%)	^{238}U, Bq/kg (%)	^{238}U, Bq/kg (%)
A1	1.37 ± 0.15 (8.8)	0.25 ± 0.04 (1.6)	9.82 ± 0.72 (62.9)	1.06 ± 0.16 (6.8)	3.12 ± 0.17 (19.9)
A2	0.76 ± 0.10 (7.4)	0.248 ± 0.037 (2.4)	4.37 ± 0.43 (42.7)	0.284 ± 0.035 (2.8)	4.56 ± 0.31 (44.6)
A3	1.29 ± 0.15 (15.5)	1.19 ± 0.12 (14.3)	4.69 ± 0.23 (56.3)	0.20 ± 0.05 (2.5)	0.96 ± 0.12 (11.5)
B	0.25 ± 0.04 (1.2)	10.8 ± 1.6 (52.0)	1.46 ± 0.10 (7.1)	8.12 ± 0.40 (39.1)	0.124 ± 0.019 (0.59)
C1	12.4 ± 1.8 (3.2)	28.2 ± 2.6 (7.4)	213 ± 29 (56.0)	41.9 ± 2.6 (11.0)	85.3 ± 6.2 (22.4)
C2	9.52 ± 0.49 (18.2)	9.1 ± 0.6 (17.3)	8.12 ± 0.40 (15.5)	8.12 ± 0.40 (15.5)	17.53 ± 1.13 (33.5)
C3	393.0 ± 1.1 (45.5)	1.48 ± 0.22 (0.17)	55.1 ± 8.3 (6.4)	135 ± 20 (15.6)	279 ± 59 (32.3)
C4	3110 ± 802 (83.0)	517 ± 56 (13.8)	86 ± 14 (2.3)	10.4 ± 1.6 (0.3)	23.02 ± 0.91 (0.61)
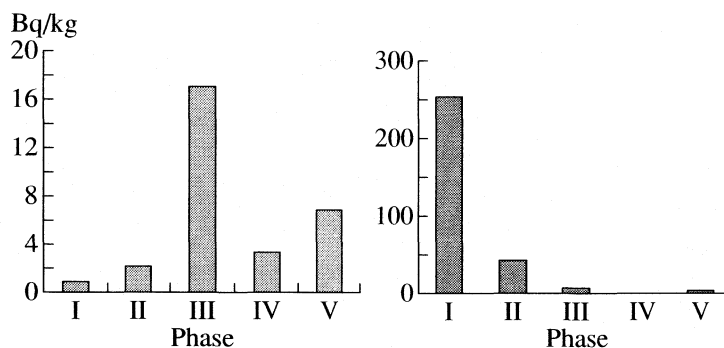
Fig. 2. Uranium distribution in five phases of sequential extraction for low and high contaminated soil samples, respectively, both taken at 50 cm depth.

cal/chemical associations in soil may greatly influence on the mobility, eco-toxicity and bioavailability than the total amount, but there are limitations is the contamination if very high.

REFERENCES

1. Betti, M. (2003) Civil use of depleted uranium, J. Environ. Radioact 64/2-3, 113–119.

2. Fetter S., Hippel F. N. (1999) The Hazard Possed by Depleted Uranium Munitions, Sci. Glob. Security 8/2, 125–161.

3. WHO-World Health Organization. (2001) Depleted uranium: sources, exposure and health effects, WHO/SDE/PHE/01.1, Geneva.

4. Tessier A., Campbell P. G. C., Bisson M., Analytical Chemistry, 1979, 54. 844–851.

5. Polić P., Investigation of heavy metal association types and identification of their substrates in alluvial sediment by using a sequential extraction procedure, Ph.D Thesis, (1991) University of Belgrade.

6. Schultz M. K., Inn K. G. W., Lin Z. C., Burnett W. C., Smith G., Beigalski S. R., Filliben J. (1998) Identification of radionuclide partitioning in soils and sediments, Applied Radiation and Isotopes, 49, 1289–1293.

7. Blanko P., Vera Tome F., Lozano J. C., Sequential extraction for radionuclide fractionation in soil samples: a comparative study. (2004) Applied Radiation and Isotopes, 61, 345–350.

8. ASTM-American Standard Test Methods Committee, (1999) Annual Book of Standards. 12.01: C 999–90; C 1000–90.

9. Radenković M., Vuković D., Šipka V., Todorović D. (1996) Ion-exchange separation of uranium, thorium and plutonium isotopes from environmental samples, Journal of Radioanalitical and Nuclear Chemistry 208/2, 467–475.

10. Chang-Kyu Kim, Takaku A., Yamamoto M., Kawamura H., Shiraishi K., Igarashi Y., Igarashi S., Takazama H., Ikeda N., Journal of Radioanalitical and Nuclear Chemistry, (1989) 132/1, 131–137.

11. Talvitie N. A., Analytical Chemistry, 1972, 44, 280–283.

12. Šipka V., Radenković M., Paligorić D., Djurić J., Proceedings of XXI Conference of JDZZ, (in Serbian) Kladovo, (2001), 69–72.

13. UNEP-United Nations Environment Programme, (2002) Depleted uranium in Serbia and Montenegro. Post-conflict environmental assessment in the Federal Republic of Yugoslavia, United Nations Report. Geneva.

14. Slavek J., Pickering W. F. (1986) Extraction of metal ions sorbed on hydrous oxides of iron (III), Water Air and Soil Pollution 28, 151–162.

15. Boruvka L., Drabek O. (2004) Heavy metal distribution between fractions of humic substances in heavily polluted soils, Plant Soil Environ 50, 339–345.

16. Lenhart J., Cabaniss S., MacCarthy P., Honeyman B. (2000) Uranium (VI) complexation with citric, humic and fulvic acids, Radiochim. Acta 88, 345–353.

COLLOID CHEMISTRY
AND ELECTROCHEMISTRY

THIN LAYER OF Ni-MODIFIED 13 X ZEOLITE ON GLASSY CARBON SUPPORT AS AN ELECTRODE MATERIAL IN AQUEOUS SOLUTIONS

© 2007   Z. Mojović*, S. Mentus**, I. Krstić***

*IChTM-Center of Catalysis and Chemical Engineering, Njegoševa 12, Belgrade, Serbia
**Faculty of Physical Chemistry, Belgrade University, Studentski trg 12, Belgrade, Serbia
***Faculty of Chemistry, Belgrade University, Studentski trg 12, Belgrade, Serbia
E-mail: slavko@ffh.bg.ac.yu

Abstract – New type of electrode material, zeolite modified by incorporation of Ni or NiO clusters into its cavities, was synthesized by multiple impregnation of zeolite 13X with Ni-acetylacetonate solution, following by solvent evaporation and thermal degradation of nickel compound. The samples with Ni / 13X mass ratio within a range 0.2 - 1.0 were synthesized. Modification by both Ni and NiO clusters may result, depending on whether reducing (H_2) or oxidizing (air) atmosphere, respectively, was used to finish the sample. After modification, the zeolite kept its original crystallografic structure, as proven by X-ray diffractommetry. The dimensions of incorporated clusters were limited by the diameter of zeolite cavities (amounting to 1.3 nm). This material, homogenized with 10 wt % of nanodispersed carbon, in a form of thin layer, was bonded to a glassy carbon disc by means of nafion, and used as an electrode material in an aqueous 0.1 M NaOH solution. The cyclovoltammograms of this thin-layer electrode resemble the ones of smooth nickel electrode in alkaline solutions.

Zeolites are aluminosilicates having porous, cavity structure, consisting of nanometer sized cages, interconnected by channels into a solid crystal framework with a huge inner surface area of several hundred $m^2 g^{-1}$. They are widely used as catalysts, ion-exchangers, adsorbents and molecular sieves, and present a specific support for metal or metal oxide clusters incorporation as well. Number of papers have shown that alkaline cations consisting the zeolite structure may, by ion-exchange procedure, be replaced with transition metal cations, which may further be reduced to metal atoms inside zeolites cages. Stoichiometric composition of zeolites limits maximum number of metal atom per zeolite cage, so only clusters of nanometer dimensions can be obtained. Metal particles in zeolites can grow up from an isolated atom to that of a cluster containing a few tens of atoms. The catalytic effectiveness of such systems in numerous, particularly organic, chemical reactions is well known [1–7]. Detailed analysis of size and location and chemical surrounding of metal clusters in zeolite was performed with the aim to explain their catalytically properties. High resolution electron microscopy techniques are most suitable for this investigation [8–12]. The complete characterization of metal aggregates comprises the determination of metal dispersion (particle size and particle location), as well as the determination of the atomic and electronic structure of the particles. The clusters containing 5–12 Pt atoms are identified also by extended X-ray adsorption fine structure spectroscopy (EXAFS) [13, 14]. There is the evidence that solid aluminosilicate framework hinders the metal nanocluster agglomeration [15].

Zeolites and their inclusion complexes were also the subject of electrochemical investigations. Xu et al. [16] investigated the oxidation of hydrazine, alcohol and hydroquinone in water solutions by means of electrode material consisting of zeolite/carbon mixture, fixed on an electronically conductive support. In several cases, such a zeolite fixed on electronically conductive support has been used to study the kinetics of redox reactions within its cavities. For example, MV/MV^{2+} (MV = methylviologen) [17] and Fe^{2+}/Fe^{3+} [18] redox pairs were studied in this particular way. Finally, platinum modified zeolite as a microscopic bipolar electrode suspended in low conducting aqueous media, was studied by Rolisson et al. [19] for water splitting.

The present authors incorporated metal clusters in zeolite cavities by impregnation of zeolites by solutions of thermodegradable complex compounds – metal acetylacetonates. They used such modified zeolites as a thin-layer electrodes, after addition of carbon black which provides its electronic conductivity [20, 21].

In this work, recently developed procedure of zeolite impregnation by Ni-acetylacetonate following by thermal decomposition of acetylacetonates was used to incorporate NiO clusters within the zeolite cavities. Zeolite NaX (faujasite type) was used as supporting material. NiO-modified zeolite was investigated as an electrode material in an aqueous electrolyte solution. Zeolites are expected to both enable to obtain effective nickel catalyst in a form of nano-dispersion, and prevent its agglomeration during the use.

Relative residual mass, %
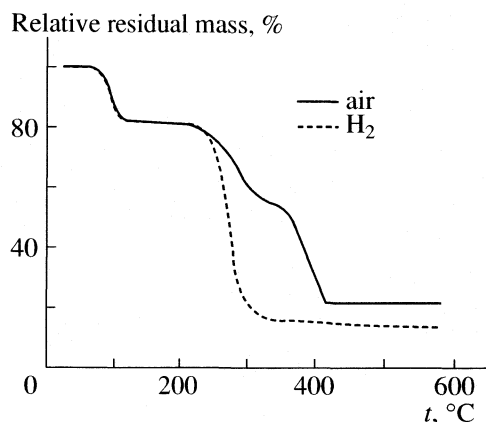
Fig. 1. Residual mass versus temperature for Ni(acac)$_2$ heated at a rate of 15 K/min, in oxidizing (air) and reducing (H$_2$) atmospheres.

EXPERIMENTAL

Nickel(II) acetylacetonate [Ni(acac)$_2$] was synthesized for purposes of this paper. The zeolite NaX, alternatively labeled 13X (Linde Co.) was heated to 350°C to remove adsorbed water, and cooled to room temperature in dry atmosphere. Then it was soaked with diluted acetone solution of Ni(acac)$_2$. Wet sample was previously dried to 90°C, to evaporate acetone, and further to 400°C with the purpose to both decompose nickel acetylacetonate and remove its gaseous decomposition products. Figure 1 illustrates the importance of the composition of atmosphere in this procedure. In this way, working in air, nanodispersed NiO clusters were incorporated into the zeolite cages. The impregnation/decomposition procedure was repeated until the weight ratios NiO/zeolite of 0.2, 0.4 and 1.0 were reached. After this procedure, the modified zeolites changed the color from white to dark gray one.

The thermogravimetric (TG) analysis of both pure and Ni(acac)$_2$ impregnated zeolite samples was performed using the device SDT 2090 (TA Instruments).

XRD diagrams of original and modified zeolites were taken by means of Philips PW 1710 diffractometer using CuK_α radiation.

In order to use the modified zeolite as an electrode material, the zeolite sample was homogeneously dispersed in a solution of Nafion (5 wt. %) in mixture of isopropyl alcohol and distilled water by means of an ultrasonic bath. 10 wt. % of carbon black Vulcan XC72 (Cabot Corp.) was added to the initial suspension to provide the electronic conductivity of the sample. The droplet of this suspension was placed on the surface of a glassy carbon disc of a rotating electrode. After the solvent removal by evaporation at 90°C, the zeolite particles, properly dispersed in a form of thin layer of the density 12 mg cm^{-2}, i.e. about 3.8 mg NiO cm^{-2}, finally resulted as pasted deposit on the glassy carbon support. An analogous way of preparation of such a powdered materials for electrochemical investigations

was already published elsewhere, for instance, in the case of galvanostatic charging and discharging of the Li-intercalate powders [22].

For electrochemical investigations in a three-electrode all glass cell compartment, glassy carbon disc, covered by a layer of homogeneous mixture of Ni-modified zeolite along with 10 wt. % carbon black, was used as a working electrode. The reference electrode was Ag/AgCl in 1 M KCl, while a platinum foil served as a counter electrode. The electrolyte was an aqueous solution 0.1 M NaOH. The electrolyte solution was purged by nitrogen stream. The device used for electrochemical measurements was 757 VA Computrace Metrohm. The polarisation curves were recorded in a sufficiently broad voltage range to encompass water electrolysis.

RESULTS AND DISCUSSION

Thermogravimetry of Ni(acac)$_2$. In order to explain properly the mass change under heating of zeolite impregnated with Ni(acac)$_2$, thermal stability of pure Ni(acac)$_2$ was analyzed thermogravimetrically in air and hydrogen atmospheres. The thermograms recorded using either oxygen or hydrogen atmospheres are presented in Fig. 1. The initial weight loss of 19% at 100°C under both air and H$_2$ flow can be associated to the acetone excess. This amount of the solvent is unavoidably present to maintain the solubility in acetone, otherwise dimeric and trimeric molecules, insoluble in acetone, may be formed [23]. Under hydrogen flow, main weight lost occurs suddenly in one step at 230°C, leaving 15% of initial weight (against theoretically expected 18%, what indicates some extent of evaporation losses). Under air flow, the weight temperature curve shows two distinguished steps, indicating the sequenced loss of two molecules of acetylacetonate. Thermal decomposition becomes complete at 430°C, leaving 23% of the initial weight, which corresponds to transformation of Ni(acac)$_2$ to nickel oxide. Namely, theoretically expected residual mass in weight percents, assuming NiO to be the final product, amounts to 23.4.

During the pocedure of NiO incorporation, it was assumed that the processes observed in the case of pure Ni(acac)$_2$, illustrated in Fig. 1, occur in the same way in the case of zeolite impregnated by Ni(acac)$_2$. Based on the thermogravimetric investigation shown in Fig. 1, Ni-modified zeolite was obtained by heating impregnated zeolite to 400°C in air. This procedure lead to incorporation of NiO. The effects of NiO incorporation were further observed by XRD and electrochemical methods.

XRD analysis of Ni-modified zeolite. The content of adsorbed water in zeolite, providing water vapor pressure equal to that of pure water, is about 20% by weight. One may assume that this amount corresponds to full volume occupation of zeolite cavities. The volume occupation of zeolite cavities by NiO in NiO-mod-
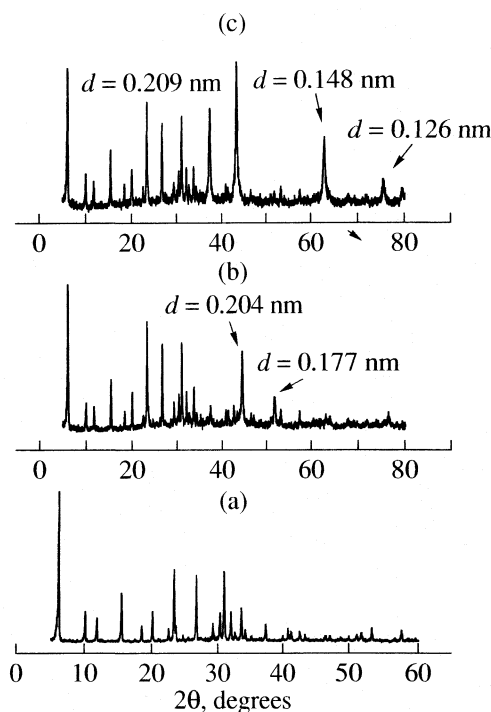
Fig. 2. Comparative X-ray diffractograms of zeolite 13X (a), 13X–20% Ni (b, prepared in hydrogen atmosphere) and 13X–40% NiO (c).

Fig. 3. Cyclic voltammograms (the 30th cycle and the next ones) of NiO-modified zeolite, with 40% of NiO, recored in deaerated 0.1 M NaOH solution, at a scan rate 50 mV/s. Final anodic potential was progressively enlarged from –0.1 to 1.0 V in steps of 0.1 V.

ified zeolite samples may be estimated owing to the density ratio of NiO toward H_2O. Namely, this ratio is 6.67/1. Thus, one may assume that total cavity volume occupation by NiO requires its weight percentage of 134%. Consequently, the percentages achieved in this work: 20, 40 and 100%, fall into the range of partial volume occupation.

The diffractograms of pure 13X zeolite, nickel-modified zeolite up to 20% (13X–20% NiO) and nickel-modified zeolite up to 40% (13X–40% NiO) are presented in Fig. 2. The comparison of the diffractograms in Fig. 2 shows that all diffraction lines characteristic of original zeolite appear with the same intensity ratios in the diffractograms of modified zeolite too. This indicates that procedure did not destroy original crystal structure of zeolite.

Zeolite with lower nickel content (20%), being prepared in air, was afterward heated in hydrogen atmosphere to reduce NiO to Ni. According to JCPDS (Joint Committee on Powder Diffraction Standards) the diffraction lines of crystalline nickel correspond to the plane distance $d = 0.204$ nm and $d = 0.177$ nm. In the diffractogram of 13X–20% Ni at these position relatively narrow peaks appear, what indicates crystal arrangement of incorporated nickel.

The zeolite sample with higher Ni content, prepared by thermal decomposition of $Ni(acac)_2$ in air, as expected from TGA measurements in Fig. 1, show the reflec-

tions at $d = 0.209$, 0.148 and 0.126 nm, which according to JCPDS belong to NiO.

The mean size of incorporated clusters was calculated by means of Scherer formula:

$$L = K\lambda/b\cos\theta$$

where is L – mean diameter along the vertical to the plane of diffraction, K – size parameter (usually 0.9), λ – wavelength of X-rays, Å; b – peak width on the half of height, θ – Brag angle.

This calculation did not confirm significant difference between the cluster sizes expected on the basis of twofold difference in weight percent of NiO, what may mean rather approximative applicability of this method in this case.

Cyclic voltammetry and RDE experiments. First time used electrode is always rather inactive. To achieve full CV response, usually 20–30 potentiodynamic cycles

The mean size (L, nm) of nickel moieties in 13X zeolite cavities calculated on the basis of X-ray diffractometric data

Sample	d, nm	2θ, grad	b, grad	L, nm
13X–20% Ni	0.204	44.4996	0.334	0.257
	0.177	51.7538	0.436	0.203
13X–40% NiO	0.209	43.3062	0.325	0.263
	0.148	62.9648	0.413	0.226
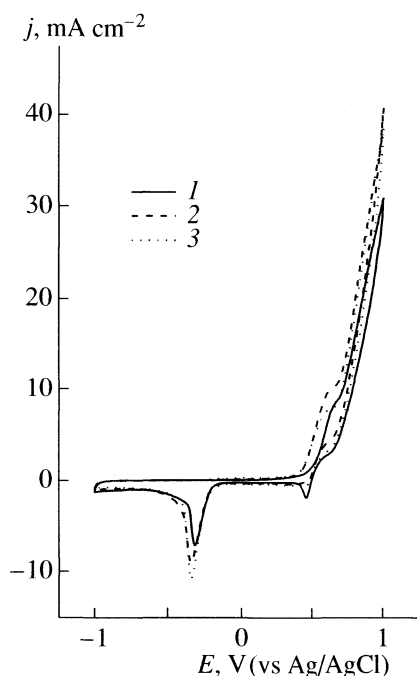
Fig. 4. Cyclic voltammograms of NiO-modified zeolite, with 20 (*1*), 40 (*2*) and 100% of NiO (*3*), recored in deaerated 0.1 M NaOH, at a scan rate 5 mV/s.

Fig. 5. Faradaic capacity of 13X–40% NiO electrode in 0.1 M NaOH as a function of final anodic potential in the region of $Ni(OH)_2$/NiOOH redox reactions.

are necessary to be performed. Regardless whether reduced or oxidized form Ni-modified zeolite is used for electrode preparation, the same steady state CV curves are always to be observed. This is due to a high reactivity of nickel in nanodispersed form, which obviously undergoes fast transformation into hydroxide when diped into aqueous solution.

The steady state cyclovoltammograms of thin layer electrode involving Ni-modified zeolite with Ni/zeolite ratio of 0.4 as an electrode material, in the potential range −1 to +1 V, recorded in dearated 0.1 M NaOH solution, are shown in Fig. 3. A wide potential range from −1.4 to 0.5 V, this electrode material show a purely capacitive behaviour, manifesting itself in a practically potential independent distance between the current values at common potentials but opposite polarisation directions. The capacitance current is proportional to the scan rate ($I_c = vC_{dl}$, where v is scan rate) and in Fig. 3 corresponds to a C_{dl} value of approx 0.1 F cm^{-2}. To reduce capacitive background current, one should use relatively low scan rate. In Fig. 4, the voltammograms recorded at a scan rate of 5 mV s^{-1}, are presented, at which, simultaneously, a rather slight influence of NiO percentage to the electrode activity was illustrated.

The processes which take place on NiO-modified zeolite electrode may be identified by comparing them with the known processes taking place on other electrodes in the same solutions.

On platinum surface, hydrogen evolution reaction may appear at potentials close to −1 V. At the same potential, NiO-modified zeolite electrode is obviously in-

active for this reaction, and cathodic potential extension beyond −1.5 V is required in order to induce visible hydrogen evolution.

On the anodic side, in a limited potential range 0.55–0.8 V, one may see a pair of anodic-cathodic peaks. As well known from the literature [24–27], in the potential range 0.55–0.8 V vs SCE, (0.4–0.65 V vs Hg/HgO) on smooth Ni electrode, reversible Ni(II) ⇔ ⇔ Ni(III) redox transformation occurs, being the basic reaction of nickel cathode of commercial power sources [28]. Using the analogy with smooth nickel electrode, the processes in 13X-Ni$_{40}$ electrode can be attributed to the following reactions:

$$\beta\text{-Ni(OH)}_2 + OH^- \Leftrightarrow \beta,\gamma\text{-NiOOH} + H_2O + e^-.$$
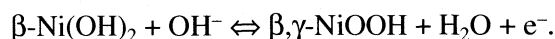
From the coulonometric analysis of the cyclovoltammograms in Fig. 3 limited to a potential range 0–0.8 V, both charging and discharging capacity of Ni-modified zeolite electrode was determined in dependence on anodic potential, and this dependence is shown in Fig. 5. Owing to the actual surface coverage by modified zeolite, these values are close to 75% of a theoretical charging/discharging capacity of this electrode (being approx 4 mC cm^{-2}).

On a smooth nickel electrode [24–27], the corresponding anodic peak is clearly separated from the current of oxygen evolution reaction, appearing at higher anodic potentials. However, at our NiO-modified zeolite electrode, the separation is absent and the current of oxidation of Ni(II), at anodic potentials higher than 0.8 V, passes gradually to the current of oxygen evolution, visible also by gas bubble deliberation. In this potential range, oxygen evolution proceeds on the basis of equation [29]:

$$4OH^- = O_2 + 2H_2O + 4e^-.$$
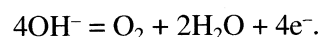
This is in accordance to the data that NiOOH is very good catalyst for oxygen evolution [30–32]. Contrary to this, on gold, oxygen evolution is much slower, un-
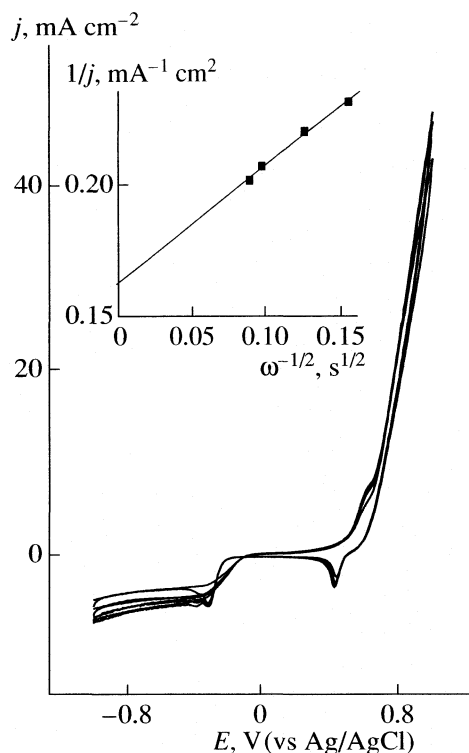
Fig. 6. Cyclic voltammogram of 13X–20% NiO obtained with rotating disc electrode in oxygen saturated 0.1 M NaOH solution at sweep rate 5 mV s^{-1} and rotation rates 400, 600, 1000 and 1200 rpm. Inserted picture: the Koutecky-Levich plot of the voltammograms for a common potential of –0.6 V.

less special cathodic treatment was applied [29]. This is only to illustrate similar catalytic activity of modified zeolite electrode, however, very probably this electrode may not mechanically withstand the extensive gas evolution.

If the polarisation is reversed upon achievement of final potential higher than 0.8 V, a cathodic peak centered at the potential of –0.5 V appears. This peak may be attributed to oxygen reduction reaction, involving oxygen which remains within the zeolite cavities thanks to a slow deliberation of oxygen from zeolite cavities. This conclusion is supported by the fact that this peak significantly decreases if rotation of the electrode is switched on.

To prove additionaly that one deals here with oxygen reduction, the voltammogram in oxygen saturated solution was recorded too, using rotation disk technique. Corresponding diagramms were shown in Fig. 6. As expected, instead of peak around –0.5 V, current plateau appears, but having a certain bias toward potential axis. The non-biased plateaus are otherwise characteristic of oxygen reduction on smooth platinum electrode [33]. For rotation rate of 600 rpm, the plateau height amounts to 5 mA cm^{-2}, which overrates for approx. 30% the plateau current observed on smooth platinum in the same solution [33]. Further to this, the de-

pendence of current on rotation rate is less pronounced than expected for diffusion controlled processes. Namely, Koutecky Lewich plot inserted in Fig. 6, has the slope much lower than one corresponding to both 2e$^-$ and 4e$^-$ route of oxygen reduction, and in addition, does not cross the origin of coordinate system. Most probably these particularities are due to a rough nature of zeolitic electrode as well as due to the aggravation of mass transport of both reactants and products through it.

CONCLUSION

Impregnation of 13X zeolite by Ni-acetylacetonate solution in acetone, following by thermal degradation in air, resulted in a new material: modified zeolite 13X with NiO clusters incorporated into the cavities of original zeolite structure. NiO may be reduced to Ni by heating in hydrogen atmosphere. By addition of 10% of carbon black, and bonded by polymeric glue (nafion) to a electronically conductive support (glassy carbon, etc.) this material was used as an electrode material. Its electrochemical performance was studied in, both deaerated and oxygen saturated, 0.1 M NaOH aqueous solution. The performance characteristic of Ni(OH)$_2$/NiOOH redox pair, as well as good catalytic activity toward both oxygen reduction and evolution were evidenced. Contrary to the expectations, the increase of NiO content above 20 wt. % did not lead to a proportional enhancement of electrochemical performance. It is reasonable to expect that solid aluminosilicate framework may protect nickel clusters of agglomeration if subjected to numerous charging/discharging cycles.

REFERENCES

1. A. M. Ferrari, K. M. Neyman, T. Belling, M. Mayer, N. Rösch, *J. Phys. Chem. B*, 103 (1999) 216.
2. A. L. Yakovlev, K. M. Neyman, G. M. Zhidomirov, N. Rösch, *J. Phys. Chem.*, 100 (1996) 3482.
3. R. E. Jentoft, M. Tsapatsis, M. E. Davis, and B. C. Gates, *J. Catal.* 179 (1998) 565.
4. W. A. Weber and B. C. Gates, *J. Catal.* 180 (1998) 207.
5. W. A. Weber, B. L. Phillips, and B. C. Gates, *Chemistry a European Journal 5* (1999) 2899.
6. W. A. Weber, A. Zhao, and B. C. Gates, *J. Catal.* 182 (1999) 13.
7. P. Gallezot, I. Mutin, G. Dalmai-Imelik, B. Imelik, *J. Microsc. Spectrosc. Electron.* 1 (1976) 1.
8. P. Gallezot, *Surf. Sci.* 106 (1981) 459.

9. A. Tonscheidt, P. L. Ryder, N. I. Jaeger, G. Schulz-Ek-loff, *Surf. Sci.* 281(1993) 51.

10. A. Tonscheidt, P. L. Ryder, N. I. Jaeger, G. Schulz-Ek-loff, *Zeolites, 16,* (1996) 271. ▪

11. V. Alfredsson, O. Terasaki, Z. Blum, Jan-Olov Bovin, G. Karlsson, *Zeolites 15* (1995) 111.

12. M. Hartman, C. Bischof, Z. Luan, L. Kevan, *Micropor. Mesopor. Mater. 44–45* (2001) 385.

13. M. Vaarkamp, F. S. Modica, J. T. Miller, D. C. Konings-berger, *J. Catal. 144* (1993) 611.

14. S. E. Deutsch, J. T. Miller, K. Tomishige, Y. Iwasawa, W. A. Weber, B. C. Gates, *J. Phys. Chem., 100,* (1996) 13408.

15. D. Barthoment, *Catal. Rev. 38* (1996) 521.

16. M. Xu, W. Horsthemke and M. Schell, Electrochim. Acta *38,* (1993) 919.

17. Z. Li, C. M. Wang, L. Persaud and T. E. Mallouk, J. Phys. Chem. 92 (1988) 2592.

18. C. Iwakura, S. Miyazaki, H. Yoneyama, J. Electroanal. Chem. 246 (1988) 63.

19. D. R. Rolison, E. A. Hayes, W. E. Rudzinski, J. Phys. Chem. 93 (1989) 5524.

20. S. Mentus, Z. Mojović, N. Cvjetićanin, Z. Tesic, Fuel Cells – from Fundamentals to Systems 1–2 (2003) 15.

21. Z. Mojovic, S. Mentus and Z. Tesic, Mat. Sci. Forum 453–454 (2004) 257.

22. D. Jugovic, N. Cvjetićanin, V. Kusigerski, S. Mentus, J. Optoelectron. Adv. Mat. 5, (2003) 337.

23. W. H. Watson, Chi-tsun Lin, Inorg. Chem. 5 (1966) 1074.

24. H. Bode, K. Dehmelt, Electrochim. Acta 11 (1966) 1079.

25. F. Hahn, B. Beden, M.J. Croisssant, C. Lamy, Electro-chim. Acta 31 (1986) 335.

26. F. Hahn, D. Floner, B. Beden, C. Lamy, Electrochim. Acta 32 (1987) 1631.

27. Yy M. Grden A. Czerwiński, J. Golimowski, E. Bulska, B. Krasnodebska-Ostrega, R. Marassi and S. Zamponi, J. Electroanal. Chem. 460 (1999) 30–37.

28. R. G. Gunther, S. Gross, (Eds.) Proc. Symp. On the Nickel Electrode, The Electrochem. Soc., Princeton, N.J. (1982).

29. A. Abu Rabi, D. Jašin, S. Mentus, J. Electroanal. Chem., in press, available online from 18 october 2006.

30. P.W.T. Lu, S. Srinivasan, J. Electrochem. Soc. 125 (1978) 1416.

31. D. Corrigan, J. Electrochem. Soc. 134 (1987) 377.

32. Y. Hu, Y. V. Tolmachev, D. A. Scherson, J. Electroanal. Chem. 468 (1999) 64.

33. N. M. Marković, P. N. Ross, Ch. 46, in Interfacial Elec-trochemistry, Theory, Experiment and Applications, Ed. A. Wieckowski, M. Dekker Inc., New York, Basel (1999) p. 821.

COLLOID CHEMISTRY
AND ELECTROCHEMISTRY

ELECTROCHEMICAL BEHAVIOUR OF 5-SUBSTITUTED 2-ALKYLIDENE-4-OXOTHIAZOLIDINE DERIVATIVES STUDIED BY CYCLIC VOLTAMMETRY

© 2007   D. M. Minić[*, **], I. Cekić[*, **], F. T. Pastor[**, ****], V. Jovanović[***], R. Marković[**, ****]

*Faculty of Physical Chemistry, University of Belgrade, Studentski trg 12, Belgrade, Serbia
E-mail: dminic@ffh.bg.ac.yu
**Center for Chemistry ICTM, P.O. Box 473, 11001 Belgrade, Serbia
***ICTM, Department of Electrochemistry, P.O. Box 815, 11000 Belgrade, Serbia
****Faculty of Chemistry, University of Belgrade, Studentski trg 16, 11001 Belgrade, Serbia

Abstract – This study demonstrated the electrochemical activity of selected 2-alkylidene-4-oxothiazolidine derivatives, containing different substituents at the C5-position, on Pt-electrode in 0.1 M TBAHFP + MeCN in the potential range from –2 V to 2 V. The mechanism of electrode processes was discussed. It was shown that chemical step was involved in the irreversible electrochemical processes. The effect of the substituent at the C5 position on reduction and oxidation potentials was also noted. The regions of the linear dependence of the current peak on concentration of the compounds examined were determined.

During the course of our studies focused on the synthesis of stereodefined *push-pull* 2-alkylidene-4-oxothiazolidines [1]

(I)
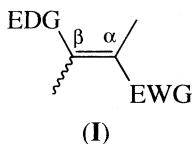
we have been interested in the assessment of the specific physico-chemical effects on the reactivity and functionalization [2, 3] of these heterocyclic compounds. Compounds of that type belong to push-pull alkenes, containing electron-donating group(s) (EDG) on C(β) and strong resonatively electron-withdrawing group(s) (EWG) on C(α) as depicted by general structure **I**.

Thus, based on the *n,π*-donor/acceptor properties of the 2-alkylidene-4-oxothiazolidines **I**, with different electron-withdrawing groups at the terminus of the C=C bond, and two electron-donating groups (NH and –S–) at the other terminus, they undergo the well-defined *Z/E*-process, controlled by the intra- and intermolecular hydrogen bonding interactions [4–7]. In addition, one of the important structural features of the compounds **1** (EWG = COPh, COOEt, etc.), related to a rather close distance between the sulfur and oxygen atoms within the *cis*-configured –S–C=C–C=O moiety, can be accounted for the facile 4-oxothiazolidine to 1,2-dithiole rearrangement (Scheme, path *E*) [8].

It is interesting to note that the 4-oxothiazolidines **1** undergo various oxidation and reduction transformations (Scheme, paths *B* and *F*, respectively). For that reason, having also in mind a broad range of biological activity of thizolidine derivatives [9] and the intrinsic

physico-chemical properties of the compounds, exemplified by specific structures **1a–c**:
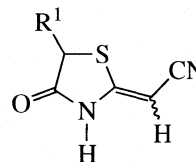
(R^1 = Me (**1a**), (**1b**) and (**1c**)); there

exist a need for the electrochemical investigation of these redox processes.
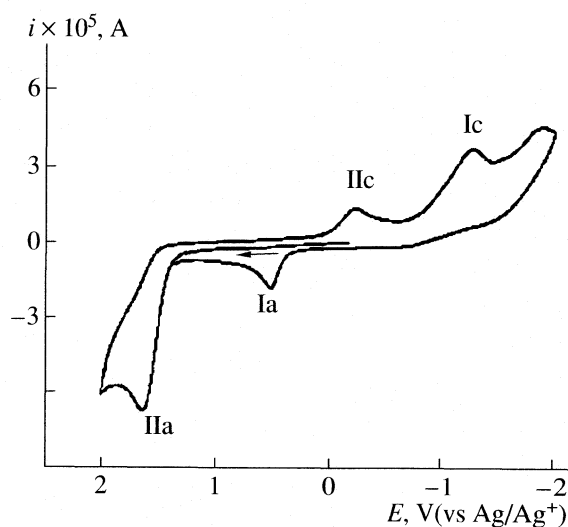
Fig. 1. Cyclic voltammogram of compound **1b**, sweep rate 100 mV/s, concentration 4 mM.

MINIĆ et al.

(4)
EWG = COPh, CONHPh, COOEt,
CONHCH$_2$CH$_2$Ph, CN; R^2 = H

(2)

(3)
EWG = COPh, CONHPh, COOEt,
CONHCH$_2$CH$_2$Ph, CN; R^2 = H

(5)
Nu = OMe, NHPh, N⏜O ;
EWG = NHPh, NHCH$_2$CH$_2$Ph; R^2 = H

(1)
EWG = COPh, CONHPh, COOEt,
CONHCH$_2$CH$_2$Ph, CN;
R^1 = H, Me, CH$_2$COOEt, R^2 = H, Me

(6a)

(6b)
R^1 = H, Me, CH$_2$CO$_2$Et

(8)
EWG = COPh, CONHPh, COOEt,
CONHCH$_2$CH$_2$Ph, CN; R^2 = H, Me

(7)
EWG = COPh, CONHPh, COOEt,
CONHCH$_2$CH$_2$Ph, CN; R^2 = H, Me
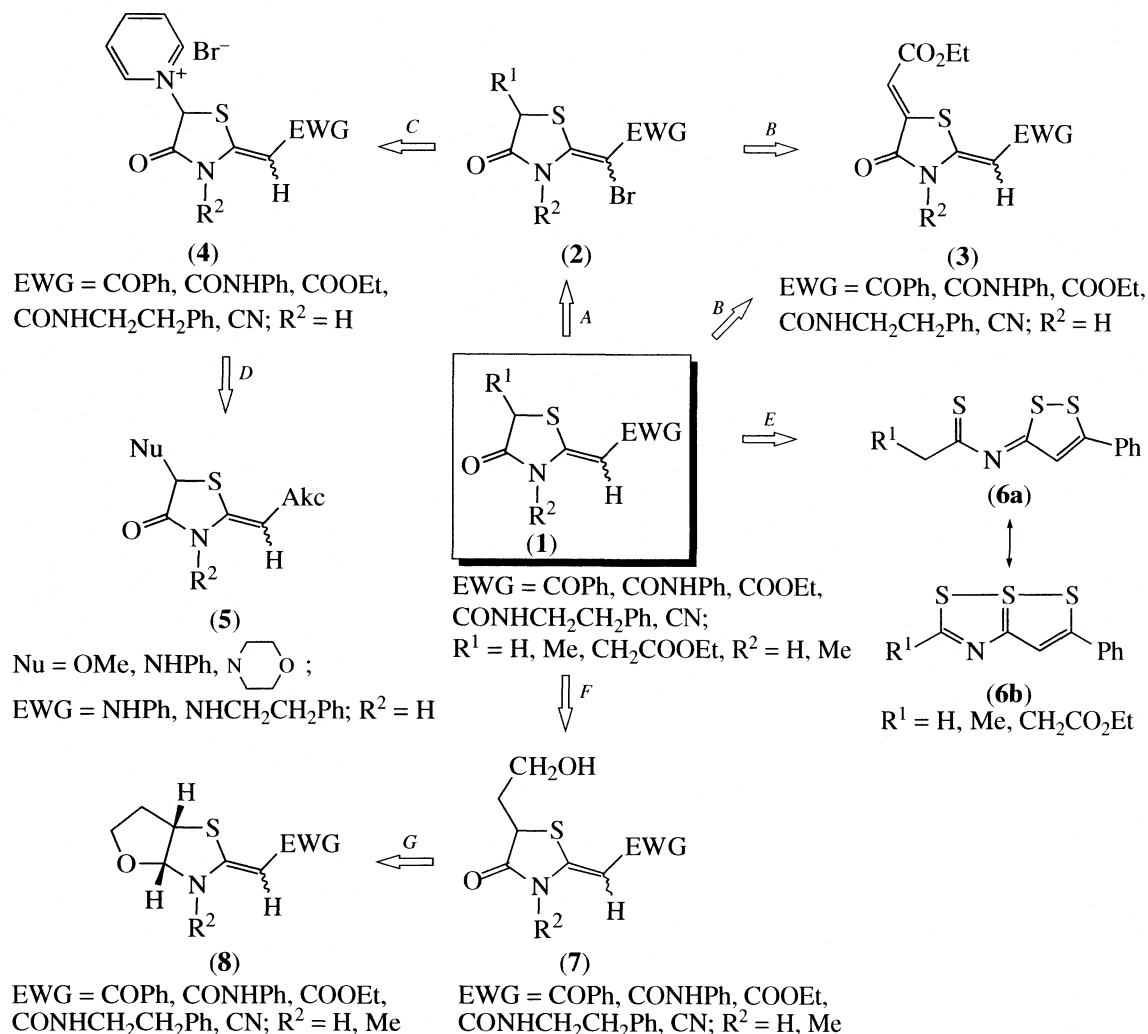
Scheme

EXPERIMENTAL

Reagents and solutions. Push-pull compounds **1a–c** were synthesized and characterized in our laboratory according to the procedure already described [1]. All the other reagents employed were of analytical grade. Anhydrous acetonitrile used as a solvent was distilled prior to use. The solutions used in cyclic voltammetry experiments were prepared by dissolving the measured amount of compounds in 0.1 M solution of TBAHFP in acetonitrile.

Apparatus. Cyclic voltammetry was performed with Electrochemistry workstation CHI760b (CHI Instrument CO., USA) using one-compartment electrolytic cell (volumetric capacity 10 ml) with a three-electrode configuration. A platinum disc (2.0 mm diameter, CH Instruments, Inc.) and a platinum flag wire were used as

Table 1. Anodic (Ia, IIa) and cathodic (Ic, IIc) peak potentials (V) and peak currents (A) at different sweep rates for the compound **1b**

Peak	v = 0.05 V/s		v = 0.1 V/s		v = 0.5 V/s	
	$i_p \times 10^5$	E_p	$i_p \times 10^5$	E_p	$i_p \times 10^5$	E_p
Ic	3.1250	−1.1424	3.828	−1.1685	8.7550	−1.2864
Ia	0.6880	0.4848	1.5540	0.4917	5.3820	0.5440
IIa	5.5000	1.6224	7.3220	1.6485	14.9700	1.7397
IIc	0.3747	−0.1227	0.9111	−0.1360	2.0370	−0.2080
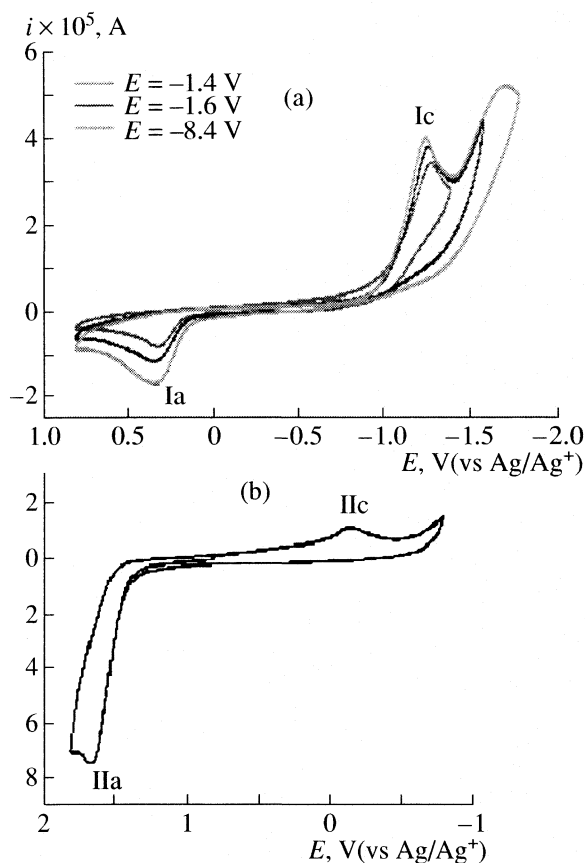
Fig. 2. Cyclic voltammograms of compound **1b**, sweep rate 100 mV/s, concentration 4 mM, cathodic (a) and anodic (b) potential range.

Fig. 3. Cyclic voltammograms for different concentrations ($1 - 0.5$, $2 - 1$, $3 - 2$; $4 - 4$, $5 - 6$, $6 - 8$ mM) of compound **1b**, sweep rate 100 mV/s.

the working and the counter electrode, respectively. A silver wire in 0.01 M AgNO$_3$ solution of TBAHFP in acetonitrile (anhydrous) served as a non-aqueous reference electrode which was separated from the test solution by a fine glass frit. All the measurements were carried out at room temperature at a sweep rates ranging from 25 to 500 mV/s in the potential range from –2 to 2 V.

RESULTS AND DISCUSSION

The electrochemical properties of the compounds **1a–c** at room temperature were investigated by the cyclic voltammetry method in acetonitrile containing the 0.1 M TBAHFP as supporting electrolyte. Based on the first scan cyclic voltammogram of 4 mM solution of 4-oxothiazolidine **1b** (Fig. 1), and potential values given in Table 1, this compound, depending on the direction of the applied polarization potential, undergoes irreversible processes of oxidation or reduction on the Pt electrode.

Consequently, as shown on Fig. 2, the different electrochemical processes were identified on the basis of the cyclic voltammograms, recorded by changing the direction and the values of the polarization potential.

According to the theory of cyclic voltammetry, the potential increment between the peak E_p and the half-peak $E_{p/2}$ is given by expression:

$$E_p - E_{p/2}, \text{V} = 0.048/\alpha n_a,$$

where α is the transfer coefficient and n_a is the number of electrons involved in the rate-determining step. The values of potential peak differences and αn_a for all compounds **1a–c** (Table 2) show that the electrode processes are very slow. With the increase of the sweep rate, the differences of the corresponding potential peaks increase, and on the other hand the ratio of the corresponding current peaks decreases. These facts indicate an enhancement of the irreversibility of the processes. The values determined for αn_a imply that the transfer of one electron in the first step of the electrode processes is the rate determining step [10].

Relatively high values for cathodic and anodic potential peaks, as shown for **1b** (Table 1, columns 3, 5 and 7) indicate an increased stability of the intermolecularly hydrogen-bonded Z- and E-isomers of the thiazolidine compounds **1a–c**. In addition, the stability of **1a–c** is attributed to hydrogen bonding interactions

Table 2. The potential increment between the peak E_p and the half-peal $E_{p/2}$ and αn_a

Compound	Δ_1,V	αn_a	Δ_2,V	αn_a
1a	0.188	0.25	0.163	0.29
1b	0.221	0.22	0.141	0.34
1c	0.096	0.50	0.088	0.54

Notes: $\Delta_1 = |E_p - E_{p/2}|_{Ic}$, $\Delta_2 = |E_p - E_{p/2}|_{IIa}$.
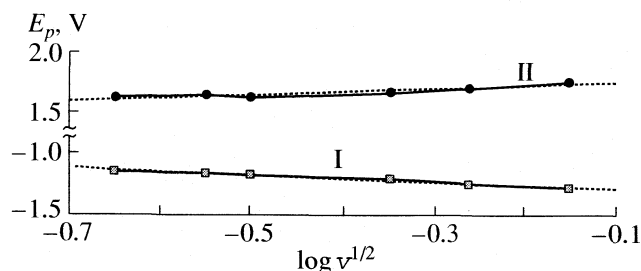
Fig. 4. The plots of E_p vs $\log v^{1/2}$ for 4 mM concentration of compound **1b**; I – cathodic peak, II – anodic peak.

with the relatively polar acetonitrile. In turn, this is the reason for the rather slow electrode processes. It should be pointed out that the potential peak shifts to the more anodic and less cathodic values, when the initial concentration of the 4-oxothiazolidines **1a–c** decreases (Fig. 3). Thus, it can be assumed that some chemical reaction can be coupled to the charge transfer step on the Pt electrode.

The nature of electrode processes were analyzed in terms of the variations of the potential peak E_p and current peak i_p with a sweep rate v by plotting E_p vs $\log v^{1/2}$ and $i_p/v^{1/2}c$ vs $v^{1/2}$ and i_p vs v for different concentrations of the thiazolidine derivative **1c** (Figs. 4 and 5).

The E_p values are function of the polarization rate and vary linearly with $\log v^{1/2}$ (Fig. 4). The current function $i_p/v^{1/2} c$ decreases with $v^{1/2}$ in such a way that is strongly dependent on the initial concentration, as shown in Fig. 5. The latter fact leads to the conclusion that the abovementioned chemical reaction, of the higher than the first order kinetics, is involved in electrochemical processes. Significant influence of the chemical step involved in the electro-reduction can be observed from the shape of the dependence $i_p/v^{1/2}c$ vs $v^{1/2}$ for different concentrations (Fig. 5). By taking into account previous studies on electro-oxidation of the related compounds [11], and the fact that dependence of i_p vs v is not linear, thus excluding the absorption, we think that the formation of the dimer of the parent compound is involved in the electrode processes.

The number of electrons of the anodic process was determined by the controlled-potential coulometry. The coulumetry was performed at +1.6 V for the 10^{-3} M acetonitrile solution of compound **1b**. The electrolysis was stopped upon the current reduction to about 3% of the

Table 3. The peak potentials (V) of the compounds **1a–c** (versus Ag/Ag$^+$)

Compound	Cathodic peaks		Anodic peaks	
	I	II	I	II
1a	−1.36	−0.24	0.49	1.69
1b	−1.17	−0.14	0.49	1.65
1c	−1.01	−	0.65	1.82
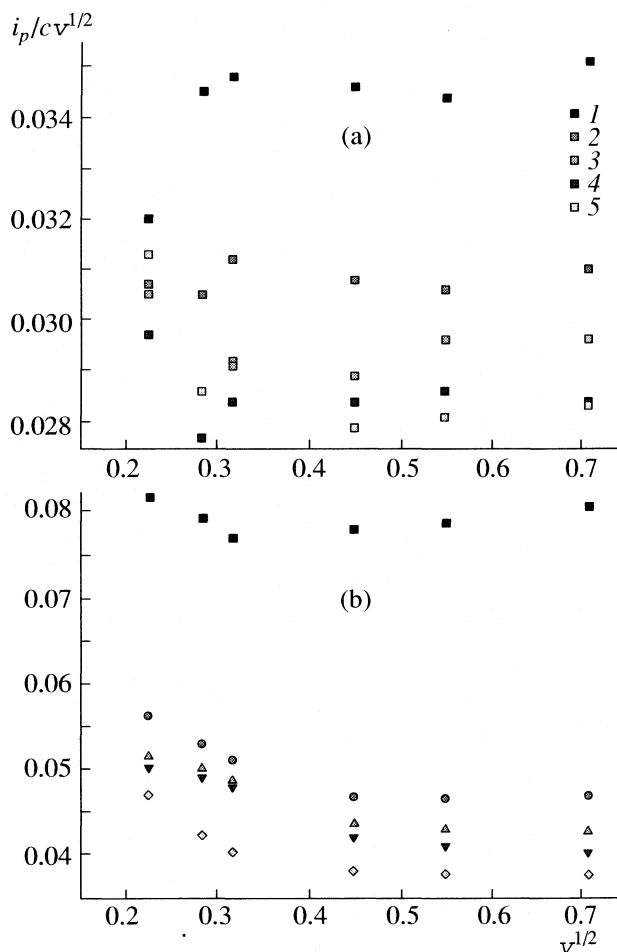
Fig. 5. The plotting $i_p/v^{1/2}c$ vs $v^{1/2}$ of cathodic I (a) and anodic (II) (b) peaks for compound **1c**; $c = 1$ (*1*), 2 (*2*), 3 (*3*), 4 (*4*) and 5 mM (*5*).

initial value. The charge passed was 2.21 C and the calculated charge was 1.94 C, assuming that $n = 2$.

It is worth mentioning that the influence of the substituents at the C5-position in the heterocyclic ring regarding ht processes of the electrochemical reduction and oxidation was investigated (Fig. 6, Table 3). The cyclic voltammograms of **1a–c** shown in Fig. 6 indicate certain regularity in the reduction potentials with respect to the substituent at the C5-position. The order of the reduction potentials of the 4-oxithiazolidines **1a–c** is as follows: **1a** > **1b** > **1c**.

The rationale for this behaviour is most likely based upon increased electron-accepting ability of the etoxycarbonylmethylidene group at C5 of **1c** *versus* that of the etoxycarbonylmethyl group in **1b**. In the case of precursor **1a**, containing the methyl group at C5, a different mode of reduction occurs, thus, making the precursor **1c** less reactive. On the other hand, the order of the oxidation potentials follows the opposite direction.

We have also tested the possibility of employing this technique for a quantitative determination of the
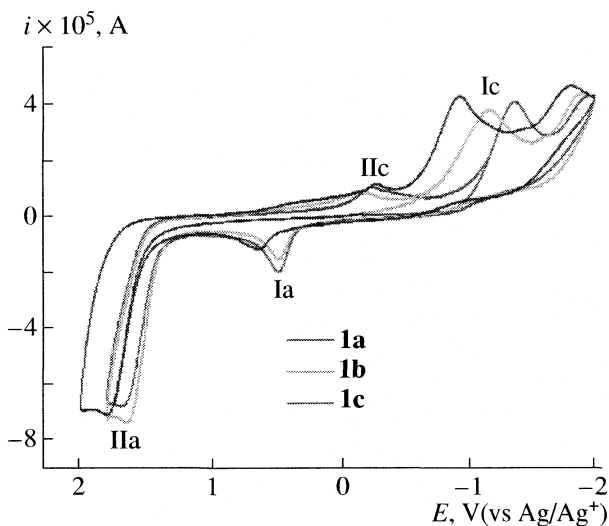
Fig. 6. Cyclic voltammograms of compounds **1a**, **1b** and **1c** in 0.1 M TBAHFP + CH_3CN, sweep rate 100 mV/s.
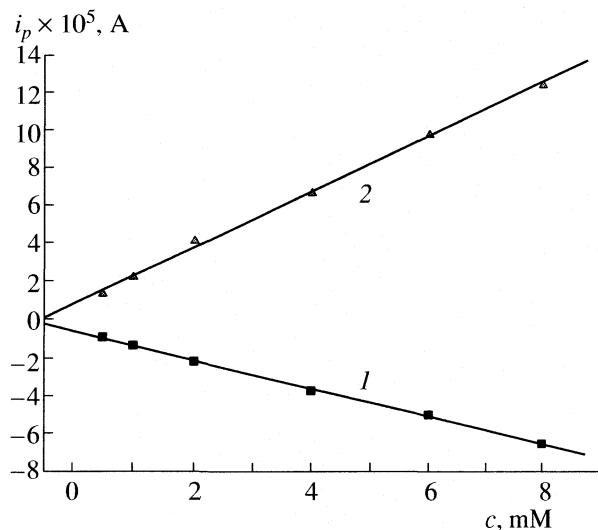
Fig. 7. Dependance of peak current on concentration for compound **1b**; *1* – Ic, *2* – IIa.

heterocyclic derivatives **1a–c** following the relationship between the current peak and substrate concentration (Fig. 7). As can be seen the concentration effect on the voltammetric signal follows the linear relationship. This linear relationship, found for the low concentrations (0.5×10^{-3} to 2×10^{-3} M), opens up the possibility for the analysis of low amounts of the thiazolidines **1a–c** in a non-aqueous solution.

ACKNOWLEDGEMENTS

REFERENCES

1. Marković, R., Dzambaski, Z., Baranac, M., *Tetrahecron* (**2001**), 57, 5833.

2. Marković, R., Baranac, M., Steel, P., Kleinpeter, E., Stojanović, M., *Heterocycles* (**2005**), 65, 2635.

3. Stojanović Baranac M., Marković, R., *Synlett* (**2006**), 729.

4. Mmarković, R., Shirazi, A., Dzambaski, Z., Baranac, M., Minić, D., *Journal of Physical Organic Chemistry* (**2004**), 17, 118.

5. Kessler, H., *Angew. Chem. Int. Ed. Engl.* (**1982**), 21, 512.

6. Zhuo, J.-C., Magn. Reson. Chem. (**1997**), 35, 311.

7. Lehn, J.-M., *Angew. Chem. Int. Ed. Engl.* (**1990**), 29, 1304.

8. Marković, R., Baranac, M., Jovetić, S., *Tetrahedron Letters* (**2003**), 44, 7087.

9. Giles, R. G., Lewis, N. J., Quick, J. K., Sasse, M. J., Urquhart, M. W. J., *Tetrahedron* (**2000**), 56, 4531.

10. Boskris, J. O'., Reddy, A. K. N., "Modern Electrochemistry", vol. 2, Plenum Press, New York (1970), p. 1081.

11. Iwakura, C., Tsunaga, M., Tamura, H., *Electrochimica Acta* (**1972**), 17, 1391.

===== BIOPHYSICAL CHEMISTRY =====

ADJUVANT ANTIPROLIFERATIVE AND CYTOTOXIC EFFECT OF ALOIN IN IRRADIATED HELAS3 CELLS

© 2007   A. Nićiforović, M. Adžić, B. Zarić, M. B. Radojčić

Laboratory of Molecular Biology and Endocrinology, VINČA Institute of Nuclear Sciences P.O. Box 522, 11001 Belgrade, Serbia

E-mail: ana@vin.bg.ac.yu

Abstract – Naturally occurring phytoanthracycline, aloin, was used to radiosensitize HeLaS3 human cervix carcinoma cells. The results indicated that the cytotoxic adjuvant effect of aloin was synergistic with gamma-ionizing radiation at all drug concentrations and comparable to the cytotoxicity of 5–10 Gy ionizing radiation alone. Radiosensitization of HeLaS3 cells was achieved by 60 μM aloin which reduced IC_{50} dose of ionizing radiation from 3.4 to 2 Gy. Ionizing radiation and aloin alone, or in combination are shown to cause perturbation of HeLaS3 cell-cycle, and increase percentage of cells in DNA synthesis (S) phase of cell cycle. While either of the agents applied alone cause programmed cell death by apoptosis, the simultaneous cell damage by both agents through the altered redox balance compromised cell capacity to conduct this program, and led to the synergic cytotoxic cell death by necrosis.

INTRODUCTION

Carcinoma of the uterine cervix is one of the most common malignancies and the second leading cause of cancer death among women worldwide [1]. Advanced stages of disease are treated with chemotherapy alone or in combination with ionizing radiation [2]. In chemotherapy of cervical cancer, several drugs have been used: but application of all these agents is limited by their nephro-, neuro-, cardio- and gastrointestinal toxicity [3]. Beneficial antitumour action of well known anthracycline such as doxorubicin, may also be the characteristic of naturally occurring anthracyclines. One such candidate is phytoanalog-aloin, a C-glycoside derivative of an anthraquinone, which showed potential cytotoxic effect in several tumour cell lines and low toxicity and the low incidence of side effects in treating mice-bearing ascites and solid Ehrlich carcinoma [4].

Among the possible mechanisms of antitumour action of the anthracyclines are interactions with cellular DNA, generation of reactive oxygen species (ROS) [5] which produce DNA strand scission, lipid peroxidation and disruption of cell membane functions and integrity. Since, aloin is a strong oxidizing agent, it can be proposed that the treatment of cells with this compound changes cellular redox balance. At the same time, HeLaS3 cells have reduced levels of apoptosis signalling protein p53, due to its ubiquitination and degradation by human papilloma virus E6 protein [6]. Since p53 under normal conditions act as repressor of antioxidant enzyme (AOE) Mn-superoxide dismutase (MnSOD), its lack of function cause high MnSOD expression. Without a concomitant increase in the peroxide-scavenging enzymes, H_2O_2 represents a major intracellular ROS in the pathway to cytotoxicity [7].

Therefore, growth-suppressive effects of overexpressed MnSOD could be the concequence of imbalance in AOE that favours H_2O_2 accumulation [8] which may inhibit anti-apoptotic transcription factor NF-κB [9].

Gamma-ionizing radiation (IR) induces dose and time dependent inhibition of HeLaS3 human cervical carcinoma cell growth [10], due to perturbation of cell-cycle and induction of apoptosis. The cell proliferation was inhibited for 50% (IC_{50}) at 3.4 Gy, while 50% cell cytotoxicity (EC_{50}) was not attainable within the dose range of 2–10 Gy. These cellular effects correlated with increased activity of mitochondrial MnSOD, which was not coupled with the respective catalase (CAT) activity. The cytosolic CuZn-superoxide dismutase (CuZnSOD) activity decreased [11]. Since IC_{50} dose is rather high the aim of the presented study was to test the adjuvant phytoanthracycline, aloin, which possess less undesirable side-effects in comparison to other currently used drugs. Aloin is shown to cause perturbation of HeLaS3 cell-cycle, and increase percentage of cells in S phase and apoptosis [12]. Since aloin diminishes tumour metastatic potential induced by IR-triggered MnSOD overexpression and that IR and aloin share, at least in part, a common pathway in the mechanism of their action, it is of interest to investigate their possible synergic activity in HeLaS3 cells.

EXPERIMENTAL

Cell culture. The human cervix uteri adenocarcinoma cell line HeLaS3 was obtained from the American Type Culture Collection (Rockville, MD, USA). The cells were maintained in 95% Ham's F12 supplemented with 5% heat inactivated fetal calf serum, 100 IU/ml penicillin/streptomycin and 2 mM L-glutamine
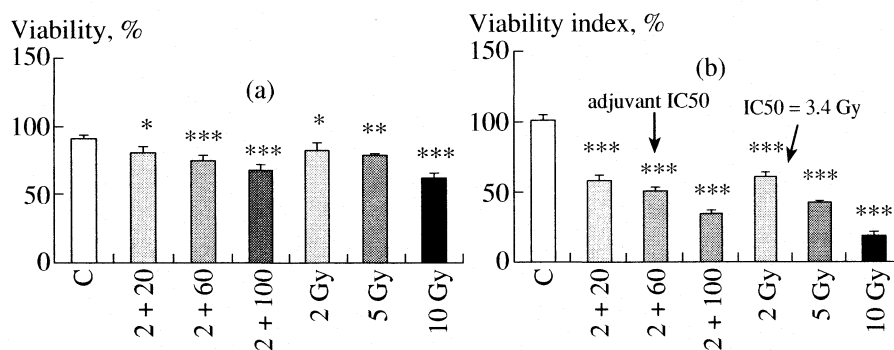
Fig. 1. Combined effect of gamma-ionizing radiation (IR in Gy) plus aloin (μM), or IR alone on HeLaS3 cell viability (a) and viability index (b). Data are presented as mean $\pm$SD (n = 6), C – control.
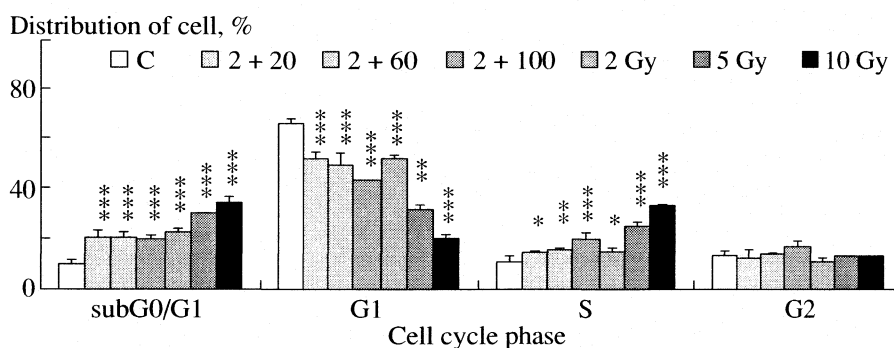
Fig. 2. Cell cycle distribution of HeLaS3 cell treated with gamma-ionizing radiation (IR in Gy) plus aloin (μM), or IR alone. Data are presented as mean $\pm$SD (n = 3).

(Sigma Aldrich Chemie, Taufkirchen, Germany). Cells were grown as monolayer in a humidified atmosphere of 95% air and 5% CO_2 at 37°C.

Cell irradiation. Cell IR was performed in the exponential phase of cell growth with 2-, 5- and 10 Gy of gamma-rays from a ^{60}Co source and a fixed dose rate of 20 Gy/h.

Drug treatment. Aloin was obtained as pure powder form *Aloe barbadensis* Miller leaves, $\geq$97% (Sigma Aldrich Chemie, Taufkirchen, Germany). Different concentration of aloin (20–100 μM) were prepared freshly in PBS and sterilized before use by filtration through 0.22 mm Millipore filters (Sarstedt, Germany).

Cell viability. The cell growth and viability in the control and IR cells was determined by the trypan blue exclusion assay. The ratio between viable cell numbers in treated and control cells was presented as the Viability index (VI).

Flow cytometry. For cell cycle analysis, the HeLaS3 cells were resuspended in 250 ml of cold PBS and fixed using 0.5 ml ice-cold 70% ethanol. After the ethanol was washed out, the fixed cells were treated with 50 mg/ml RNAse A at 37°C, incubated with 50 mg/ml propidium iodide (PI) at 4°C for 30 min and then analyzed by a FACS Calibur flow cytometer (Becton Dickinson, San Jose, CA, USA). Cell cycle distribution was deter-

mined using ModFIT software (Verity Software House, Inc. Topsham, ME, USA).

Statistical analysis. The data were presented as mean $\pm$ SD. Analysis of variance (one-way ANOVA) and Tukey's post-hoc test were used to determine statistically significant differences ($p < 0.05$).

RESULTS AND DISCUSSION

The results presented in this paper indicate that ionizing radiation (IR) induces dose and time dependent inhibition of HeLaS3 cells viability and proliferation, and that the cytostatic effect of IR in HeLaS3 is more pronounced than cell cytotoxicity. The adjuvant effect of aloin (20–100 μM) on HeLaS3 cells irradiated with standard clinical fraction dose of 2 Gy was tested via determination of cell viability (% of viable cells, Fig. 1a) and viability index (ratio of viable cells in treated vs. control sample, Fig. 1b). The results clearly indicated that the cytotoxic adjuvant effect of aloin was synergistic with IR at all drug concentrations and comparable to the cytotoxicity of 5–10 Gy IR alone. Moreover, 60 μM aloin as adjuvant reduced IC_{50} dose of IR from 3.4 to 2 Gy.

Flow-cytometric analysis of propidium iodide (PI) stained HeLaS3 cells indicated a dose-dependent perturbation of the cell cycle (Fig. 2, Table), transient delay predominantly in S phase and increased apoptotic

Cell cycle distribution of HeLaS3 cell treated with gamma-ionizing radiation (IR in Gy) plus aloin (µM), or IR alone. Data are presented as mean ±SD ($n = 3$)

Treatment	SubG0/G1	G0/G1	S	G2/M
Control	9.9 ± 2.0	65.7 ± 1.9	11.0 ± 2.0	13.3 ± 1.6
2 Gy + 20 µM	20.5 ± 3.0***	51.9 ± 2.2***	14.7 ± 0.9*	12.8 ± 2.9
2 Gy + 60 µM	20.6 ± 2.1***	49.4 ± 4.8***	16.2 ± 0.8**	14.0 ± 0.8
2 Gy + 100 µM	19.9 ± 1.6***	43.4 ± 0.2***	20.2 ± 2.4***	16.5 ± 2.4
2 Gy	22.5 ± 1.9***	51.4 ± 2.1***	15.3 ± 1.3*	10.9 ± 1.8
5 Gy	29.8 ± 0.3***	31.9 ± 1.6***	25.4 ± 1.0***	13.0 ± 0.2
10 Gy	34.0 ± 2.6***	20.1 ± 1.5***	32.8 ± 0.8***	13.1 ± 0.3

cell death (subG0/G1 peak). The IR induced late S phase arrest in HeLaS3 cells was also previously observed by Ianzini and Mackey [13]. In our study the S phase HeLaS3 cell cycle arrest correlated with IR-induced down regulation of NF-κB (p65) expression and increased activity of MnSOD (data not shown). They are likely the consequence of IR-induced alterations in cell redox equilibrium via increased ROS concentration. NF-κB triggered cycline D pathway is known to enhance cell cycle progression primarily through G1 but it may also regulate S phase transition in widely different cell types [14]. Thus, the down-regulated NF-κB may be responsible for HeLaS3 cell arrest in S phase observed in our study. In addition to that the S phase arrest in HeLaS3 cells may also be due to the increased MnSOD activity which is not coupled to the respective catalase (CAT) activity. Such situation leads to the increased cellular level of untoxified H_2O_2 which on its turn may be related to cell cycle arrest in S phase via Cip1 (p21) and cyclines D3 inhibition [15]. Irradiation of HeLaS3 cells also increased cell apoptosis in a dose-dependent manner. Since in our HeLaS3 study, IR did not induce expression of p53, increased apoptosis may be explained by the activity of alternative p53 independent pathways. One of the possible reasons could again be the down-regulation of anti-apoptotic protein NF-κB. Namely, although it is not clear how NF-κB regulates apoptotic pathways, its inhibition has been shown to enhance the sensitivity of tumours to apoptosis induced by gamma-IR [15].

The adjuvant effect of aloin was observed predominantly in the S phase of cell cycle, at all drug concentrations. It is known that aloin exerted its cytotoxicity through topoisomerase II (topo II) catalytic inhibition [16], enzyme required during DNA replication, chromosome dysfunction at mitosis, and essential for the survival of eukaryotic cells.

The synergic effect of aloin plus IR on cell viability and S phase cell cycle arrest indicated that both agents may share a common regulatory pathway. Since, HeLaS3 cells constitutively have enhanced activity of MnSOD, and since either IR or IR plus aloin caused its further elevation (which was not followed by the respective CAT activity) both agents caused H_2O_2 accu-

mulation. Increased concentration of this toxic ROS may lead to their synergism in cytotoxicity. High H_2O_2 concentration could also be the reason for down-regulation of CuZnSOD observed in either IR or IR plus aloin treated cells. Decreased CuZnSOD activity could contribute to decreased cell proliferation, emphasizing the importance of CuZnSOD in HeLaS3 cell growth [17].

Although, IR or aloin alone increased subG0/G1 peak, their synergic effect on cell apoptosis was not observed. This result indicates that the mechanism of apoptosis induction by IR and aloin are probably different. Due to that, simultaneous cell damage by both agents could compromise cell capacity to conduct programmed cell death by apoptosis, and instead may lead to the synergic cytotoxic cell death by necrosis. The synergism of IR plus aloin induced cell cytotoxicity is reflected in reduction of IC_{50} dose to 2 Gy by 60 µM aloin.

CONCLUSION

The adjuvant effect of aloin in irradiated HeLaS3 cells is reflected in the reduction of IC_{50} cytotoxicity dose from 3.4 Gy to 2 Gy in the presence of 60 µM aloin. Its radiosensitizing effect is achieved through up-regulation of antioxidant enzyme Mn-superoxide dismutase activity leading to accumulation of toxic H_2O_2. This toxic reactive oxygen species, either directly or through down-regulation of CuZn-superoxid dismutase activity, causes decrease in cell proliferation. Ionizing radiation and aloin alone, or in combination are shown to cause perturbation of HeLaS3 cell-cycle, and increase percentage of cells in S phase of cell cycle. While either of the agents applied alone cause programmed cell death by apoptosis, the simultaneous cell damage by both agents compromises HeLaS3 cell capacity to conduct this program, and instead led to the synergic cytotoxic cell death by necrosis.

ACKNOWLEDGEMENT

REFERENCES

1. P. Pisani, F. Bray, and D. M. Parkin, *Int. J. Cancer.* **97** (1), 72 (2002).

2. J. H. Maduro, E. Pras, P. H. B. Willemse, and E. G. H. de Vries, *Cancer Treatment Reviews.* **29** (6), 471 (2003).

3. P. J. Eifel, *Radiat Res.* **154** (3), 229 (2000).

4. A. Y. Esmat, S. M. El-Gerzawy, and A. Rafat, *Cancer Biology and Therapy.* **4** (1), 108 (2005).

5. G. Powis, In: *Metabolism and action of Anti-cancer drugs* (Eds. Powis, G., and Prough, R.A. Taylor and Francis, London 1987).

6. M. Scheffner, B. A. Werness, J. M. Huibregtse, A. J. Levine, and P. M. Howley, *Cell.* **63** (6), 1129 (1990).

7. P. Amstad, R. Moret, and P. Cerutti, *J. Biol. Chem.* **269** (3), 1606 (1994).

8. L. A. Ridnour, T.D. Oberley , and L. W. Oberley, *Antioxid Redox Signal.* **6** (3), 501 (2004).

9. J. J. Li, L. W. Oberley, M. Fan and N. H. Colburn, FASEB J. **12** (15), 1713 (1998).

10. A. Nićiforović, B. Zarić, A. Dakić, N. Tisma, and M. B. Radojčić, *Jugoslov. Med. Biohem.* 23 (2), 135 (2004).

11. A. Niciforovic, M. Adzic, S. D. Spasic, M. B. Radojcic submitted to *J. Serb. Chem. Soc.*

12. A. Niciforovic, M. Adzic, M. Spasic, M. B. Radojcic, submitted to *Canc. Biol. Ther.*

13. F. Ianzini and M. A. Mackey, *Int. J. Radiat. Biol.* **72** (4), 409 (1997).

14. D. Joyce, C. Albanese, J. Steer, and M. Fu, B. Bouzahzah, and R.G. Pestell, *Cytokine & Growth Factor Rev.* **12** (1), 73 (2001).

15. S. K. Manna, H. J. Zhang, T. Y. Larry, W. Oberley, and B. B. Aggarwa, *The Journal of Biological Chemistry.* **273** (21), 13245 (1998).

16. A. Esmat, C. Tomasetto, and M. Rio, *Cancer Biol. Ther.* **5** (1), 97 (2006).

17. T. T. Huang, M. Yasunami, E. J. Carlson, A. M. Gillespie, A. G. Reaume, E. K. Hoffman, P. H. Chan, R. W. Scott, and C. J. Epstein, *Arch. Biochem. Biophys.* **344** (2), 424 (1997).

=========== BIOPHYSICAL CHEMISTRY ===========

HTB140 MELANOMA CELLS UNDER PROTON IRRADIATION AND/OR ALKYLATING AGENTS

© 2007 L. Korićanac*, I. Petrović*, G. Privitera**, G. Cuttone***, A. Ristić-Fira*

*Vinca Institute of Nuclear Sciences, P.O.Box 522, Belgrade, Serbia
**Institute of Radiology and Radiation Oncology, University of Catania, Italy
***Istituto Nazionale di Fizica Nucleare, LNS, Catania, Italy
E-mail: aristic@vin.bg.ac.yu

Abstract – Chemoresistance is a major problem in the treatment of malignant melanoma. The mainstay of treatment for melanoma is DNA-alkylating agent dacarbazine (DTIC). Fotemustine (FM), member of chloro-ethylnitrosourea group of alkylating agents, also has demonstrated significant antitumoral effects in malignant melanoma. However, intrinsic and acquired resistance of melanoma limits clinical application of these drugs. Melanomas are also extremely radioresistant. With the objective to enhance growth inhibition of melanoma cells, combined treatments of FM or DTIC with proton irradiation, were investigated. These effects were studied on HTB140 melanoma cell viability and proliferation. Cells exposed to treatment with FM and protons have shown inhibition of cell growth, and significant reduction of proliferation capacity, compared to single irradiation or drug treatment. Treatment with DTIC and protons has shown improved growth inhibition compare to appropriate single drug treatment while the effects of single proton irradiation have been the most pronounced.

Malignant melanoma is the most aggressive form of human skin cancer, and its incidence is increasing more rapidly than in any malignancy, representing around 2% of all cancers in the USA and Europe [1]. Metastatic disease is practically incurable with short median survival of 6 to 9 months. Prognoses of advanced melanoma are generally poor, because this tumor commonly exhibits intrinsic or acquired resistance to chemotherapy [2].

Chemotherapy with alkylating agents is considered the most efficient treatment in malignant melanoma, but with low response rates being less than 25% for all agents [3]. Biological effects differ strongly among the various alkylating agents. The activity of these chemotherapeutic compounds depends primarily on their capacity to transfer alkyl groups, such as methyl, ethyl or chloroethyl, to DNA [4]. Dacarbazine, DNA-methylating drug, has become the standard chemotherapy for metastatic melanoma with usually partial tumor response, which lasts only for a few months. Other tested agents, including platinum analogues, vinca alkalloids, nitrosoureas and taxanes, did not have as good response rate as dacarbazine [2]. Fotemustine is a member of the chloroethylnitrosourea class of alkylating agents, which gave encouraging responses in phase I and II drug trials for a number of tumor types, particularly metastatic melanoma [5]. However, toxicity and drug resistance limit clinical efficiency of all alkylating agents used in chemotherapy, which is the principal reason for the failure of anti-cancer therapy [6]. Although various combined chemotherapeutic protocols increase response rates in some clinical cases, they also increase toxicity exhibiting insignificant response duration or survival benefit [7].

However, some forms of specially localized melanoma tumors, such as uveal melanoma and other eye tumors are curable to a certain extent by protons [8]. Proton irradiation offers several advantages over conventional radiotherapy, mainly delivering a uniform radiation dose to the entire tumor volume, thus causing minimal radiation damage to the surrounding normal tissue. These advantages are based on physical properties of proton beam, such as well defined range, small lateral scattering and especially, high energy deposition, at the precisely controlled position, just before the end of the range, known as Bragg peak. To treat malignant tumors with uniform dose of protons Bragg peak, initialy being only a few milimeters wide, is spread-out by modifaing proton energy. This energy modulation results in superposition of a number of monoenergetic proton beams of closely spread energies [9].

In order to find new ways to modify and improve therapeutic protocols the aim of this study was to contribute to investigations of combined treatments of either DTIC or FM and proton irradiation on the human melanoma cell growth *in vitro*.

MATERIALS AND METHODS

Cell culture and experimental conditions. HTB140 human melanoma cells were maintained as monolayer in RPMI 1640 medium supplemented with 10% fetal calf serum, penicillin/streptomycin and L-glutamine at 37°C in humidified atmosphere with 5% CO_2. For single drug treatment cells were plated in a 96-well assay plate (3×10^3 cells/well) and 24 h later were treated with increasing concentrations of fotemustine (FM, Ital farmaco S.p.A., Milano, Italy) or dacarbazine (DTIC,

Aventis Pharma S.p.A., Milano, Italy), ranging from 0.05–2 mM. Cell viability and cell proliferation assays were assessed 48 h after drug administration.

For the analysis of the combined effects of FM or DTIC (100, 250 μM) and proton irradiation cells were treated 24 h after seeding and were grown for additional 24 h, when they were irradiated with protons. Proton irradiations were performed within the spread-out Bragg peak (SOBP) of the 62 MeV proton beam, produced by the superconducting cyclotron at the CATANA (Centro di Adro Terapia e Applicazzioni Nucleari Avanzati) facility at INFN – LNS, Italy. Delivered single doses were 12 and 16 Gy, at dose rate of 15 Gy/min. Irradiation position in the middle of SOBP was simulated by interposing 16.3 mm thick Perspex plate (Polymethyl methacrylate – PMMA) between the final collimator and cell monolayer, thus obtaining corresponding relative dose of $99.42 \pm 0.58\%$, with the mean energy of protons 34.88 ± 2.15 MeV. Reference dosimetry was performed by using plane-parallel PTW 34045 Markus ionization chamber calibrated according to IAEA code of practice [10, 11]. Immediately after irradiation cells were replated at 3×10^3 cells per well in 96 – well plates and grown for further 7 days, when cell viability and cell proliferation assays were performed. Effects of combined treatment were compared to corresponding single drug treatments or proton irradiations.

Viability assays. In the preliminary experiments cell viability was determined by the MTT assay (Roche Diagnostics GmbH, Mannheim, Germany), which is based on the ability of viable cells to reduce 3-(4,5-dimethylthiazol-2-y1)-2,5-diphenyltetrazolium bromide (MTT) into blue-purple formazan crystals. The assay was performed according to manufactures' procedure and compared with results obtained by the other colorimetric method, sulforhodamine B (SRB) assay, based on quantifying total protein content of viable cells and performed according to the method of Skehan et al. [12]. The absorbance was measured using microplate reader (Victor, Wallac) at 550 nm.

Proliferation assay. Proliferative activity of cells was monitored by quantification of 5'-bromo-2'-deoxyuridine (BrdU)-incorporation into the genomic DNA during cell growth. DNA synthesis was assessed by a colorimetric cell proliferation ELISA assay (Roche Diagnostics GmbH, Mannheim, Germany) according to the manufacturer's instructions. The absorbance was analyzed using microplate reader (Victor, Wallac) at 450 nm.

Statistical analysis. Quadruplicate measurements were made during each experiment, and all experiments were repeated at least twice. Independent Student's t-test was performed to assess the significance of differences among all analysed experimental groups. The level of significance was set at $p < 0.05$. Results were presented as the Mean $\pm$ SD (standard deviation).

RESULTS AND DISCUSSION

Effects of FM and DTIC on cell viability. Cell viability after single treatment with FM or DTIC was analyzed at 6, 24, 48, 72, 96 h and 7 days using MTT and SRB assays (data not presented). Cells were treated with increasing concentrations of drugs, ranging from 0.05 to 2 mM. The best inhibitory effects with both drugs were obtained 48 h after treatment. Analyzis of chemosensitivity using MTT assay has shown that only 2mM DTIC significantly influens cell viability producing high level of cell inactivation. When estimated by SRB, cell number was significantly reduced after DTIC treatment in the whole range of doses applied. Significant cell growth inhibition was also obtained after 0.1–2 mM FM treatment, as estimated by SRB assay. These results have also shown that MTT is less sensitive method for studing HTB140 melanoma chemosensitivity than SRB. They are in agreement with literature data sugesting that SRB showes better linearity and higher sensitivity than tetrazolium-based assays, including MTT [13]. Based on these results, in following experiments, cell viability after combined treatments was evaluated using SRB assay.

Effects of combined treatment with FM or DTIC and protons on cell viability and cell proliferation. Concentrations of 100 and 250 μM drugs were chosen for analysis of combined treatment of drugs and protons. These concentrations were close to 50% growth inhibition concentration (IC_{50}). Results obtained with FM are consistent with those previously reported in literature. Similar IC_{50} were obtained for CALL77 (90 μM) and A375 human melanoma cells (220 μM) [14] as well as for B16/F10 mouse melanoma cells [15]. Significantly higher IC_{50} were obtained for SK-MEL-1 and SK-MEL-28 melanoma cells, being 930 and 774 μM respectively [15]. Evaluated IC_{50} values for DTIC in our experiments were also close to those reported for HeLa MR cells [16] and G361 human melanoma cells [17].

HTB140 melanoma cells have shown very high level of radio resistance with surviving fraction at 2 Gy proton irradiation (SF2) being 0.931 ± 0.006 [18]. In this study cells were irradiated with 12 and 16 Gy protons, which produce near 50% inhibition of HTB140 cells [18]. Doses of 12 and 16 Gy, at the dose rate of 15 Gy/min are in the range of those commonly used in proton therapy of eye melanoma [11].

In previous experiments, combined treatments with FM or DTIC and protons on HTB140 human melanoma cell viability were examined 48 h after irradiation [19]. This experimental set up was appropriate for the evaluation of the effects of drug treatment. Data obtained in these experiments did not show significant changes of cell viability as compared to each single treatment. Therefore, in our present study, combined treatments of tested drugs and protons were estimated 7 days after irradiation. Chosen time point is appropriate for evaluation of radiobiological survival, i.e. sur-
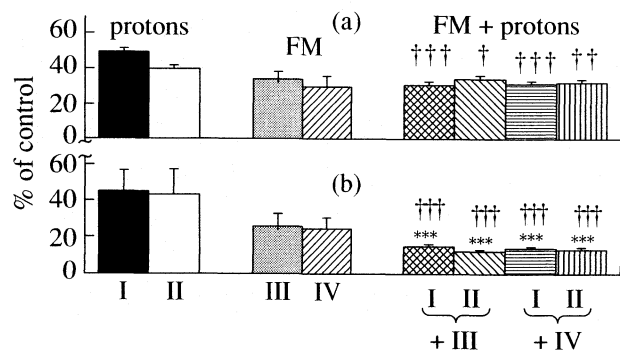
Fig. 1. Viability and cell proliferation of HTB140 cells estimated by SRB (a) and BrdU (b) assay respectively after single and combined treatments with FM and protons. Applied irradiation doses were 12 (I) and 16 Gy (II), while drug concentrations were 100 (III) and 250 μM IV); * – combined treatments vs. single drug treatment, † – combined treatments vs. proton irradiation); $0.01 < p < 0.05$ (*, †), $0.001 < p < 0.01$ (**, ††), $p < 0.001$ (***, †††).

Fig. 2. Viability and cell proliferation of HTB140 cells estimated by SRB (a) and BrdU (b) assay respectively after single and combined treatments with DTIC and protons. Notes see Fig. 1.

vival after at least six doubling times following irradiation.

Obtained results implicated that cell viability and cell proliferation of HTB140 cells exposed to single FM treatment or irradiation, as well as combined treatments with FM and protons, were significantly reduced, as compared to untreated control ($p < 0.001$). Irradiated cells, pretreated with FM have shown increased cell growth inhibition, as compared to single proton irradiation. Treatments with 100 or 250 μM FM and 12 Gy protons have shown very high level of statistical significance of growth inhibition, as compared to single 12 Gy proton irradiation ($p < 0.001$ for both drug concentrations). Combined treatments of FM with 16 Gy protons have also shown significant, drug concentration dependent growth inhibition, compared to adequate single proton irradiation ($p < 0.05$ for 100 μM FM, $p < 0.01$ for 250 μM FM). Effects of FM and protons on cell viability were not significantly improved, regarding FM treatment for both analyzed concentrations (Fig. 1a). However, proliferation of these cells is significantly inhibited, comparing to relevant single drug treatments ($p < 0.001$ for all combined treatments) and adequate doses of protons ($p < 0.001$ for all combined treatments) (Fig. 1b).

Viability of HTB140 cells after single DTIC treatment did not decrease, as compared to untreated control. Cells exposed to both DTIC and protons, have shown significant growth inhibition when compare to untreated control, as well as to relevant single DTIC treatment ($p < 0.001$ for all combined treatments). However, cell viability after combined treatment was increased when comparing the evaluated data with those obtained for single proton irradiation ($p < 0.001$ for all combined treatments) (Fig. 2a).
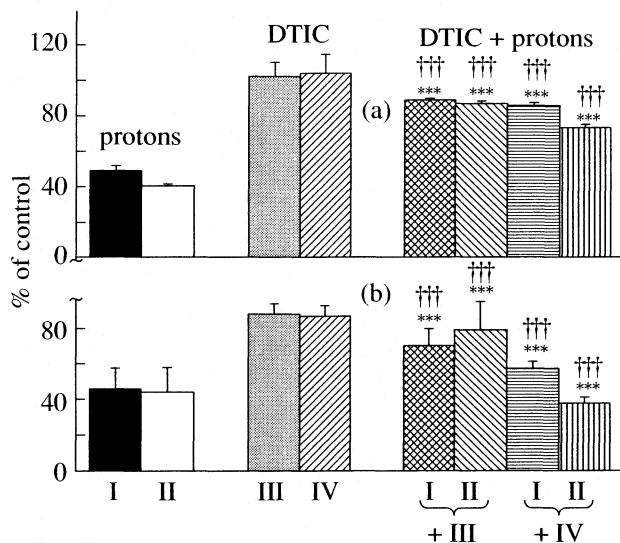
Proliferation capacity of treated cells is significantly reduced for all analyzed single and combined treatments with DTIC, when comparing to untreated control. Effects of treatment with both DTIC and protons on cell proliferation were more pronounced than corresponding effects of single DTIC application ($p < 0.001$ for all analyzed samples). However, cells exposed to combined treatment have shown weaker inhibition of proliferation than cells that were only irradiated with protons. When irradiated with 12 Gy, cells pretreated with 100 or 250 μM DTIC have shown increased proliferation capacity as compared to those only irradiated with 12 Gy protons ($p < 0.05$). Cells irradiated with 16 Gy, pretreated with 100 μM DTIC also have shown increased proliferation capacity, as compared to relevant single proton irradiation ($p < 0.01$). Treatment with 250 μM DTIC followed by irradiation with 16 Gy protons has shown proliferation level in the range of single 16 Gy proton irradiation ($p > 0.05$) (Fig. 2b).

This relatively weak effect of combined treatment with DTIC and protons on cell growth inhibition and cell proliferation might be explained through the activation of repair mechanism after DTIC treatment, because expression of DNA repair protein O^6-alkylguanine-DNA-alkyltransferase is inducible by DNA damaging agents, such as DTIC and ionizing radiation [20].

CONCLUSION

Obtained results have shown that FM and protons significantly affected HTB140 cell viability and proliferation, while combined treatment with DTIC and protons improved inhibition of cell viability and proliferation, compared to single DTIC treatment, not reaching inactivation level induced by proton irradiation.

REFERENCES

1. M. B. Atkins, The treatment of metastatic melanoma with chemotherapy and biologics. Curr. Opin. Oncol. **9(2)**, 205–213 (1997)

2. D. Bafaloukos, D. Tsoutsos, H. Kalofonos, S. Chalkidou, P. Panagiotou, E. Linardou, E. Briassoulis, E. Efstathiou, A. Polyzos, G. Fountzilas, C. Christodoulou, C. Kouroussis, T. Iconomou and H. Gogas, Temozolomide and cisplatin versus temozolomide in patients with advanced melanoma: a randomized phase II study of the Hellenic Cooperative Oncology Group, Ann. Oncol. **16**, 950–957 (2005).

3. R. M. MacKie, Melanoma and the dermatologist in the third millennium, Arch. Dermatol. **136**, 71–73 (2000).

4. B. J. Sanderson and A. J. Shield, Mutagenic damage to mammalian cells by therapeutic alkylating agents, Mutat. Res. **355**, 41–57 (1996).

5. M. T. Hayes, J. Bartley, P. G. Parsons, G. K. Eaglesham and A. S. Prakash, Mechanism of action of fotemustine, a new chloroethylnitrosourea anticancer agent: evidence for the formation of two DNA-reactive intermediates contributing to cytotoxicity, Biochemistry. **36**, 10646–10654 (1997).

6. M. Christmann, M. Pick, H. Lage, D. Schadendorf and B. Kaina, Acquired resistance of melanoma cells to the antineoplastic agent fotemustine is caused by reactivation of the DNA repair gene MGMT, Int. J. Cancer. **92**, 123–129 (2001).

7. S. M. Lee, D. C. Betticher and N. Thatcher, Melanoma: chemotherapy, Br Med. Bull. **51**, 609–630 (1995).

8. L. Kodjikian, P. Roy, F. Rouberol, J. G. Garweg, P. Chauvel, L. Manon, B. Jean-Louis, R. E. Little, A. J. Sasco and J. D. Grange, Survival after proton-beam irradiation of uveal melanomas, Am. J. Ophthalmol. **137**, 1002–1010 (2004).

9. A. Ristić-Fira and I. Petrović, Efficiency of proton irradiation in killing malignant cells, Arch. Biol. Sci. **52 (3)**, 123–132 (2000).

10. IAEA Technical Report Series N. Absorbed dose determination in external beam radiotherapy: an international code of practice for dosimetry based on standards of absorbed dose to water. **398**, 135–150 (2000).

11. G. A. P. Cirrone, G. Cuttone, P. A. Lojacono, S. Lo Nigro, V. Mongelli, V. Patti, G. Privitera, L. Raffaele, D. Rifuggiato, M. G. Sabini, V. Salamone, C. Spatola and L. M. Valastro, A 62 MeV proton beam for the treatment of ocular melanoma at Laboratori Nazionali del Sud-INFN.IEEE Transactions on Nuclear Science **51 (3)**, 860–865 (2004).

12. P. Skehan, R. Storeng, D. Scudiero, A. Monks, J. McMahon, D. Vistica, J. T. Warren, H. Bokesch, S. Kenney and M. R. Boyd, New colorimetric cytotoxicity assay for anticancer-drug screening, J. Natl. Cancer Inst. **82**, 1107–1112 (1990).

13. K. T. Papazisis, G. D. Geromichalos, K. A. Dimitriadis and A. H. Kortsaris, Optimization of the sulforhodamine B colorimetric assay, J. Immunol. Methods. **208**, 151–158 (1997).

14. J. Y. Winum, J. L. Bouissiere, I. Passagne, A. Evrard, V. Montero, P. Cuq and J. L. Montero, Synthesis and biological evaluation of Fotemustine analogues on human melanoma cell lines, Eur. J. Med. Chem. **38**, 319–324 (2003).

15. J. Rodriguez-Vicente, V. Vicente-Ortega and M. Canteras-Jordana, The effects of different antineoplastic agents and of pretreatment by modulators on three melanoma lines, Cancer, **82**, 495–502 (1998).

16. M. Sanada, Y. Takagi, R. Ito and M. Sekiguchi, Killing and mutagenic actions of dacarbazine, a chemotherapeutic alkylating agent, on human and mouse cells: effects of Mgmt and Mlh1 mutations, DNA Repair (Amst), **3**, 413–420 (2004).

17. H. Shibuya, Y. Kato, M. Saito, T. Isobe, R. Tsuboi, M. Koga, H. Toyota and J. Mizuguchi, Induction of apoptosis and/or necrosis following exposure to antitumour agents in a melanoma cell line, probably through modulation of Bcl-2 family proteins, Melanoma Res. **13**, 457–464 (2003).

18. I. Petrović, A. Ristić-Fira, D. Todorović, L. Valastro, P. Cirrone and G. Cuttone, Radiobiological analysis of human melanoma cells on the 62 MeV CATANA proton beam, Int. J. Radiat. Biol. **82**, 251–265 (2006).

19. I. Petrović, L. Korićanac, D. Todorović, A. Ristić-Fira, L. Valastro, G. Privitera and G. Cuttone, Viability of a human melanoma cell after single and combined treatment with fotemustine, dacarbazine and proton irradiation, Ann. N.Y. Acad. Sci. **1095**, 154–164 (2007).

20. J. A. Rafferty, A. R. Clarke, D. Sellappan, M. S. Koref, I. M. Frayling and G. P. Margison, Induction of murine O^6-alkylguanine-DNA-alkyltransferase in response to ionising radiation is p53 gene dose dependent, Oncogene **12**, 693–697 (1996).

OTHER PROBLEMS
OF PHYSICAL CHEMISTRY

STUDY OF THE DISPERSITY OF IRON OXIDE
AND IRON OXIDE-NOBLE METAL (Me = Pd, Pt) SUPPORTED SYSTEMS

© 2007   Z. P. Cherkezova-Zheleva*, M. G. Shopska*, J. B. Krstić**, D. M. Jovanović**,
I. G. Mitov*, G. B. Kadinov*

*Institute of Catalysis, Bulgarian Academy of Sciences, Acad. G. Bonchev St., Block 11, 1113 Sofia, Bulgaria
**IChTM-Center of Catalysis, Njegoseva 12, 11000 Belgrade, Republic of Serbia
E-mail: zzhel@ic.bas.bg

Abstract – Samples of one (Fe) and two-component (Fe–Pd and Fe–Pt) catalysts were prepared by incipient wetness impregnation of four different supports: TiO_2 (anatase), γ-Al_2O_3, activated carbon and diatomite. The chosen synthesis conditions resulted in formation of nanosized supported phase – iron oxide (in one-component samples) or iron oxide-noble metal (in two-component ones). Different agglomeration degree of this phase was obtained as a result of thermal treatment. Ultradisperse size of supported phase was kept in some samples, while a process of partial agglomeration occurred in the others giving rise to nearly bidisperse (ultra- and highdisperse) supported particles. The different texture of the used supports and their chemical composition are the reasons for different stability of nanosized supported phases. The samples were tested as heterogeneous catalysts in total benzene oxidation reaction.

The morphology and valence band structure of nanosized (1–10 nm) metal and metal oxide particles differ fundamentally from those of large particles in terms of short-range ordering [1–5]. Their catalytic activity and selectivity, based upon these new magnetic, optic, electric, and other properties, can be changed due to the critically small size. Thus an enhanced catalytic activity and selectivity in hydrocarbons oxidation is expected from the nanosized metal/metal oxide supported particles. As far as iron oxide based systems are concerned, the formation of highly active sites is associated with the formation of highly dispersed iron oxide because of the strong iron-support interaction [6]. Nowadays, the research interest is focused on deeper look insight the preparation techniques for highly active and selective catalysts, as well as into the way to stabilize this highly disperse and highly active nanosized phase.

On the other hand, the emission levels of volatile and semi-volatile organic compounds such as benzene, formaldehyde and polycyclic aromatic hydrocarbons in the air are under strict legislation and control in many countries [7, 8]. Therefore the complete hydrocarbon oxidation is of great importance for the environmental protection. The investigation of transition metal oxide-noble metal supported catalysts is a question of theoretical and practical interest, because of the expected synergetic effect between the components leading to an improvement of their catalytic performance in the hydrocarbon oxidation due to formation of such nanosized metal/metal oxide supported particles.

The main factors for the preparation of high dispersity and stable active phase are the method and the conditions for precursor deposition, calcination, reduction, support pre-treatment, etc. The impregnation is a clas-

sical preparation method, but it has unused possibilities to prepare active phases in nanosized region. Because of its simplicity and accessibility the method is not in largely substituted by new techniques – like laser ablation, "ion assisted" preparation (sol/gel techniques, sol precursors, zeolite encaged metal particles, etc.).

The aim of the present study was to investigate the influence of support characteristics and thermal treatment on the active phase dispersity and its stability, in order to obtain different catalytic properties of supported active phase.

EXPERIMENTAL

Sample Preparation. Four different supports were used – TiO_2 (anatase, BDH Chemical Ltd., England), γ-Al_2O_3 (type 20-1/83P, G-3, Poland), activated carbon (NORIT PKDA, The Netherlands) and diatomite. The used diatomite support is a natural substance (Barosevac, the "Kolubara" Coal Basin – field B, Lazarevac, Serbia). The crude diatomite has relatively high humidity level and is preliminary ground, chemically (with an aqueous solution of HCl) and thermally (at 1073 K) treated in order to obtain an activated support before catalyst synthesis. The chemical composition (wt. %) of the diatomite after activation is: 93.07% SiO_2, 3.87% Al_2O_3, 0.56% Fe_2O_3, 0.59% CaO, 0.80% MgO, 0.05% Na_2O, 0.56% K_2O.

The fraction of supports with particle size 0.63–0.8 mm is used. The catalysts were prepared by incipient wetness impregnation of the supports with aqueous solutions of $Fe(NO_3)_3 \cdot 9H_2O$ and $Pd(NO_3)_2 \cdot 2H_2O$ or $(NH_3)_4PtCl_2 \cdot H_2O$, respectively. The samples were dried at 343 K in vacuum, heated in vacuum for 3 hours

Table 1. Physical characteristics of supports

Parameters	TiO$_2$	Diatomite	γ-Al$_2$O$_3$	AC
s_{BET}, m^2/g	11.9	16.8	303.9	923.4
V_{tot}, cm^3/g	0.054	0.102	0.618	0.750
V_{mic}, cm^3/g	0.004	0.006	–	0.400
d_0, nm	UD	2–4 (33.6%)	3–6 (69.5%)	<3 (47.0%)
		4–6 (14.2%)	6–10 (21.4%)	3–6 (34.8%)

Notes: AC – activated carbon, d_0 – predominant pore size, UD – uniform distribution.

at 493 K (as prepared samples) and calcined in air for 3 hours at 713 K (thermally treated samples). The metal loading was 8 wt. % Fe and 0.7 wt. % noble metal.

Support characterization. The total pore volume of all samples, were determined by nitrogen adsorption/desorption isotherms at 77 K using the Sorptomatic 1990 apparatus (ThermoQuest, CE Instruments). The specific surface area of samples s_{BET}, was calculated according to Brunauer–Emmett–Teller method from the linear part of the nitrogen isotherms [9]. The pore size distribution for mesopores was calculated according to Barett–Joyned–Halenda (BJH) method [10, 11] from desorption branch of the isotherm. The micropore volume was calculated using Dubinin–Radushkevich equation [12].

Active phase composition. The chemical composition of the prepared systems was analyzed by atomic emission spectrometer (AES) with ICP, model 3410 (ARL, USA). The as prepared and calcinated samples were studied before and after catalytic tests by Moessbauer spectroscopy (MS), X-ray diffraction (XRD) and X-ray photoelectron spectroscopy (XPS).

MS measurements were carried out on Wissenschaftliche Elektronic GmbH instrument, operating in a constant acceleration mode (^{57}Co/Cr source, α-Fe standard). The following parameters of hyperfine interactions of spectral components were determined by computer fitting: isomer shift (*IS*), quadrupole splitting (*QS*), effective hyperfine magnetic field (H_{eff}), line widths (FWHM) and component relative weights (*G*).

XRD patterns were obtained on TUR M62 apparatus, HZG-4 goniometer with Bregg-Brentano geometry, CoK_α radiation and Fe filter. JCPDF data base was used for the phase identification [13].

XPS study was performed on ESCALAB-MkII spectrometer (VG Scientific), by unmonochromatized MgK_α radiation (1253.6 eV). The total instrumental resolution was 1.5 eV (measured from the Ag5$d_{5/2}$ line width). The energy scale was calibrated by the C1s line (285 eV).

Catalytic activity. The catalytic activity in total benzene oxidation was studied in a flow type glass reactor at atmospheric pressure in the temperature range 373–773 K.

Reaction mixture of C$_6$H$_6$, N$_2$ and air (2.88–3.57 mol/h C$_6$H$_6$) at a total flow rate of 7.2 l/h (120 ml/min) was used. Catalyst loading was about 140 mg. The reaction products were analyzed by a gas chromatograph Varian Model 3700 equipped with TCD ($T_{filament}$ = 353 K, T = = 333 K) and FID (T = 453 K) and 2 m Porapak Q (0.150–0.180 mm, Riedel-de Haën AG D-3016 Seelze 1) column operating at 443 K. Nitrogen (30 ml/min) was used as carrier gas, whereas benzene (Merck, for spectroscopy) was used for oxidation and calibration.

RESULTS AND DISCUSSION

The calculated values about s_{BET}, the total pore volume and the amount of predominant pore diameters for the used supports are presented in Table 1. Presented data shows differences between used supports. TiO$_2$ has smallest specific surface area, as well as smallest total pore volume of all tested supports. Compared to TiO$_2$, diatomite has similar specific surface area, but the total pore volume and the pore size distribution are significantly different. It is obvious that these differences are due to the existence of meso- and macropores in the diatomite. γ-Al$_2$O$_3$ is a typical mesoporous material. Up to 90% of total pore volume is in the mesoporous region and 80% of all pores have diameter in the range 3–10 nm. Activated carbon possess total pore volume comparable to γ-Al$_2$O$_3$. All the three pore types (micro-, meso- and macropores) are present.

The metal loading obtained by AES was in the range of 5.5–6.5% for the iron and 0.65–0.7% for the noble metal (palladium or platinum) in the studied catalysts.

The XRD patterns of all as prepared and calcined alumina- and titania-supported samples showed the characteristic pattern of the carrier only. The supported metal-oxide phase was X-ray amorphous, because of the small crystallite size. There was a difference in the XRD patterns of the samples supported on diatomite and activated carbon only. The samples, which are thermally treated (Figs. 1b and 2c), exposed the patterns of the support (for comparison see Fig. 1a and 2a) and broadened lines of low intensity, belonging to a highly dispersed iron oxide phase. This is a hematite phase (PDF#72-0469) in the case of diatomite supported sam-
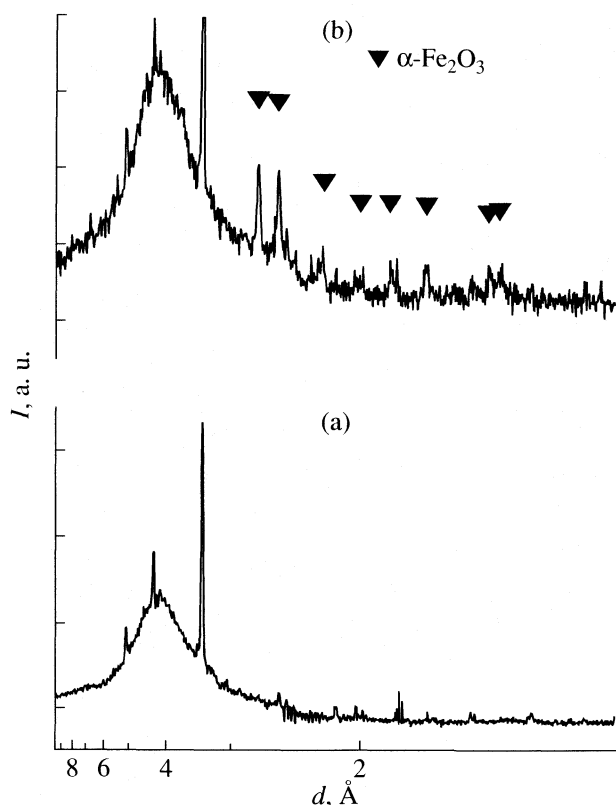
Fig. 1. XRD patterns of diatomite support (a) and 8% Fe/diatomite (b) after calcination at 713 K.
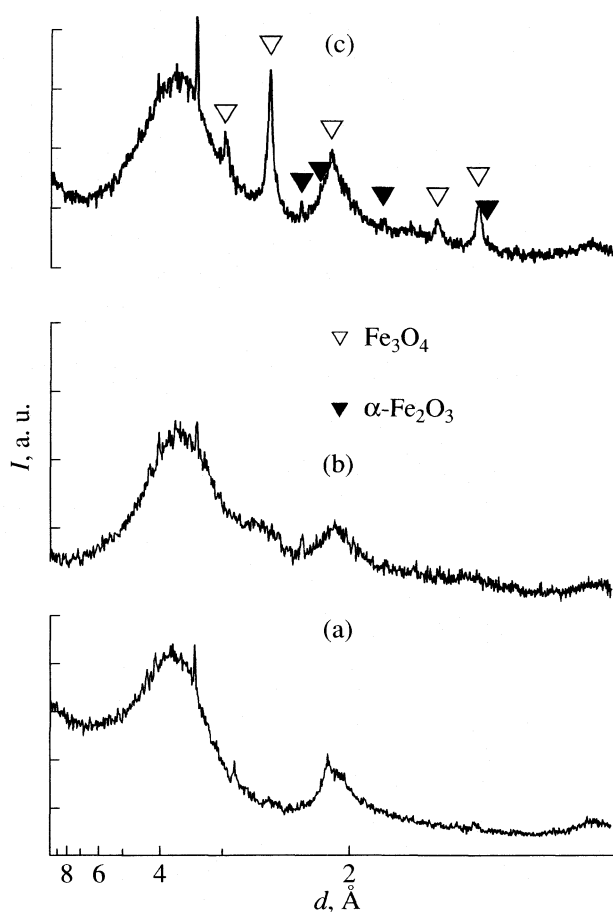
Fig. 2. XRD of activated carbon (a), 8% Fe/activated carbon (b) after heating in vacuum at 493 K (as prepared sample) and 8% Fe/active carbon after calcination at 713 K (c).

ples (Fig. 1b) or hematite (PDF#72-0469) and magnetite (PDF#82-1533) on the activated carbon supported ones (Fig. 2c). According to the Scherrer equation [14] the average crystallite size of hematite was calculated about 12 nm in the diatomite supported samples (Fig. 1b). In the samples supported on activated carbon (Fig. 2c) the particle size of α-Fe_2O_3 and Fe_3O_4 were about 12 and 14 nm, respectively.

There were no reflexes of any phases, characteristic for the respective noble metal in the XRD patterns.

The obtained Moessbauer spectra of the samples at various stages of preparation, thermal pre-treatment and after the catalytic test show the presence of ultradisperse iron oxide phase and its evolution in the course of treatment. The spectra include superposition of doublet lines or doublet and sextet part [15–18].

The experimentally obtained spectra of all as prepared samples (i.e. heated in vacuum for 3 hours at 493 K) have an optimal fit with two quadrupole doublets (Dbl.), regardless of the used support. The determined hyperfine parameters of two sets of doublet lines can be assigned to ultradisperse hematite-like α-Fe_2O_3 particles ($D < 10$ nm) with superparamagnetic (SPM) behaviour [1, 2, 19]. It is known that when the magnetic anisotropy barrier (KV), where K is anisotropy constant and V is the particle volume, is smaller or comparable to the average thermal energy (E_{th}) of the particles ($KV \leq E_{th}$), the

magnetic moment flips rapidly so that the effective moment during the time of measurement becomes zero. This causes the collapse of a six-line pattern to a superparamagnetic doublet. In this case core-shell model [19–21] can be applied to explain the presence of two components in quadrupole doublet. They belong to iron ions from the "core" and the interface ("shell layers") of nanoparticles. The doublet with $IS = 0.33$–0.34 mm/s and lower $QS = 0.61$–0.75 mm/s belongs to iron ions from the "core" of the particles. The doublet with $IS = 0.34$–0.35 mm/s and larger $QS = 1.01$–1.29 mm/s can be assigned to interface (from the "shell" layers) ferric ions. The lower symmetry in the environment of "surface" iron ions results in a change in the electric field gradient and therefore in a shift of the QS value. The obtained ratio of the relative weights of these two quadrupole doublets, corresponding to the "inner" and "outer" iron ions, is about 1 : 1 (50%/50%). Therefore, according to the used model, the hematite-like particle size is below 3–4 nm [21].

The ultradisperse iron oxide phase, supported on different carriers, shows different stability in the course of thermal treatment and catalytic test. The 3–4 nm particle

size of hematite-like phase, supported on the γ-Al_2O_3, does not change (see Table 2) [15]. The appearance of a sextet component (Sxt.) in the spectra of thermally treated samples, supported on TiO_2, activated carbon and diatomite shows partial agglomeration of iron oxide particles (Table 2) [16–18]. The calculated hyperfine parameters of this sextet part of the spectrum of the TiO_2 and diatomite supported samples belong to α-Fe_2O_3 phase ($IS = 0.35$ mm/s, $QS = -0.10$ mm/s, $H_{eff} = 498$–507 kOe). However, the sextet part of Moessbauer spectra of activated carbon supported samples includes a number of components. One of the sextuplets has hyperfine parameters ($IS = 0.36$ mm/s, $QS = -0.10$ mm/s, $H_{eff} = 482$ kOe), which are characteristic for the presence of α-Fe_2O_3 phase. The other two sextuplets ($IS_1 = 0.26$ mm/s, $QS_1 = 0$, $H_{eff1} = 466$ kOe and $IS_2 = 0.64$ mm/s, $QS_2 = 0$, $H_{eff2} = 435$ kOe) belong to Fe_3O_4 phase. Reduction of the hyperfine effective magnetic field values of all sextet components in comparison to the bulk ones is observed [14, 22]. It can be understood in terms of collective magnetic excitations, where the thermal energy is comparable with the total magnetic anisotropy energy of the particle. The thermal energy is not enough to flip the magnetic moments around the easy axis and hence does not lead to superparamagnetism but causes the moments to oscillate around the easy axis, giving rise to a reduced hyperfine effective magnetic field [23, 24].

Therefore, different agglomeration degree of the active phase was obtained as a result of the thermal treatment. The ultradisperse size of supported phase (about 3–4 nm) was preserved in alumina supported samples. The process of partial agglomeration resulted in nearly bidisperse (ultra- and highdisperse) active phase in the case of TiO_2 and diatomite supported samples. The evidences of this are the relatively narrow lines of spectral components (low values of FWHM – about 0.35–0.45 mm/s). Along with the particles of $D \approx 3$–4 nm, particles with size about 10–20 nm exist, too. On the contrary, the activated carbon supported samples show poly-disperse particle size distribution of the active phase in thermally treated samples.

The crystallite size in the iron oxide phase decreases in the order: Fe sample > Fe–Pt sample > Fe–Pd sample for all studied supports. The agglomeration degree in the samples decreases in the same order. This mode of distribution could be explained with the presence of hematite-like ultradisperse particles in the pores and on the external surface. The latter part could agglomerate with the increase of temperature. The iron oxide particles in Fe and Fe–Pt samples are both in the pores and on the external surface of the support, whereas in Fe–Pd samples they are predominantly in the pores. Another reason for the different ratio between ultradisperse and highdisperse particles in the samples can be the presence of the noble metal (Pd or Pt) and/or the nature of the used noble metal precursors [25].

Table 2. Size distribution of iron oxide particles in thermally treated samples (i.e. after agglomeration) according to Moessbauer data

Sample	Components	D, nm	G, %
γ-Al_2O_3			
Fe	I	3–4	100
Fe–Pd	I	3–4	100
Fe–Pt	I	3–4	100
TiO_2			
Fe	I	3–4	72
	II	10–20	18
Fe–Pd	I	3–4	90
	II	10–20	10
Fe–Pt	I	3–4	80
	II	10–20	20
Diatomite			
Fe	I	3–4	49
	II	10–20	51
Fe–Pd	I	3–4	94
	II	10–20	6
Fe–Pt	I	3–4	52
	II	10–20	48
Activated carbon			
Fe	I	3–4	34
	III	3–6	12
	IV	6–10	17
	II	10–20	7
	V	10–20	30
Fe–Pd	I	3–4	85
	V	10–20	15
Fe–Pt	I	3–4	76
	V	10–20	24

Notes: D – particle size; I – Dbl. – hematite-like, II – Sxt. = α-Fe_2O_3, III – Dbl. – magnetite-like, IV – Sxt. – Fe–O, V – Sxt. = Fe_3O_4.

The mean effective particle size was calculated from the detailed XPS spectra, according to the Kirchoff–Moulijne model [26, 27]. The size of iron oxide particles was about 3–9 nm. From the detailed XPS

spectra the size of noble metal particles was calculate, too: for platinum it was about 1.2–1.8 nm and about 0.7–1.4 nm for palladium. In the course of thermal treatment and the catalytic test, the initial high dispersity of the samples slightly decreased in the case of TiO_2, activated carbon and diatomite support, but it was not significantly changed in the case of Al_2O_3 support [28, 29].

The results about particle sizes of iron oxide, obtained by the above mentioned methods, are in very good conformity.

Most of the samples were tested as catalysts in the process of complete oxidation of benzene [15, 17, 30]. Low catalytic activity was observed for the catalysts containing iron oxide only. The calcination at 713 K of these samples had slightly negative influence on their catalytic performance. To evaluate the effect of nanosized iron oxide on the oxidation process several samples were prepared by mixing of Fe_2O_3 and respective support. The general trend was that the catalysts containing nanosized particles worked at lower reaction temperature – about 50 degrees. Therefore, the higher activity was probably due to the higher dispersion of the active phase.

During the catalytic test, the two-component samples exhibited the so called "ignition of the reaction" behaviour that was realized in the temperature interval 500–630 K. Most of systems showed nearly 100% benzene conversion in the temperature interval 530–570 K. In general, the procedure of thermal pretreatment had not significant influence on the catalyst activity. The obtained results allow us to suppose that the catalytic activity in this case is due to the noble metal, mainly. However, both components have stabilizing effect on each other as far as the particle size is concerned.

CONCLUSIONS

Supported catalysts containing nanosized iron oxide particles and noble metal Pt or Pd particles were synthesized by wetness impregnation. No data have been obtained for appearance of mixed phases between the active phase and the support. However, influence of the chemical composition and dispersity of the used support on the catalytic behaviour of synthesized active phase has been observed, which results in different agglomeration degree of the supported iron oxide phase. Alumina-supported ultradisperse hematite-like particles do not change their size during thermal treatment. An agglomeration process occurs in the iron oxide phase on titania, diatomite and activated carbon giving rise to bi- or poly-disperse distribution of the particles size. The noble metal dispersion is not significantly changed after thermal treatment.

Catalytic tests for total benzene oxidation with one-component (iron oxide) samples containing supported nanosized active phase and the respective mechanical

mixtures of an active phase and a support reveal a positive effect of the high dispersity. A comparison of one- and two-component samples shows that the catalytic activity is due to the noble metals, mainly. Since the thermal pretreatment had no significant influence on the catalyst activity, a mutual stabilizing effect on the dispersion of the nanosized iron(III) oxide and the noble metal was supposed.

REFERENCES

1. I. P. Suzdalev, V. N. Buravtsev, Yu. V. Maksimov, A. A. Zharov, V. K. Imshennik, S. V. Novichikhin and V. V. Matveev, J. Nanoparticle Res. **5**, 485 (2003).
2. I. P. Suzdalev, V. N. Buravtsev, Yu. V. Maksimov, V. K. Imshennik, S. V. Novichikhin, V. V. Matveev and A. S. Plachinda, Ross. Khim. Zh. **45**, 66 (2001).
3. B. Bachiller-Baeza, A. Guerrero-Ruiz and I. Rodriguez-Ramos, Appl. Catal. A: General **192**, 289 (2000).
4. L. Guczi, G. Petë, A. Beck, and Z. Pàszti, Top. Catal. **29**, 129 (2004).
5. L. Guczi, Chem. Inform. **36**, 30 (2005).
6. G. Waychunas, C. Kim and J. Banfield, J. Nanoparticle Res. **7**, 409 (2005).
7. S. Kim, J. Hazardous Mater. **91**, 285 (2002).
8. A. Hinz, P.-O. Larsson, B. Skarman and A. Andersson, Appl. Catal. B: Env. **34**, 161 (2001).
9. F. Rouquerol, J. Rouquerol and K. Sing, *Adsorption by Powders and Porous Solids*, (Academic Press, London, 1999).
10. E. P. Barett, L. G. Joyner, P. P. Halenda, J. Am. Chem. Soc. **73**, 353 (1951).
11. A. Lecloux, J. P. Pirard, J. Colloid Interface Sci. **70**, 265 (1979).
12. M. M. Dubinin, *Progress in Surface and Membrane Science,* Vol. 9, (Academic Press, New York, 1975).
13. Powder Diffraction Files, Joint Committee on Powder Diffraction Standards, Philadelphia PA, USA, 1997.
14. U. Schwertmann and R. Cornell, *Iron Oxides in the Laboratory*, (Weinheim, New York–Basel–Cambridge, 1991).
15. Z. Cherkezova-Zheleva, M. Shopska, B. Kunev, I. Shtereva, G. Kadinov, I. Mitov, L. Petrov, in *"Nanosci. Nanotechnol."*, Vol 4 , (Heron Press, Sofia 2004), p. 101.
16. Z. Cherkezova-Zheleva, M. Shopska, B. Kunev, I. Mitov, G. Kadinov and L. Petrov, in: *"Physical Chemistry 2004"*, Vol. II, (Mrljes Print. & Publ. Comp., Belgrade, 2004), p. 478.
17. M. Shopska, Z. Cherkezova-Zheleva, B. Kunev, I. Shtereva, D. Jovanović, J. Krstić, Z. Mojović, Z. Vuković, G. Kadinov, I. Mitov, L. Petrov, Bulg. Chem. Commun. **37**, 178 (2005).

18. Z. Cherkezova-Zheleva, M. Shopska, J. Krstić, D. Jovanović, I. Mitov, G. Kadinov, in "*Nanosci. Nanotechnol.*", Vol. 7, (Heron Press, Sofia, 2007), in press.

19. A. Van der Kraan, Phys. Status Solidi A **18**, 215 (1973).

20. J. Dumesic and H. Topsoe, Adv. Catal. **26**, 122 (1977).

21. J. Niemantsverdriet and A. Van der Kraan, J. Phys. Chem. **89**, 67 (1985).

22. E. Murad, Hyperfine Interactions **117**, 39 (1998).

23. S. Mørup, J. Magn. Magn. Mater. **37**, 39 (1983).

24. C. Upadhyay, H. C. Verma and S. Anand, J. Appl. Phys. **95**, 5746 (2004).

25. A. Lecloux, J. P. Pirard, J. Colloid Interface Sci. **70**, 265 (1979).

26. Handbook of the Elements and Native Oxides, XPS International Inc., 1999.

27. J. Scofield, J. Electron Spectrosc. **8**, 129 (1976).

28. Z. Cherkezova-Zheleva, M. Shopska, G. Gouliev, I. Donchev, G. Kadinov, I. Mitov, L. Petrov, in "*Nanosci. Nanotechnol.*", Vol. 5, (Heron Press, Sofia, 2005), p. 148.

29. G. Gouliev, Z. Cherkezova-Zheleva, M. Shopska, B. Kunev, I. Mitov, G. Kadinov, L. Petrov, in "*Nanosci. Nanotechnol.*", Vol. 6, (Heron Press, Sofia, 2006), p. 172.

30. M. Shopska, Z. Cherkezova-Zheleva, I. Shtereva, B. Kunev, G. Kadinov, I. Mitov and L. Petrov, in: "*Physical Chemistry 2004*", Vol. II, (Mrljes Print. & Publ. Comp., Belgrade, 2004), p. 481.

УДК 541.15

NEURAL NETWORKS DATA ANALYSIS FOR CLASSIFICATION OF SOILS BASED ON THEIR RADIONUCLIDE CONTENT

© 2007   S. Dragović*, A. Onjia**

*Institute for the Application of Nuclear Energy – INEP, Banatska 31b, 11080 Belgrade, Serbia
**Vinča Institute of Nuclear Sciences, P.O. Box 522, 11001 Belgrade, Serbia
E-mail: sdragovic@inep.co.yu; onjia@vin.bg.ac.yu

Abstract – Artificial neural network (ANN) data analysis method was used to recognize and classify soils of unknown geographic origin. A total of 103 soil samples were differentiated into classes, according to regions in Serbia and Montenegro from which they were collected. Their radionuclide (^{226}Ra, ^{238}U, ^{235}U, ^{40}K, ^{134}Cs, ^{137}Cs, ^{232}Th and ^{7}Be) activities detected by gamma-ray spectrometry were then used as the inputs in ANN. Five different training algorithms with different numbers of samples in training sets were tested and compared, in order to find the one with the minimum root mean square error (RMSE). The best predictive power for the classification of soils from fifteen regions was achieved using a network with seven hidden layer nodes and 2500 training epochs, using the online back-propagation randomized training algorithm. With the optimized ANN, most soil samples not included in the ANN training data set were correctly classified at an average rate of 92%.

A number of analytical techniques and methods may be used in the classification of soil samples of different taxonomy and/or geographic origin [1]. In the last few years, concentration profiles of chemical substances in conjunction with pattern recognition methods have been widely employed to classify soils [2–7].

The use of artificial neural networks (ANNs) for pattern recognition has attracted considerable attention recently. ANN classifiers have some important advantages over other statistical methods. Whereas statistical classification techniques typically require prior information about the pattern distribution, neural network classifiers work well without any knowledge of the distribution [8–10]. ANNs have the ability to adapt automatically to new data using non-rigid assumptions about the underlying data distribution and build models without knowing the actual modeling function [11]. Unlike traditional statistical procedures, ANNs adjust themselves to available data and do not require any specification of the functional or distributional form of the population. Even though the topologies and algorithms of ANN may vary, they work as follows: pattern statistics are achieved from a set of training samples and then new patterns are classified on the basis of these statistics. ANNs are now widely used in soil science for the prediction of soil attributes and the probability of soil classes from environmental data, as well as for the classification of soils from different geographical regions [2–6]. In gamma-ray spectrometry ANNs have been used to identify radioactive isotopes automatically from their spectra, employing pattern recognition of the entire spectrum instead of analyzing individual peaks [12, 13], for optimization of experimental conditions [14], and for the quantitative spectrometry analysis [15, 16].

In this study ANNs were employed to classify soil samples based on their radionuclide contents determined by gamma-ray spectrometry. A predominant part of the radioactivity in soil is derived from the decay of the primordial radionuclides, ^{238}U, ^{232}Th and ^{40}K. Significant amounts of ^{137}Cs are also present in soil as a result of nuclear weapon tests and nuclear accidents. There are a few studies on employing the neural network approach to describe the correlation between locations and contamination [17]. The feasibility of using artificial neural networks as a method to predict soil origin based on its radionuclide content was examined here.

EXPERIMENTAL

Samples. Soil samples ($n = 103$) were collected from fifteen geographical regions of Serbia and Montenegro: 1 – Slatina ($n = 7$), 2 – Beljanica ($n = 6$), 3 – Željevica ($n = 6$), 4 – Kopaonik (n = 10), 5 – Avala ($n = 6$), 6 – Devojački Bunar ($n = 8$), 7 – Bukulja ($n = 8$), 8 – Kosmaj ($n = 7$), 9 – Stara Planina ($n = 5$), 10 – Surdulica ($n = 5$), 11 – Bogićevica ($n = 6$), 12 – Durmitor ($n = 8$), 13 – Kosovska Kamenica ($n = 7$), 14 – Kukavica ($n = 5$) and 15 – Loznica ($n = 9$).

Measuring setup. After grinding and drying, the soil samples were placed in 1L Marinelli beakers. The beakers were closed and sealed and the samples measured 4 weeks later, when an equilibrium between ^{226}Ra and ^{238}U was reached. Measurements were performed using an HPGe gamma-ray spectrometer [ORTEC-AMETEK model GEM 25 (34% relative efficiency and 1.65 keV FWHM for ^{60}Co at 1.33 MeV, 8192 channels)]. All samples were measured for 17 hours. The spectra

Table 1. Descriptive statistics of radionuclide activities (Bq/kg) in soil samples

Variable	Mean	SD	Min	Max	Medn.	Skwn	Krts
^{226}Ra	30.8	9.14	13.6	54.9	29.9	0.42	−0.45
^{238}U	29.7	9.42	14.6	53.4	30.2	0.44	−0.33
^{235}U	1.37	0.46	0.51	2.61	1.38	0.53	0.22
^{40}K	567	164	271	919	593	−0.17	−0.73
^{232}Th	40.7	13.5	18.3	83.4	39.7	1.20	2.18
^{134}Cs	0.09	0.07	0.02	0.26	0.05	0.91	−0.56
^{137}Cs	48.3	26.2	5.25	112	42.9	0.44	−0.39
^{7}Be	1.79	1.05	0.54	3.94	1.50	0.66	−0.91

Notes: SD – standard deviation, Min – minimum value, Max – maximum value, Medn. – median, Skwn – skewness, Krts – kurtosis.

obtained were processed using Gamma Vision 32 software, Version 5.3 (ORTEC, Oak Ridge, USA).

Artificial neural networks. The architecture of ANN models used in this study is a fully connected feed-forward system, in which the signals propagate from the input layer through the hidden layer to the output layer. A node thus receives signals via connections or weights from other nodes (or from the external world for the nodes of the input layer). The net input for a node j is given by

$$net_j = \sum_i w_{ji} o_i, \qquad (1)$$

where i represents the nodes in a previous layer, w_{ji} is the weight associated with the connection from node i to node j, and o_i is the output of node i. The output of a node is determined by a nonlinear transfer function and the net input of the node. A sigmoidal function is used as the transfer (activation) function in this application

$$o_j = f(net_j) = 1/\{1 + \exp[-(net_j + \theta_j)]\}, \qquad (2)$$

where θ is a bias term or threshold value of the node j responsible for accommodating nonzero offsets in the data [18].

One pass through the set of training patterns along with the updating of weights is called the cycle or epoch. In the testing phase, the trained neural network is fed by a separate set of data. In this phase, the neural network predictions (using the trained weights) are compared with the target output values. The neural network will produce almost instantaneous results of the outputs for practical inputs provided. Once the training and testing phases are found successful, the neural network can be put to use in practical applications. The root mean square error (RMSE) was used to estimate the success of the training process. It is computed as

$$RMSE = \left[\sum_{i=1}^{n} (d_i - o_i)/n\right]^{1/2} /x, \qquad (3)$$

where d_i is the desired output (experimental values) in the training or testing set, o_i is the actual output (ANN predicted values) in the training or testing set, n is the number of data in the training or testing set, and x is the average value of the desired output in the training or testing set.

Five different training algorithms were tested and compared: online backpropagation (OBP), online backpropagation randomized (OBPR), batch backpropagation (BBP), resilient propagation (RP), and quick propagation (QP) [19]. The idea of the back-propagation algorithms is to propagate the error back through the network and to adjust the weights of each layer as it propagates. OBP updates the weights after each pattern is presented to the network. In the OBPR algorithm, the order of input patterns is randomized prior to each epoch, which makes the learning process stochastic. In the BBP algorithm, weight updates occur after each epoch. RP is an adaptive learning rate method where weight updates are based only on the sign of the local gradients, not on their magnitude. Each weight has its own updated value, which varies with time. QP is a training method with a fixed learning rate that needs to be chosen to suit the problem.

RESULTS AND DISCUSSION

Basic statistics. Table 1 shows the activities (Bq/kg) of radionuclides in the analyzed soil samples. In general, radionuclide activities in these soils varied by a factor of up to 3–5 for ^{226}Ra, ^{238}U, ^{235}U, ^{40}K and ^{232}Th, 7 for ^{7}Be, 13 for ^{134}Cs, and 21 for ^{137}Cs. The standard deviation was the greatest for ^{40}K and the smallest for ^{134}Cs. The arithmetic mean and the standard deviation of the activities for all samples and locations were used to describe the central tendency and variation of the data (Table 1). The distribution parameters (skewness and kurtosis) indicated normal (Gaussian) distribution.

ANN architecture. The classifier used was a three-layer network architectured by an input layer consisting of the radionuclide activities in the soil samples, a hidden layer, and an output layer composed of regions the

Table 2. RMSE of test set predictions as a function of the training algorithm and the number of objects in training/testing set (N)

N	RMSE				
	OBP	OBPR	BBP	RP	QP
85/18	0.116	0.108	0.123	0.159	0.135
75/28	0.092	0.087	0.096	0.125	0.102
65/38	0.102	0.102	0.106	0.138	0.118
55/48	0.119	0.115	0.118	0.143	0.137
45/58	0.125	0.121	0.126	0.152	0.147
35/68	0.143	0.135	0.141	0.172	0.159
25/78	0.144	0.141	0.152	0.181	0.186

samples were collected from. The strategy used for the classification of soils was the so-called one-of-many encoding [20]. The output of the network was a multidimensional vector and each vectorial dimension class was assigned to a class. In the network training file, the class membership of a single item of data was coded in a numerical format assigning 1 to the belonging class and 0 to all the others. In the network testing file, the membership of an input data set was assigned to the class with the greatest network output.

Random selection within each region was applied as the division method for the selection of objects (training set) used for building the model. The advantage of this method is its simplicity and the property that a group of data randomly taken from a larger set retains the population distribution of the entire set [21]. The 103 objects were divided into the training and test

sets in seven different ways: 85 vs. 18, 75 vs. 28, 65 vs. 38, 55 vs. 48, 45 vs. 58, 35 vs. 68 and 25 vs. 78, respectively. The "leave-10%-out" method was applied for cross-validation. With this method, 10% of the data in the training set are not used to update the weights. Therefore, this 10% can be used as an indication of whether or not memorization is taking place. When an ANN memorizes the training data, it may produce acceptable results for the training data, but poor results when tested on unseen data.

Selection of the training algorithm. The RMSE for the prediction on the test set applying five training algorithms to different training sets are presented in Table 2. It can be seen that the OBPR training algorithm gave the lowest RMSE. Another trend also evident is an increase in RMSE with decrease in the number of objects in the training set. This is understandable, since the modeling area is more evenly covered when more data are used in the training set. On the other hand, the best model was not obtained with the largest training set (85 vs. 18) but with the next largest division, i.e. 75 vs. 28. When too many training data are presented to the network, it tends to learn the specific data set better than the general problem.

The differences in RMSE values within a training/testing set of fixed size cannot distinguish between the specific training algorithms in a significant manner. The greatest difference reached a factor of 1.5 (case 85/18; the best RMSE = 0.1080, the worst RMSE = = 0.1586), while the most homogenous RMSE values were obtained with the training set of 55 objects, where the best and the worst RMSE did not differ by more than 19%. This means that a thorough investigation for the proper selection of the training set size should be made as well as for the most suitable training algorithm.

ANN model optimization. The ANN model using the OBPR algorithm, which gave the lowest RMSE, was further optimized with 75 objects in the training set. Different combinations of the learning rate and momentum were used to find the best configuration for model optimization, in order to allow the solution to escape the local minima of the error function. For this study, the learning rate and momentum were set to 0.1. The number of epochs and number of nodes in the hidden layer were also optimized. Each topology was repeated five times to avoid random initialization of weights. The obtained results are presented in Fig. 1. Through the above process, it was found that the optimum number of hidden layer nodes was 7, and the number of learning epochs 2500.

ANN optimized in this study is schematically represented in Fig. 2. The input layer consists of eight nodes representing the radionuclide activities. The output layer consists of fifteen nodes representing the regions the samples were collected from. In addition, there is also a bias (neuron activation threshold) connected to the
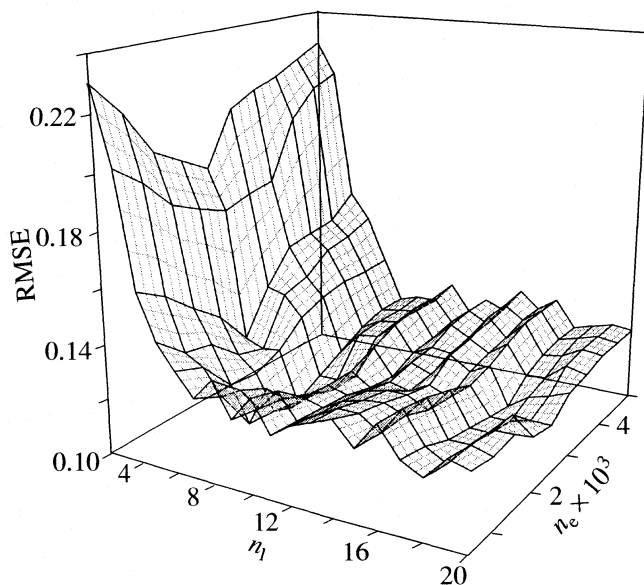
Fig. 1. The influence of number of epochs (n_e) and number of hidden layer nodes (n_l) on RMSE.
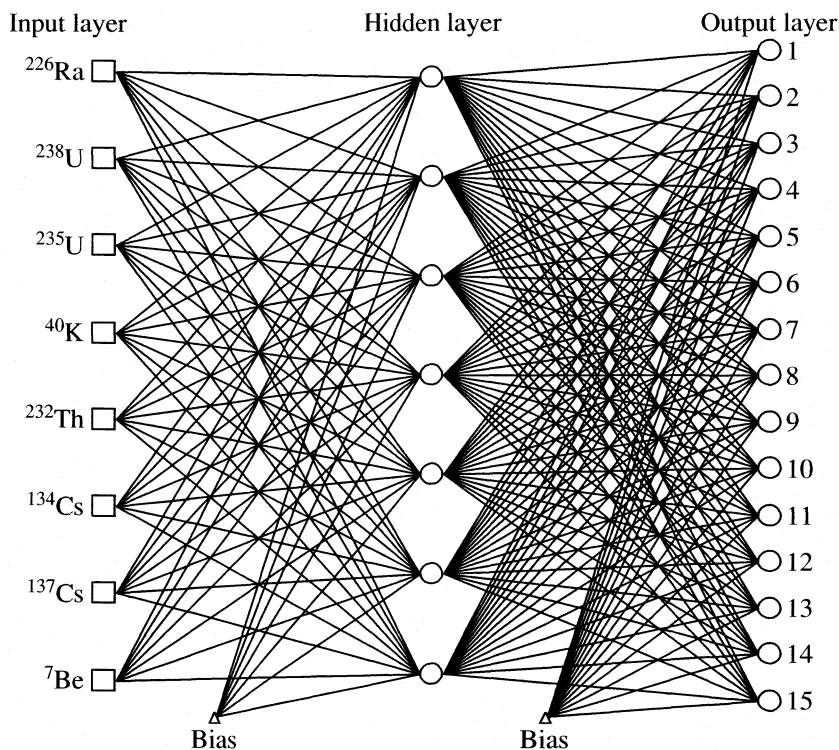
Fig. 2. Schematic representation of a three-layer feed-forward neural network used in this study, samples *1–15* – see Experimental.

nodes in hidden and output layers (but not in the input layer) via modifiable weighted connections.

ANN model validation. After the learning process, a dataset not used in the training process was employed to test the reliability of the trained algorithm. This process was repeated 10 times using different sets of randomly chosen objects. The overall performance of the predictive classifier based on ANNs can be appreciated

Table 3. Classification matrix obtained by online back-propagation randomized network. The values are averaged for different training/testing set combinations (non-zero values are in bold)

Actual classes	Output of classifier, %														
	1	2	3	4	5	6	7	8	9	10	11	12	13	14	15
1	**92**	0	**6**	**2**	0	0	0	0	0	0	0	0	0	0	0
2	0	**87**	0	0	0	0	0	0	**10**	0	0	0	0	**1**	**2**
3	0	**1**	**94**	0	0	0	0	0	0	0	0	0	0	0	**5**
4	0	0	0	**90**	0	0	**4**	**6**	0	0	0	0	0	0	0
5	0	**8**	0	0	**92**	0	0	0	0	0	0	0	0	0	0
6	0	0	0	0	0	**90**	0	0	0	**6**	**3**	0	0	0	**1**
7	**4**	0	0	0	0	0	**96**	0	0	0	0	0	0	0	0
8	0	0	0	**8**	0	0	0	**92**	0	0	0	0	0	0	0
9	0	0	0	0	**8**	**1**	0	0	**88**	0	0	0	0	**3**	0
10	**2**	0	0	0	0	0	0	0	0	**94**	0	**4**	0	0	0
11	0	**4**	0	0	0	0	0	0	0	0	**96**	0	0	0	0
12	0	0	0	0	0	0	0	**2**	0	0	**1**	**90**	**7**	0	0
13	0	0	0	0	0	0	0	0	0	0	0	**6**	**93**	0	**1**
14	**2**	0	0	0	0	0	0	0	**2**	0	0	0	0	**96**	0
15	0	0	0	0	0	**9**	0	0	0	0	0	0	0	0	**91**

in detail by the classification matrix, in which the classes predicted by the ANN classifier are compared to the actual classes. An ideal classifier will produce a classification matrix in which all diagonal elements are 100%, while all off-diagonal elements are 0%. The matrix in Table 3 is not ideal, but the origin of most soil samples was correctly classified. Namely, the average classification rate, defined as the ratio of the number of correctly identified patterns to that of all test patterns (the average of diagonal elements in the classification matrix) was $92.1 \pm 5.23\%$. This value represents the average classification rate for different training/testing set combinations as shown in Table 2. It was shown that the performance of ANNs outperformed principal component analysis (PCA) for the same dataset. This method produced 86.4% of correctly classified soil samples (unpublished data).

The ANN method have shown many adventages over traditional method for the analysis of gamma-ray spectra. Compared with usual automatic spectra analysis methods, ANNs use full-parallel computing, are simple to implement and contain nonlinearities [22]. This approach appears to be useful when a fast response is required with reasonable accuracy. The resistance to noise is certainly one of the most powerful characteristics of this type of analysis. In hazardous environments automated pattern recognition systems (such as neural network) have a distinct adventage over traditional sampling and laboratory analysis methods since an environment can be monitored without risk to human operators.

CONCLUSION

The correct classification performance of over 90% in this study, for different training/testing set ratios, indicates that gamma-ray spectrometry with back-propagation ANN is a viable tool for soil classification. Some soil samples were incorrectly assigned to one or two wrong classes that were not always geographic neighbours. This misidentification of the soil origin indicates that other soil characteristics also influence the pattern of activities of the eight commonly detected radionuclides.

ACKNOWLEDGEMENTS

REFERENCES

1. H. Eswaran, T. Rice, R. Shrens, B.A. Stewart, *Soil Classification: A Global Desk Reference* (CRC Press, 2002).

2. A.X. Zhu, Water Resour. Res. **36**, 663 (2000).

3. P. H. Fidêncio, I. Ruisãnchez, R. J. Poppi, Analyst **126**, 2194 (2001).

4. Z. Ramadan, X. H. Song, P. K. Hopke, M. J. Johnson, K. M. Scow, Anal. Chim. Acta **446**, 233 (2001).

5. O. Antonić, N. Pernar, S. D. Jelaska, Ecol. Model. **170**, 363 (2003).

6. A. C. McBratney, M. L. Mendonça Santos, B. Minasny, Geoderma **117**, 3 (2003).

7. L. Slavković, B. Škrbić, N. Miljević, A. Onjia, Environ. Chem. Lett. **2**, 105 (2004).

8. C. M. Bishop, *Neural Networks for Pattern Recognition* (Oxford Univ. Press, Oxford, 1995).

9. J. Kim, A. Mowat, P. Poole, N. Kasabov, Chemom. Intell. Lab. Syst. **51**, 201 (2000).

10. P. K. Goel, S. O. Prasher, R. M. Patel, J. A. Landry, R. B. Bonnel, A. A. Viau, Comp. Electr. Agric. **39**, 67 (2003).

11. J. Zupan, M. Novič, I. Ruisanchez, Chemom. Intell. Lab. Syst. **38**, 1 (1997).

12. P. Olmos, J. C. Diaz, J. M. Perez, P. Aguayo, P. Gomez, V. Rodellar, IEEE Trans. Nucl. Sci. **41**, 637 (1994).

13. P. Olmos, J. C. Diaz, J. M. Perez, P. Gomez, V. Rodellar, P. Aguayo, A: Bru, G. Garcia Belmonte, J. L. de Pablos, IEEE Trans. Nucl. Sci. **38**, 971 (1991).

14. S. Dragović, A. Onjia, S. Stanković, I. Aničin, G. Bačić, Nucl. Instr. Meth. Phys. Res. A **540**, 455 (2005).

15. V. Pilato, F. Tola, J. M. Martinez, M. Huver, Nucl. Instr. Meth. Phys. Res. A **422**, 423–427 (1999).

16. E. Yoshida, K. Shizuma, S. Endo, T. Oka, Nucl. Instr. Meth. Phys. Res. A **484**, 557 (2002).

17. M. Kanevski, R. Arutyunyan, L. Bolshov, V. Demyanov, M. Maignan, Geoinform. **7**, 5 (1996).

18. F. Despagne, D. L. Massart, Analyst **123**, 157R (1998).

19. QwikNet Version 2.23, Craig Jensen, Redmond, USA, 1999.

20. C. Di Natale, A. Macagnano, E. Martinelli, E. Proietti, R. Paolesse, L. Castellari, S. Campani, A. D'Amico, Sens. Act. B **77**, 561 (2001).

21. K. Rajer-Kanduč, J. Zupan, N. Majcen, Chemom. Intell. Lab. Syst. **65**, 221 (2003).

22. V. Vigneron, J. Morel, M. C. Lepy, J. M. Martinez, Nucl. Instr. Meth. Phys. Res. A **369**, 642 (1996).

OTHER PROBLEMS
OF PHYSICAL CHEMISTRY

CHARACTERISTICS OF WINTERTIME POLYCYCLIC AROMATIC HYDROCARBONS ASSEMBLAGE IN AEROSOL OF SOUTHERN ADRIATIC

© 2007   V. Ž. Jovanović*, P. A. Pfendt*,**, A. J. Filipovic***

*Graduate School of Advanced Technology and Science, The University of Tokushima,
2–1 Minamijosanjima-cho, Tokushima 770–8506, Japan
**Faculty of Chemistry, University of Belgrade, Studentski trg 12–16, 11000 Belgrade, Serbia
***Institute of Public Health of Belgrade, Bulevar Despota Stefana 54a, 11000 Belgrade, Serbia
E-mail: vladimir@eco.tokushima-u.ac.jp ; jovanovicvlada@yahoo.com

Abstract – Features of the polycyclic aromatic hydrocarbon (PAH) assemblage in the aerosol samples collected from the atmosphere of Herceg Novi during winter months of two successive years were studied. The results showed almost the same concentration profiles of identified PAHs for samples from the two periods analyzed, generally suggesting similar origin. Diagnostic ratios indicated combustion of wood and coal, emissions from petrol and diesel engines and dust resuspension as sources that predominantly contributed to the atmospheric PAH concentrations.
Statistical analysis, principal component analysis (PCA) in particular, allowed us to identify the impact of meteorological parameters on PAH abundance.

PAH are compounds formed mainly by anthropogenic processes, especially the combustion of organic fuels with high concentrations corresponding to urban and industrial areas. They are however ubiquitous contaminants of the environment also detected in rural [1], as well as in remote [2] or even marine regions [3] because of their relatively high persistence in the environment and their ability to be transported over long distances. PAHs occur in both gaseous phase and adsorbed to particles in the atmosphere, depending on the volatility of the species. Particulate PAH were considered to be the more abundant and hazardous to human health [4, 5]. Their occurrence in ambient air has caused specific concern due to the continuous nature of exposure and the size of population at risk, especially in urban, suburban and industrial areas.

In order to assess the significance of PAHs in ambient air it is necessary to evaluate the physical and chemical characteristics of airborne PAH as well as to identify the major emission sources. The contribution of any PAH source to the atmosphere will depend on a number of factors including the emission rate of the source, its geographical location and the local climatic conditions [6].

The results presented in this paper are a part of our integrated study on chemical characterization of the Mediterranean aerosol in the South Adriatic region [7] for which, to our best knowledge, no data are available in literature. The results are based on investigation of the organic part of aerosol, with a focus on PAHs in order to determine the origin and contribution of their dominant sources in the Herceg Novi environment (Adriatic coast of Montenegro) during the winter months of two successive years. The data resulting from the study of summertime PAH assembly are reported elsewhere [8].

In a suburban environment, such as the area investigated, the PAH features affected by the local sources (traffic, fossil fuel and biomass combustion in power plants, wood-stoves and fireplaces for home heating, unregulated burning of tyre, waste, wood, etc.) may be greatly modified by the meteorological conditions. We therefore also asses the influence of meteorological parameters on the abundance and distribution of specific particle-bound PAHs.

STUDY REGION

The sampling site, located in the eastern suburb of Herceg Novi (HN), is included in a network of stations of the World Meteorological Organization program for monitoring and investigating air pollution in the Mediterranean (MED POL). It is of special importance ecochemically, since it represents a point of overlapping of the effects of urban, marine, and local pollution with the effects of pollution transfer from greater distances.

The town HN (18°33' N, 42°27' E) is situated in the south-west Montenegro at the entrance of Boka Kotorska, the largest gulf in the Adriatic Sea (Fig. 1). More detail on the geographical location is given in [8].

A high number of sunny hours (about 2400–2500 annually) in the HN region results in relatively high average annual air temperatures, not below 14°C for the whole region. In January, the temperatures show mild maritime characteristics (averaging 8.6°C in Herceg Novi) but they fall rapidly at the steep mountainsides. In higher zones they fluctuate around 0°C. The annual mean precipitation in HN is 1974 mm and average hu-
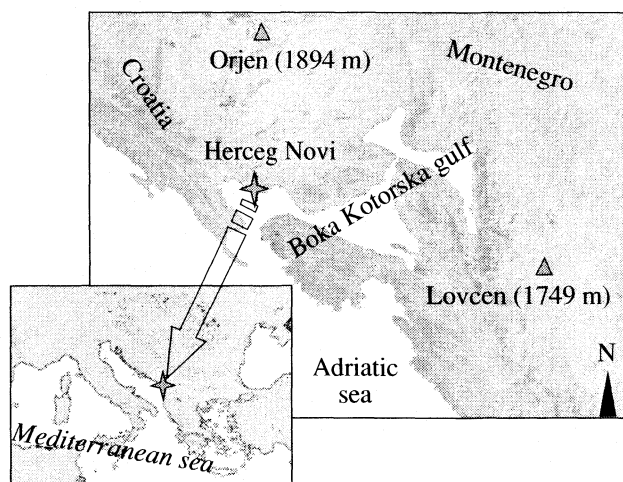
Fig. 1. Location of sampling site.

midity about 70%. According to Magas [9], southerly winds (S, SE, SW) are prevalent in this region with frequency of about 51%. The westerly winds participate with 15% and easterly with 14%. The less frequent northerly winds (N) and north-western winds (NW), with 11 and 4% respectively, are most present in winter.

The whole region is semi-functional, with extensive tourism and free from any industrial activities. The main traffic pathways are the Bar railway, Adriatic highway, with significant transit traffic, whereas the main terminals are the Bar seaport and the Tivat airport.

EXPERIMENTAL

Sampling methodology and extraction. A total of 30 aerosol samples were analysed for the purpose of our investigation. Fifteen samples were taken during the winter months (January-March) of 1998, and the other fifteen during the same period of 1999. The sampling equipment was placed on the rooftop of the Meteorological station building at about 5 m above ground, less than 15 m from the coast, and about 100 m away from the nearest traffic thoroughfare. Aerosol particulate matter was collected on quartz fiber filters (20×25 cm, Schleicher & Schuell type G6) using a high-volume sampler AQUERO model 400XT. The system was operated at a flow rate of 50 m^3 h^{-1} over a 24 h period, yielding sampled air volumes ranging from 1190 to 1295 m^3. The sampling frequency was 1-in-6 days. Meteorological parameters: temperature (T), relative humidity (RH), wind direction (WD) and wind velocity (WV) were measured at the sampling site during the collection.

Total content of suspended particles (TSP) was quantified gravimetricaly with a sensitivity of 0.01 mg. Quality control was assured by measurements of three blank filters, which were kept together with the samples in the desiccator, at a temperature of $20 \pm 1°C$.

The organic part was extracted from the filter material by dichloromethane in an ultrasonic bath. The extracts were dried over anhydrous sodium sulphate (Na_2SO_4), filtered and concentrated to a volume of approximately 1ml using a rotary evaporator. The total organic extracts (TOE) were transferred to a pre-weighted 5 ml conical vial and the solvent evaporated under a stream of nitrogen gas. The extracts were quantified gravimetrically and analysed using a standard GC-MS system.

Instrumental analysis. The operating GC-MS conditions and analytical procedure are described elsewhere [8]. PAHs that were difficult to separate by gas chromatography and were of identical quality, were presented as the total amount of the isomers, and one of the isomers was used as a standard because of their identical responses to the flame ionization detector [10, 11]. Field blanks, filter blanks and solvent blanks were also determined. PAHs were not detectable in either.

RESULTS AND DISCUSSION

TSP and TOE. Contents of the TSP and TOE in the aerosol samples and corresponding meteorological data are listed in Table 1. Samples collected during rainy days were not taken into account, for reasons of consistency. The data show that the TSP and TOE contents differ slightly between the samples from 1998 and 1999. The 24 h average concentrations of TSP in air did not exceed the limit value of 120 μg m^{-3}, recommended by the WHO (World Health Organisation) during the whole period of investigation, and amounted to 48.2 ± 16.9 and 54.6 ± 11.9 μg m^{-3} for both years. The TOE content did not exceed 15% of the total aerosol mass in the samples, and amounted to 9.4 ± 1.8 and $8.9 \pm 2.2\%$ on average for 1998 and 1999, respectively. These values are comparable to those reported in literature for wintertime aerosol samples from some urban and semiurban localities in the Mediterranean area, collected and analysed by a similar method [12, 13].

PAHs. The results of GS-MS analysis are summarized in Fig. 2. The PAHs are listed according to their elute order from gas-chromatographic column, i.e. to the order of their MS identification. It is observable that the relative concentration profiles of the PAHs detected in the samples from both years are almost the same, (confirmed statistically by the Student t test, $p > 0.05$) indicating a similar type of PAH sources and dispersion processes in the periods analysed.

The samples contain mostly PYR, FLT, BxF and CHR with 67 and 71% of the total PAHs in 1998 and 1999, respectively. PYR and FLT, were consistently the most prominent of all identified PAHs in all samples. Both compounds tend to dominate the PAH profiles. Thus, the differences in the mean PAHs concentration (Fig. 2) mainly reflect their variations. Certain authors [14, 15] explained the dominance of these

Table 1. Contents of TSP and TSOE in aerosol samples and meteorological data

Parameter	Winter 1998 ($n = 13$)			Winter 1999 ($n = 11$)		
	Min–Max	Mean	±SD	Min–Max	Mean	±SD
TSP, $\mu g\ m^{-3}$	31.09–81.26	48.16	16.86	33.73–70.82	54.63	11.88
TOE, $\mu g\ m^{-3}$	2.01–7.87	4.48	1.64	2.96–10.50	4.91	1.99
TOE, %	6.5–12.8	9.4	1.8	6.2–14.8	8.9	2.2
T, °C	5.9–13.2	10.2	2.0	3.1–12.7	8.1	2.6
RH, %	45.0–83.3	64.8	11.6	36.7–87.3	68.7	19.3
WV, m s^{-1}	3.1–9.3	5.5	1.6	2.8–12.5	6.5	3.9

Notes: n – number of samples analysed, T – average daily temperature, RH – relative humidity, WV – maximum wind velocity; SD – standard deviations.

PAHs by their high rate of emission in ambient air and their weak reactivity in the atmosphere. However, these two dominant PAHs are toxicologically and ecochemicaly of minor importance [16].

With the aim to obtain indication of possible sources of the PAH contamination, diagnostic ratios of the characteristic PAHs were calculated. The values are given in Table 2. Compared to literature data, the value obtained for the diagnostic ratio FLT/(FLT + PYR) in samples of the periods analysed indicates burning of wood and resuspension of road dust as the sources of PAHs. According to Manoli et al. [17], the ratio of these PAHs from wood burning is in the range from

0.40 to 0.50, and for resuspended dust in the range from 0.42 to 0.52.

The average values of the INP/(INP + BGP) in our samples are 0.56 and 0.52, which, according to literature data indicate coal burning as the source [18], as well as dust resuspension [17], but also traffic, i.e. diesel-engine emissions [19].

Traffic as the source of PAHs in this period is also confirmed by the diagnostic ratios BeP/(BeP + BaP) (0.78 for both sample groups), BaA/(BaA + CHR) (0.36 and 0.37) and BGP/BaP (2.96 and 2.50), which are characteristic to emissions from petrol and diesel engines, and road dust [19–21]. The ratio BxF/BGP
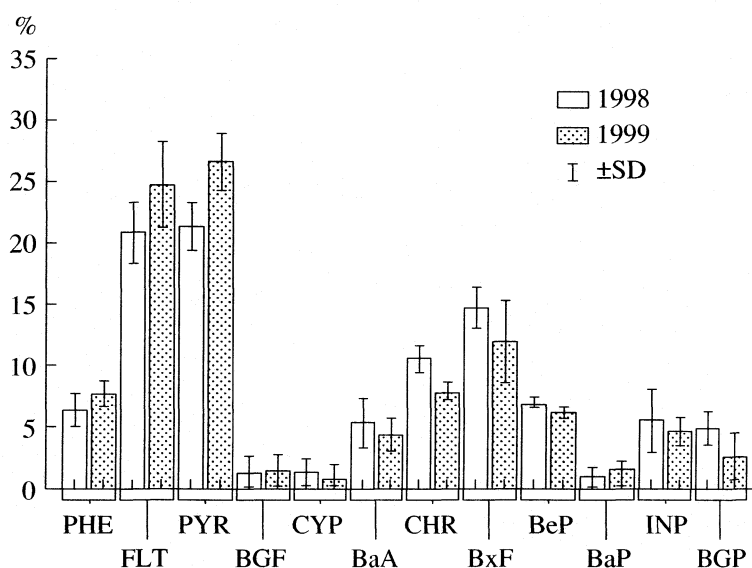
Fig. 2. Average relative PAH composition in the TSP for winter samples of 1998 and 1999 Error bars correspond to standard deviation.

PHE – phenanthrene + anthracene (determined cumulatively as unresolved by gas chromatographic analysis); FLT – fluoranthene; PYR – pyrene; BGF – benzo[ghi]fluoranthene; CYP – cyclopenta[cd]pyrene; BaA – benz[a]anthracene; CHR – chrysene + triphenylene; BxF – benzo(j)fluoranthene + benzo(b)fluoranthene + benzo(k)fluoranthene; BeP – benzo(e)pyrene; BaP – benzo(a)pyrene; INP – indeno[1,2,3-cd]pyrene; BGP – benzo[ghi]perylene.

Table 2. Diagnostic ratios of characteristic PAHs identified in HN aerosols

Dijagnostic Rations	Winter 1998	Winter 1999
FLT/(FLT + PYR)	0.49 ± 0.02	0.48 ± 0.03
BeR/(BeP + BaP)	0.78 ± 0.04	0.78 ± 0.08
INP/(INP + BGP)	0.56 ± 0.04	0.52 ± 0.04
BaA/(BaA + CHR)	0.36 ± 0.03	0.37 ± 0.03
BGP/BaP	2.96 ± 0.31	2.50 ± 0.48
BxF/BGP	2.69 ± 0.47	2.72 ± 0.42
BaP/BGP	0.34 ± 0.10	0.42 ± 0.07

(2.68 and 2.78) in our samples corresponds to motor oil burning [19].

Principal component analysis. A PCA with a Varimax rotation was applied to 12 identified PAHs, TSP, TOE and meteorological parameters mentioned earlier, aimed at finding groups of PAHs with similar behavior, and investigating the existence and magnitudes of effects of meteorological conditions on PAH patterns during the periods analysed. The analysis was performed using the SPSS 10.0 statistics package.

According to Kaiser criterion [22], four principal components (PCs) were selected for the set data of 1998 and three PCs for the 1999 data. They account for 91.9 and 89.5% of the total percentage of variance in the set data of 1998 and 1999, respectively (Table 3).

Results of the analysis for 1998. The first principal component (PC1) accounts for 60.7% of the total variance and includes all the identified PAHs with high loadings (>0.70). An exception is CYP, which is correlated with moderate loading (0.65) and which appears negatively correlated with the PC2 (−0.48) and positively correlated with PC3 (0.38). Finding all PAHs in the same component, with highly significant mutual correlation (except for CYP), indicates the effect of

Table 3. PCA results for HN winter aerosol

Parameter	Winter 1998				Winter 1999		
	PC 1	PC 2	PC 3	PC 4	PC 1	PC 2	PC 3
TSP	0.16	0.92	−0.16	0.23	0.41	0.80	0.01
TOE	0.31	0.92	0.12	0.16	0.48	0.37	0.63
PHE	0.79	0.32	0.15	0.21	0.85	0.14	0.45
FLT	0.89	0.03	0.04	−0.30	0.87	0.15	0.42
PYR	0.98	0.06	0.06	0.02	0.94	0.22	−0.13
BGF	0.91	−0.14	0.14	0.22	0.94	−0.15	0.13
CYP	0.65	−0.48	0.38	−0.09	0.69	0.03	0.69
BaA	0.97	0.09	−0.03	−0.16	0.82	0.42	−0.07
CHR	0.96	−0.04	−0.20	0.00	0.85	0.32	0.38
BxF	0.95	0.04	−0.26	0.06	0.80	0.21	0.34
BeP	0.97	0.01	−0.19	−0.06	0.95	0.24	0.13
BaP	0.91	−0.08	0.11	0.23	0.86	0.06	0.44
INP	0.91	0.11	−0.10	−0.30	0.87	0.40	0.09
BGP	0.93	0.22	0.01	0.01	0.96	0.11	0.19
T	−0.10	0.49	−0.04	0.82	−0.30	0.89	−0.10
RH	0.79	0.37	−0.01	0.33	0.20	0.90	−0.02
WV	−0.56	0.62	0.32	−0.27	−0.41	−0.80	−0.05
WD	0.07	−0.02	−0.96	0.01	0.01	0.36	−0.84
Initial Eigenvalue	10.99	3.11	1.43	1.01	11.61	3.19	1.31
% of variance	60.75	15.95	7.96	7.24	54.32	21.14	14.04
Cumulative, %	60.75	76.70	84.66	91.90	54.32	75.45	89.49

Rotation Method: Varimax with Kaiser normalization Eigenvalue > 1.

predominantly the same sources and/or relative non-selectivity of the factors that control the attaching of PAHs to particles.

In addition to the PAHs, the PC1 is characterised by two meteoparameters: RH, which is highly positively correlated (0.79), and wind velocity (WV), which is moderately negatively correlated (−0.56). Significant association of PAHs with air humidity results from the fact that RH is one of the factors that affect the attaching of the substances to particles, i.e. which affects the formation and size of particles. The adsorption capacity, namely, can be expected to decrease with an increase of RH. Its increase also may favour other mechanisms of attachment (sticking, scavenging) that are non-selective by nature [23]. This follows from the correlation analysis [7] that PAHs are non-selectively correlated with RH, i.e. that no difference in attachment is observed between semi volatile PAHs (lower molecular mass) and those that are found exclusively in the particulate phase.

A moderate negative correlation of PC1 with WV indicates a decrease of PAH concentrations due to wind induced dillution. In addition, the conditions of low wind velocity increase the effect of local emissions with respect to remote transport, leading to the clonclusion that the PAHs identified originate mostly from local sources.

The second principal component (PC2), which accounts for 15.9% of the variance, is characterised by TSP and TOE with a high loadings (>0.90), CYP with (−0.48), and meteoparameters: WV (0.62), T (0.49), and RH (0.37).

The same direction of dependence of TSP on T and RH seems logical if one has in mind the fact that RH is not an independent parameter, but represents a ratio of the current partial pressure of water vapour in air and the maximum possible pressure of water vapour at a given temperature (expressed as percentage), meaning that it implicitly includes temperature.

On the other hand it could be expected that an increase of RH induces a decrease in the content of suspended particles, due to inhibited resuspension. The observed positive correlation is most likely a consequence of association of T and other meteoparameters through complex interdependent effects, which affect the TSP content. Agglomeration of particles by mutual attachment probably has a significant role.

The correlation between TSP and WV can be explained by the assumption that at higher wind velocities and absence of precipitation, remote transport and resuspension are predominant. It means that TSP and TOE originate from local sources (resuspension) but, partialy, also from remote transport. Quantitative determination of the contributions of remote transport and resuspension requires detailed analysis of physical and chemical characteristics of dust particles from the immediate environment of the measuring point, which is not a subject of the present paper.

Except for CYP, none of the PAHs is found in the same component together with TSP and TOE, most likely because PAHs comprise only about 2% of TOE in the winter period, which represents less than 10% TSP. CYP is characterised by an exceptionally rapid reaction with the $NO_3^{\bullet}$ radical (or N_2O_5) [23] which results in its loss, and the consequent absence of significant correlation with other PAHs.

All of the above indicates that TSP concentration depends on T, RH, and WV, but without a systematic relationship between particulate aerosol content and these meteoparameters, which has been recognised earlier [24], so that only the effect of the meteoparameter set on TSP content can be considered. The PC3 and PC4 account for 7.9 and 7.2% of the variance, and are characterised only by meteorological parameters WD (in PC3) and T (in PC4). The TSP, TOE, and PAHs are not correlated with WD most probably because of the continuous change of the dominant directions in this period.

Results of the analysis for 1999. The first principal component (PC1) accounts for 54.3% of the variance (Table 3) and, as the PC1 for the previous year, it is in highly positive correlation with all the PAHs. Several PAHs are also in correlation with PC2 and PC3. As for the other variables, PC1 is characterised by TSP, TOE with low loadings, and by meteoparameter WV, which is negatively correlated with low loading (−0.41).

PC2 accounts for 21.1% of the variance and includes a highly correlateed TSP (0.80), weakly correlated TOE (0.37), as well as a highly positively correlated T (0.89), RH (0.90), and a highly negatively correlated WV (−0.80). As for the PAHs, PC2 includes low correlated BaA (0.42) and INP (0.40).

PC3 accounts for 14.0% of the variance and is highly negatively correlated with WD (−0.84), moderately positively with TOE (0.63), weakly with PHE (0.45), BaP (0.44), FLT (0.42) and CHR (0.32), and moderately with CYP (0.69).

The results obtained with PCA show that two groups of PAHs exist.

The first group includes PAHs that are significantly correlated only with PC1 and no other component. They are PYR, BGF, BeP, and BGP, comprising 37% of the total PAH content. Weak individual correlations of these PAHs with meteorological parameters indicates that the contribution of neither of the PAHs is directly dependent on meteorological parameters. Their source are most probably traffic emissions in the immediate vicinity of the measuring point, controlled mostly by vehicle throughput and engine factors (eg. model, type, age, maintenance, capacity, etc). Another PAH group consists of two subgroups, according to the correlation with PC2 and/or PC3 (Table 3).

One subgroup includes BaA and INP, comprising 9% of the total PAH content. These PAHs correlate significantly with PC1 and less significantly (~0.40) with

PC2, which is characterised by highly positive correlations with T (0.89) and RH (0.90), as well as by a negative correlation with WV (–0.80), which indicates existence of a certain dependence of these two PAHs on meteorological parameters, or a stronger association with TSP (resuspension).

The other subgroup comprises PHE, FLT, CYP, CHR, and BaP, which are significantly correlated with PC1, and less significantly with PC3, which is moderately correlated with TOE (0.63) and highly negative (–0.84) with WD. These PAHs constitute, on average, 54% of the total PAHs in the period analysed. It is not possible to associate this combination of PAHs with specific sources because each compound might have a different origin. Therefore, PC3 suggests a multiple source impact. Their contribution in the aerosol of the measuring point explicitly depended on WD. The negative correlation with WD is probably associated with dominant wind directions of the north-easterly (NE) sector, i.e. direction of the wider HN area (Fig. 1).

CONCLUSION

The following conclusions can be drawn from this study.

1. There are no significant differences in PAH compositions between aerosol samples collected during the winter months of 1998 and 1999, indicating similar type of sources for both periods. It was found that the samples of both years quantitatively mostly contain PYR, FLT, BxF, and CHR, with 67 and 71%, respectively.

2. Diagnostic ratios of the characteristic PAHs suggest that main PAH sources were combustion of wood and coal, emissions from petrol and diesel engines and dust resuspension.

3. PCA indicate that the TSP concentration depends on meteoparameters T, RH, or WV but that there is also no systematic relationship between particulate aerosol and these meteoparameters, so that only the effect of the meteoparameter set on TSP content can be considered. The dominant impact on the distribution of PAHs during winter months of 1998 was attributed to wind velocity (WV) and relative humidity (RH), while the wind velocity (WV) and wind direction (WD) had prevalent influence in 1999.

REFERENCES

1. B. R. T. Simoneit and M. A. Mazurek, *Organic matter of the troposphere II: Natural background of biogenic lipid matter in aerosols over the rural western United States.* Atmos. Environ. **16**, 2139–2159 (1982).

2. E. Aamot, E. Steinnes and R. Schmid, *Polycyclic aromatic hydrocarbons in Norwegian forest soils: impact of long range atmospheric transport.* Environ. Pollut. **92**, 275, (1996).

3. C. J. Halsall, A. J. Sweetman, L. A. Barrie, K. C. Jones, *Modelling the behaviour of PAHs during atmospheric transport from the UK to the Arctic.* Atmos. Environ. **35**, 255 (2001).

4. W. Cautreels, and K. Van Cawenberghe, Atmos. Environ. **12**, 1133, (1978).

5. R. J Lyall, M. A. Hooper and S. J Mainwaring, Atmos. Environ. **22**, 2549, (1988).

6. R. Harkov, and A. Greenberg, J. Air Pollut. Control Assoc. **35**, 238. (1985).

7. V. Jovanović, *Determining of the ecochemical indicator potential of hydrocarbons from Mediterranean aerosol,* M. Sc. Thesis, Faculty of Chemistry, University of Belgrade, (2006).

8. V. Ž. Jovanović, *Summertime PAH assembly in Mediterranean air: the Herceg Novi sampling station as an example,* J. Serb. Chem. Soc. **72**, 2, 193–204 (2007).

9. D. Magaš, *Natural-geographic characteristics of the Boka Kotorska area as the basis of development.* Geoadria **7** (1), 51–81, (2002).

10. H. Yamasaki, K. Kuwata and H. Miyamoto, *Effects of Ambient Temperature on Aspects of Airborne Polycyclic Aromatic Hydrocarbons. Environ. Sci. Technol.* **16**, 190, (1982).

11. H. Schonbuchner, G. Guggenberger, K. Peters, H. Bergmann, W. Zech, *Particle-size distribution of PAH in the air of a remote Norway spruce forest in northern Bavaria. Water Air Soil Poll.* **128**, 358, (2001).

12. A. Gogou, N. Stratigakis, M. Kanakidou, E. G. Stefanou, *Organic aerosols in Eastern Mediterranean; components source reconciliation by using molecular markers and atmospheric trajectories.* Org. Geochem. **25**, 79–96, (1996).

13. J. Mantis, A. Chaloulakou and C. Samara, *PM10-bound polycyclic aromatic hydrocarbons (PAHs) in the Greater Area of Athens, Greece.* Chemosphere, **59**, 593–604, (2005).

14. G. Kiss, Z. Varga-Puchony, B. Tolnai, B. Varga, A. Gelencser, Z. Krivacsy, J. Hlavay, *The seasonal changes in the concentration of polycyclic aromatic hydrocarbons in precipitation and aerosol near Lake Balaton, Hungary.* Environ. Poll. **114** (1), 55–61 (2001).

15. A. Motelay-Masseia, D. Ollivonb, B. Garbanb, M. Chevreuil, *Polycyclic aromatic hydrocarbons in bulk deposition at a suburban site: assessment by principal component analysis of the influence of meteorological parameters.* Atmos. Environ. **37**, 3135–3146 (2003).

16. J. F. Muller, D. W. Hawker and D. W. Connell, *Polycyclic Aromatic Hydrocarbons in the Atmopspheric Environment of Brisbane, Australia.* Chemosphere **37**, 7, 1369–1383, (1998).

17. Manoli, E., A. Kouras, C. Samara. *Profile analysis of ambient and source emitted particle-bound polycyclic aromatic hydrocarbons from three sites in northern Greece. Chemosphere* **56**, 867–878, (2004).

18. Kavouras I. G., Lawrance J., Koutrakis P., Stephanou E. G., Oyola P., *Measurement of particulate aliphatic and polynuclear aromatic hydrocarbons in Santiago de Chile: Sources reconciliation and evaluation of sampling artifacts.* Atm. Environm. **33**, 4977–4986 (1999).

19. W F. Rogge, M. L. Hilldemann, M. A. Mazurek, and G. R. Cass. *Sources of fine organic aerosols: 2. Noncatalyst and Catalyst-Equipped Automobiles and Heavy-*

Duty Diesel trucks. Environ. Sci. Techno., **27**, 636–651, (1993).

20. C. Venkataraman, J. M. Lyons, S. K. Friedlander, *Size distributions of polycyclic aromatic hydrocarbons and elemental carbon 1. Sampling, measurement methods, and source characterization.* Environ. Sci. Techno., **28**, 555–562, (1994).

21. N. R. Khalili, P. A. Scheff, T. M. Holsen. *PAH source fingerprints for coke ovens, diesel and gasoline engines, highway tunnels, and wood combustion emissions.* Atmos. Environ., **29**, 533–542 (1995).

22. L. G Grim and P. R. Yarnold. *Reading and understanding multivariate statistics.* American Psychological association, Washington. p. 99 (2004).

23. B. J. Finlayson-Pitts, and J. N. Pitts. *Chemistry of the Upper and Lower Atmosphere: Theory, Experiments and Applications.* San Diego, Calif.; London, *Academic Press.* (2000).

24. D. A. Braaten, U. K. T. Paw and R. H. Shaw, *Particle resuspension in a turbulent boundary layer-observed and modeled.* Journal of Aerosol Science 21: 613–628 (1990).

OTHER PROBLEMS
OF PHYSICAL CHEMISTRY

PRACTICAL APPLICATIONS OF RADIATION CHEMISTRY

© 2007   A. G. Chmielewski

Institute of Nuclear Chemistry and Technology
Department of Chemical and Process Engineering, University of Technology, Warsaw, Poland
E-mail: <a.chmielewski@ichtj.waw.pl>

Abstract – Physical, chemical and biological effects of ionizing radiation on the matter are the basis of many practical applications. The number of applications is growing and radiation sources; gamma, electron beam and X-rays are becoming an industrial equipment operated in the harsh, demanding environment. They play important role in the economical development of many countries.

Radiation chemistry is a part of the physical chemistry like photo-chemistry, plasma-chemistry, ultrasonic-chemistry etc. Shortwave high energy electromagnetic (gamma radiation or X-rays) or high penetration corpuscular (electrons) radiation transfer the energy into the continuous, even high density matter.

FUNDAMENTAL

Ionizing radiation, X-rays, gamma radiation, high energy electrons produce abundant secondary electrons. The collision of a photon with a molecule usually causes an electron to be ejected via Compton effect. Thus, nearly all of the physical and chemical changes in the system are produced by the energetic electron and not by the initial photon. The kinetics of reactions induced by high-energy photons are therefore similar to those obtained if high-energy electrons are used as the primary radiation Therefore there is not a big difference in the effects caused by these different forms of radiation. Depending to the energy transferred, molecules can undergo ionization, excitation or thermal transfer. The interaction with the matter can be divided in the time scale in the following stages; initial physical processes, pre-chemical reactions, chemical reactions and finally radical diffusion. The time scale for the physical stage is on the order of 10^{-16} s. The electron excitation occurs in the range shorter than $\sim 10^{-10}$ s and vibrational excitation in the range of 10^{-14} to 10^{-11} s. Molecular dissociation takes place in the range of 10^{-14} to 10^{-6} centered to 10^{-10} s. Reactions governed by diffusion take place in the range of $\sim 10^{-10}$ to $\sim 10^{-6}$ s. In a liquid systems, it takes an ion pair about 10^{-5} s to separate and become free ions. Following these primary events, the ions, secondary electrons and excited molecules undergo further transformations, exchanging charges and energy and reacting with surrounding molecules, thereby producing free radicals and other reactive species which finally evolve into new stable products.

RADIATION SOURCES

Three main sources of radiation are applied for radiation processing. These are electron accelerators, gamma sources and X-ray unit based on e^-/X conversion process. Accelerators are available supplying electron beams in the energy range up to 10 MeV [1] and sources of the radionuclides Co-60 and Cs-137 emitting gamma rays 1.17/1.33 and 0.662 MeV respectively [2]. The introduction of new X-ray (Bremsstrahlung) powerful radiation sources opens new, until now unexplored fields as well [3]. Electron beams are corpuscular radiation and are characterized by limited penetration The whole energy of high-energy electrons is deposited in relatively thin layers of material. In the case of X-rays and gamma rays, ionizing radiation is provided by photons which have no mass and are thus able to penetrate deeper into materials [4].

The cobalt-60 emitted gamma rays penetrate ~300 mm of unit density material on an equal entrance-equal exit basis. In contrast, the highest electron energy used in commercial applications, 10 MeV, penetrates ~38 mm only. Dose rates are for gamma and X-rays 4 to 5 orders of magnitude lower as compared to EB. Therefore throughput efficiencies of gamma and X-rays are significantly lower than those of e-beams, electron beams are capable of delivering 100 kGy per second, whereas typical dose rate for gamma rays is 2.8×10^{-3} kGy per second or ~10 kGy per hour. The radiation dose rate generated by the electron accelerator of 15 kW power is approximately equal to that generated by 1 MCi of the cobal source. X-ray target conversion efficiencies vary with the atomic number of the metal used, they are typically no higher that 5–8%. In practice this means that in order for an X-ray to process products with the same speed as a 10 MeV, 50 kW e-beam, it will need to have 625 kW of power.

POLYMERS

Radiation processing was used early on for polymer modification [5]. The irradiation of polymeric materi-

als with ionizing radiation (gamma rays, X-rays, accelerated electrons, ion beams) leads to the formation of very reactive intermediates, free radicals, ions and excited states. These intermediates can follow several reaction paths that result in disproportion, hydrogen abstraction, arrangements and/or the formation of new bonds. The degree of these transformations depends on the structure of the polymer and the conditions of treatment before, during and after irradiation. Thorough control of all of these factors facilitates the modification of polymers by radiation processing. Nowadays, the modification of polymers covers radiation cross-linking, radiation-induced polymerization (graft polymerization and curing) and the degradation of polymers. The success of radiation technology for the processing of synthetic polymers can be attributed to two reasons, namely the easiness of processing in various shapes and sizes and, secondly, most of these polymers undergo cross-linking reaction upon exposure to radiation.

On the other hand, naturally occurring polymers were difficult to process and degraded when exposed to high-energy radiation. In recent years, natural polymers are being looked at again with renewed interest because of their unique characteristics like inherent biocompatibility, biodegradability and easy availability. A further progress in natural polymers' processing is foreseen. Many processes of radiation treatment of natural polymers, though known for a long time, have not yet been commercialized, either because of the high cost of irradiation (high dose) or because of the reluctance on part of the industry to adapt to the radiation technology. It is therefore of importance to consider combining the beneficial effects of conventional technology along with radiation technology to overcome such problems. Recently, some products based on radiation processed cellulose derivatives or chitosan have been developed and introduced to the market.

A significant difference exists between electron beam and gamma processing of polymers, which is related to dose rate and often to oxidative degradation of material at or near the surface for reactions conducted at low dose-rates. The introduction of new X-ray (Bremsstrahlung) powerful radiation sources opens new, until now unexplored fields of polymer processing as well [6]. New applications are foreseen in the field of nanotechnology [7].

STERILIZATION

Radiation sterilization of a product means destruction of all viable organisms present on that product (mainly microorganisms) by using ionizing radiation. Both types of ionizing radiation, i.e. gamma radiation from isotopic sources and electron beams from accelerators are used for radiation sterilization. It is now universally accepted that the deoxyribonucleic acid (DNA) in the chromosomes represents the most critical "target" for ionizing radiation. Effect on the cytoplas-

mic membrane appears to play an additional role in some circumstances.

The destruction of microorganisms by physical or chemical agents follows an exponential law. Accordingly, one can calculate a finite probability of a surviving organism regardless of the magnitude of the delivered sterilization dose or treatment. The probability of survival is a function of the number and types (species) of microorganisms present on the product (bioburden), the sterilization process lethality, and, in some instances, the environment in which the organisms exist during treatment. It follows that the sterility of an individual item in a population of products sterilized cannot be ensured in the absolute sense. A sterility assurance level (SAL) is derived mathematically and it defines the probability of a viable microorganism being present on an individual product unit after sterilization. SAL is normally expressed as 10^{-n}.

Commercial radiation sterilization has been used for more than 50 years. Over the decades, there has been enormous growth in the disposable medical products market. With this, there has been significant growth in the use of ionizing radiation as a method for sterilization. At present, 40 to 50% of all disposable medical products manufactured in North America are radiation-sterilized. Worldwide, there are now some 160 commercial cobalt-60 irradiators for radiation sterilization operating in 47 countries containing approximately 240 to 260 million curies $((8.9–9.6) \times 10^{18}$ Bq) of the gamma emitting cobalt-60. Included in this are service type facilities operated in R&D centres. Because of the ability to down-scale cobalt-60 units, there are many R&D and pilot-scale small facilities as well, almost equal in number (~150).

When other uses are taken into account, there are in total over 300 gamma irradiators being operated for a variety of purposes in 55 different countries. Syringes, surgical gloves, gowns, masks, band aids, dressings, medical tetra packs, bottle teats for premature babies, artificial joints, food packaging, raw materials for pharmaceuticals and cosmetics, and even wine corks are gamma sterilized. An increasing number of electron beam (EB) accelerators are also being used, but at present EB is used for only a minority of radiation sterilized product [8].

FOOD IRRADIATION

Joint FAO/IAEA/WHO Expert Committee approved the use of radiation treatment of foods up to 10 kGy dose in 1980 [9]. After 1980, new regulations allowed the irradiation of foods, which were not approved for this process before in the US. Approval of irradiation for treatment of packaged fresh or frozen uncooked poultry in 1990 and for treatment of fruits, vegetables and grains in 1986 are some of the examples for these new regulations. Today, more than 40 countries permitted the use of irradiation of over 60 food products. More-

over, the use of irradiation is becoming a common treatment to sterilize packages in aseptic processing of foods and pharmaceuticals. The biggest amount of food product treated are spices [10].

ENVIRONMENTAL APPLICATIONS

Over the last few decades, extensive work has been carried out for utilizing electron beam technology for environmental remediation. This includes application of this technology for flue gas treatment, purification of drinking water and wastewater and hygienization of sewage sludge for use in agriculture [11].

Flue gas treatment. Fossil fuels, which include coal, natural gas, petroleum, shale oil and bitumen, are the main primary source of heat and electrical energy production, are responsible for emitting a large number of pollutants into the atmosphere with off-gases from industries, power stations, residential heating systems and vehicles. All these fuels contain major constituents (carbon, hydrogen, oxygen) as well as other materials, such as metal, sulphur and nitrogen compounds. During the combustion process different pollutants like fly ash, sulphur oxides (SO_2 and SO_3), nitrogen oxides ($NO_x = NO_2 + NO$) and volatile organic compounds are emitted. Wet and dry deposition of inorganic pollutants leads to acidification of environment. These phenomena affect human health, increase corrosion, and destroy plants and forests.

Wet flue gas desulfurization (FGD) and selective catalytic reduction (SCR) can be applied for flue gas treatment and SO_2 and NO_x emission control. All these technologies are complex chemical processes and waste, like wastewater, gypsum and used catalyst are generated.

Electron beam flue gas treatment technology (EBFGT) is a dry-scrubbing process of simultaneous SO_2 and NO_x removal, where no waste except the by-product are generated. Studies show that irradiation of flue gases with an electron beam can bring about chemical changes that make removal of sulfur and nitrogen oxides easier. The main components of flue gases are N_2, O_2, H_2O, and CO_2, with much lower concentration of SO_x and NO_x. NH_3 may be present as an additive to aid removal of the sulfur and nitrogen oxides. Radiation energy is absorbed by gas components in proportion to their mass fraction in the mixture. The fast electrons slow down and secondary electrons are formed which play important role in overall energy transfer. After irradiation, fast electrons interact with gas creating various ions and radicals, the primary species formed include e-, N_2+, $N+$, O_2+, $O+$, H_2O+, $OH+$, $H+$, CO_2+, $CO+$, N_2^*, O_2^*, N, O, H, OH, and CO.

In the case of high water vapour concentration the oxidising radicals $OH^•$ and $HO_2^•$ and excited ions as $O(^3P)$ are the most important products. These species take part in a variety of ion-molecule reactions, neutral-

ization reactions, dimerization. The SO_2, NO, NO_2, and NH_3 present cannot compete with the reactions because of very low concentrations, but react with N, O, OH, and HO_2 radicals. After humidification and lowering its temperature, flue gases are guided to reaction chamber, where irradiation by electron beam takes place. Ammonia is injected upstream the irradiation chamber. Partly NO is reduced to atmospheric nitrogen. The byproduct formed in the process is a mixture of ammonium sulfate and nitrate which is a good fertilizer component. The electron beam flue gas treatment industrial plants are also operating in the coal-fired plants in China and Poland. The power of accelerators installed at the Polish plant is bigger than 1 MW, therefore it is the largest plasma flue gas treatment facility ever built. The plant treats approx. 270000 Nm3/h of flue gases. The installation consists of four main, separated systems: flue gas conditioning unit, ammonia storage and injection unit, process vessels and by-product collecting and storage unit.

The tests carried on the industrial installation showed, that the way of ammonia adding affects the pollutants (especially, SO_2) removal efficiency. The by-product aerosol is collected by the electrostatic precipitator and after granulation and storage is shipped to the NPK fertilizers production plant. The by-product consists mainly of ammonium sulfate and ammonium nitrate. The high efficiency of SO_x and NO_x removal was achieved (up to 95% for SO_x and up to 70% for NO_x) and by-product is a high quality fertilizer [12]. The other possibility is application of the process for VOC removal. Coal combustion is one of the biggest sources of VOCs, which are emitted with various concentrations, polynuclear aromatic hydrocarbons (PAH) are known as the most dangerous, and among them, e.g. benzo(a)pyrene $C_{20}H_{12}$, benzo(g,h,I)perylene $C_{22}H_{12}$ or dibenzo(a,h)anthracene $C_{22}H_{14}$ are the most toxic according to EPA.

Recent years have brought new regulations concerning PAH emission, and European countries have signed an international treaty, covering PAH emission. Tests at the pilot plant constructed at a coal-fired power station were performed with the purpose of estimating the influence of electron beam on VOCs present in flue gas, during SO_2 and NO_x removal. The influence of electron beam on the global toxicity factor of flue gas has been analysed. The removal efficiencies have been ranged from 40 up to 98% [13]. The chlorocarbons may be removed with the high efficiency as well [14].

Wastewater treatment. Increasing urbanization in the last two centuries has been accompanied by expansion of sewerage collection systems without any or adequate treatment. Liquid waste loads have become so large that the self-purification capacity of receiving streams downstream of large populations can no longer prevent adverse effects on water quality. These wastes now constitute significant sources of water pollution. The industrial effluents carry chemical contaminations such as heavy metals, organic pollutants, petrochemi-
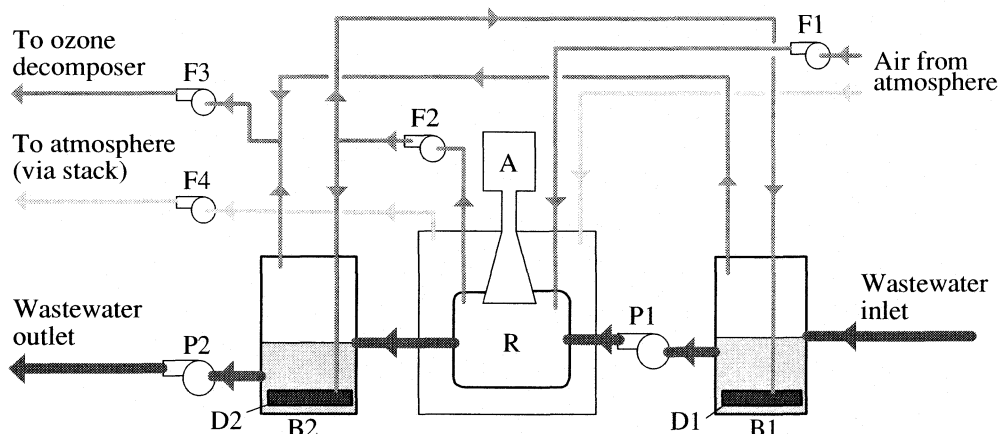
Simplified technological scheme of the industrial plant in Daegu, Korea; F1–F4 – air fans; P1–P2 – water pumps; D1 and D2 – diffusers; A – accelerator, R – reactor, B1 and B2 – primary and secondary basins.

cals, pesticides and dyes, while discharge of sewage and sludge gives rise to microbiological contamination of water bodies. The discharge of such materials into water bodies is responsible for risk of infection, health effects caused by contaminated drinking water and offensive odours. Therefore all these industrial and municipal wastewater need adequate treatment. Radiation processing of wastewater treatment is non-chemical, and uses fast formation of short-lived reactive species that can interact with a wide range of pollutants [15].

High-energy irradiation produces instantaneous radiolytic transformations by energy transfer from high energy photons or accelerated electrons to orbital electrons of water molecules. Absorbed energy disturbs the electron system of the molecule and results in breakage of inter-atomic bonds. The most important products of the fragmentation and primary interactions (radiolytic products):

$$H_2O \xrightarrow{EB} e_{aq}^-, {}^{\bullet}H, {}^{\bullet}OH, HO_2^{\bullet}, H_2O_2, H_2$$
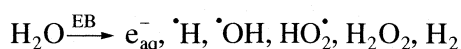
with yields (G value) of $0.28(e_{aq}^-)$, $0.062(H)$; $0.28(OH)$, $0.072(H_2O_2)$, in units of $\mu mol/J$. High reactivity is characteristic of water radiolysis products. Typical time of their reactions with the impurities in water is, as the rule, less than 1 μs. At the same time, reactivity of radiolytic products has quite different characteristics. Hydrogen peroxide, H_2O_2, radicals ${}^{\bullet}OH$ and $HO_2^{\bullet}$ are oxidizing species, while H atom and e_{aq}^- are reducing in nature. Simultaneous existence of strong oxidants and strong reductants within wastewater under treatment is remarkable and one of the important characteristics of radiation processing. Such reactive radicals are strong oxidizing or reducing agents that can transform the pollutants in the liquids wastes [16].

A large number of substances such as hard surfactants, lignin, pesticides cannot be degraded by conventional biochemical methods and thus escape from de-

composition in biological treatment. Biodegradation quality of wastewater depends on oxidation level and structure of pollutants and preliminary oxidation and fragmentation of biologically resistant molecules contribute to improvement of their biodegradability. Above mentioned mechanism of radiolytical oxidation shows possibility for the just required transformation of various pollutants.

Research and industrial treatments testify significant improvement of pollutant biodegradability after radiation-oxidation in aerated wastewater. Usually a dose of abort 1 ~ 2 kGy is necessary for complete transformation of pollutants by biological resistant to a biodegradable state. In December 2005 EB TECH Co, DYETEC, and KAERI finished the installation of high power accelerator (1 MeV, 400 kW) and wastewater treatment system in Daegu Dyeing Industrial Complex (DDIC), Korea, and started operation of the plant (Figure). This plant treats up to 10000 m³ of textile dyeing wastewater (from the total of 80000 m³) per day and shows good removal of non-degradable organic impurities. This is a breakthrough in the technology implementation worldwide and the biggest wastewater treatment plant based on electron emission unit ever built [17].

Sludge hygenization and biohazards. Research has shown that sewage sludge can be disinfected successfully by exposure to high-energy radiation. At a plant near Munich, doses of 2–3 kGy destroy more than 99.9% of bacteria present in sewage sludge, and at a plant near Boston a slightly higher dose (4 kGy) was used. Higher doses (up to 10 kGy) are required to inactivate more radiation resistant organisms at plants in Albuquerque and Ukraine.

Both gamma sources (Co-60, Cs-137) and electron accelerators can be used for the irradiation of sewage sludge. Gamma sources have better penetration allowing thicker layers of sludge to be irradiated [18], although they are less powerful and take longer irradiation time than electron sources [19]. The pilot plant us-

ing gamma source is operated in India. The irradiator system can be easily integrated with conventional treatment plant with flexibility of operation. Various dose treatment can be imparted to sludge with addition of sensitizing agents such as oxygen, air, ozone etc. About 3 kGy of absorbed dose in sewage sludge removes 99.99% of pathogenic bacteria consistently and reliably in a simple fashion. The irradiated sludge being pathogen free can be beneficially used as manure in the agricultural fields as it is rich in nutrients required for the soil. Since the irradiated sludge is free from bacteria, this can also be used as a medium for growing soil useful bacteria like rhizobium and azetobactor to produce bio-fertilizers, which can be used to enhance the crop yields.

Special applications regards biohazards combat. Anthrax that was sent in mail in October 2001 caused several deaths and big economical losses in the USA. Radiation proved to be very effective for mail decontamination. About 4000 tons of letter mail and 200 tons of parcels had been sanitized by the end of 2003 [20], the units are in operation nowadays as well.

REFERENCES

1. Zimek, Z. and Chmielewski, A. G., 1993, Electron accelerators for radiation processing, Nukleonika, 38(2), 3–19.

2. IAEA, 2005, Gamma irradiators for radiation processing, Vienna, ISBN 83-909690-6-8.

3. Stichelbaut, S., F., Bol, J.-L., Cleland, M. R., Gregoire, O., Herer, A. S., Jongen, Y., Mullier, B., 2004, The Palletron(tm): a high-dose uniformity pallet irradiator with X-rays, Radiat. Phys. Chem. 71 (1–2), 291–295.

4. Mehta, K., 2005, Radiation: Basics principles, J. Vascular Surgery, 1237–1238.

5. Zaman Haji Mohd Dahlan, K., 2004, Radiation processing, Physical Sciences, Engineering and Technology Resources, in Encyclopedia of Life Support Systems (EOLSS), Developed under the Auspices of the UNESCO, Eolss Publishers, Oxford, UK, [http://www.eolss.net].

6. Chmielewski, A. G., Haji-Saeid, M., Shamshad, A., 2005, Progress in radiation processing of polymers, Nucl. Instr. Meth. in Phys. Res. B, 226, 44–54.

7. Chmielewski, A. G., Michalik, J., Buczkowski, M. Chmielewska, D. K, 2005, Ionizing radiation in nanotechnology, Nucl. Instr. Meth. Phys. Res. B236, 329–332.

8. Chmielewski, A. G., Haji-Saeid, M., 2004, Radiation technologies: past, present and future, Radiat. Phys. Chem., 71(1–2) 17–21.

9. FAO/IAEA/WHO, 1999, High-dose irradiation: wholesomeness of food irradiated with doses above 10 kGy, WHO Technical Reports Series no 890, Geneva, Switzerland.

10. Chmielewski, A. G., Migdał, W., 2005, Radiation decontamination of herbs and species, Nukleonika, 50(4), 179–184.

11. Chmielewski, A. G., 2005, Application of ionizing radiation to environment protection, Nukleonika, 50 (suppl. 3), S17–S22.

12. Chmielewski, A. G., Licki, J., Pawelec, A., Tymiński, B., Zimek, Z., 2004, Operational experience of the industrial plant for electron beam flue gas treatment, Radiat. Phys. Chem., 71 (1–2), 441–444.

13. Chmielewski, A. G., Ostapczuk, A., Licki, J., Zimek, Z., Kubica, K., 2002, Reduction of VOCs in flue gas from coal combustion by electron beam treatment, Radiat. Phys. Chem., 63(3–6), 653–655.

14. Sun, Y, Chmielewski, A. G., 2004, 1,2-Dichloroethylene decomposition in air mixture by using ionization technology, Radiat. Phys. Chem., 71(1–2), 433–436.

15. Getoff N., 1996, Radiation-induced degradation of water pollutants–state of the art, Radiat. Phys. Chem., 47(4), 581–593.

16. Wasiewicz M., Chmielewski, A. G., Getoff, N., 2006, Radiation-induced degradation of aqueous 2,3-dihydroxynaphthalene, Radiat. Phys. Chem., 75(2), 201–209.

17. Han, B., Kim, Y. R, Kim, R. A., Salimov, R. A., Kuksanov, N. K, Nemytov, P. I., 2005, Electron beam treatment of textile dyeing wastewater: Operation of pilot plant and industrial plant construction, in TECDOC-1473, IAEA, Vienna, 101–110.

18. Sabharwal, S., Shah, M. R., Kumar, N., Patel, J. B., Technical and economic aspects of radiation hygenization of municipal sewage sludge using gamma irradiator, in TECDOC-1473, IAEA, Vienna, 119–124.

19. Chmielewski A. G., Zimek, Z., Bryl-Sandalewska, T., Kosmal, W., Kalisz, L, Kazimierczuk, M., 1995, Disinfection of municipal sludges in installation equipped with electron accelerator, Radiat. Phys. Chem., 46, 1071–1074.

20. Desrosiers, M. F., 2004, Irradiation applications for homeland security, Radiat. Phys. Chem., 71 (1–2), 479–482.

OTHER PROBLEMS
OF PHYSICAL CHEMISTRY

DETERMINATION OF Fe, Hg, Mn AND Pb IN TREE-RINGS OF POPLAR (*Populus alba* L.) BY U-SHAPED DC ARC

© 2007   D. M. Marković*, I. Novović*, D. Vilotić**, Lj. Ignjatović***

Institute of Physics, P.O. Box 68, Pregrevica 118, 11080 Belgrade, Serbia
E-mail: markovic@phy.bg.ac.yu
**Faculty of Forestry, University of Belgrade, Kneza Višeslava 1, 11030 Belgrade, Serbia*
***Faculty of Physical Chemistry, University of Belgrade, Studentski trg 12–16, 11000 Belgrade, Serbia*

Abstract – The U-shaped DC arc with aerosol supply was applied for determination of Fe, Hg, Mn and Pb in poplar (*Populus alba* L.) tree-rings. By optimization of the operating parameters and by selection of the most appropriate signal integration time (20s for Fe, Mn, Pb and 30s for Hg), the obtained limits of detection for Fe, Hg, Mn and Pb are 5.8, 2.6, 1.6 and 2.0 ng/mL, respectively. The detection limits achieved by this method for Fe, Hg, Mn and Pb are comparable with the detection limits obtained for those elements by such methods as: inductively coupled plasma-atomic emission spectrometry (ICP-AES), direct coupled plasma-atomic emission spectrometry (DCP-AES) and microwave induced plasma-atomic emission spectrometry (MIP-AES). We have chosen the tree-rings of poplar from two different locations. The first one is in the area close to the power plant "Nikola Tesla" TENT A, Obrenovac, while the other one is in the urban area of Novi Sad. In almost all cases from the location Obrenovac are registered elevated average concentrations of Fe, Hg, Mn and Pb in the tree-rings of poplar.

Heavy metals are natural components of the environment, but are of concern lately because they are being added to soil, water and air in increasing amounts. This is because of the rapid growth of population, increased urbanization, expansion of industrial activities, and more. Anthropogenic emission (primary sources are the combustion of fossil fuels and automobile exhaust emission in certain areas) of most trace metals now exceed or equal their natural emission [1]. The majority of metals that can be found in natural sources are toxic or harmful even at very low concentrations [2]. Heavy metals that get into the plants, animals and environment are not degraded pointing to their accumulation.

Tree-rings represent a unique, widely available, cheap and simple source of long-term data for monitoring trace metal levels in the atmosphere. Tree-ring chemistry may be used to monitor historical changes in trace metal levels. The use of vegetation monitors provides the cheapest and simplest indicator for monitoring trace metal levels in the atmosphere. A basic assumption in dedrochemistry is that the chemical make-up of the annual woody increment at least partly reflects the chemistry of the environment during the year of formation [3].

Current demands required from control and protection of the environment is strict. Therefore, the methods enabling the detection of low element concentration are very useful. In order to determine the low concentrations of Fe, Hg, Mn and Pb we modulated and utilized earlier developed spectrochemical method [4], where U-shaped DC arc plasma stabilized with an argon stream and aerosol supply was used as an excitation

source. The operating conditions of U-shaped DC arc plasma were optimized. Applying the appropriate computer program that enables the time integration of registered signal the reduction of the Fe, Hg, Mn and Pb detection limit was achieved.

EXPERIMENTAL

Apparatus. An U-shaped low current (7.5 A) argon DC arc with aerosol supply was applied as excitation source. The main characteristics of the arc are presented in the paper [5]. A laboratory modified spectrograph PGS-2 (Carl Zeiss, Jena) with holographic gratings: Spectrogon (2100 grooves/mm, VIS, Fe, Mn and Pb) and Carl Zeiss (2100 grooves/mm, UV, Hg), was used as spectrometer. The intensity of the analyte spectral line was recorded by photomultiplier (Hamammatsu R-3788) and AD conversion card (ED-300) connected with PC. The recorded signal intensities were accumulated during the integration time of 20 s for Fe, Mn, Pb and 30 s for Hg, by application of the appropriate computer program. The slit width was 0.15 mm. Spectral lines intensities are measured for Fe I ($\lambda = 371.99$ nm), Mn I ($\lambda = 403.08$ nm) and Pb I ($\lambda = 405.78$ nm) at 4 mm and for Hg I ($\lambda = 253.6$ nm) at 2 mm from the axis of the arc.

Solutions. A series of reference solutions (Fe, Hg, Mn and Pb) were prepared in the range from 5 to 5000 ng/ml, by appropriate dilution of the stock solutions (1 mg/ml Merck). Each of the solutions contained 0.5% potassium chloride as spectroscopic buffer. The nebulization of the solution was performed by a Meinhard nebulizer (TR 30 K2) connected with a double-pass spray chamber.
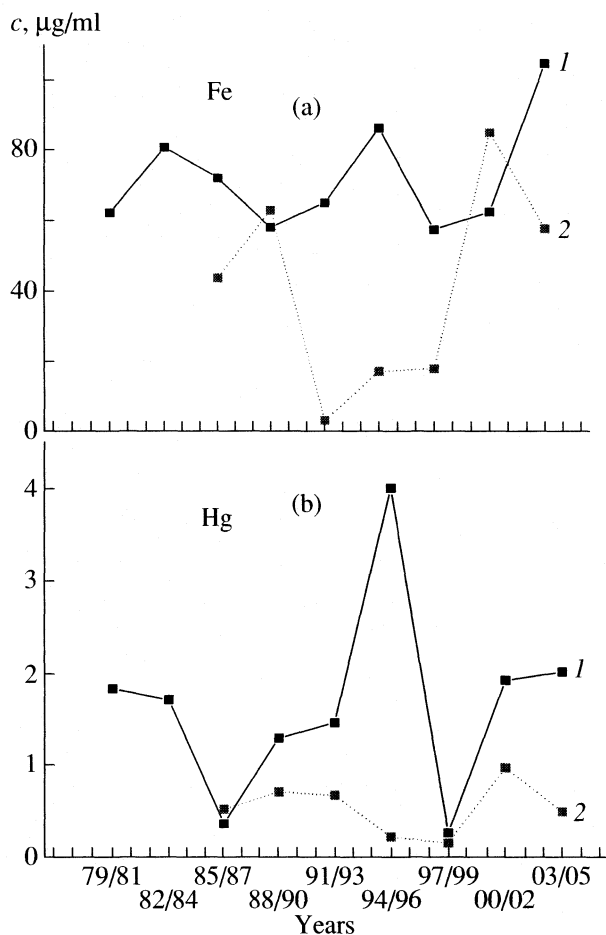
Fig. 1. Fe and Hg mean concentration in poplar (*Populus al-ba* L.) tree-rings for the location Obrenovac from 1979 (*1*) and for the location Novi Sad from 1985 to 2005 (*2*).

Sampling locations. Tree-rings samples were collected in march 2005 from two locations. First one was in the area of power plant "Nikola Tesla A" (TENT-A), located on the bank of the Sava river, in Obrenovac, 42 km upstream from the Serbian capital Belgrade. Power plant was built in 1970 and produces approximately 5000 kt of ash per year [6]. Coal ash is transported to the dump after being suspended in the water taken from the Sava river, in the approximate ratio 1 : 10 [7]. Coal combustion in power plants generates large amounts of ash that is stored more or less unprotected in the environment where it can represent a significant source of heavy metals, PAHs and other pollutants [7]. The second one location was in the urban area of Novi Sad in the Institute for lowland forestry and environmental protection plantation. Novi Sad is located on the bank of the Danube river, 80 km upstream from the Serbian capital Belgrade. The cores were taken from each poplar tree at the breast hight (1.3 m). Each poplar core was divided into 3 years segments starting from 1979 for poplar from Obrenovac and from 1985 for the location of Novi Sad.

Samples preparation. Tree-rings samples (3 years segments) were placed in pre-washed (15% H_2SO_4) 50 ml borosilicate glass tube dried at 70°C for 48h and weighed. Samples were suspended in 10 ml of 70% HNO_3 at 80°C for 24 h. The cold solution was filtered through acid washed (10% HNO_3) Whatmam No. 42 filter paper and diluted to 50 ml with bidistilled water [8].

RESULTS AND DISCUSSION

After the optimization of the operating conditions, two series of standard aqueous solutions of Fe, Hg, Mn and Pb, containing 0.5% KCl as spectroscopic buffer, were measured at appropriate wavelength with different integration times (t_1 = 1 s, t_2 = 10 s, t_3 = 20 s and t_4 = 30 s). The obtained calibration curves were straight lines in an extensive concentration range. With increasing integration time the slope of the lines increases i.e. the concentration sensitivity is enlarged. According to the obtained results the detection limit is defined using the following relation [9, 10]:

$$c_L = k \times 0.01 s_r c_o / p, \qquad (1)$$

where k represents a constant with value 2, s_r relative standard deviation of the background signal, c_o – concentration, and p – the signal-to-background ratio at c_o. The lowest detection limits for Fe, Mn and Pb are achieved for the integration time of 20 s reaching the values 5.8, 1.6 and 2.0 ng/ml, respectively. The lowest detection limit for Hg is obtained for the integration time of 30 s and amounts 2.6 ng/ml. The achieved detection limits, using our spectrochemical method, for Fe, Mn and Pb are within the detection limits accomplished with ICP-AES [11], DCP-AES [12] and MIP-AES [13] methods. Obtained results point out that our spectrochemical method can be used successfully for determination of very low metal concentrations in different samples.

Tree-rings are a unique source of long-term data and have often been used in studies for understanding and quantifying of air pollution on forests [14]. The concentrations of Fe, Hg, Mn and Pb in poplar tree-rings from locations Obrenovac and Novi Sad, were determined in this paper.

In Fig. 1, 2 are presented average concentrations of Fe, Hg, Mn and Pb in white poplar tree-rings for the locations Obrenovac from 1979 and for the location Novi Sad between 1985 and 2005. From Fig. 1a it can be seen that almost in all cases the obtained average concentrations of Fe in tree-rings taken from the location Obrenovac are higher. The average Fe concentration value in poplar tree-rings from the location Obrenovac is 72.43 μg/g, while from the location Novi Sad is 41.34 μg/g. Comparing the mutual relationship of their average concentration values one can get the value 1.75.

From Fig. 1b it can be also seen much higher average Hg concentration in poplar tree-rings from the location Obrenovac. There is also one pronounced maxi-
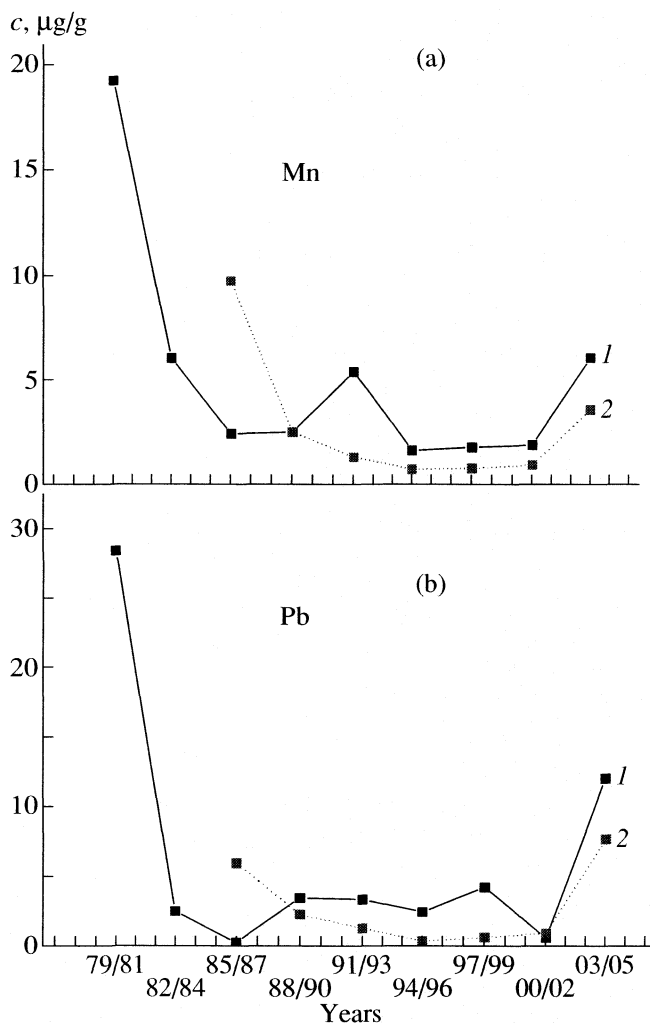
Fig. 2. Mn and Pb mean concentration in poplar (*Populus alba* L.) tree-rings for the location Obrenovac from 1979 (*1*) and for the location Novi Sad from 1985 to 2005 (*2*).

Fig. 3. The relationship of average concentrations of Fe, Hg, Mn and Pb in poplar tree-rings from the locations Obrenovac and Novi Sad.

mum for the period 1994–1996 from the location Obrenovac. The average value of Hg concentration in poplar tree-rings from the location Obrenovac is 1.66 µg/g, and from the location Novi Sad is 0.54 µg/g. Their average concentration ratio is 3.07. This value is the highest in comparison with other obtained ratios for Fe, Mn and Pb.

Like wise in case of Fe and Hg in case of Mn (Fig. 2a) the average concentration is higher in poplar tree-rings from the location Obrenovac. The average Mn concentrations are 5.25 µg/g, for the location Obrenovac and 2.83 µg/g for the location Novi Sad while their ratio is 1.86. From Fig. 2 it can be observed the similar trend of Mn concentration for the period 1994–2005.

In Pb case (Fig. 2b), analogously with all above mentioned cases, are obtained higher average concentration values in poplar tree-rings from the location Obrenovac. Average value of Pb in tree-rings from location Obrenovac is 6.44 µg/g and from the location
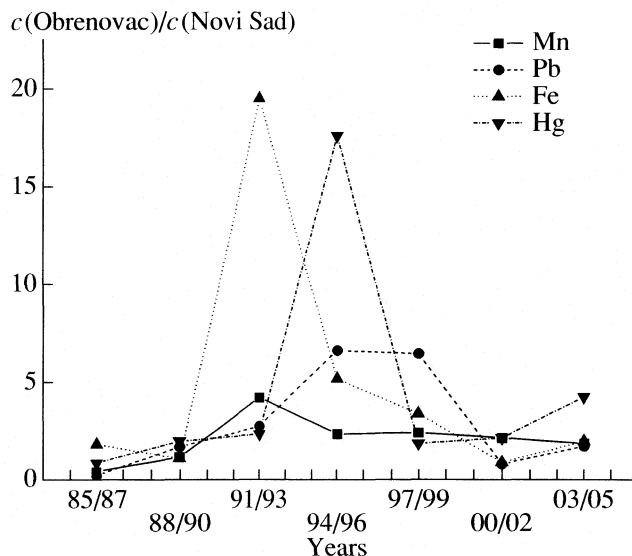
Novi Sad 2.80 µg/g while their ratio is 2.30. As well as in the Mn case in Pb case it can be seen the similar concentration rising trend in poplar tree-rings from both locations for the period 1988–2005.

In Fig. 3 is presented the relationship of average concentrations of Fe, Hg, Mn and Pb in poplar tree-rings from the locations Obrenovac and Novi Sad for the period 1985–2005. From Fig. 3 are clearly seen maxima in Fe and Mn concentrations for a period 1991–1993, while the maximal concentration of Hg is obtained for a period 1994–1996. In a case of Pb the maximal concentration ratio has a plateau rather than distinctly pronounced maximum between 1994 and 1999. On the basis of obtained results given in Fig. 3 it can be deduced that the maximal value of average concentration ratio of Fe, Mn and Hg in poplar tree-rings from locations Obrenovac and Novi Sad are. concentrated in a period between 1991 and 1996. For Pb this period is extended from 1996 to 1999.

The results obtained from our present study clearly indicate that in the samples of poplar tree-rings taken from location Obrenovac, the average Fe, Mn, Hg and Pb concentrations are higher than from location Novi Sad. We used tree-rings of poplar as an indicator of environmental pollution. These results present an answer to continuous activity of power plant Nikola Tesla in Obrenovac for many years i.e. decades.

ACKNOWLEDGEMENTS

Ministry of Science and Environmental Protection of Serbia.

REFERENCES

1. Odukoya O. O., Arowolo T. A. and Bamgbose O., *Environ. Internat.*, 2000, vol. 26, no. 1–2, p. 11.

2. Kakkar P. and Jaffery F. N., *Environ. Toxicol. Pharmacol.*, 2005, vol. 19, no. 2, p. 335.

3. Watmough S. A., *Environ. Pollut.*, 1999, vol. 106, no. 3, p. 391.

4. Tripković M., Holclajtner-Antunović I., Marinković M. and Marković D., *J. Serb. Chem. Soc.*, 2001, vol. 66, no. 4, p. 249.

5. Marinković M. and Antonijević V., *Spectrochim. Acta B*, 1980, vol. 35, no. 3, p. 129.

6. Ilica M., Cheeseman C., Sollarsb C. and Knightb J., *Fuel*, 2003, vol. 82, no. 3, p. 331.

7. Popovic A., Djordjevic D. and Polic P., *Environ. Internat.*, 2001, vol. 26, no. 4, p. 251.

8. Orlandi M., Pelfini M., Pavan M., Santilli M. and Colombini M. P., *Microchem. J.*, 2002, vol. 73, no. 1–2, p. 237.

9. Boumans P. W. J. M. and Vrakking J. J. A. M., *Spectrochim. Acta B*, 1984, vol. 39, no. 9–11, p. 1261.

10. Boumans P. W. J. M. and Vrakking J. J. A. M., *Spectrochim. Acta B*, 1985, vol. 40, no. 8, p. 1085.

11. Seubert A., *Tr AC*, 2001, vol. 20, no. 6–7, p. 274.

12. Lajunen L. H. J., *Spectrochemical Analysis by Atomic Absorption and Emission*, Cambridge: Royal Society of Chemistry, 1992, p. 230.

13. Jin Q., Duan Y. and Olivares J. A., *Spectrochim. Acta B*, 1997, vol. 52, no. 2, p. 131.

14. Forretti M., Innes J. L., Jalkanen R., Saurer M., Schaffer J., Spiecker H. and Wilpert K., *Dendrochronologia*, 2002, vol. 20, no. 1–2, p. 159.

METHODS AND TECHNIQUES
OF PHYSICOCHEMICAL INVESTIGATIONS

CHEMICAL OXYGEN-IODINE LASER:
RECENT ADVANCES AS A CHEMICAL DEVICE

© 2007 M. Endo

*Department of Physics, School of Science, Tokai University, 1117 Kitakaname, Hiratsuka 259–1292, Japan*
E-mail: <endo@tokai.ac.jp>

Abstract – Recent advances of Chemical Oxygen-Iodine Laser (COIL) are reviewed. In this paper, developments of COIL as a unique chemical device, whose product is not chemical substance, but coherent photons, is emphasized. The key component of COIL is singlet oxygen generator (SOG). Unique principles of modern SOG are reviewed. For high-efficiency operation, rapid mixing of oxygen and iodine is of primarily important. Latest mixing enhancement techniques are reviewed. Applications of ultra high-power COIL are presented.

1. INTRODUCTION

Chemical oxygen-iodine laser (COIL) is an unusual chemical device. Although it comprises of series of chemical reaction chambers, the output of COIL is not a chemical substance. Instead, it produces extremely high-power, coherent photon flux in near-infrared region, at 1.315 μm. As a chemical laser, COIL is unique because it is the only electronic transition chemical laser. In other chemical lasers, population inversion is attained between vibrational levels of active molecule, thus the wavelength is in the range of mid-infrared. Because the operating wavelength is in the minimum loss band of silica optical fiber, long-distance fiber delivery of the laser output is possible and that makes COIL promising for unique applications.

Fig. 1 shows the schematic drawing of typical modern supersonic COIL. It comprises of Singlet Oxygen Generator (SOG), iodine injector, supersonic expansion nozzle, laser cavity and vacuum pump. The energy source of the COIL is aqueous basic hydrogen peroxide (BHP). The gas-liquid surface reaction between BHP and gaseous chlorine produces electronically excited oxygen molecules, $O_2(^1\Delta)$ by the following overall reaction,

$$H_2O_2 + 2KOH + Cl_2 \longrightarrow 2H_2O + 2KCl + O_2(^1\Delta). \quad (1)$$
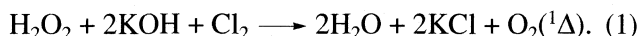
The $O_2(^1\Delta)$ is mixed with inert buffer gas such as nitrogen or helium, and transferred to the laser cavity under a low partial pressure (less than 2 kPa) to avoid collisional deactivation. Then molecular iodine carried with inert gas is injected into the main flow, and the mixture is supersonically expanded. The iodine is dissociated by a complex, collisional process involving $O_2(^1\Delta)$[1] described as

$$nO_2(^1\Delta) + I_2 \longrightarrow nO_2(^3\Sigma) + 2I(^2P_{3/2}), \quad (2)$$
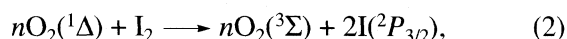
where $O_2(^3\Sigma)$ is a ground-state oxygen and n is believed to be 6 to 10. In the typical COIL operation, the ratio of

I_2 to O_2 is approximately 2%. As shown above, part of the energy contained in $O_2(^1\Delta)$ is used to dissociate the iodine, and the rest is used to excite iodine atoms via the near-resonant energy transfer reaction

$$O_2(^1\Delta) + I(^2P_{3/2}) \underset{k_b}{\overset{k_f}{\rightleftharpoons}} O_2(^3\Sigma) + I(^2P_{1/2}), \quad (3)$$
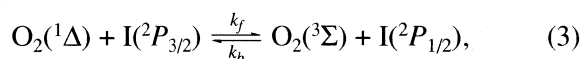
where the equilibrium constant $k_f/k_b = 0.75\exp[403/T]$. Population inversion is established between excited $I(^2P_{1/2})$ and ground-state $I(^2P_{3/2})$ to stimulate laser action,

$$I(^2P_{1/2}) + h\nu \longrightarrow I(^2P_{3/2}) + 2h\nu. \quad (4)$$
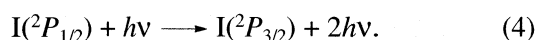
Supersonic expansion of the laser medium is employed mainly to achieve a high efficiency since the gasdynamic cooling of the medium shifts the equilibrium condition of Eq. (3) to the right-hand side as indicated by

$$K_e = \frac{[O_2(^3\Sigma)][I(^2P_{1/2})]}{[O_2(^1\Delta)][I(^2P_{3/2})]} = 0.75\exp\left[\frac{403}{T}\right], \quad (5)$$

a change that results in a higher gain and more complete energy extraction from $O_2(^1\Delta)$. The figure-of-merit of COIL is measured by "Chemical Efficiency". It is defined as the number of emitted photons divided

Fig. 1. Schematic drawing of a supersonic COIL device.

Fig. 2. Schematic drawing of the gas-liquid surface reaction of $O_2(^1\Delta)$ generation.

Fig. 3. Singlet oxygen generator of the early age.

by the number of chlorine molecules input. Chemical efficiency of typical COIL is on the order of 20%.

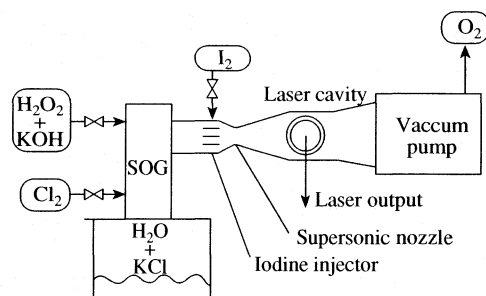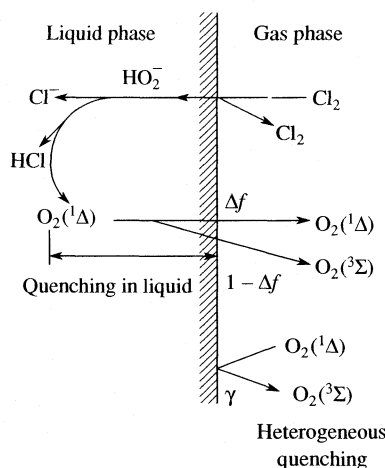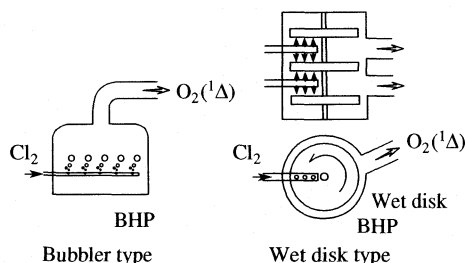The first COIL was demonstrated in 1977 by McDermott et al. at the U. S. Weapons Laboratory [2]. Because he was a chemist, the first COIL apparatus looks quite familiar to them, but it does not resemble to any other lasers. Since the operational parameter was not optimized, the output power of the first COIL was merely 4 mW. In the first 10 years, COIL was scaled-up by simply increasing the size of the apparatus, and finally a 4.6 kW output was reported by an apparatus with a 4 m-width laser duct [3]. Further scale up by simply increase the size of the apparatus was prohibitive.

In the mid 80's a breakthrough technology, supersonic expansion was introduced. The merit of supersonic expansion was twofold. The gasdynamic cooling of the laser medium shifted the equilibrium of oxygen-iodine energy transfer more favorable to energy extraction, and the energy flow density through gas transport duct was increased tenfold. A 1.6 kW apparatus was developed in the mid 80's [3], but the width of the flow duct was only 25 cm.

Another breakthrough in SOG technology boosts the output of the COIL tenfold. In the ancient SOG, the density of oxygen generation was restricted by the sur-face area of the gas-liquid interface. The bottleneck was broken by the advent of "Jet SOG" and it is currently employed most of the COIL devices around the world.

As of 2006, an output of several hundreds kW is demonstrated by a single COIL device, and multi-MW device is being developed by operating those devices in series. The multi hundred kW COIL module was developed by TRW [4]. Its size is surprisingly compact compared to other ultra high-power lasers.

2. SOG TECHNOLOGY

Singlet oxygen is generated by the gas-liquid surface reaction between HO_2^- ion in the BHP and gaseous chlorine (Fig. 2). The reaction cross section is so large that Cl_2 molecule could penetrate into the liquid phase only a few molecular layers if the surface HO_2^- ion is not depleted. Therefore, the technical challenges of SOG is summarized as:

1. Making as large surface area as possible in a unit volume of reaction chamber.

2. Prevention of HO_2^- ion depletion by constant renewal of the gas-liquid interface.

3. Detachment of generated $O_2(^1\Delta)$ as fast as possible to prevent heterogeneous quenching at the gas-liquid interface.

SOG technology has been evolved over the years from a very simple sparger to modern sophisticated chemical devices. Fig. 3 shows the schematic drawing of early SOGs. The first successful SOG was based on simple sparger, in which bubbler is located near the liquid surface to prevent heterogeneous deactivation of $O_2(^1\Delta)$. Then variety of "wet surface" type SOGs shown in Fig. 3 has been developed. In those types, thin layer of BHP is generated on the vertically held plates so that they could pack much more surface area per unit volume than bubbler type.

In 1991, Zagidullin et al. developed revolutionary "Jet SOG" [5]. The principle was very simple, but quite effective. Fig. 4 shows the schematic drawing of the Jet SOG. Dense row of holes are punched at the jet plate and mounted on the top of the SOG. BHP jet shower fills the reaction volume and Cl_2 gas flows from bottom of the reaction volume. More than 90% of Cl_2 is converted to oxygen within 10 cm of interaction length. The properties of Jet SOG are characterized by its large surface-to-volume ratio and fast renewal of the liquid surface. The Jet SOG is so successful that almost all the COIL research sites in the world are now employing this type SOG. In Tokai University, a Jet SOG is operating with the following specifications: Reaction zone cross section 10 cm^2, Cl_2 input molar flow rate 20 mmol/s, pressure 20 Torr, O_2/Cl_2 yield 90%, $O_2(^1\Delta)/O_2$ yield 60%.

Today's challenge for SOG is higher operational pressure and higher throughput per reaction volume without degradation of the yield. To achieve these re-

quirements, modern SOGs use centrifugal force to maintain gas-liquid interface under very high flow of Cl_2 gas. Fig. 5a shows the schematic drawing of the "TA-SOG" [6]. In this SOG, BHP jet flows from the hub of the screw perpendicularly to its axis. Cl_2 gas is forced to go up by the rotating vane, and reacts with BHP droplets. Due to the strong centrifugal force, droplets are not entrained by the gas flow, thus high throughput is possible. Fig. 7b shows the schematic of the centrifugal bubbler SOG [7]. The principle of this SOG is same as the ancient bubbler SOG, except that the liquid surface is held vertically under the strong centrifugal force. The maximum operation pressure thus throughput is boosted considerably by the false gravitational force.

3. MIXING OF OXYGEN/IODINE

Rapid mixing of oxygen and iodine is critical to the performance of supersonic COIL. During the first 15 years of supersonic COIL developments, the shape of the expansion nozzle was simple Laval nozzle with holes of iodine injectors. The optimization of the iodine holes was achieved mainly by the cut-and-try basis experiments. Since the late 1990's, evolution of the personal computers changed the situation. Three-dimensional Computational Fluid Dynamics (CFD) became available for COIL researchers who were not specialized in fluid dynamics. Since then, number of unique mixing concepts has been proposed.

We have developed so-called "X-wing" mixing nozzle [8]. Fig. 6 shows the schematic drawing. Thin wedges are set in an alternating fashion across the flow duct. Because those wedges resemble the letter "X" viewed from the side, we call this component the "X-wing". The assembly of wedges primarily functions as the supersonic expansion nozzle, but also doubles as a streamwise vortex generator. The secondary flow is injected at the nozzle exit plane (NEP) perpendicularly to the main flow. The contact surface between the primary and secondary flows is immediately enlarged by the streamwise vortices, a change that should lead to rapid completion of iodine dissociation. Notably, the streamwise vortex has a much longer life than the transverse vortex in the supersonic flow, and it is the most effective factor in enhancing the mixing in the supersonic stream. By employing this mixing nozzle, we have achieved record chemical efficiency of 33%.

Another trend of oxygen/iodine mixing is so-called "Ejector COIL" [9–11]. Ejector COIL is motivated to overcome the drawback of the conventional supersonic COIL. Because of the collisional deactivation, cavity pressure of COIL is limited at less than 1 kPa. Vacuum pumps to evacuate the active medium to atmospheric pressure is rather large and that limits the mobility of COIL. In ejector COILs, supersonic expansion of the active medium is done by the ejector effect of hypersonic nitrogen flow injected into the flow channel. Mixing of iodine into the supersonic flow of oxygen
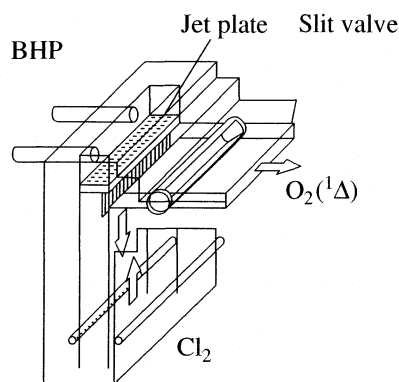
Fig. 4. Schematic drawing of a jet SOG.

(a) TA-SOG

(b) Centrifugal bubbler SOG
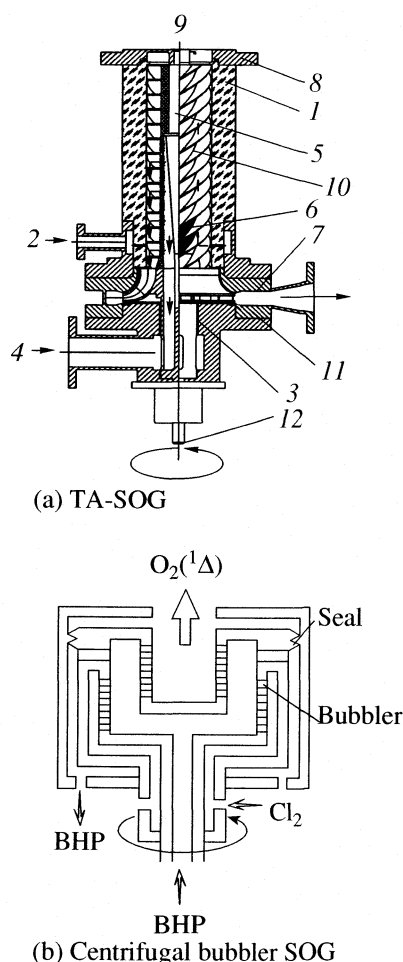
Fig. 5. Advanced SOGs. *1*: reactor body; *2*: chlorine source; *3*: BHP injection unit; *4*: BHP source; *5*: hollow rotor; *6*: holes in rotor's wall; *7*: BHP collector; *8*: singlet oxygen output unit; *9*: singlet oxygen; *10*: multiple-thread screw; *11*: liquid pump; *12*: rotor's shaft.

ejected by the nitrogen in a limited period is a very interesting problem. A number of nozzles are developed by the aid of CFD as shown in Fig. 7. Typically, 25% of chemical efficiency are achieved and pressure at downstream of the supersonic diffuser reaches at 13 kPa.
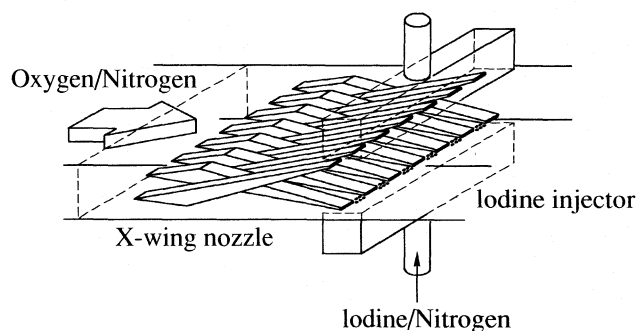
Fig. 6. Schematic drawing of X-wing supersonic mixing nozzle.

4. ELECTROCHEMICAL BHP REGENERATION

In every COIL system, singlet oxygen generator (SOG) is operated with a predetermined quantity of dense BHP solution (approx. 6M) that is continuously recirculated within the system and reacts with Cl_2. During a batch operation of COIL, the molarity of HO_2^- in the BHP decreases. Since the absorbability of the gaseous Cl_2 depends on the HO_2^- ion concentration at the gas-liquid interface, the efficiency of the $O_2(^1\Delta)$ production depends on the HO_2^- molarity. When HO_2^- molarity is decreased to a point (approx. 3M), residual BHP is drained and replaced with fresh one. Continuous regeneration of the BHP with an electrochemical reaction may extend the continuous operation period of COIL outstandingly, and leads to a drastic reduction of the operational costs.

Motivated by those facts, we have been studying the electrochemical regeneration of BHP [12]. Fig. 8 shows the schematic drawing of the electrochemical BHP regenerator. BHP is refreshed by the following three-phase contact reaction on the carbon-felt cathode,

$$O_2 + e^- \longrightarrow O_2^-, \tag{6}$$

$$2O_2^- + H_2O \longrightarrow O_2 + HO_2^- + OH^-, \tag{7}$$

$$O_2^- + H_2O + e^- \longrightarrow HO_2^- + OH^-. \tag{8}$$

The key for successful regeneration of high molarity BHP is the control of decomposition of BHP on the car-bon-felt surface. We have found that adding caffeine is effective to prevent decomposition. Currently, positive gain of molarity is achieved up to 3.6 M of BHP with electric current efficiency of 67%.

5. APPLICATIONS

COIL is a highly scalable laser operating at the lowest loss band of silica optical fiber. Moreover, it is independent of electrical input to pump the active medium. Various applications are projected to exploit the characteristics of this unique laser. The most distinctive COIL application should be the "Airborne Laser" [13]. A multi-megawatt COIL system is carried on the modified B–747 aircraft, and kill the hostile ballistic missiles at the boost phase from a few hundreds km away. The laser module and platform are already completed and it will be deployed in 2011.

The mobility and optical fiber deliverability of COIL could be used for decommission and dismantlement of the ceased nuclear plants. There was an extensive research done by Kawasaki Heavy Industries in 1990's [14].

We have proposed "Optical Power Network" concept on the basis of ultra high-power COIL facility [15]. It is like today's electric power network, a supplier generates coherent photons and users buy them through optical fiber delivery. The initial and running costs of high-power laser for general industrial uses would be greatly reduced due to the scale merit. A 1 kW, 1km delivery of COIL output is already demonstrated [16]. In this concept, the nature of COIL, an open-cycle chemical laser, is a drawback for continuous operation. The motivation of the electrochemical regeneration of BHP comes partly from our proposal.

In addition to those applications, excavation of the underwater natural resource [17] and space debris removal [18] by COIL are proposed.

6. SUMMARY

The paper has been aimed at introducing the unique features of chemical oxygen-iodine laser (COIL) as a chemical device, and presenting latest achievements. Trends of singlet oxygen generator (SOG) develop-
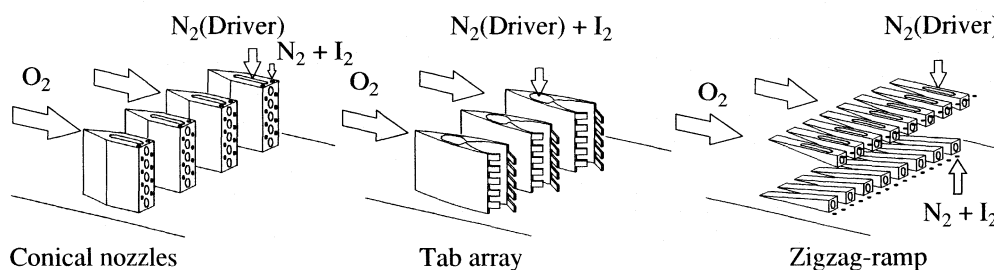

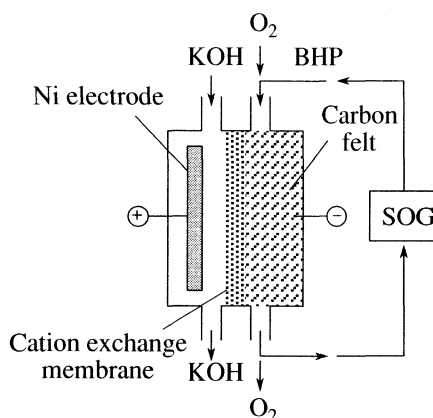**Fig. 7.** Various nozzle configurations of "Ejector COIL".

Fig. 8. Electrochemical BHP regenerator.

ments and oxygen-iodine mixing concepts are highlighted. Some briefly described projects of COIL applications demonstrate the unique characteristics of this chemical device.

REFERENCES

1. R. F. Heidner III, C. E. Gardner, G. I. Segal and T. M. El-Sayed, J. Phys. Chem. 87, pp. 2348–2360, 1983.

2. W. E. McDermott, N. R. Pchelkin, D. J. Benard and R. R. Bousek, Appl. Phys. Lett. 32, pp. 469, 1978.

3. K. A. Truesdell, C. A. Helms and G. D. Hager, Proc. SPIE 2502, pp. 217–237, 1994.

4. G. Koop, J. Hartlove, C. Clendening, P. Lohn, C. C. Shih, J. Rothenflue, K. Hulick, K. Truesdell and R. Walter, AIAA–00–2421, 31st Plasmadynamics and Lasers Conference, Denver CO., 2000.

5. M. V. Zagidullin, A. Yu. Kurov, N. L. Kupriyanov, V. D. Nikolaev, M. I. Svistun and N. V. Erasov, Sov. J. Quant. Electern. 21, pp. 747–753, 1991.

6. F. Wani, M. Endo, B. Vyskubenko, S. Ilyn, I. Krukovsky, S. Takeda and T. Fujioka, IEEE J. Quant. Electron. 34, pp. 2130–2137, 1998.

7. V. D. Nikolaev, M. I. Svistun, M. V. Zagidullin and G. D. Hager, Appl. Phys. Lett. 86, 231102 (2p), 2005.

8. M. Endo, T. Masuda and T. Uchiyama, IEEE J. Quant. Electron. pp. 71–77, 2006.

9. V. D. Nikolaev, M. V. Zagidullin, T. J. Madden and G. D. Hager, AIAA2000–2427, 2000.

10. T. T. Yang, R. A. Dickerson, L. F. Moon and Y. S. Hsia, AIAA–2000–2425, 2000.

11. M. Endo, H. Nagaoka, T. Osaka, T. Dabamoto, S. Takeda and F. Wani, AIAA2003–3618, 2003.

12. M. Endo, M. Hano, S. Wakita, M. Uno and S. Takeda, Proc. SPIE 5777, pp. 66–69, 2004.

13. S. J. Thornton, Proc. SPIE 5777, pp. 1008–1010, 2004.

14. J. Adachi, N. Takahashi, K. Yasuda and T. Atsuta, Progress in Nuclear Energy 32, pp. 517–523, 1998.

15. M. Endo, S. Nagatomo, S. Takeda, F. Wani, K. Nanri and T. Fujioka, Proc. SPIE 3268, pp. 106–114, 1998.

16. N. Takeuchi, K. Tei, D. Sugimoto, O. Vyskubenko and T. Fujioka, Proc. SPIE 5777, pp. 298–301, 2004.

17. K. Josui, T. Fujioka, K. Tei and D. Sugimoto, Proc. SPIE 5777 pp. 302–306, 2004.

18. W. L. Bohn, Proc. SPIE 3612, pp. 79–84, 1999.

ХИМИЧЕСКАЯ КИНЕТИКА И КАТАЛИЗ

СИНТЕЗ УГЛЕРОДНЫХ НАНОТРУБОК С МАЛЫМ ЧИСЛОМ СЛОЕВ КАТАЛИТИЧЕСКИМ ПИРОЛИЗОМ МЕТАНА И КИНЕТИКА ИХ НАКОПЛЕНИЯ

© 2007 г.   Ю. В. Гаврилов*, Д. А. Гришин*, Х. Джиан**, Н. Г. Дигуров*, А. Г. Насибулин**, Е. И. Кауппинен**, ***

*Российский химико-технологический университет им. Д.И. Менделеева, Москва
**Государственный технический научно-исследовательский институт Финляндии, Эспоо
***Группа наноматериалов, Лаборатория физики и Центр новых материалов,
Хельсинский университет технологии, Эспоо, Финляндия
E-mail: dag@fromru.com

Путем прямых термогравиметрических измерений в сочетании с электронно-микроскопическими исследованиями получены кинетические зависимости накопления массы углерода в процессе пиролиза CH_4 в смеси с H_2 на Мо–Со/MgO-катализаторе с атомным соотношением Мо : Со : Mg = 3 : 1 : 76 при атмосферном давлении, температуре 900°С и различных парциальных давлениях CH_4 и H_2. Показано, что основными твердыми продуктами пиролиза являются углеродные нанотрубки с числом слоев от двух до пяти. Внешний диаметр нанотрубок изменялся от ~3 до 9 нм. Предложена кинетическая модель накопления углерода, в которой учитывается образование двух продуктов – нанотрубок и углерода, отлагающегося на их поверхности. Показаны обратимость процесса и дезактивация катализатора образующимися нанотрубками.

Углеродные нанотрубки (НТ) являются одним из наиболее изучаемых объектов и связано это, прежде всего, с перспективой создания на их основе материалов, которые смогли бы унаследовать их уникальные свойства. Синтез НТ в граммовых количествах уже не является проблемой: предложено множество способов, которые были успешно реализованы в лабораторных масштабах [1], однако цена одного грамма таких НТ до сих пор колеблется от нескольких десятков до нескольких сотен долларов [2]. Высокая цена и отсутствие промышленного производства сдерживают применение НТ в областях, где они оказались эффективнее традиционных материалов. Решением этой проблемы может стать создание технологии непрерывного получения НТ каталитическим пиролизом углеводородов с использованием доступного сырья и высокоэффективных катализаторов (Kt). Самым простым и наиболее доступным углеводородным сырьем является природный газ, основным компонентом которого является метан. Наиболее эффективными катализаторами представляются системы, которые могут быть описаны общей формулой Мо–Со/MgO [3–6].

В настоящее время изучению влияния различных параметров каталитического пиролиза метана на выход и морфологию НТ посвящено достаточно большое количество работ [7–10]. Однако для создания технологии производства НТ необходима кинетическая модель накопления НТ, которая могла бы позволить определить режимы проведения процесса пиролиза и рассчитать основные размеры аппаратов.

Целью этой работы являлось создание кинетической модели накопления НТ в процессе пиролиза CH_4 в стационарном слое Мо–Со/MgO-катализатора.

ЭКСПЕРИМЕНТАЛЬНАЯ ЧАСТЬ

Для синтеза Kt выбран метод сжигания, который был разработан Кинсли и Патилом для синтеза оксида алюминия [11], и впоследствии нашел широкое применение для синтеза различных оксидных композиций [12, 13], в том числе Kt синтеза НТ [3–6]. Оксидный катализатор с атомным соотношением Мо : Со : Mg = 3 : 1 : 76 синтезировали согласно следующей методике. В керамической чаше на 250 мл смешивали 10.000 г $Mg(NO_3)_2 \cdot 6H_2O$ ("ч.д.а"), 0.149 г $Co(NO_3)_2 \cdot 6H_2O$ ("ч.д.а."), 0.272 г $(NH_4)_6Mo_7O_{24} \cdot 4H_2O$ ("х.ч.") и 5.730 г NH_2CH_2COOH ("ч."), добавляли 2.5 мл дистиллированной H_2O и нагревали до полного растворения компонентов. Керамическую чашу с раствором вносили в предварительно разогретую до 550 ± 10°С муфельную печь, выдерживали 20 мин, затем охлаждали на воздухе и переносили в герметичную емкость.

Для изучения кинетики роста НТ использовали установку, позволяющую непрерывно измерять массу твердых углеродных продуктов пиролиза CH_4. Установка включала вертикальный трубчатый реактор из кварцевого стекла с внутренним диаметром 34 мм и длиной 430 мм, печь резистивного нагрева длиной 200 мм, торсионные весы с диапазоном измерения 0.000–0.500 г и оборудование для регулирования температуры и расхода газов. В нижней части реактора имелся карман для термопары. В верхней части реактора располагалась съемная крышка из фторопласта-4, в центре которой находилось отверстие диаметром 2 мм, через которое в реактор вводилась хромель-алюмелевая нить, на один конец которой прикреплялся контейнер из медной фольги (диаметр 20 мм и высота 5 мм) с навеской катализатора, а другой прикреплялся к рычагу торсионных весов. Газ подавался через штуцер, расположенный в нижней части реактора, и выводился через его верхнее отверстие.

Источником CH_4 служил природный газ из московской городской сети. Водород получали растворением Al ("ч.д.а.") в ~20%-ной HCl ("х.ч.") в аппарате Киппа. Для очистки H_2 от паров H_2O и HCl его пропускали через твердый KOH.

В ходе предварительных экспериментов установлено, что заметное отложение углерода на синтезированном Kt начинается при температуре ~850°C, и уже при 900°C удельная скорость его накопления $(d(m_C/m_{Kt})/d\tau)$ является достаточной для проведения кинетических экспериментов.

Для проведения кинетических экспериментов необходимо было знать массу, которую будет иметь Kt при температуре проведения эксперимента. Оказалось, что при нагреве Kt в атмосфере H_2 до 900°C он теряет $18 \pm 1\%$ своей массы. Потеря массы Kt может быть отнесена к удалению сорбированной влаги, химически связанной воды, разложению карбонатов металлов, которые могут образовываться при синтезе Kt методом сжигания, восстановлению с образованием активных центров. Таким образом, для того чтобы масса Kt при проведении эксперимента составляла, например, 50 мг, необходимо взять $50/(1 - 0.18) = 61$ мг исходного катализатора.

Прямым экспериментом установлено, что некаталитического отложения углерода в заметном количестве в условиях проведения процесса пиролиза не происходит. Так, масса 50 мг MgO, синтезированного сжиганием нитрата магния с глицином, за 1 ч изотермической выдержки при 900°C в токе смеси CH_4 и H_2 (1 : 4 об.) с суммарным расходом 400 мл/мин в пределах чувствительности торсионных весов, не изменилась.

Для определения кинетической области протекания процесса навеску катализатора уменьшали (уменьшалась высота слоя катализатора), а расход смеси CH_4 и H_2 (1 : 4 об.) увеличивали до тех пор, пока начальная удельная скорость отложения углерода не стала постоянной. Так, было установлено, что при исходной навеске Kt 61 мг (50 мг при 900°C) и суммарном расходе смеси CH_4 и H_2 400 мл/мин реакция протекает в кинетической области. Все последующие эксперименты проводили при этих условиях.

Кинетические эксперименты проводили согласно следующей методике. Медный контейнер с навеской катализатора 61 мг помещали в верхнюю (холодную) зону реактора, устанавливали суммарный расход реакционной смеси 400 мл/мин заданного состава и нагревали до 900°C. Разбавление CH_4 и H_2 до нужной концентрации (парциального давления) производили He (99.995%). После того как температура установилась, контейнер опускали в горячую зону, а второй конец нити прикрепляли к рычагу торсионных весов и фиксировали изменение массы в течение 1 часа.

Для проведения микроскопических исследований и определения удельной поверхности продукты пиролиза очищали от основной массы катализатора кипячением 15 мин в ~23%-ной HCl, промывали дистиллированной водой и 96%-ным этиловым спиртом при центрифугировании (Janetzki T30, 6400 об./мин) и сушили на воздухе при 110–115°C.

Для изучения морфологии продуктов пиролиза использовали просвечивающий электронный микроскоп на полевой эмиссии (ПЭМ) высокого разрешения Philips CM200 FEG. Измерение удельной поверхности проводили методом низкотемпературной десорбции азота на установке Газохром-1.

ОБСУЖДЕНИЕ РЕЗУЛЬТАТОВ

Полученный катализатор имел насыпную плотность 0.054 ± 0.005 г/см^3 и удельную поверхность 140 ± 40 м^2/г.

Микроскопические исследования (рис. 1) показали, что основными твердыми продуктами пиролиза являлись НТ с числом слоев от двух до пяти. Их внешний диаметр изменялся от ~3 до 9 нм. В большинстве случаев НТ организованы в сростки. В некоторых местах НТ покрыты неупорядоченным углеродом. Можно предположить, что это продукты пиролитической поликонденсации или сильно искривленные графеновые слои. В продуктах пиролиза также встречались червеобразные частицы, которые в некоторых случаях имели многочисленные внутренние перегородки. Их внешний диаметр мог превышать 10 нм, а число слоев достигать 10 и более. Морфологическое
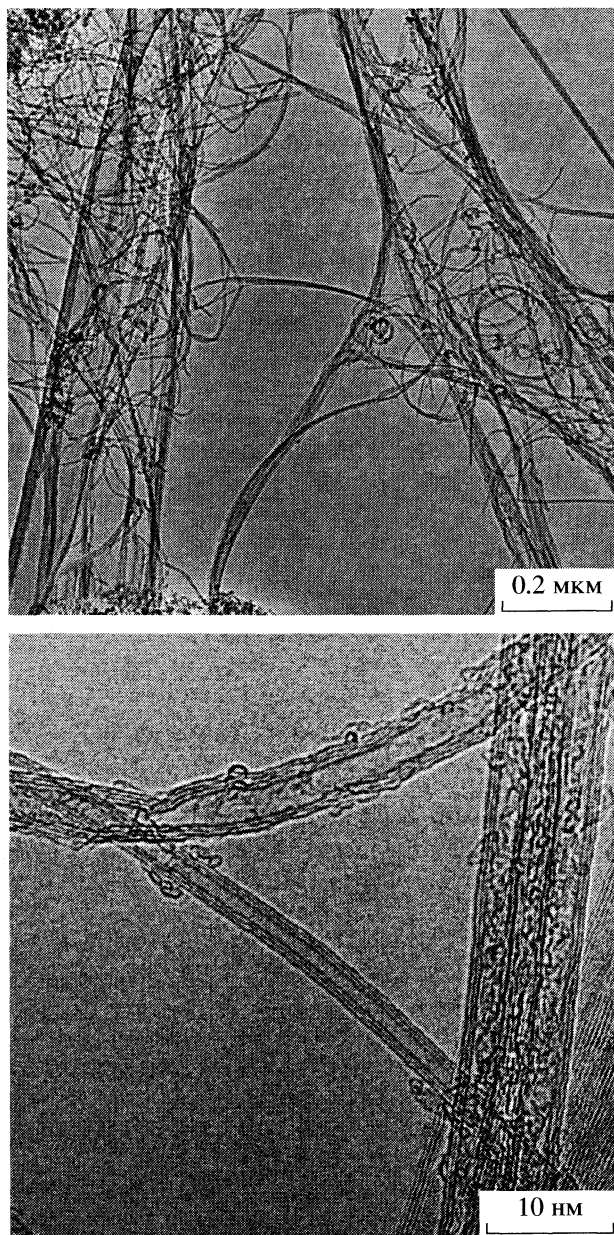
Рис. 1. Типичные ПЭМ микрофотографии твердых продуктов пиролиза; p_{CH_4} = 19.9 кПа (20 об. %), p_{H_2} = 79.6 кПа (80 об. %).

Рис. 2. Кинетические зависимости накопления массы углерода при различных парциальных давлениях CH_4: *1* – 19.9 (20 об. %), *2* – 14.9 (15 об. %), *3* – 9.9 (10 об. %), *4* – 7.5 кПа (7.5 об. %), p_{H_2} = 79.6 кПа (80 об. %), Не – остальное.

разнообразие продуктов пиролиза дополняли луковичные структуры и инкапсулированные частицы катализатора. Вместе с тем анализируемые образцы не содержали нановолокон большого диаметра и НТ с большим числом слоев.

Удельная поверхность углеродных продуктов, полученных при концентрации CH_4 20 об. %, а H_2 80 об. %, составила 500 ± 50 м²/г, что соответствует удельной поверхности НТ с малым числом слоев [14].

На рис. 2 и 3 представлены зависимости массы отложившегося углерода от времени, построенные с учетом данных параллельных экспериментов. Обработка параллельных опытов позволила определить доверительный интервал для всех значений количества углерода во времени.

Для обработки результатов вначале использовался дифференциальный метод. Из данных, представленных на рис. 2 и 3, видно, что скорость реакции образования углеродной массы ($dm_C/d\tau$) уменьшается со временем процесса, увеличивается с увеличением парциального давления CH_4 и уменьшается с увеличением парциального давления H_2 в газовой реакционной смеси. Начальные скорости накопления массы углерода (рис. 4 и 5) линейно зависят от парциального давления CH_4 и обратной величины парциального давления H_2. Экстраполяция полученных зависимостей (рис. 4 и 5, пунктирная линия) показывает, что существуют критические (предельные) парциальные давления метана ($p_{CH_4}^*$) и водорода ($p_{H_2}^*$), при которых накопление углерода с заметной скоростью не наблюдается, что, по-видимому, связано с тем, что процесс образования НТ является равновесным. Действительно, при парциальном давлении CH_4 ниже критического (p_{CH_4} < 6400 Па) накопления углерода в прямом эксперименте не наблюдалось.

Согласно данным, представленным на рис. 4 и 5, зависимость начальной скорости накопления углерода ($r_0 = dm_C/d\tau$ при $\tau = 0$) от состава газовой
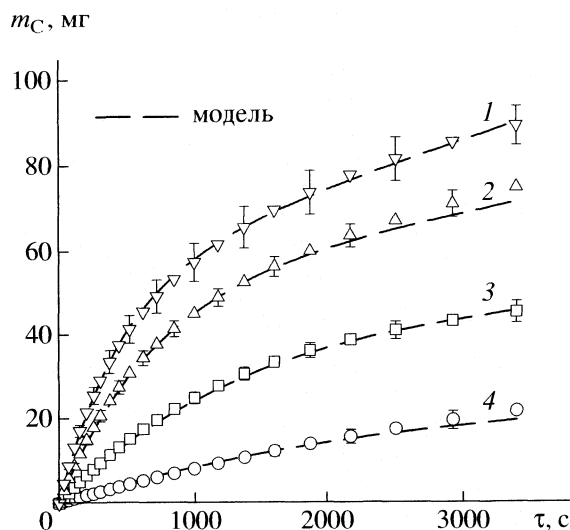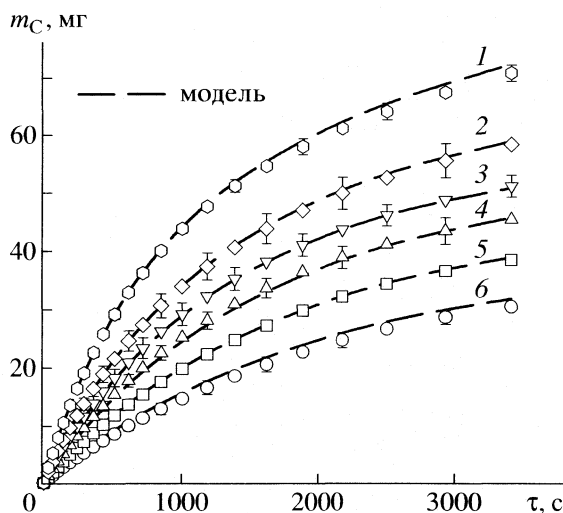
Рис. 3. Кинетические зависимости накопления массы углерода при различных парциальных давлениях H_2: *1* – 59.7 (60 об. %), *2* – 69.6 (70 об. %), *3* – 74.6 (75 об. %), *4* – 79.6 (80 об. %), *5* – 84.5 (85 об. %); *6* – 89.5 кПа (90 об. %), p_{CH_4} = 9.9 кПа (10 об. %), He – остальное.
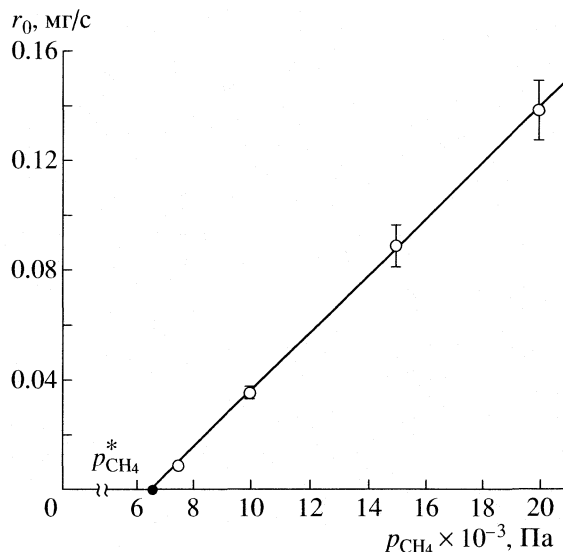
Рис. 4. Зависимость начальной скорости накопления углерода от парциального давления CH_4; p_{H_2} = = 79.6 кПа (80 об. %), He – остальное.

реакционной смеси может быть аппроксимирована следующей функцией:

$$r_0 = k_0(p_{CH_4} - p^*_{CH_4})(1/p_{H_2} - 1/p^*_{H_2}), \qquad (1)$$

где k_0 – константа скорости накопления массы углерода, мг/с.

Наличие p_{H_2} в знаменателе уравнения (1) может быть объяснено сорбцией H_2 на поверхности Kt, что затрудняет доступ к его активным центрам молекул CH_4.

При построении зависимости скорости накопления углерода от его массы было установлено, что на начальных участках она линейно убывает и описывается уравнением

$$\frac{dm_C}{d\tau} = r_0 - \alpha r_0 m_C = r_0(1 - \alpha m_C), \qquad (2)$$

где α – удельная доля дезактивированного Kt на единицу массы НТ, мг$^{-1}$. Такая зависимость, по-видимому, связана с дезактивацией Kt образующимися НТ, например, в результате его инкапсулирования.

Анализ микрофотографий (рис. 1) показал, что углерод может отлагаться и на поверхности растущих НТ. Этот процесс, по всей видимости, является каталитическим, так как некаталитического отложения углерода в условиях кинетических экспериментов не наблюдали. Роль катализатора при этом, вероятнее всего, сводится к образованию на его поверхности полупродуктов пиролиза CH_4, которые десорбируются в объем, отлагаются на развитой поверхности НТ и уплот-

няются. Не исключено, что этот процесс может приводить к росту числа слоев НТ.

Прямым экспериментом показано, что образующийся в процессе пиролиза метана углерод может газифицироваться водородом. Так, при прекращении подачи CH_4 23 мг отложившегося к этому моменту на Kt углерода потеряли за 18 мин пребывания в атмосфере H_2 6 мг своей массы. Зависимость потери массы от времени носила экспоненциальный характер, причем, по-видимому,
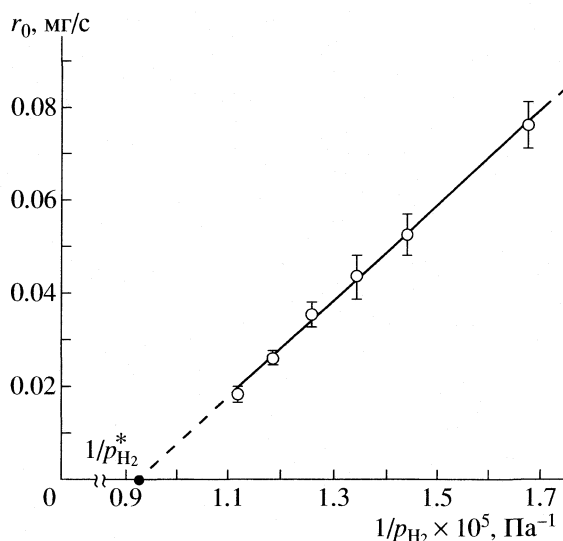

Рис. 5. Зависимость начальной скорости накопления углерода от обратной величины парциального давления H_2; p_{CH_4} = 9.9 кПа (10 об. %), He – остальное.

газификации могут подвергаться как НТ, преимущественно в местах скопления дефектов и местах контакта с катализатором, так и углерод, отлагающийся на их поверхности. Ранее газификацию пиролитически полученных НТ водородом наблюдали в [10].

Учитывая уравнения (1) и (2), возможность отложения углерода на поверхности НТ, возможность газификации НТ и отлагающегося на их поверхности углерода водородом, можно записать зависимость скорости накопления углерода от состава реакционной газовой смеси в виде системы уравнений:

$$dm_C/d\tau = dm_1/d\tau + dm_2/d\tau, \qquad (3)$$

$$\frac{dm_1}{d\tau} = k_0(p_{CH_4} - p^*_{CH_4})\left(\frac{1}{p_{H_2}} - \frac{1}{p^*_{H_2}}\right)(1 - \alpha m_1) - \\ - k_1 m_1 p_{H_2}, \qquad (4)$$

$$\frac{dm_2}{d\tau} = k_2(p_{CH_4} - p^*_{CH_4})\left(\frac{1}{p_{H_2}} - \frac{1}{p^*_{H_2}}\right)m_1 - k_3 m_2 p_{H_2}, \quad (5)$$

где k_1 – константа скорости газификации НТ водородом, k_2 – константа скорости отложения углерода на поверхности НТ, k_3 – константа скорости газификации углерода, отлагающегося на поверхности НТ, водородом, m_1, m_2 – соответственно масса НТ и масса углерода, отлагающегося на их поверхности.

Найденные дифференциальным методом константы использовались как начальные приближения при оптимизации констант в системе дифференциальных уравнений (3)–(5). В результате оптимизации были получены следующие значения констант для температуры 900°C:

$$p^*_{CH_4} = 6385 \pm 33 \text{ Па}, \quad p^*_{H_2} = 109481 \pm 711 \text{ Па},$$

$$k_0 = 2.778 \pm 0.066 \text{ мг с}^{-1},$$

$$\alpha = 1.62 \times 10^{-2} \pm 0.06 \times 10^{-2} \text{ мг}^{-1},$$

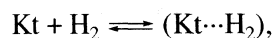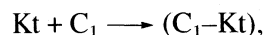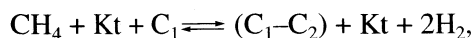$$k_1 = 2.98 \times 10^{-9} \pm 0.20 \times 10^{-9} \text{ Па}^{-1}\text{c}^{-1},$$

$$k_2 = 5.18 \times 10^{-3} \pm 0.79 \times 10^{-3} \text{ c}^{-1},$$

$$k_3 = 1.02 \times 10^{-9} \pm 0.65 \times 10^{-9} \text{ Па}^{-1} \text{ c}^{-1}.$$

Сравнение всех экспериментальных и расчетных данных (рис. 2 и 3) показало, что полученные при расчете по модели значения укладываются в доверительный интервал.

С учетом полученных кинетических зависимостей предлагается схема протекания процесса пиролиза, состоящая из четырех стадий. В ней учитывается обратимость процессов образования

двух продуктов – НТ и углерода, отлагающегося на их поверхности, и сорбция H_2 на поверхности Kt, а также дезактивация Kt образующимися НТ:

$$CH_4 + Kt \rightleftharpoons C_1 + Kt + 2H_2,$$

$$CH_4 + Kt + C_1 \rightleftharpoons (C_1\text{–}C_2) + Kt + 2H_2,$$

$$Kt + C_1 \longrightarrow (C_1\text{–}Kt),$$

$$Kt + H_2 \rightleftharpoons (Kt\cdots H_2),$$
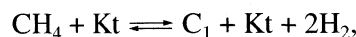
где C_1 – углеродные НТ, Kt – катализатор в активной форме, $(C_1\text{–}Kt)$ – дезактивированная форма катализатора, $(C_1\text{–}C_2)$ – нанотрубки с углеродом, отложившимся на их поверхности, $(Kt\cdots H_2)$ – катализатор с сорбированным на нем водородом.

Предложенная кинетическая модель не учитывает всех возможных процессов, протекающих при пиролизе CH_4 в смеси с H_2 на Kt, и ограничена использованным Kt, температурой 900°C, интервалом парциальных давлений метана 7.5–19.9 кПа и водорода 59.7–89.5 кПа, однако, она не противоречит имеющимся в литературе данным и может быть использована для расчета аппаратов непрерывного синтеза НТ.

Таким образом, исходя из данных кинетических экспериментов и данных, полученных путем математической обработки, следует, что образование НТ, а также иных форм углерода, образующихся одновременно с ними, является обратимым процессом, который может быть охарактеризован через предельные концентрации (парциальные давления) CH_4 и H_2, соответствующие, по-видимому, равновесным условиям образования НТ. Скорость роста НТ в системе CH_4–H_2–He характеризуется первым порядком по CH_4 и обратно пропорциональна концентрации H_2 в газовой фазе. Образующиеся в процессе пиролиза НТ и другие формы углерода могут газифицироваться водородом. По-видимому, газификация полученной углеродной массы водородом может являться одним из способов очистки НТ от сопутствующих им углеродных примесей. Предлагаемая в работе система дифференциальных уравнений может быть использована для расчета аппаратов непрерывного синтеза НТ.

СПИСОК ЛИТЕРАТУРЫ

1. *Раков Э.Г.* // Успехи химии. 2000. Т. 69. С. 41.

2. *Раков Э.Г.* // Хим. технология. 2003. № 10. С. 2.

3. *Tang S., Zhong Z., Xiong Z. et al.* // Chem. Phys. Lett. 2001. V. 350. P. 19.

4. *Flahaut E., Peigney A., Bacsa W.S. et al.* // Mater. Chem. 2004. V. 14. P. 646.

5. *Flahaut E., Laurent Ch., Peigney A.C.* // Carbon. 2005. V. 43. P. 375.

6. *Гришин Д.А., Гаврилов Ю.В., Насибулин А.Г. и др.* // Поверхность. Рентгеновские, синхротронные и нейтронные исследования. 2005. № 12. С. 52.

7. *Peigney A., Laurent Ch., Rousset A.* // J. Mater. Chem. 1999. V. 9. P. 1167.

8. *Liu W., Cai W., Yao L. et al.* // J. Mater. Sci. 2003. V. 38. P. 3051.

9. *Huang S., Woodson M., Smalley R., Liu J.* // Nano Lett. 2004. V. 4. № 6. P. 1025.

10. *Nagy J.B., Bister G., Fonseca A. et al.* // J. Nanosci. Nanotechnol. 2004. V. 4. P. 326.

11. *Kingsley J.J., Patil K.C.* // Mater. Lett. 1988. V. 6. P. 427.

12. *Zhang Y., Stangle G.C.* // J. Mater. Res. 1994. V. 9. P. 1997.

13. *Patil K.C., Aruna S.T., Mimani T.* // Curr. Opinion in Solid State & Mater. Sci. 2002. V. 6. P. 507.

14. *Peigney A., Laurent Ch., Flahaut E. et al.* // Carbon. 2001. V. 39. P. 507.

УДК 544.723+544.4

РАЗЛОЖЕНИЕ ГАЗООБРАЗНЫХ ПРОДУКТОВ ХИМИЧЕСКОЙ ТРАНСПОРТНОЙ РЕАКЦИИ H_2O_2/ZnO НА ПОВЕРХНОСТИ СИЛИКАГЕЛЯ

© 2007 г.   О. А. Камалян

Ереванский государственный университет
E-mail: kamalyan@ysu.am

Поступила в редакцию 24.07.2006 г.

Изучен процесс разложения газообразных продуктов химической транспортной реакции, протекающей при взаимодействии паров H_2O_2 с ZnO, на поверхности силикагеля. Показано, что в начальной стадии разложения промежуточного комплекса химической транспортной реакции H_2O_2/ZnO происходит заметное увеличение удельной поверхности сорбента и одновременный сдвиг максимума распределения пор по размерам в сторону меньших пор. Установлено, что с увеличением времени выдержки силикагеля в потоке газообразных продуктов химической транспортной реакции H_2O_2/ZnO наблюдается обратная картина. Показано, что обработка кремнеземного сорбента промежуточным комплексом H_2O_2/ZnO существенно влияет на фрактальную размерность его поверхности.

Ранее нами показано [1], что обработка кремнеземного сорбента газообразными продуктами химической транспортной реакции (ХТР) H_2O_2/ZnO приводит к существенным изменениям его текстурных параметров, что является следствием разложения газообразного пероксосольвата ZnO в порах сорбента с образованием вторичной текстуры поверхности. На основании изучения изотерм адсорбции бензола при 373 К на поверхности модифицированного кремнезема показано, что если после такой обработки исходной подложки удельная поверхность снижается на 15 м²/г, то удельный объем пор, наоборот, увеличивается на 0.042 см³/г.

Гетерогенная реакция паров H_2O_2 с оксидами, солями и халькогенидами – сложный и малоизученный процесс. В зависимости от природы гетерогенного контакта и температуры реакции могут протекать два процесса [2–4]. В одном случае на твердом контакте происходит разложение H_2O_2 на воду и кислород, а в другом – пероксид водорода вступает в прямую реакцию с веществом поверхности, приводя к образованию новых соединений [5–7], которые в условиях реакции частично переходят в газовую фазу. В объеме газа они проявляют достаточную устойчивость, однако легко разлагаются при соприкосновении с твердыми веществами, выделяя исходное твердое соединение. В потоке газа промежуточное соединение может перемещаться на большие расстояния. Следовательно, эту реакцию можно отнести к типичным ХТР [8], главной отличительной особенностью которой является то, что она протекает при низких температурах (в некоторых случаях даже ниже комнатной) и легко управляема. Немаловажно и то, что для всех соединений транспортером вещества является одно и то же доступное соединение – пероксид водорода. Помимо несомненного теоретического значения эта реакция открывает новые возможности получения различных покрытий и пленок, поверхностно-модифицированных сорбентов и неподвижных фаз для хроматографии, металлоксидных катализаторов нового поколения. Например, в [9] с помощью этой реакции модифицирована поверхность таблетки аэросила и показано, что таким способом можно получить различные каталитические системы с заданными свойствами. Причем одну и ту же поверхность можно модифицировать различными активными соединениями одновременно или в отдельности, с нужным количеством и последовательностью, что очень важно для регулирования свойств катализаторов.

В настоящем сообщении приведены данные исследования изменений текстурных параметров подложки при разложении на ее поверхности газообразных продуктов ХТР, протекающей при взаимодействии паров H_2O_2 с ZnO.

ЭКСПЕРИМЕНТАЛЬНАЯ ЧАСТЬ

Эксперименты проводились на вакуумно-проточной установке, позволяющей провести гравиметрические измерения в ходе процесса, упрощенная схема которой представлена на рис. 1. Смесь паров пероксида и воды ($H_2O_2 : H_2O = 1 : 1$) из ампулы *1* под давлением ~80 Па пропускали через реактор *2*, где помещен таблетированный об-

разец высокодисперсного порошка оксида цинка чистотой 99.999% фирмы Aldrich.

Газовый поток после реактора направлялся в гравиметрический узел (весы Мак-Бена), где находится таблетированный силикагель *4*, подвешенный к тонкой кварцевой спирали *5* (чувствительность – 4.35×10^{-3} г/см). Таблетка силикагеля массой ~0.1 г и размерами $1 \times 1 \times 0.1$ см^3 изготовлена прессованием измельченного особо чистого SiO_2 под давлением 1500 кг/см^2. Удельная поверхность препарированного образца по азоту составляла 250 м^2/г, удельный объем пор – 0.690 см^3/г.

Вакуумная установка снабжена соответствующими узлами регулирования давления и скорости потока, температуры реактора и таблетки SiO_2. Концентрация ZnO в потоке определялась отдельным опытом с помощью атомно-адсорбционного спектрометра AAS-30 следующим образом: за один час конденсации газового потока в ловушке при температуре 77 K накапливается достаточное для анализа количество комплекса ZnO с H_2O_2 (~10^{-9} моль). После прекращения опыта температуру конденсата повышали до комнатной. В этих условиях конденсат превращается в жидкость и комплексное соединение легко разлагается с выделением исходного ZnO. Так как оксид цинка плохо растворяется в воде, то его превращали в растворимую соль растворением в соляной кислоте. Затем с помощью спектрометра AAS-30 определяли концентрацию цинка в полученном растворе, следовательно, и количество перенесенного в ходе эксперимента вещества. После этого, зная скорость и давление газового потока, рассчитывали концентрацию комплекса в потоке газа.

Фрактальную размерность исходного и модифицированного SiO_2, характеризующую степень раздробленности поверхности сорбента, определяли по методике [10], из изотерм адсорбции N_2, $CHCl_3$, C_6H_6, C_6H_{14}(н-гексан) и C_9H_{12} (кумол), используя зависимость удельной поверхности пористого тела от размера молекулы адсорбтива

$$S_{уд} = N_м \sigma \sim \sigma^{(2 - D)/2},$$

где $N_м$ – число молекул в монослое для одного грамма адсорбента, σ – площадь, занимаемая одной молекулой адсорбата, D – фрактальная размерность поверхности адсорбента. Удельную поверхность и остальные текстурные параметры образцов определяли, используя уравнение полимолекулярной адсорбции БЭТ, которое описало процесс адсорбции до относительных давлений паров адсорбтива $p/p_s = 0.25$.

Реакция химического переноса ZnO осуществлена в условиях (время контакта ~10^{-2} с, давление паров эквимолярной смеси пероксида и воды – 80 Па, температура реактора – 293 K), которые позволяют осуществить модифицирование поверхности
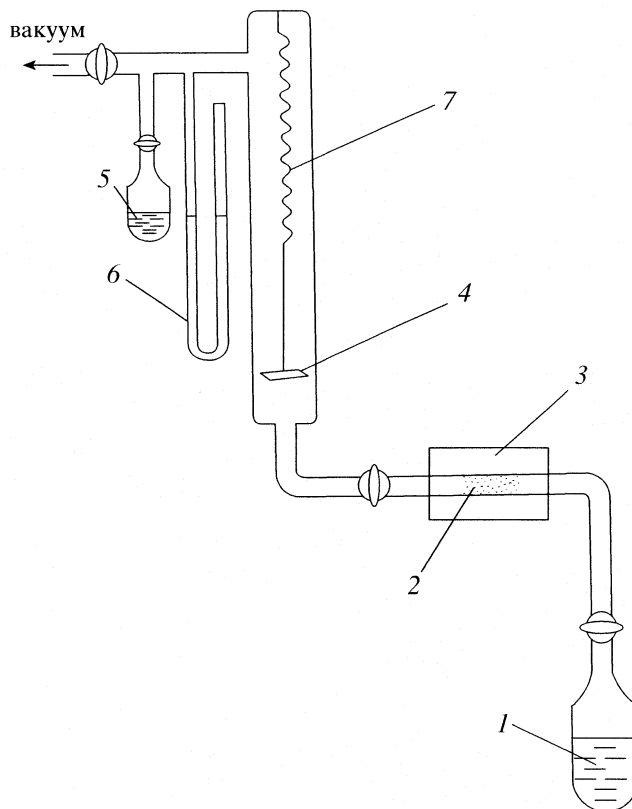
Рис. 1. Схема вакуумно-проточной установки: *1* – узел подачи паров H_2O_2, *2* – реактор с таблетированным ZnO, *3* – термостат, *4* – таблетированный силикагель, *5* – ампула с адсорбтивом, *6* – масляный манометр, *7* – кварцевая спираль.

силикагеля оксидом цинка. В стационарном режиме химического переноса концентрация промежуточного соединения – переносчика вещества в объеме газа в наших условиях составила ~3×10^{10} молек/см^3, а скорость переноса – 4×10^{12} молек/(см^3 с). При этом за 1 ч потоком газов переносится ~10^{-9} моль ZnO, а количество накопленного на кремнеземной подложке – и того меньше (что ниже предела чувствительности примененных нами весов Мак-Бена). По этому не удалось надежно наблюдать за изменением массы сорбента в ходе его обработки газообразными продуктами ХТР H_2O_2/ZnO.

ОБСУЖДЕНИЕ РЕЗУЛЬТАТОВ

На рис. 2 приведены изотермы адсорбции азота на исходном (*1*) и модифицированном газовыми продуктами ХТР H_2O_2/ZnO на первой стадии (*2*, в течение 6 ч) и в конце модифицирования (*3*, в течение 30 ч). Модифицирование сильно меняет текстуру исходного сорбента, что проявляется в изменении не только относительного давления начала капиллярной конденсации, но и формы петли гистерезиса. Причем на первой стадии модифицирования наблюдается уменьшение относи-

Рис. 2. Изотермы адсорбции азота на исходном кремнеземе (*1*) и после его обработки газообразными продуктами ХТР H_2O_2/ZnO в течение 6 (*2*) и 30 (*3*) ч.

Рис. 3. Зависимости распределения пор по размерам от времени обработки кремнезема газообразными продуктами ХТР H_2O_2/ZnO: *1* – исходный SiO_2, *2* – 6 ч, *3* – 30 ч.

тельного давления начала капиллярной конденсации, что является прямым следствием образования на поверхности кремнезема новой микропористой структуры вследствие разложения промежуточных соединений ХТР H_2O_2/ZnO в порах больших размеров.

Дальнейшее увеличение времени модифицирования приводит к обратной картине, т.е. к смещению относительного давления начала капиллярной конденсации в сторону пор с большими размерами. Такие изменения поведения изотермы адсорбции азота в зависимости от времени обработки кремнезема, по-видимому, можно объяснить тем, что некоторые поры закрываются, а размеры некоторых пор уменьшаются или они меняют свою форму, т.е. происходит новое поверхностное структурообразование. Об этом свидетельствуют также соответствующие кривые распределения пор по размерам (рис. 3).
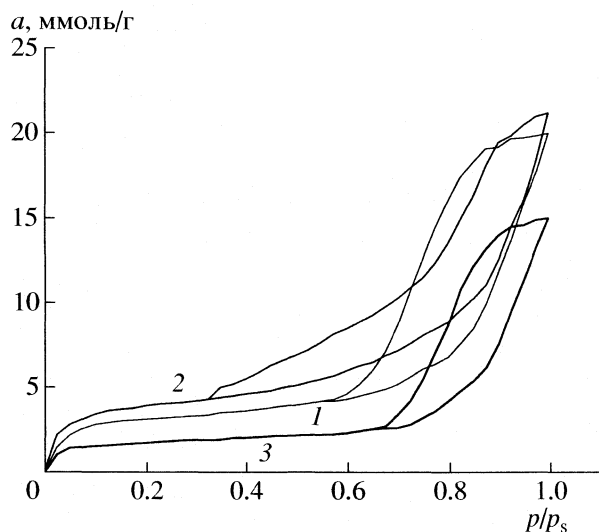
На первой стадии модифицирования (6 ч) наблюдается смещение максимума на кривой распределения пор по радиусам с 40 до 20 Å. При увеличении продолжительности модифицирования до 30 ч максимум смещается в сторону больших размеров (70 Å), с одновременным расширением распределения. Исходя из кривых распределения пор по радиусам можно заключить, что в результате разложения промежуточных соединений ХТР H_2O_2/ZnO на поверхности кремнезема происходит не только изменение текстурных параметров исходного кремнезема за счет изменения морфологии пор, но и образование новой текстуры поверхности за счет ZnO, осаждаемого на поверхности. Однако, учитывая то, что количество ZnO, образованное на поверхности, очень мало, можно предположить, что изменение текстурных харак-

теристик сорбента в основном обусловлено закрытием некоторых щелевидных и бутылкообразных пор, что и является главной причиной уменьшения удельной поверхности.

Доказательством такого предположения может являться также и вид зависимости удельного адсорбционного объема кремнеземной подложки от времени модифицирования (таблица). На начальной стадии (10 ч) наблюдается некоторое увеличение удельного адсорбционного объема с 0.69 до 0.75 см³/г. В дальнейшем этот объем уменьшается и после 30 ч модифицирования составляет ~0.52 см³/г.

Другим, более надежным доказательством сказанного является изменение удельных поверхностей, рассчитанное по адсорбции веществ с разными величинами площадей, занимаемых их молекулами (рис. 4). На первой стадии модифицирования (6 ч) наблюдается некоторое увеличение удельной поверхности с 250 до 270 м²/г (по азоту). В дальнейшем удельная поверхность уменьшается до 160 м²/г, после модифицирования в течение 30 ч. Во всех случаях наблюдается уменьшение удельной поверхности SiO_2 с увеличением времени модифицирования, хотя изменение удельной поверхности, определенное по адсорбции различных сорбатов, происходит по-разному. Однако наблюдаемая разница изменения удельной поверхности от времени модифицирования в случае разных адсорбтивов свидетельствует об изменении фрактальной размерности поверхности.

Изменение текстуры SiO_2 при обработке газообразными продуктами ХТР H_2O_2/ZnO (R – коэффициент корреляции, σ – среднеквадратичная ошибка)

| t, ч | $S_{уд}$, м²/г, по разным адсорбтивам | | | | | $V_{уд}$, см³/г (по N_2) | D | $-R$ | σ |
	N_2 (16.2 Å²)	$CHCl_3$ (28.5 Å²)	C_6H_6 (41 Å²)	C_6H_{14} (51.5 Å²)	C_9H_{12} (62.3 Å²)				
0	250	220	208	200	190	0.690	2.14 ± 0.091	0.99852	0.00285
6	270	220	200	190	180	0.710	2.59 ± 0.095	0.99924	0.00316
10	230	190	178	165	165	0.740	2.51 ± 0.056	0.99793	0.00432
15	215	209	200	190	188	0.700	2.25 ± 0.047	0.99936	0.00131
20	205	200	195	190	195	0.580	2.10 ± 0.060	0.99535	0.00247
30	158	156	150	145	150	0.520	2.07 ± 0.024	0.98605	0.00252

На рис. 5 приведены прямые зависимости $\lg S_{уд}$ от $\lg\sigma$, из которых рассчитаны значения фрактальной размерности поверхности образцов после их модифицирования. На начальной стадии модифицирования поверхности SiO_2 происходит увеличение фрактальности, а с увеличением времени обработки сорбента газообразными продуктами ХТР H_2O_2/ZnO наблюдается сглаживание поверхности, т.е. Уменьшение его фрактальной размерности, о чем было сделано предположение в [1].

На основании полученных данных (таблица) по адсорбционному изучению процесса разложения на поверхности кремнезема газообразных продуктов ХТР H_2O_2/ZnO сделан вывод о том, что на первой стадии разложения газообразных продуктов ХТР H_2O_2/ZnO на поверхности пористого кремнезема происходит увеличение удельной поверхности и удельного адсорбционного объема

за счет образования новой текстуры поверхности с увеличенной фрактальной размерностью. Разложение промежуточного комплекса ХТР H_2O_2/ZnO на начальной стадии происходит преимущественно в порах с радиусами >40 Å. Дальнейшее увеличение времени выдержки исходного сорбента в токе газообразных продуктов ХТР H_2O_2/ZnO приводит к нивелировке поверхности, доказательством чего являются уменьшение удельной поверхности и одновременное уменьшение фрактальной размерности поверхности.

Таким образом, реакцию разложения газообразных продуктов ХТР с участием пероксида водорода и оксидов различных металлов можно использовать для нанесения нанопленок на поверхности различных твердых тел, в частности, на пористые материалы. Это может быть эффективным способом получения различных катали-

Рис. 4. Изменения удельной поверхности в зависимости от времени обработки, рассчитанные по изотермам адсорбции различных адсорбтивов.
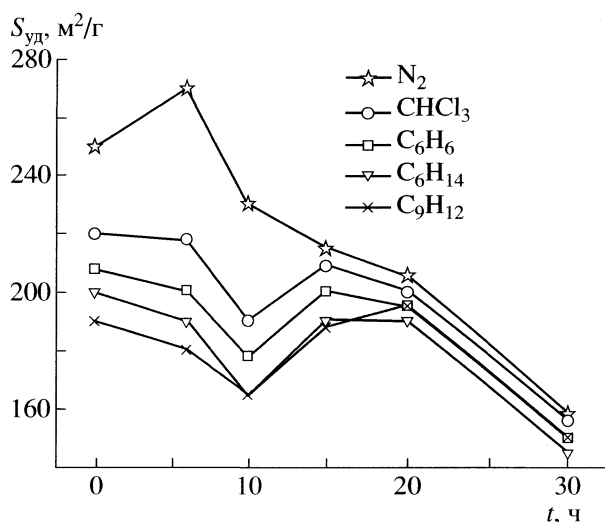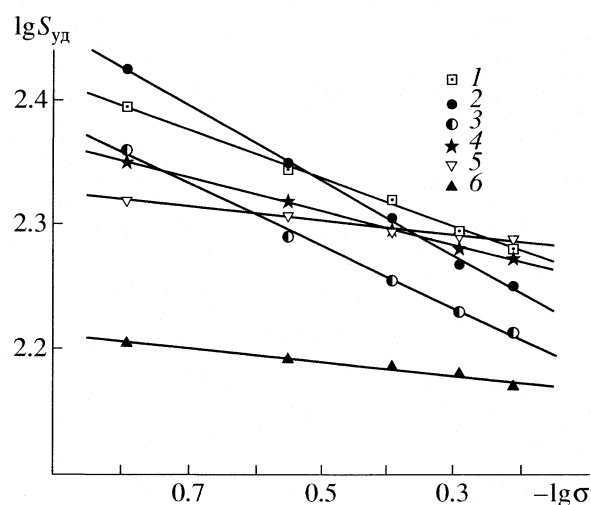
Рис. 5. Прямые для расчета фрактальной размерности поверхности кремнезема, обработанного при разных временах: 1 – исходный образец (D = 2.39), 2 – 6 ч (D = 2.61), 3 – 10 ч (D = 2.51), 4 – 15 ч (D = 2.27), 5 – 20 ч (D = 2.12), 6 – 30 ч (D = 2.10).

заторов, избирательных сорбентов, хроматографических неподвижных фаз и других материалов.

Работа выполнена при финансовой поддержке МНТЦ (проект А-629).

СПИСОК ЛИТЕРАТУРЫ

1. *Григорян Г.Л., Камялян Т.О., Камялян О.А., Гукасян П.С.* // Журн. физ. химии. 2005. Т. 79. № 10. С. 1908.

2. *Григорян Г.Л., Налбандян А.Б.* // Докл. АН СССР. 1977. Т. 235. № 2. С. 381.

3. *Григорян Г.Л.* // Хим. журн. Армении. 1996. Т. 49. № 4.

4. *Арутюнян А.Ж., Газарян К.Г., Гарибян Т.А. и др.* // Кинетика и катализ. 1988. Т. 29. № 4. С. 860.

5. *Абрамян А.Н., Григорян Г.Л., Налбандян А.Б.* // Докл. АН СССР. 1986. Т. 289. С. 896.

6. *Саркисян Н.Я., Абрамян А.Н., Григорян Г.Л.* // Журн. физ. химии. 1990. Т. 64. С. 2548.

7. *Григорян Г.Л., Абрамян А.Н., Саркисян Н.Я., Григорян Г.С.* // Хим. журн. Армении. 1998. Т. 51. № 3–4. С. 240.

8. *Шеффер Г.* Химические транспортные реакции. М., 1964. 190 с.

9. *Саркисян Н.Я., Абрамян А.Н., Григорян Г.Л.* // Кинетика и катализ. 1992. Т. 33. № 5–6. С. 1205.

10. *Nagai M., Yamatoto Y., Aono A.* // Coll. and Surfaces A; Physicochem. Eng. Aspects. 2004. V. 241. P. 257.

ХИМИЧЕСКАЯ КИНЕТИКА И КАТАЛИЗ

ГЕТЕРОГЕННО-КАТАЛИТИЧЕСКОЕ ОКИСЛЕНИЕ ПРОПИЛЕНА ПРИ НАЛИЧИИ СИНГЛЕТНОГО КИСЛОРОДА В РЕАКЦИОННОЙ СМЕСИ

© 2007 г.   О. В. Удалова, Е. В. Хаула, Ю. Н. Руфов

Российская академия наук, Институт химической физики им. Н.Н. Семенова, Москва

E-mail: haula@polymer.chph.ras.ru

Поступила в редакцию 24.07.2006 г.

Опробованы три способа подачи синглетного кислорода в реакционную смесь: термическая генерация синглетного кислорода самим катализатором, введение синглетного кислорода в реакционную смесь от внешнего источника и фотогенерация синглетного кислорода на катализаторе. Использованы цеолиты с введенными добавками Mo, Bi, V, Ni и нанесенными на SiO_2 Mo, V, Bi. Установлено, что общей закономерностью при наличии синглетного кислорода в реакционной смеси является увеличение концентрации продуктов глубокого окисления. На катализаторе Bi/SiO_2 при фотоокислении пропилена отмечено резкое увеличение выхода продуктов мягкого окисления. Установлено, что генерация синглетного кислорода, осуществляемая при облучении в диапазоне 240–260 нм, приводит только к глубокому окислению; появление продуктов мягкого окисления возможно лишь при освещении полным светом ртутной лампы.

Реакционная способность электронно-возбужденных молекул в гетерогенном катализе мало изучена, чему есть причины. Основные из них – сравнительно малое время жизни и малая концентрация возбужденных частиц в экспериментах. В этом контексте синглетный кислород $O_2(^1\Delta_g)$ имеет определенное преимущество по сравнению с другими молекулами, так как его радиационное время составляет 64.6 мин при энергии 0.977 эВ.

Возбужденное состояние $O_2(^1\Sigma_g^+)$ имеет радиационное время ~7 с при внутренней энергии 1.626 эВ [1], поэтому практически не учитывается в гетерогенных процессах.

Интерес к $O_2(^1\Delta_g)$ обусловлен также его электронной структурой, проявляющейся в селективном окислении по двойной связи органических молекул. Эти свойства молекулы позволяют надеяться на специфику реакций с их участием в гетерогенном каталитическом окислении. Существует несколько молекул с сопоставимыми радиационными временами возбужденных состояний (Ne–430 с, Xe–149 с, C–3230 с), но они не представляют интереса для гетерогенного катализа.

Ранее работы по исследованию роли $O_2(^1\Delta_g)$ в гетерогенном окислении проводились либо при низких давлениях [2], либо при малых концентрациях в реакционной смеси [3–5]. Трудность проведения подобных работ состоит в увеличении концентрации $O_2(^1\Delta_g)$ в реакционной смеси.

В предлагаемой работе использованы различные методы увеличения концентрации $^1O_2$ при реакции:

1) подбор катализаторов с максимальной термогенерацией $O_2(^1\Delta_g)$ при температуре катализа;

2) введение синглетного кислорода от внешнего источника в реакционную смесь;

3) облучение катализаторов с максимальной фотогенерацией $O_2(^1\Delta_g)$ в ходе реакции.

В процессе работы опробованы цеолиты типа Y с введенными добавками Zn, Ni, Ca, силикагель и Al_2O_3 с нанесенными ионами V, Bi, Mo.

ЭКСПЕРИМЕНТАЛЬНАЯ ЧАСТЬ

Исходными материалами для приготовления образцов замещенных цеолитов служила Na-форма цеолита Y с отношением Si/Al = 2.6, синтезированная из водных силикаалюмогелей при 80–110°C. Zn-форму Y-цеолита получали однократной обработкой ($t \sim 22$°C) NaY раствором $Zn(NO_3)_2 \cdot 6H_2O$, концентрация Zn в котором в 10 раз превышала эквивалентное количество Na в цеолите (продолжительность обработки составляла 24 ч). Во всех опытах навеска цеолита составляла 3 г, объем раствора соли – 200 мл. Ni [Ca]-формы Y-цеолита получали обработкой навески NaY (3 г) тремя порциями раствора $Ni(NO_3)_2 \cdot 6H_2O$ [$CaCl_2$]
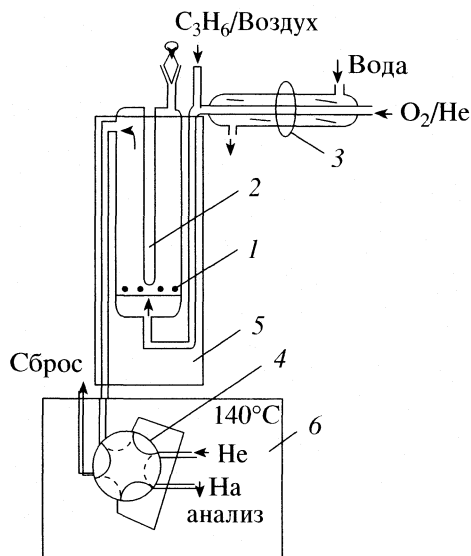
Рис. 1. Кварцевый реактор для изучения гетерогенно-каталитического окисления пропилена при термогенерации $O_2(^1\Delta_g)$ самим катализатором и введении $O_2(^1\Delta_g)$ в реакционную смесь от внешнего источника: *1* – слой катализатора, *2* – карман для термопары, *3* – галогеновые лампы, *4* – шестиходовой кран отбора пробы на хроматографический анализ, *5* – печь реактора.

Рис. 2. Кварцевый реактор для изучения гетерогенно-каталитического окисления пропилена при фотогенерации $O_2(^1\Delta_g)$ самим катализатором: *1* – слой катализатора, *2* – термопара.

по 100 мл с промежуточной декантацией. Обмен проводили при 60°C в течение 4 ч. Каждая порция раствора содержала количество Ni [Ca], эквивалентное количеству Na в цеолите.

В работе исследована серия катализаторов, представляющая собой оксиды металлов и переходных элементов, нанесенные на силикагель. Приготовлены следующие образцы: V_2O_5/SiO_2, MoO_3/SiO_2, Bi_2O_3/SiO_2. В качестве подложки нами использован силикагель "Силохром С-120". Нанесение производили осаждением солей из водного раствора. Количество соли, необходимое для приготовления раствора, рассчитывали исходя из того, что итоговая концентрация нанесенных оксидов по отношению к силикагелю должна составлять 1.5 мол. % ($N_M/N_{Si} + N_M$). Силикагель фракции 0.15–0.25 мм помещали в раствор соответствующей соли, затем, периодически перемешивая его магнитной мешалкой, испаряли воду в течение 12 ч при 110°C. После этого образцы прокаливали 5 ч при 400 и 500°C. Для приготовления нанесенного оксида висмута в качестве исходной соли использовался нитрат, ванадиевого и молибденового образцов – ванадат аммония и молибдат аммония соответственно [6].

Гетерогенно-каталитическое окисление пропилена при термической генерации $O_2(^1\Delta_g)$ самим катализатором изучали на установке проточного типа с использованием кварцевого реактора объемом 20 см³ с карманом для термопары (рис. 1). Диаметр реактора – 12 мм при средней длине слоя

катализатора ~1 см. Термопара располагалась в центре слоя катализатора. Продукты окисления поступали на анализ непосредственно из реактора в термостат хроматографа, нагретого до 140°C. Для изучения каталитической активности образцов при введении синглетного кислорода в реакционную смесь от внешнего источника в реактор был впаян дополнительный вход. Экспериментально установлено, что при температуре катализа (~400°C) гибели синглетного кислорода до катализатора не происходит, что связано с генерацией синглетного кислорода на нагретом кварце реактора.

Фотохимический генератор синглетного кислорода состоял из стеклянной трубки диаметром 15 мм и длиной 180 мм, внутренняя поверхность которой матирована и обработана спиртовым раствором красителя метиленовый голубой, и водяной рубашки по всему периметру трубки. Освещение производили шестью галогеновыми лампами мощностью 50 Вт. Введение $O_2(^1\Delta_g)$ в реакционную смесь осуществлялось за счет потока He + O_2 с оптимальной (учитывающей гибель $O_2(^1\Delta_g)$ в газовой фазе) концентрацией O_2 ~ 2.5%. При потоке 210 см³/мин фотогенерация $O_2(^1\Delta_g)$ составила 1.2×10^{13} молек/см³.

Для облучения специально подобранных катализаторов в ходе реакции гетерогенно-каталитического окисления пропилена использовали кварцевый реактор (рис. 2) объемом 115 см³ и диаметром 3.5 см. Реактор имел перегородку с пластиной из кремнезема, на которой и располагался катализатор. Термопара помещалась в слое кремнезема. Источником ультрафиолетового излучения служила ртутная лампа (марка ПРК-8).

Непрерывная регистрация синглетного кислорода $O_2(^1\Delta_g)$ осуществлялась хемилюминесцентным методом. При реакции $O_2(^1\Delta_g)$ с сенсибилизатором 10-метоксиметил-10^1-метил-9,9^1-биакридилиден испускается квант, регистрируемый ФЭУ, сигнал от которого усиливается и через АЦП подается на компьютер. Подробное описание уста-

Рис. 3. Зависимости фотогенерации $O_2(^1\Delta_g)$ от температуры для оксидов металлов и переходных элементов, нанесенных на силикагель.

Рис. 4. Зависимости фотогенерации $O_2(^1\Delta_g)$ от температуры для замещенного цеолита Y.

новки дано в работе [7]. При давлении воздуха в реакторе 80–90 мм рт. ст. скорость потока составляла 3–3.3 см^3/с. Данное давление оптимально, так как при его увеличении сказывается гибель синглетного кислорода в газовой фазе.
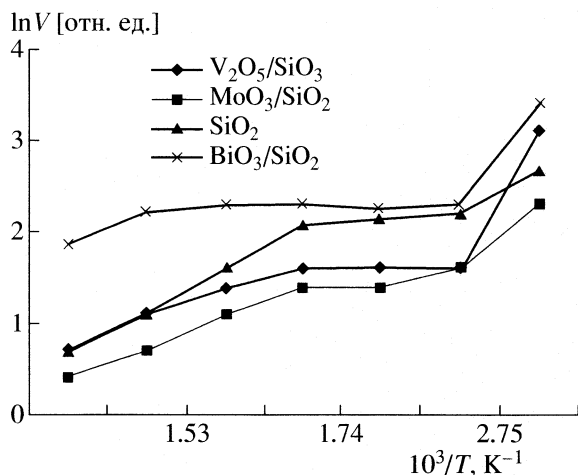
ОБСУЖДЕНИЕ РЕЗУЛЬТАТОВ

При сравнении результатов экспериментов по влиянию синглетного кислорода на каталитическое окисление пропилена выбраны условия, наиболее эффективно проявляющие влияние $^1O_2$. Фотокаталитическое окисление пропилена пришлось проводить при пониженных температурах, так как выше 200–250°C происходит снижение фотогенерации $O_2(^1\Delta_g)$ на всех исследованных катализаторах. Температурная зависимость фотогенерации $O_2(^1\Delta_g)$ может быть обусловлена хемосорбционным механизмом дезактивации синглетного кислорода.

Как показано в [8], десорбция паров воды освобождает центры для дезактивации синглетного кислорода. По-видимому, этот процесс имеет место при сравнительно низких температурах (до ~100°C). При более высоких температурах для всех образцов с небольшим разбросом в энергиях активации (4–7 ккал/моль) наблюдается падение генерации $O_2(^1\Delta_g)$. Возможно, это падение связано с освобождением поверхности от адсорбированных газов. При освещении не исключена также возможность интенсификации диссипации энергии возбуждения в твердое тело, не связанной с образованием синглетного кислорода (рис. 3 и 4).

Концентрация синглетного кислорода, участвующего в каталитическом процессе, остается невыясненной по следующим обстоятельствам.

Во-первых, каталитический процесс протекает при атмосферном давлении, тогда как определение концентрации синглетного кислорода осуществляется при пониженных давлениях (~80 мм. рт. ст.) для исключения газофазной гибели $^1O_2$. Эту трудность формально можно обойти простой экстраполяцией концентрации $^1O_2$ к атмосферному давлению. Во-вторых, остается неясным вопрос о реальной концентрации синглетного кислорода, участвующего в каталитическом процессе, так как возможна гибель $^1O_2$ на пути к каталитическому центру.

Как показывают результаты, представленные в таблице, образование $O_2(^1\Delta_g)$ происходит наиболее эффективно при облучении в УФ-области (<240 нм) практически на всех исследованных системах, как нанесенных, так и массивных. Это позволяет предположить, что образование $^1O_2$ происходит в комплексах с переносом заряда по механизму, описанному в [1]. Перенос заряда, приводящий к образованию CO_2, предполагался в работах [7, 9].

Дополнительное освещение катализатора в видимой области спектра приводит к незначительному увеличению выхода CO_2. Возможно, что образование CO_2 происходит через возбуждение комплекса с переносом заряда [9].

Анализ данных таблицы показывает, что независимо от способа увеличения концентрации $^1O_2$ оно приводит (в первом приближении) к росту содержания продуктов глубокого окисления (CO и CO_2). Обнаружено одно исключение: на образце Bi_2O_3/SiO_2 почти на порядок растет выход акролеина при увеличении конверсии в 1.5 раза. Выход CO при освещении повышается в 1.5 раза.

Рентгеновский анализ образца Bi_2O_3/SiO_2, при концентрации 6 ат. % Bi_2O_3, обнаружил образование мобильной фазы $SiBiO_5$, которая, возможно, и ответственна за каталитический процесс. С этой фазой связано, по-видимому, сверхравновес-

Продукты гетерогенно-каталитического окисления пропилена при разных способах подачи синглетного кислорода

Образец	Осве-щение	$N \times 10^{-11}$	x, %	[CO], %		[CO$_2$], %		[C$_3$H$_4$O], %		[C$_2$H$_4$O$_2$], %		[C$_3$H$_4$O$_2$], %	
				E	S	E	S	E	S	E	S	E	S
Фотогенерация синглетного кислорода при 200°C													
SiO$_2$	I		0.0	0.0	0.0	0.0	0.0	0.0	0.0	0.0	0.0	0.0	0.0
	II	4.9	0.7	0.0	0.0	0.0	0.0	0.3	40.1	0.2	32.3	0.2	27.7
ZnY	I		45.1	7.9	17.6	34.2	75.9	1.4	3.0	0.3	0.6	1.3	2.9
	II	5.1	46.5	11.3	24.3	32.1	69.0	1.7	3.7	0.4	0.8	1.0	2.1
NiY	I		65.7	9.1	13.8	55.1	83.9	0.2	0.4	0.3	0.4	0.9	1.4
	II	0.7	65.5	17.3	26.4	46.1	70.5	0.4	0.6	0.6	0.9	1.0	1.6
MoO$_3$/SiO$_2$ (1.5%)	I		0.8	0.0	0.0	0.0	0.0	0.1	9.9	0.7	82.6	0.1	7.6
	II	0.03	6.1	2.6	42.9	2.7	44.2	0.1	1.7	0.5	9.0	0.1	2.3
	III		6.0	1.4	23.9	3.6	60.3	0.2	2.7	0.5	8.1	0.3	5.0
	IV		5.6	1.3	23.6	3.7	65.8	0.0	0.4	0.4	6.6	0.2	3.7
V$_2$O$_5$/SiO$_2$ (1.5%)	I		12.5	5.1	40.9	5.1	40.9	1.0	8.1	0.4	3.1	0.9	6.8
	II	0.4	15.6	6.4	40.8	7.4	47.2	1.2	7.5	0.3	1.8	0.4	2.8
	III		12.3	4.3	34.7	6.6	53.6	1.0	8.5	0.3	2.6	0.1	0.6
	IV		7.3	1.5	20.4	5.6	75.9	0.2	2.2	0.0	0.5	0.1	1.1
Bi$_2$O$_3$/SiO$_2$ (1.5%)	I		6.0	1.8	30.6	3.8	38.9	0.1	2.5	0.2	3.4	0.0	0.4
	II	0.6	7.8	2.7	34.6	3.8	48.7	0.9	11.3	0.3	3.5	0.1	1.2
	III		5.7	2.5	44.1	2.9	53.9	0.1	2.1	0.1	1.7	0.1	1.1
	IV		3.3	0.9	27.9	2.2	35.4	0.0	0.0	0.1	3.5	0.0	1.4
	V		7.6	2.1	28.1	4.5	24.7	0.8	10.0	0.1	1.5	0.1	1.1
Термогенерация и фотогенерация O$_2$($^1\Delta_g$) от внешнего источника при 420°C													
CaY		<1	78.8	30.9	39.6	45.5	58.3	0.0	0.0	0.8	1.1	0.0	0.0
	VI	123	79.7	42.4	53.3	55.8	70.0	0.0	0.0	1.0	1.2	0.0	0.0
ZnY		223	32.1	26.0	81.3	32.2	98.1	0.0	0.0	1.3	4.1	0.0	0.0
	VI	346	35.1	31.1	88.5	27.5	78.1	0.0	0.0	1.2	3.5	0.0	0.0
NiY		74	70.2	17.7	25.2	51.7	73.7	12.1	17.2	0.6	0.9	0.0	0.0
	VI	197	70.5	24.5	34.8	52.1	73.9	6.5	9.2	0.5	0.7	0.0	0.0

Обозначения: x – конверсия, E – выход, S – селективность, N – концентрация синглетного кислорода (молек/см^3).
I – без освещения ртутной лампой (рт. л.), II – освещение рт. л., III – рт. л. с фильтром УФС-1, IV – рт. л. с фильтром БС-8, V – к освещению ртутной лампой добавлено освещение галогеновой лампой, VI – термогенерация + внешний источник синглетного кислорода.

ная генерация синглетного кислорода при повышенных температурах [10].

При всех сделанных выше предположениях о концентрации синглетного кислорода, участвую-

щего в реакции, его концентрация остается на несколько порядков меньше, чем концентрация основных реагентов. Поэтому наблюдаемое влияние синглетного кислорода может быть объяснено ли-

бо модифицированием им каталитических центров, либо выходом в объем продуктов разложения диоксетанов, где они могут вести объемные реакции [11]. Более тщательный анализ процесса возможен при сопоставимых концентрациях синглетного кислорода и основных реагентов.

СПИСОК ЛИТЕРАТУРЫ

1. *Якуничев М.В., Мясников И.А., Цивенко В.И.* // Журн. физ. химии. 1986. Т. 60. № 4. С. 1017.

2. *Якуничева М.В.* Фотостимулированная эмиссия синглетного кислорода с поверхности нанесенных оксидов переходных металлов (фотокатализаторов). Дис. ... канд. физ.-мат. наук. М.: НИФХИ им. Л.Я. Карпова, 1986.

3. *Удалова О.В., Хаула Е.В., Быховский М.Я. и др.* // Журн. физ. химии. 2003. Т. 77. С. 1018.

4. *Вишнецкая М.В., Емельянов А.Н., Щербаков Н.В. и др.* // Журн. физ. химии. 2004. Т. 78. С. 2152.

5. *Вишнецкая М.В., Емельянов А.Н., Щербаков Н.В. и др.* // Хим. физика. 2004. Т. 23. С. 40.

6. *Hisao Yoshida, Chizu Murata, Tadashi Hattori* // J. Catal. 2000. V. 194. P. 364.

7. *Романов А.Н., Руфов Ю.Н.* // Журн. физ. химии. 1998. Т. 72. № 11. С. 2094.

8. *Ryskin M.E., Kurenyova T.Y., Kustarev V.G. et al.* // Proc. 8th Int. Congress on Catalysis. Berlin (West). 1984. V. 3. P. 311.

9. *Kreuzke L.D., Keulke G.W.* // J. Catal. 1980. V. 64. P. 295.

10. *Щербаков Н.В., Емельянов А.Н., Хаула Е.В. и др.* // Журн. физ. химии. В печати.

11. *Dewar M.J.S., Thisl W.* // J. Am. Chem. Soc. 1975. V. 97. P. 3978.

ХИМИЧЕСКАЯ КИНЕТИКА
И КАТАЛИЗ

TIME-OF-FLIGHT SECONDARY ION MASS SPECTROMETRY AS A NEW TECHNIQUE FOR THE INVESTIGATIONS OF DEACTIVATION PROCESS OF HYDRODECHLORINATION CATALYSTS

© 2007   J. Grams, J. Góralski, B. Szczepaniak

Institute of General and Ecological Chemistry, Technical University of Łódź, Poland

E-mail: jgrams@mail.p.lodz.pl

Received October 27, 2006

Abstract – Time-of-flight secondary ion mass spectrometry (ToF-SIMS) was applied to the investigations of deactivation process of hydrodechlorination catalysts. It appeared that owing to the use of ToF-SIMS technique a simultaneous monitoring of various reasons of catalyst deactivation was possible in one measurement. As a model catalyst Pd/Al_2O_3 sample was chosen. ToF-SIMS studies revealed an increase in the amount of Cl and $PdCl_2$ on the catalyst surface during hydrodechlorination reaction. Moreover, a drop in the quantity of surface accessible Pd was observed.

Time-of-flight secondary ion mass spectrometry (ToF-SIMS) is applied in the studies of a large group of solid materials. The ToF-SIMS popularity is connected with the possibility of this technique to characterise upper layers of the investigated surface [1–3]. It is generally known that in many cases surface properties of solids are decisive for the course of various industrial processes. Therefore, especially for catalysts, the recognition of the surface structure is necessary to work out the most effective systems. For this purpose various techniques may be used (i.e. XPS, XRD, TPR, TEM, SEM, etc.). However, owing to ToF-SIMS obtainment of additional information about the investigated surface is possible [4]. In the case of catalysts this technique enables the determination of chemical composition of analysed surface and presence of contaminants, estimation of an active phase distribution, comparison of a metal reduction degree and observation of an existence and nature of the interactions between an active phase and support (in the case of bimetallic catalysts the interactions between metals can be also determined) [5–13]. Moreover, ToF-SIMS may be very useful in the studies of catalyst deactivation processes. In such a case changes in the composition of the upper layer of the investigated surface (formation of new compounds, increase in the quantity of various contaminants and catalyst poisons) can be determined.

The aim of this work was to show the potentialities of ToF-SIMS to the investigations of the surface of hydrodechlorination catalysts and to find out reasons for its deactivation during the hydrodechlorination process. As a model catalyst the Pd/Al_2O_3 sample was chosen. Palladium supported on aluminium oxide is one of the most widely used catalyst in the removal of chlorine atoms from the environmentally dangerous substances [14–20]. Unfortunately, such a system is susceptible to deactivation [21]. The main reasons for catalyst deacti-

vation during the hydrodechlorination reaction are: chlorine adsorption on the catalyst surface, formation of Pd–Cl bounds, decrease in the amount of palladium, arising of carbon deposit, a considerable drop of surface area and deterioration of Pd dispersion. It appeared that except the investigations of the amount of carbon deposit other processes which caused the deactivation of the catalyst can be determined during one ToF-SIMS measurement. It becomes a capital advantage of the utilization of time-of-flight secondary ion mass spectrometry to the surface studies of hydrodechlorination catalysts in comparison with the techniques used earlier. In the case of ToF-SIMS, measurements are relatively fast and do not demand a special operation during samples preparation before introducing them inside the apparatus.

EXPERIMENTAL

2% Pd/Al_2O_3 catalyst was prepared by the incipient wetness impregnation method. $PdCl_2$ (POCh Gliwice) was introduced onto Al_2O_3 (Fluka 507C). Samples were aging for 48h at room temperature. After evaporation of water, the support was dried under atmospheric pressure at 110°C for 2h. Then, the sample was calcined in the flow of O_2 at 500°C for 4h and reduced in the flow of H_2 in the same conditions. The metal content was confirmed by an inductively coupled plasma emission spectroscopy (ICP-AES). The surface areas of catalysts were established by a nitrogen adsorption method.

The catalysts were deactivated in the hydrodechlorination of CCl_4. The reaction was carried out at 100°C using CCl_4/H_2 (1 : 10) as a reactant mixture. The activity tests were conducted in a flow reactor using a gas

chromatograph Chrom 5 (Laboratorni Pristroje Praha) equipped with FID detector under atmospheric pressure. Details of the procedure were described in [22].

ToF-SIMS measurements were performed using an ION-TOF GmbH instrument (TOF-SIMS IV) equipped with 25 kV pulsed $^{69}Ga^+$ primary ion gun in the static mode (primary ion dose about 3.6×10^{11} ions/cm^2). The analysed area corresponds to a square of 500 μm × × 500 μm in the case of secondary ion mass spectra collecting and surface imaging. For each sample five spectra from different surfaces areas were made. To obtain the plain surface of catalysts (then better mass resolution could be achieved), powder samples were tableted before the measurements. The tablets were attached to a sample holder using a double-sided tape. Because the samples were insulating an application of charge compensation during the measurements was necessary (a pulsed electron flood gun was used). In order to compare the quantity of chlorine and palladium present on the surface of "fresh" and "used" catalysts, the number of counts of selected ions obtained from collected mass spectra was normalised on the basis of the value of total counts.

The amount of carbon deposited on the surface of the investigated catalysts was measured by an automatic carbon analyser TOC 5000 (Shimadzu) equipped with a solid sample module.

RESULTS AND DISCUSSION

In the beginning the catalyst was put to the activity test. It appeared that the main product of hydrodechlorination of CCl_4 was CH_4. For about 120 minutes the stable work of the catalyst was observed [22]. However, after this time a considerable decrease in the conversion of CCl_4 was noticed (a drop of conversion degree from about 100–90% to below 40% after 160 minutes). This phenomenon is strictly connected with the deactivation process, which occurred on the investigated surfaces during the hydrodechlorination reaction. In order to explain reasons for the catalyst deactivation fresh and used (collected after reaction) samples were investigated using ToF-SIMS technique.

The differences in the amount of chlorine adsorbed on the surface of fresh and used catalyst are shown in Fig. 1. It appeared that in the case of the sample subjected to the hydrodechlorination reaction the amount of chlorine deposited on the surface after 250 minutes of work was almost 3 times higher (Cl^- – 0.12) than in the case of fresh sample (Cl^- – 0.34). A similar situation was observed for Cl_2^- ion ($m/z = 70$), but in this case a change of the emission intensity was considerably bigger. The initial amount of chlorine was introduced onto the surface of the fresh sample during the catalyst preparation process. A further increase in the quantity of

Table 1. Normalized intensity ($I \times 10^3$) of ions selected from the mass spectra of 2% Pd/Al_2O_3 catalyst

Ions	Fresh	Used
Cl^-	120	340
Cl_2^-	0.22	21
$PdCl_2^-$	0.15	0.61
$^{105}Pd^+$	2.1	0.8
$^{106}Pd^+$	2.7	1.1
$^{108}Pd^+$	2.5	1.0

chlorine was caused by the course of hydrodechlorination reaction.

The next problem connected with a deactivation of hydrodechlorination catalysts is a formation of Pd–Cl bounds on the catalyst surface exposed to contact with reaction products. On the fragment of the mass spectrum (at $m/z > 100$) collected from the surface of the fresh sample (Fig. 1a) a certain amount of $PdCl^-$ and $PdCl_2^-$ ions was observed. It is caused by the presence of a residue of metal precursor, which was introduced on the catalyst surface in the preparation process. The investigations of the used sample (Fig. 1b) revealed that during the hydrodechlorination reaction, besides an increase in Cl content, a bigger amount of the $PdCl_2$ was formed on the analysed surface. The normalized intensity of $PdCl_2^-$ bore out the results presented in Fig. 1.

It appeared that the quantity of $PdCl_2^-$ ions on the mass spectrum collected from the surface of the used catalyst is 4 times higher than in the case of the surface of the fresh sample. Contrary to Pd/Al_2O_3 in the case of ToF-SIMS investigations of $Pd/ZrO_2–Al_2O_3$ catalyst [23] a growth of the amount of $PdCl_2$ was not observed. It could be the reason why this system maintained catalyst activity on a satisfactory level for a considerably longer time (conversion degree of CCl_4 at the level of 60% even after 100 hours of work). However, in spite of the lack of $PdCl_2$ on the investigated surface, after some time $Pd/ZrO_2–Al_2O_3$ catalyst undergoes deactivation. It means that not only the formation of Pd–Cl bounds can lead to the loss of catalytic activity. Other possible reasons will be discussed below.

Fig. 2 shows a fragment of the positive secondary ion mass spectrum of 2% Pd/Al_2O_3 catalyst. A decrease in the intensity of the signal originating from Pd isotopes ($m/z = 102–110$) observed in the case of the used sample seems to be very interesting. It appeared that emission intensity of $^{106}Pd^+$ ions decreased about 60% in comparison with the fresh sample (Table 1).
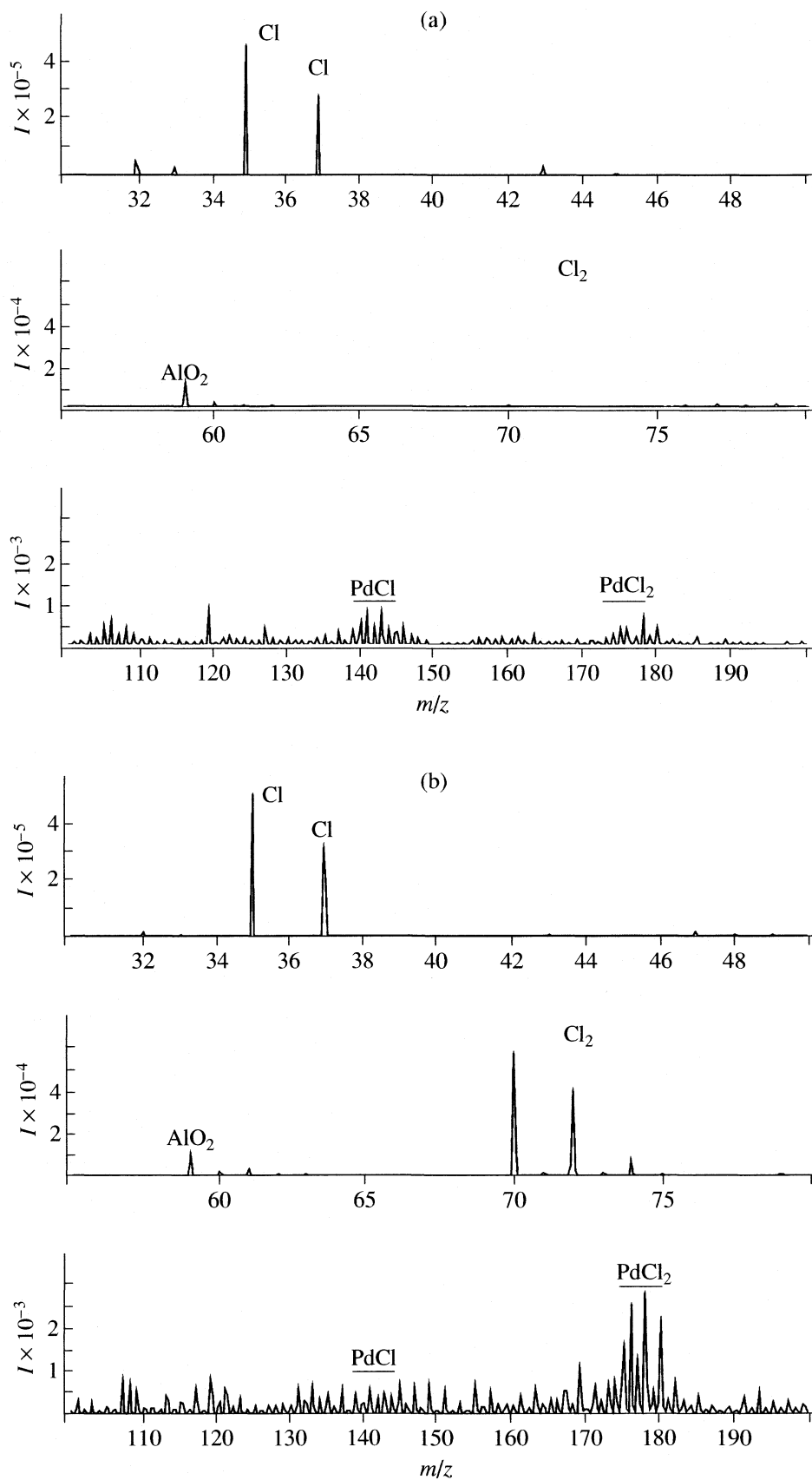
GRAMS et al.

Fig. 1. The fragments of the negative secondary ion mass spectrum of fresh (a) and deactivated (b) 2% Pd/Al_2O_3 catalyst.
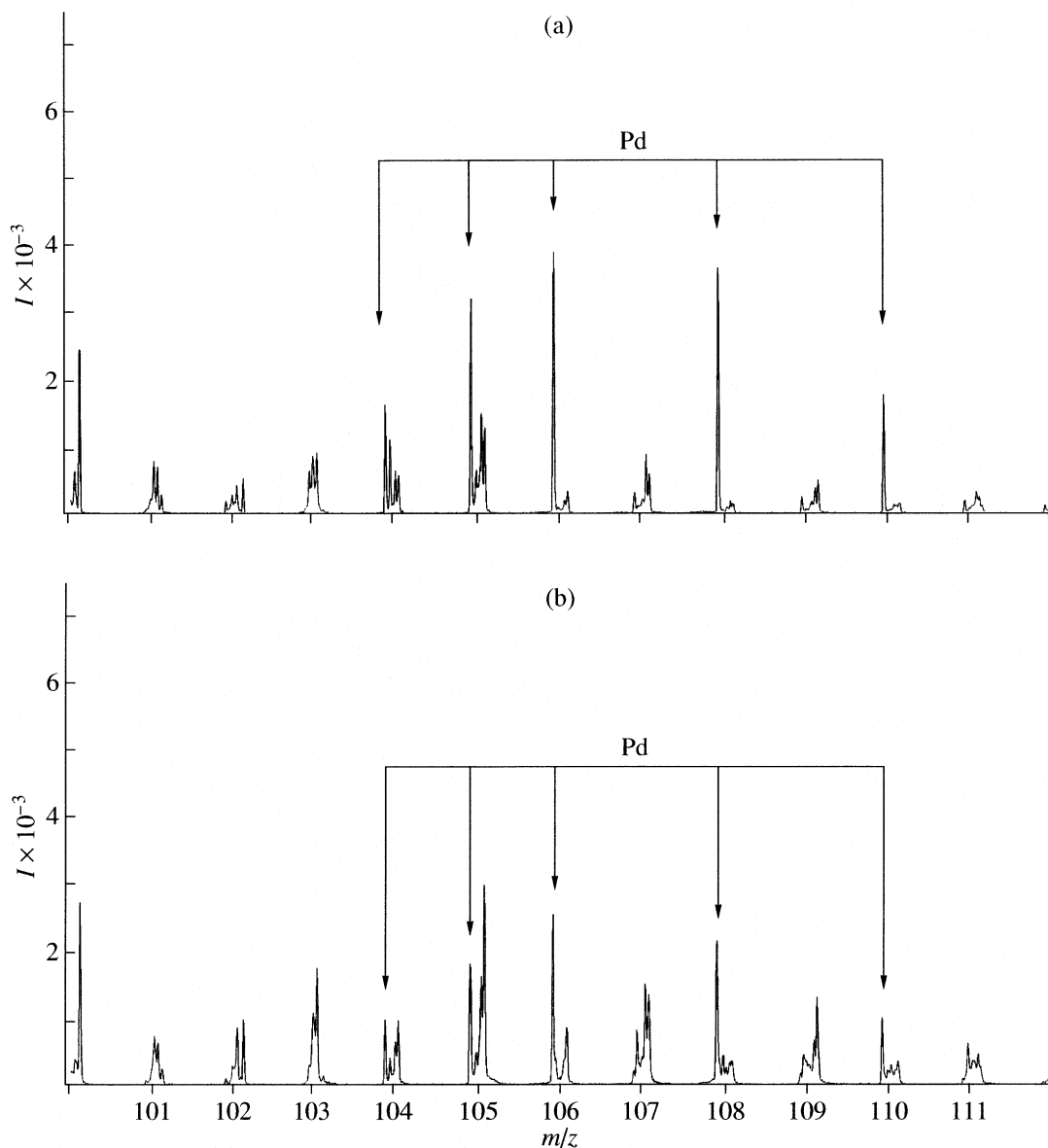
Fig. 2. The fragments of the positive secondary ion mass spectrum of fresh (a) and deactivated (b) 2% Pd/Al_2O_3 catalyst.

A similar situation was observed for Pd/ZrO_2–Al_2O_3 catalyst [23]. It indicated that some part of Pd might be covered by arising carbon deposit and adsorbed chlorine or was removed during the reaction.

A drop of the content of surface accessible Pd during the hydrodechlorination reaction was accompanied by a decrease in the surface area of the catalyst, which changed from 98 m^2/g in the case of the fresh sample to only 7 m^2/g for the used catalyst (Table 2). Such a fall of the surface area and a possibility of the formation of Cl containing compounds on the surface of the investigated samples could influence the distribution of Pd. As a tool for an estimation of Pd dispersion also ToF-SIMS technique was used. Fig. 3 and 4 present ToF-SIMS surface images of 2% Pd/Al_2O_3 catalyst. They revealed

that during the hydrodechlorination process a dispersion of palladium changes noticeably. Contrary to the fresh sample in the case of the used catalyst Pd atoms were distributed non-homogenously on the analyzed surface and a certain number of bigger Pd clusters was observed.

Table 2. Content of carbon (c, %) and surface area (s, m^2/g) of fresh and used 2% Pd/Al_2O_3 catalyst

Catalyst	c	s
Fresh	–	98
Used	1.1	7

Field of view: 500 × 500 μm

Na
tc: 975293

Al
tc: 2360245

AlH
tc: 258792

^{105}Pd
tc: 32487

^{106}Pd
tc: 40805

^{108}Pd
tc: 36663

total ion
tc: 11829270
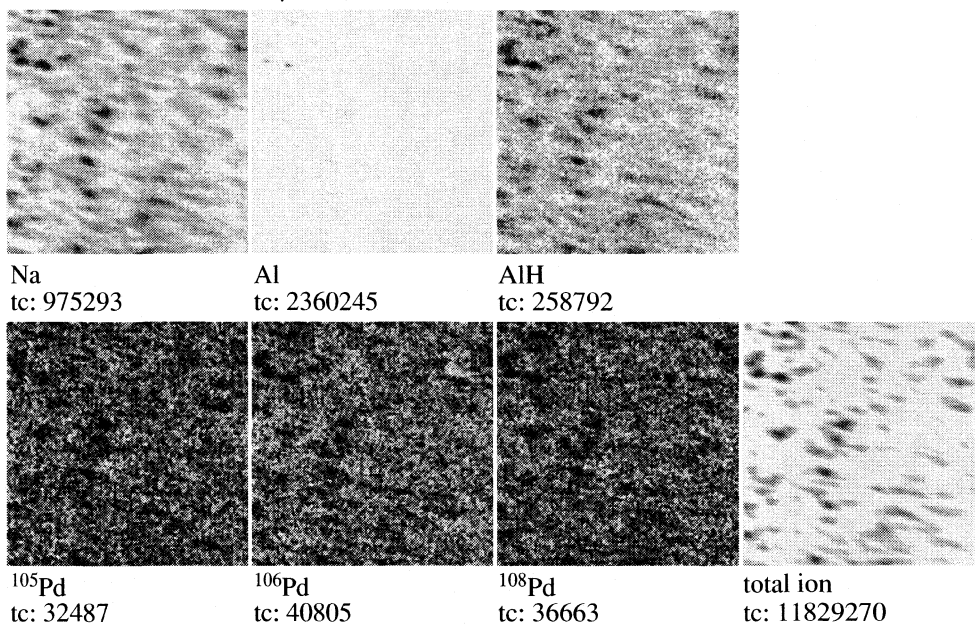
Fig. 3. ToF-SIMS surface images of the fresh 2% Pd/Al$_2$O$_3$ catalyst. Bright colour indicates investigated ions.

Field of view: 500 × 500 μm

Na
tc: 1091848

Al
tc: 3878768

AlH
tc: 364114

^{105}Pd
tc: 33179

^{106}Pd
tc: 41550

^{108}Pd
tc: 39563

total ion
tc: 28632623
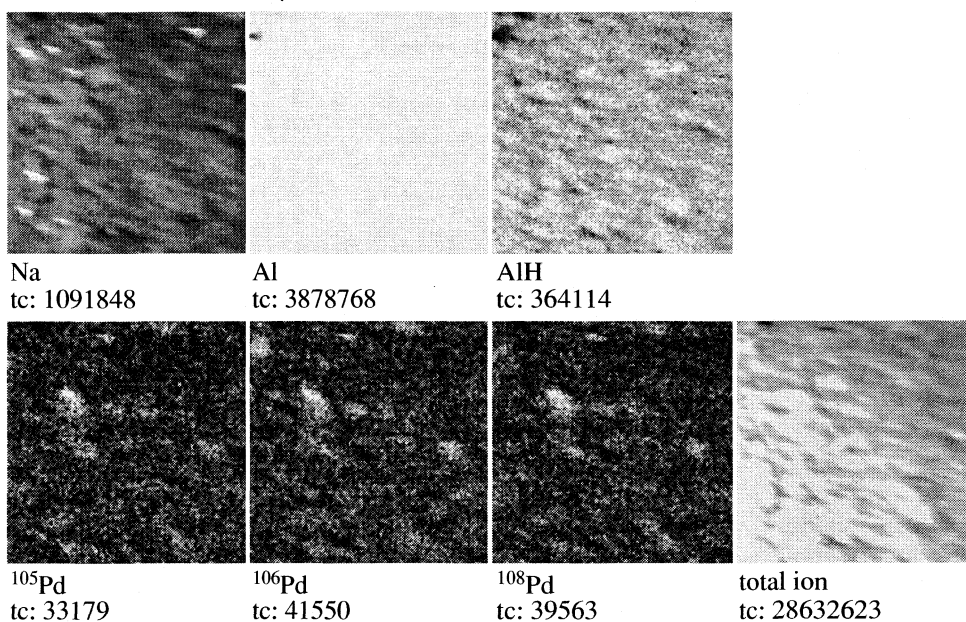
Fig. 4. ToF-SIMS surface images of the deactivated 2% Pd/Al$_2$O$_3$ catalyst. Bright colour indicates investigated ions.

CONCLUSION

Time-of-flight secondary ion mass spectrometry has been proved to be a universal and very useful tool in the characterisation of the surface of catalysts applied in hydrodechlorination reaction. The capital advantage of ToF-SIMS technique is the possibility of simultaneous monitoring of various changes of the analysed surface leading to the catalyst deactivation. In the case of Pd/Al$_2$O$_3$ catalyst not only a change of Cl content but also an increase in the amount of PdCl$_2$ were estimated. Owing to ToF-SIMS a considerable drop in the amount of surface accessible Pd was also observed during the

hydrodechlorination reaction. Moreover, ToF-SIMS surface images allowed to observe a deterioration of Pd distribution on the surface of catalyst after reaction in comparison with the fresh sample.

ACKNOWLEDGEMENT

REFERENCES

1. J.C. Vickerman, and D. Briggs, (Eds.), TOF-SIMS Surface Analysis by Mass, IM Publications and SurfaceeSpectra Limited, Chichester, 2001.

2. A. Benninghoven, Angew. Chem. Int. Ed. Engl. 33 (1994) 1023.

3. T. Paryjczak, M.I. Szynkowska, Przem. Chem. 82(3) (2003) 199.

4. J. Grams, J. Góralski, T. Paryjczak, Surf. Sci. 549 (2004) L21.

5. J. Grams, J. Rogowski, M. I. Szynkowska, E. Lesniewska, T. Paryjczak, React. Kinet. Catal. Lett. 84(2) (2005) 237.

6. A.A. Galkin, A.O. Turakulova, V.V. Lunin, J. Grams, Russ. J. Phys. Chem. 79(6) (2005) 881.

7. J. Rynkowski, D. Rajski, I. Szyszka, J.R. Grzechowiak, Catal. Today 90 (2004) 159.

8. W.K. Jóźwiak, W. Ignaczak, D. Dominiak, T.P. Maniecki, Appl. Catal. A 258 (2004) 33.

9. S. Karski, I. Witonska, J. Rogowski, J. Gołuchowska, J. Mol. Catal. A 240 (2005) 155.

10. Y. Zhou, M.C. Wood, N. Winograd, J. Catal. 146 (1994) 82.

11. Y.L. Leung, B.J. Flinn, P.C. Wong, K.A.R. Mitchell, K.J. Smith, Appl. Surf. Sci. 125 (1998) 293.

12. A.N. Kharat, P. Pendleton, A. Badalyan, M. Abedini, M.M. Amini, J. Catal. 205 (2002) 7.

13. L.T. Weng, P. Bertrand, O. Tirions, M. Devillers, Appl. Surf. Sci. 99 (1996) 185.

14. Z. Karpinski, K. Early, J.L. d'Itri, J. Catal. 164 (1996) 378.

15. W. Juszczyk, A. Malinowski, Z. Karpiński, Appl. Catal. A 166 (1998) 311.

16. F.J. Urbano, J.M. Marinas, J. Mol. Catal. A 173 (2001) 329.

17. H. Yu, E.M. Kennedy, Md.A. Uddin, B.Z. Dlugogorski, Catal. Today 88 (2004) 183.

18. S.C. Shekhar, J.K. Murthy, P.K. Rao, K.S.R. Rao, Appl. Catal. A 271 (2004) 95.

19. V.Y. Borovkov, P.P. Kulkarni, V.I. Kovalchuk, J.L. d'Itri, J. Phys. Chem B 108 (2004) 4811.

20. S. Ordonez, F.V. Diez, H. Sastre, Ind. Eng. Chem. Res. 41 (2002) 505.

21. Y. Ukisu, S. Kameoka, T. Miyadera, Appl. Catal. B 27 (2000) 97.

22. B. Szczepaniak, J. Góralski, T. Paryjczak, S. Szafran, T. Maniecki, Ann. Pol. Chem. Soc. 3 (2004) 583.

23. J. Grams, J. Góralski, B. Szczepaniak, T. Paryjczak, Pol. J. Env. Stud. 14 (2005) 89.

ХИМИЧЕСКАЯ КИНЕТИКА
И КАТАЛИЗ

ОПТИМИЗАЦИЯ ПОЛУЧЕНИЯ АЛКЕНОВ НА ЦЕОЛИТЕ HZSM-5 В ПРОЦЕССЕ СОВМЕСТНОЙ КОНВЕРСИИ МЕТАНОЛА И НИЗШИХ АЛКАНОВ

© 2007 г. В. В. Болотов, В. В. Поддубный, Л. М. Коваль

Томский государственный университет
E-mail: bolotov_vv@bk.ru

Поступила в редакцию 11.07.2006 г.

Изучен процесс совместной конверсии метанола и низших алканов C_3–C_4 на HZSM-5 с $SiO_2/Al_2O_3 = 50$. Методом параболической аппроксимации нахождения максимума поверхности отклика определены оптимальные технологические параметры (температура, объемная скорость подачи метанола) проведения процесса, обеспечивающие максимальную селективность по алкенам.

Процессы конверсии метанола и индивидуального превращения алканов C_3–C_4, а также катализаторы цеолитной природы для данных процессов хорошо изучены [1–3]. Совместная конверсия – новый альтернативный способ превращения метанола и алканов на цеолитах семейства пентасил. Этот процесс сочетает конверсию метилового спирта с расщеплением низших алканов C_3–C_4 и отличается высоким выходом алкенов в определенных условиях.

Значения технологических параметров процесса – температуры, объемной скорости подачи исходного сырья играют существенную роль в получении тех или иных продуктов каталитической конверсии. Нахождение оптимальных условий процесса, характеризуемого многими параметрами, целесообразно осуществлять привлечением математических методов планирования, позволяющих за короткий временной интервал и наиболее точно решить поставленную задачу.

В связи с этим цель данной работы – определение оптимальных значений температуры и объемной скорости подачи метанола для получения алкенов в процессе совместной конверсии метанола и низших алканов.

В качестве катализатора использовали высококремнеземный цеолит типа ZSM-5 с мольным отношением $SiO_2/Al_2O_3 = 50$, приготовленный по методике [4]. Образец испытывали в установке проточного типа со стационарным слоем катализатора при атмосферном давлении. В качестве сырья использовали пропан-бутановую фракцию и метанол. Влияние технологических параметров на процесс совместной конверсии метанола и пропан-бутановой смеси изучали в интервале температур 773–923 K и объемных скоростей подачи метанола $V = 0.6$–1.8 ч$^{-1}$. Объемную скорость подачи пропан-бутановой фракции поддерживали

постоянной во всей серии экспериментов (240 ч$^{-1}$). Результаты исследования приведены в таблице.

Несмотря на то, что при различных температурах эксперимента характер изменения степени конверсии (η) и селективности (S_i) по продуктам различен, можно выделить в нем характерные тенденции. С увеличением объемной скорости подачи метанола с 0.6 до 1.4 ч$^{-1}$ наблюдается рост селективности процесса по олефинам C_2–C_4 от 8.3 до 13.0 мас. % при 773 K, от 12.5 до 20.0 мас. % при 823 K, от 15.7 до 18.7 мас. % при 923 K и еще в большей степени при 873 K. Напротив, селективность образования ароматических углеводородов C_6–C_{10} с увеличением объемной скорости подачи метанола падает, минимальное значение наблюдается при 873 K и объемной скорости метанола 1.4 ч$^{-1}$ и составляет 12.9 мас. %. Вместе с этим при дальнейшем увеличении скорости подачи метанола до 1.8 ч$^{-1}$ в системе наблюдается незначительное снижение селективности по алкенам, которое составляет ~3–5 мас. %.

Для определения оптимальных значений технологических параметров образования алкенов в процессе совместной конверсии метанола и низших алканов использовали метод параболической аппроксимации нахождения максимума поверхности отклика, который, несомненно, можно отнести к одним из методов планирования эксперимента.

Суть используемого метода заключается в следующем: при приближении к максимуму поверхности отклика, т.е. в условиях адекватности параболического приближения, возникает задача нахождения и уточнения положения максимума поверхности отклика. В этих условиях естественно использовать метод наименьших квадратов (МНК) для уточнения вида параболической по-

Влияние технологических параметров ($V = 0.6$–1.8 ч$^{-1}$ – объемная скорость подачи CH_3OH) на распределение продуктов (мас. %) в процессе совместной конверсии метанола и алканов C_3–C_4 на НВКЦ-50 (η– степень конверсии, %)

Продукты	0.6	1.0	1.4	1.8	0.6	1.0	1.4	1.8	0.6	1.0	1.4	1.8	0.6	1.0	1.4	1.8
	500 K				550 K				600 K				650 K			
Водород	15.3	14.6	12.5	12.9	19.3	12.5	14.9	10.2	7.8	7.7	13.9	9.3	10.2	7.1	12.4	12.3
Метан	27.7	31.1	28.8	34.0	20.0	28.5	22.8	17.1	29.4	32.3	27.1	24.8	23.2	28.1	26.6	24.4
Этан	17.6	19.6	20.7	18.6	21.2	19.1	20.9	21.0	24.5	20.4	14.9	20.9	24.5	21.2	18.1	20.0
Этилен	3.1	3.4	6.0	7.1	8.0	8.5	10.2	11.9	9.0	10.7	13.7	14.2	11.3	10.1	11.8	9.2
Пропилен	5.2	7.2	6.3	5.9	4.5	6.0	8.6	8.1	7.6	6.5	8.8	6.2	4.4	7.3	6.9	5.3
Изобутан	14.3	9.5	10.3	9.3	5.3	7.6	8.4	11.8	5.9	8.2	8.7	10.3	8.2	7.8	9.1	8.4
Бензол	5.5	2.8	3.5	2.3	3.3	2.0	2.0	2.0	3.0	2.2	1.1	1.4	3.2	5.4	4.1	4.3
Толуол	6.4	5.9	7.0	6.8	10.0	7.6	6.1	6.6	5.5	5.8	6.6	4.8	7.1	6.8	5.3	5.9
Ксилолы	4.8	3.5	2.3	2.1	5.8	4.7	4.1	9.9	5.5	5.2	4.0	6.7	5.8	3.8	3.8	6.1
Арены C_{9+}	1.1	2.4	2.6	1.1	2.6	3.5	2.0	1.4	1.8	1.0	1.2	1.4	2.1	2.4	1.9	4.1
Алкены C_2–C_4	8.3	10.6	12.3	13.0	12.5	14.5	18.8	20.0	16.6	17.2	22.5	20.4	15.7	17.4	18.7	14.5
Арены C_6–C_{10}	17.8	14.6	15.4	12.2	21.7	17.8	14.2	19.9	15.8	14.2	12.9	14.3	18.2	18.4	15.1	20.4
η	58	60	62	57	64	71	75	75	65	66	76	67	52	50	62	59

верхности отклика и нахождения положения максимума.

Пусть искомая зависимость в общем виде выглядит следующим образом:

$$A_{ij} = A(T_i, V_j) + \varepsilon_{ij},$$

где A_{ij} – выход алкенов в зависимости от температуры эксперимента (T_i) и объемной скорости подачи метанола (V_j). В нашем конкретном примере

$$A(T, V) = a_{11}T^2 + a_{22}V^2 + a_{12}TV + a_{01}T + a_{02}V + a_{00},$$

где a_{ij} – искомые коэффициенты регрессии. Отклонения:

$$\varepsilon_{ij} = A_{ij} - A(T_i, V_j) = A_{ij} - a_{11}T_i^2 - a_{22}V_j^2 - $$
$$- a_{12}T_iV_j - a_{01}T_i - a_{02}V_j - a_{00}.$$

Затем, согласно методу наименьших квадратов,

$$\varepsilon^2 = \sum_{i, j = 1}^{n} \varepsilon_{ij}^2 \Rightarrow \min(a_{11}, \ldots, a_{00}).$$

Составим систему уравнений, обеспечивающих минимум ε^2 (систему шести уравнений для шести неизвестных коэффициентов):

$$\left.\begin{array}{l} \partial\varepsilon^2/\partial a_{11} = 0, \\ \ldots\ldots\ldots\ldots, \\ \partial\varepsilon^2/\partial a_{00} = 0 \end{array}\right\}.$$

Введем обозначение:

$$A_{ij} - a_{11}T_i^2 - a_{22}V_j^2 - a_{12}T_iV_j - a_{01}T_i - a_{02}V_j - a_{00} \equiv \Psi_{ij},$$

тогда $\varepsilon^2 = \sum_{i, j = 1}^{n} \Psi_{ij}^2$, т.е.

$$\left\{\begin{array}{l} \partial\varepsilon^2/\partial a_{11} = -2\sum_{i, j}\Psi_{ij}T_i^2 = 0, \\[2mm] \partial\varepsilon^2/\partial a_{22} = -2\sum_{i, j}\Psi_{ij}V_j^2 = 0, \\[2mm] \partial\varepsilon^2/\partial a_{12} = -2\sum_{i, j}\Psi_{ij}T_iV_j = 0, \\[2mm] \partial\varepsilon^2/\partial a_{01} = -2\sum_{i, j}\Psi_{ij}T_i = 0, \\[2mm] \partial\varepsilon^2/\partial a_{02} = -2\sum_{i, j}\Psi_{ij}V_j = 0, \\[2mm] \partial\varepsilon^2/\partial a_{00} = -2\sum_{i, j}\Psi_{ij} = 0. \end{array}\right.$$

В итоге после проведения дифференцирования получим уравнение, которое в матричном виде будет выглядеть следующим образом:

$$\frac{1}{n^2}\begin{pmatrix} \sum_{i,j} T_i^4 & \sum_{i,j} T_i^2 V_j^2 & \sum_{i,j} T_i^3 V_j & \sum_{i,j} T_i^3 & \sum_{i,j} T_i^2 V_j & \sum_{i,j} T_i^2 \\ \sum_{i,j} T_i^2 V_j^2 & \sum_{i,j} V_j^4 & \sum_{i,j} T_i V_j^3 & \sum_{i,j} T_i V_j^2 & \sum_{i,j} V_j^3 & \sum_{i,j} V_j^2 \\ \sum_{i,j} T_i^3 V_j & \sum_{i,j} T_i V_j^3 & \sum_{i,j} T_i^2 V_j^2 & \sum_{i,j} T_i^2 V_j & \sum_{i,j} T_i V_j^2 & \sum_{i,j} T_i V_j \\ \sum_{i,j} T_i^3 & \sum_{i,j} T_i V_j^2 & \sum_{i,j} T_i^2 V_j & \sum_{i,j} T_i^2 & \sum_{i,j} T_i V_j & \sum_{i,j} T_i \\ \sum_{i,j} T_i^2 V_j & \sum_{i,j} V_j^3 & \sum_{i,j} T_i V_j^2 & \sum_{i,j} T_i V_j & \sum_{i,j} V_j^2 & \sum_{i,j} V_j \\ \sum_{i,j} T_i^2 & \sum_{i,j} V_j^2 & \sum_{i,j} T_i V_j & \sum_{i,j} T_i & \sum_{i,j} V_j & \sum_{i,j} 1 \end{pmatrix} \times \begin{pmatrix} \hat{a}_{11} \\ \hat{a}_{22} \\ \hat{a}_{12} \\ \hat{a}_{01} \\ \hat{a}_{02} \\ \hat{a}_{00} \end{pmatrix} = \frac{1}{n^2}\begin{pmatrix} \sum_{i,j} A_{ij} T_i^2 \\ \sum_{i,j} A_{ij} V_j^2 \\ \sum_{i,j} A_{ij} T_i V_j \\ \sum_{i,j} A_{ij} T_i \\ \sum_{i,j} A_{ij} V_j \\ \sum_{i,j} A_{ij} \end{pmatrix}$$

или в сокращенном виде:

$$M \times \hat{a} = B,$$

откуда можно легко найти столбец оценок искомых коэффициентов регрессии:

$$\hat{a} = M^{-1} \times B.$$

Таким образом, получаем поверхность, уравнение которой имеет следующий вид:

$$\hat{A}(T, V) = \hat{a}_{11} T^2 + \hat{a}_{22} V^2 + \hat{a}_{12} TV + {} $$
$$ + \hat{a}_{01} T + \hat{a}_{02} V + \hat{a}_{00}.$$

Далее наша задача сводится к нахождению максимума полученной поверхности:

$$\begin{cases} \partial\hat{A}/\partial T = 2\hat{a}_{11} T + \hat{a}_{12} V + \hat{a}_{01}, \\ \partial\hat{A}/\partial V = 2\hat{a}_{22} V + \hat{a}_{12} T + \hat{a}_{02}, \end{cases}$$

$$\begin{pmatrix} 2\hat{a}_{11} & \hat{a}_{12} \\ \hat{a}_{12} & 2\hat{a}_{22} \end{pmatrix} \times \begin{pmatrix} T^* \\ V^* \end{pmatrix} = -\begin{pmatrix} \hat{a}_{01} \\ \hat{a}_{02} \end{pmatrix},$$

где T^* и V^* – соответственно температура и объемная скорость подачи метанола в точке максимума. Отсюда имеем

$$\begin{pmatrix} T^* \\ V^* \end{pmatrix} = -\begin{pmatrix} 2\hat{a}_{11} & \hat{a}_{12} \\ \hat{a}_{12} & 2\hat{a}_{22} \end{pmatrix}^{-1} \times \begin{pmatrix} \hat{a}_{01} \\ \hat{a}_{02} \end{pmatrix}.$$

Можно показать, что при достаточно малых флуктуациях положения максимума матрица ковариации его оценок вычисляется по формуле:

$$\begin{pmatrix} \sigma_{T*}^2 & \sigma_{T*}\sigma_{V*} r \\ \sigma_{T*}\sigma_{V*} r & \sigma_{V*}^2 \end{pmatrix} = G \times K\hat{a} \times G^T,$$

где σ_{T*}, σ_{V*} – среднеквадратичные ошибки оценивания положения максимума; r – коэффициент корреляции между оценками T^* и V^*; $K\hat{a} = (\hat{\sigma}^2/n^2)M^{-1}$ – матрица ковариации оценок $\hat{a}$; $\hat{\sigma}^2$ – оценка дисперсий флуктуаций поверхности

$$\hat{\sigma}^2 = \frac{1}{n^2 - 1} \sum_{i,j=1}^{n} (A_{ij} - \hat{A}(T_i, V_j))^2,$$

G – вспомогательная матрица

$$G = \begin{pmatrix} 2\hat{a}_{22} & \hat{a}_{12} \\ \hat{a}_{12} & 2\hat{a}_{11} \end{pmatrix}^{-1} \times \begin{pmatrix} \partial\varphi(T^*, V^*)/\partial T \\ \partial\varphi(T^*, V^*)/\partial V \end{pmatrix},$$

в которой $\varphi(T, V) = (T^2, V^2, TV, T, V, 1)$ – вектор-строка в представлении $\hat{A}(T, V) = \varphi(T, V) \times \hat{a}$ в виде скалярного произведения векторов φ и $\hat{a}$.

Относительные погрешности оценок положения максимума параболической поверхности отклика:

$$\delta_{T*} = \sigma_{T*}/T^*, \quad \delta_{V*} = \sigma_{V*}/V^*.$$

Заметим, что матрица

$$I = \frac{1}{\sigma^2} \sum_{i,j=1}^{n} \varphi^T(T_i, V_j) \times \varphi(T_i, V_j) = \frac{n}{\sigma^2} M$$

является информационной матрицей Фишера [5, 6], которая выражает количество информации, со-
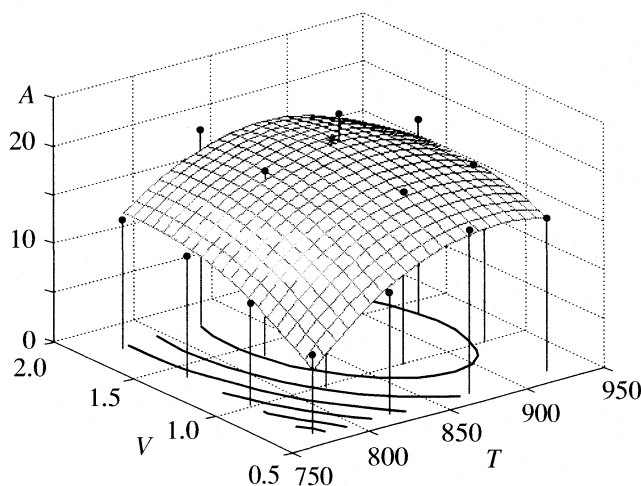
Рис. 1. Рассчитанная параболическая поверхность отклика; $T_r = 870.0456$, $V_r = 1.415$, $\hat{A}_r = 19.8545$, $T_{ex} = 873$, $V_{ex} = 1.4$, $A_{ex} = 22.5$.

держащееся в наблюдениях T, V и A, о коэффициентах параболической модели поверхности отклика. Поскольку $K\hat{a} = I^{-1}$, то неравенство Крамера–Рао [5] переходит в равенство, что свидетельствует о минимальности ошибок оценивания параметров a по методу наименьших квадратов.

При помощи программы, написанной в среде MatLab 7.01, для HZSM-5 была построена параболическая поверхность отклика и рассчитан ее максимум, координаты которого соответствуют оптимальным значениям технологических параметров процесса совместной конверсии.

Полученная параболическая поверхность в различных интерпретациях представлена на рис. 1 и 2, где T_r, V_r, A_r – рассчитанные оптимальные значения температуры эксперимента, объемной скорости подачи метанола и максимального выхода алкенов соответственно; T_{ex}, V_{ex}, A_{ex} – оптимальные параметры, полученные экспериментально; $\text{sigma}T_m/T_m$ и $\text{sigma}V_m/V_m$ – относительные погрешности оценок положения максимума параболической поверхности. Расчетные оптимальные значения сопоставимы с экспериментальными данными. Довольно низкие значения относительных погрешностей оценок положения максимума свидетельствуют о достаточно высокой точности эксперимента.
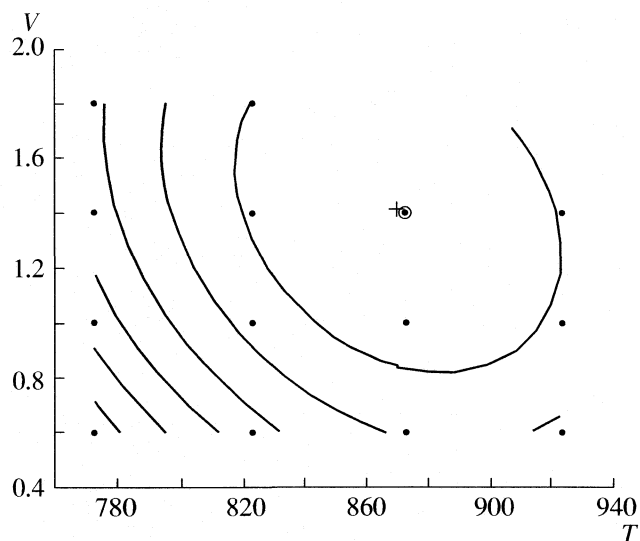

Рис. 2. Рассчитанная параболическая поверхность, представленная в виде контурных линий; точки – экспериментальные значения; $T_m = 870.0456$, $\text{sigma}T_m/T_m = 0.21594\%$, $V_m = 1.415$, $\text{sigma}V_m/V_m = 2.183\%$; знаком "+" отмечен максимум поверхности, "○" – экспериментально определенный максимум.

Таким образом, изучая влияние технологических параметров на процесс сопряженной конверсии метанола и низших алканов, можно подобрать такие условия, при которых будет получаться максимально возможная величина селективности в образовании требуемого продукта.

СПИСОК ЛИТЕРАТУРЫ

1. *Миначев Х.М., Дергачев А.А.* // Нефтехимия. 1994. Т. 34. № 5. С. 387.

2. *Миначев Х.М., Дергачев А.А.* // Успехи химии. 1990. Т. 59. С. 1522.

3. *Пономарева О.А., Московская И.Ф., Романовский Б.В.* // Кинетика и катализ. 2004. Т. 45. № 3. С. 426.

4. *Ерофеев В.И., Антонова Н.В., Рябов Ю.В., Коробицина Л.А.* Способ получения высококремнеземных цеолитов типа ZSM-5 // ПАТ. 1527154 Россия, МКИ С 01 В 33/28.

5. *Крамер Г.* Математические методы статистики. М.: Мир, 1975. 648 с.

6. *Ван-дер-Варден Б.Л.* Математическая статистика. М.: Изд-во иностр. лит., 1960. 436 с.

ФИЗИЧЕСКАЯ ХИМИЯ
ПОВЕРХНОСТНЫХ ЯВЛЕНИЙ

АДСОРБЦИЯ H₂O И D₂O ПОРИСТЫМИ ПОЛИСТИРОЛЬНЫМИ АДСОРБЕНТАМИ

© 2007 г.   И. А. Бардина, О. С. Жукова, Н. В. Ковалева, С. Н. Ланин

Московский государственный университет им. М.В. Ломоносова, Химический факультет
E-mail: SNLanin@phys.chem.msu.ru

Поступила в редакцию 19.07.2006 г.

Газохроматографическим методом изучена адсорбция H_2O и D_2O на пористых полимерах: хромосорбе-102 (сополимере стирола с дивинилбензолом) и MN-200 (сверхсшитом полистироле). Для оценки свойств поверхности этих полимеров в качестве тестовых адсорбатов использованы *н*-алканы (C_6–C_9), C_6H_6 и полярные соединения: $CHCl_3$, CH_3NO_2, CH_3CN, $(CH_3)_2CO$, $C_2H_5COOCH_3$, $(C_2H_5)_2O$. Из экспериментальных данных по удерживанию сорбатов определены вклады энергий дисперсионных и специфических межмолекулярных взаимодействий в общую энергию адсорбции для изученных систем. Определены электронодонорные K_D и электроноакцепторные K_A характеристики поверхности хромосорба-102 и MN-200. На основании полученных значений K_D и K_A эти полимеры отнесены к слабоспецифическим адсорбентам с преобладанием электроноакцепторных свойств. Измерены изотермы адсорбции H_2O и D_2O при 55, 67 и 80°C на этих полимерах. Определены зависимости их изостерических теплот адсорбции Q_{st} от величины адсорбции. Сделан вывод о том, что H_2O взаимодействует с поверхностью этих полимеров по адсорбционному механизму, а в удерживание D_2O заметный вклад, возможно, вносит абсорбция.

Авторы работы [1] сообщили, что спиновые изомеры воды (*орто-* и *пара*-вода) могут быть разделены хроматографически. Это обстоятельство вызвало интерес к различию адсорбционных свойств и хроматографического поведения изотопомеров, в том числе и воды – легкой (H_2O) и тяжелой (D_2O).

Известно, что адсорбционные свойства изотопомеров водорода H_2, HD и D_2 [2, 3] а также свойства обычных и дейтерированных углеводородов [4–6] несколько различаются. В зависимости от массы и строения молекулы, природы поверхности адсорбента и температуры дейтерированные молекулы могут адсорбироваться как слабее, так и сильнее, чем соответствующие их легкие изотопомеры. На графитированной саже дейтероуглеводороды адсорбируются слабее, чем соответствующие обычные углеводороды, однако на сильно полярных адсорбентах некоторые дейтероуглеводороды адсорбируются сильнее, чем их легкие изотопомеры [7, 8].

Изотопомеры воды, несмотря на близость их физико-химических свойств, нашли применение в качестве компонентов подвижной фазы в ВЭЖХ [9, 10]. Так, в [9] исследовано использование дейтеризованных растворителей CD_3OD и D_2O в качестве компонентов подвижных фаз в обращенно-фазовой (ОФ)-микро-ВЭЖХ. Показано, что свойства подвижных фаз с органическим компонентом CD_3OD или CH_3OH различаются немного. Однако при использовании в качестве водного компонента подвижной фазы D_2O (вместо H_2O) разделение ароматических углеводородов улучшается примерно до 30%. Отмечено, что D_2O является особенно эффективным растворителем для разделения дейтеризованных и недейтеризованных соединений. Также преимущества подвижных фаз, содержащих D_2O, проявились при разделении катехоламинов и комплексов металлов [10]. Обнаруженное различие свойств подвижных фаз, содержащих в качестве водного компонента H_2O или D_2O, по-видимому, связано с межмолекулярными взаимодействиями в объеме подвижной фазы и на поверхности сорбента [11].

Цель работы – исследование газохроматографическим методом адсорбции изотопомеров воды (H_2O и D_2O) на двух полимерных адсорбентах: Хромосорбе 102 (сополимере стирола с дивинилбензолом) и сверхсшитом полистироле MN 200 [12] и зависимости адсорбции легкой и тяжелой воды от донорно-акцепторных свойств поверхности сорбентов, оцениваемых по специфической и неспецифической адсорбции ряда тестовых органических соединений (*н*-алканов, а также азот-, хлор- и кислородсодержащих соединений алифатического, ароматического и гетероциклического рядов), молекулы которых обладают различными электронодонорным и электроноакцепторными свойствами.

ЭКСПЕРИМЕНТАЛЬНАЯ ЧАСТЬ

В качестве адсорбатов использовали изотопомеры воды H_2O (99.1%) и D_2O (99.9%). Для оценки

Таблица 1. Характеристика тестовых адсорбатов

Адсорбат	M	μ, D	α, Å^3	DN, ккал/моль	AN	DN/AN
$n\text{-}C_6H_{14}$	86.18	0	11.9	0	0	0
$n\text{-}C_7H_{16}$	100.20	0	13.7	0	0	0
$n\text{-}C_8H_{18}$	114.23	0	15.6	0	0	0
$CHCl_3$	119.38	1.15	8.23	0	23	0
CH_3NO_2	61.04	3.54	7.2	2.7	20.5	0.13
CH_3CN	41.05	3.90	5.4	14.1	18.9	0.74
$(CH_3)_2CO$	58.08	2.80	6.6	17.0	12.5	1.36
$CH_3COOC_2H_5$	88.11	1.80	9.0	17.1	9.3	1.82
$(C_2H_5)_2O$	74.12	1.70	9.5	19.2	3.9	4.92

Обозначения: M – молекулярная масса, μ – дипольный момент, α – общая поляризуемость молекулы, AN и DN – электроно-акцепторные и электронодонорные характеристики (числа), характеризующие способность этих молекул к электронодонорным и к электроноакцепторным взаимодействиям [13].

характеристики поверхности исследуемых адсорбентов в качестве тестовых адсорбатов использовали н-алканы, проявляющие с поверхностью любого адсорбента только неспецифические (дисперсионные) взаимодействия, а также бензол, тетрагидрофуран и полярные соединения алифатического ряда, способные вступать в специфические межмолекулярные взаимодействия с поверхностью адсорбентов. Некоторые физико-химические характеристики тестовых адсорбатов приведены в табл. 1. В качестве адсорбентов исследованы пористые полимерные адсорбенты: сополимер стирола и дивинилбензола Хромосорб-102, обладающий в основном мезопорами и сверхсшитый полистирольный полимер MN-200 с преобладающей микропористостью, аналог сорбента Purosep-200 [14]. Структурные характеристики адсорбентов приведены в табл. 2.

Адсорбционные свойства полимеров исследовали методом газовой хроматографии (ГХ) на хроматографе ЛХМ с детектором по теплопроводности. Сигнал детектора регистрировали и обрабатывали с помощью программного комплекса "Мультихром 1.52m". В качестве ГХ-колонок применяли стеклянные трубки длиной 35 см и внутренним диаметром 2 мм. Навеска адсорбента составляла 0.2349 и 0.2913 г для Хромосорба-102 и MN-200 соответственно. Скорость газа-носителя (гелия) поддерживали постоянной при значении ~25 мл/мин. Перед экспериментом адсорбент кондиционировали в хроматографической колонке в токе гелия при 200°C в течение 20 ч. Пробу адсорбатов объемом 2–10 мкл вводили в инжектор хроматографа микрошприцем.

Для всех адсорбатов определены удельные удерживаемые объемы V_m в интервале температур 50–100°C по Хромосорбе 102 и 100–200°C на MN-200 (для проб 2 мкл). Из линейной зависимо-

сти $\ln V_m$ от $1/T$ рассчитаны дифференциальные мольные изменения внутренней энергии адсорбции $-\Delta U$, равные дифференциальной мольной теплоте адсорбции Q_v. Из зависимости Q_v от поляризуемости молекул определены вклады энергий дисперсионных (Q_{disp}) и специфический (Q_{spec}) взаимодействий в общую энергию адсорбции.

Для H_2O и D_2O определили изотермы адсорбции из проявительных хроматограмм (пробы 0.2–10 мкл) в интервале температур 55–80°C по известной методике [15]. А затем из изотерм адсорбции рассчитали изостерические теплоты адсорбции при различных заполнениях поверхности сорбентов.

ОБСУЖДЕНИЕ РЕЗУЛЬТАТОВ

Величину эффективной удельной поверхности и параметры пористой структуры полимерных сорбентов определили из экспериментальных изотерм адсорбции н-гексана и бензола при повышенных температурах. Они приведены в табл. 3. Удельную поверхность (s) рассчитали по уравнению

$$s = a_m \omega N,$$

Таблица 2. Структурные характеристики полимерных адсорбентов, рассчитанные из низкотемпературной адсорбции азота

Адсорбент	S^*, $м^2/г$	V_{total}, $см^3/г$	d, нм	V_{micro}, $см^3/г$	d_{micro}, нм
Хромосорб-102	364	3.3	9		
MN-200*	1050	1.1		0.4	0.15

* По данным для Purosep-200, аналогом которого является MN-200 [14].

БАРДИНА и др.

Таблица 3. Характеристика пористой структуры полимерных адсорбентов

Сорбат	t, °C	Уравнение	Параметр	Хромосорб-102	MN-200
$н$-Гексан	100 (150)	Ленгмюра	a_m, ммоль/г	0.200	0.631
			s, м^{2}г	64	200
Бензол	150	Дубинина–Радушкевича	a_0, ммоль/г	0.4	1.9
			E_0, кДж/моль	13	13.8
			L, нм	6.8	4.5

Обозначения: t – температура измерения, величина в скобках – температура на MN-200, a_0 – емкость микропор, E_0 – характеристическая энергия адсорбции стандартного вещества – бензола, L – ширина микропоры.

где N – число Авогадро, ω – площадь, занимаемая молекулой сорбата в плотном монослое, определенная из плотности жидкости при плоской ориентации молекулы (для $н$-гексана $\omega = 52$ Å^2 [16]), a_m – емкость монослоя для $н$-гексана рассчитали из изотерм сорбции по уравнениям Ленгмюра, БЭТ, Арановича и получили близкие значения:

0.631, 0.636, 0.633 ммоль/г на MN-200 и 0.200, 0.202, 0.204 ммоль/г на Хромосорбе-102.

Параметры микропористой структуры оценили по уравнению теории объемного заполнения микропор Дубинина–Радушкевича [16]. Величину L рассчитали из зависимости E_0 от размера пор [17]. Из табл. 2 видно, что общая удельная поверхность, определенная из низкотемпературной адсорбции азота [14], значительно превышает рассчитанную из изотерм $н$-гексана, измеренных при повышенных температурах. Эта рассчитанная эффективная поверхность составляет только 15–20% от общей удельной поверхности. Для MN-200 она близка к удельной поверхности мезопор, равной 190 м^2/г, определенной из низкотемпературной адсорбции азота [12]. Причиной этого может быть уменьшение значения константы адсорбционного равновесия с ростом температуры [18].

Изотермы адсорбции H_2O и D_2O на Хромосорбе-102 и MN-200, приведенные на рис. 1, обращены выпуклостью к оси давления сорбата, что свидетельствует о более сильном взаимодействии адсорбат–адсорбат, чем адсорбат–адсорбент.

При одинаковых равновесных давлениях адсорбция D_2O на обоих пористых полимерах больше адсорбции H_2O, причем эта разница увеличивается с ростом температуры и давления.

Теплоты адсорбции. Из изотерм адсорбции H_2O и D_2O рассчитали изостерические теплоты адсорбции при разных заполнениях поверхности полимеров по уравнению Клаузиуса–Клапейрона:

$$d\ln p/dT = Q_{st}/RT^2. \qquad (1)$$

Зависимости Q_{st} от величины адсорбции a приведены на рис. 2. Во всей области заполнения теплота адсорбции пара воды на этих адсорбентах больше теплоты конденсации ($L_{H_2O} = 10.14$ ккал/моль), что указывает на полярный характер поверхности этих полимеров. На неполярном непористом адсорбенте с однородной поверхностью, графитированной термической саже, Q_{st} во всей области заполнения значительно меньше теплот конденсации [19].
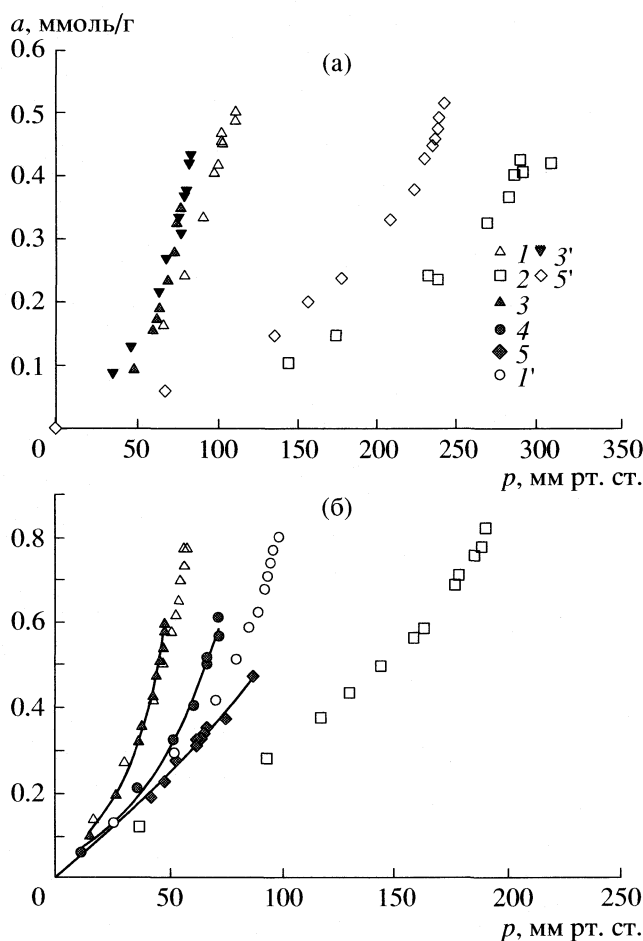

Рис. 1. Изотермы адсорбции H_2O (*1*, *1'*, *2*) и D_2O (*3–5*, *3'*, *5'*) на Хромосорбе-102 (а) и MN-200 (б) при 50 (*1*, *3*, *3'*), 60 (*1'*, *4*), 70°C (*2*, *5*, *5'*); *3'* и *5'* – первая серия опытов.

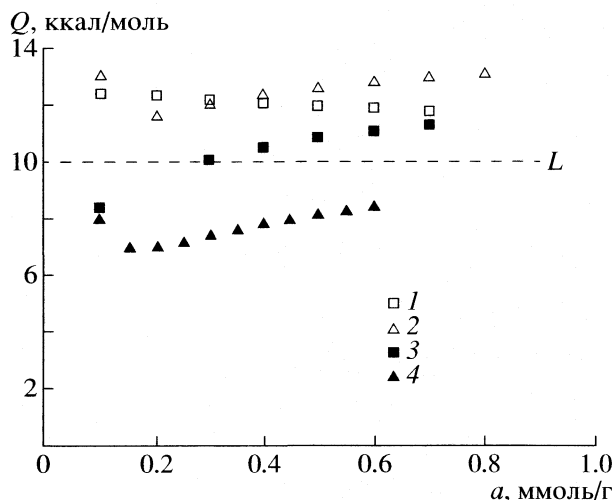**Рис. 2.** Зависимости теплот адсорбции H$_2$O (*1, 2*) и D$_2$O (*3, 4*) на полимерных адсорбентах Хромосорбе-102 (*1, 3*) и MN-200 (*2, 4*).

Рис. 3. Изотермы сорбции H$_2$O (а) и D$_2$O (б) на MN-200 (*1–3*) и Хромосорбе-102 (*4, 5*) при разных температурах: 55 (*1, 4*), 67 (*2*), 80°C (*3, 5*).

Теплота адсорбции D$_2$O на Хромосорбе-102 (рис. 2) при низких заполнениях ниже теплоты конденсации (L_{D_2O} = 10.26 ккал/моль), с ростом заполнения она увеличивается и несколько превышает L_{D_2O} при более высоких заполнениях (*a* > > 3 ммоль/г). На MN-200 величина Q_{st} для D$_2$O при низких заполнениях значительно ниже теплоты конденсации, с ростом заполнения Q_{st}, так же как и в случае Хромосорба-102, увеличивается, но не достигает L_{D_2O}.

Величины Q_{st} для D$_2$O при всех заполнениях значительно меньше, чем Q_{st} для H$_2$O, особенно на MN-200, в то время как адсорбция D$_2$O превышает адсорбцию H$_2$O (рис. 1), и эта разница увеличивается с ростом температуры. Вероятно, это связано с изменением механизма удерживания D$_2$O на этих сорбентах с ростом температуры.

Известно, что в случае пористых полимеров имеет место не только адсорбция на поверхности, но и растворение сорбатов во всем объеме частиц полимера [20]. Оба механизма сорбции (адсорбция и абсорбция) могут осуществляться одновременно. В работе [21] показано, что полимеры на основе стирола и дивинилбензола при низких температурах ведут себя как адсорбенты, а при более высоких температурах кроме адсорбции может происходить растворение некоторых веществ в объеме частиц полимера (например, бензол удерживается на Полисорбе-4K, сополимере стирола с дивинилбензолом, при 80°C по адсорбционному механизму, а при 180°C растворяется в объеме полимера). Сорбция D$_2$O с температурой увеличивается, а теплоты сорбции остаются меньше теплот адсорбции на обоих полимерных сорбентах. А H$_2$O, по-видимому, взаимодействует с по-
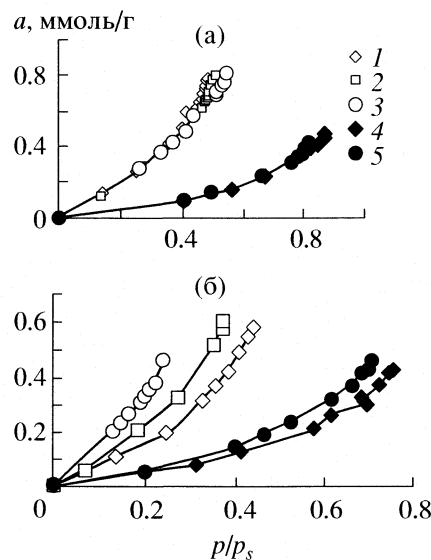
верхностью исследуемых полимеров по адсорбционному механизму (рис. 3). В случае D$_2$O при низких температурах (55°C) также преобладает процесс адсорбции, а при более высоких температурах заметный вклад в удерживание вносит растворение, причем в случае MN-200 абсорбция проявляется в большей степени. Это отчетливо видно из сравнения изотерм адсорбции H$_2$O и D$_2$O в координатах $a = f(p/p_s)$, представленных на рис. 3. Изотермы адсорбции H$_2$O на обоих полимерах при всех температурах близки, изотермы адсорбции D$_2$O – отличаются. При более высоких температурах это различие усиливается.

Для того чтобы оценить роль дисперсионных и специфических взаимодействий при адсорбции H$_2$O и D$_2$O на исследуемых сорбентах, были определены зависимости $\ln V_m$ от $1/T$ для H$_2$O, D$_2$O и тестовых адсорбатов при малых заполнениях поверхности сорбентов, при которых еще заметно не проявляются взаимодействия адсорбат–адсорбат.

Зависимости $\ln V_m$ от $1/T$ для всех адсорбатов на Хромосорбе-102 и MN-200 в исследуемом интервале температур линейны:

$$\ln V_m = A + B/T, \qquad (2)$$

где $A = (\Delta S + R)/R$ и $B = -\Delta U/R = Q_v/R$. Вычисленные из этой зависимости величины теплот адсорбции для H$_2$O и тестовых адсорбатов приведены в табл. 4 и 5.

Теплоты адсорбции всех адсорбатов на Хромосорбе-102 меньше, чем на MN-200. *н*-Алканы взаимодействуют с поверхностью этих полимеров (так же как и со всеми другими адсорбентами) только за счет дисперсионных сил и их адсорбция

Таблица 4. Зависимость Q_{st} для H_2O и D_2O (ккал/моль) от величины адсорбции (a, ммол/г) на Хромосорбе-102 и MN-200

a, ммоль/г	$Q(H_2O)$	$Q(D_2O)$	$Q(H_2O)-Q(D_2O)$
Хромосорб-102			
0.1	12.4	8.4	4.0
0.2	12.4		
0.3	12.2	10.1	2.1
0.4	12.1	10.5	1.6
0.5	12.0	10.9	1.1
0.6	11.9	11.1	0.8
0.7	11.8	11.3	0.5
MN-200			
0.1	13.1	8.0	5.1
0.2	11.7	7.0	4.7
0.3	12.1	7.4	4.7
0.4	12.4	7.8	4.6
0.5	12.7	8.2	4.5
0.6	12.9	8.4	4.5

определяется геометрической структурой и общей поляризуемостью молекул *н*-алканов. Более высокие теплоты адсорбции *н*-алканов на MN-200 по сравнению с Хромосорбом-102 свидетельствуют о том, что MN-200 обладает более узкими микропорами (в которых происходит более значительное усиление адсорбционного потенциала), чем Хромосорб-102. Зависимости Q_{disp} от общей поля-

ризуемости (α) молекул сорбатов линейны и описываются следующими уравнениями

для Хромосорба-102:

$$Q_{disp} = 0.7713\alpha + 2.1541, \quad n = 4, \quad R^2 = 0.9995, \tag{3}$$

для MN-200:

$$Q_{disp} = 1.162\alpha - 0.4633, \quad n = 4, \quad R^2 = 0.9995. \tag{4}$$

При адсорбции полярных адсорбатов проявляются дисперсионные и специфические взаимодействия. Вклады энергии специфического взаимодействия (Q_{spec}) определяли по формуле: $Q_{spec} = Q_v - Q_{disp}$, где Q_v – теплота адсорбции искомого полярного соединения Q_{disp} – определяется по уравнению (3) в случае Хромосорба-102 и по уравнению (4) в случае MN-200 для гипотетического *н*-алкана, поляризуемость которого равна поляризуемости этого полярного адсорбата. Эти данные приведены в табл. 5 и 6, из которых видно, что на MN-200 происходит более сильное, чем на Хромосорбе-102, специфическое взаимодействие функциональных групп тестовых полярных адсорбатов с адсорбционными центрами.

На поверхности использованных полимеров расположены в основном фенильные группы, которые могут вступать в специфические взаимодействия с функциональными группами полярных адсорбатов за счет участия π-электронов. Однако на обоих полимерах значение Q_{spec} для всех тестовых адсорбатов значительно больше, чем на неполярном Хромосорбе-103 (поперечносшитом полистироле), и близки к соответствующим величинам для Хромосорба-105 (полиароматическом эфире) [22], но значительно меньше,

Таблица 5. Теплоты адсорбции и вклады в них дисперсионных и специфических взаимодействий на Хромосорбе-102

Адсорбат	Q, ккал/моль	α, Å^3	Q_{disp}, ккал/моль	Q_{spec}, ккал/моль	Q_{spec}/Q, %
C_6H_{14}	11.4	11.9		0	
C_7H_{16}	12.6	13.7		0	
C_8H_{18}	14.2	15.6		0	
C_6H_6	10.2	10.4	10.2	0	
$CHCl_3$	10.6	8.2	8.5	2.1	19.8
CH_3NO_2	10.3	7.2	7.7	2.6	25.2
CH_3CN	9.4	5.4	6.3	3.1	33.0
$(CH_3)_2CO$	10.0	6.6	7.2	2.8	28.0
$CH_3COOC_2H_5$	12.5	9.0	9.1	3.4	27.2
H_2O	12.1	1.5	3.3	8.8	72.7
ТГФ	12.5	7.7	8.1	4.4	35.2
$(C_2H_5)_2O$	8.2	9.5	9.5	–1.3	

Обозначения: ТГФ – тетрагидрофуран.

Таблица 6. Теплоты адсорбции и вклады в них дисперсионных и специфических взаимодействий на MN-200

Адсорбат	Q, ккал/моль	α, Å³	Q_{disp}, ккал/моль	Q_{spec}, ккал/моль	Q_{spec}/Q, %
C_6H_{14}	13.4	11.9	13.4	0	
C_7H_{16}	15.5	13.7	15.5	0	
C_8H_{18}	17.7	15.6	17.7	0	
C_6H_6	12.3	10.4	11.6	0.7	5.6
$CHCl_3$	11.6	8.2	9.1	2.5	21.5
CH_3NO_2	11.2	7.2	7.9	3.3	29.5
CH_3CN	11.0	5.4	5.8	5.2	47.2
$(CH_3)_2CO$	11.6	6.6	7.2	4.4	37.9
$CH_3COOC_2H_5$	14.4	9.0	10.0	4.4	30.5
H_2O	12.2	1.5	1.3	10.9	89.3
ТГФ	12.2	7.7	8.4	3.6	29.5
$(C_2H_5)_2O$	12.3	9.5	10.6	1.7	13.8

чем для Хромосорба-104, на поверхности которого расположены нитрильные группы [21]. Вероятно, высокие энергии специфического взаимодействия обусловлены не только наличием на поверхности исследуемых полимеров π-электронов фенильных колец, но и наличием более активных центров – функциональных групп: кетонных, эфирных, спиртовых, обнаруженных методами ¹³C ЯМР и ИК-фурье-спектроскопии [23]. Значительный вклад специфических π–π-взаимодействий в механизм удерживания органических веществ в условиях обращенно-фазовой ВЭЖХ на MN-200 был обнаружен и в [24].

Таким образом, согласно полученным данным, Хромосорб-102 и MN-200 можно отнести к слабоспецифическим адсорбентам по классификации [18]. H₂O адсорбируется на этих полимерах в основном за счет специфических взаимодействий: (Q_{spec}) на Хромосорбе-102 составляет 72%, а на MN-200 89% от общей энергии адсорбции.

Энергия специфического взаимодействия определяется донорно-акцепторными взаимодействиями сорбат–сорбент

$$Q_{spec} = K_D AN + K_A DN \qquad (5)$$

или

$$Q_{spec}/AN = K_D + K_A DN/AN, \qquad (6)$$

где AN и DN – электроноакцепторные и электронодонорные числа молекул адсорбатов [25], а K_D и K_A – электронодонорные и электроноакцепторные характеристики поверхности адсорбентов.

На рис. 4 представлены зависимости Q_{spec}/AN от отношения DN/AN; они линейны (коэффициент корреляции 0.95). Определенные из этих зависимостей K_A и K_D представлены в табл. 7. На основании этих данных можно заключить, что по-

верхности обоих полимеров обладают как электроноакцепторными, так и электронодонорными свойствами. Энергетические характеристики этих центров немного выше на MN-200, чем на поверхности Хромосорба-102.

Таким образом, из полученных результатов следует, что H₂O взаимодействует с поверхностью Хромосорба-102 и сверхсшитого полистирола по адсорбционному механизму, в удерживание D₂O, по-видимому, заметный вклад вносят процесс адсорбции, который увеличивается с повышением температуры эксперимента.
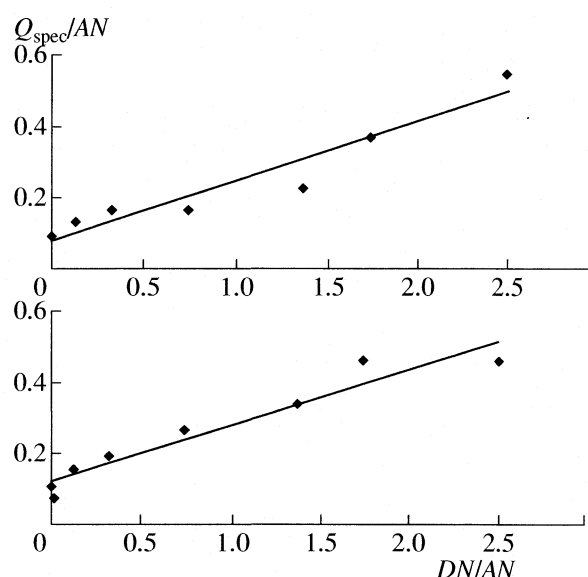

Рис. 4. Зависимости Q_{spec}/AN от отношения DN/AN на Хромосорбе-102 (а) и MN-200 (б).

Таблица 7. Электронодонорные K_D и электроноакцепторные K_A характеристики поверхности полимерных адсорбентов

Адсорбент	K_A	K_D
MN-200*	0.20	0.12
MN-200**	0.20	0.10
Хромосорб-102*	0.17	0.08
Хромосорб-102**	0.16	0.06
Хромосорб-103	0.08	0.07
Хромосорб-104	0.22	0.42
Хромосорб-105	0.08	0.15
Технический углерод ДГ-100	0.01	0.02

* Без учета данных по $(C_2H_5)_2O$.
** Без учета данных по $(C_2H_5)_2O$ и ТГФ.

СПИСОК ЛИТЕРАТУРЫ

1. *Tikhonov V.I., Volkov A.A.* // Science. 2002. V. 296. P. 2363.

2. *Moore W.R., Ward H.R.* // J. Am. Chem. Soc. 1958. V. 80. P. 2909.

3. *Панченков Г.М., Толмачев А.М., Зотова Т.В.* // Журн. физ. химии. 1964. Т. 38. С. 1361.

4. *Constabaris G., Sams J.R., Halsey G.D.* // J. Phys. Chem. 1961. V. 65. P. 367.

5. *Bruner F., Ceccioli P., Corcia A.* // Anal. Chem. 1972. V. 44. P. 894.

6. *Киселев А.В., Худяков В.Л., Яшин Я.И.* // Журн. физ. химии. 1974. Т. 48. С. 757.

7. *Bruner F., Cartoni G.P.* // J. Chromatogr. 1965. V. 18. P. 390.

8. *Сакодынский К.И., Картони Дж.Р., Пела А.* // Журн. физ. химии. 1966. Т. 40. С. 2887.

9. *Jinno K.* // J. HRC & CC. 1982. V. 5. P. 364.

10. *Jinno K., Fujimoto C.* // J. Liquid Chromatogr. 1984. V. 7. P. 2059.

11. *Ланин С.Н.* //100 лет хроматографии / Под ред. Б.А. Руденко. М.: Наука, 2003. С. 407.

12. *Белякова Л.Д., Волощук А.М., Ларионов О.Г. и др.* // Тр. IX Международ. конф. по теорет. вопросам адсорбции и адсорбционной хроматографии. Москва, 2001. С. 121.

13. *Gutmann V.* // Coord. Chem. Rev. 1991. V. 18. P. 225.

14. *Белякова Л.Д., Волощук А.М., Воробьева Л.М. и др.* // Журн. физ. химии. 2002. Т. 76. № 9. С. 1674.

15. *Киселев А.В., Яшин Я.И.* Газоадсорбционная хроматография. М.: Наука, 1967. 256 с.

16. *Дубинин М.М.* // Carbon. 1983. V. 21. P. 359.

17. *Stoekli H.M., Rebstein P., Bullerini L.* // Ibid. 1990. V. 28. P. 907.

18. *Киселев А.В.* Межмолекулярные взаимодействия в адсорбции и газовой хроматографии. М.: Высш. школа, 1986. 360 с.

19. *Belyakova L.D., Kiselev A.V., Kovaleva N.V.* // Bull. Soc. Chim. France. 1967. P. 285.

20. *Сакодынский К.И., Панина Л.И.* Полимерные сорбенты для молекулярной хроматографии. М.: Наука, 1977. 164 с.

21. *Гвоздович Т.Н.* Исследование адсорбционных свойств пористых полимеров. Дис. ... канд. хим. наук. М.: МГУ, 1975. 173 с.

22. *Бардина И.А., Ковалева Н.В., Никитин Ю.С.* // Журн. физ. химии. 1997. Т. 71. № 7. С. 1282.

23. *Streat M., Sweetland L.A.* // Trans. J. Chem. Eng. 1998. V. 76(B). P. 115.

24. *Пеннер Н.А.* Сверхсшитые полистирольные сорбенты для ВЭЖХ. Дис. ... канд. хим. наук. М.: МГУ, 2000. 178 с.

25. *Gutmann V.* // Electrochimica Acta. 1991. V. 21. P. 661.

ФИЗИЧЕСКАЯ ХИМИЯ
ПОВЕРХНОСТНЫХ ЯВЛЕНИЙ

АДСОРБЦИЯ ГАЗОВ НА ПОВЕРХНОСТИ ТВЕРДЫХ РАСТВОРОВ И БИНАРНЫХ СОЕДИНЕНИЙ СИСТЕМЫ GaSb–ZnTe

© 2007 г.   И. А. Кировская, Л. В. Новгородцева, М. В. Васина

Омский государственный технический университет

E-mail: phiscem@omgtu.ru

Изучена адсорбция аммиака, оксида углерода (II) и кислорода на пленках твердых растворов и бинарных соединений системы GaSb–ZnTe. На основе анализа изобар, равновесных и кинетических изотерм, термодинамических и кинетических характеристик адсорбции, электрофизических, кислотно-основных и других физико-химических характеристик адсорбентов и электронной природы молекул адсорбатов установлены механизм и закономерности адсорбционных процессов в зависимости от условий протекания и состава системы. Выявлены общность с бинарными соединениями (GaSb, ZnTe) и специфические особенности в поведении твердых растворов $(GaSb)_x(ZnTe)_{1-x}$ как многокомпонентных систем. О специфических особенностях свидетельствует наличие экстремумов на диаграммах "адсорбционная характеристика – состав". Использование таких диаграмм привело к открытию наиболее активных по отношению к NH_3, CO, O_2 компонентов изученной системы и созданию на их основе высокочувствительных и селективных сенсоров-датчиков.

Система GaSb–ZnTe к началу данной работы не была получена. Поэтому ее объемные и, тем более, поверхностные свойства не изучались. Как и другие сложные системы на основе алмазоподобных полупроводников, таящие в себе неожиданные свойства [1–3], система GaSb–ZnTe представляет интерес в плане поиска новых адсорбентов, катализаторов и материалов современной техники, в частности, сенсорной электроники, включая сенсоры-датчики экологического назначения [2]. Создание таких сенсоров-датчиков, базирующееся на необходимых сведениях об адсорбционных и других физико-химических свойствах поверхности полупроводников, в настоящее время, в связи с экологическим кризисом, особенно актуально. Соответственно и выбранные адсорбаты (CO, NH_3, O_2) интересны не только как отличающиеся по электронной природе, но и как компоненты окружающей и технологических сред.

ЭКСПЕРИМЕНТАЛЬНАЯ ЧАСТЬ

Адсорбцию изучали методами пьезокварцевого микровзвешивания [2] (чувствительность 1.23×10^{-11} г/(см^2 Гц), интервал температур 252–393 K и давлений 1.1–10.7 Па). Адсорбенты представляют собой пленки ($d = 0.18$–0.22 мкм) GaSb, ZnTe и твердых растворов $(GaSb)_x(ZnTe)_{1-x}$ (5, 10, 15, 90, 95 мол. % GaSb), полученные дискретным термическим напылением в вакууме ($T_{конд} = 298$ K, $p = 1.33 \times 10^{-3}$ Па) на электродные площадки пьезокварцевых резонаторов (АТ-среза, собственная частота колебаний 4.5 МГц) с последующим отжигом в парах исходного материала при соот-

ветствующих режимах [2, 4]. На этих же образцах одновременно исследовали изменения электропроводности и соответственно заряда поверхности под влиянием адсорбированных газов. Порошки твердых растворов получали методом изотермической диффузии бинарных компонентов в вакуумированных запаянных кварцевых ампулах при температурах, превышающих температуру плавления легкоплавкого компонента (GaSb) [1]. Их состав определялся пределами взаимной растворимости GaSb и ZnTe.

Идентификацию твердых растворов осуществляли по результатам рентгенографического анализа, измерения электропроводности (четырехзондовым методом Ван-дер-Пау) и определения pH изоэлектрического состояния поверхности (методом гидролитической адсорбции). Адсорбаты получали по известным методикам [5]: оксид углерода (II) – разложением муравьиной кислоты в присутствии нагретой концентрированной серной кислоты; аммиак – разложением аммонийных солей (хлорида или сульфата аммония) оксидом кальция; кислород – разложением перманганата калия с последующим хроматографическим анализом. Воспроизводимость результатов проверяли дублированием опытов. Расчеты и статистическую обработку результатов проводили с применением ЭВМ.

ОБСУЖДЕНИЕ РЕЗУЛЬТАТОВ

Величины адсорбции изученных газов на всех компонентах системы GaSb–ZnTe составляют 10^{-4}–10^{-3} моль/м^2. Опытные зависимости адсорб-
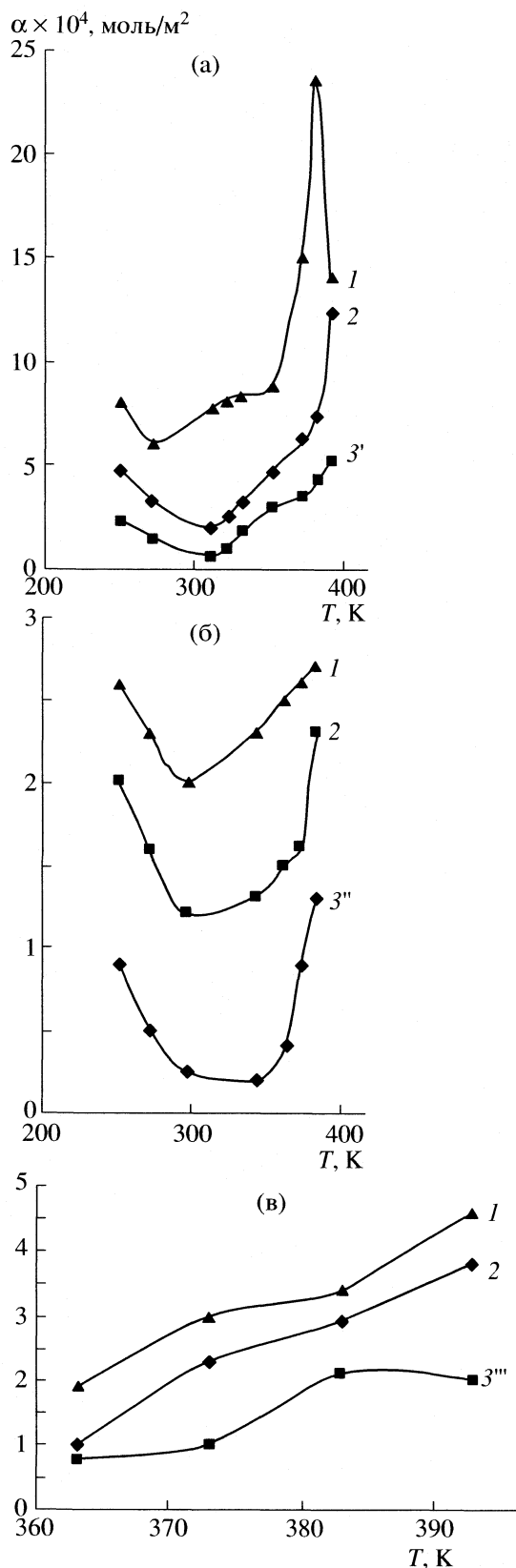
Рис. 1. Изобары адсорбции NH_3 (а), CO (б), O_2 (в) на GaSb (*1*), ZnTe (*2*) и твердых растворах $(GaSb)_{0.95}(ZnTe)_{0.05}$ (*3'*), $(GaSb)_{0.15}(ZnTe)_{0.85}$ (*3''*), $(GaSb)_{0.90}(ZnTe)_{0.10}$ (*3'''*) при $p_н = 8$ Па.

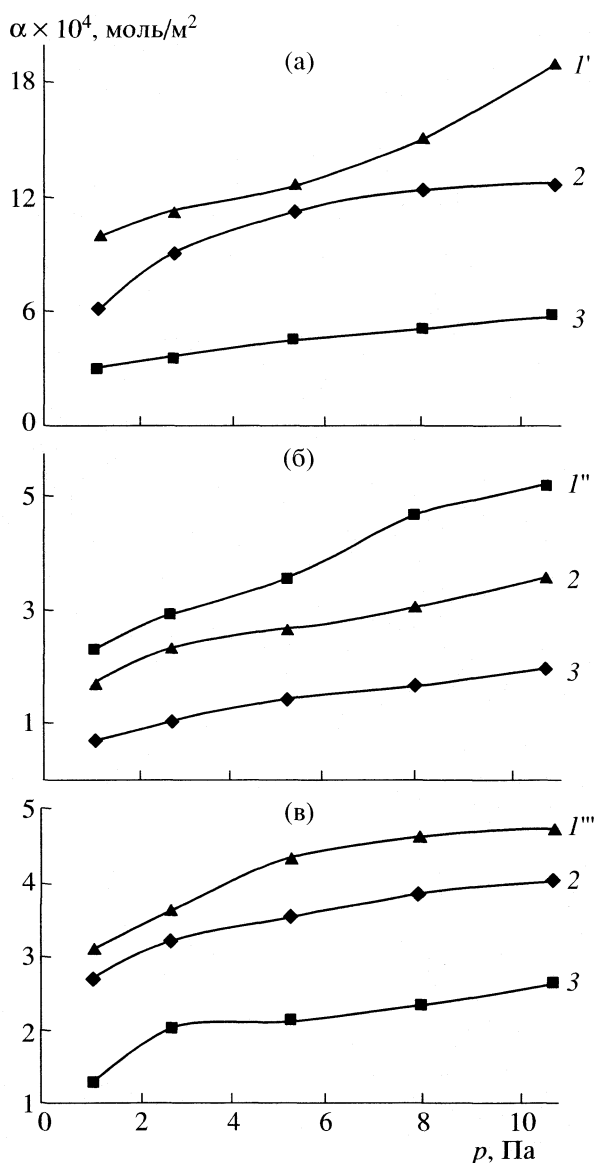**Рис. 2.** Равновесные изотермы адсорбции NH_3 (а), CO (б), O_2 (в) на твердых растворах $(GaSb)_{0.95}(ZnTe)_{0.05}$ (*1'*), $(GaSb)_{0.15}(ZnTe)_{0.85}$ (*1''*), $(GaSb)_{0.90}(ZnTe)_{0.10}$ (*1'''*) и *2* – GaSb, *3* – ZnTe при 393 K.

ции $\alpha_p = f(T)$, $\alpha_T = f(p)$, $\alpha_T = f(t)$ (типичные представлены на рис. 1–3) данного газа на всех компонентах системы GaSb–ZnTe имеют сходный характер. Они свидетельствуют о росте величины адсорбции с температурой, т.е. о ее преимущественно химической активированной природе, начиная с 313, 323–343 и 363 K для аммиака, оксида углерода и кислорода соответственно. В системе NH_3–$(GaSb)_{0.95}(ZnTe)_{0.05}$ необратимая химическая адсорбция при 383 K переходит в обратимую.

Преимущественно химическую активированную природу адсорбции газов в заданных температурных условиях подтверждают результаты ана-

лиза равновесных и кинетических изотерм, расчетов энергии активации (E_a) и термодинамических характеристик адсорбции (q_a, ΔS_a).

Равновесные изотермы адсорбции описываются в основном уравнением Лэнгмюра (частично, в области средних давлений – Фрейндлиха), **кинетические изотермы адсорбции** – уравнением Рогинского–Зельдовича–Еловича [6]. Выполнение последнего позволило использовать созданный С.З. Рогинским для неоднородных поверхностей метод "контролирующей полосы" и вытекающее из него уравнение [7]

$$E_a = RT\ln(t + t_0)/\tau_0,$$

где t_0 – поправка, которая находится из тангенса угла наклона кинетических изотерм в координатах $\alpha{-}\lg t$, $\tau_0 = 1/K_0$ – величина, обратная предэкспоненциальному множителю, имеющая размерность времени, для нахождения средних значений **энергии активации адсорбции** при различных заполнениях поверхности (величинах адсорбции α).

Теплоты адсорбции определяли по уравнению Клапейрона–Клаузиуса для нисходящих участков кривых $\alpha_p = f(T)$, из температурных зависимостей адсорбционных коэффициентов и по уравнению, предложенному в [6], для всего исследованного интервала температур. Там же описан способ расчета изменения энтропии адсорбции. Порядок величин E_a, q_a (с поправкой на возможные заниженные значения теплот химической адсорбции на алмазоподобных полупроводниках [8]) (таблица) подтверждает химическую природу адсорбционного взаимодействия NH_3, CO, O_2 с поверхностью компонентов системы GaSb–ZnTe. В согласии с ними находятся и отрицательные величины изменений энтропии адсорбции (таблица), обусловленные, скорее всего, частичным или полным торможением вращательных и поступательных степеней свободы адсорбированных молекул и соответственно образованием относительно прочных связей [2, 6].

Отмечаемые рост энергии активации и уменьшение теплоты адсорбции с ростом степени заполнения поверхности указывают на неоднородный характер поверхности и присутствие на ней различных по силе и энергетическому состоянию активных центров. Об этом же свидетельствуют и результаты исследования кислотно-основных свойств поверхности данных адсорбентов [9]. Выполненные с использованием методов ИК-спектроскопии, определения рН-изоэлектрического состояния, механохимии, кондуктометрического титрования они указали на наличие на поверхности, по крайней мере, трех типов кислотных центров, ответственными за которые, как и на других алмазоподобных полупроводниках [10], должны выступ-
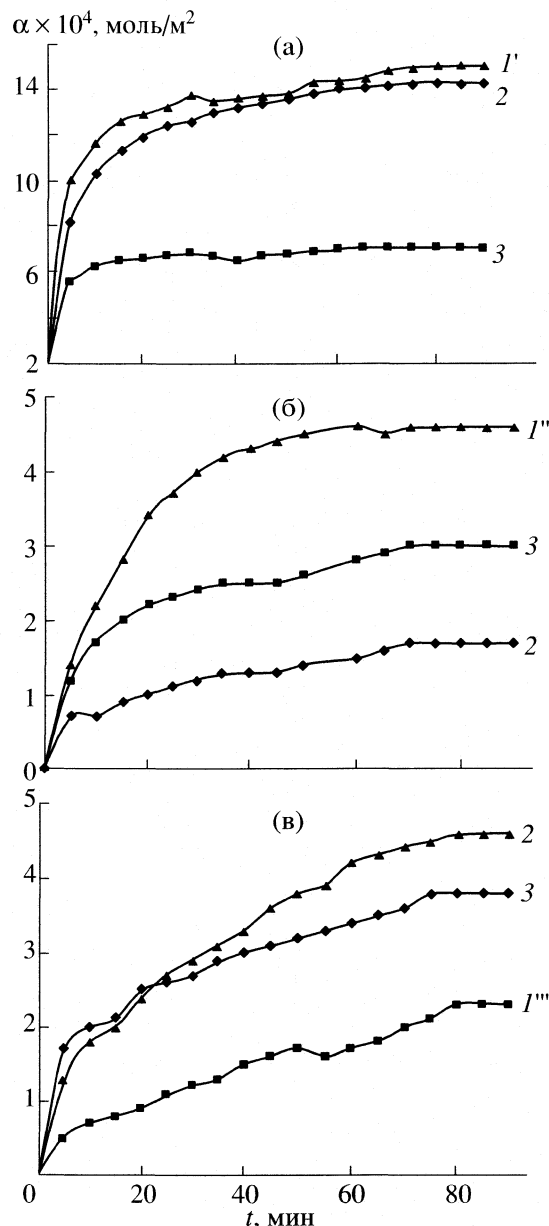

Рис. 3. Кинетические изотермы адсорбции NH_3 (а), CO (б), O_2 (в) на твердых растворах $(GaSb)_{0.95}(ZnTe)_{0.05}$ (*1'*), $(GaSb)_{0.15}(ZnTe)_{0.85}$ (*1''*), $(GaSb)_{0.90}(ZnTe)_{0.10}$ (*1'''*) и 2 – GaSb, *3* – ZnTe при $p_н =$ = 8 Па и 393 К.

пать координационно-ненасыщенные атомы с окружающими их вакансионными дефектами (льюисовские центры) и адсорбированные молекулы H_2O, группы OH^- (бренстедовские центры).

На основе анализа полученных результатов с учетом кислотно-основных свойств поверхности адсорбентов и электронного строения молекул адсорбатов можно утверждать, что адсорбция NH_3, CO, по аналогии с адсорбцией CO_2 [2, 8], протекает по донорно-акцепторному механизму с участием в качестве акцепторов преимуществен-

Энергия активации (E_a) и термодинамические характеристики (q_a, ΔS_a) адсорбции газов на компонентах системы GaSb–ZnTe в интервалах температур 313–393 K и величин адсорбции (1.3–5.8) × 10^{-4} моль/м²

Компонент системы GaSb–ZnTe	E_a, кДж/моль	q_a, кДж/моль	$-\Delta S_a$, Дж/(моль K)
Аммиак			
GaSb	53.3–80.8	2.8–15.9	48.9–65.6
(GaSb)$_{0.95}$–(ZnTe)$_{0.05}$	34.9–66.5	4.2–17.6	45.8–61.9
(GaSb)$_{0.90}$–(ZnTe)$_{0.10}$	50.7–67.1	3.4–16.1	47.3–64.5
(GaSb)$_{0.15}$–(ZnTe)$_{0.85}$	56.8–88.6	2.7–9.8	51.5–66.3
ZnTe	81.7–95.5	1.9–7.6	58.8–69.2
Оксид углерода (II)			
GaSb	61.1–109.4	1.1–10.9	53.8–73.3
(GaSb)$_{0.95}$–(ZnTe)$_{0.05}$	57.4–91.6	2.1–11.5	52.6–65.9
(GaSb)$_{0.90}$–(ZnTe)$_{0.10}$	59.1–81.2	3.9–13.3	48.1–62.6
(GaSb)$_{0.15}$–(ZnTe)$_{0.85}$	52.9–62.1	6.7–15.1	38.9–58.7
ZnTe	91.1–96.5	4.4–12.8	49.5–64.7
Кислород			
GaSb	85.4–103.4	0.4–7.2	62.4–73.6
(GaSb)$_{0.95}$–(ZnTe)$_{0.05}$	73.7–96.6	0.5–8.1	58.6–68.1
(GaSb)$_{0.90}$–(ZnTe)$_{0.10}$	60.5–95.1	0.6–10.2	54.2–65.6
(GaSb)$_{0.15}$–(ZnTe)$_{0.85}$	87.8–106.1	0.3–8.5	59.9–68.9
ZnTe	96.2–112.6	0.3–5.3	66.7–74.7

но поверхностных атомов A (со свободными d- и p-орбиталями и с более выраженными металлическими свойствами) и в качестве доноров – молекул адсорбатов:
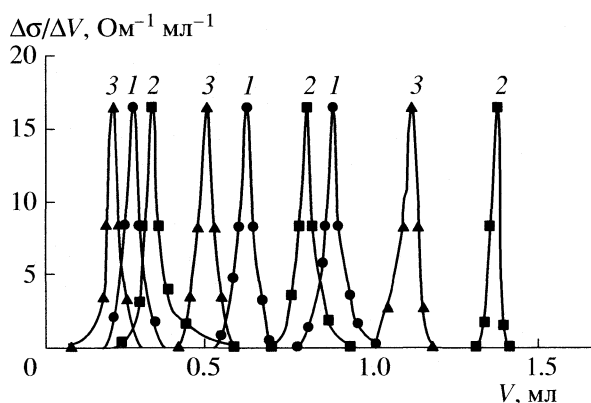
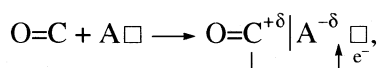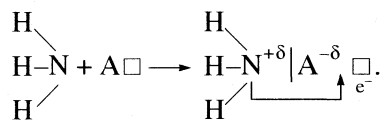$$O{=}C + A\square \longrightarrow O{=}C^{+\delta}\big|A^{-\delta}\,\square,$$

**Рис. 4.** Дифференциальные кривые кондуктометрического титрования компонентов системы GaSb–ZnTe, экспонированных на воздухе: *1* – GaSb, *2* – (GaSb)$_{0.95}$(ZnTe)$_{0.05}$, *3* – (GaSb)$_{0.90}$(ZnTe)$_{0.10}$.

$$\begin{array}{c}H\\ \diagdown\\ H{-}N \\ \diagup\\ H\end{array} + A\square \longrightarrow \begin{array}{c}H\\ \diagdown\\ H{-}N^{+\delta}\big|A^{-\delta}\,\square.\\ \diagup\\ H\end{array}$$

О преимущественно донорном действии молекул NH_3 и CO свидетельствуют результаты измерения электропроводности (σ) [11]: в условиях химической адсорбции NH_3 и CO величина σ растет.

При различной координационной ненасыщенности поверхностных атомов (тем более в многокомпонентных системах) возможно образование нескольких донорно-акцепторных связей, отличающихся степенью делокализации электронов и прочностью, что согласуется с наличием на дифференциальных кривых кондуктометрического титрования исследуемых адсорбентов трех пиков (рис. 4).

Механизм адсорбции кислорода, как и в [8], можно представить следующим образом:

$$O_2(г) + F \longrightarrow O_2^-(адс),$$

$$O_2^-(адс) + F \longrightarrow 2O^-(адс),$$
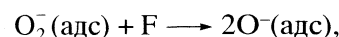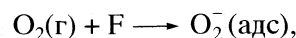
где F – вакансия атома B, захватившая электрон, т.е. так называемый F-центр. При этом нельзя исключить и взаимодействия кислорода со сверхстехиометричными атомами B с образованием связей $O_2^{-\delta}$–$B^{+\delta}$ или $O^{-\delta}$–$B^{+\delta}$ (B – Sb, Te).

При *сопоставлении бинарных соединений и твердых растворов системы GaSb–ZnTe* как адсорбентов по отношению к изученным газам (NH_3, CO, O_2) установлены сходство и различие в их поведении. О сходстве свидетельствуют аналогичный вид опытных зависимостей (изобар, равновесных и кинетических изотерм), порядок величин адсорбции, термодинамических и кинетических характеристик, одинаковые природа активных центров, механизм и закономерности адсорбционного взаимодействия. Отражением специфических особенностей твердых растворов, как многокомпонентных систем, является наличие экстремумов на диаграммах "адсорбционная характеристика – состав" (рис. 5).

Как следует из этих диаграмм, максимумам адсорбционной активности отвечают максимумы теплот и минимумы энергий активации адсорбции NH_3, CO, O_2, приходящиеся на твердые растворы, содержащие соответственно 95, 15, 90 мол. % GaSb.

Отклонения от линейных зависимостей "адсорбционная характеристика – состав", согласно [1], могут быть связаны с наибольшими дефектностью структуры, координационной ненасыщенностью поверхностных атомов и, тем самым, возникновением наибольшего количества активных центров. Отмеченные явления, в свою очередь, есть следствие изменения степени упорядоченности и дефектности структуры исходных би-
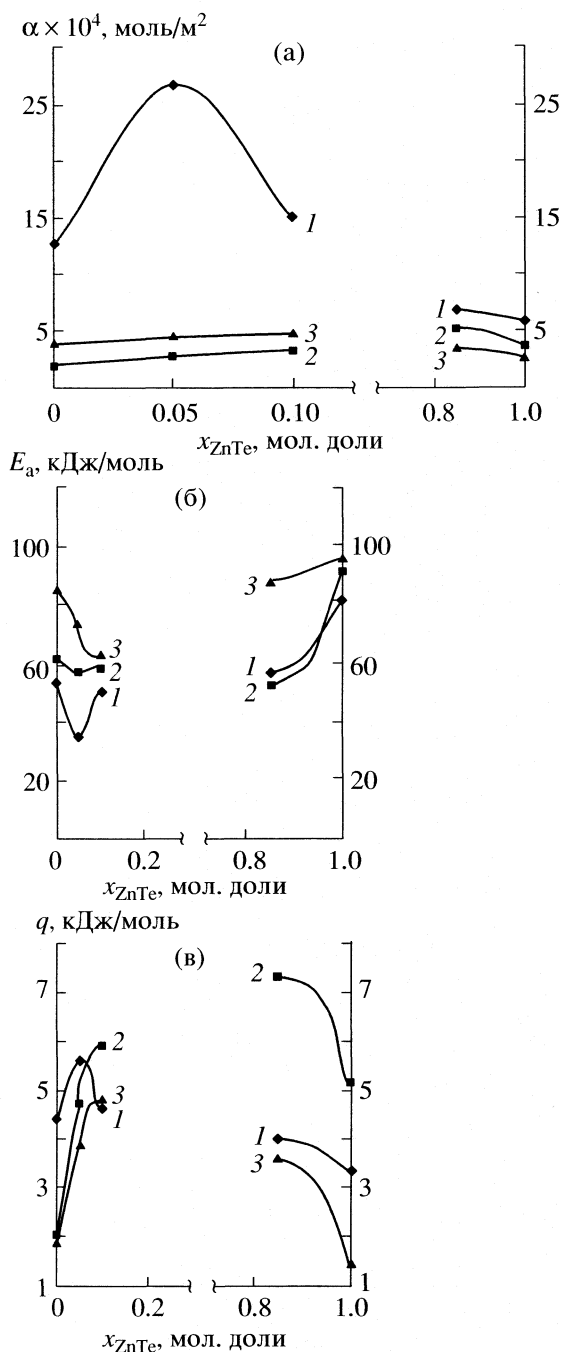
Рис. 5. Зависимости величин адсорбции (а), энергии активации адсорбции (б) и теплоты адсорбции (в) NH_3 (*1*), CO (*2*), O_2 (*3*) от состава системы GaSb–ZnTe.

нарных соединений под влиянием атомов-заместителей при образовании твердых растворов [1].

Использование диаграмм "адсорбционная характеристика – состав" позволило найти наиболее активные по отношению к NH_3, CO, O_2 компоненты системы – твердые растворы $(GaSb)_{0.95}(ZnTe)_{0.05}$, $(GaSb)_{0.15}(ZnTe)_{0.85}$, $(GaSb)_{0.90}(ZnTe)_{0.10}$ соответственно, на основе которых созданы сенсоры-датчики на микропримеси указанных газов.

СПИСОК ЛИТЕРАТУРЫ

1. *Кировская И.А.* Поверхностные свойства алмазоподобных полупроводников. Твердые растворы. Томск: Изд-во ТГУ, 1984. 160 с.

2. *Кировская И.А.* Поверхностные явления. Омск: Изд-во ОмГТУ, 2001. 175 с.

3. *Кировская И.А.* Катализ. Полупроводниковые катализаторы. Омск: Изд-во ОмГТУ, 2004. 272 с.

4. Тонкие пленки антимонида индия. Получение, свойства, применение / Под ред. В.А. Касьяна, П.И. Кетруша, Ю.А. Никольского, Ф.И. Пасечника. Кишинев: Штиинца, 1989. 162 с.

5. *Раппопорт Ф.М., Ильинская А.А.* Лабораторные методы получения чистых газов. М.: Госхимиздат, 1963.

6. *Кировская И.А.* Адсорбционные процессы. Иркутск: Изд-во ТГУ, 1995. 300 с.

7. *Рогинский С.З.* Адсорбция и катализ на неоднородных поверхностях. М.: Изд-во АН СССР, 1948. 643 с.

8. *Кировская И.А.* Поверхностные свойства алмазоподобных полупроводников. Адсорбция газов. Иркутск: Изд-во ИГУ, 1984. 186 с.

9. *Кировская И.А., Новгородцева Л.В.* // Докл. АН ВШ РФ. 2006. № 2(7). С. 1.

10. *Кировская И.А.* Поверхностные свойства алмазоподобных полупроводников. Химический состав поверхности. Катализ. Иркутск: Изд-во ТГУ, 1988. 220 с.

11. *Кировская И.А., Шубенкова Е.Г., Новгородцева Л.В.* // Матер. IV Всерос. школы-семинара "Новые материалы. Создание, структура, свойства – 2004". Томск, 2004. С. 226.

ФИЗИЧЕСКАЯ ХИМИЯ
ПОВЕРХНОСТНЫХ ЯВЛЕНИЙ

ВЛИЯНИЕ СТРОЕНИЯ ПОВЕРХНОСТИ ГИДРОФИЛЬНО-ГИДРОФОБНЫХ КРЕМНЕЗЕМОВ НА АДСОРБЦИЮ ХОЛЕВОЙ КИСЛОТЫ

© 2007 г.   Л. А. Белякова, Л. Н. Бесараб

*Национальная академия наук Украины, Институт химии поверхности, Киев*
E-mail: v-bel@mail.kar.net; v-bel@mail.vtv.kiev.ua

Синтезированы гидрофильно-гидрофобные кремнеземы с равномерным и островковым размещением функциональных групп по поверхности, а также с изменяющейся степенью ее гидрофобности. Изучена адсорбция холевой кислоты гидрофильно-гидрофобными кремнеземами в зависимости от равновесной концентрации в растворе. Показано, что адсорбция происходит в основном за счет дисперсионного взаимодействия между гидрофобными участками поверхности и стероидными сегментами холевой кислоты. Обнаружено повышение адсорбционной способности для гидрофильно-гидрофобного кремнезема с мозаичным строением поверхности, обусловленное вкладом геометрических "отпечатков" холевой кислоты в суммарную адсорбцию.

Холевая кислота (НСА, первичная желчная кислота, $pK_a = 5.0$) является амфифильным соединением [1], а потому удобной тест-молекулой для оценки сродства поверхности органокремнеземов к веществам, адсорбирующимся как за счет дисперсионного притяжения, так и посредством специфических взаимодействий. В настоящей работе изучено влияние степени гидрофобности и строения поверхности гидрофильно-гидрофобных кремнеземов на адсорбцию холевой кислоты.
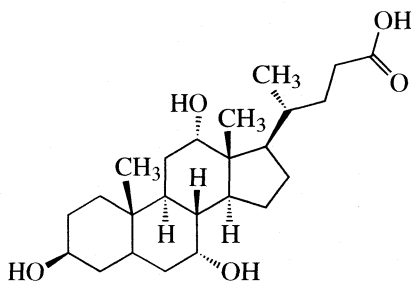
ЭКСПЕРИМЕНТАЛЬНАЯ ЧАСТЬ

Исходным кремнеземом служил непористый высокодисперсный аэросил А-300 с удельной поверхностью 300 м²/г и концентрацией силанольных групп 940 мкмоль/г. Холевую кислоту с содержанием основного вещества 99.7% ("Fluka") использовали без дополнительной очистки. Адсорбционное и химическое модифицирование поверхности кремнезема контролировали с помощью ИК-спектроскопии (спектрофотометр Thermo Nicolet NEXUS FT-IR). Записывали ИК-спектры спрессованных пластинок плотностью 25–30 мг/см² в интервале частот 4200–1200 см⁻¹.

Степень замещения (α, %) силанольных групп кремнезема на триметилсилильные (реакция с гексаметилдисилазаном (HMDS)) рассчитывали по формуле:

$$\alpha = [(D_0 - D)/D_0] \times 100,$$

где D_0 и D – оптические плотности полосы поглощения изолированных OH-групп (3750 см⁻¹) до и после реакции с HMDS соответственно. Для устранения влияния массы пластинки кремнезема и приборных погрешностей оптическую плотность полосы поглощения 3750 см⁻¹ определяли как отношение [2]: D_{Si-OH}(3750 см⁻¹)/$D_{Si-O-Si}$(1860 см⁻¹).

Адсорбцию паров воды и гексана изучали при 25°С в вакуумной адсорбционной установке с пружинными кварцевыми весами Мак-Бена–Бакра [3] (чувствительность спиралей 0.45–0.55 мм/мг).

Краевой угол смачивания θ поверхности исходного и модифицированных кремнеземов определяли капельным методом [4]. Адсорбцию холевой кислоты изучали методом отдельных навесок. Навески кремнеземов (0.1 г) приводили в контакт с увеличивающимися объемами (от 10 до 250 мл) 0.1 мМ водного раствора НСА с рН 5. Полученные суспензии выдерживали при 20°С в течение 5 ч до установления адсорбционного равновесия. Содержание холевой кислоты в исходных и равновесных растворах определяли по образованию окрашенного комплекса с концентрированной серной кислотой при λ = 389 нм [5] (спектрофотометр Specord М-40).

Гидрофильно-гидрофобные кремнеземы синтезировали двумя различными способами: 1) взаимодействием гидроксилированного кремнезема с
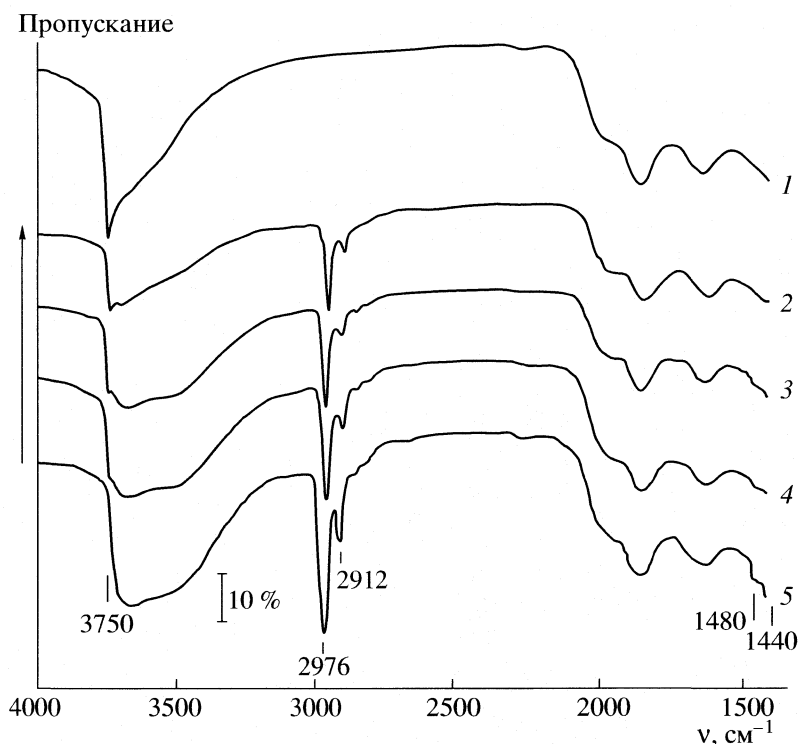
Рис. 1. ИК-спектры кремнезема до (*1*) и после (*2–5*) взаимодействия с гексаметилдисилазаном (нумерация спектров соответствует адсорбентам в таблице).

гексаметилдисилазаном в мягких условиях; 2) гидрофобизацией свободных участков поверхности кремнезема после адсорбции холевой кислоты (аппликационный синтез).

Модифицирование кремнезема, предварительно вакуумированного при 400°C для удаления с его поверхности адсорбированной воды, парами HMDS осуществляли при 50°C [6]:
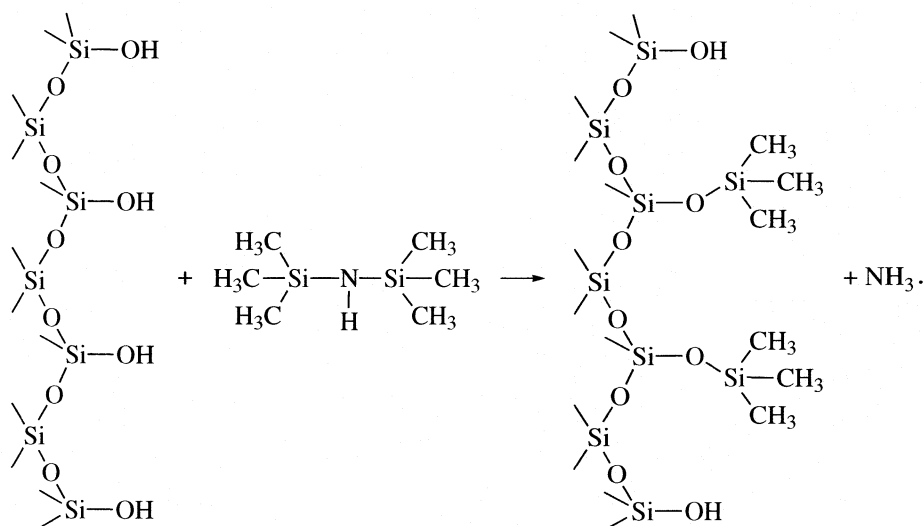
Содержание триметилсилильных групп варьировали, изменяя время контакта кремнезема с HMDS от 1 мин до 2 ч.

ОБСУЖДЕНИЕ РЕЗУЛЬТАТОВ

В ИК-спектрах модифицированных кремнеземов (рис. 1) наблюдается уменьшение интенсив-

Физико-химические характеристики гидрофильно-гидрофобных кремнеземов

Адсорбент	c, мкмоль/г	α, %	θ, град	K_d, мл/г
1	0	0	25	8
2	380	40	55	50
3	490	52	78	105
4	610	65	85	200
5	940	100	95	300
6	470	50	–	520

Обозначения: c – концентрация $Si(CH_3)_3$-групп; α – степень замещения ОН-групп триметилсилильными; θ – краевой угол смачивания (по воде); K_d – коэффициент распределения для адсорбции холевой кислоты.

ности полосы поглощения изолированных силанольных групп (3750 см$^{-1}$) и появляются характеристические полосы поглощения валентных (2976, 2912 см$^{-1}$) колебаний связи С–Н в привитых триметилсилильных группах [7].

С увеличением содержания триметилсилильных групп растет краевой угол смачивания поверхности гидрофильно-гидрофобных кремнеземов (таблица), а также уменьшается адсорбция воды (рис. 2), так как снижается содержание центров специфической адсорбции (силанольных групп) в результате триметилсилилирования поверхности кремнезема. Адсорбция $н$-гексана происходит не в непосредственной близости к поверхности гидрофильно-гидрофобных кремнеземов, а на некотором расстоянии от нее, лимитируемом
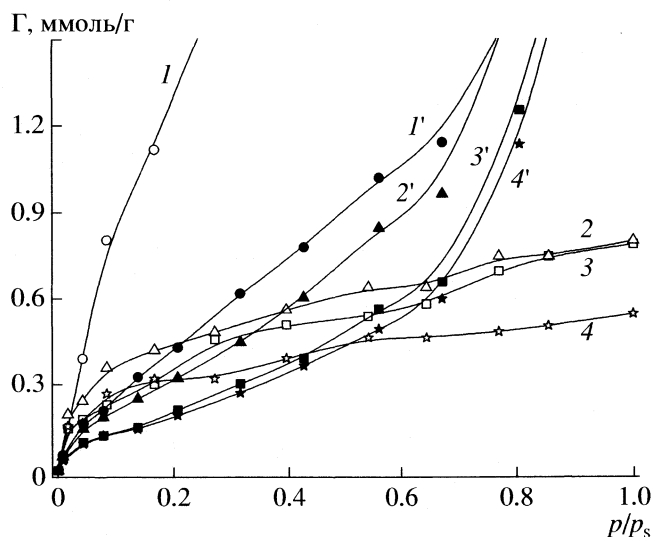

Рис. 2. Изотермы адсорбции воды (*1–4*) и $н$-гексана (*1'–4'*) для гидроксилированного кремнезема (*1*, *1'*), а также гидрофильно-гидрофобных кремнеземов, содержащих 40 (*2*, *2'*), 65 (*3*, *3'*) и 100% (*4*, *4'*) триметилсилильных групп.

размерами триметилсилильных групп. Поэтому дисперсионное взаимодействие $н$-гексана происходит с меньшим числом атомов поверхности модифицированных кремнеземов [8], а адсорбция $н$-гексана уменьшается с увеличением плотности прививки триметилсилильных групп (рис. 2).

При аппликационном синтезе гидрофильно-гидрофобного кремнезема с островковой (мозаичной) структурой поверхностного слоя в качестве молекулы-аппликатора использовали холевую кислоту. После адсорбции НСА (из расчета 50%-ного покрытия поверхности) проводили химическое модифицирование свободных участков поверхности кремнезема с помощью HMDS, а затем десорбцию холевой кислоты. После адсорбции холевой кислоты в ИК-спектре кремнезема появляется характеристическая полоса поглощения 1720 см$^{-1}$ $\nu(C=O)$, а также полосы поглощения валентных (2940 и 2875 см$^{-1}$) и деформационных (1450, 1410 и 1380 см$^{-1}$) колебаний связей С–Н в метильных и метиленовых группах НСА (рис. 3). Интенсивность полосы поглощения изолированных силанольных групп (3750 см$^{-1}$) при этом уменьшается, что свидетельствует об их участии в образовании водородной связи при адсорбции НСА.

Модифицирование поверхности кремнезема HMDS приводит к увеличению интенсивности полос поглощения валентных колебаний связей С–Н и исчезновению полосы поглощения $\nu(O–H)$ силанольных групп, что является следствием замещения протона силанольных групп триметилсилильными радикалами на участках поверхности кремнезема, свободных от адсорбированных молекул холевой кислоты. При удалении молекул аппликатора с поверхности кремнезема интенсивность полосы поглощения валентных колебаний связи С=О карбоксильной группы НСА уменьшается; кроме того, появляется полоса поглощения валентных колебаний связи О–Н в изолированных силанольных группах. На основании характера ИК-спектральных изменений в процессе аппликационного модифицирования можно сделать вывод о наличии на поверхности кремнезема участков компактного расположения гидрофильных (силанольных) и гидрофобных (триметилсилильных) групп.

На рис. 4, 5 представлены изотермы адсорбции холевой кислоты для гидрофильно-гидрофобных кремнеземов с равномерным и островковым размещением функциональных групп по поверхности. Сигмоидальный вид изотерм адсорбции НСА и существенное увеличение поглощения холевой кислоты с уменьшением содержания силанольных групп на поверхности гидрофильно-гидрофобных кремнеземов может свидетельствовать о преимущественном вкладе в адсорбцию дисперсионных взаимодействий между гидрофобными участками поверхности кремнеземов и стероид-
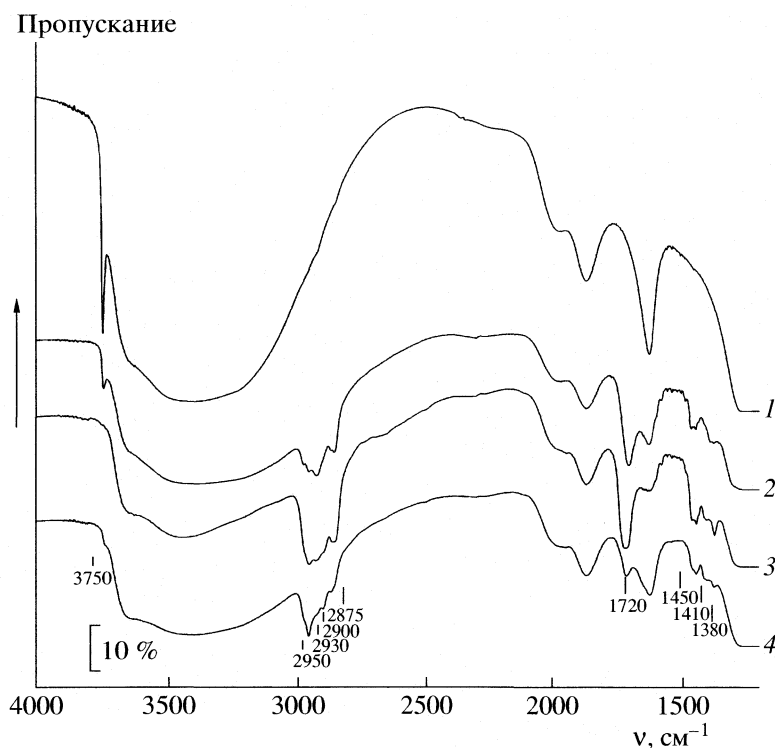
Пропускание

Рис. 3. ИК-спектры гидроксилированного кремнезема до (*1*) и после адсорбции холевой кислоты (*2*), дополнительно модифицированного триметилсилильными группами (*3*), после десорбции холевой кислоты (*4*).
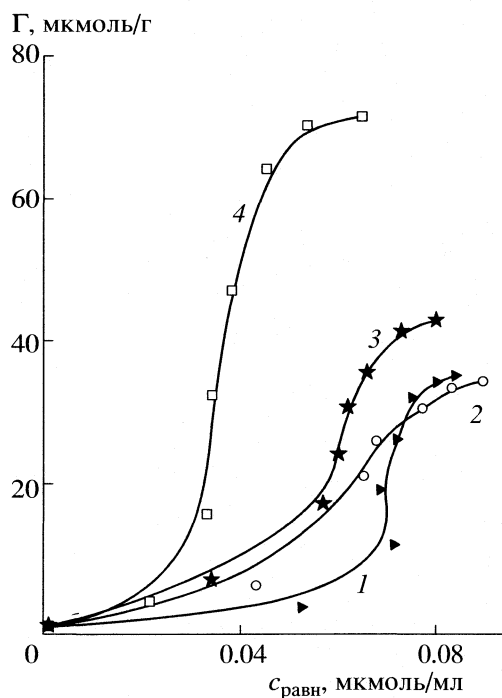

Рис. 4. Изотермы адсорбции холевой кислоты для кремнеземов с различным содержанием триметилсилильных групп: *1* – 40, *2* – 52, *3* – 65, *4* – 100%.
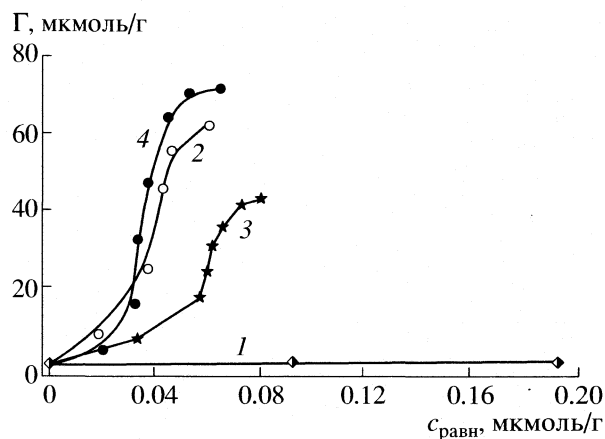

Рис. 5. Изотермы адсорбции холевой кислоты для исходного кремнезема (*1*), а также гидрофильно-гидрофобных кремнеземов с мозаичной структурой поверхности (*2*) и равномерным размещением функциональных групп: *3* – 52, *4* –100% триметилсилильных групп.

ными сегментами молекул холевой кислоты. При pH 5 силанольные группы поверхности кремнезема переходят в ионизированное состоя-

ние, так же как и холевая кислота, а потому специфической адсорбции HCA не происходит (рис. 5).

Адсорбция холевой кислоты на кремнеземе с мозаичным строением поверхности (рис. 5, таблица, адсорбент 6) существенно превышает адсорбцию для кремнезема 3, несмотря на практически одинаковое содержание триметилсилильных групп в адсорбентах. Максимальная величина адсорбции для адсорбента 6 примерно такая же, как

для кремнезема со 100%-ным замещением силанольных групп триметилсилильными (адсорбент 5). Коэффициент распределения в области Генри для адсорбции холевой кислоты увеличивается симбатно с гидрофобностью поверхности модифицированных кремнеземов. Следует отметить, что величина K_d для кремнезема с островковым распределением функциональных групп наибольшая. Более высокое сродство поверхности "мозаичного" кремнезема к НСА свидетельствует о наличии дополнительных центров адсорбции. Такими центрами, по-видимому, являются геометрические "отпечатки" холевой кислоты на поверхности гидрофильно-гидрофобного кремнезема. Возможен незначительный вклад в суммарную адсорбцию неионизированных силанольных групп, которые в случае островкового размещения функциональных групп по поверхности не экранированы триметилсилильными радикалами.

Таким образом, установлена симбатная зависимость адсорбции холевой кислоты от гидрофобности поверхности триметилсилилированных кремнеземов. Осуществлен аппликационный синтез гидрофильно-гидрофобного кремнезема с мо-

заичным строением поверхности. Доказан вклад геометрических "отпечатков" молекул аппликатора в суммарную адсорбцию холевой кислоты.

СПИСОК ЛИТЕРАТУРЫ

1. *Hofmann A.F.* // News Physiol. Sci. 1999. V. 14. P. 24.

2. *Davydov V.Ya., Kiselev A.V., Zhuravlev L.T.* // Trans. Faraday Soc. 1964. V. 60. № 12. P. 2254.

3. Экспериментальные методы в адсорбции и молекулярной хроматографии / Под ред. А.В. Киселева, В.П. Древинга. М.: Изд-во МГУ, 1973.

4. *Adamson A.W.* Physical Chemistry of Surfaces. N. Y.: Wiley, 1976.

5. *Рипатти П.О., Попова Р.А., Каган Т.Б., Бехтерева З.А.* // Вопросы мед. химии. 1969. Т. 15. № 5. С. 630.

6. *Тертых В.А., Белякова Л.А.* Химические реакции с участием поверхности кремнезема. Киев: Наукова думка, 1991.

7. *Киселев А.В., Лыгин В.И.* Инфракрасные спектры поверхностных соединений и адсорбированных веществ. М.: Наука, 1972.

8. Курс физической химии. Т.1 / Под ред. Я.И. Герасимова. М.: Химия, 1969.